AIX-MARSEILLE UNIVERSITÉ

ECOLE DOCTORALE 352 “PHYSIQUE ET SCIENCES DE LA MATIERE”

Thèse de Doctorat

Discipline : Physique et Sciences de la Matière
Spécialité : Astrophysique et Cosmologie

présentée pour obtenir le grade de docteur de l’Université d’Aix-Marseille par

Jesús Alberto GOMEZ LOPEZ

Titre de la thèse :

Les propriétés cinématiques de l’échantillon de galaxies *Herschel* Reference Survey (HRS)

The kinematical properties of the Herschel Reference Survey (HRS)

Soutenue le 20/09/2019 devant le jury composé de :

Philippe AMRAM	LAM	Directeur de thèse
Paola ANDREANI	ESO	Examinatrice
Médéric BOQUIEN	U. Antofagasta	Examinateur
Alessandro BOSELLI	LAM	Directeur de thèse
Laurent CHEMIN	U. Antofagasta	Rapporteur
Benoit EPINAT	LAM	invité
Giuseppe GAVAZZI	UNIMO	Rapporteur
Margarita ROSADO	IA-UNAM	Directrice de thèse
Annie ZAVAGNO	LAM	Présidente

Contents

Acknowledgements

One upon a time,
in a very small town in the middle of Mexico,
a five years old little boy had an enormous dream: to become an astronomer.
Twenty five years later, that small-town boy continues pursuing his dream...

First of all, I would like to thank my partner, my best friend, my support...

Alfonso, honey, my beloved husband, I do not have enough words to express my gratitude... When opportunities came to me and I was very frightened and doubtful, you always pulled me, telling: “My dear, you are able to achieve anything you want... Let’s do it!”.

Now I am here next to you, and I am who I am because of the man you are. Thank you so much, I love you much more than the concept “love” could cover... You and I are both oneself, and I beg you to continue sharing your life with me until my last day of life...

Mother, thank you for giving me the privilege of life, and thank you for being the best person over the world. You are the strongest and the noblest person I have ever known, always fighting against the hardest situations, hardly working everyday from sunrise to sunset in order to providing by everything to my brothers and me...

Thank you for always protecting us from the precarious situations, my brothers and me are who we are because of the woman you are...

Mom, thank you for being my mom, and for giving me the purest love that could exist... You are the most important person in my life.

Father, you are so strict, disciplined and have a very hard character. My childhood was not nice at all because of that reason...

Nevertheless, I have grown up and today, being 30 years old, I am aware that it is really difficult to fight against the hardest and most precarious situations while you are trying to raising three children and provide them by education, maintenance, and trying to become your dreams into reality at the same time. Father, I admire you, and I love you. Your tenacity brought me until here...

Iris, Isaac, my brothers, my friends, you are my treasure. You are my second parents, my role models, and I love you so much, I have the best family that I could have...

Alessandro, Philippe, Margarita: thank you for your patience, for your advices, for hours and hours of fruitful discussions, you have been more than my supervisors during these four years. Thank you for making my dreams come true.

Equally, I would like to say thank you to Benoit, Michel, Samuel, Denis, Veronique, Jean-Luc, Olivier, Médéric, Laurent, Paola, and many other GECO's at LAM that helped me to develop this PhD project.

Francoise, Laurene, Jean-Luc, Melody, when I was far from my family and close friends, you were here for making me feel like I was at home... Dear friends, thank you very much...

I thank also CONACYT for the scholarship provided for this PhD project, CNRS for the facilities during these four years, and the project DGAPA-UNAM PAPIIT IN 109919.

THANK YOU TO ALL OF YOU!

Résumé en français

Une galaxie est un ensemble d'étoiles, de gaz, de poussière et d'autres formes de matières liées gravitationnellement. Ces galaxies sont très diverses en taille, luminosité et masse. En effet, certaines galaxies naines sont composées d'environ 10^7 étoiles alors que des galaxies très massives peuvent contenir jusqu'à 10^{12} étoiles. Cependant, il est possible de les classer selon leur morphologie comme le fit Hubble (1936). Les galaxies sont regroupées en galaxies elliptiques, galaxies lenticulaires, galaxies spirales et galaxies irregulières (Fig. 1.1). Sur ce diagramme, le rapport de taille entre le bulbe et le disque augmente de droite à gauche, de meme pour la luminosité dans le visible. La quantité de gaz et de poussière ainsi que le nombre de bras spiraux diminuent de droite à gauche. Plutôt historiquement que physiquement, les galaxies elliptiques et lenticulaires sont dites de types précoces, alors que les galaxies spirales et irrégulières sont dites de types tardifs.

L'étude de l'Univers a pour but de comprendre comment celui-ci s'est formé, comment il a évolué pour arriver jusqu'à l'état dans lequel nous l'observons à notre époque. L'objectif d'un modèle cosmologique réaliste est donc de proposer un scénario qui permette de prédire le plus précisément possible l'ensemble des observations. Il doit pouvoir expliquer la cosmologie dite primordiale, notamment en montrant comment pendant le Big Bang l'Univers a pu se trouver dans l'état très homogène que l'on observe grace au fond diffus cosmologique (CMB, Fig. 1.6), pourquoi à cette époque des anisotropies sont apparues et enfin il doit pouvoir justifier la présence des différentes formes de matières (matière baryonique, matière noire, neutrinos, photons) issus du Big Bang. Cependant, un modèle complet doit pouvoir aussi expliquer les observations faites, et prendre en compte la répartition actuelle des galaxies, amas de galaxies et super amas révélée par les catalogues de galaxies, leurs propriétés physiques (taille, masse, température, etc), ainsi que l'évolution de leur répartition que l'on observe en comparant la répartition actuelle de ces objets à celle qu'ils avaient par le passé.

Aujourd'hui, le modèle standard de la cosmologie donnant une description de cette évolution est le modèle ΛCDM (Λ Cold Dark Matter, Riess et al., 1998; Perlmutter, 1999). Il s'appuie sur le principe cosmologique statuant que l'Univers est homogène et isotrope à grande échelle (>100 Mpc) et présente une courbure nulle, lorsque des grandes anisotropies et inhomogénéités sont trouvées à plus petites échelles (<100 Mpc, filaments des galaxies, galaxies isolées ou en groupes et super groupes). L'Univers contient de la matière noire et de l'énergie noire au meme titre que la matière baryonique (Fig. 1.5).

Dans ce contexte de modélisation de l'évolution de l'Univers, l'étude des propriétés physiques des galaxies locales, et donc de l'Univers actuel, permet d'obtenir des observations idéales et d'étudier leur dynamique et cinématique ansi que toutes leurs composantes : étoiles, gaz, poussière, métaux, etc. Enfin, la proximité d'amas tel que celui de la Vierge, allié aux avantages que présentent l'étude de l'Univers local, permet de comprendre l'impact de l'environnement sur les propriétés des galaxies. Ainsi, l'Univers local représente l'état "final" de l'évolution que les modèles cosmologiques doivent absolument prédire. C'est pourquoi les modèles d'évolution doivent etre fortement contraints à $z = 0$.

La connaissance détaillée de la phénoménologie des galaxies proches, qui représente l'état présent de l'évolution des galaxies, est de première importance pour contraindre les modèles d'évolution. Les observations des galaxies à grand redshift ont montré que leur masse est le paramètre principal qui déterminera leur évolution (Gavazzi et al., 1996; Cowie et al., 1996; Boselli et al., 2001). Afin d'étudier les différents scenari d'évolution des galaxies, il est nécessaire d'avoir un échantillon complet en masse et d'analyser les propriétés de chacune de ses galaxies en fonction de ce paramètre. Les observations en proche infrarouge sont dominées par l'émission des vieilles étoiles de la séquence principales ainsi que les géantes rouges (Bruzual & Charlot, 1993). Elle permet de tracer directement la masse dynamique de celles-ci (a l'intérieur du rayon optique, Gavazzi et al., 1996). En choisissant un ensemble de galaxies afin d'avoir une fonction de luminosité proche infrarouge complète, nous sommes donc assurés d'avoir un échantillon complet en masse. C'est l'approche qui a été choisie pour constituer le *Herschel* Reference Survey (Fig. 2.2), dont la description complète est présentée dans Boselli et al. (2010). Je reprends ici brièvement les caractéristiques principales de sélection de l'échantillon.

Les galaxies du survey HRS ont été sélectionnées afin de répondre à trois critères. Le premier est un critère sur la distance imposant une sélection limitée en volume. Les galaxies doivent se situer à distance telle que $15 \leq D \leq 25$ Mpc. Cette limitation permet de réduire les incertitudes sur les distances dues à des mouvements locaux particuliers, ainsi que d'assurer la présence de galaxies de faible luminosité telles que les galaxies naines, non visible à haut redshift. En appliquant une limite inférieure à la distance, les galaxies proches très étendues et donc très longues à observer sont éliminées.

Ensuite les galaxies ont été sectionnées selon leur luminosité en bande K afin d'obtenir un échantillon complet en masse stellaire. En effet, les magnitudes en bandes K permettent d'obtenir directement l'information sur la masse stellaire totale des galaxies (Gavazzi et al., 1996). Etant données les études optiques sur l'extinction ainsi que les observations en infrarouge lointain à des longueurs d'ondes ≤ 200 μm (Sauvage & Thuan, 1994), on s'attend à ce que les galaxies de types tardifs contiennent beaucoup plus de poussières que les galaxies de types précoces (Sauvage & Thuan, 1994). Deux magnitudes K limites (à partir des données 2MASS) ont donc été choisies pour sélectionner les galaxies : $K_{mag} \leq 12$ pour les galaxies spirales (Sa-Sd-Im-BCD)

et $K_{mag} \leq 8.7$ pour les galaxies elliptiques (E-S0-S0a), en magnitudes Vega (Fig. 2.4, Boselli et al., 2010).

Enfin, afin de limiter la contamination due aux nuages de la Voie Lactée émettant en infrarouge lointain, les galaxies ont été choisies à hautes latitudes galactiques (b > +55°) et dans des régions de faible extinction galactique ($A_B < 0.2$; Schlegel et al., 1998).

La Fig. 2.2 présente la répartition des galaxies du survey HRS dans le ciel. Certaines sont isolées et serviront de références pour l'étude des galaxies se trouvant dans des milieu très denses, comme celles de l'amas de la Vierge (croix rouges et vertes). Au final, le HRS comprend 323 galaxies, 62 galaxies de types précoces et 261 galaxies de types tardifs. L'échantillon couvre tous les types morphologiques (Fig. 2.4, Boselli et al., 2010), et contient des galaxies isolées de champs tout comme des galaxies d'amas (82).

Des observations résolues multi-fréquences des galaxies HRS ont été réalisées afin de fournir à la communauté le plus grand nombre possible de données à toutes les longueurs d'ondes et donc d'analyser aussi bien leurs propriétés de manière global. Pour bien arriver à la compréhension de la formation, de l'évolution et de la stabilité des galaxies, il faut avoir des données spectroscopiques à haute résolution spatial et spectral. Malheureusement, ces données manquent pour le HRS, afin de tracer la cinématique de manière précise d'estimer la masse dynamique des galaxies, incluant leur matière sombre et leur matière visible, en permetant également de qualifier le support dynamique et de quantifier le moment angulaire, ainsi que de suivre l'évolution dynamique des galaxies par rapport aux autres propriétés physiques.

Deux types de spectromètres basés sur le phénomène d'interférences optiques permettent naturellement de faire de la spectroscopie à champ intégral. Il s'agit du spectromètre à transformée de Fourier, dit IFTS, et de l'interféromètre de Fabry-Perot. Ces interféromètres ne font que moduler le flux et ne perturbent donc pas le caractère imageur des instruments dans lesquels ils sont placés.

Un spectromètre à transformée de Fourier est un interféromètre de Michelson: ce type d'instrument est composé d'une lame semi-réfléchissante et de deux miroirs, dont un mobile, formant deux voies. La lumière va être décomposée par la lame en deux faisceaux envoyés dans chacune des voies et recomposée après réflexion sur les miroirs, à leur retour sur la lame: les ondes en provenance des deux voies interfèrent. En faisant varier la différence de chemin optique grâce au miroir mobile, il est possible d'enregistrer une série d'interférogrammes. Celle-ci contient la transformée de Fourier du spectre de la lumière en chaque point du champ de vue : pour chaque exposition, l'information enregistrée concerne donc l'ensemble du spectre.

Un spectromètre de Fabry-Perot est un système dynamique composé d'une paire de lames semi-réfléchissantes parallèles (Fig. 3.5). La lumière traversant ce système subit des réflexions multiples entre les lames qui interfèrent à la sortie de l'interféromètre.

Pour chaque espacement des lames, seules certaines longueurs d'onde sont transmises par l'interféromètre. Le spectre sur l'ensemble du champ est donc obtenu en faisant varier séquentiellement l'espacement entre les lames. Ce type d'instrumentation est idéal pour étudier la cinématique d'objets étendus (aussi bien les nébuleuses que les galaxies) car le domaine de longueurs d'onde utile peut être ajusté à la dynamique en vitesse de l'objet observé et au bénéfice d'un champ de vue important.

L'interféromètre de Fabry-Perot a été inventé en 1896 par Charles Fabry (1867-1945) et Alfred Perot (1863-1925) dans le domaine de la métrologie, afin de mesurer très précisément des variations d'épaisseur. Ils pressentent alors déjà la possibilité de placer leur interféromètre au foyer d'un télescope. Les applications de cet interféromètre s'avèrent nombreuses. En 1909, les inventeurs de cet interféromètre l'utilisent dans le but de comparer une lumière monochromatique au mètre étalon, afin d'améliorer la précision des mesures réalisées par Michelson en 1893 (Amram & Georgelin, 2000).

La technique d'observation a été redécouverte par Courtès (1972) afin d'étudier les régions de gaz ionisé (régions HII) de notre Galaxie mais également dans d'autres galaxies. Jusqu'alors, ces observations utilisaient un interféromètre de Fabry-Perot dont l'espacement entre les lames est fixe également appelé étalon. Les premières utilisations d'un Fabry-Perot à balayage datent respectivement de 1980, avec le développement de l'instrument TAURUS initialement pour le foyer Cassegrain du télescope de 2.5m Isaac Newton (INT), et de 1982 avec le développement de l'instrumentation CIGALE par Boulesteix et al. (1984) et ses collaborateurs pour le foyer Cassegrain du télescope de 3.6 m du CFHT, prémices d'une longue pratique d'observations utilisant le Fabry-Perot à balayage au sein de l'équipe Interférométrie du LAM (Boulesteix et al., 1987;Laval et al., 1987; Georgelin et al., 1987; Marcelin et al., 1987; Amram, 1991; Le Coarer et al., 1992; Plana, 1996;Russeil, 1998; Garrido et al., 2003; Epinat et al., 2008b,a), ainsi que au sein de l'Observatorio Astronómico Nacional au Mexique en charge de l' instrument PUMA (Rosado et al., 1995; Fuentes-Carrera et al., 2001).

La raie Hα est le nom que les physiciens utilisent pour faire référence à la raie d'émission produite par les atomes d'hydrogène neutre correspondant à la transition de Balmer a observable dans le rouge (656.3 nm). Elle est générée par la désexcitation des électrons passant du niveau d'énergie n = 3 au niveau n=2. Le rayonnement ultra-violet d'énergie supérieure à 13.6 eV émis par les étoiles jeunes de type OB ionise le gaz d'hydrogène neutre à partir duquel elles ont été formées dans les régions HII.

La raie Hα, qui a une intensité élevée par rapport aux autres raies d'émission du domaine visible, est d'autant plus adaptée aux études cinématiques puisqu'une mesure précise des moments de raies nécessite un rapport signal sur bruit qui augmente avec l'ordre du moment. Toutefois, par rapport aux raies d'absorption stellaires, les raies d'émission présentent l'inconvénient de tracer principalement la cinématique du gaz, donc des structures telles que les spirales, dont les mouvements ne sont pas purement circulaires.

Par ailleurs, comme toutes les données spectroscopiques, les données Fabry-Perot nécessitent une réduction adaptée. Jacques Boulesteix développa ADHOC en 1993 puis l'adapta pour Windows (ADHOCw) en 1999. Ce logiciel très éprouvé et très didactique bénéficie de très bons outils de visualisation et de manipulation des données, ainsi que de programmes connexes extrêmement utiles lors des observations. Parallèlement, un autre outil de réduction a été développé sous UNIX en langage C à partir de 1988, puis C++ à partir de 2000 par Étienne Le Coarer pour le dépouillement des données CIGALE observées avec le télescope de 36 cm de la Silla (ESO) correspondant au sondage du plan Galactique et aux nuages de Magellan (Le Coarer et al., 1992). Ce programme dispose d'outils spécifiques pour la visualisation et la décomposition des profils. Il cherche a minimiser l'occupation de l'espace disque par les produits de réduction en utilisant un algorithme de compression et en n'enregistrant que le produit final.

Afin de pouvoir étudier l'échantillon complet de façon homogène, des procédures de réduction et d'analyse des données ont été développées récemment (Daigle et al., 2006b) sous IDL. Ces nouvelles procédures tendent à être le plus automatisé possible afin de rendre les résultats indépendants de la personne qui analyse les données

La réduction des données a pour objectif de créer un cube de données calibré à partir des interférogrammes d'observation et d'en extraire les cartes cinématiques.

Un cube de données possède deux dimensions spatiales et une dimension spectrale. Ainsi, un spectre est mesuré pour chaque élément de résolution spatiale ou pixel (Fig. 3.7). Pour chaque pixel, on va utiliser le spectre pour mesurer le flux émis par la raie, sa position en longueur d'onde et sa largeur, et ainsi obtenir des cartes pour chacune de ces grandeurs. La méthode utilisée sur l'échantillon HRS pour extraire ces grandeurs est la méthode des moments: le flux est l'ordre 0 du spectre, le barycentre est l'ordre 1 et la dispersion est l'ordre 2. On déduit la vitesse et la dispersion de vitesses à partir des mesures en longueur d'onde grâce à l'effet Doppler-Fizeau. La technique de lissage adaptatif est utilisée pour avoir un rapport signal sur bruit donné même dans les régions où le flux est faible, en particulier pour le gaz diffus ionisé qui n'est pas aisé à détecter. Il s'agit d'une accrétion de pixels : tant que le rapport signal sur bruit recherché dans le spectre n'est pas atteint, les pixels sont accrétés. Ainsi, le spectre des régions de faible flux n'est pas corrélé avec les régions à fort flux.

L'analyse dont il est question ici consiste à extraire les paramètres cinématiques déduits des champs de vitesses et leurs erreurs associées. Ces paramètres sont les paramètres de projection de la galaxie (inclinaison, angle de position du grand axe, vitesse globale de la galaxies dite vitesse systémique) ainsi que la courbe de rotation de la galaxie.

Un modèle de disque fin avec une courbe de rotation paramétrique est ajusté aux données par une méthode des moindres carrés afin de déterminer ses paramètres. L'algorithme utilisé est l'algorithme de Levenberg-Marquardt (Vetterling et al., 1989; Press et al., 1992), qui permet d'effectuer l'ajustement de modèles non linéaires aux

données. La librairie IDL de Markwardt MPFIT a été utilisée. Cet algorithme utilise les dérivées partielles par rapport aux variables pour converger vers une vallée de moindres carrés.

Cette méthode a été développée pour deux raisons (Epinat et al., 2008a,b). Jusqu'à présent, deux méthodes étaient couramment utilisées. La première est une détermination manuelle des paramètres afin de symétriser au mieux la courbe de rotation. Un premier inconvénient de cette méthode est que la détermination des paramètres est dépendante de l'utilisateur, mais le principal problème est que les erreurs ne peuvent pas vraiment être mesurées. Une solution serait la détermination des paramètres indépendamment par plusieurs utilisateurs, ce qui, en pratique, demande beaucoup de temps et de ressources humaines.

La seconde méthode, utilisée par le logiciel GIPSY, est une méthode dite de "tilted ring model". La galaxie est découpée en anneaux. Pour chaque anneau, un jeu de paramètres est alors ajusté par une méthode de moindres carrés, avec une erreur statistique pour chaque paramètre et pour chaque couronne. Cette méthode est particulièrement adaptée aux données possédant beaucoup de points afin d'avoir une statistique suffisante pour chaque anneau, ce qui est le cas des données HI pour lesquelles un gauchissement des disques est potentiellement observable. De tels gauchissements sont bien plus rares dans le disque optique et donc en Hα. La décomposition en anneaux engendre donc une difficulté quant à une définition unique des paramètres de projection pour chaque galaxie. Il était donc nécessaire de faire l'ajustement d'un modèle possédant une seule inclinaison, un seul grand axe, une seule vitesse systémique et un seul et unique centre pour chaque galaxie. Par ailleurs, une détermination robuste et réaliste des erreurs a été mise au point en utilisant la carte des résidus du modèle.

Grâce à ces méthodes, j'ai pu réduire et analyser l'ensemble de l'échantillon. Un article publié dans un journal avec comité de lecture (Section 4.1.3) et un autre en preparation (Section 4.2.1) ont résulté de ces travaux. Ces articles présentent:

a) Les cartes déduites de la réduction des données ainsi que la comparaison des paramètres de projection déduits de la cinématique et de la morphologie. Des commentaires galaxie par galaxie sont présentés.

b) La relation Tully-Fisher (TF, Tully & Fisher, 1977), souvent utilisé pour contraindre les modèles et les simulations de l'évolution des galaxies, est une relation étroite entre la masse baryonique et la masse dynamique des systèmes de type tardif. Cette relation d'échelle a été dérivée dans différentes bandes photométriques (optique, infrarrouge proche, masse stellaire et masee baryonique). Nous avons vérifié d'abord la comparaison entre les limites statistiques du survey HRS et ceux des échantillons utilisés dans la littérature qui reposent généralement sur plusieurs centaines/milliers de galaxies. Le HRS est bien représentatif de ces échantillons, et le seul pour lequel chaque composant baryonique peut être mesuré avec telle précision. Compte tenu de la nature

complète du survey HRS, nos relation Tully-Fisher sont d'accord avec les prédictions des simulations hydrodynamiques cosmologiques EAGLE (Schaye et al., 2015). Nous avons comparé la masse baryonique par rapport à la masse dynamique de l'échantillon, en constatant que la fraction de baryons est inférieure dans les galaxies de faible masse et riches en gaz ($\sim$ 20-25 % de la masse dynamique totale) que dans les galaxies de grande masse avec un faible SFR ($\sim$ 35-45 % de la masse dynamique totale).

c) La masse est l'un des principaux moteurs de l'évolution des galaxies (e.g. Cowie et al., 1996; Gavazzi et al., 1996; Boselli et al., 2001). Conformément à ces résultats d'observation, les simulations cosmologiques hydrodynamiques suggèrent que l'évolution des galaxies est principalement gouvernée par le halo de matière noire dans lequel elles résident (Governato et al., 2012; Brooks & Zolotov, 2014; Christensen et al., 2014). Il est donc intéressant de dériver la relation "main-sequence", qui relie la masse des galaxies et son taux de formation d'étoiles, en utilisant des masses dynamiques et baryoniques plutôt que des masses stellaires. La pente de cette relation d'échelle évidente (les galaxies plus grandes ont plus de tout), sa flexion à hautes luminosités, sa dispersion et sa variation en fonction du redshift et de l'environnement sont souvent utilisées pour suivre l'évolution des galaxies avec le temps cosmique.

Ce travail est en cours. J'ai initié des études cinématiques à partir de l'échantillon HRS durant ma thèse (Section 4.1.3, Section 4.2.1). On présentera plusieurs études pendant 2020 dont la forme finale sera probablement très différente de la forme actuelle puisque chaque domaine d'investigation sera développé pour donner éventuellement lieu, au final, à plusieurs articles disjoints (par exemple, dériver une "Universal Rotation Curve" pour le HRS, étudier son moment angulaire, mouvements non circulaires des galaxies situées dans environnements différents, etc).

L'un des principaux processus régulant l'évolution des galaxies et le cycle de la matière dans les galaxies est la formation d'étoiles. La loi de Kennicutt-Schmidt (Schmidt, 1959; Kennicutt, 1989, 1998b; Fig 5.1) associe le taux de formation d'étoiles (SFR) à la densité du gaz dans les galaxies de type tardif. En dépit des efforts considérables déployés par notre communauté pour améliorer nos connaissances, tant du point de vue théorique qu'observationnel, il reste encore plusieurs questions en suspens à résoudre, telles que: quel est le mécanisme déclencheur de l'effondrement de nuages moléculaires géants (GMC) ? Quel est le processus de formation des étoiles dans les systèmes de type tardif?

Plusieurs mécanismes physiques ont été proposés pour répondre à ces questions. Parmi eux, il y a des indications théoriques selon lesquelles la relation entre la formation d'étoiles et la quantité de gaz est modulée à grande échelle par la rotation différentielle du disque et la compression du gaz dans les ondes de densité associées aux bras spiraux, tandis qu'à des échelles plus petites, cette relation est contrôlée par des mouvements non circulaires dus à l'instabilité du gaz dans les GMC (Wyse, 1986; Larson, 1992; Kennicutt, 1998b; Boissier & Prantzos, 1999; Tan, 2000; Kennicutt & Evans, 2012).

Nous allons nous concentrer sur ces mécanismes.

Bien que la vitesse de rotation soit facile à mesurer, la turbulence (dispersion de vitesse) nécessite une résolution angulaire et spectrale suffisamment élevée. L'échelle typique d'un GMC est de 80 pc et peut aller jusqu'à 200 pc, ce qui correspond à 0.8" et 2" à une distance de 20 Mpc, la distance moyenne du survey HRS. Pour effectuer une étude précise du rôle de la cinématique sur la loi Kennicutt-Schmidt en galaxies proches, il est impératif de le faire à des échelles de GMC et une résolution spectrale de quelques km s^{-1}, autrement dit pixel par pixel.

Il y a donc quatre paramètres à déterminer pour étudier le rôle de la cinématique sur le processus de formation d'étoiles et du gaz à l'échelle des GMCs, pour un échantillon bien représentatif des galaxies de type tardif situées dans des environnements différents dans l'univers local, à savoir, le HRS:
1) La densité de SFR Σ_{SFR}.
2) La densité de colonne du gaz Σ_{CO}.
3) La vitesse de rotation V_r et la dispersion de vitesse σ.

Nous allons utiliser deux méthodes pour obtenir le Σ_{SFR} et comparer les résultats de chaque technique:

a) Utilisation des images Hα. Les luminosités Hα peuvent être transformées en SFR en utilisant un facteur qui dépend de la fonction de masse initiale (IMF), fonction qui décrit la distribution initiale des masses pour une population d'étoiles, et du modèle stellaire. Cette technique a l'avantage de nous permettre de calculer le SFR à des échelles de $\sim$ 80pc. Désavantage: il n'y a pas de données disponibles à résolution spatiale élevée pour corriger l'atténuation de [NII] et la poussière aux échelles $\sim$ 80pc. Pour ce dernier point, nous proposons une solution utilisant une combinaison des corrections de atténuation basées sur le Décrément de Balmer et la luminosité de 24 μm, ainsi que la contribution [NII], de manière radiale pour traiter ces corrections.

b) CIGALE SED-fitting code (Noll et al., 2009). Ceci est la méthode la plus cohérente et la plus précise pour calculer le SFR, en modelant la Distribution Spectrale d'Énergie (SED) de l'UV au FIR en combinant plusieurs populations stellaires anciennes et jeunes et en tenant compte d'un équilibre énergétique entre l'énergie émise par les jeunes populations stellaires et celle absorbée par la poussière cosmique puis réémise dans le FIR (Fig. 1.10); ce code permet d'estimer avec précision et de manière cohérente le SFR et le M_{star} des galaxies, deux paramètres clés dans l'étude de la relation entre Σ_{SFR} et Σ_{gas} (R, V_{rot}, σ, M_{star}) aux échelles GMC. Malheureusement, pour une analyse si précise, le fit de la SED doit avoir toutes les images multifréquences de l'UV au FIR à la même résolution angulaire qui correspond au FIR (dans notre cas, le PACS-100 qui a une résolution angulaire de $\sim$ 9" correspondant à l'échelle d'un kpc (Fig. 1.11).

La Σ_{gas} peut être calculée à partir du gaz moléculaire, qui est tracé par les données de CO. Notre analyse est actuellement limitée par les données résolues CO (1-0) et CO(2-1), qui ne sont disponibles que pour un sous-échantillon de 26 galaxies HRS, à

savoir: HERACLES (Leroy et al., 2009), BIMA-SONG (Helfer et al., 2003), Nobeyama CO Atlas (Kuno et al., 2007) et sur les bases de données ALMA. Toutes ces échantillons fournissent une résolution spatiale différente qui va de ∼ 1 ” (100 pc, permettant de résoudre les GMC) à ∼ 15 ” (échelles kpc, voir Fig. 1.13). Heureusement, la collaboration PHANGS-ALMA (Leroy et al. 2018) recueille des données de CO(2-1) haute résolution pour des dizaines d'objets situés dans l'amas de la Vierge.

Enfin, nous avons completé l'échantillon cinématique Hα Fabry-Perot de l'HRS, à partir duquel nous déduisons la vitesse de rotation et la dispersion de vitesse des galaxies, avec une résolution angulaire de ∼ 1-3 ” et une résolution spectrale de ∼ 5-10 km s^{-1}.

Vu qu'il y a plusieurs facteurs à considérer de caractère technique et physique qui pourraient biaiser notre étude (résolution angulaire et facteurs de conversion, par exemple), nous avons besoin de bien definir la méthodologie à suivre et quantifier ces facteurs et minimiser leur impact, avant de faire un étude detaillé sur la Loi Kennicutt-Schmidt. Pour cela, il faut choisir une galaxie de type tardif avec un taux élevé de formation stellaire, sans être fortement perturbée ou en cours d'interaction, avec une grande couverture spatiale sur le ciel pour pouvoir quantifier les effets de résolution angulaire, et à inclination moyenne (c'est à dire, afin d'éviter des exemplaires face-on ou edge-on) pour pouvoir bien tracer la cinématique.

Nous avons fait un étude préliminaire du rôle de la cinématique sur le processus de formation d'étoiles et du gaz à l'échelle des GMCs:

1) Nous avons d'abord étudié si la résolution joue un rôle important pour la loi de Kennicutt-Schmidt originale. La galaxie NGC4254 a une grande couverture spatiale (diamètre ∼ 6') et elle possède un vaste ensemble de données résolues spatialement, du FUV à FIR, donc le cible idéal pour étudier le rôle de la résolution angulaire sur la loi de Kennicutt-Schmidt.

2) Les lignes d'émission de CO peuvent également être utilisées pour tracer la cinématique avec précision. L'inconvénient est que nous avons besoin d'instruments très grands et très demandés, tels que l'interféromètre ALMA, afin d'obtenir des cubes de données CO avec une résolution angulaire suffisante (et donc la raison pour laquelle les données ALMA ne sont disponibles que pour quelques galaxies HRS uniquement); de plus, ALMA ne couvre qu'une couverture spatiale souvent plus petite que le diamètre des objets proches. Nous avons vérifié si la cinématique du gaz froid (CO, traceur de la composante moléculaire) est comparable à la cinématique du gaz chaud (Hα, traceur des régions HII) calculé à partir des techniques de Fabry-Pérot.

3) Nous avons quantifié l'influence de la cinématique sur la loi de Kennicutt-Schmidt, en testant différentes relations théoriques existant dans la littérature.

Dans cette première tentative:

a) Nous avons essayé de traiter des facteurs à caractère technique et physique qui pourraient biaiser notre étude (résolution angulaire, facteurs de conversion et correction, etc) pour bien calculer et comparer la Σ_{SFR} et Σ_{H_2} aux résolutions de 1 kpc et GMCs. Nous avons trouvé que ces facteurs à caractère technique et physique ne jouent pas un rôle important concernant la loi de Kennicutt-Schmidt originale. À partir d'ici, Nous continuons l'étude aux échelles de GMCs.

b) La cinématique du gaz chaud et celle du gaz froid est similaire. Le gaz chaud (Hα) est lié directement aux régions HII lesquelles sont des traceurs de la formation stellaire récente. Donc notre étude continue en utilisant la cinématique du gaz chaud.

c) Nous avons quantifié l'influence de la cinématique sur la loi de Kennicutt-Schmidt en testant deux relations théoriques différentes qui prennent en compte la time scale d'effondrement τ sous la forme $\Sigma_{SFR} \propto \Sigma_{gas}\,\tau^{-1}$: formation d'étoiles auto-régulée (via V_{rot} sous la forme $\tau \propto \kappa^{-1}$) et gravitation versus dispersion (via σ sous la forme $\tau \propto \sigma^{-0.5}$). Nous avons trouvé que la cinématique a bien un impact direct sur l'effondrement des nuages de gaz et puis le processus de formation d'étoiles en galaxies de type tardif.

Ce travail est en cours. Une fois que la méthodologie à suivre soit bien définie, nous procéderons à effectuer une étude plus étendue à un échantillon plus grand de galaxies HRS situées dans environnements différents (prenant en compte que la galaxie NGC 4254 est une galaxie d'amas qui est perturbée) pour étudier le rôle de l'environnement sur la Loi Kennicutt-Schmidt. En plus des données résolues CO(2-1) à libérer par la collaboration PHANGS, nous allons appliquer pour temps d'observation aux intruments ALMA, NOEMA et APEX pendant 2020, pour bien plus étendre l'échantillon CO à haute résolution pour le HRS.

Abstract

The study of the universe is important to understand how it was formed and evolved until the current scenario of matter distribution that is observed at our epoch. Nearby galaxies represent the last scenario of the galaxy evolution that the cosmological and semi-analytical models must predict, and current observing facilities give us the opportunity to study and robustly constrain the statistical properties of galaxies in an extremely accurate and detailed way.

The Herschel Reference Survey (HRS) is a complete K-band-selected, volume-limited ($15 < D < 25$ Mpc) sample of 323 nearby galaxies spanning a wide range in morphological type (from E to Sd-Im-BC) and stellar mass ($10^8 < M_{star} < 10^{11}$ $M_\odot$). It has been selected to be observed as part of the guaranteed time Herschel/SPIRE program in several far-infrared bands (100-500 microns), and has been the target of pointed imaging and spectroscopic observations at several other wavelengths, from the UV to the radio centimetric. Thanks to its complete nature, the HRS is now becoming the reference for several nearby and high redshift studies of galaxies.

We have gathered and analysed high-resolution 2D Perot-Fabry spectroscopic H-alpha data for the star forming objects (261 galaxies) of the HRS providing a complementary kinematical information to the sample (since December 2015, at the OHP 1.93m telescope, and with coordinated observations at the SPM 2.1m telescope in Mexico). We checked the consistency of the rotation curves by comparing our maximum rotational velocities to those derived from HI data, and computing the i-band, NIR, stellar and baryonic Tully-Fisher relations. We use this set of kinematical data combined to those available at other frequencies to study for the first time the relation between the dynamical and the total baryonic mass (stars, atomic and molecular gas, metals and dust), and derive the baryonic and dynamical main sequence on a representative sample of the local universe.

These kinematica data, combined with the available multifrequency data spanning the whole electromagnetic spectrum (from UV GALEX to far-IR Herschel, including HI and CO), and multizone chemo-spectrophotometric models of galaxy evolution as well as with the CIGALE SED fitting code, are allowing us to study the role played by velocity rotation and turbulence at GCM scales in the process of star formation occurring in normal late-type galaxies, since star formation is tightly correlated to the gas column density according to the Kennicutt-Schmidt law, and probably modulated by the kinematics. For this purpose, we are studying first the case of the late-type

galaxy HRS 102 (NGC 4254). We explored the influence of kinematics on the star formation process and the gas content at low resolution (down to kpc scales using the CIGALE SED-fitting code) and at high resolution (GMC scales using the VESTIGE Ha image). Since the gas emits through the CO and HI emission, we calculate the gas column density using the available high resolution ALMA CO data. The results are be presented in the present work and the study will be extended to a larger sample of HRS galaxies situated in different environments.

1 Introduction

1.1 Classification of galaxies

A galaxy is a system composed by millions of stars, gas, dust and other kind of matter, linked by gravity. Galaxies are distributed in groups or isolated, and they cover a wide range in size, morphology, luminosity and mass, containing from 10^7 to 10^{12} stars. Nowadays, it is well possible to classify galaxies according to their morphology just as done by Hubble (1936): ellipticals (or early-types), lenticulars, spirals (or late-types) and irregulars. In the Hubble diagram (Fig. 1.1), the bulge/disc ratio, defined as the contribution of the bulge and disc components to the total luminosity of a galaxy (Boselli, 2011), increases from the right to the left, as well as the luminosity in the optical band. On the other hand, the gas and dust content (Fig 1.2, Boselli et al., 2014c, Ciesla et al., 2012), and the spiral arms number, decrease from the right to the left. We are going to do a brief description of each galaxy type.

Elliptical galaxies (E, Fig 1.3, bottom-left panel) are classified according to the index $n = 10(1 - b/a)$, where b/a is the axial ratio, $n = [0, 7]$ (Liller, 1966) going for the spherical to the flattest galaxies. They represent the ∼10% of systems in the universe and are mainly composed by evolved stellar populations (Boselli, 2011; Young et al., 2011). The luminosity profile of these systems follows a de Vacouleurs's $r^{1/4}$, or the Sersic profile $r^{1/n}$ where the n manages the profile curvature: at bigger n values, the luminosity of galaxies is more concentrated in the core.

Lenticular galaxies (S0, Fig 1.3, bottom-left panel) are characterised by a prominent bulge and a flat diffuse region similar to a disc but without any spiral structure, dominated by old stellar populations, generally devoid of gas and dust; some of them present even a bar. Lenticulars can also be classified according to the dust attenuation of their disc (Ciesla et al., 2012) and represent the ∼20% of galaxies in the universe (Boselli, 2011).

Spiral galaxies (S, Fig 1.3, top right panel) are divided in normal spirals and barred spirals (SB). The sequence from Sa to Sm is a sequence in the bulge/disc ratio, the strength and resolution of spiral arms, gas and dust content, as well as the presence of star forming regions. Indeed the total luminosity of a galaxy decreases from Sa to Sm (this classification includes Sd and Sm, which are rich in gas and dust, and have starburst episodes, containing mainly young stellar populations). The morphology and luminosity profile of a bulge are reminiscent to elliptical galaxies, although at a smaller scale, and this picture does not apply to pseudo-bulges. On the other hand, the luminosity profile

of the disc follows the relation $I = I_0 e^{-r/r_0}$ with r_0 as the scale length (Freeman, 1970). Spiral galaxies represent $\sim$ 70% of the total systems (Boselli, 2011).

Irregular galaxies (Irr, Fig 1.3, bottom-right panel) do not have a distinct regular shape, unlike a spiral or an elliptical galaxy. Irregular galaxies do not fall into any of the regular classes of the Hubble sequence, and they are often chaotic in appearance. Irregular galaxies contain abundant amounts of gas and dust (Hunter, 1997).

Galaxies can also be considered as active when they host an active nucleus (AGN): an accretion mass disc onto the central supermassive black hole.

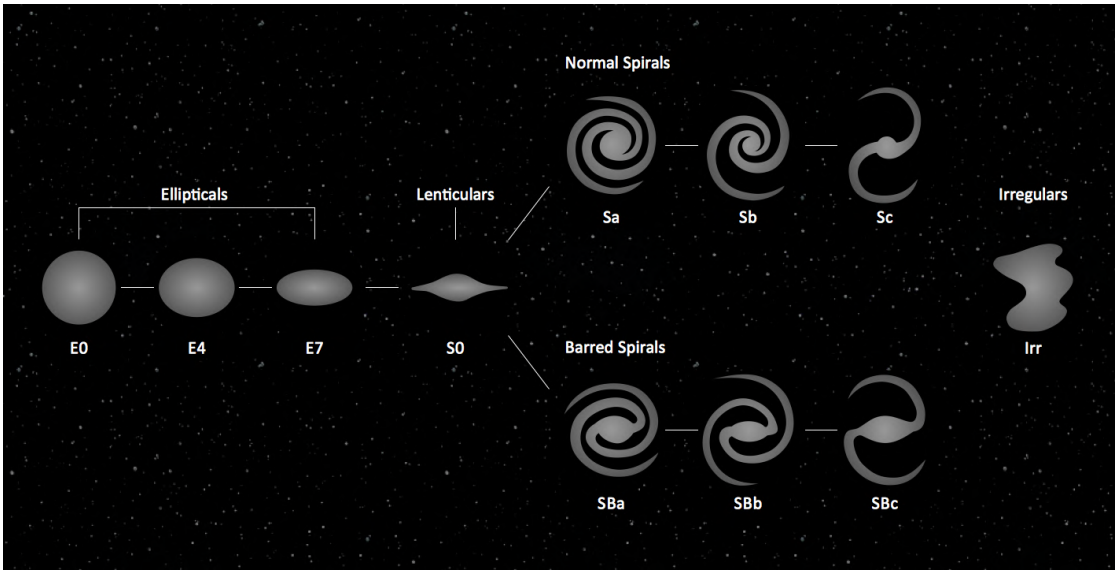

Figure 1.1 – Morphological classification of galaxies as done by Hubble (1936).

1.2 Why studying nearby galaxies is important?

Nowadays, the standard model of cosmology giving the best description of the evolution of the universe is the Λ Cold Dark Matter (ΛCDM): the universe started 13.8 billion years ago (Jarosik et al., 2011; Planck Collaboration et al., 2016) with a Big Bang and is expanding since then, it is homogeneous and isotropic at large scales ($>$ 100 Mpc) with no curvature, containing baryonic (stars, gas, metals, dust), dark matter, as well as dark energy which is causing the acceleration of the expansion of the universe (Riess et al., 1998; Perlmutter, 1999). According to the observations, at present, the proportions of each component of the universe is as illustrated in Fig. 1.5. On the other hand, the universe is highly unhomogeneous at scales $<$ 100 Mpc, where we observe clear anisotropies and large scale structures across the cosmic web (Fig 1.4)

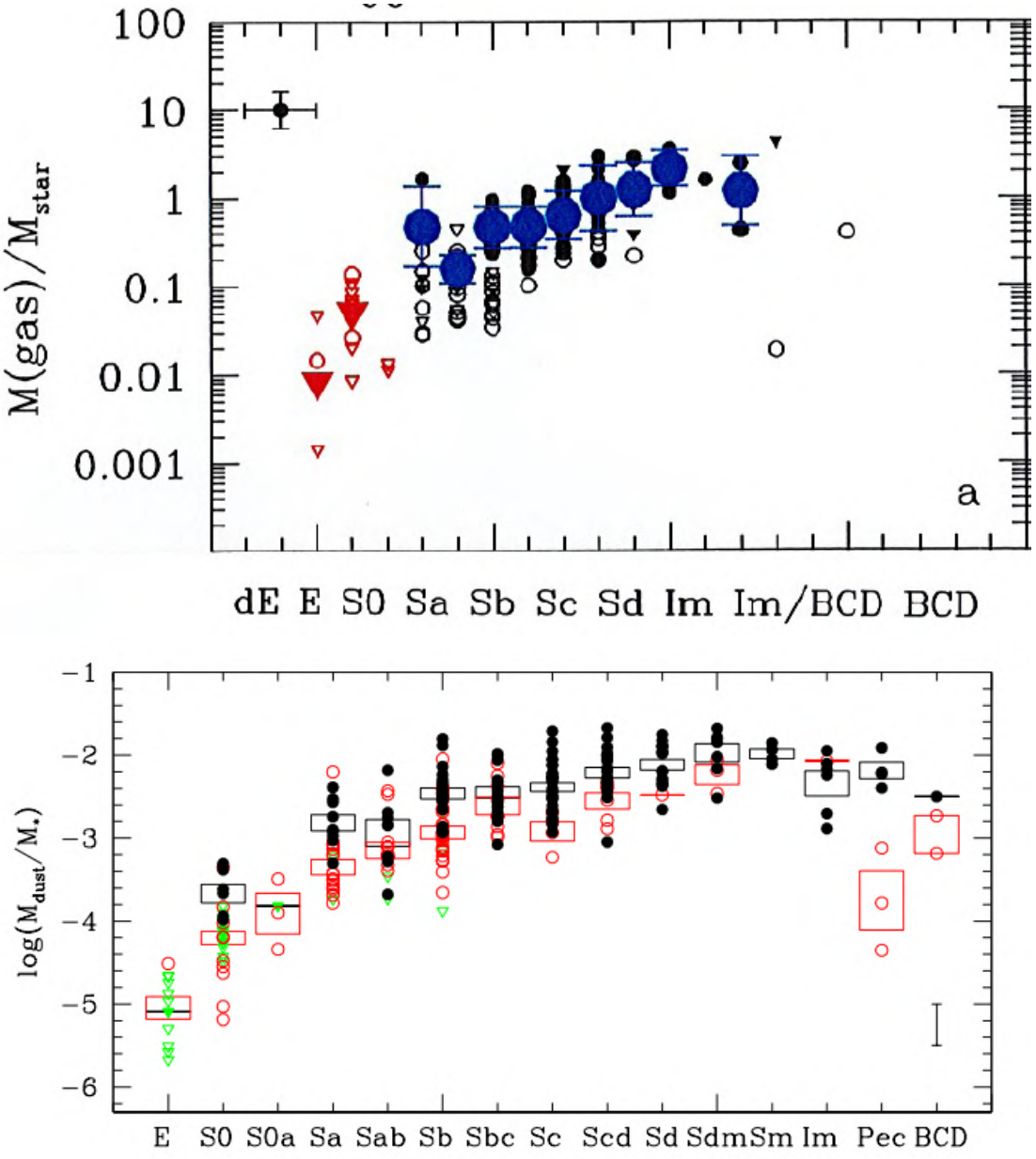

Figure 1.2 – The gas (top panel) and dust (bottom panel) content decrease as a function of galaxy type, from the left to the right, just as in the Hubble diagram. Figures taken from Boselli et al. (2014c) and Ciesla et al. (2012).

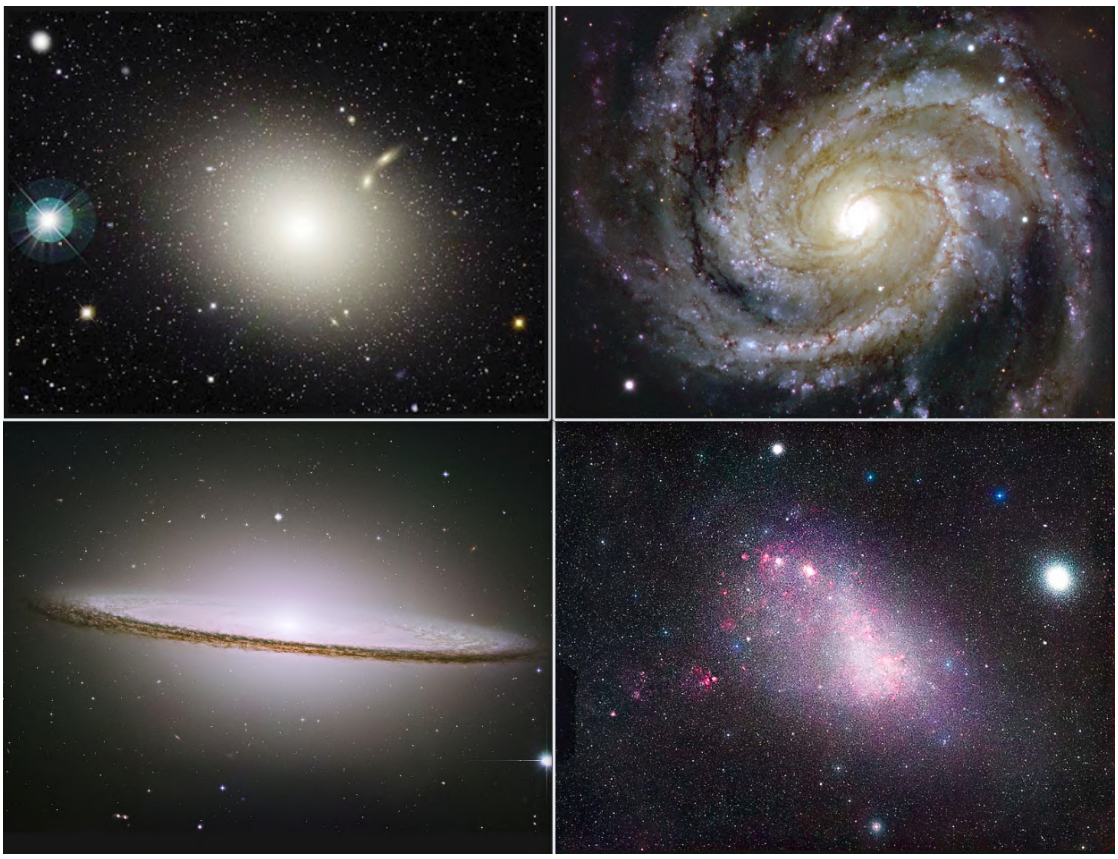

Figure 1.3 – Example of an elliptical (top-left panel, M 87), spiral (top-right panel, M 104), lenticular (bottom-left panel, M 83) and irregular galaxy (bottom-right panel, Small Magellanic Cloud). Images taken by the Hubble Space Telescope ACS in the optical BVR bands; credits by NASA/ESA and The Hubble Heritage Team (STScI/AURA).

such as big empty regions surrounded by filaments populated by isolated galaxies or systems situated into voids, groups, clusters and superclusters.

So far, new generation of ground-based and space facilities allow to observe galaxies at redshifts >5 in an accurate way (Giavalisco et al., 2004; Scoville et al., 2007), meaning that we are able to observe how the universe looked when it was ∼1 Gyr old. The observations of galaxies at high redshift have shown that mass and environment are the main drivers of galaxy evolution (Cowie et al., 1996).Now we can link the distribution of the matter from the local universe at $z = 0$ (Gavazzi et al., 1996; Boselli et al., 2001) to epochs far away than $z > 5$ and even until the recombination epoch captured in the Cosmic Microwave Background (CMB at z∼1100, Fig. 1.6, Planck Collaboration et al., 2016).

The study of the universe is important to understand how it was formed and evolved until the current scenario of matter distribution that is observed at our epoch. The objective of a realistic cosmological model is to propose a scenario which allows the prediction of the observations from CMB (z∼1100) to z∼0, reproducing the primordial cosmology and the observed evolution of the universe at different redshifts, from the homogeneous structure observed in the CMB to the current observed anisotropies in the local cosmic web.

Nearby galaxies represent the last stage of the galaxy evolution that the cosmological and semi-analytical models must predict, and current observing facilities give us the opportunity to study and robustly constrain the statistical properties of galaxies in an extremely accurate and detailed way (i.e. their kinematics and dynamics, as well as their components: stars, gas, dust, metals), properties that such models must reproduce. In addition, low surface brightness galaxies, which are very gas-rich systems and the most numerous galaxies in the universe, are only detectable in the local universe and must be taken into account in order to constrain properly the galaxy evolution. On the other hand, nearby objects are spatially resolved enough to accurately study and understand the impact of the environment on the galaxy properties. Because of these reasons, it is crucial to study nearby galaxies.

Studying the properties of nearby galaxies and its evolution requires an accurate analysis of the different processes involved in galaxy evolution (not only for nearby galaxies, but also for systems at any redshift). Thus, the key process of galaxy evolution across the time is the matter cycle: Giant Molecular Clouds in galaxies (GMC) collapse to form stars of different sizes, temperature and luminosities. Then, these stars enrich the InterStellar Medium (ISM) by new elements, latter aggregated to form dust. Dust also absorbs the interstellar radiation, being an important parameter in the cooling process of the gas (Boselli, 2011). Massive stars inject a large amount of kinetic energy into the interstellar medium, favouring the ionisation of the surrounding gas and the dissociation of the molecular component. On the other hand, the matter cycle is modulated by the environment; In high density environments both gravitational interactions and interactions with the intergalactic medium of clusters can heavily affect

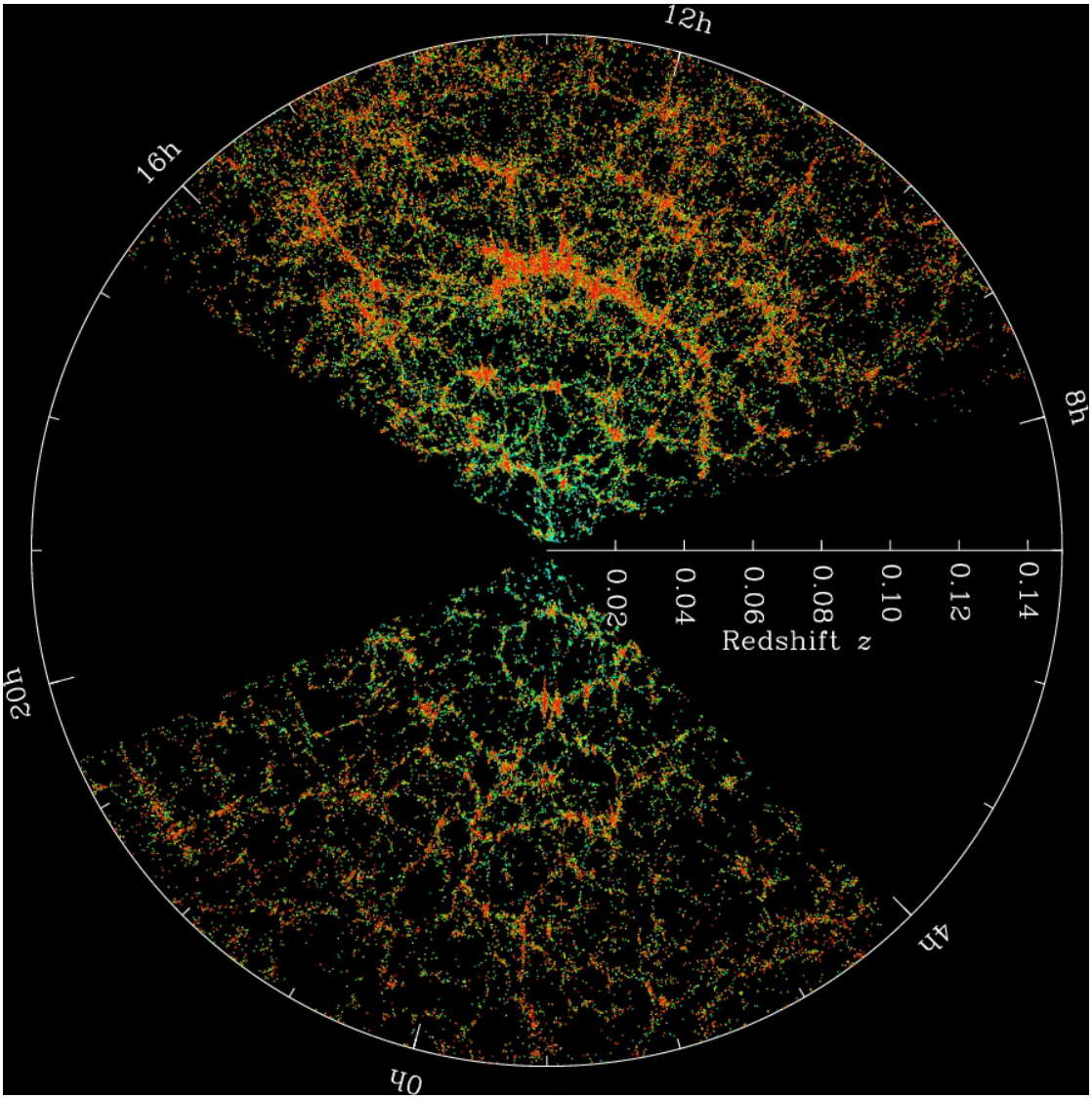

Figure 1.4 – Cosmic web across the local universe, containing filaments populated by isolated galaxies or systems situated into voids, groups and clusters, pictured by SDSS.

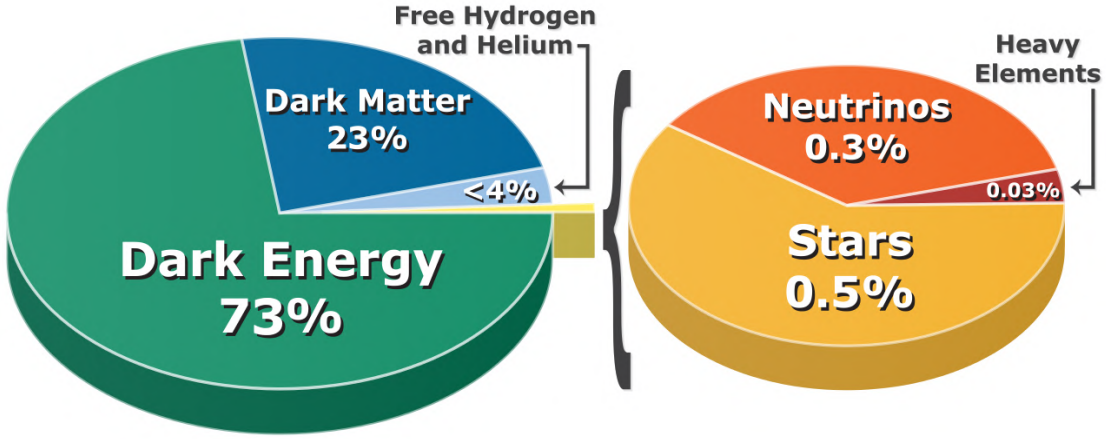

Figure 1.5 – Composition of the universe following the ΛCDM cosmological model, according to Planck Collaboration et al., 2016. Picture by ESA/PLANCK COLLABORATION.

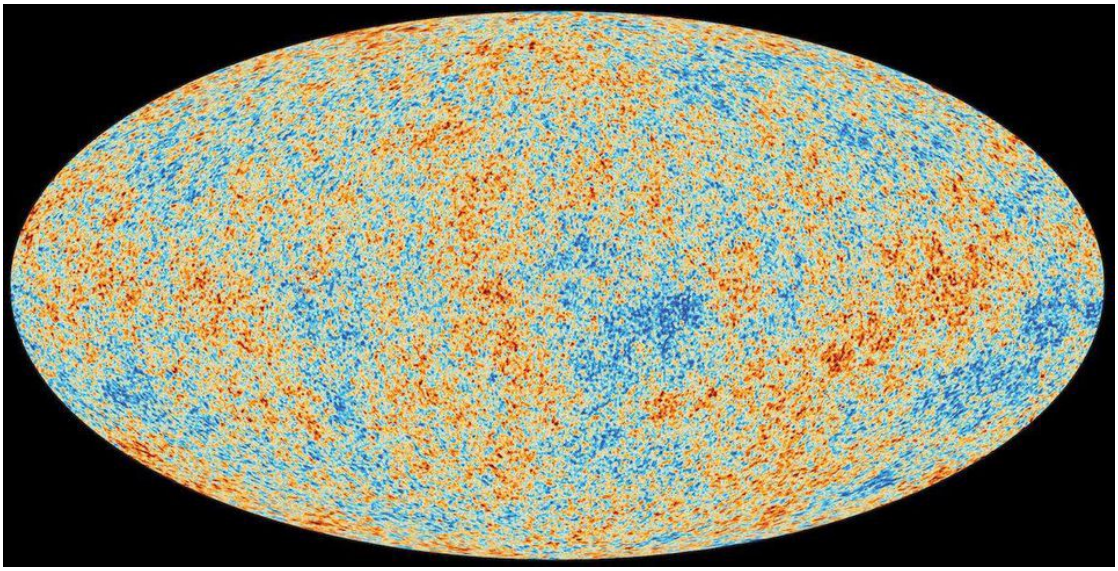

Figure 1.6 – The leftover glow from the Big Bang, the CMB, is uniform, but has tiny imperfections and temperature fluctuations on the scale of a few hundred microkelvin. Planck detected and measured these fluctuations to better precision than ever before. (ESA/PLANCK COLLABORATION).

the physical properties of galaxies:

a) Ram pressure stripping and starvation (the cluster acts on large scales by removing any extended gaseous halo surrounding a galaxy) quenches the star formation process and truncates gaseous galaxy discs. This causes that cluster galaxies migrate from the blue cloud (high star formation) to the green valley (medium star formation) and, eventually, to the red sequence (passive galaxies). Molecular gas is removed less efficiently than neutral gas. Ram pressure, rather than starvation, is the dominant process driving the evolution of cluster galaxies (Boselli et al., 2009, 2014b; Fumagalli et al., 2014).

b) The dynamical interactions between close companions plays a fundamental role in the star formation process and the gas content. The gas is ripped and the star formation process is triggered at the tails of stripped gas, where the gas embedded in the hot intracluster medium is compressed and transformed into stars (Boselli et al., 2018b,a).

c) Since the work of Dressler (1980), it is clear that clusters of galaxies are dominated by early-type systems (ellipticals and lenticulars) which are relatively rare in the field (Whitmore et al., 1993).

All the physical processes regulating the matter cycle, including the perturbations induced by the environment, must be considered and studied at the same time. Fortunately and wonderfully, all the information necessary in order to study all these phenomena can be quantified along the spectrum; from X-rays to Radio-centimetric, it contains information about each element, component, etc. The Spectral Energy Distribution (SED) of a system is plenty of information (Fig. 1.7): the continuum from UV to FIR provide information about stellar populations, while the emission and absorption lines allow to study chemical abundances and their ratios, as well as the kinematics, allowing us to constrain different parameters such as stellar mass, star formation activity, dust attenuation and mass, among many others. With this information, we can quantify different properties and scaling relation (structural, chemical, kinematical and spectrophotometrical properties combined and analysed) of galaxies, as we will see carefully in Chapter 1.

1.3 The ideal survey to study the properties of nearby galaxies

In order to study the properties of nearby galaxies in a robust statistical way (priority to well constraint the models of evolution), one needs a well representative sample of systems spanning a wide range of morphology and mass, containing isolated and cluster objects, and for which a spatially resolved imaging and spectroscopic dataset is available at different wavelengths.

The Virgo cluster and the surrounding clouds are the ideal laboratory to study the

Domain λ	X-ray 0.1–10 keV (1–100 Å)	UV 912–3500 Å	Visible 3500–7500 Å	NIR 0.75–5 μm	MIR 5-20 μm	FIR-submm 20 μm–1 mm	Radio 1 mm–1 m
			Continuum				
Process	Black body	Black body	Black body	Black body	Thermal emission	Modified black body	Synchrotron
	Thermal bremsstrahlung						Free–free
Emitting source	Accretion disk in binary systems	Young stars	Intermediate age stars	Old stars	PAH, hot dust grains	Cold dust grains	Relativistic electrons in weak magnetic fields
	Hot gas						HII regions
			Main emission lines				
Emission lines		Atomic hydrogen, metals	Atomic hydrogen, metals	Atomic and molecular hydrogen, molecules	PAH	[CII], CO, molecules	HI(21 cm)
Origin		HII regions	HII regions	HII regions	PDR	Giant molecular clouds	Diffuse ISM
Absorption lines		Hydrogen, metals	Hydrogen, metals	Hydrogen			HI(21 cm)
Origin		Stellar atmosphere, ISM, IGM	Stellar atmosphere	Stellar atmosphere			Diffuse ISM

Notes: PAH: Polycyclic Aromatic Hydrocarbons; PDR: photodissociation region; ISM: interstellar medium; IGM: intergalactic medium.

Figure 1.7 – Emitting sources and emission processes related to different wavelengths through a SED. Table taken from Boselli (2011).

nature of the different kind of perturbations acting on galaxies in different environments. Located at a distance of 16.5 Mpc (Gavazzi et al., 1999; Mei et al., 2007), Virgo is the closest concentration of galaxies to the Milky Way. Thanks to its proximity, all galaxies in Virgo and surrounding clouds, including those objects down to the dwarf population, can be easily resolved at different frequencies.

In this context, the *Herschel* Reference Survey (HRS, Boselli et al., 2010, Fig. 2.2), a *Herschel* Guaranteed Time Key Project, is a complete sample defined with the purpose of studying the relationship between the star formation process and the different components of the interstellar medium (ISM), as well as the main drivers of galaxy formation and evolution. The HRS has been observed in the IR with PACS and SPIRE instruments by *Herschel* (Ciesla et al., 2012; Cortese et al., 2014), as well as IRAC and MIPS by *Spitzer* (Bendo et al., 2012; Ciesla et al., 2014). To provide the community with the largest possible set of homogeneous data, multifrequency observations of the whole HRS have been carried out in the UV with GALEX (Cortese et al., 2012; Boselli et al., 2011), HI and CO single-dish data have been gathered (Boselli et al., 2014a), medium resolution integrated spectroscopy (Boselli et al., 2013) and Hα imaging data (Boselli et al., 2015), while optical, near and mid-IR, and radio centimetric data are available from the SDSS (Abazajian et al., 2009), NGVS (Ferrarese et al., 2012), 2MASS (Skrutskie et al., 2006), WISE (Ciesla et al., 2014) and NVSS all-sky surveys (Condon et al., 1998). VESTIGE (Boselli et al., 2018c) will provide high resolution deep Hα imaging for the Virgo Cluster objects, while PHANGS-ALMA will provide CO(2-1) datacubes for dozens of galaxies situated in the Virgo clouds.

Thanks to its statistical completeness, the HRS is becoming the ideal reference for local and high-redshift studies as well as for models and simulations.

1.4 Kennicutt-Schmidt Law and kinematics of nearby galaxies

One of the main processes regulating galaxy evolution and the matter cycle in galaxies is the star formation. The Kennicutt-Schmidt Law (Schmidt, 1959; Kennicutt, 1989, 1998b; Fig 5.1) relates the Star Formation Rate (SFR) with the gas column density in late-type galaxies: $\Sigma_{SFR} \propto \Sigma_{gas}$. Despite the huge effort that our community has done in order to improve our knowledge, from the theoretical and observational point of view, still remain several open questions that need to be addressed concerning: what is the mechanism that triggers the GMC collapse and then the star formation processes in late-type systems?

Several physical mechanisms have been proposed to answer those questions. Among them, there are theoretical indications that the Kennicutt-Schmidt Law is modulated at large scales by the differential rotation of the disc and the compression of the gas in the density waves associated to spiral arms, while at smaller scales such relation is driven by

non-circular motions through the instability of the gas in GMCs (Wyse, 1986; Larson, 1992; Kennicutt, 1998b; Boissier & Prantzos, 1999; Tan, 2000; Kennicutt & Evans, 2012).

While the rotation is easy to measure, turbulence (velocity dispersion) requires a sufficiently high angular and spectral resolution (R∼10000). The typical scale of a GMC is ∼ 80 pc and could reach up to ∼ 200pc, equivalent to ∼ 0.8" and ∼ 2" at a standard distance of 20 Mpc, the average distance of the HRS. Because of the latter, in order to perform an accurate statistical study of the role of kinematics on the star formation process and gas content in nearby galaxies, it is imperative to constrain the analysis at GMCs scales down to a couple of km s^{-1}.

1.5 The two aims of the PhD project

As previously said, out of the 323 galaxies composing the HRS sample, 261 objects are late-type systems with an ongoing star formation activity, as indicated by their strong Balmer line emission (Boselli et al., 2015). This PhD project is devoted to these 261 star-forming objects in order to study, in an accurate and statistical way, the role of kinematics on the star formation process and gas content in late-type galaxies.

1.5.1 An Hα kinematic survey of the HRS

Despite a panchromatic dataset for the whole HRS sample is already available (Sec. 1.3), spatially resolved 2D spectroscopic observations lack in order to trace the kinematics. Constructing an Hα kinematic survey for the HRS star-forming sample is the first aim of my PhD project.

For this purpose, we use Fabry-Perot interferometry (extensively described in Chapter 2), which have a fundamental advantage over other Integral Field Spectroscopy (IFS) techniques: gathering not only high spatial but also high spectral resolution datacubes using relatively small telescopes (diameter of ∼2m) with a typical exposure per extended source of ∼ 2 hours and at a high spatial coverage. Despite the spectral range is much narrower in Fabry-Perot interferometry, high spectral resolution is crucial to trace accurately the kinematical properties of galaxies at GMCs scales, thus the Fabry-Perot technique is ideal to construct a resolved kinematical dataset for the HRS.

During my PhD we have been gathering and analysing Hα Fabry-Perot spectroscopic observations for the star-forming sample in order to trace the kinematics of such galaxies: we have derived Hα data cubes from which are computed Hα maps, radial velocity fields (Fig, 1.8), rotation curves and kinematical parameters for the sample. The Fabry-Perot dataset for the HRS is presented in Chapter 3, which in combination with the multifrequency data of the HRS, will allow to accurately:

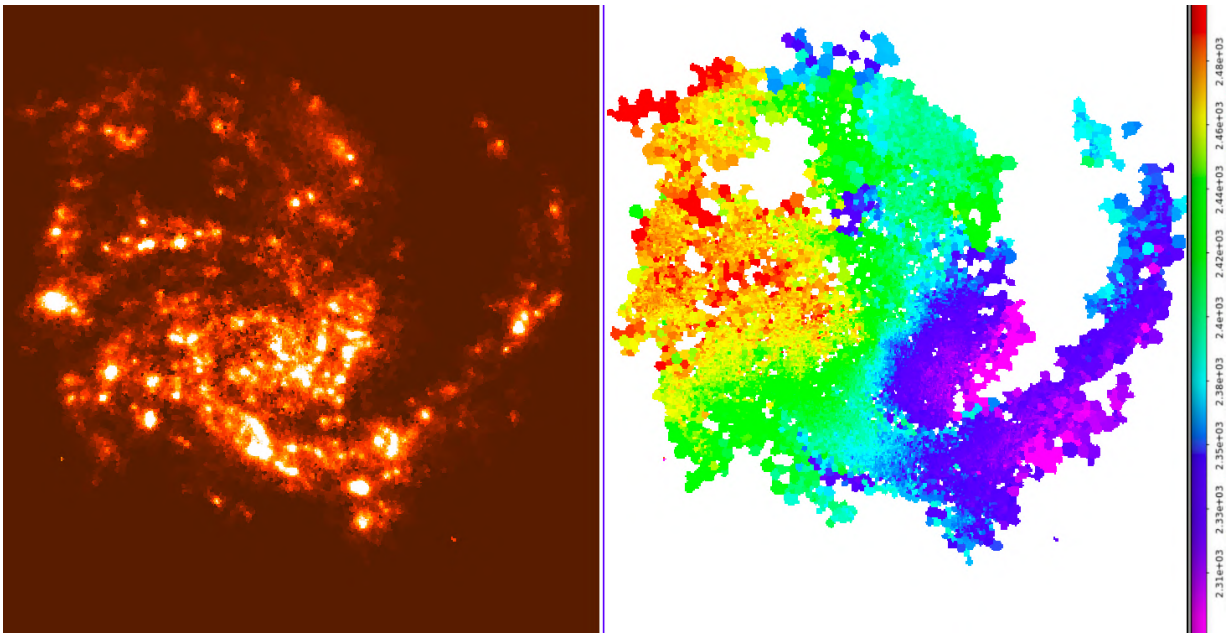

Figure 1.8 – The Hα line (6563Å) is the most prominent of the Balmer lines in star-forming galaxies (like NGC 4254), therefore perfect to be scanned with Fabry Perot techniques in order to trace the kinematics at a spatial resolution of ∼1-3" and at a spectral resolution of ∼5-10 km s^{-1}. Left panel: monochromatic image. Right pannel: velocity map of the galaxy; the colorbar indicates km s^{-1}.

a) Determine the dynamical mass distribution of our sample of star-forming objects and compare it to those of the other components (stellar, atomic and molecular gas, dust masses, star formation rate, metallicity, etc.) to characterise the statistical properties of our sample. The dynamical masses could be then used to quantify the dark-to-baryonic mass content. These statistical properties could be then compared to the predictions of cosmological and semi-analytical models of galaxy evolution.

b) Study the effects of the environment on the dark matter content of galaxies by comparing cluster and isolated galaxies selected according to similar criteria. This comparison can be done either through the analysis of global quantities (total baryonic and dark matter content for instance), or by comparing the radial variation of their dark and baryonic mass profiles.

c) Quantify the role of rotation velocity and velocity dispersion (turbulence) in the process of star formation and the gas surface density of the galaxies. Observations then could be compared to the predictions of 2D chemo-spectrophotometric models of galaxy evolution (Boissier et al., 2003). The multifrequency HRS dataset can allow us to determine in a self consistent way, and with unprecedented precision, the 2D-distribution of the different galaxy components (stellar, atomic, molecular, dust masses), the dust attenuation, and several other properties critical for the study of the radial variation of the star formation history of these galaxies.

d) For the largest objects, where the angular resolution of *Herschel/PACS* data allows the pixelisation of the images down to ~1 kpc, and for which high resolution CO and HI imaging data are available, the relation between gas column density, star formation and rotation could be analysed in 2D using the CIGALE SED fitting code (Noll et al., 2009).

1.5.2 Study of the role of kinematics on the Kennicutt-Schmidt Law in nearby galaxies at GMC scales.

A detailed study of the relation between star formation, gas column density and kinematics of nearby galaxies requires to derive four properties of each galaxy of the sample at GMCs scales:

a) The SFR density Σ_{SFR}, computed from Hα luminosities and by SED-fitting.
b) The gas column density Σ_{CO} computed from CO data in our case (further details below).
c) rotation velocity V_{rot} and velocity dispersion σ from Fabry-Perot data.

1.5.2.1 The SFR density

We will derive the Σ_{SFR} in two ways and compare the results of each technique, since both of them have advantages and disadvantages:

a) Using Hα imaging. Hα luminosities can be transformed into Σ_{SFR} using a factor which depends on the assumed Initial Mass Function (IMF, function that describes the initial distribution of masses for a population of stars) and the stellar model. This technique has the advantage of allowing us to compute the Σ_{SFR} at scales of $\sim$ 80 pc. Such Σ_{SFR} is valid only under the assumption that the mean star formation activity of the emitting galaxies is constant over a timescale of a few Myr (Boselli et al., 2009; Boissier, 2013; Boquien et al., 2014), the typical age of O-B stars. On the other hand, and unfortunately, since the UV radiation that ionises the HII regions influences an area much bigger than 80 pc, if we could compute the Σ_{SFR} from UV or radio-continuum maps at 80 pc – they are other SFR tracers for which there is no resolved data at such high resolution– the calculated Σ_{SFR} for each pixel may differ a lot from that computed using Hα; we assume that this factor is not very relevant according to Boselli et al. (2015), since the integrated $SFR_{H\alpha} \simeq 1.1 \times SFR_{FUV,radio}$ for the HRS sample (Fig. 1.9). In addition, we do not count with resolved data to correct by [NII] and dust attenuation at ~80pc scales. For the latter, in Chapter 4 we propose a solution using a combination of both the Balmer decrement and 24μm corrections, as well as [NII] contamination, in a radially way $A_{BD+24\mu m}(r)$ and $\frac{[NII]}{H\alpha}(r)$ to deal with these disadvantages.

b) CIGALE SED-fitting code. This is the most self-consistent and more accurate way to compute the Σ_{SFR}. CIGALE fits the SED from the UV to the FIR by combining several old and young stellar populations, and considering an energetic balance between the energy emitted by the young stellar populations which is absorbed and re-emitted in the FIR by dust; this code allows to accurately estimate in a consistent way the SFR and the $M_\star$ of galaxies, two key parameters in the study of the relation between Σ_{SFR} and $\Sigma_{gas}(r, V_{rot}, \sigma, M_\star)$ at GMC scales per galaxy (Fig. 1.10). Unfortunately, this method suffers from energy transfer problems, and in addition, SED-fitting needs to have all the multifrequency imaging from UV to FIR at the same coarsest angular resolution (kpc scales, Fig. 1.11), not allowing to resolve GMCs and HII regions.

It is important to mention that we do not expect to have a remarkable difference between the Σ_{SFR} computed from Hα at high resolution and the Σ_{SFR} computed from SED-fitting at low resolution, according to Boselli et al. (2015), since the integrated $SFR_{SED} \simeq 0.96 \times SFR_{H\alpha}$ for the HRS sample (Fig. 1.12).

1.5.2.2 The gas column density

The gas column density can be computed from the molecular gas, which is traced by the CO data, through a conversion factor X_{CO}. Since such factor depends on the metallicity (Boselli et al., 2002b), we must apply a radially conversion factor based on measurements of $Z(r)$. In addition, our analysis is limited by the CO data only available for a subsample of 26 HRS late-type galaxies on HERACLES (Leroy et al., 2009), BIMA-SONG (Helfer et al., 2003), Nobeyama CO Atlas (Kuno et al., 2007) and ALMA databases. All these CO surveys provide different spatial resolution going from ~1" (100 pc or GMCs/HII regions scales) to ~15" (kpc scales) so there is no CO

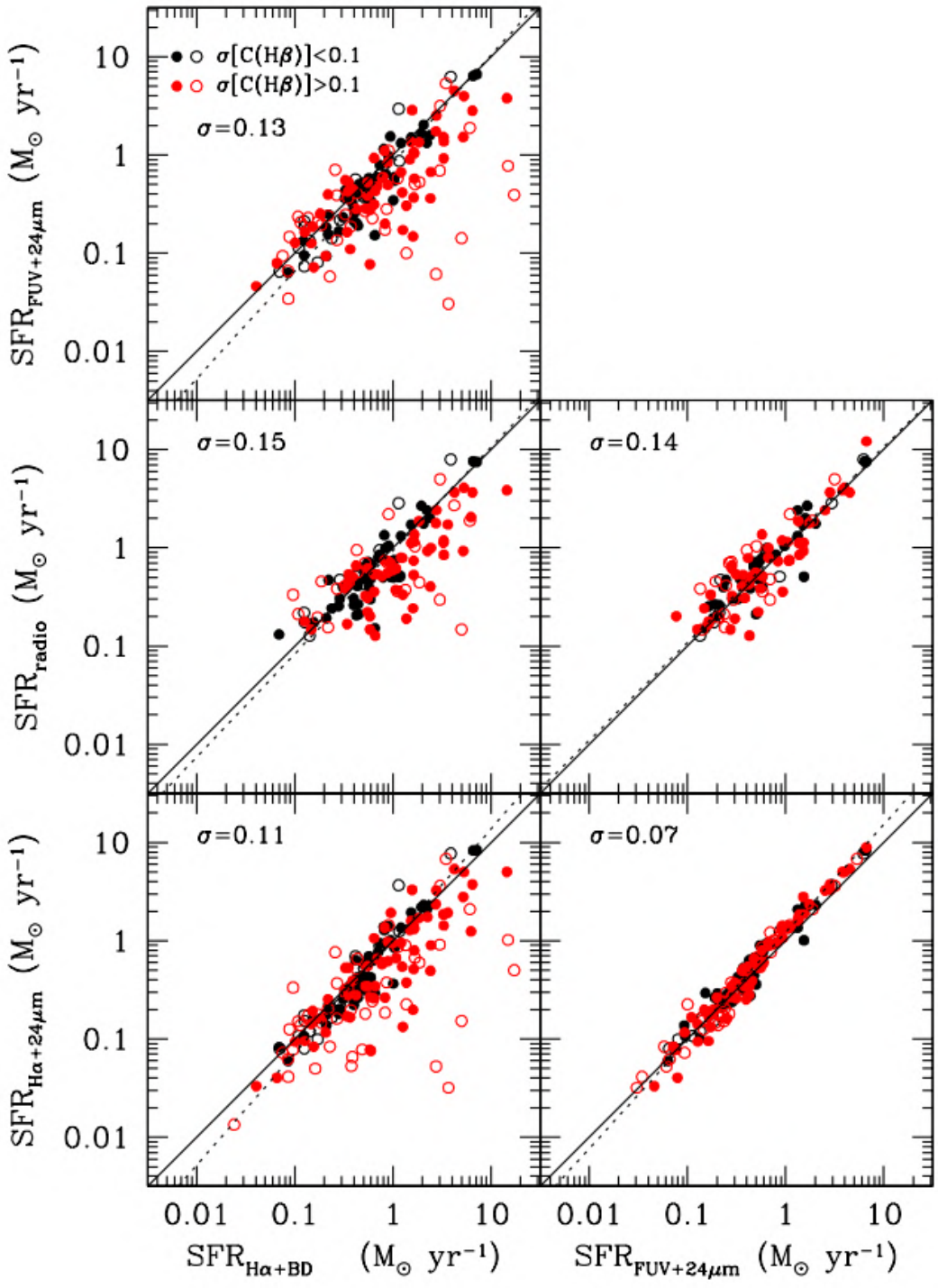

Figure 1.9 – Comparison between integrated SFR of the HRS galaxies using different tracers. For each case, the solid line is the 1-1 relation, and the dashed line is the bisector fit. Taken from (Boselli et al., 2015).

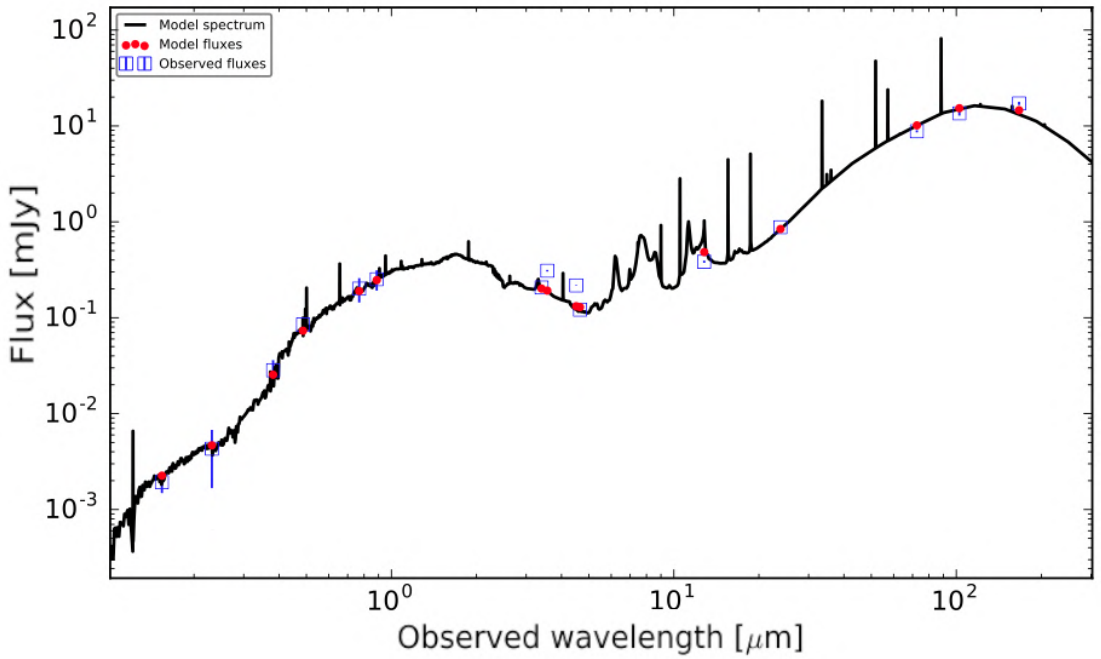

Figure 1.10 – The SED-fitting of a single pixel at GMC scales of the galaxy NGC 4254, from FUV to FIR, using CIGALE (Gómez-López et al., in prep.).

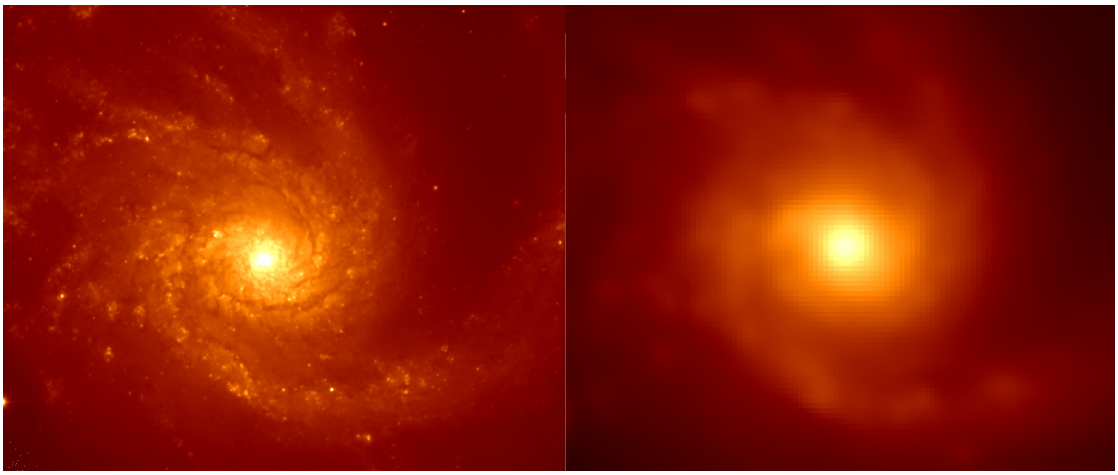

Figure 1.11 – Galaxy NGC 4254 in the NGVS I-band at the original angular resolution (~0.6”, left panel) and degraded to PACS-100 resolution (right panel).

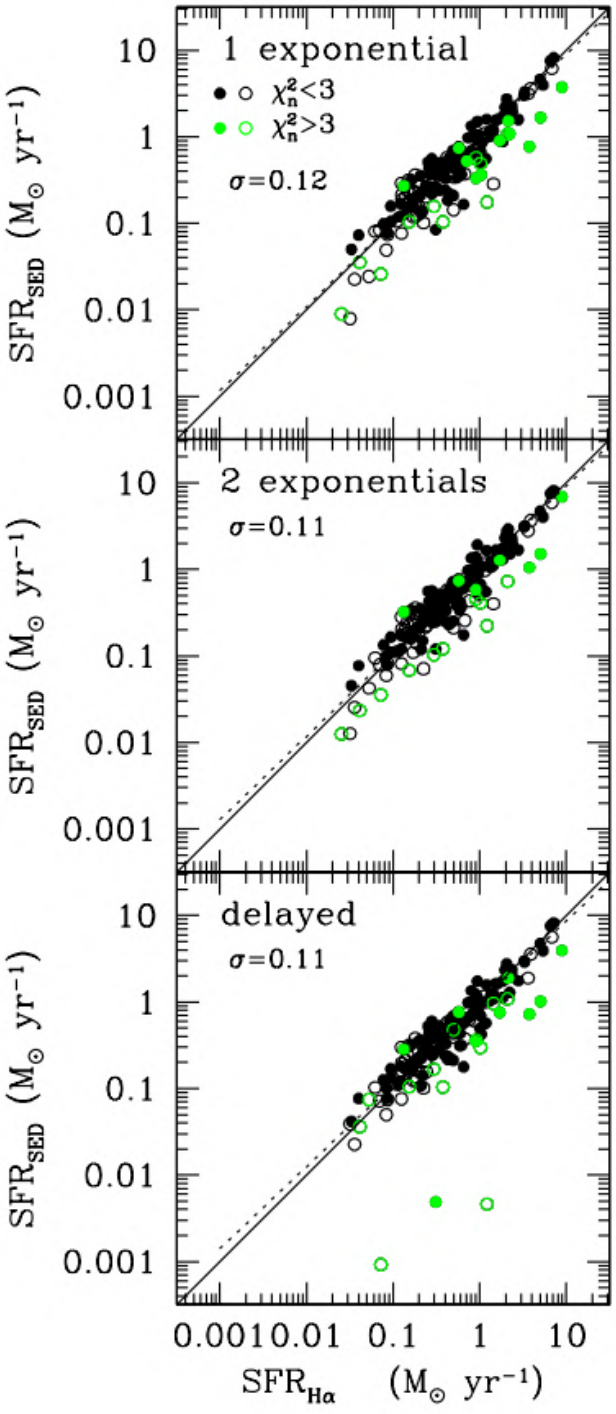

Figure 1.12 – Comparison between integrated SFR of the HRS galaxies computed from Hα luminosities and from SED-fitting. For each case, the solid line is the 1-1 relation, and the dashed line is the bisector fit. Taken from Boselli et al. (2015).

database with a homogeneous spatial resolution for a significant subsample of HRS galaxies and the loss of resolution power is brutal from 1" to 15" as we can see in Fig. 1.13. Fortunately, the PHANGS-ALMA survey (Leroy et al. 2018) is gathering high spatial resolution CO(2-1) data for dozens of HRS objects.

1.5.2.3 V_{rot} and σ

Finally, we have completed the Hα Fabry-Perot kinematic survey of the HRS, from which we derive the rotation velocity and velocity dispersion of the ionised gas in galaxies, with an angular resolution of ~1-3" (enough to resolve GMCs and HII regions) and a spectral resolution of ~5-10 km s^{-1} (in order to well constrain the velocity dispersion).

1.5.2.4 Methodology

Since the role of technical (spatial and spectral resolution) and physical problems (conversion factors, energy transfer, dust attenuation, etc.) must be analysed and traited/corrected carefully in order to perform a correct study of the role of kinematics on the Kennicutt-Schmidt Law, it is worth to study such technical and physical effects on one representative galaxy: NGC 4254 (HRS 102). We make a preliminary study proceeding as follows:

1) We must see first if the spatial resolution (GMC scales versus kpc scales) plays an important role for the original Kennicutt-Schmidt Law.

2) The CO emission lines can also be used to accurately trace the kinematics. We will see if the kinematics of cold gas (CO, tracer of the molecular component) is comparable to the kinematics of warm gas (Hα, tracer of HII regions) computed with Fabry-Perot techniques.

3) We will quantify the influence of kinematics on the Kennicutt-Schmidt Law, testing different theoretical relations existing in the literature.

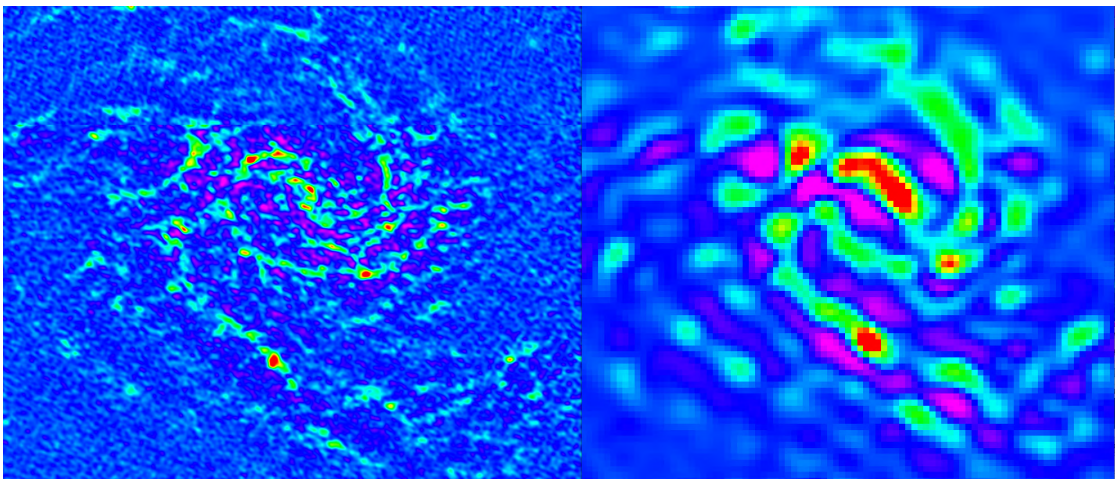

Figure 1.13 – Galaxy NGC 4254 observed with ALMA at the original angular resolution (∼1”, left panel) and degraded to NOBEYAMA resolution (∼15”, right panel).

2 The Herschel Reference Survey (HRS)

Nearby galaxies represent the last stage of galaxy evolution that the cosmological and semi-analytical models must predict. In addition, low surface brightness galaxies, which are very gas-rich systems and the most numerous galaxies in the universe, are only detectable in the local universe. On the other hand, nearby objects are spatially resolved enough to accurately study and understand the impact of the environment on galaxies.

In order to study the properties of nearby galaxies in a robust and statistical way –a priority to well constrain the models of evolution– one needs a well representative sample of systems spanning a wide range in morphology and mass, containing isolated and cluster objects, and for which a spatially resolved imaging and spectroscopic dataset is available at different wavelengths. In this context is defined the HRS, containing galaxies situated into the Virgo cluster and the surrounding clouds, which together are the ideal laboratory to study the nature of the different kind of perturbations acting on galaxies in different environments. Located at a distance of 16.5 Mpc (Gavazzi et al., 1999; Mei et al., 2007), Virgo is the closest concentration of galaxies to the Milky Way. Thanks to its proximity, all galaxies in Virgo and surrounding clouds, including those objects down to the dwarf population, can be easily resolved at different frequencies.

Thanks to its statistical completeness and to the multifrequency data already available, the HRS is becoming the ideal reference for local and high-redshift studies as well as for models and simulations.

2.1 The Survey

The HRS, a *Herschel* Guaranteed Time Key Project [1], extensively described in Boselli et al. (2010), was selected according to the following criteria:

1. The HRS is complementary to other two *Herschel* Key Projects: the KINGFISH (imaging/spectroscopic survey of 61 nearby galaxies at D < 30 Mpc, chosen to cover a wide range of galaxy properties and local ISM environments found in the nearby universe, is the *Herschel* extension of SINGS, Kennicutt et al., 2011) and the VNGS (twelve galaxies within 25 Mpc and the archetypal starburst galaxy Arp 220) samples, optimized for the study of the different phases of the ISM in individual galaxies. These three key projects were thought to provide the community with a unique dataset for studying the ISM properties of galaxies in the local universe.

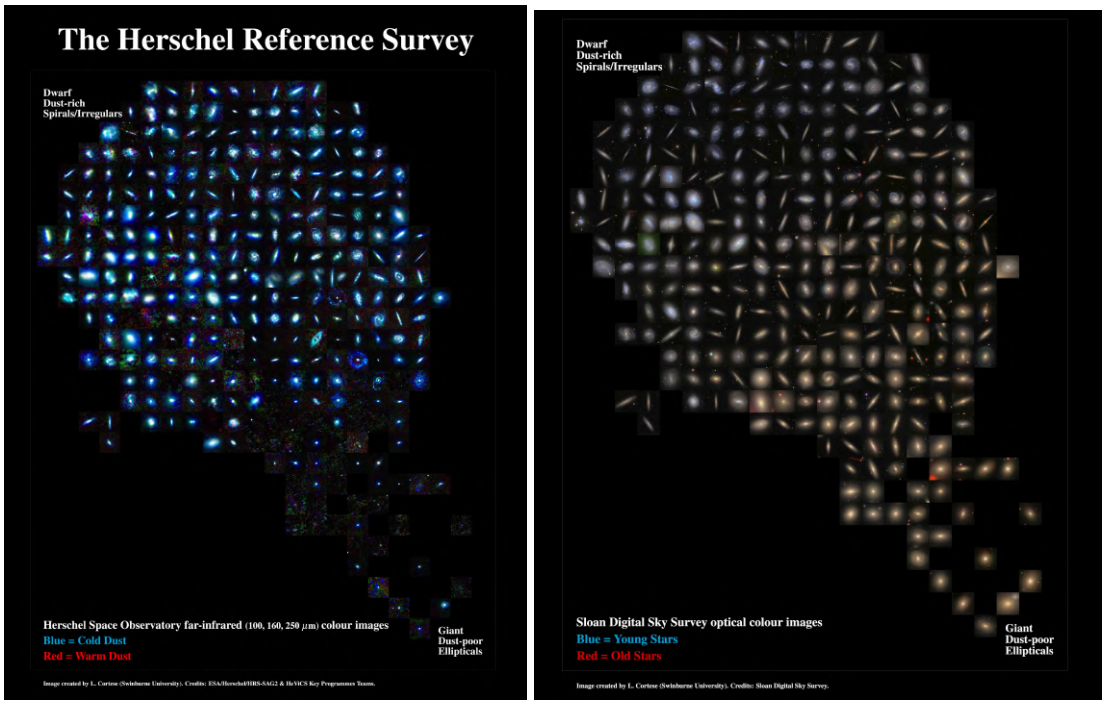

Figure 2.1 – Collage of HRS galaxies at infrared/submillimetre wavelengths by Herschel (top panel) and at visible wavelengths from the SDSS (bottom panel). The Herschel image is coloured with blue representing cold dust and red representing warm dust; the SDSS image shows young stars in blue and old stars in red. Together, the observations plot young, dust-rich spiral/irregular galaxies in the top left, with giant dust-poor elliptical galaxies in the bottom right. Images created by L. Cortese in collaboration with ESA/Herschel/HRS-SAG2 & HeVICS Key Programmes Teams and SDSS.

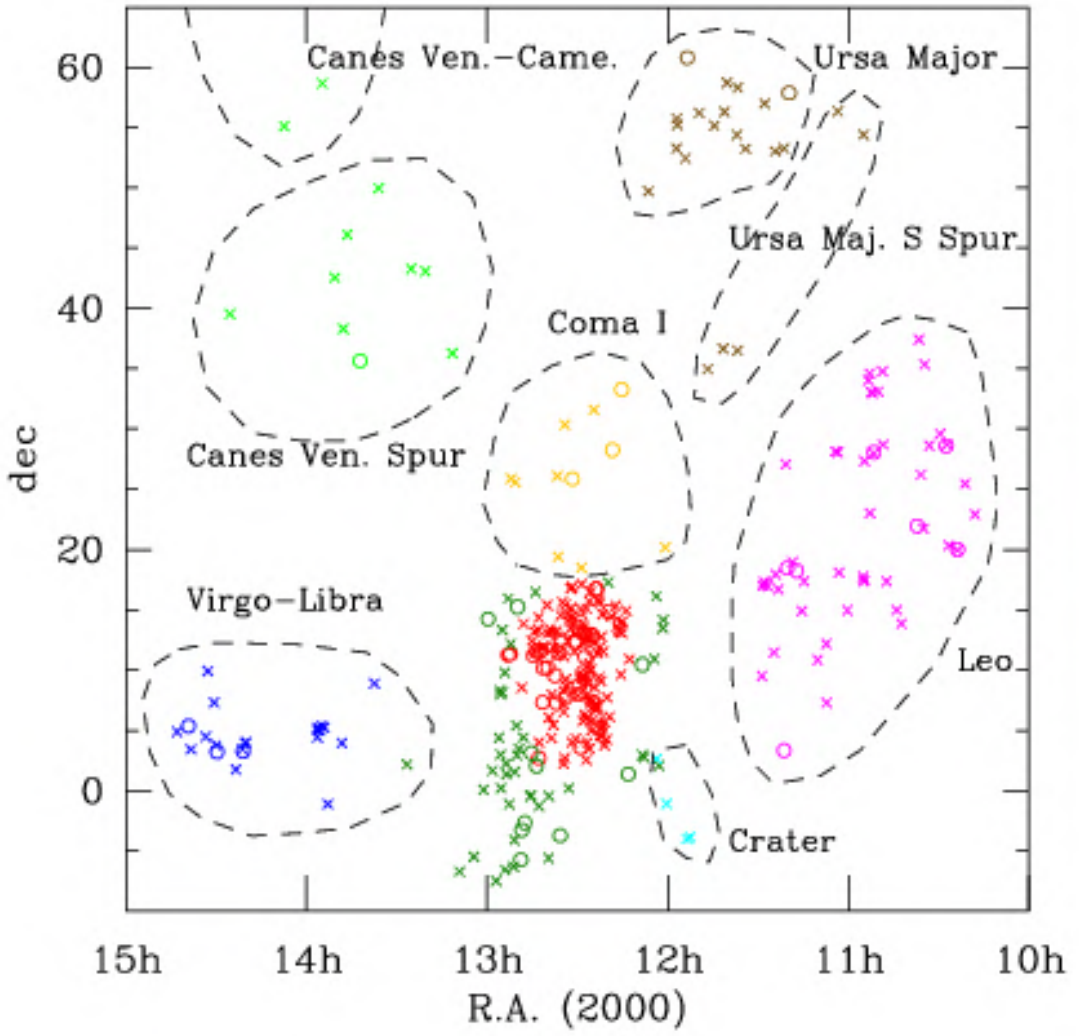

Figure 2.2 – Sky distribution of the HRS, taken from Boselli et al. (2010). Early type galaxies are represented with circles, while late-type galaxies with crosses. The red and green points corresponds to the Virgo cluster and its outskirts. The orange symbols corresponds to galaxies situated in Coma I cloud, magenta for Lyon cloud, brown for Ursa Major clouds, cyan for the Crater cloud, clear green for the Canes Venatici Spur and Camelopardalis clouds, and blue for the Virgo-Libra cloud.

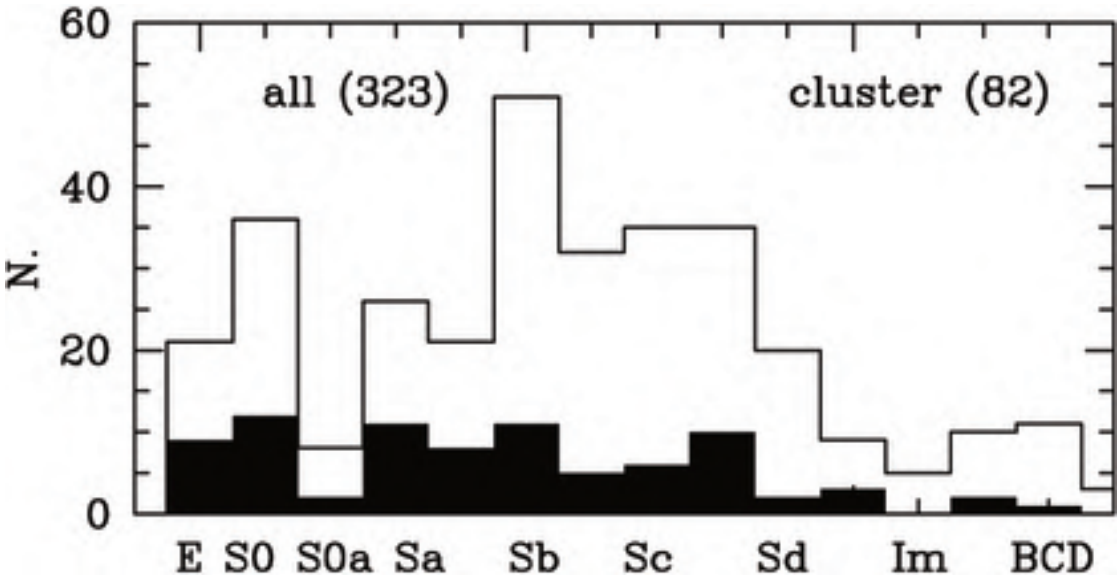

Figure 2.3 – Galaxy distribution in morphologycal type for the whole sample (empty histogram) and for cluster galaxies (black histogram). Figure taken from Boselli et al. (2010).

i) Volume-limited in order to reduce distance uncertainties due to local peculiar motions and ensure the presence of low-luminosity dwarf galaxies which are not accessible at high redshift. By applying a lower distance (D) limit, Boselli et al. (2010) excluded the very extended sources (for which many observing time is generally needed). They also selected objects with an optical recessional velocity between 1050 km s^{-1} and 1750 km s^{-1} for which, in the absence of peculiar motions, a value of H_0 = 70 km s^{-1} Mpc^{-1}, corresponds to 15 $\leq$ D $\leq$ 25 Mpc. In the Virgo cluster region (12h $< \alpha$(J2000) $<$ 13h; $0° < \delta < 18°$), where peculiar motions are dominant, the authors included all galaxies with vel $<$ 3000 km s^{-1} and belonging to cluster A, the North (N) and East (E) clouds and the Southern extension (S) (17 Mpc) and Virgo B (23 Mpc), where the subgroup membership has been taken from Gavazzi et al. (1999). W and M clouds objects, at a distance of 32 Mpc, have been excluded.

ii) K-band luminosity selection in order to obtain a mass complete sample. Across the different studies of extinction in optical and FIR bands, late-type galaxies are much more dusty than early-type ones (Sauvage & Thuan, 1994). Given the expected low dust content of quiescent galaxies, whose emission would be hardly detectable within reasonable integration times, a more stringent limit has been adopted for early-types than for star forming galaxies. The K-band ($\sim$ 2.1 μm) enable to derive the total stellar mass of a galaxy (Gavazzi et al., 1996), so two 2MASS K-band limited magnitudes were chosen in order to perform the galaxy selection: mag $K \leq 12$ for spiral galaxies (Sa-Sd-Im-BCD) and mag $K \leq 8.7$ for elliptical galaxies (E-S0-S0a), both in Vega system (Fig. 2.4, Boselli et al., 2010).

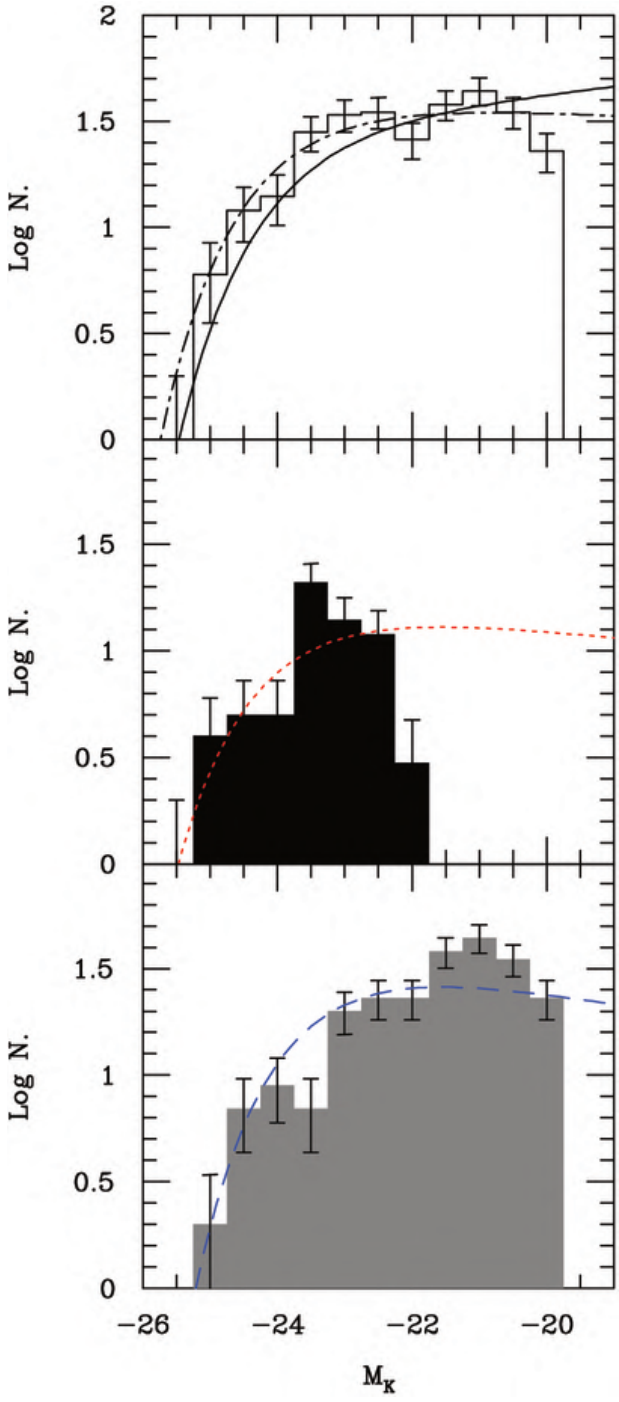

Figure 2.4 – Luminosity distribution in K-band Boselli et al. (2010) for the whole HRS sample (top panel), early-type (middle panel) and late-type galaxies (top panel). Luminosity functions from Kochanek et al. (2001) (black solid line) and Cole et al. (2001) (crosshatched line) are plotted on top panel; Kochanek et al. (2001) (red dashed line) on middle panel as well as on bottom panel (dashed blue line).

iii) High Galactic latitude. With the purpose to avoid the Milky way IR contamination, HRS galaxies have been selected at high Galactic latitudes ($b > +55°$) and at low Galactic extinction regions ($A_B < 0.2$, Schlegel et al., 1998.)

The resulting sample is composed of 323 galaxies (Fig. 2.1) located in the sky region between 10h17m < α(J2000) < 14h43m and -6° < δ < 60° (Fig. 2.2), of which 62 are early-type (E, S0 and S0a) and 261 are late-type (Sa-Sd-Im-BCD) (Fig. 2.3). The only galaxies which are clearly undersampled are blue compact galaxies and dwarf irregulars, the most numerous galaxies in the nearby universe. As selected, the sample spans a large range in environment since it includes the Virgo cluster, many galaxy groups and pairs as well as relatively isolated objects (Fig. 2.2). Using the Virgo cluster membership criteria defined in Gavazzi et al. (1999), the HRS includes 82 members of cluster A and B (Fig. 2.3). The other galaxies are members of nearby clouds such as Leo, Ursa Major and Ursa Major Southern Spur, Crater, Coma I, Canes Venatici Spur and Canes Venatici - Camelopardalis and Virgo-Libra Clouds (Tully, 1988). As defined, the sample is thus ideal for environmental studies (Boselli et al., 2014b; Boselli et al., 2016).

2.2 HRS: the ideal survey to study the properties of the local universe.

The HRS is well representative of the galaxy population and is unbiased versus cosmic variance. This is necessary since, as selected, the HRS may be biased versus galaxies located in a high density environment (Virgo clouds). Boselli et al. (2010) tested this by seeing whether the luminosity distributions at different wavelengths in the HRS are similar to the local galaxy luminosity functions at the corresponding frequencies.

Fig. 2.4 displays a comparison of the HRS luminosity distribution in the K-band (histogram) to the K band luminosity function of Cole et al. (2001) and Kochanek et al. (2001), this last also considering separately early- and late-types. When considered from the perspective of the K-band, the HRS is a good approximation to a volume-limited sample down to an absolute magnitude of $M_K \simeq$ -20. This absolute magnitude limit is relatively high and explains why the HRS is under-represented in Im and BCD galaxies (Fig. 2.3). The sample includes only the brightest ellipticals and lenticulars, whose K band luminosity function ends at $M_K \sim$ -18, while it does not include any quiescent dwarf system ($M_K \geq$ -20). In summary, since the K-band light traces stellar mass, the good agreement between the HRS luminosity distribution and K-band luminosity function implies that the HRS can be treated as a representative sample down to a stellar mass of $\sim 10^8 M_\odot$.

The HI-deficiency parameter is defined as the logarithmic difference between the average HI mass of a reference sample of isolated galaxies of similar type and linear dimension and the HI mass actually observed in individual objects. Most of the

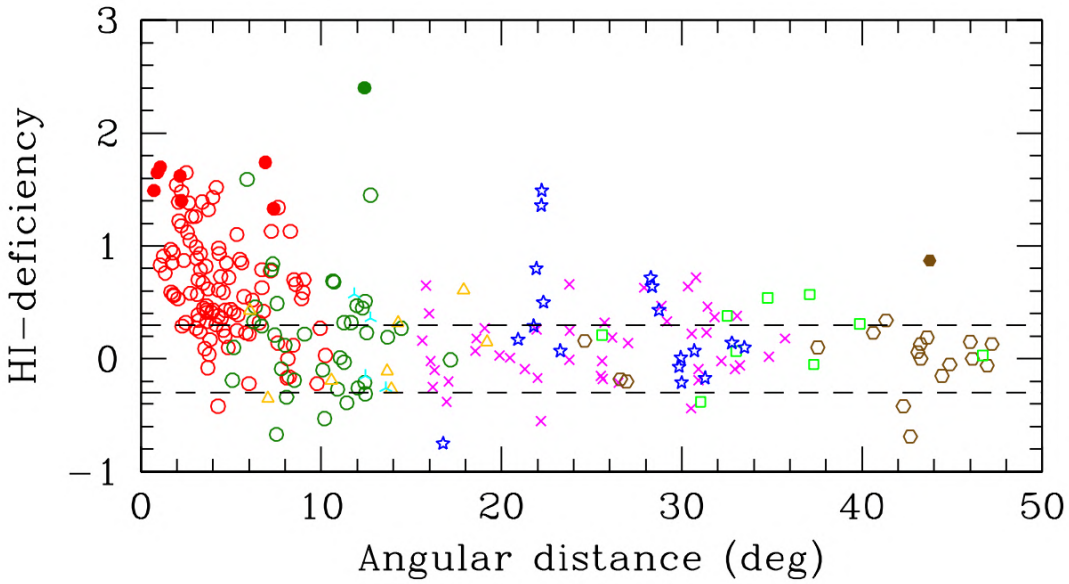

Figure 2.5 – The variation of the HI-deficiency parameter as a function of the angular distance from the core of the Virgo cluster (M87). Red circles are for Virgo cluster galaxies (Virgo A, B, N, S and E), dark green circles for galaxies in the Virgo outskirts, orange triangles for the Coma I Cloud, magenta crosses for the Leo Cloud, brown hexagons for Ursa Major Southern Spur and Cloud, cyan three skeletal for the Crater Cloud, light green squares for Canes Venatici Spur and Camelopardalis and blue stars for the Virgo-Lybra Cloud. Taken from Boselli et al. (2010).

late-type HI-deficient objects (HI-deficiency ≥ 0.4) in the HRS are indeed located in the core of the Virgo cluster as shown in Fig. 2.5. Galaxies in the outskirt of the Virgo cluster or in the surrounding clouds have a normal HI gas content and can be generally considered as unperturbed objects (unless belonging to groups or pairs) in the study of the effects of the environment on the physical properties of galaxies. Indeed, despite the relatively poor statistics, the average HI-deficiency of late-type galaxies in the Coma I Cloud, Leo Cloud, Ursa Major Cloud and Southern Spur, Crater Cloud, Canes Venatici Spur, Canes Venatici - Camelopardalis Cloud and Virgo - Libra Cloud is consistent with that of unperturbed galaxies in the reference sample of Haynes & Giovanelli (1984) (HI-deficiency ≤ 0.3). The HI-deficiency of late-type galaxies in the different substructures of the Virgo cluster are generally consistent with those observed in a larger sample by Gavazzi et al. (1999). The only exception is Virgo E, found dominated by HI-deficient objects. The presence of HI-deficient and normal objects makes the HRS ideal for studying the effects of the environment properties of nearby galaxies.

The lack of very luminous galaxies in the HRS is because Luminous (LIRGs) and Ultra Luminous (ULIRGs) Infrared Galaxies are quite rare in the nearby universe and in particular inside rich clusters (Boselli & Gavazzi, 2006). Nevertheless, The HRS have two bright radio galaxies; M84 and M87.

Across this section, a brief summary of each available dataset for the HRS will be presented and graphically exemplified using the galaxy NGC 4254 in order to visualise the resolution and features of each band. All those datasets are available in the HRS-dedicated website `https://hedam.lam.fr/HRS/`.

2.3 The panchromatic dataset for the HRS

2.3.1 Far and Near Ultraviolet observations (FUV-NUV)

The UV emission comes from the most bright and young massive stars (O-B type, with an age $< 10^8$ y) and is thus a direct tracer of the current Star Formation Rate (SFR) (Kennicutt, 1998a; Boselli et al., 2009; Kennicutt et al., 2011). Dust absorbs an important fraction of this radiation to reemit it in the IR. It is fundamental to take the latter into account in order to well constrain and accurately recover the star formation activity.

Cortese et al. (2012) presented *Galaxy Evolution Explorer* (GALEX) FUV ($\lambda = 1539$ Å with $\Delta\lambda = 442$ Å) and NUV ($\lambda = 2316$ Å with $\Delta\lambda = 1069$ Å) photometry for the whole HRS (Fig. 2.7).

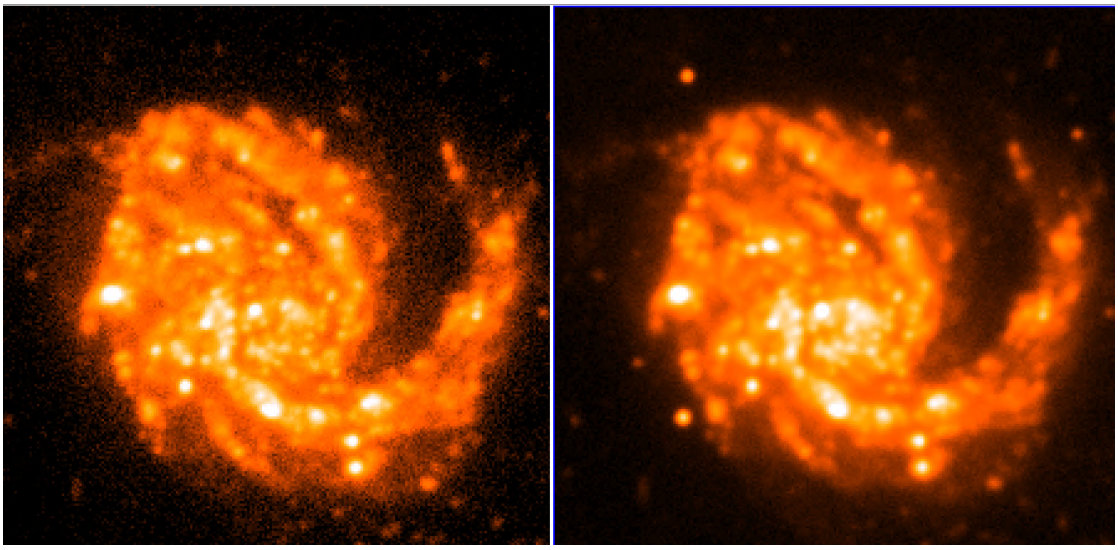

Figure 2.6 – Galaxy NGC4254 in GALEX FUV (left panel, angular resolution ~4.5”) and NUV (right panel, angular resolution ~6.5”) bands, provided by Cortese et al. (2012).

Figure 2.7 – Galaxy NGC4254 in SDSS-*gri* bands with a median angular resolution of ~1.3”, provided by Cortese et al. (2012).

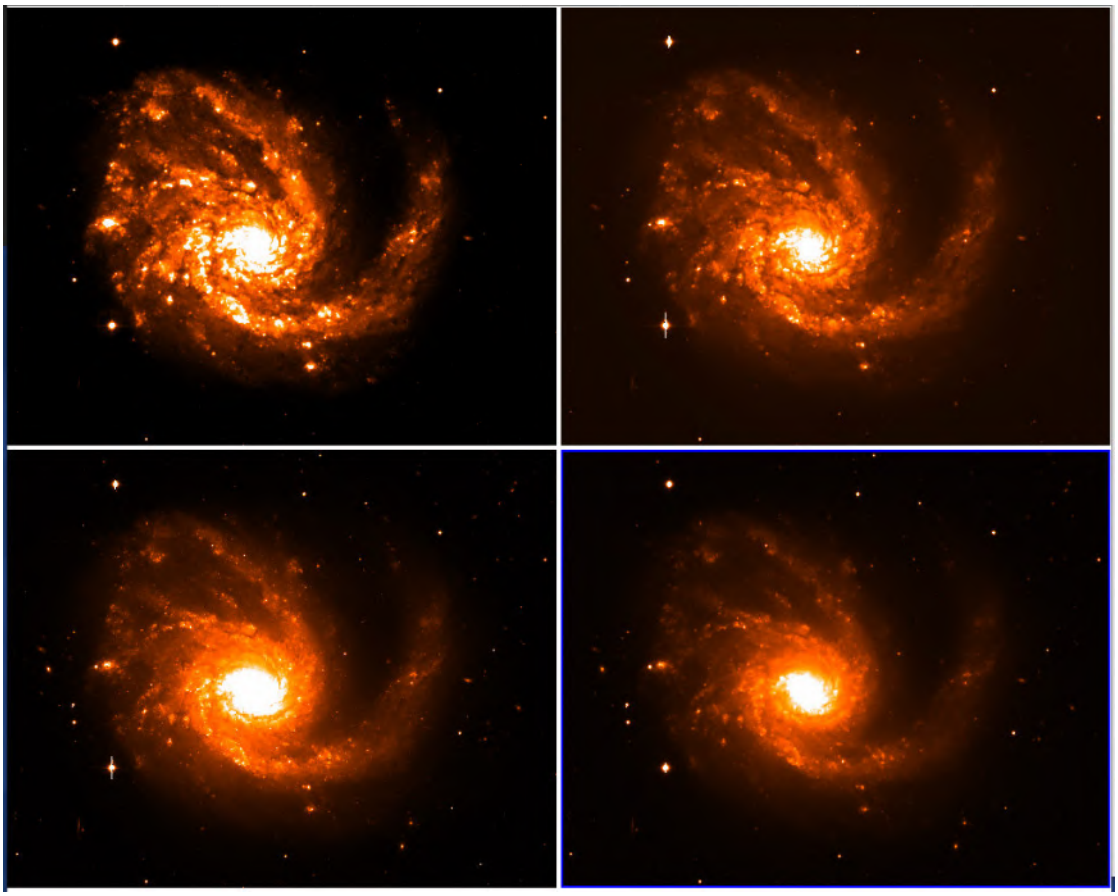

Figure 2.8 – Galaxy NGC4254 in NGVS *u*- (top left panel), *g*- (top right panel), *i*- (bottom left panel) and *z*-(bottom right panel) bands, with a typical angular resolution ~0.6", provided by Ferrarese et al. (2012).

2.3.2 Optical observations ($g - r - i$ bands)

The optical emission comes from middle-age stars ($\sim 10^9$ y). In this spectral range, as well as in UV and NIR, the ISM modulates the emission absorbing and diffusing the stellar radiation. Several emission and absorption lines are present in the optical range.

Cortese et al. (2012) also presented the optical photometry in the g ($\lambda = 4686$ Å), r ($\lambda = 6165$ Å) and i ($\lambda = 7481$ Å) bands from the *Sloan Digital Sky Survey* (SDSS) for the whole HRS (Fig.2.7). The spatial resolution of the data is on average 2". SDSS data in the u ($\lambda = 3551$ Å) and z ($\lambda = 8391$ Å) are also available for the HRS ((Abazajian et al., 2009)).

Concerning the Virgo cluster objects, (Ferrarese et al., 2012) provided a deep optical imaging survey carried out using the MegaPrime/MegaCam at the Canadian-France-Hawaii Telescope (CFHT): the *Next Generation Virgo Cluster* (NGVS), covering a circular region with radius $r = 5.383°$. The data have a high spatial resolution ($\sim 0.5''$, enabling the possibility to disentangle individual HII regions) in the bands u, g, i, z and a detection limit of ~ 29 mag arcsec^{-2} in the g-band (Fig.2.8).

2.3.3 Hα observations

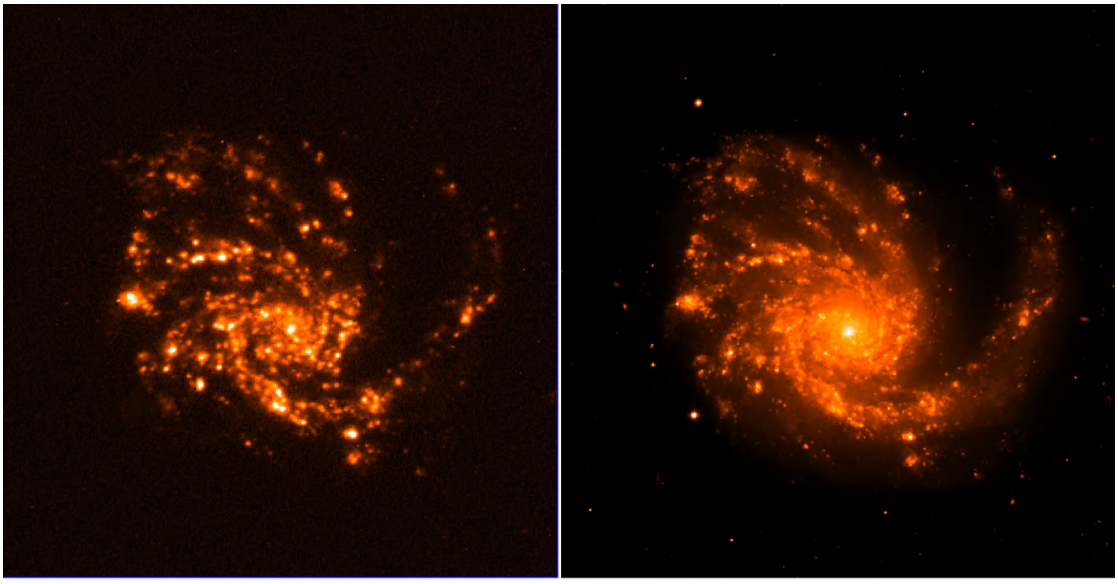

Figure 2.9 – Galaxy NGC4254 in Hα emission (Boselli et al., 2015, left panel, at an angular resolution of ~1.5"; Boselli et al., 2018d, right panel, at angular resolution of ~0.6").

The Hα emission $\lambda = 6562.78$Å comes from HII regions and across diffuse emission escaping from such regions, where the hydrogen atom is photoionised by the strong UV

radiation produced by O-B stars, thus indicating directly a recent star formation event ($< 4 \times 10^6$ yr, Kennicutt, 1998a). The Hα emission is thus an ideal tracer of SFR.

Boselli et al. (2015) presented Hα+[NII] imaging data for the whole HRS (observed with a filter $\lambda = 6603$Å with $\delta\lambda = 90$Å). These observations were carried out at 1.5m and 2.1m telescopes at San Pedro Martir Observatory in Mexico, or collected from previous surveys of the Virgo cluster (; Boselli et al., 2002a; Gavazzi et al., 2002, 2006), with a spatial resolution of ~ 1.5" (Fig.2.9, left panel).

On the other hand, an undergoing independent project of deep Hα+[NII] imaging, the *Virgo Environmental Survey Tracing Ionised Gas Emission* (CFHT-VESTIGE, Boselli et al., 2018c), is covering the whole Virgo cluster region from its core to one virial radius (104 deg^2). The sensitivity of the survey is $\sim 4\times10^{-17}$ erg sec^{-1} cm^{-2} (5σ detection limit) for point sources and $\Sigma(H\alpha) \sim 2 \times 10^{-18}$ erg sec^{-1} cm^{-2} arcsec^{-2} (1σ detection limit) for extended sources, making VESTIGE the deepest and largest blind narrow-band survey of a nearby cluster. The spatial resolution of VESTIGE data is ~ 0.6", providing the HRS by extremely resolved Hα imaging for the cluster objects, allowing to disentangle the HII regions with a diameter of $\sim$80 pc (Fig.2.9, right panel).

2.3.4 Integrated and Nuclear Spectroscopy (spectral range 3600-6900Å)

Boselli et al. (2013) and Gavazzi et al. (2018) presented integrated and nuclear spectroscopy of the HRS galaxies, covering a spectral range of 3600-6900Å at a resolution $R \simeq 1000$, thus suitable to resolve several absorption/emission lines within that range. They measured the fluxes and the equivalent widths of the lines [OII] ($\lambda = 3727$Å), Hβ ($\lambda = 4861$Å), [OIII] ($\lambda = 4959$Å and $\lambda = 5007$Å), [NII]($\lambda = 6548$Å), Hα, [NII]($\lambda = 6584$Å), [SII] ($\lambda = 6717$Å and ($\lambda = 6731$Å). Boselli et al. (2013) studied the distribution of equivalent widths of such lines, the Balmer decrement C(Hβ), the underlying Balmer absorption under Hβ (EW Hβ_{abs}), the relation of C(Hβ) and EW Hβ_{abs}, the metallicity of galaxies, etc. all those properties as a function of the morphological type, stellar mass, stellar surface density, SFR, birthrate parameter, atomic and molecular gas content, etc. in galaxies situated into different environments. This is crucial to trace ratios of different parameters, scaling relations, among others properties, in other words, this is crucial to characterise the galaxy evolution.

2.3.5 Near and Middle Infrared observations (NIR and MIR)

Low luminosity old stars in the main sequence (age $> 10^{10}$ yr) and red giants emit in the NIR. These stellar populations are dominant in early-type galaxies, allowing to trace the stellar mass of them (Gavazzi et al., 1996).

All the HRS galaxies have been observed by the project *Two Micron All-Sky Survey* (2MASS, Jarrett et al., 2003) in the J ($\lambda = 1.25\mu$m), H ($\lambda = 1.65\mu$m) and K ($\lambda =$

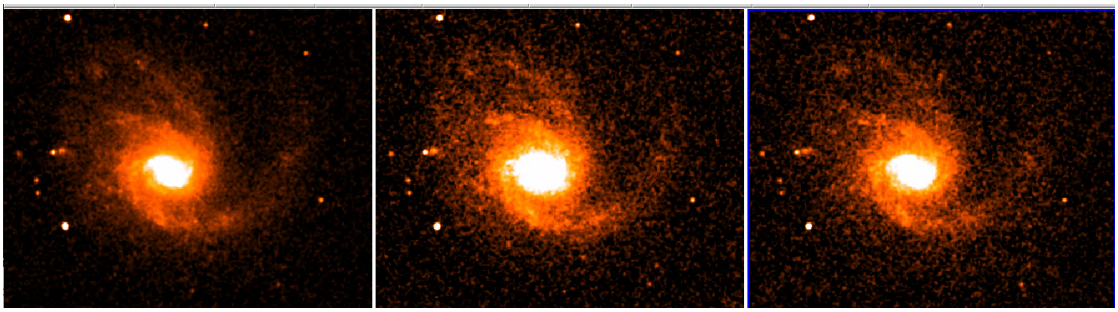

Figure 2.10 – Galaxy NGC4254 in 2MASS J- (left panel), H- (middle panel) and K- (right panel) bands, with a median angular resolution of ~5”-6”, provided by Jarrett et al. (2003).

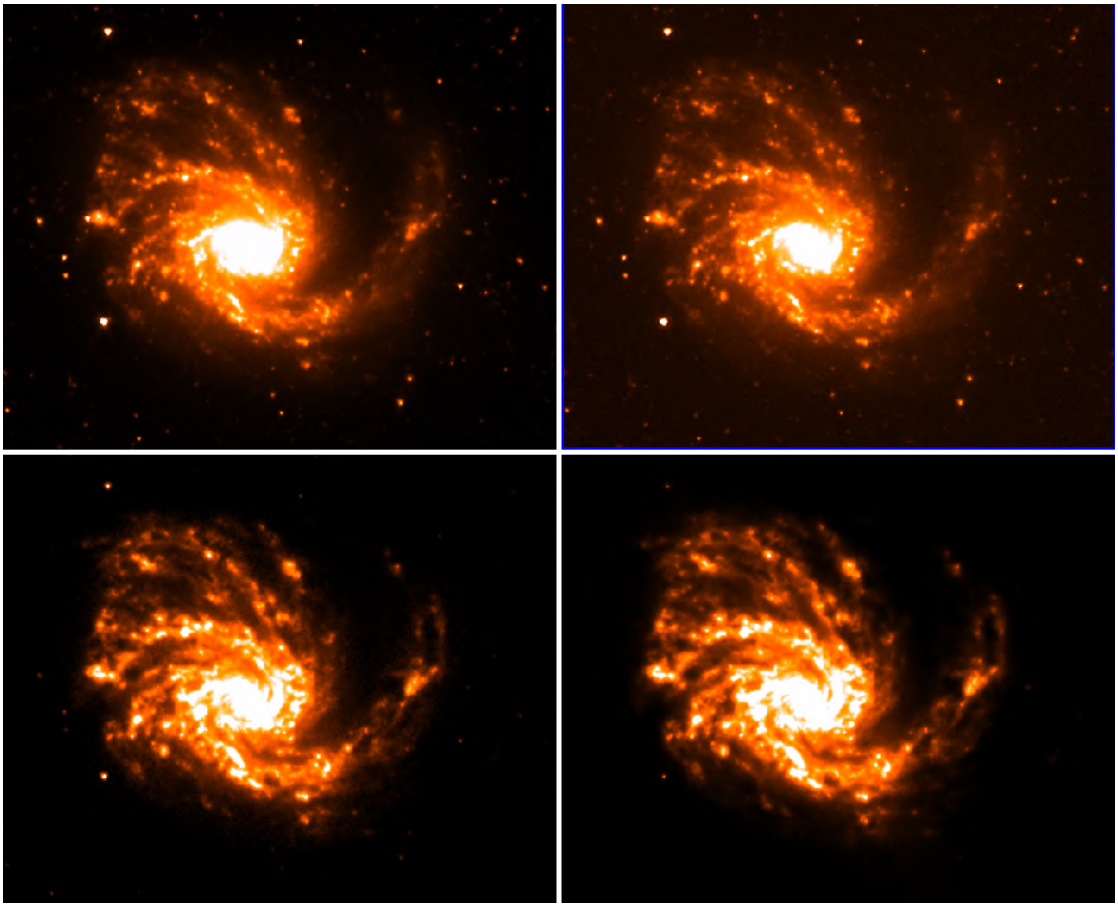

Figure 2.11 – Galaxy NGC4254 in S4G 3.6μm (top left panel), S4G 4.5μm (top right panel), IRAC-3 (bottom left panel) and IRAC-4 (bottom right panel) bands, with at typical angular resolution of ~2”, provided by Sheth et al. (2010) and Fazio et al. (2004).

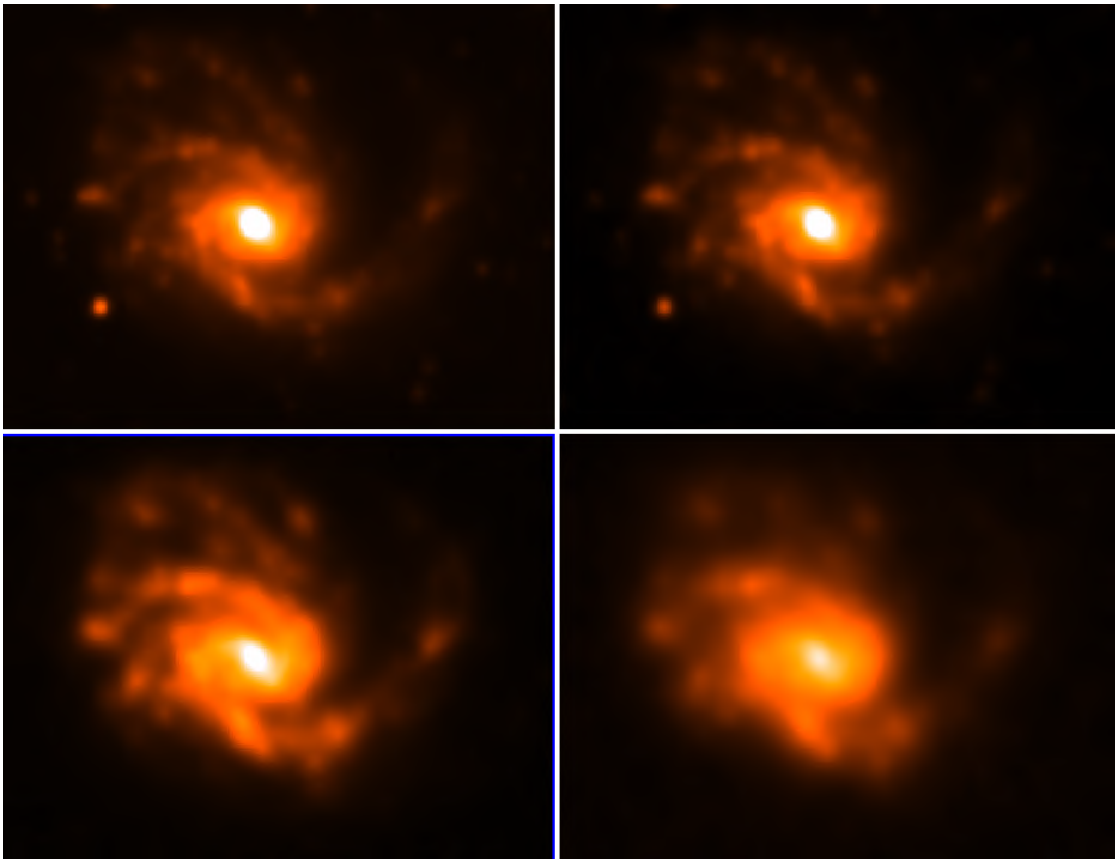

Figure 2.12 – Galaxy NGC4254 in WISE-1 (top left panel, angular resolution ~6.1”), WISE-2 (top right panel, angular resolution ~6.4”), WISE-3 (bottom left panel, angular resolution ~6.5”) and WISE-4 (bottom right panel, angular resolution ~12”) bands, provided by Ciesla et al. (2014).

2.17μm) bands, with a spatial resolution of ~2-3" (Fig.2.10).

Until 5μm, the emission is due to old stars. At longer wavelengths, the emission comes from hot dust, particularly from Polycyclic Aromatic Hydrocarbons (PAHs) (until 10μm) and Very Small Grains (VSG). The dust plays an important role as a catalyser in the transformation process of neutral hydrogen into molecular hydrogen, absorbing the UV and optical avoiding the dispersion of molecular clouds, and contributing to the cooling and heating of the ISM. Because of the latter, emission between 5μm and 10 μm is indispensable to characterize the PAHs emission (the PAHs most important emission line wavelength is 7.7μm) and, on the other hand, observations around 24μm are crucial to constrain VSG emission.

The *Spitzer Survey of Stellar Structure in Galaxies* (S4G, Sheth et al., 2010), carried out using the Infrarred Array Camera (IRAC), provided deep 3.6μm and 4.5μm imaging for 2331 galaxies, among which there are 301 galaxies belonging to the HRS. The S4G data have a typical detection limit of $\mu_{AB} \sim 27$ mag arcsec^{-2}, and a spatial resolution of $\sim$ 1.9". On the other hand, IRAC images are available at 5.8μm for 131 HRS galaxies, and at 8.0μm for 129 HRS galaxies (Fazio et al., 2004) (Fig.2.11).

The *Wide-field Infrared Survey Explorer* (WISE, Wright et al., 2010) observed the whole sky in NIR and MIR bands: 3.4, 4.6, 12 and 22μm with a spatial resolution of 6.1", 6.4", 6.5" and 12" and a 5σ point source sensitivities better than 0.08, 0.11, 1, and 6 mJy, respectively. The whole HRS has been observed in those bands by WISE (Ciesla et al., 2014) (Fig.2.12).

2.3.6 Far Infrared (FIR) and Submilimetre (sub-mm) observations

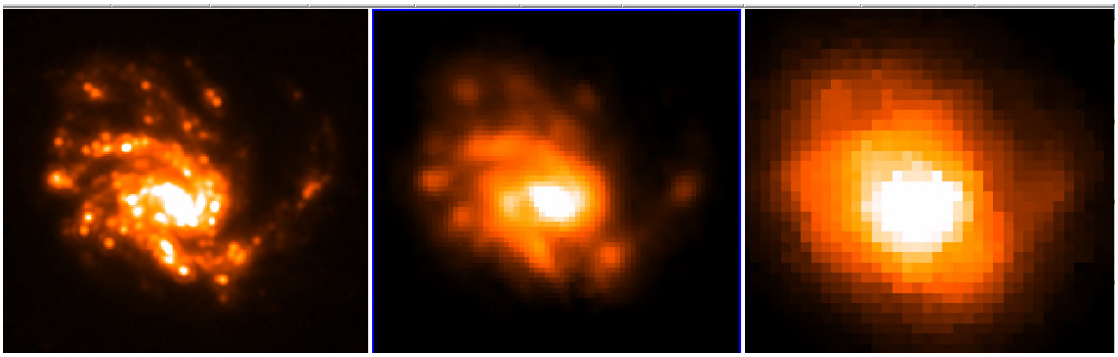

Figure 2.13 – Galaxy NGC4254 in MIPS 24μm (left panel, angular resolution ~6"), 70μm (middle panel, angular resolution ~18") and 160μm (right panel, angular resolution ~38") bands, provided by Bendo et al. (2012).

The FIR and sub-mm emission (until ~1.0mm) is due to colder dust composed by bigger grains. It is crucial as well to cover this spectral range in order to constrain the

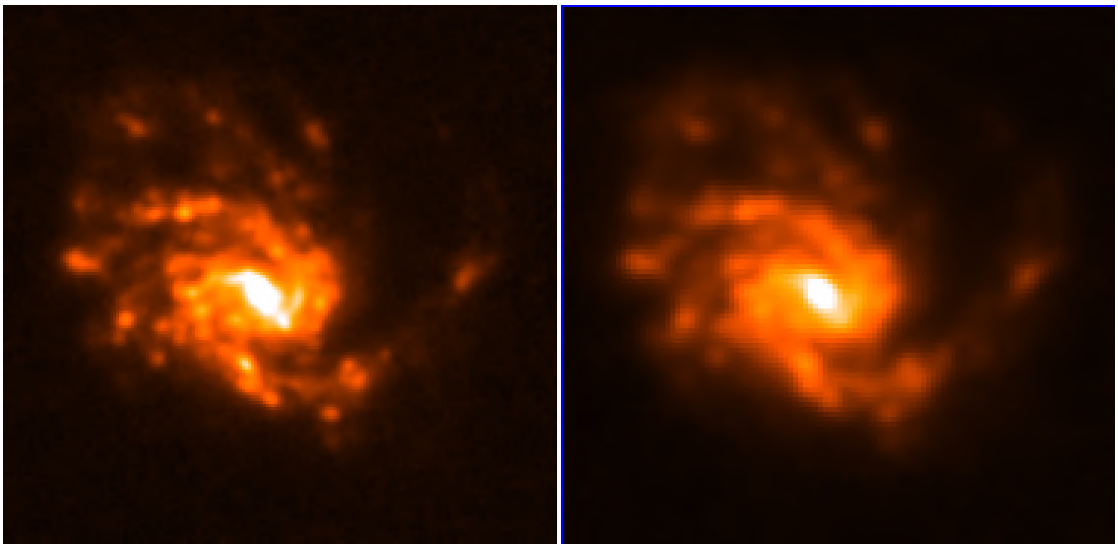

Figure 2.14 – Galaxy NGC4254 in PACS 100μm (left panel, angular resolution ~9") and 160μm (right panel, angular resolution ~12") bands, provided by Cortese et al. (2014).

totality of the dust emission and therefore its mass.

The *Infrared Astronomical Satellite* (IRAS, Neugebauer et al., 1984) observed the whole sky in the bands 12, 25, 60 and 100 μm, allowing to have integrated flux densities (Moshir & et al., 1990; Thuan & Sauvage, 1992; Soifer et al., 1989; Young et al., 1996; Sanders et al., 2003) for the HRS galaxies.

Bendo et al. (2012) provided imaging and photometry of the *Spitzer Multiband Imaging Photometer* (MIPS) for *Herschel-SPIRE* and *Herschel Virgo Cluster Survey* (HeVICS) local galaxies at 24, 70, and 160μm with a spatial resolution of 6", 18" and 38", respectively. From this catalog, 167 galaxies belonging to the HRS have been observed at 24μm, as well as 107 a 70μm and 100 at 160μm (Fig.2.13).

Cortese et al. (2014) presented observations and integrated photometry in the 100μm and 160μm bands of the *Herschel Photodetector Array Camera and Spectrometer* (PACS) for the whole HRS sample, with a spatial resolution of ~9" and ~12" respectively, and a detection limit of ~0.01 mJy arcsec^{-2} in both cases (Fig.2.14).

Ciesla et al. (2012) presented imaging and flux densities for the whole HRS in the three bands of the *Herschel Spectral and Photometric Imaging Receiver* (SPIRE) at 250μm, 350μm and 500μm, with a spatial resolution of ~18", ~25" and ~36" respectively (Fig. 2.15).

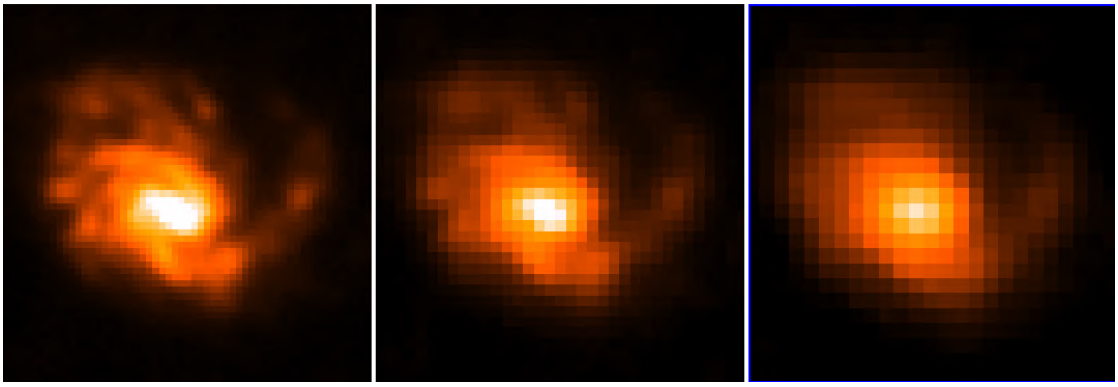

Figure 2.15 – Galaxy NGC4254 in SPIRE 250μm (left panel, angular resolution ~18"), 350μm (middle panel, angular resolution ~25") and 500μm (right panel, angular resolution ~38") bands, provided by Ciesla et al. (2012).

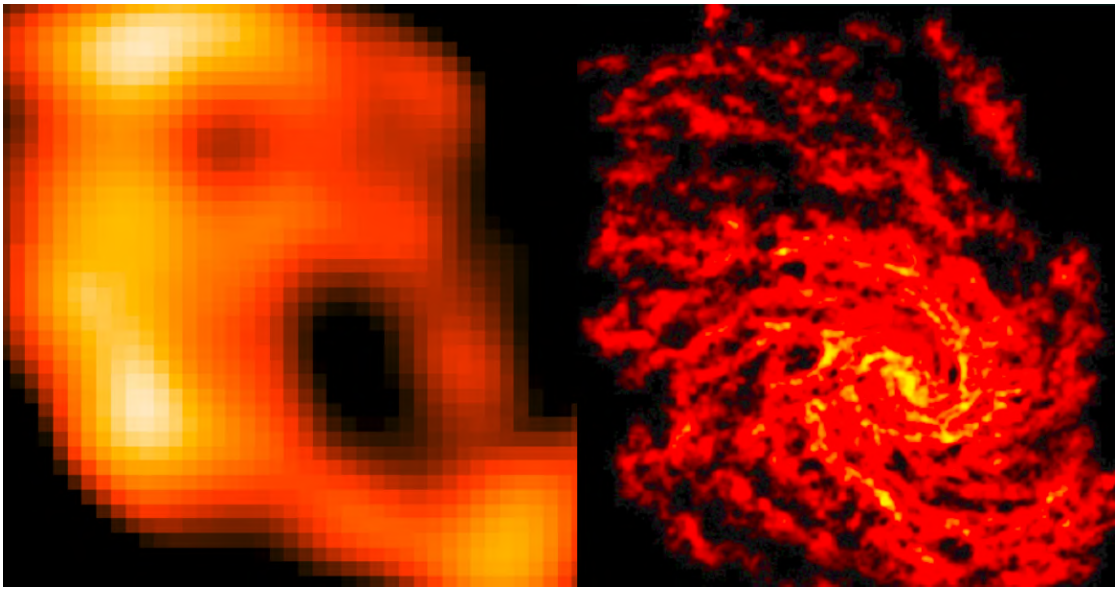

Figure 2.16 – Galaxy NGC4254 in HI (left panel, angular resolution ~15", Chung et al., 2009), and PHANGS-ALMA CO(2-1) (right panel, angular resolution ~1", Sun et al., 2018, Utomo et al., 2018).

2.3.7 HI, CO observations (mm and cm)

One of the most observable molecules is the carbon monoxide (CO) thanks to its strong dipolar moment. The CO strong rotational lines are situated in the milimetric i.e. for the transitions CO(1-0) at 2.6 mm and CO(2-1) at 1.3mm (Lequeux, 2005). The carbon monoxide emission allows to trace the molecular gas content using a conversion factor X_{CO} between the CO intensity and the H_2 gas column density. Such factor depends on the metallicity and the gas temperature (Wilson, 1995; Boselli et al., 2002b; Kennicutt et al., 2011).

The neutral hydrogen 21 cm emission line enables to trace the atomic gas in the universe. It is caused by a forbidden hyperfine transition of the hydrogen atom. This phenomenon is produced in a timescale of 10^7yr but this emission is well plentiful in the universe (Fig. 2.16, left panel).

Both HI and H_2 compose the total hydrogen gas mass. Boselli et al. (2014a) presented CO(1-0) and HI integrated observations for the whole HRS, providing also paramaters such as HI and H_2 gas mass as well as integrated profile widths (related to the rotation velocity amplitude of galaxies, Boselli & Gavazzi, 2014).

On the other hand, an undergoing independent project using the *Atacama Large Millimeter Array* (ALMA) interferometer, the *Physics at High Angular resolution in Nearby GalaxieS using the Atacama Large Millimeter/Submillimeter Array* (PHANGS-ALMA) is gathering high spectral ($R \sim 3 \times 10^7$) and spatial resolution (~1") CO(2-1) data for dozens of Virgo cluster objects, providing the HRS by resolved H_2 data for the cluster galaxies (Fig. 2.16, right panel).

2.3.8 Metallicity and dust

Hughes et al. (2013) provided integrated metallicity (Z) values $12 + log(O/H)$ for the whole HRS, by using integrated drift-scan optical spectroscopy (Boselli et al., 2012, 2013) and the base metallicity calibrations of Kewley & Ellison (2008).

Cortese et al. (2012), Cortese et al. (2014) and Ciesla et al. (2014), making use of WISE, MIPS, PACS and SPIRE datasets, constrained the integrated properties of dust (dust masses, attenuation, etc.) for the whole HRS using the CIGALE SED-fitting code Noll et al. (2009), and studied the dust scaling relations for nearby galaxies as well.

2.3.9 Necessity of high spatially and spectrally resolved data for the HRS

Despite a very big panchromatic dataset for the HRS is already available and perfectly suited to perform statistical studies of galaxies in the local universe, the HRS lacks of spatially resolved kinematical data, which are crucial to study the different processes involved in galaxy formation and evolution.

As mentioned in the Introduction, we will use Fabry-Perot interferometry to construct a kinematical database for the HRS. In the next Chapter we explain everything about this technique.

3 Fabry-Perot Interferometry

3.1 Integral Field Spectroscopy

The integral Field Spectroscopy (IFS) is an observing technique which allows to obtain, in a single and relatively quick exposition (around 1 hour), the spectra of many spatial elements (pixels or spaxels) of an extended source. The resulting data is a datacube: a big quantity of images belonging to the same source but at different wavelengths. Thus, a datacube is composed by three dimensions: two spatial dimensions (right ascension and declination) and wavelength (Fig 3.1).

There are several IFS methods such as image slicer, lenslet array and fibers; these methods are/have being exploited to construct several large surveys of galaxies situated at different redshifts i.e. CALIFA (Sánchez et al., 2012), MaNGA (Bundy et al., 2015), SAMI (Bryant et al., 2015), and to develop instruments as MUSE (Bacon et al., 2017), among others. Thanks to the wide spectral range covered by these surveys, it is possible to trace 2D maps of kinematics, age, metallicity, star formation history and rate, dust extinction, surface brightness, etc. deriving thus many properties of galaxies belonging to those surveys, and allowing to disentangle the phenomena involved in galaxy evolution at different redshifts and environments.

Other IFS techniques rely on interferometry, using electro-mechanical scanning techniques i.e. Imaging Fourier transform spectroscopy (IFTS) employing a Michelson interferometer layout, and Fabry-Perot interferometry. The IFTS is an interferometer of two beams, meanwhile the Fabry-Perot is an interferometer of multiple beams. The IFTS transfer function is sinusoidal, while the Fabry-Perot one is an Airy Function which is more selective.

SITELLE (Drissen et al., 2019), an IFTS is available at the CFHT 3.6m. SITELLE is a Michelson-type interferometer able to reconstruct the spectrum of every light source within its 11' field of view in filter-selected bands of the visible (350 to 900 nm). The spectral resolution can be adjusted up to $R = 10000$ and the spatial resolution is seeing-limited and sampled at 0.32 arcsec per pixel.

The Fabry-Perot technique has a fundamental advantage over the others surveys/instruments mentioned before, concerning the kinematics: gathering not only high spatial but also high spectral resolution datacubes using not very demanded and relatively small telescopes (diameter of ~2m) with a typical exposure per extended source of ~2 hours and covering big spatial coverages (diameters of ~5'-10'). Despite the spectral range of the data is much narrower in Fabry-Perot interferometry than

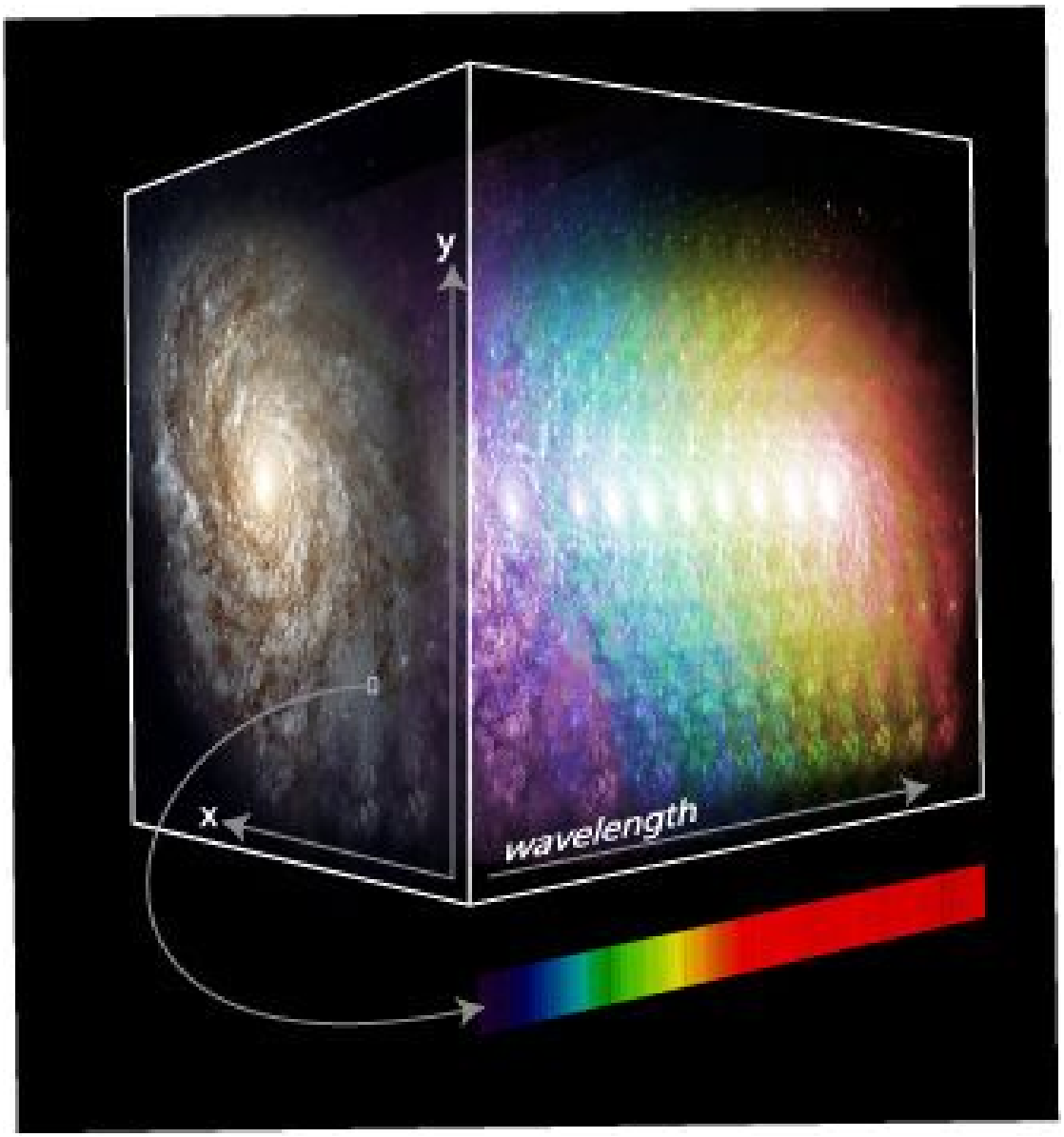

Figure 3.1 – A datacube contains the information of an extended source (i.e. a galaxy) within two spatial and one spectral dimension. Credit: Marc White (RSAA-ANU).

those of the data of the surveys mentioned above, the spectral resolution is crucial to trace accurately the kinematical properties of extended objects like galaxies. In addition, Fabry-Perot is a technique extensively proved concerning observations of diffuse emission of galactic (Russeil et al., 2005) and extragalactic (Marcelin et al., 1987) ionised gas. Thus, the Fabry-Perot technique is ideal to construct a resolved kinematical dataset for a complete reference survey such as the HRS.

3.2 Historical review of the Fabry-Perot interferometer

The principles of this interferometer lies on the fact that light behaves as waves, a principle established by Thomas Young (1773-1829). The theoretical frame of wave optics is developed later by Augustin Fresnel (1788-1827) and the mathematical frame of the Fabry-Perot interferometry is determined in 1831 by Georges Airy (1801-1892) describing the coherent addition of multiple reflections between two flat surfaces thanks to the eponymic function.

The Fabry-Perot interferometer has been invented in 1896 by Charles Fabry (1867-1945) and Alfred Perot (1863-1925) in the frame of meteorology, in order to accurately measure the thickness variations, and presenting the possibility to place the interferometer in the focal plane of a telescope.

Buisson et al. (1914) made the first utilisations of the Fabry-Perot for astronomical purposes observing the Orion nebula with a interferometer placed on a 80cm Foucault telescope at Marseille Observatory. These observations allowed them to measure the kinematics of the nebula ionised gas. Fabry-Perot techniques were used then by Courtès (1972) in order to study the ionised gas regions of the Milky Way and other very nearby galaxies. Until this point of the history, Fabry-Perot observations were done using an interferometer with fixed plates denominated “etalon”.

The first scanning Fabry-Perot interferometer was developed at the London Imperial College, controlled remotely by an automatic system (Hicks et al., 1976). CIGALE instrument (extensively described in Chapter 3) was developed by Boulesteix et al. (1984) for the CFHT Cassegrain telescope.

All these premises gave place to expert teams of scanning Fabry-Perot interferometry at LAM (Boulesteix et al., 1987;Laval et al., 1987; Georgelin et al., 1987; Marcelin et al., 1987; Amram, 1991; Le Coarer et al., 1992; Plana, 1996;Russeil, 1998; Garrido et al., 2003; Epinat et al., 2008b,a) and at OAN-SPM in Mexico (Rosado et al., 1995; Fuentes-Carrera et al., 2001).

3.3 Interference

3.3.1 Formalism of interference

Interference is produced when radiation follows more than only one path (e.g. two beams) from its origin and is superposed until the detection point. The intensity in the superposition regions could vary from maximums getting over the individual intensities to minimums like zero. The shining and shadowy observed bands are called interference bands. This phenomena is always seen in superposed monochromatic beams.

3.3.2 Interference of multiple beams

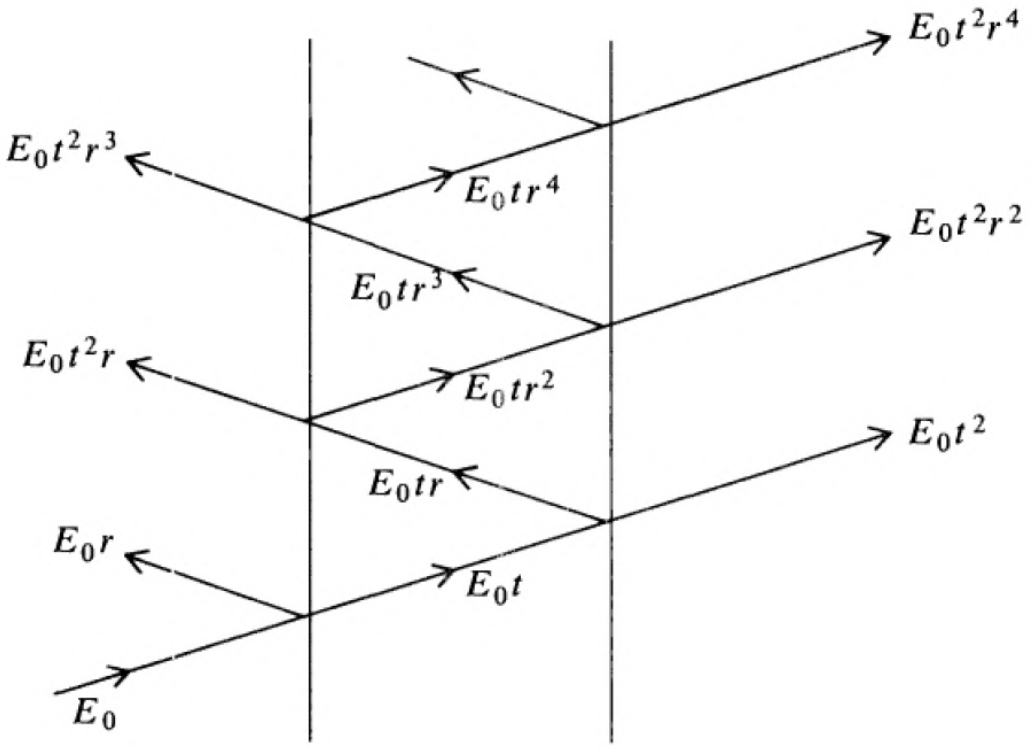

Figure 3.2 – Paths of light in the multiple reflection between two semi-reflecting plates (Fowles, 1989).

The interference of multiple beams take place when many waves mutually coherent interfere. The usual method to do that is the division of amplitude using two semi-reflective plates (Fig. 3.2). The amplitude of the primary beam is E_0; if the coefficient of reflection is r and the coefficient of transmission is t, then the amplitudes

of the successive beams reflected internally are E_0t, E_0tr, E_0tr^2, ... , while the amplitudes of the transmitted beams are E_0t^2, $E_0t^2r^2$, $E_0t^2r^4$, ...

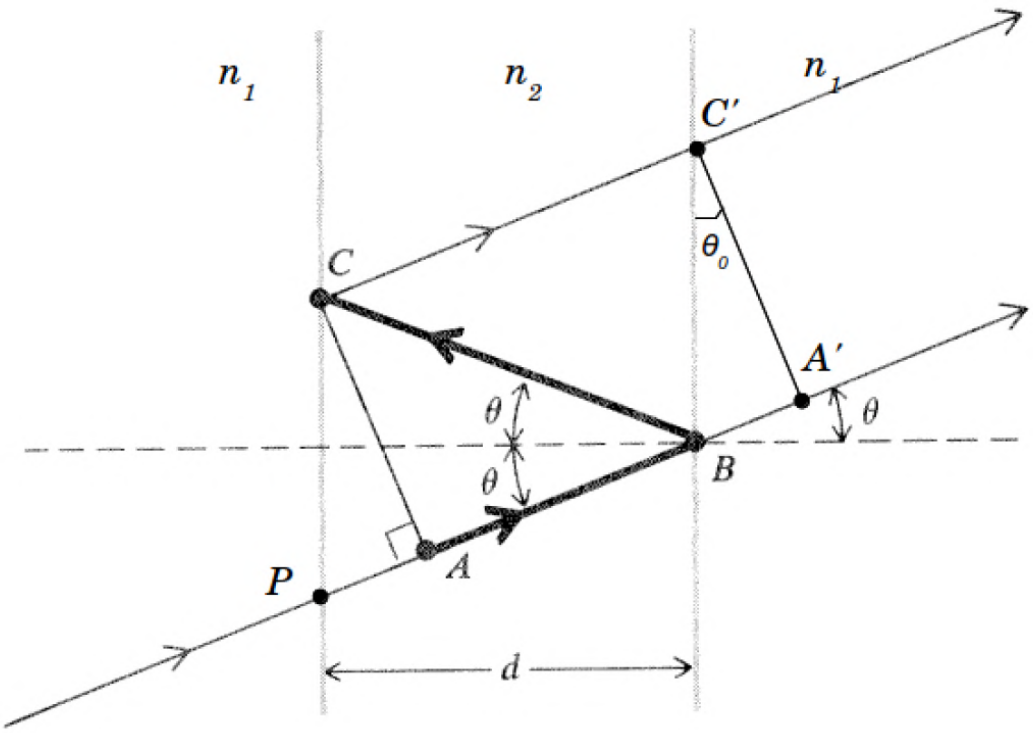

Figure 3.3 – Difference of optical path between two successive waves (Fowles, 1989).

We can start analyzing the phase difference between two interfering waves. The difference of optical path is Δ; from Fig. 3.3 we can define the beam $PABA'$ and the beam $PABCC'$. If n_1 and n_2 are the refraction index inside and outside the plates respectively, then:

$$\Delta = n_2(\overline{BC} + \overline{CC'}) - n_1\overline{BA'} = 2n_2\overline{BC} - n_1BA' \tag{3.1}$$

where

$$sin\,\theta_0 = \frac{\overline{BA'}}{\overline{C'B}} = \frac{\overline{BA'}}{2\,dtan\theta} \quad and \quad cos\,\theta = \frac{d}{\overline{BC}}. \tag{3.2}$$

Factorizing and using the Snell relation, we finally obtain:

$$\Delta = \frac{2\,d}{cos\,\theta}n_2[1 - sin^2\theta] \;\Rightarrow\; \Delta = 2\,d\,n_2\,cos\,\theta, \tag{3.3}$$

where d is the separation between the two semi-reflecting plates and θ is the angle between a beam reflected internally and the normal surface. The phase difference δ taking into account Δ is:

$$\delta = \frac{2\,\pi}{\lambda_0}\,\Delta = \frac{4\,\pi}{\lambda_0}\,n_2\,d\,cos\,\theta, \tag{3.4}$$

where λ_0 is the wavelength in the vacuum.

Finally, taking this phase difference as a factor $e^{i\delta}$ and summing the amplitudes of the transmitted beams, we obtain the total amplitude E_T and the total transmitted intensity $I_T = |E_T|^2$:

$$E_T = E_0\,t^2 + E_0\,t^2\,r^2\,e^{i\delta} + ... = \frac{E_0 t^2}{1 - r^2 e^{i\delta}} \quad \Rightarrow \quad I_T = I_0 \frac{|t|^4}{|1 - r^2 e^{i\delta}|^2}. \tag{3.5}$$

However, a phase change could happen during the reflection ($\delta_r/2$), so in general r is a complex number $r = |r|e^{i\delta_r/2}$. We can denote R as the reflectancy and Θ as the transmitancy of a surface, in terms of r and t, so that $R = |r|^2 = rr*$ and $\Theta = |t|^2 = tt*$, where the asterisk denote the conjugated complex. The total transmitted intensity can be rewritten as follows:

$$I_T = I_0 \frac{\Theta^2}{|1 - R^2 e^{i(\delta - \delta_r)}|} = I_0 \frac{\Theta^2}{(1 - R^2)} \frac{1}{(1 + F sin^2(\frac{\delta - \delta_r}{2}))} \tag{3.6}$$

where F is called the contrast coefficient and it measures the intensity of the interference bands, and the last factor of Eq. 3.6 is called the Airy function $A(\delta - \delta_r)$, which measures the density of the transmitted flux (Fig 3.4):

$$F = \frac{4R}{(1 - R)^2} \quad ; \quad A(\delta - \delta_r) = \frac{1}{(1 - F sin^2(\frac{\delta - \delta_r}{2}))} \tag{3.7}$$

The condition for a maximal band is $(\delta - \delta_r)/2 = m\pi \;\Rightarrow\; 2m\pi = (4\pi/\lambda_0)\,n\,d\,cos\,\theta + \delta_r$, where m is an integer known as the interference order, which is equivalent to the path difference, in wavelength, between two successive beams.

3.3.3 The Airy function

The Airy function $A(\delta - \delta_r)$ (Fig 3.4, Eq. 3.7) represents the distribution of flux density transmitted between two plates. The complementary function is $[1 - A]$. When $(\delta - \delta_r)/2 = \pi m$, the Airy function is equal to 1 for all the F (and therefore r) values. When such function is close to 1 , the density of transmitted flux is very small, except

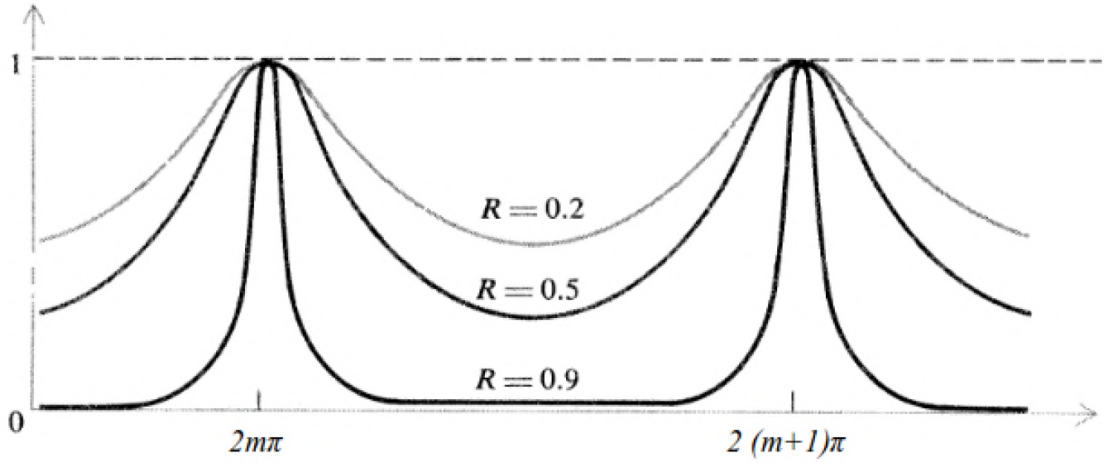

Figure 3.4 – The Airy function (Fowles, 1989) normalised to $A(\delta - \delta_r) = I_T / I_{T_{max}}$ as a function of the phase δ (X-axis) for different values of the reflectancy R.

into sharp maximums centered in $(\delta - \delta_r)/2 = \pi m$.

The Airy function depends on θ_t (transmission angle) and/or θ_i (incidence angle) due to its dependence with $\delta - \delta_r$. Each maximum of the density flux curve corresponds to a determined $\delta - \delta_r$ and a θ_i. In the case of flat parallel plates, the transmitted bands will consist instead in a series of bright rings on a almost black background, while the reflected bands will consist in narrow dark bands on an almost homogeneous bright background. In the case of monochromatic beams inciting on the plates (not mattering θ_i), the Airy function describes a parabolic surface (Bland & Tully, 1989).

3.4 The Fabry-Perot fundamental relations

The interferometer implements interference of multiple beams. It is used for measurements of wavelengths with high precision and for the study of the fine structure of spectral lines. A Fabry-Perot interferometer is composed by two parallel transparent plates with flat surfaces, separated by a distance d. The internal surfaces are covered by a high-reflectancy coating. The large number of interfering beams produces an interferometer with a very high spectral resolution. The plates can be fixed (étalon Fabry-Perot) or vary the separation between them (scanning Fabry-Perot).

The interferometer is mounted in general between a collimation lens and a focal lens as showed in Fig. 3.5. If an extended source of light is used, the waves coming from the source suffer multiple reflections between the plates, and this reflections are recollected by the focal lens making them to coincide in a "screen". The interference rings appears in a concentric way in the focal plane of the focal lens. Each ring corresponds to a

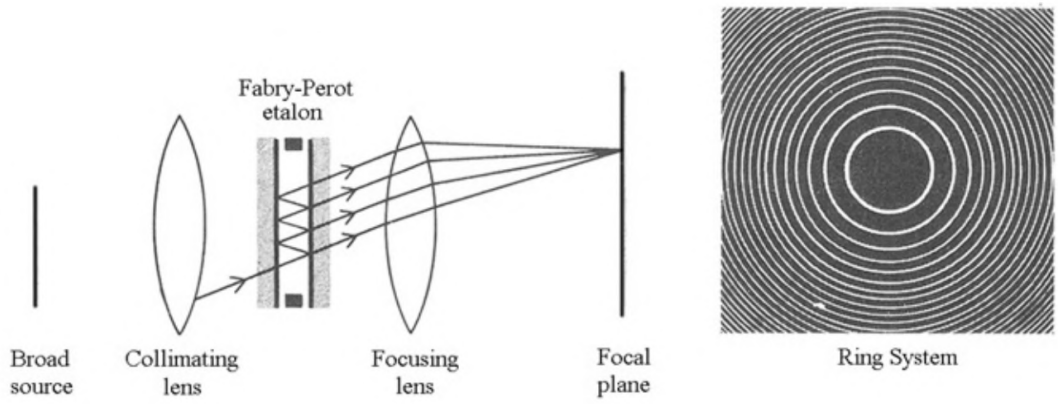

Figure 3.5 – The scanning Fabry-Perot interferometer (Fowles, 1989). The distance between the plates varies in order to let transmit different wavelengths to the focal plane. After multiple interferences, the beams are collimated onto the focal plane as concentric rings, where the central ring corresponds to the biggest m value which decreases as rings are more external.

constant value θ_i. The condition to obtain an interference maximum is:

$$2n_2\, d\, cos\, \theta_i = m\, \lambda_0. \tag{3.8}$$

where d is the distance between the plates, and m is the interference order (an integer) which is equivalent to the path difference between two successive beams. The Free Spectral Range (FSR) of the Fabry-Perot is defined as the separation between contiguous interference orders. This parameter corresponds to the maximum difference in wavelength that the interferometer is able to measure without ambiguity; if two wavelengths are separated by a bigger interval than the FSR, we will obtain an incorrect result when measuring the $\delta - \delta_r$ between them. The FSR corresponds, in terms of $\delta - \delta_r$ and the frequency, to:

$$(\delta - \delta_r)_{m+1} - (\delta - \delta_r)_m = 2\pi \quad \Rightarrow \quad \nu_{m+1} - \nu_m = \frac{c}{2n_2\, d\, cos\, \theta_i}, \tag{3.9}$$

and in the cases where θ_i is small, then $cos\, \theta_i \sim 1$.

The Finesse F_R is a measurement of sharpness of the interference rings and is measured experimentally by the ratio of the FSR to the full width at half maximum (FWHM) of the transmission profile:

$$F_R = \frac{\pi}{2} F^{1/2} = \pi \frac{R^{1/2}}{1 - R}. \tag{3.10}$$

The spectral resolving power of the Fabry-Perot is given by:

$$R_P = \frac{\lambda}{|\delta\lambda|} = mF_R. \tag{3.11}$$

3.4.1 Scanning Fabry-Perot interferometer

In a scanning Fabry-Perot interferometer, the transmitted wavelength depends on the separation d between the plates:

$$\lambda_{trans} = \frac{2nd}{m} \tag{3.12}$$

As mentioned before, for a monochromatic source, the Airy function describes a parabolic surface. When the light is not monochromatic, we obtain a series of concentric paraboloids depending either on d or θ_i.

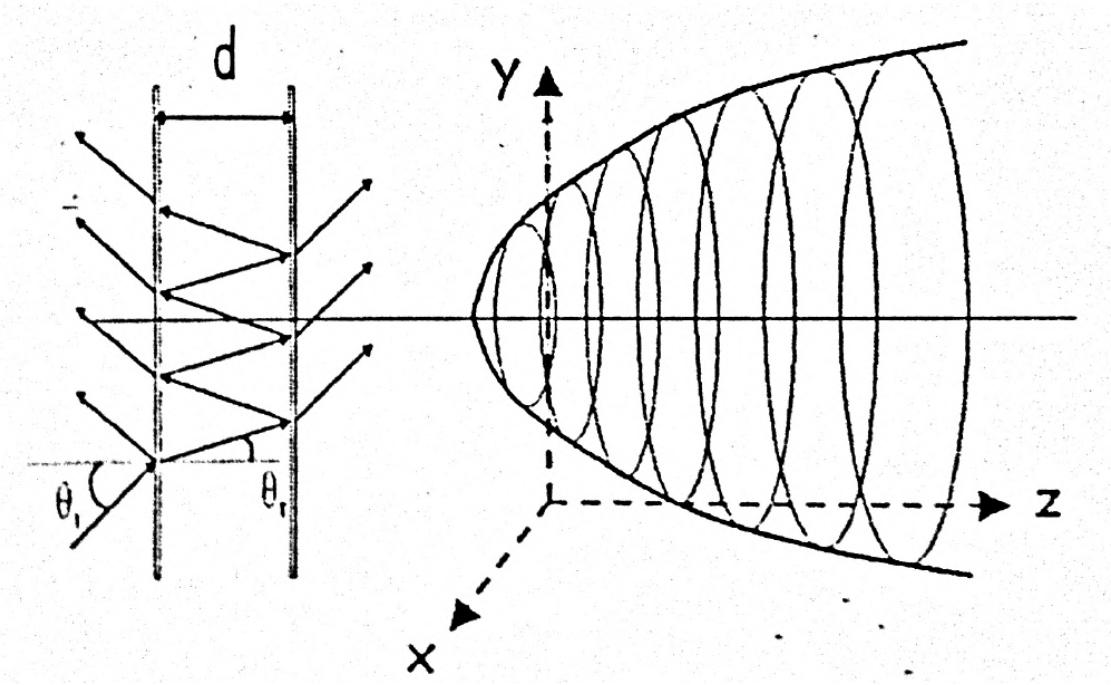

Figure 3.6 – Paraboloid described by the Airy function maximal transmissivity for a constant wavelength (Fuentes-Carrera et al., 2003). Each ring corresponds to an order m.

If we define z as a variable which is related to the plates separation as $d(z) = d(z_0)+bz$, where b is an arbitrary constant and z_0 denotes a z value on the optical axes, so that $m\lambda = 2nd(z_0)$, the Airy function describes a paraboloid for a constant λ (Bland & Tully, 1989) which depends on the θ_i (Fig. 3.6). This paraboloid is given by $z = z_0 + K_z r^2$ where r is the radius between the optical axes of the instrument and a given pixel and K_z is the "radius-quadrant" relation (Atherton et al., 1982; Bland et al., 1987) defined as $K_z = (m/2)\Delta z_0(p_\mu^2/f_{cam}^2)$ where p_μ is the pixel size and f_{cam} the focal length of the camera.

For the light coming from a galaxy and passing through the interferometer plates, for each scanned d one galaxy image is taken. These images are saved as a "datacube" with coordinates (x, y, z). The (x,y) coordinates are the spatial coordinates of the sky, and the z coordinate is related to d which is related to the λ passing through the plates. The (x,y) plane is called a "channel" of the datacube. For each pixel of the datacube, an emission profile is obtained (Fig. 3.7).

Each channel of the datacube does not correspond to the same λ, since for a d between the plates, the λ passing through depends on θ_i too. Because of that, in order to obtain a certain λ per channel, it is necessary to calibrate the datacube considering a calibration cube obtained from a monochromatic source; in this way, the paraboloid shape for a given λ is determined and the differences due to θ_i can be corrected in the datacube.

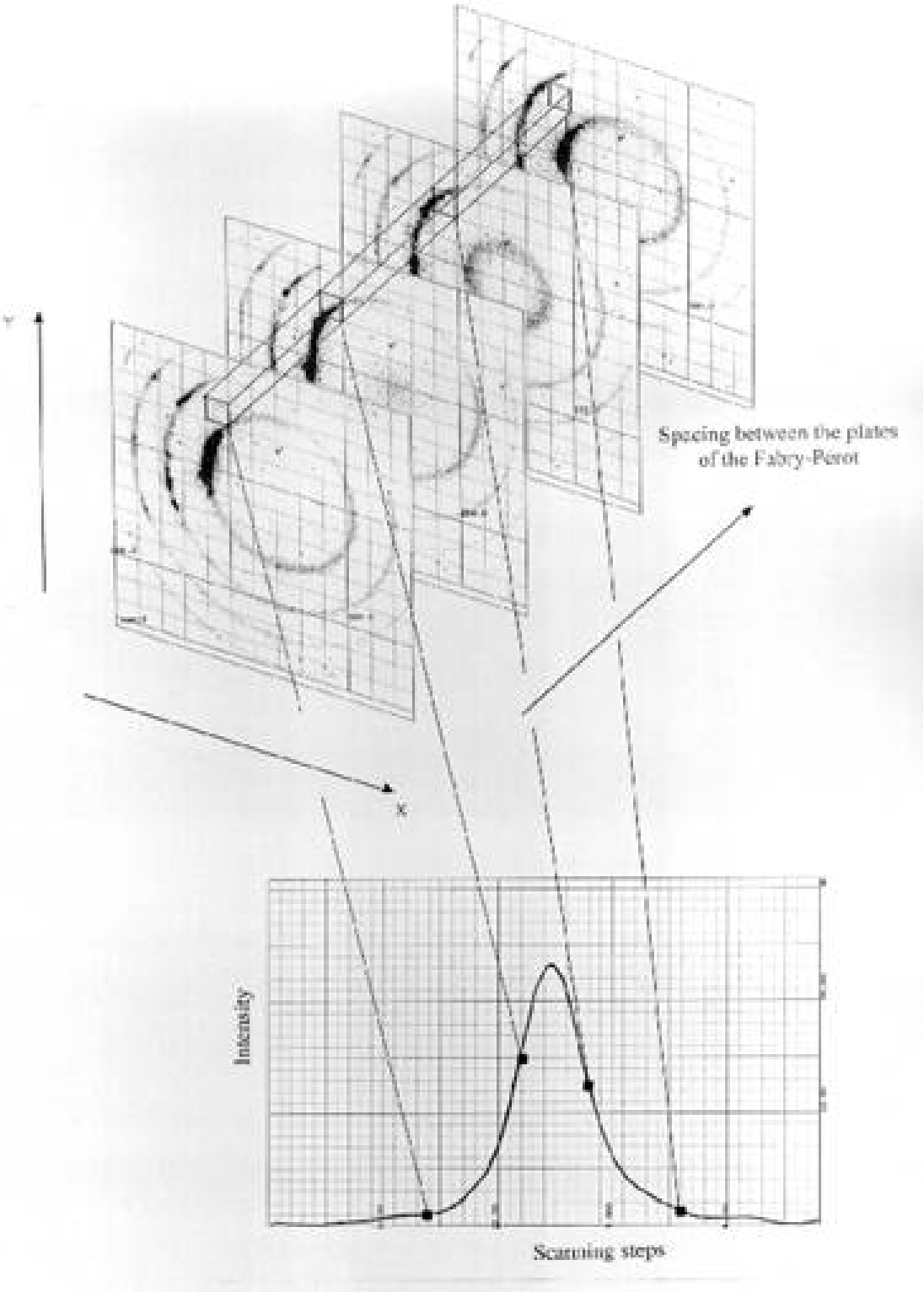

Figure 3.7 – Datacube obtained by a scanning Fabry-Perot interferometer (Fuentes-Carrera et al., 2003). For each pixel, an emission profile is obtained according to the flux detected in each channel.

4 Hα kinematic survey of the HRS

Hydrogen recombination lines are present in HII regions where the temperature of gas reaches 10000 K. The hydrogen atom is photoionised by the strong FUV radiation produced by O-B stars (effective temperature between 25000 K – 50000 K and $M_{star} > 10\,M_{\odot}$) with a maximum lifetime of $\sim 10^7$ Myr, thus indicating a recent star formation process. The Hα line (6563Å) is the most intense of the Balmer lines and more intense than other emission lines in the optical domain, therefore ideal for radial velocity measurements in galaxies and recovering the diffuse gas emission (Epinat et al., 2008b).

Out of the 261 HRS late-type objects, 40 galaxies (15.33% of the star-forming survey) had already been observed with Fabry-Perot techniques and the datacubes were already published during the following Fabry-Perot surveys of nearby galaxies: GHASP (Garrido et al., 2005, Epinat et al., 2008b,a), GHASP/SINGS (Daigle et al., 2006a), Virgo cluster (Chemin et al., 2006) and Loose Groups (Marino et al., 2013). These data are already available in the LAM Fabry-Perot webpage database http://cesam.lam.fr/fabryperot/.

During my PhD, we have observed 221 galaxies and then completed an Hα Fabry-Perot dataset for all the HRS star-forming sample through coordinated campaings started on winter 2015 and finished on summer 2019 carried out by an international collaboration between LAM at the Observatoire de Haute Provence (OHP) in France, and UNAM at the Observatorio Astronómico Nacional de San Pedro Mártir (SPM) in Mexico. In summary, we spent 107 observing nights at OHP and 59 nights at SPM to complete the HRS kinematic survey. Each galaxy was observed with a typical exposure of 2 hours in order to get, after Voronoi binning, a Signal-to-Noise ratio (S/N) > 7. The new data will be available in fall 2019 on the HRS dedicated webpage https://hedam.lam.fr/HRS/ and the FP database http://cesam.lam.fr/fabryperot/.

We will describe in this section the features of the instruments used during the observations, the data reduction and analysis, and the paper(s) (accepted, submitted, in prep.) presenting the HRS Fabry-Perot kinematic survey.

4.1 HRS galaxies observed at OHP

4.1.1 Scanning Fabry-Perot GHASP

The instrument GHASP, extensively described in the GHASP survey publications and in the Paper I of this PhD project (Subsection 4.1.3), is composed by a focal reducer (collimator + camera) coupled to a scanning Fabry-Perot interferometer with a QueensGate constant of 9.15. The instrument and camera are constantly cooled in order to avoid humidity into the piezoelectric control and the overheating of the camera. GHASP covers a Field of View (FoV) of 5.8'×5.8' with a pixelsize of 0.68'×0.68" for an image of 1024×1024 pixels. The interference order of the instrument is 798 for Hα with an Image Photon Counting System (IPCS, Gach et al., 2002) detector of a Free Spectral Range (FSR) of 8.24 (376 km s^{-1}) and a spectral resolution of 0.26Å (10 km s^{-1}); the effective finesse is 12. A typical exposure for a galaxy is ~2 hours scanning 32 or 48 channels, with a detection limit of ~2.5×10^{-17} erg s^{-1} cm^{-2} arcsec^{-2}.

The instrument is controlled by a Windows-based software (nIPCS), in order to control the filter wheel, indicate the number of channels to be scanned, the exposure time, spatial pixel binning (usually 4×4 pixels = 1.19"×1.19"), number of cycles (i.e. 1 cycle of 32 channels where each channel is scanned during 10 seconds has a total exposure of ~5.33 minutes), among others.

4.1.2 Observation, data reduction and analysis

Fabry-Perot observations were carried out from 2015 to 2019 for 177 objects (67.82% of the HRS star-forming sample) at OHP using GHASP instrument. 10 different narrow band filters with FWHM=15 were used to cover a spectral range from 6555 to 6655, representing a velocity amplitude of ~4600 km s^{-1}. All the galaxies were observed in general in good photometrical conditions, with a seeing of ~2". A neon lamp and a filter centered at 6598 were used to obtain the calibration cubes.

The observation outputs are ".ADA files" which contain the frames got by the IPCS. Data reduction was done using the IDL-based softwares *reducWizard* and *computeeverything* as in previous GHASP survey publications, specially designed to correct, sort and merge the ".ADA" files. The different momenta of the data were computed, as well as the integrated Hα profiles, kinematical models and rotation curves for each galaxy. In order to take into account the Line Spread Function (LSF) of the instrument, we computed the different "momenta" of the calibration cubes; then, we calculated the mean dispersion of these "momenta" (FWHM$_{inst}$ ~33 km s^{-1}, σ_{inst} ~14 km s^{-1}) and we did a Root Squared Difference (RSD) between the velocity dispersion maps of the galaxies and the mean dispersion of the instrument as follows:

$$\sigma_{pix_{corr}}(km\,s^{-1}) = \sqrt{(\sigma_{pix}(km\,s^{-1}))^2 - (\sigma_{inst}(km\,s^{-1}))^2} \tag{4.1}$$

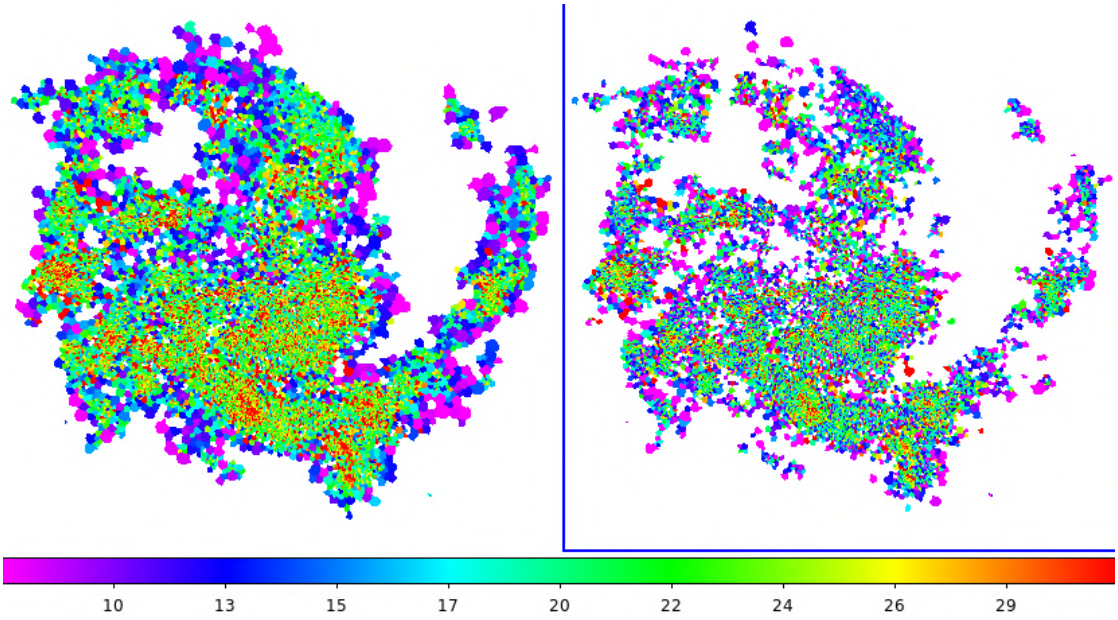

Figure 4.1 – Velocity dispersion field of the galaxy NGC 4254 after removing (left panel) and before removing (right panel) the instrumental contribution. Colorbar units are in km s^{-1}.

removing in this way the contribution due to the instrument (Fig. 4.1).

Further details about the observations and data reduction are extensively described in the Paper I of this PhD project (Subsection 4.1.3).

4.1.3 Paper I: An Hα kinematic survey of the *Herschel* Reference Survey – I. Fabry-Perot observations with the 1.93m telescope at OHP

This is the first of a serie of publications called "An Hα kinematic survey of the *Herschel* Reference Survey–". This paper presents the observations and data reduction for 152 late-type galaxies observed at OHP. Different kinematical parameters, momenta, integrated fluxes, individual comments, as well as the rotation curves were obtained/computed/done/written for these galaxies. The Appendix displays the totality of the different figures obtained for each galaxy. We used the Tully-Fisher relationship to test whether the HRS is well representative of other larger samples in the literature, obtaining a positive and consistent result. The HRS is the only one survey where the stellar an baryonic mass can be very accurately measured/computed, thus we took advantage of the high quality of our kinematical data to trace, with an unprecedented precision, the relation between the baryonic and dynamical mass of

a representative sample of the local universe, having very good agreement with the literature (observations, semi-analytic models and hydrodinamical simulations of galaxy evolution in a ΛCDM context). And for the very first time, a stellar, baryonic and dynamical "main sequence" was traced, obtaining similar results between slopes and intrinsic scatters.

Astronomy & Astrophysics manuscript no. JAGL_aa_V_2.0
August 29, 2019

An Hα kinematic survey of the *Herschel* Reference Survey – I. Fabry-Perot observations with the 1.93m telescope at OHP*.

Gómez-López, J. A.[1]**, Amram, P.[1], Epinat, B.[1], Boselli, A.[1], Rosado, M.[2], Marcelin, M.[1], Boissier, S.[1], Gach, J.-L.[1], Sánchez-Cruces, M.[1], and Sardaneta, M. M.[1]

[1] Aix Marseille Univ, CNRS, CNES, LAM, Marseille, France. e-mail: jesus.gomez-lopez@lam.fr, philippe.amram@lam.fr, benoit.epinat@lam.fr, alessandro.boselli@lam.fr, michel.marcelin@lam.fr, monica.sanchez-cruces@lam.fr, minerva.munoz@lam.fr
[2] Instituto de Astronomía, Universidad Nacional Autonoma de México (UNAM), Apdo. Postal 70-264, 04510, Mexico City, Mexico. e-mail: margarit@astro.unam.mx

Received May 10, 2019; accepted August 22, 2019

ABSTRACT

Aims. We present new 2D high resolution Fabry-Perot spectroscopic observations of 152 star-forming galaxies which are part of the *Herschel* Reference Survey (HRS), a complete *K*-band selected, volume-limited sample of nearby galaxies, spanning a wide range in stellar mass and morphological type.
Methods. Using improved data reduction techniques that provide adaptive binning based on Voronoi tessellation, using large field-of-view observations, we derive high spectral resolution (R>10,000) Hα datacubes from which we compute Hα maps and radial 2D velocity fields that are based on several thousand independent measurements. A robust method based on such fields allows us to accurately compute rotation curves and kinematical parameters, for which uncertainties are calculated using a method based on the power spectrum of the residual velocity fields.
Results. We check the consistency of the rotation curves by comparing our maximum rotational velocities to those derived from HI data, and computing the *i*-band, NIR, stellar and baryonic Tully-Fisher relations. We use this set of kinematical data combined to those available at other frequencies to study for the first time the relation between the dynamical and the total baryonic mass (stars, atomic and molecular gas, metals and dust), and derive the baryonic and dynamical main sequence on a representative sample of the local universe.

Key words. Galaxies: fundamental parameters – Galaxies: kinematics and dynamics – Galaxies: spiral – Galaxies: general – Galaxies: statistics – Galaxies: evolution.

1. Introduction

One of the main processes regulating galaxy evolution is star formation. The gas located along the disc of spiral galaxies collapses inside molecular clouds to form stars following the Kennicutt-Schmidt law (Schmidt 1959; Kennicutt 1989). Besides enriching the Inter Stellar Medium (*ISM*) with chemical elements, massive evolved stars and supernovae inject a large amount of kinetic energy into the *ISM* (van den Bosch 2000), driving the formation and evolution of new generations of stars. Finally, the star formation process affects also the Inter Galactic Medium (*IGM*, Boselli 2011).

We are still far from fully understanding the complexity of the star formation process. It is still unclear which mechanism triggers the collapse of the gas inside molecular clouds to form new stars; nowadays, this topic is still under debate. The kinematical properties in late-type galaxies seems to play a crucial role in triggering the star formation process, at large scales through the instability of the rotating disc (Toomre 1964, Larson 1992; Kennicutt 1998a,b; Tan 2000; Boissier et al. 2003) and the dynamical influence of the spiral arms (Wyse 1986; Tan 2000), while at small scales through turbulence (Wang & Silk 1994; Corbelli 2003; Leroy et al. 2008; Krumholz & McKee 2005; Krumholz et al. 2012; Elmegreen 2015).

The study of the relations between the star formation rate (SFR), the gas column density (Σ_{gas}), and the kinematical properties of galaxies on strong statistical basis would require a well representative sample having multifrequency resolved images and 2D-spectroscopic observations. The distribution of the atomic and molecular gas can be derived using HI and CO observations, while that of the star formation activity using direct tracers such as the Balmer Hα emission line or the UV emission, properly corrected for dust attenuation using for instance the far-infrared emission, or using SED fitting codes when multifrequency data are available.

The *Herschel* Reference Survey (HRS, Boselli et al. 2010) is a complete sample of 323 nearby galaxies defined with the purpose of studying the relation between the star formation process and the different components of the interstellar medium (ISM). This sample has been observed at all frequencies to provide the community with the largest possible set of homogeneous data. This unique dataset includes photometric data in the UV and in the optical bands (Cortese et al. 2012; Boselli et al. 2011, Ferrarese et al. 2012), in the mid- and far-IR (Ciesla et al. 2012; Cortese et al. 2014b; Bendo et al. 2012; Ciesla et al. 2014), and in the Hα line(Boselli et al. 2015).

* Based on observations collected at the Observatoire de Haute Provence (OHP) (France), operated by the CNRS.
** Alternative e-mail: jagl.c06@gmail.com

Spectroscopic data are also avalibale in the visible (Boselli et al. 2013, Gavazzi et al. 2004, 2018) and in the radio at 21 cm (HI) and at 2.6 mm (CO) (Boselli et al. 2014a).

Two-dimensional kinematical data are however still lacking. For this purpose, we are undertaking an Hα kinematic survey of the HRS star-forming galaxies using Fabry-Perot interferometry. This technique is perfectly adapted for this sample since it allows to gather, using typical integration times of ~2 hours per galaxy and a 2m-class telescope, seeing-limited (~2 arcsec) datacubes of galaxies, within a large field-of-view (FoV~5.8×5.8 arcmin^2), i.e. surrounding by their nearby environment, with high a spectral resolution ($R > 10,000$). The large FoV allows to get high resolution Hα spectra for hundreds to thousands independent spatial elements.

This paper presents new Fabry-Perot data for 152 HRS star-forming galaxies gathered during 9 observing runs at the Observatoire de Haute Provence (OHP). These data are used to derive the kinematical properties of the ionised gas at high spatial and spectral resolution. Combining this new set of data with other Fabry-Perot data available in the literature we study the relation between the dynamical and the baryonic mass, this last directly measured using multifrequency observations. We also derive, for the first time in the literature, the dynamical mass main sequence for a representative sample of the local universe.

The paper is organised as follows. Section 2 describes the HRS sample, section 3 the observations and data reduction. In section 4 we derive the kinematical parameters. In section 5 we compare several kinematical scaling relations derived for the HRS with those proposed in the literature. The summary and conclusions are given in Section 6. All the data products, including comments on individual objects, are given in the different Appendices.

Consistently with our previous works, all the Fabry-Perot data will be made available on the HRS dedicated database HeDAM (`https://hedam.lam.fr/`), and on the Fabry-Perot database (`https://cesam.lam.fr/fabryperot`).

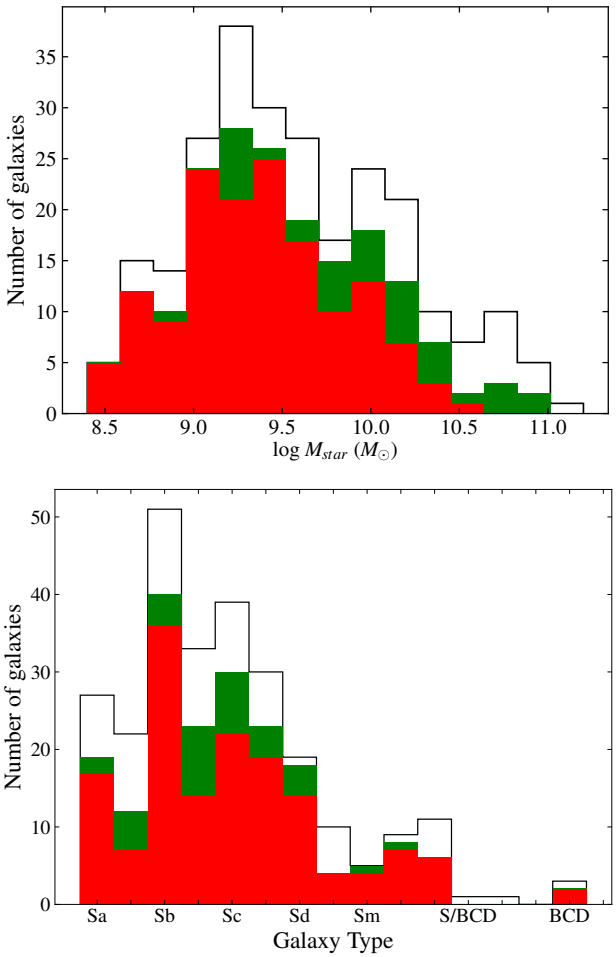

Fig. 1. Top panel: Histogram of the stellar mass distribution of the HRS star-forming sample. Bottom panel: Histogram of the galaxy type distribution. Out of the 261 galaxies (white histograms), 152 have been observed at the OHP and are presented in this work (red), while 40 observations are available in the literature (green).

2. The Sample

The *Herschel* Reference Survey (HRS) is a *K*-band-selected (where the *K*-band is a proxy of stellar mass, Gavazzi et al. 1996), volume-limited ($15 < D < 25$ Mpc) complete sample of 323 galaxies spanning a wide range in morphological type (from ellipticals to late-type spirals and irregulars) and stellar mass ($10^8 < M_{star} < 10^{11}$ M$_\odot$). The sample, which has been extensively presented in Boselli et al. (2010), includes galaxies belonging to different environments, from the Virgo cluster to isolated systems in the field. Out of the 323 galaxies of the sample, 261 objects are late-type systems, with an ongoing star formation activity, as indicated by their strong Balmer line emission (Boselli et al. 2015). These late-type systems are thus adapted targets for a kinematical survey of the ionised gas using a Fabry-Perot interferometer. Thanks to its statistical completeness, the HRS is becoming the ideal reference for local and high-redshift studies as well as for models and simulations. It is thus a tailored sample for tracing the kinematical scaling relation of a complete sample of nearby galaxies.

In this work we present new Fabry-Perot data for 152 star forming galaxies observed at the OHP (see Table E.1). Fabry-Perot are also available in the literature for other 40 galaxies from the following references: GHASP (Garrido et al. 2005; Epinat et al. 2008b), SINGS (Daigle et al. 2006a), Virgo cluster (Chemin et al. 2006), and Loose Groups (Marino et al. 2013). So far, Fabry-Perot data are thus available for 192 out of the 261 star-forming galaxies of the sample (73.6% complete). Figure 1 compares the distribution in morphology and stellar masses (taken from Cortese et al. 2012) of the HRS galaxies to the Fabry-Perot dataset presented in this paper and available from the literature. This figure shows that the available kinematical data constitue a representative subsample of the HRS, suitable for statistical studies, since they already include a large number of galaxies spanning a wide range in morphological type and stellar mass.

3. Observations and Data Reduction

Fabry-Perot observations scanning the Hα emission line of 152 late-type galaxies have been obtained along 91 nights at the OHP (9 runs from February 2016 to April 2018). The observations have been carried out in good photometric conditions and with a typical integration time of 2 hours per galaxy. The journal of the observations is given in Table E.2.

3.1. GHASP Instrumental Setup

Fabry-Perot observations provide datacubes with dimensions x (right ascension α), y (declination δ) and z (wavelength λ), containing Hα profiles for each pixel along the field-of-view (FoV). The instrument we use at OHP is GHASP, a focal reducer containing a scanning Fabry-Perot interferometer attached at the Cassegrain focus of the 1.93m telescope. The principles and characteristics of the GHASP instrument are extensively explained in Garrido et al. (2002, 2003, 2004, 2005) and Epinat et al. (2008b). The focal reducer has an aperture ratio of $f/3.9$, with a FoV of ≃5.9×5.9 arcmin in a 512×512 pixels window with a pixel size of ≃0.69 arcsec/pix. The angular resolution is limited by the seeing, typically ranging between ≃1.5 and ≃3 arcsec. The interference order of the Fabry-Perot interferometer we used is 798 at Hα rest wavelength, giving a free spectral range (FSR) of 376 km s^{-1}, reaching a spectral resolution of R ≃10,000 (velocity sampling ≃10 km.s^{-1} for a resolution of ≃30 km.s^{-1}). The pattern of interference rings varies along the FoV when the separation of the plates is changed by applying different voltage on the piezoelectric actuators. Because of that, the wavelength varies according to the position on the FoV, so we must calibrate the Hα profiles for each pixel by comparing them with reference profiles given by a monochromatic source such as a neon lamp (6598.95 Å) in order to give the same wavelength origin (or phase) to all the pixels and associate a specific wavelength to each spectral channel. Two calibration cubes are taken, one before and one after each galaxy exposure, to account for flexion conditions and temperature variations.

The detector, an Image Photon Counting System (IPCS), has the significant advantage of zero readout noise and enables to scan the interferometer quickly, taking 10s per scanning step, typically 32 (for 146 galaxies) or 48 channels (for 6 galaxies) to cover the whole FSR, so that we can repeat the FSR scanning many times (or cycles) and then add up the successive exposures, enabling to greatly reduce the effects of variation in atmospheric transmission and to correct any eventual telescope drift in a very efficient manner.

To cover the Hα line in the range 6565Å to 6635Å, we use seven different interference filters having a typical FWHM ~15Å, allowing to scan the isolated Hα line of ionised hydrogen (6562.78Å) and rejecting other emission lines (e.g. [NII] contaminating contribution) as well as the sky background emission (mainly OH lines). If necessary, we tilt by a couple of degrees the corresponding filter to blue shift the central wavelength of the transmitivity peak the closest to the systemic velocity (V_{sys}) of the corresponding galaxy, as indicated in Table E.2.

3.2. Comparison With Other Integral Field Spectrographs

The gain in FoV is significant with respect to other seeing-limited IFS instruments; e.g. CALIFA (Sánchez et al. 2012), MaNGA (Bundy et al. 2015), SAMI (Bryant et al. 2015) and MUSE (Bacon et al. 2017) have a FoV~1.30×1.30, 0.20×0.20 or 0.53×0.53, 0.25×0.25, and 1.0×1.0 arcmin[2] respectively. The large FoV of our instrument enables to cover the galaxies of the HRS up to their optical limit r_{opt}[1] , ranging from 0.16 to 2.55 arcmin, with a mean/median value of 1.08/0.99 arcmin. In terms of effective radius r_{eff}, r_{opt} spans from 1.47 to 4.26 r_{eff}, with a mean spatial coverage of 2.56±0.59 r_{eff}. The mean/median radius reached in HRS sample is nevertheless smaller than the mean/median one in the GHASP sample (Epinat et al. 2008a,b), this is due to the galaxy environment. Galaxies in the GHASP sample are mainly located in an isolated environment while 25.8% galaxies of our HRS sample are situated at a projected distance smaller that 3.4 Mpc from the Virgo center and are furthermore potentially affected by environmental effects (ram pressure stripping, tidal stripping, quenching, etc.).

In order to quantify the spatial coverage of our observations, for each galaxy, we compute the number of independent seeing elements, hereafter refereed as N_{beams}. N_{beams} is the total number of pixels covering a galaxy with a signal-to-noise ratio per bin>7 (see next paragraph) divided by the number of pixels per seeing element, for each observation. N_{beams} are listed in Table E.3, they range from 66 to 21153 with a mean/median value of 3138/2066. For comparison, the half of the FoV[2] of CALIFA, MaNGA and SAMI gives N_{beams} equal to 234, 75 and 33, respectively.

Within a narrow spectral domain around Hα, the gain in spectral resolution R is also significant with respect to other IFS instruments: CALIFA (R~850-1650), MaNGA (R~2000), SAMI (from R~1700 to R~4500), MUSE (R~3000). This allows to study the kinematics down to the scale of single HII regions (σ ≃30 km.s^{-1}, Boselli et al. 2010).

3.3. Data reduction

The Fabry-Perot data reduction procedure[3] basically follows the same used in Daigle et al. (2006b) and in Epinat et al. (2008b). The reduction procedure consists of:

i) Obtaining the phase map. Such a map is computed from the rings of calibration cubes. The consistency of both calibrations is checked and the phase is calculated by averaging the two calibration exposures. The phase map gives the reference scanning channel as origin wavelength for the spectrum of each pixel.

ii) Sorting and merging the data. This is done by removing strong variations in atmospheric transmission by comparing the recorded successive individual frames of the observations. Those frames having an inconsistent flux compared with the median flux are deleted and replaced by frames of adjacent cycles automatically.

iii) Correcting from any telescope drift and/or instrumental flexures along the different successive frames by using reference stars or bright HII regions. According to subsection 3.1, the wavelength varies with the position across the FoV, thus this correction from telescope drift implies a phase correction for each cycle (i.e. each ≃5 or 8 minutes for 32 or 48 scanning channels per cycle respectively).

iv) Obtaining wavelength calibrated cubes. The latter is done by calibrating the interference rings of the galaxy observation by using the phase map. The same wavelength origin is assigned for each pixel.

[1] The definition we adopt in this work for r_{opt} is given in section 4.1.7.

[2] In order to make a rough approximation, we estimate for those instruments that, in average, half of the spaxels gives a spectrum with an acceptable signal-to-noise ratio.

[3] The Fabry-Perot data reduction pipeline is composed by the IDL based program *computeeverything* and *reducWizard* interface, both of them available on websites `https://projets.lam.fr/projects/computeeverything` and `https://projets.lam.fr/projects/fpreducwizard`, respectively.

v) Performing a one-spectral-element Hanning smoothing of the spectrum which preserves the flux.

vi) Subtracting night skylines. The data cube is divided into sky-dominated and galaxy-dominated regions. Then a sky cube is built by fitting the sky dominated regions (polynomial fitting of 2^{nd} order in our case) and then making an interpolation of the sky spectrum on the galaxy-dominated regions. Such a sky cube is finally subtracted.

vii) Eventually, suppressing ghosts due to reflection at the interfaces air/glass of the interferometer when necessary.

viii) Computing the astrometry to find the correct World Coordinate System for each galaxy dataset, making use of XDSS *R*-band images. This is done using *KOORDS* routine of *KARMA*[4] (Gooch 1996) by a systematic comparison between field stars that are present in both the broad-band XDSS images and our continuum images.

ix) Data processing of adaptive spatial binning based on Voronoi tesselation on the data. The latter preserves the spatial resolution of bright regions while the weak emission of diffuse gas areas is recovered. Due to the small ratio between the number of channels containing continuum and the channels containing the emission line, the criterion used for GHASP data relies on an estimate of the signal-to-noise ratio as the square root of the flux in the line, which is a simple estimation of the Poisson noise at the line flux. We aim to recover a signal-to-noise ratio≥ 7 per spatial bin. Two kind of maps are generated: the binned maps with *N* independent bins, where all the pixels belonging to each bin are affected to the same value and the bin-centroid maps, for which only one pixel per bin corresponding bin-centroid position, contains a value (the other pixels being set to NaN). Those later maps are the ones that are used in practice, in order to provide the same statistical weight to each bin and not to each pixel.

x) Computation of the different momenta maps (flux, radial velocity, radial velocity dispersion, continuum).

xi) FSR corrections on velocity fields, since some Hα profiles present FSR overlaps causing velocity jumps at some pixels.

xii) The semi-automatic cleaning system of the velocity fields in order to delimitate the outskirts of the galaxy where there is no more Hα emission. The latter is done by a continuity velocity process on the velocity field, based on a cut-off value between contiguous velocity bins (typically ∼30 km s^{-1} for a velocity field with an amplitude of ∼300 km s^{-1}). Regions with too low emission and very large bins are also discarded and thus masked.

xiii) Correction of the velocity dispersion from the Line Spread Function (LSF) broadening. This is done by a quadratic difference between the velocity dispersion values of the observation maps and the mean dispersion due to the instrumental contribution.

3.4. Flux Calibration and Hα Profiles

During the OHP runs, in order to maximize the observing time on the galaxies themselves, we do not observe flux calibration sources but we use instead the high quality Hα photometry, available for the whole HRS sample (Boselli et al. 2015). Thus we perform an indirect calibration of the total Hα flux for the 152 datacubes in a similar way as in Epinat et al. (2008a), but using in our case the calibrated fluxes from Boselli et al. (2015).

[4] *KARMA* tools package is available on website `https://www.atnf.csiro.au/computing/software/karma/`.

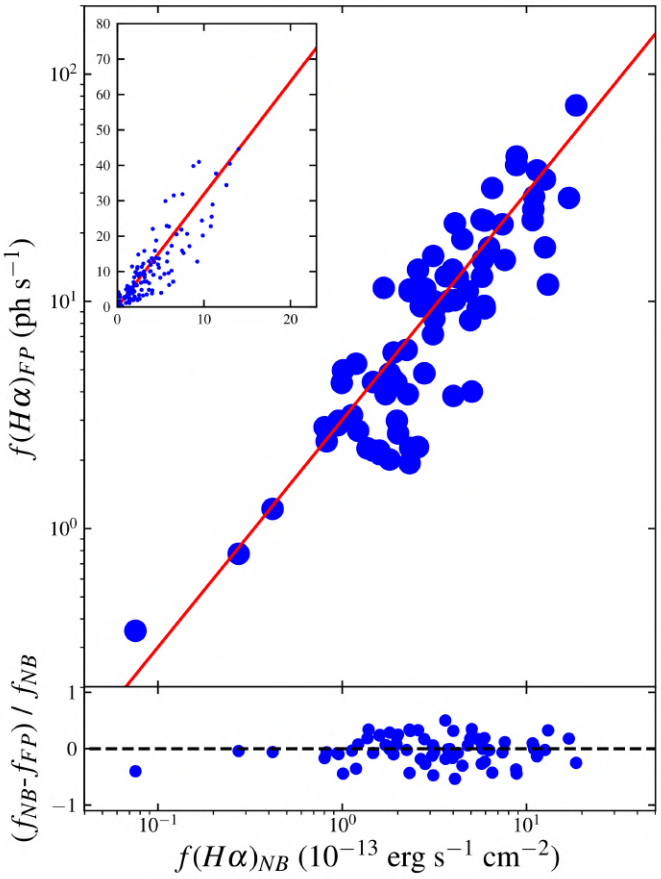

Fig. 2. Top panel (and top-left insert): Hα integrated fluxes measured by GHASP compared with Hα integrated fluxes from Boselli et al. (2015); the solid red line represents the OLS bisector linear regression on the data from which results our calibration; the insert at the top-left shows the same calibration plot but using a linear scale. Bottom panel: normalised residual values, where f_{NB} are fluxes from Boselli et al. (2015) and f_{FP} are GHASP calibrated fluxes.

We correct their Hα + [NII] fluxes for [NII] contamination (6584 and 6548 Å) using the [NII]/Hα ratio derived from spectroscopic observations (Boselli et al. 2013); for galaxies where there is no available [NII]/Hα ratio, we calculate it according to the $[NII]/H\alpha$ *vs* M_{star} relation in the *B*-band given in Boselli et al. (2009).

For each galaxy, the total Hα emission is computed by integrating the flux for each spatial element of the datacubes as described in Epinat et al. (2008a), taking into account:

i) the response of the instrument,
ii) the aperture of the instrument,
iii) the exposure time (given in Table E.2),
iv) using the velocity field to disentangle the FSR overlaps when necessary.
v) the shift of the interference filter spectral range due to the tilt (if any) and the temperature,
vi) the subtraction of the continuum contribution.

To minimize the foreground sky contamination, we only consider the spatial elements not masked in the final momenta maps (shown in Appendix D). The integrated Hα profiles per galaxy are shown in Appendix C.1. Figure 2 shows the

comparison between the Fabry-Perot fluxes and those from Boselli et al. (2015). The response of the GHASP camera being linear and since we are not comparing quantities having the same units, we use an Ordinary Least Squares (OLS) bisector linear regression, represented on the figure with a solid red line, to calibrate the Fabry-Perot Hα fluxes. The fit is forced to pass through the origin for obvious physical reasons; the calibration coefficient is 1 $ph\ s^{-1} = 0.50 \pm 0.05 \times 10^{-13}\ erg\ cm^{-2}\ s^{-1}$. The integrated fluxes estimated for each galaxy using our calibration are given in Table E.3.

We measure the sensitivity of our Fabry-Perot dataset using two methods. The first one consists in computing the detection limits from the isophotes of VESTIGE Hα narrow band images (Boselli et al. 2018b) for galaxies in common with the HRS, while the second method consists in calculating such limits directly on all our Hα monochromatic images using our estimated calibration. We find for each case a surface brightness detection limits of $\sim 2.5 \pm 0.2 \times 10^{-17}$ erg s^{-1} cm^{-2} arcsec^{-2} and $\sim 2.3 \pm 0.2 \times 10^{-17}$ erg s^{-1} cm^{-2} arcsec^{-2} for a typical 2 hours exposure time, thus comparable to the typical sensitivity of narrow-band imaging. This sensitivity is close to that reached by Epinat et al. (2008a) using similar integration times and predicted by Fig. 2 in Gach et al. (2002) for a signal-to-noise ratio between 1 and 2.

4. Data Analysis

4.1. Kinematical Models and Rotation Curves

4.1.1. Kinematical Models

Rotation curves are computed from the velocity fields following the method described in Epinat et al. (2008b), which is a synthesis adapted to Hα data between the angular sector method, tilted-ring models and the fitting method used by Barnes & Sellwood (2003). In 21cm-HI discs where warps are frequently observed at a distance from the center larger than the optical radius, the position angle (PA) and galaxy inclination (i) might vary as a function of the galacto-centric radius. Within the optical radius, the situation is different, as in Epinat et al. (2008b), we do not allow the PA nor i to vary because these variations are slight throughout the optical disc plane and due mainly to non-circular motions and velocity dispersion that behave as oscillations around a median value.

For each bin situated in the frame of the galactic plane of a disc, assuming that at first order the expansion velocity component and vertical motions are negligible, the velocity vector projected on the line-of-sight can be described as follows:

$$V_{obs}(r) = V_{sys} + V_{rot}(r)\ cos\,\theta\ sin\,i \quad (1)$$

where V_{sys} is the systemic velocity of the galaxy, i is the inclination, and r and θ are the polar coordinates in the plane of the galaxy, both measured from the PA, i and the kinematical center (α, δ) of the galaxy. $V_{rot}(r)$ is modeled assuming a four-parameters modified Zhao function (Epinat et al. 2008a) on the whole velocity field:

$$V_{rot}(r) = v_t \frac{(r/r_t)^g}{1 + (r/r_t)^a} \quad (2)$$

where v_t is the effective "turnover" velocity, r_t is the transition radius between the rising and flat part of the rotation curve g and a are coefficients that parametrise the sharpness of the turnover. This leads to a model of nine free parameters: four projection parameters (PA, i, galaxy center α and δ) and five kinematical parameters (V_{sys}, v_t, r_t, g, a). The model parameters are obtained with a χ^2 minimization based on the Levernberg-Marquardt method (Press et al. 1992), computing an iterative 3.5 σ clipping on the observed bin-centroid velocity field. The number of unknowns will depend on how many initial guess parameters are fixed or let as free for Eqs. 1 and 2: in our case, the galaxy center is carefully computed from the continuum image and always fixed; PA and/or i are taken from the literature and generally let as free or fixed in some cases (see subsection 4.2). These initial guesses of projection parameters are used to fit the modified Zhao function to the velocity field in order to obtain the V_{rot} starting parameters v_t, r_t, g and a, which are then let always as free.

4.1.2. Residual Velocity Fields

Since the kinematical models are calculated with a prior assumption that circular motions are dominant and those due to non-axisymetric perturbations are not part of a large scale pattern, the residual velocity field computed by subtracting the modeled velocity field to the original one reflects well the deviation from circular velocities. Since our model is simple, the resulting statistical uncertainties of kinematical parameters are too small. For that reason, the calculation of uncertainties is done by computing the power spectrum of the residual velocity fields and then considering several random phases, in order to compute residual fields that present the same kind of structure but placed differently. Through a Monte-Carlo method, we estimate robustly the standard deviations of the kinematical parameters over hundreds of simulated velocity fields (see Epinat et al. 2008a for details). For consistency with Epinat et al. (2008a) and with section 4.1.3, the residual velocities have been computed using the bin centroid maps.

4.1.3. Rotation Curves

Once the best set of parameters is derived using the method previously described, the rotation curve is extracted from the velocity field. Since the velocity field is decomposed into rings, we consider the bin centroid velocity fields in order to avoid any artificial oversampling of rings. We use n uncorrelated velocity bins per ring (or annulus) to provide each rotation velocity; n = 25 optimizes the compromise between the higher signal-to-noise ratio and the lower spatial resolution per ring (Epinat et al. 2008a). Rotation curves are computed without correction from the non-circular motions along the disc.

4.1.4. Quality Flags on the Rotation Curves

With the purpose of quantifying the quality of each rotation curve, we attribute a quality Flag using an automatic classification method extensively described in Appendix A, that goes from Flag “1" (accurate estimation of the rotation curve) to Flag “4" (poor estimation of the rotation curve), and attributing a supplementary Flag “A" and Flag “B", the latter corresponding to those peculiar cases leading to a non-realistic kinematical fitting such as the presence of a bar, asymmetries, high or low inclination, etc.

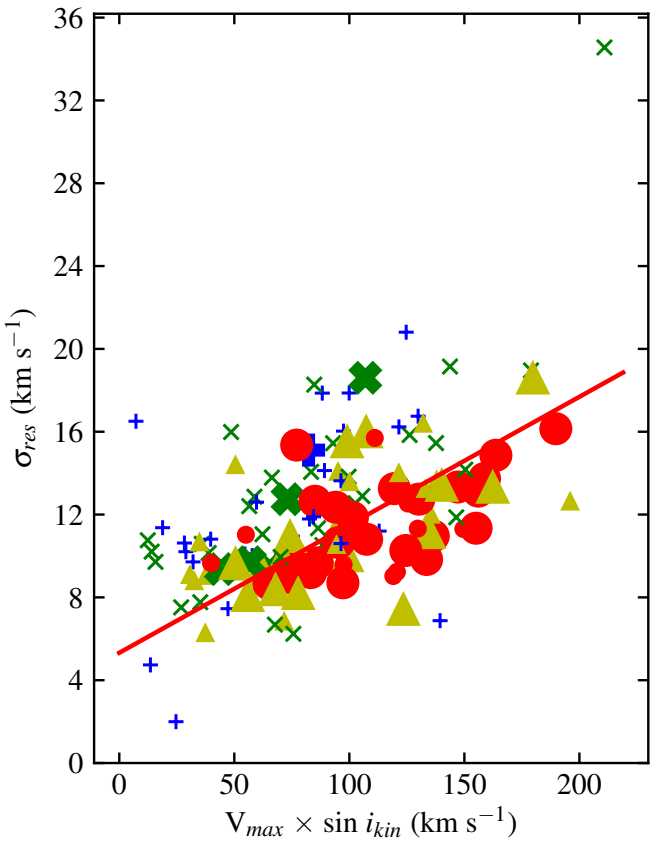

Fig. 3. Standard deviation of each residual velocity field as a function of the mean amplitude of the velocity field. The colors correspond to the different quality Flags: red dots are galaxies with Flag "1", yellow triangles are galaxies with Flag "2", green "x" symbols are galaxies with Flag "3" and blue "+" symbols are galaxies with Flag "4". The size of the symbols corresponds to the complementary Flag"A" (big symbols) and "B" (small symbols). The solid red line represents the bisector linear regression on the Flag "A" data.

For 11 cases over 152 (HRS 32, 35, 104, 136, 164, 184, 195, 249, 282, 291 and 300), characterised by a poor signal-to-noise ratio, the model does not match the rotation of the galaxy because of lack of Hα emission, thus no model is computed, neither residual velocity field nor rotation curve can be plotted, and no kinematical parameters can be calculated.

4.1.5. Quality Checks of the Residual Velocity Fields

For each residual velocity field, the average value ($\overline{Res}$) and the standard deviation of all the bins (σ_{res}) are computed (see Table E.3). Figure 3 displays, for the whole dataset, the correlation between σ_{res} (with a mean value ~12.6 ± 2.7 km s^{-1}, which is similar to the velocity of 13 km s^{-1}, computed in Epinat et al. 2008a) and the mean amplitude of the velocity field (which is the maximum rotation velocity V_{max}[5] multiplied by the *sin* i_{kin}). The bisector linear regression traces a trend which indicates that, in general, high velocity amplitude values are correlated with high σ_{res} values. Nevertheless, many points for which $V_{max} \times sin\ i_{kin} <$ 150 km s^{-1} are situated above the regression line, corresponding to galaxies with quality Flags "3-B" and "4-B", so that the distribution of such points with respect to the Y-axis seems to be related to the quality of the data and not to the line-of-sight velocity, thus resulting in a high σ_{res} value (i.e. the outlier with σ_{res} ~35 km s^{-1} is the galaxy HRS 59, an almost edge-on object with a chaotic rotation curve and flagged as "3-B"); these specific cases are extensively described in Appendix B. The correlation is in agreement with Epinat et al. (2008a) and Epinat et al. (2008b), and it does not depend on the galaxy type (Epinat et al. 2008a).

4.1.6. Maximum Rotation Velocity

In order to compute our Hα V_{max} without being perturbed by local variations in the rotation curves due for instance to crossing spiral arms, we fit the rotation curve with analytic functions, between $r = 0$ and r_{RC}, the radius corresponding to the last ring of the rotation curve. For this purpose, we select the Courteau profile (Courteau 1997). The original Courteau function describes the line-of-sight velocities from long-slit observations; because we are working with deprojected data, we used the following modified Courteau function:

$$v(r) = v_c \frac{\left(1 + \frac{r_t}{r}\right)^{\beta}}{\left(1 + \left(\frac{r_t}{r}\right)^{\gamma}\right)^{1/\gamma}} \quad (3)$$

where the four free parameters are v_c, the asymptotic velocity; r_t the transition radius between the rising and flat part of the rotation curve; β, the drop-off or steady rise of the outer part of the rotation curve and γ, the sharpness of turnover beyond the r_t radius. Because it does not affect much the result and decrease by one the degree of freedom, we used $\beta = 0$ as suggested by Courteau (1997). Furthermore, V_{max} is defined by the maximum rotation velocity reached by the fitted modified Courteau profile within the optical radius.The best fit is represented in Fig. 4 and Figures in Appendix D with a black solid curve that goes through the velocity points in each rotation curve.

It is important to mention that the choice of a given fitting function may introduce systematic biases in the estimation of V_{max}, particularly when extrapolations are necessary where data do not extent further enough at large radii. For instance, modified Zhao and Courteau profiles have four free parameters. A fair comparison of both functions should be done in reducing the degeneracy but in keeping the same number of free parameters, we furthermore set it at three; we fixed the parameters that have the weaker influence on the shape of the rotation curves, namely $g = 0$, for the modified Zhao function and $\beta = 0$ for the modified Courteau function. We conclude that this 3-parameters Zhao function is more sensitive to local oscillations that the 3-parameters Courteau one. In other words, when the modified Zhao function is used to extrapolate the rotation curves outside the last observing radius, V_{max} tends to follow the trend of the last data points rather than the general trend of the plateaus and, at the opposite, the modified Courteau function averages the mean trend of the whole outer rotation curves. In short, the modified Courteau function tends to extrapolate a flatter rotation curve and flatten local oscillation than the modified Zhao function and this have an impact on V_{max}. We choose the Courteau function because it provides a more conservative solution, as well as and for consistency with previous works on the GHASP sample.

Alternatively to Zhao and Courteau profiles used in this work, other analytic functions are used in the literature to fit

[5] Defined in paragraph 4.1.6

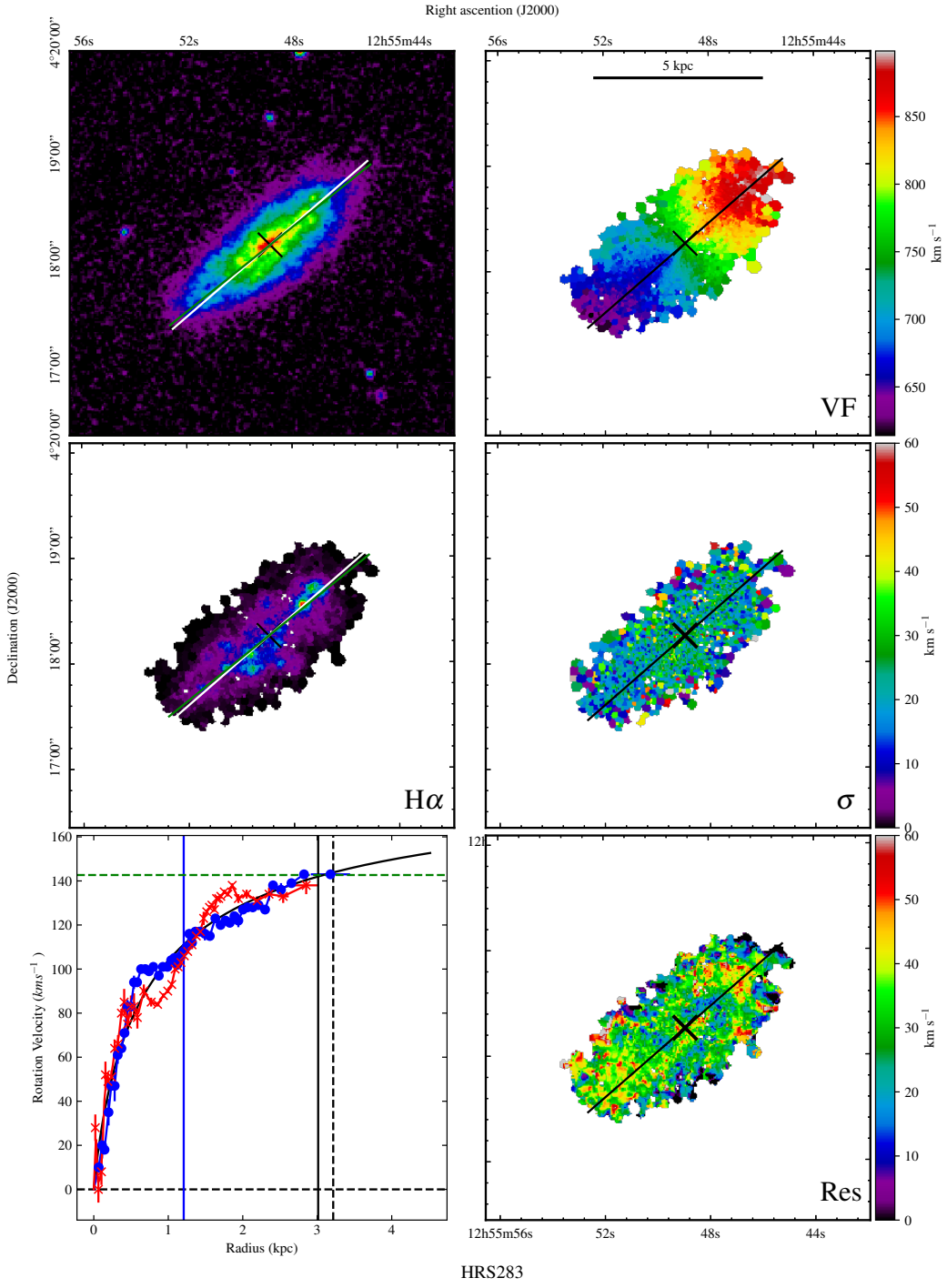

Fig. 4. Example of the products derived from Fabry-Perot observations. Top left: XDSS *R*-band image. Top right: Hα velocity field. Middle left: Hα monochromatic image. Middle right: Hα velocity dispersion field. Bottom left: rotation curve. Bottom right: residual velocity field.The black cross is the kinematical center. In the maps, the green line is the morphological major axis, while the black/white line is the estimated kinematical major axis, its length represents the $2 \times r_{opt}$. On the rotation curve, blue dots indicate the approaching side while red crosses the receding side, the black solid vertical line represents the r_{opt}, and the black dashed line represents the r_{25}; the blue solid line the r_{eff} and the green horizontal line the HI V_{max}; the solid black curve is the Courteau function best fit to the rotation curve. The maps and plots for the all the galaxies of the HRS are online material, available at the CDS, on the HRS dedicated database HeDAM (`https://hedam.lam.fr/`), and on the Fabry-Perot database (`https://cesam.lam.fr/fabryperot`).

rotation curves like the empirical Polyex function (Giovanelli & Haynes 2002; Catinella et al. 2005; Catinella et al. 2006 and Masters et al. 2006). Polyex profiles fit well a large variety of rotation curve shapes (94% of the cases, including those declining at large radii, according to Catinella et al. 2005). A comparison between Polyex and the other fitting expressions is beyond the scope of this paper.

4.1.7. Presentation of the Data

We present in the Appendix D (online material at the CDS), for each galaxy (as in Fig. 4), six frames per Figure containing the XDSS image in the *R*-band, the Hα line-of-sight velocity field, the Hα monochromatic image (free of continuum, [NII] and night skylines contributions), the line-of-sight velocity dispersion field, the rotation curve of the galaxy and the Hα residual velocity field. The white/black cross indicates the calculated kinematical center, while the solid green line traces the optical radius (called hereafter r_{opt}. For consistency with previous HRS works we choose $r_{opt} = r_{24}$, which is in fact $D_{24}/2$ in *r*-band, taken from Cortese et al. 2012. Nevertheless r_{24} is not available for 5 galaxies, thus we used r_{25} which is $D_{25}/2$ in *B*-band, taken from Boselli et al. 2010) and convert it to r_{24} following the relation $r_{24} = 0.920 \pm 0.01\ r_{25}$, obtained by comparing both radii for the whole HRS sample and fitting a bisector regression. The black/white solid line traces the kinematical major-axis deduced from our velocity field analysis; the *PA* is the one calculated from our kinematical models (see subsection 4.2). In the rotation curve plots (bottom left panel in Fig. 4 and all Figures in Appendix D), both sides are superimposed in the same quadrant, using red crosses for the receding side and blue dots for the approaching side. The solid vertical black line represents the r_{opt}; the black dashed line represents the r_{25} in *B*-band, in order to compare the extent between r_{24} and r_{25}. When available in Cortese et al. (2012), the effective radius r_{eff} is plotted with a solid blue vertical line. If available in Boselli et al. (2015), the HI V_{max} is plotted as a horizontal green dashed line. We present the tables of the rotation curves in Appendix E. When no kinematical model can be derived, we plot instead the photometrical center and the *PA* taken from Cortese et al. (2012) without any residual velocity field nor rotation curve.

4.2. Kinematical Projection Parameters

As we saw in subsection 4.1.1, we need a set of initial guess parameters in order to compute our kinematical models. Such a set is composed either by parameters taken from high quality data available in the literature for the HRS (morphological measurements extracted from surface brightness photometry PA_{morph}, i_{morph}), systemic velocity from long-slit spectroscopy V_{sys}, or carefully calculated by us using morphological and kinematic parameters. The galaxy center α and δ is computed either as the nucleus in the continuum image or as the kinematical center of the velocity field. Table E.3 shows the morphological parameters PA_{morph} and ellipticity ϵ used to compute i_{morph} for each galaxy, taken from Cortese et al. (2012). We computed i_{morph} from the ϵ value following the procedure as in Masters et al. (2010):

$$cos^2\, i_{morph} = \frac{(1-\epsilon)^2 - q^2}{1 - q^2} \quad (4)$$

where q depends on the galaxy type (Haynes & Giovanelli 1984; Masters et al. 2010).

We use the initial guesses of projection parameters to derive a rotation curve on which is fitted the modified Zhao function to obtain starting parameters v_t, r_t, g and a. The different kinematical projection parameters computed by our models are accurately determined from different symmetry properties of the line-of-sight velocity field: typical accuracy reached by our

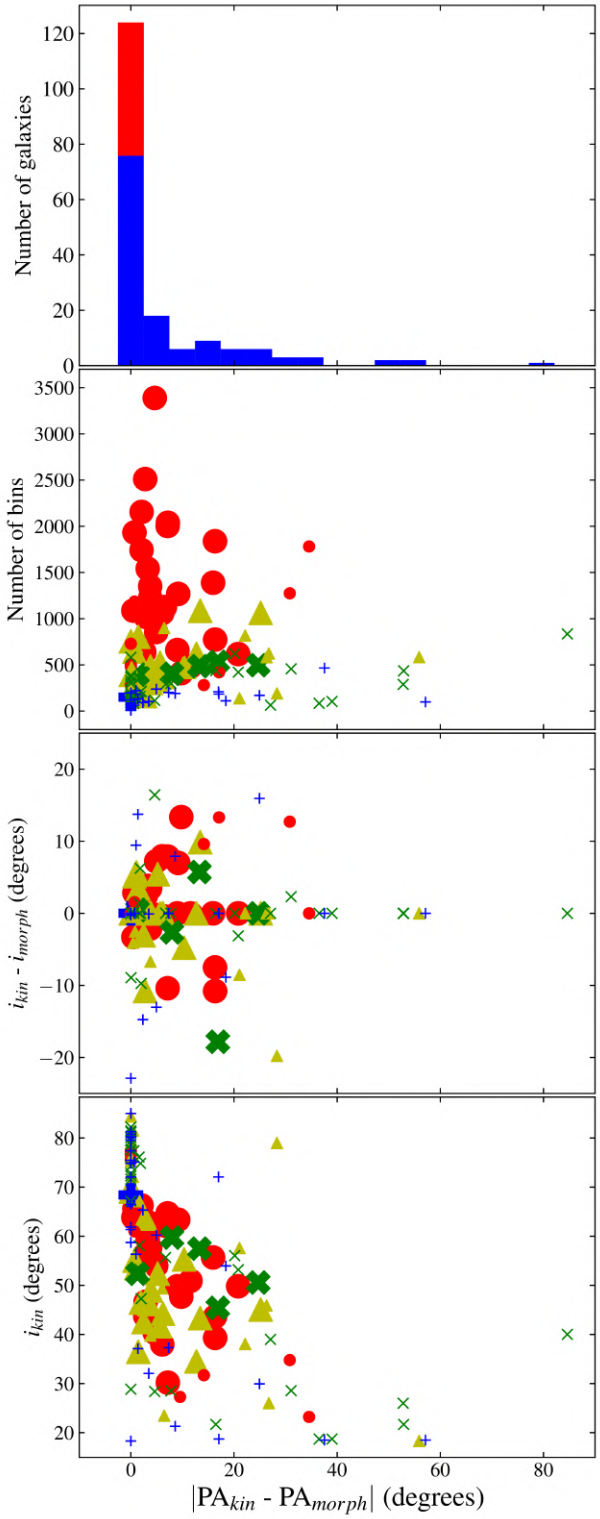

Fig. 5. Top panel: Histogram of the the difference between the kinematical and morphological PA, where the red part of the histogram represent galaxies for which the kinematical *PA* has been fixed to the morphological one. The X-axis in the last three panels represents the difference between the kinematical and morphological *PA*, as a function of: (top middle panel) the number of bins per velocity field, (bottom middle panel) the difference between the kinematical and morphological inclination and (bottom panel) the kinematical inclination. The conventions of color, symbol and marker size are as in Fig. 3.

method are sub-seeing for the coordinates of the galaxy center, ∼0.5 arcsec along the major axis and ∼1 arcsec along the minor one; ∼3 km s^{-1} for V_{sys}; ∼2° for PA and 5°-10° for kinematical inclination i_{kin}. We control those parameters using the method described in Warner et al. (1973), van der Kruit & Allen (1978) and van der Kruit (1990), which is based on the fact that residual velocity fields present characteristic patterns when one of several of those parameters is/are incorrectly determinated. Non-circular motions, mainly due to bar structures, spiral arms, HII complexes, are not considered in the kinematical models since we expect that, except in very low mass dwarf galaxies, such motions are low with respect to rotational ones in rotating systems. The modeled velocity is a purely rotating disk that optimally fits the observed velocity fields. Non-circular motions are thus embedded in the residual velocity field, which is the difference between the observed velocity and the model. For the HRS, the mean velocity dispersion of the residual velocity field is 12.55±2.60 km s^{-1}; such motions may become more important in perturbed galaxies and systems in interaction, which rare in the HRS sample (<11%, Boselli et al. 2010). However, non-circular motions are taken into account in the determination of the uncertainties (Epinat et al. 2008a,b).

Table E.3 gives also the kinematical output parameters of the models and the best reduced χ^2_{red} giving the goodness of fit of the Levernberg-Marquardt method. In general, the PA and i values of the galaxy are left as free parameters when computing the best fitting. Nevertheless, for 42 galaxies (out of which 37 are Flag "B" objects), we fix the kinematical PA to the morphological value during the model computation because of the following reasons:

i) $i \geq 70°$ (39 objects), because galaxies with high inclination have a low spatial coverage along their minor axis; and some of them have a spatial coverage actually too small (i.e. less than 150 velocity bins),

ii) poor signal-to-noise ratio (3 galaxies), because their kinematical model easily leads to non-realistic kinematical parameters.

On the other hand, for 78 galaxies, we fix the kinematical i to the morphological value during the fit process because:

i) $i \geq 70°$ or $i \leq 30°$ (63 objects), because an underestimation of the inclination leads to a overestimate on velocities and vice versa (Tully & Pierce 2000).

ii) 15 galaxies showing velocity fields dominated by non-circular features.

As already mentioned, some of galaxies relevant from those two later cases have in addition a spatial coverage or/and a signal-to-noise ratio too low.

The details about those special cases are given in the Appendix B, and the parameters PA_{kin} or i_{kin} are flagged with an asterisk in Table E.3 when fixed during the model computation.

Figure 5 shows in the top panel the histogram of the $|PA_{kin}$ - $PA_{morph}|$ distribution. For 42 galaxies over 140, the PA_{kin} is fixed to the morphological one (red part of the histogram). Ignoring such galaxies, the peak of the histogram remains at $|PA_{kin}$ - $PA_{morph}| = 0$ because the bin width centered at zero includes 44 galaxies with $|PA_{kin}$ - $PA_{morph}| \leq 3°$; in fact, $|PA_{kin}$ - $PA_{morph}| \leq 10°$ for 105 galaxies over 140, and the median of the distribution is 2.47° and the dispersion 7.85°. Figure 5 also displays the comparison of the difference between the kinematical PA_{kin} and the morphological PA_{morph} as a function of several parameters:

i) Number of bins per velocity field. The $|PA_{kin}$ - $PA_{morph}|$ values, as well as the quality flag, depend on the number of bins, which are related to the spatial coverage and signal-to-noise ratio of the galaxy. Objects with a low number of bins are usually Flag "B" for which PA is not fixed, showing a $|PA_{kin}$ - $PA_{morph}| > 25°$, representing 11.4% of the whole sample. Cases for which $|PA_{kin}$ - $PA_{morph}| > 50°$ belong to galaxies which are almost face-on with faint emission (HRS 68, HRS 154, HRS 255) or emission concentrated in the inner part (HRS 19, HRS 256); the details about these cases with Flag "3-B" and "4-B" are extensively described in Appendix B; nevertheless their velocity fields are good enough to allow the determination of PA_{kin} values.

ii) Difference between the kinematical and the morphological inclination ($i_{kin} - i_{morph}$). In this plot, if we do not take into account the data for which i_{kin} has been fixed to the morphological one, we see that a possible under or over-estimation of the inclination does not depend on $|PA_{kin}$ - $PA_{morph}|$. Despite the fact that the median difference between the kinematical and morphological inclinations is almost equal to zero (−0.2°), meaning that we probably do not introduce statistical biais to compute the inclination regardless the method used (morphological or kinematical), the dispersion of the $i_{kin} - i_{morph}$ distribution is quite large (8.3°).

iii) The kinematical inclination. $|PA_{kin}$ - $PA_{morph}|$ becomes larger as i_{kin} decreases, showing good agreement with Epinat et al. (2008a,b).

We also compare $|PA_{kin}$ - $PA_{morph}|$ as a function of the Galaxy Type and the Distance to the Virgo Cluster (A or B clouds), but we do not find any correlation with these two parameters and we do not show those plots here.

Figure 6 displays the histogram of the variation between the morphological and the kinematical inclinations. For 78 galaxies over 140, i_{kin} is fixed to the morphological value (red part of the histogram). In order to test whether there was a correlation or not between the galaxy inclination (either i_{kin} or i_{morph}) and the maximum rotational velocity V_{max}, we perform several OLS bisector regressions comparing both i_{kin} and i_{morph} values versus V_{max} (not plotted here). We do not observe any significant relation, on the whole sample neither any of the subsamples as defined by their different quality flags.

Bars and Bulges are usually bright with respect to the disks, nevertheless, bulges contain a low content of warm gas while bars could be warm gas-poor or -rich. In case of low gas content, Voronoi tessellations minimise the impact of the non-rotating bulge and of the bar on the determination of the disk parameters. In case of high gas content, Voronoi techniques do not spread out the impact of non-circular motions to outer regions. On the other hand, despite the accuracy of the PA and i computation, these two parameters may be inadequate in presence of multiple non-axisymmetric structures in the kinematics or/and in the morphology. For instance, in the case of a strong bar, the determination of the i and the PA could vary with the radius within the bar, nevertheless we take this fact into account by measuring the i and PA outside the bar since our rotation curves are extended enough. Indeed, the bar length reaches the outskirt of the warm disk in only 2/152 galaxies. In addition, the estimation of V_{max} is not significantly biased because of the presence of a bar; indeed, a peak followed by a decrease on the rotation curve is usually linked to the presence of a bar (i.e. galaxy HRS 60) and furthermore identified as such; otherwise the effect of the bar modify the inner slope of the rotation curve

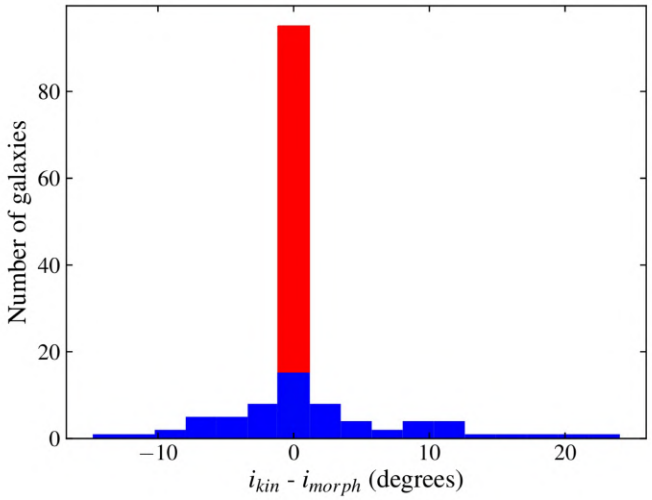

Fig. 6. Histogram of the difference between the kinematical and morphological inclination; the red part of the histogram represents the galaxies for which the kinematical inclination was fixed to the morphological one.

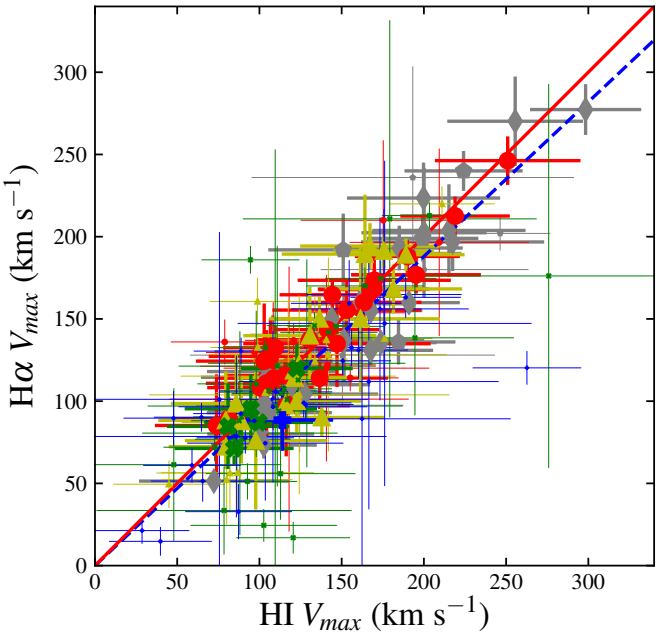

Fig. 7. Relation between $V_{max,HI}$ and $V_{max,H\alpha}$. The red solid and blue dashed lines represent the OSL bisector regression applied to a) the whole Fabry-Perot sample, and b) ignoring galaxies with Flag "B". Colors, symbols and markers are as in Fig. 3. Fabry-Perot data from the literature (grey symbols) are classified as: stars for galaxies belonging to the Loose Groups Survey, rhombuses for galaxies belonging to the Virgo Survey, and pentagons for galaxies belonging to the GHASP survey.

and possibly shift V_{max} at a different radius (i.e. galaxy HRS 287), as described by Dicaire et al. (2008), Randriamampandry et al. (2015) and Korsaga et al. (2019). Finally, we use a model to fit V_{max} rather than fitting the raw rotation curve, precisely to average local non-circular motions. The position of the galaxy center is usually weakly affected by non-circular motions. In conclusion, the methods we use minimise the effects dues to non-circular motions.

5. Discussion: Dynamical Masses

Several models, simulations and multifrequency observations consistently indicate the mass as the principal driver of galaxy evolution (i.e. Cowie et al. 1996, Gavazzi et al. 1996, Boselli et al. 2001 for observations; Navarro et al. 1996, Boissier et al. 2003, Dutton 2012, Moster et al. 2013, Dutton & Macciò 2014 for models and simulations). The mass of galaxies is generally measured through the stellar mass which is derived from optical and near-IR imaging data. Nevertheless other components are present. These include dark matter, which is generally dominant at large radius, the mass of the different gas phases (atomic and molecular hydrogen, helium, ionised and hot gas, metals), and the mass of dust. The unique dataset available for the HRS allows us to directly measure most of the baryonic components: HI and CO data are available for most of the star forming galaxies of the sample (Boselli et al. 2014a), the dust mass has been estimated from SED fitting using the far-IR data by Ciesla et al. (2014), and metallicities have been derived using integrated long slit spectroscopy by Hughes et al. (2013). The kinematical data gathered in this work can be used to roughly estimate the total dynamical mass of a system using relation (9)

In this section, we use the HRS to study the main scaling relations between the dynamical mass, the baryonic mass, and the star formation rate generally used to constrain models of galaxy formation and evolution. The unique multifrequency coverage, which allows at the same time the accurate determination of the different baryonic components, of the star formation activity, and of the dynamical mass, combined with the sample definition (see sect. 2) and the statistics (~200 objects spanning a wide range in morphological type and mass), make the HRS the best sample available in the literature for this purpose.

To study the dynamical properties of the sample in the context of galaxy evolution, we proceed as follows:

i) Since we lack of Fabry-Perot data for 26.4% of the HRS, we first test whether the HI kinematical data can be used to derive the total dynamical mass of the missing galaxies without introducing any systematic bias.

ii) We check the statistical significance of our sample by comparing the Tully-Fisher relations to those derived in other representative samples generally used in the literature.

iii) We then study the stellar and baryonic Tully-Fisher relations, the relation between the baryonic and dynamical mass, and finally we derive the main sequence for the first time using the dynamical mass [6].

5.1. $V_{max,HI}$ versus $V_{max,H\alpha}$

Boselli et al. (2014a) published a homogenised catalog of HI data for the whole HRS. Their work provides line widths W_{HI} measured at 50% of the peak flux per galaxy. We compute $V_{max,HI}$ assuming that $W_{HI} = 2\, V_{max,HI}\, sin(i)$; where

[6] For a fair comparison, all references in the literature are scaled to H_0 = 70 km s^{-1} Mpc^{-1} used in this work, and stellar masses are corrected by a factor of 0.061 *dex* (Bell et al. 2003; Gallazzi et al. 2008) consistently with the Chabrier IMF used in this work.

$V_{max,HI}$ is the maximal HI rotation velocity. On the other hand, we compute the maximal Hα rotation velocity $V_{max,H\alpha}$ from rotation curves derived from 2D velocity fields, thus intrinsically calculated in a more accurate way.

Uncertainties on $V_{max,H\alpha}$ are calculated as the quadratic combination between the i_{kin} error and the median dispersion of the rotation curve rings beyond r_t, as in Epinat et al. (2008b). This is a much more realistic estimate of the uncertainty on the maximal rotational velocity than the one derived from the integrated HI line profile W_{HI}, which is very low (< 5 km s^{-1}). For that reason, in order to have comparable errors for both quantities, we derive $V_{max,HI}$ uncertainties considering the combination of the dispersion between $V_{max,HI}$ and $V_{max,H\alpha}$ values modulated by the inclination (sin i_{kin}) and the uncertainties associated to inclination.

$V_{max,HI}$ and $V_{max,H\alpha}$ are computed comparing the kinematics of cold and warm gas phases respectively and using different methods; thus likening both quantities might present biases. A bias could come from the way $V_{max,HI}$ is computed using HI emission lines; such measurements are done at certain percentage of the peak flux, here we measure it at 50% of the peak flux but it could have been done at for instance 20% and this might have an impact on $V_{max,HI}$ if the edges of HI profiles are not sharp enough. In comparing $V_{max,HI}$ and $V_{max,H\alpha}$, we check whether systematic biases appear. Fig. 7 shows the comparison between HI and Hα V_{max} values using different symbols according to the quality of the Hα rotation curves. The OSL bisector regression for the whole sample (Flag "A" + "B") gives $V_{max,H\alpha} = 0.95 \pm 0.02\ V_{max,HI}$ with an intrinsic scatter of 0.82, while for Flag "A"-only galaxies $V_{max,H\alpha} = 0.9975 \pm 0.01\ V_{max,HI}$ with an intrinsic scatter of 0.11. The two sets of data give consistent results; however, for Flag "A" galaxies the slope of the relation is closer to one and the scatter is smaller than for the whole sample. We conclude that no systematic biases are present in the measurements and to explain the difference of slope between Flag "A"-only and Flag ("A" + "B") galaxies, we favour an explanation related to galaxy environments. Indeed, Flag "B" galaxies are mainly Virgo cluster objects which can be highly perturbed by their surrounding environment (Boselli & Gavazzi 2006, 2014). There are indeed clear indications that in cluster galaxies the star forming disc is radially truncated with respect to isolated objects (Fossati et al. 2013, Boselli et al. 2015) because of the oustide-in removal of the gas (Boselli & Gavazzi 2006). For this reason, their Hα and HI rotation curves do not always reach the plateau, making the estimate of the maximal rotational velocity quite uncertain. The HI-deficiency parameter is generally used to measure the degree of perturbation in cluster objects: galaxies with $HI - Def > 0.4$ have a HI gas content at least 2.5 times smaller than similar objects in the field (Haynes & Giovanelli 1984). Most of the Flag "B" galaxies with a rotation curve truncated at $r < 0.6\, r_{opt}$ have indeed an HI-deficiency parameter $HI - Def > 0.4$ and are thus cluster perturbed galaxies. Since we wish to trace the statistical properties of unperturbed systems, we on purpose avoid HI-deficient cluster galaxies which are known to have a lower baryonic mass than field objects (gas deficient objects, Boselli & Gavazzi 2006, Boselli et al. 2014b). For this reason, we will ignore galaxies with Flag "B" or $HI - Def > 0.4$ in the following analysis. The resulting sample includes 123 objects, out of which 80 (65%) with Hα rotation curves.

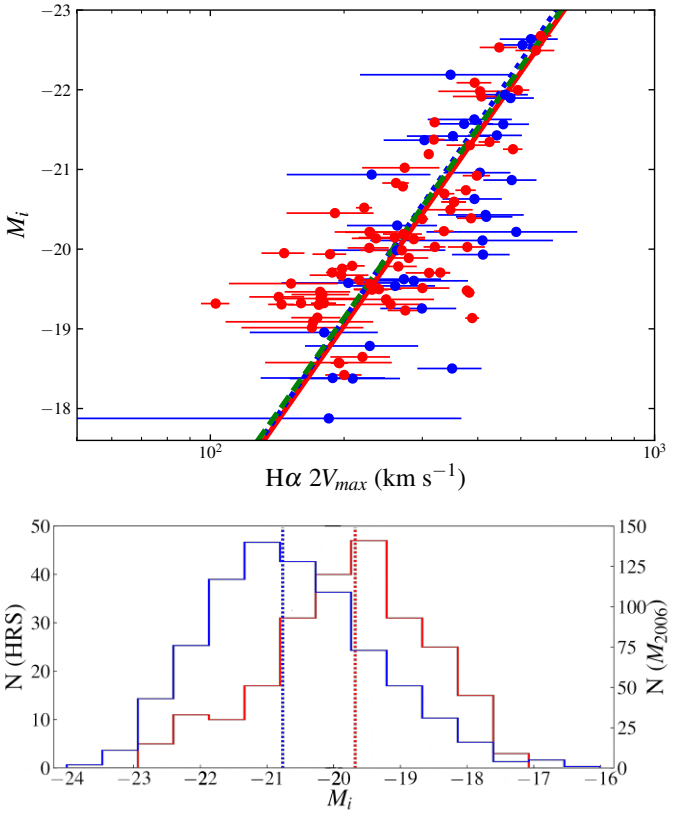

Fig. 8. Top panel: *i*-band Tully-Fisher relation. Red and blue dots indicate HRS galaxies with Hα and HI kinematical data. The solid red line indicates the OLS bisector regression to the HRS data. The dotted blue line represents the template *I*-band TF relation for the nearby galaxy sample of Masters et al. (2006) but using an OSL bisector method (instead of the bivariate method used by those authors). The dashed green line represents the median OSL bisector fit computed from the 100 subsamples of 135 galaxies matching our galaxy luminosity distribution, randomly selected from the Masters et al. (2006) sample. Bottom panel: M_i distributions of the HRS (red) and the Masters et al. (2006) samples M_{2006} (blue); dotted lines indicate the median value of the corresponding distribution (HRS = -19.67, M_{2006} = -20.76).

5.2. The Optical and NIR Tully-Fisher Relation

The Tully-Fisher relation (TF, Tully & Fisher 1977), often used to constrain models and simulations of galaxy evolution, is a tight relation between the baryonic and the dynamical masses of late-type systems. This scaling relation has been derived in different photometric bands using different samples (e.g. Giovanelli et al. 1997a,b, Steinmetz & Navarro 1999, McGaugh et al. 2000, Sakai et al. 2000, Bell & de Jong 2001, McGaugh 2005, Masters et al. 2006, McGaugh 2012, Cortese et al. 2014a, Sorce et al. 2014, Ponomareva et al. 2017, Aquino-Ortíz et al. 2018), but comparisons with prior studies are really challenging.

In the present study we use maximal rotation velocities derived from homogenous FP Hα rotation curves deduced for 2D velocity fields. Samples available in the literature often come from (i) heterogeneous sources, including Hα long slit spectrography or HI integrated line widths, (ii) they are different in absolute magnitude range, (iii) are based on slightly different photometric bands and (iv) have been studied using different

Table 1. *i*-band Tully-Fisher relation.

Authors	$\alpha \pm \sigma_\alpha$	$\beta \pm \sigma_\beta$	Fitting method	Number of galaxies
This work	-7.99 ± 0.15	-20.63 ± 0.19	OSL bisector	123
Giovanelli et al. (1997a,b)	-7.67 ± 0.33	-20.83 ± 0.32	bi-variate	782
Masters et al. (2006)	-7.85 ± 0.10	-20.68 ± 0.05	bi-variate	807
Masters et al. (2006)	-8.14 ± 0.28	-20.73 ± 0.05	OSL bisector	807
Masters et al. (2006)/HRS subsamples	-7.91 ± 0.18	-20.71 ± 0.08	OSL bisector	123

Note about Table 1: Coefficients obtained for the i-band TF relation $M_i = (\beta \pm \sigma_\beta) + (\alpha \pm \sigma_\alpha)\ (log2V_{max} - 2.5)$ *in the literature and this work. The last line has been computed by averaging 100 subsamples randomly extracted from Masters et al. (2006) and matching exactly our luminosity galaxy distribution.*

Table 2. NIR Tully-Fisher relation.

Authors	$\alpha \pm \sigma_\alpha$	$\beta \pm \sigma_\beta$	Fitting method	Number of galaxies
This work	-9.23 ± 0.26	-20.19 ± 0.18	OSL bisector	123
Sorce et al. (2014)	-9.77 ± 0.19	-20.14 ± 0.09	Inverse fitting	319
Sorce et al. (2014)	-9.89 ± 0.21	-20.17 ± 0.11	OSL bisector	319
Sorce et al. (2014)/HRS subsample	-9.31 ± 0.30	-20.25 ± 0.10	OSL bisector	89

Note about Table 2: Coefficients obtained for the NIR S4G-1 band TF relation $M_{3.6\mu m} = (\beta \pm \sigma_\beta) + (\alpha \pm \sigma_\alpha)\ (log2V_{max} - 2.5)$ *in the literature and this work.*

fitting methods. For example, Giovanelli et al. (1997a,b) used rotational velocities derived either from 21 cm spectra or optical emission line long–slit spectra; ∼60% of the galaxies in use in Masters et al. (2006) have their rotational velocities measured using HI, the other ∼40% using Hα long-slit data. Giovanelli et al. (1997a,b) and Masters et al. (2006) used bi-variate fittings in *I*- and *i*-bands respectively while Sorce et al. (2014) used inverse fitting methods and photometry in the 3.6μm-band.

A direct comparison galaxy per galaxy with several previous works is difficult because often galaxy names are not given or the number of galaxies in common is quite reduced. For instance, Aquino-Ortíz et al. (2018) using CALIFA data, and Cortese et al. (2014a), using SAMI data, do not specify the name of the galaxies they used to compute the kinematics of gas. We have only three galaxies in common (NGC 3370, 4535 and 4536) with Ponomareva et al. 2017 who used resolved HI data, for which V_{max} is respectively 152±4, 195±6 and 161±10 km s^{-1}, while we reach V_{max} values of 160±9, 201±15 and 160±7 km s^{-1}, thus compatible with our results. On the other hand, rotation curves deduced from IFUs typically only extend up to smaller radius r_{opt} (e.g. $r_{opt} \sim r_{eff}$, Cortese et al. 2014a); furthermore, V_{max} measured from IFU surveys are often measured at radii where the maximum of the rotation curve is not reached yet. While, thanks to the large FoV of our instrument, we know the actual size of the warm disk because it is not limited by the FoV.

Aquino-Ortíz et al. (2018) and Ponomareva et al. (2017) samples are smaller than our HRS one (respectively 42 and 32 galaxies with gas kinematics) while Cortese et al. (2014a) sample, with its 193 galaxies, is comparable to ours. But even more important than the sample size is the galaxy luminosity distribution. To compare different galaxy samples, an important issue is thus to compare the galaxy luminosity distributions of the samples. It is indeed known that the slope of the TF relation is known to slightly change with luminosity (e.g. Schaye et al. 2015). We check hereafter how the statistically limited HRS compares with works which are generally based on several hundreds of galaxies.

We directly compare the HRS data with two other samples, one in the optical (Masters et al. 2006) and the other in the IR (Sorce et al. 2014), see Figures 8 and 9, Tables 1 and 2. We use the Masters et al. (2006) sample because it has been qualified by these authors as a "template calibrator sample", by the way this sample is partially extracted from the Giovanelli et al. (1997a,b) sample. It consists of 807 galaxies while the present HRS consists of 123 objects. In order to fairly compare the results we compute the TF relationship on the whole Masters et al. (2006) sample using the OSL bisector. The result we obtain is, as expected, different from the one those authors found using the bivariate method.

We hereafter quantify how the difference in the TF relationships are related to the statistical significance of the sample and mostly, to their galaxy luminosity distribution using the same fitting method, the OSL bisector. To quantify those effects, we randomly pick up one hundred subsamples of 123 galaxies from the Masters et al. (2006) sample with exactly the same luminosity distribution, magnitude bin per magnitude bin, as the HRS. For each of those one hundred subsamples we refit the data and compute the TF slopes and intercepts. Averaging these 100 iterations and computing their r.m.s., we obtained a slope and zero point values closer to the ones obtained with the HRS than the ones for the whole Masters et al. (2006) sample. We see that the values obtained using the HRS sample are within the 1-σ uncertainty for both parameters. Both whole sample and subsamples agree quite well, which means that the impact of the sample is not important in this magnitude range.

Using always the OSL bisector method, we make a similar check in the 3.6 μm-band using the sample of Sorce et al. (2014) containing 319 galaxies. The Sorce et al. (2014) sample is larger than the HRS but not large enough to randomly simulate the same galaxy magnitude distribution as the HRS. We furthermore build subsamples of 89 galaxies matching approximatively our magnitude distribution. Despite the impact of sample selection seems larger for the Sorce et al. (2014) sample then for the Masters et al. (2006) sample, the results are nevertheless similar to those obtained for the *i*-band.

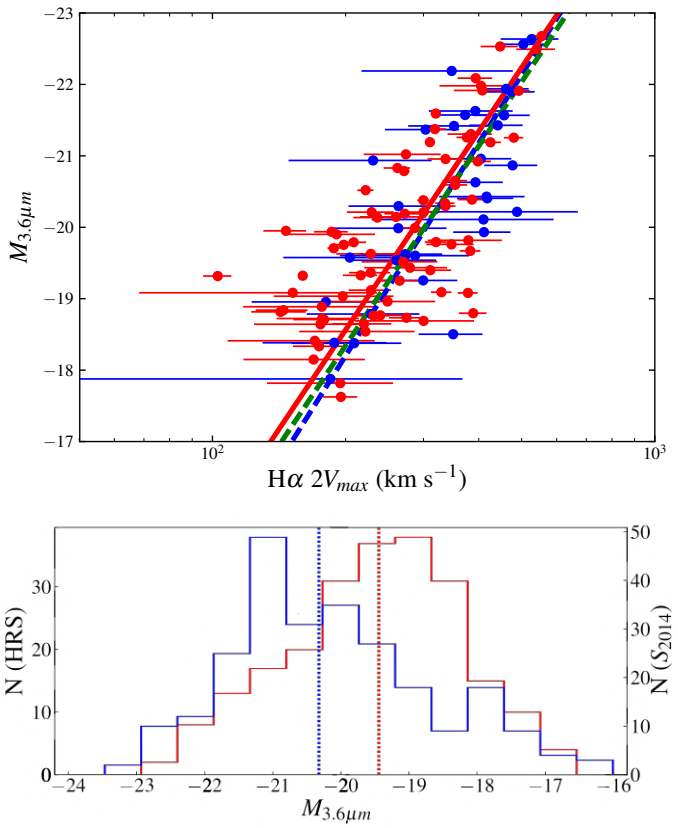

Fig. 9. NIR S4G-3.6μm band Tully-Fisher relation. The dashed blue line represents the Tully-Fisher relation determined by Sorce et al. (2014) for nearby galaxies, while the solid red line the OLS bisector regression to our data. Colors and symbols as in Fig. 8. Bottom panel: $M_{3.6\mu m}$ distributions of the HRS (red) and the Sorce et al. (2014) sample (S_{2014}, blue); dotted lines indicate the median value of the corresponding distribution (HRS is = -19.44, S_{2014} = -20.32).

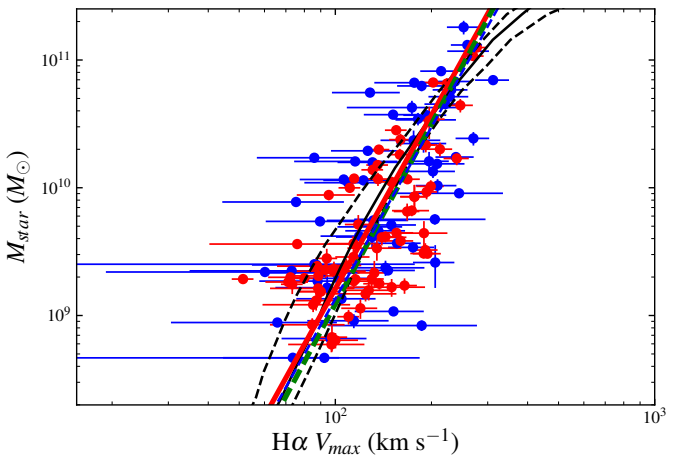

Fig. 10. Stellar Tully-Fisher relation. The dashed green line represents the relation determined by Bell & de Jong (2001), the dashed blue line that of McGaugh et al. (2000), the solid red line the OLS bisector regression to our sample. Colors and symbols are as Fig. 8.The solid black line shows the predictions from the EAGLE cosmological hydrodynamical simulations for galaxies at $z \sim 0$ (Schaye et al. 2015, with dashed lines 16% and 84% percentiles).

We can thus conclude from these analyses that, despite the difference in luminosity distribution and our smallest sample, the HRS represents well other larger samples generally used as reference in the literature.

5.3. Stellar and Baryonic Tully-Fisher Relations

5.3.1. The Stellar Tully-Fisher Relation

Figure 10 shows the stellar TF relation for the HRS. Stellar masses (from Cortese et al. 2012) have been derived using the *i*- and *g*-band SDSS photometry following the prescription of Zibetti et al. (2009) (Chabrier IMF). The OSL bisector regression and the best fit published in the literature are given in Table 3. As for the *i*- and 3.6μm-bands, the stellar TF relation derived for the HRS is in good agreement with compute the generally taken as reference in the literature (Bell & de Jong 2001; McGaugh et al. 2000). It well matches also that derived on a much smaller sample with Fabry-Perot data by Torres-Flores et al. (2011).

We also compare our data with the predictions of the EAGLE cosmological hydrodynamical simulations (Schaye et al. 2015, Ferrero et al. 2017) on $z \sim 0.1$ late-type galaxies (Fig. 10). The agreement between the slope (4.51 ± 0.68) and intrinsic scatter ($\sim$ 0.16 dex) of the HRS stellar TF relationship and the EAGLE TF predictions (mean slope $\sim$ 4.84 and intrinsic scatter $\sim$ 0.14 dex) is very good.

5.3.2. The Baryonic Tully-Fisher Relation

We can also derive the baryonic TF relation (Fig. 11), where the baryonic mass is defined as:

$$M_{bar} = M_{star} + M_{gas} + M_{dust}, \quad (5)$$

and the gas mass is defined as follows:

$$M_{gas} = M_{HI} + M_{H_2} + M_{He} + M_z, \quad (6)$$

where M_{HI} is the atomic gas mass, M_{H_2} the molecular gas mass, M_{He} the helium mass and M_z the metal mass. The hydrogen mass $M_H = M_{HI} + M_{H_2}$ is directly measurable (Boselli et al. 2014a, where M_{H_2} is measured using a luminosity dependent X_{CO} conversion factor, Boselli et al. 2002). M_{He} is derived from the primordial nucleosynthesis helium fraction, $Y \equiv M_{He}/M_{gas} \simeq 0.28$ (Pagel 2009), using the relation:

$$M_{gas} = \frac{1}{1 - Y - Z} \times M_H, \quad (7)$$

where $Z = M_z/M_{gas}$ is the metal fraction which can be derived from metallicity measurements using the relation (McGaugh et al. 2000):

$$log\,(Z/Z_\odot) = log\,(O/H) - log\,(O/H)_\odot, \quad (8)$$

taking $Z_\odot = 1.34 \times 10^{-2}$ and $12 + log\,(O/H)_\odot = 8.69$ from Asplund et al. (2009).

As previously mentioned, all baryonic components are directly measurable for the HRS, with the exception of the

Table 3. Stellar Tully-Fisher relation.

Authors	$\alpha \pm \sigma_\alpha$	$\beta \pm \sigma_\beta$	Number of galaxies.
This work	4.51 ± 0.68	0.19 ± 0.64	123
McGaugh et al. (2000)	4.47 ± 0.54	0.19 ± 1.23	~550
Bell & de Jong (2001)	4.68 ± 0.40	−0.27 ± 0.88	79
Torres-Flores et al. (2011)	4.48 ± 0.38	0.21 ± 0.83	40
Schaye et al. (2015)[a]	~ 4.84		EAGLE simulation
Ferrero et al. (2017)	4.10 ± 0.05	0.28 ± 0.02	867 simulated galaxies

Coefficients obtained for the stellar TF relation $log\ M_{star}(M_\odot) = (\beta \pm \sigma_\beta) + (\alpha \pm \sigma_\alpha)\ (logV_{max})$ in the literature and this work, assuming a Chabrier IMF.
[a] Mean slope and intrinsic scatter calculated using 8 quantiles situated within $8.0 > log\ M_{star}\ (M_\odot) > 11.5$.

Table 4. Mean contribution of the baryonic components.

Baryonic comp	Average %	Average mass ($M_\odot$)
M_{star}	65 ± 15%	$5.24 \pm 1.27 \times 10^9$
M_{HI}	19 ± 6%	$1.53 \pm 0.45 \times 10^9$
M_{He}	11.4 ± 3.3%	$9.19 \pm 2.67 \times 10^8$
M_{H_2}	5.2 ± 2.8%	$4.45 \pm 2.25 \times 10^8$
M_z	0.87 ± 0.35%	$7.03 \pm 2.83 \times 10^7$
M_{dust}	0.16 ± 0.07%	$1.32 \pm 0.58 \times 10^7$

Average contribution of each baryonic component to the total baryonic mass in percentages and solar masses.

ionised and hot gas masses which we consider as negligible. Table 4 lists the average contribution of each baryonic component to the total baryonic mass. The mean mass and percentage of each baryonic component has been computed using the whole HRS. We note that the gas (plus dust) content represents more than the half of the stellar content $(M_{gas=HI+H_2+He} + M_z + M_{dust})/M_{star}$ ≃56% and the metal content represents 2% of the total gas (plus dust) content $(M_z/(M_{gas=HI+H_2+He} + M_z + M_{dust})$ ≃0.02).

The OLS bisector regression to the data is compared to the values published in the literature in Table 5. In these published works, the baryonic mass is generally derived summing the contribution of the stellar mass to that of the HI gas mass, and assuming a constant $M(HI)/M(H_2)$ contribution for the molecular gas component. These works also lack of high quality 2D velocity fields. Despite these major differences, these works give results consistent with ours.

We can also compare our results to the predictions of models and simulations. According to Dutton & Macciò (2014), Moster et al. (2013) and Zu & Mandelbaum (2015), N-body simulations predict for the baryonic TF relation an intrinsic scatter of ~ 0.15, consistent with the dispersion of our sample (0.16).

5.4. Baryonic versus Dynamical Masses

Dynamical masses are computed following the prescription of Lequeux (1983), which is a variation of the Virial theorem that attempt to account for a variety of galaxy mass distribution, from a purely flat to a purely spherical model :

$$M_{dyn}(M_\odot) = \alpha\ r_{opt}\ V^2_{max}\ /\ G, \quad (9)$$

where G is the gravitational constant and α is a coefficient which depends on the model flatness of mass distribution ($0.6 \leq \alpha \leq 1.0$). Figure 12 shows the relationship between baryonic and dynamical masses. Since we are taking into account neither luminosity profiles nor models of mass distribution, we chose for the comparison the spherical model $\alpha = 1.0$. In order to quantify the impact of this extreme assumption, we plot a cyan shaded area representing the interval $0.6 \leq \alpha \leq 1.0$. The values of the OLS bisector fit are given in Table 6. The two variables are strongly correlated. The fraction of baryons is lower in low-mass-gas-rich galaxies (~20-25% of the total dynamical mass) than in high-mass galaxies with low SFR (~35-45% of the total dynamical mass), consistently with what seen in the previous TF relations (Figs. 8, 9, 10 and 11). Figure 13 shows how the contribution of each baryonic component changes as a function of the dynamical mass and of the stellar mass (color symbols) within the HRS. Using a simple linear regression (not plotted for clarity), we estimate the trend of the y-axis (respectively, from the top to the bottom: the fraction of stars M_{star}/M_{bar}, neutral gas $M_{\rm HI}/M_{bar}$, molecular gas M_{H2}/M_{bar}, metals M_z/M_{bar} and dust M_{dust}/M_{bar}) as a function of the

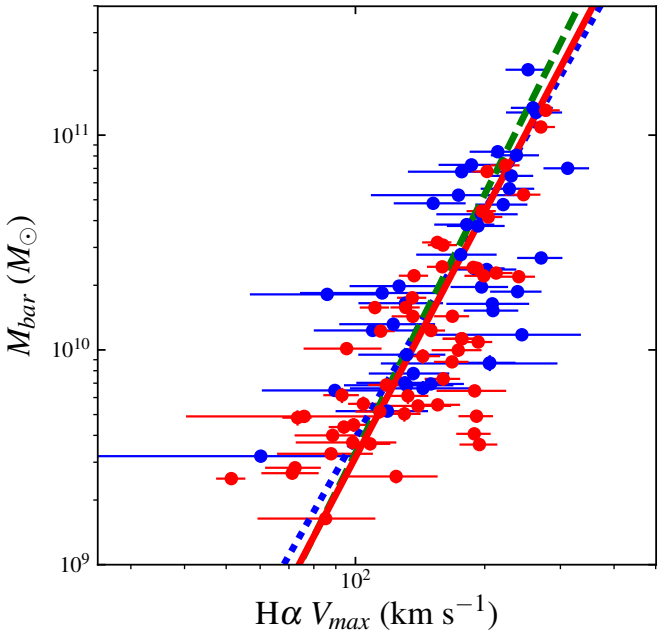

Fig. 11. Baryonic Tully-Fisher relation. The dashed green line represents the relation determined by McGaugh et al. (2000), the dotted blue line that of Bell & de Jong (2001), the solid red line the OLS bisector regression to our sample. Colors and symbols are as Fig. 8.

Table 5. Baryonic Tully-Fisher relation.

Authors	$\alpha \pm \sigma_\alpha$	$\beta \pm \sigma_\beta$	Nb galaxies	M_{bar}
This work	3.79 ± 0.39	1.91 ± 0.63	123	$M_{star} + 1.4(M_{HI} + M_{H_2}) + M_z + M_{dust}$
McGaugh et al. (2000)	3.98 ± 0.12	1.42 ± 0.25	~550	$M_{star} + 1.4\,M_{HI}$
Bell & de Jong (2001)	3.53 ± 0.20	2.56	79	$M_{star} + M_{HI}$
McGaugh (2005)	3.19 ± 0.14	3.06	74	$M_{star} + 1.4\,M_{HI}$
Torres-Flores et al. (2011)	3.64 ± 0.37	1.95 ± 0.61	40	$M_{star} + (\sim 1.4\,M_{HI})$
Zaritsky et al. (2014)	3.50 ± 0.20	2.96	1468	$M_{star} + M_{HI}$
McGaugh & Schombert (2015)	4.04 ± 0.09	1.44 ± 0.18	26	$M_{star} + 1.33\,(M_{HI} + M_{H_2})$
Lelli et al. (2016)	3.71 ± 0.08	2.10 ± 0.18	118	$M_{star} + 1.33\,M_{HI}$
Papastergis et al. (2016)	3.75 ± 0.11		97	$M_{star} + M_{HI}$
Ponomareva et al. (2018)	2.99 ± 0.20	2.71 ± 0.56	32	$M_{star} + M_{HI} + 1.4\,M_{H_2}$

Coefficients obtained for the baryonic TF relation $log\ M_{bar}(M_\odot) = (\beta \pm \sigma_\beta) + (\alpha \pm \sigma_\alpha)\ (logV_{max})$ in the literature and this work.

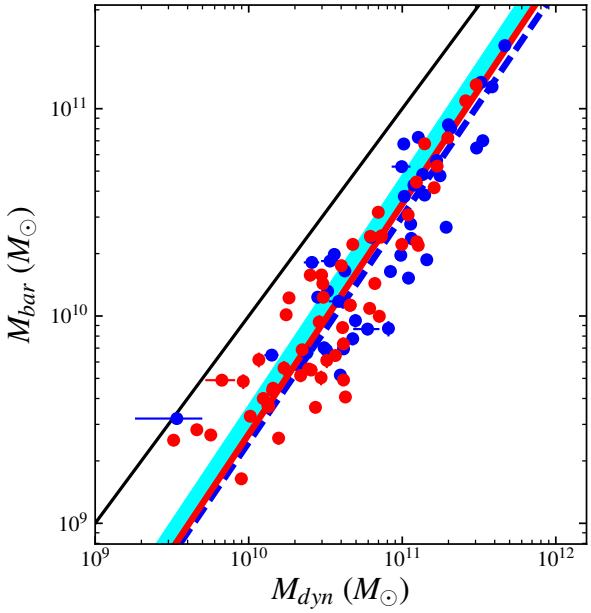

Fig. 12. Baryonic versus dynamical mass. Colors and symbols are as in Fig. 8. The dashed blue line represents the best fit of Torres-Flores et al. (2011), while the solid red line the OLS bisector regression fit to our sample. The solid black line shows the 1-1 relation, and the cyan shaded area the mass interval $0.6 \leq \alpha \leq 1.0$. M_{bar} are computed within r_{opt}, while M_{dyn} from V_{max} computed by Courteau's profile extrapolation within r_{opt}.

Table 6. Baryonic versus Dynamical Masses

Authors	$\alpha \pm \sigma_\alpha$	$\beta \pm \sigma_\beta$
This work	1.11 ± 0.12	−1.67 ± 0.59
Torres-Flores et al. (2011)	1.09 ± 0.04	−1.34 ± 0.42

Coefficients obtained for relation $M_{bar}(M_\odot) = (\beta \pm \sigma_\beta) + (\alpha \pm \sigma_\alpha)\ log\ M_{dyn}$ by Torres-Flores et al. (2011) and this work.

dynamical mass (log M_{dyn}). A positive correlation is only observed between the fraction M_{star}/M_{bar} and the dynamical mass, with a statistical coefficient of determination $R^2 \sim 0.42$. Weak negative correlations are found in the fourth next cases. Both slope and R^2 coefficient become increasingly weaker from the second top panel to the bottom one. The bottom one, i.e. M_{dust}/M_{bar}, is in fact compatible with a zero slope ($R^2 \sim$ 0.03). The gaseous components as well as the metal and dust components, are relatively more abondant, relatively to the baryonic component, in low mass galaxies (log $M_{dyn} < 10.5 M_\odot$), while the stellar component does in massive objects. The correlation and the dispersion around this correlation between the stellar and the dynamical masses, already observed in Fig. 12, is again underlined by these plots. This is indeed expected given the rapid evolution in the past of massive galaxies, which already transformed most of the gas into stars, with respect to a fairly constant star formation activity in low mass systems possible thanks to their large gas reservoirs (Sandage 1986; Gavazzi et al. 1996, 2002; Boselli et al. 2001; Boissier et al. 2003).

Dynamical masses are computed within r_{opt} and furthermore do not provide the total masses since they only account for the visible part of galaxies. In addition, dynamical masses do not take into account possible variation in the bulge-to-disc ratio nor in the actual disk or spherical shape of the baryonic matter distributions. Despite those rough approximations, the observed dispersion in the relation (~0.12 dex) is comparable to that predicted by semi-analytic models of galaxy formation in a ΛCDM context (~0.15 dex, Dutton 2012, Dutton & Macciò 2014).

5.5. Baryonic and Dynamical Mass Main Sequences

The tight relationship between SFR and M_{star} is generally called main sequence (i.e. Guzmán et al. 1997; Brinchmann & Ellis 2000; Bauer et al. 2005; Bell et al. 2005; Papovich et al. 2006; Reddy et al. 2006; Noeske et al. 2007; Salim et al. 2007; Elbaz et al. 2007; Daddi et al. 2007; Pannella et al. 2009; Rodighiero et al. 2010; Peng et al. 2010; Karim et al. 2011; Whitaker et al. 2012; Speagle et al. 2014; Torrey et al. 2014; Gavazzi et al. 2015; Renzini & Peng 2015; Sparre et al. 2015; Cano-Díaz et al. 2016; Hsieh et al. 2017; Medling et al. 2018). The slope of this obvious scaling relation (bigger galaxies have more of everything), its bending at high luminosities, its scatter, and its variation as a function of redshift and environment, are often used to trace the evolution of galaxies with cosmic time. Observational evidence indicates mass as a principal driver of galaxy evolution (e.g. Cowie et al. 1996; Gavazzi et al. 1996; Boselli et al. 2001). Consistently with these obervational results, hydrodynamic cosmological simulations suggest that the evolution of galaxies is mainly gouverned by the dark matter halo in which they reside (Governato et al. 2012; Brooks & Zolotov 2014; Christensen et al. 2014). It would thus be

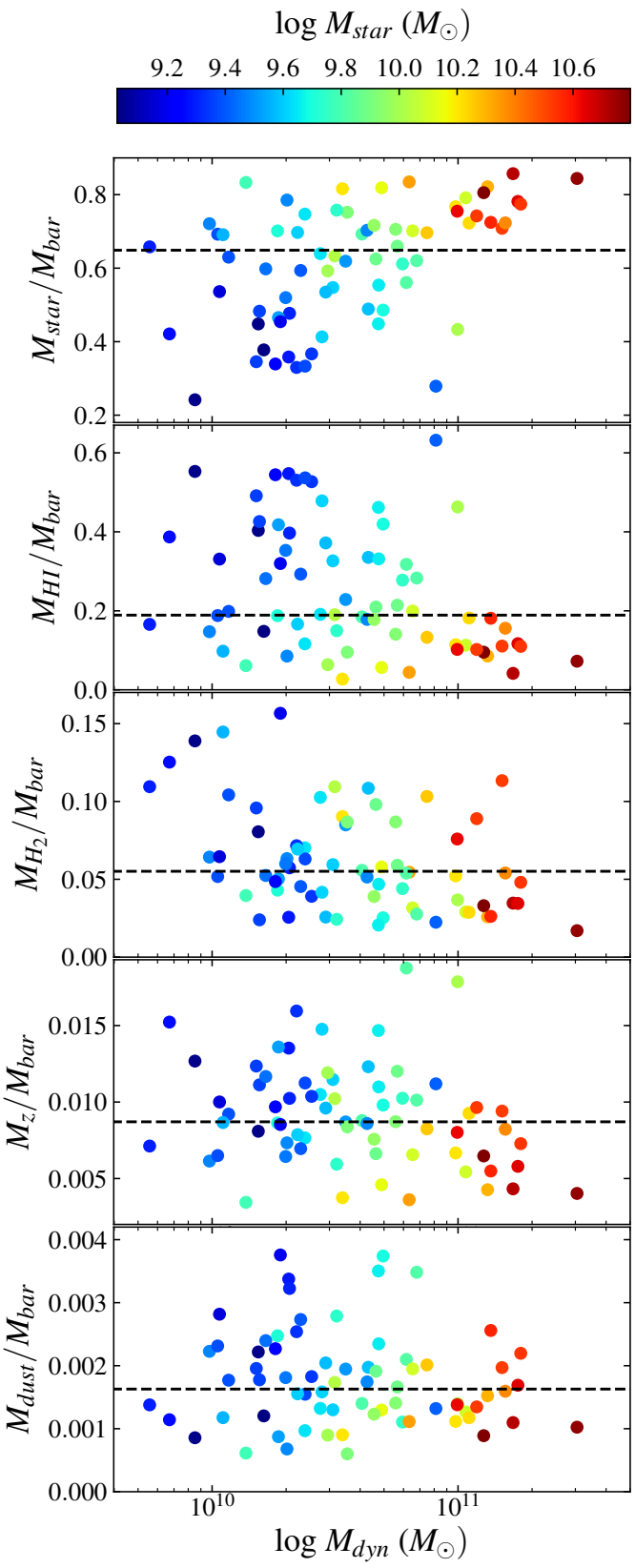

Fig. 13. Variation of the different baryonic components to the total baryonic mass of the total dynamical mass, from top to bottom: stellar (first panel), HI (second panel), H_2 (third panel), metal elements (fourth panel), and dust (fifth panel). The black dashed line shows the mean contribution of the corresponding baryonic component. The colors represent the stellar masses in logarithmic scale.

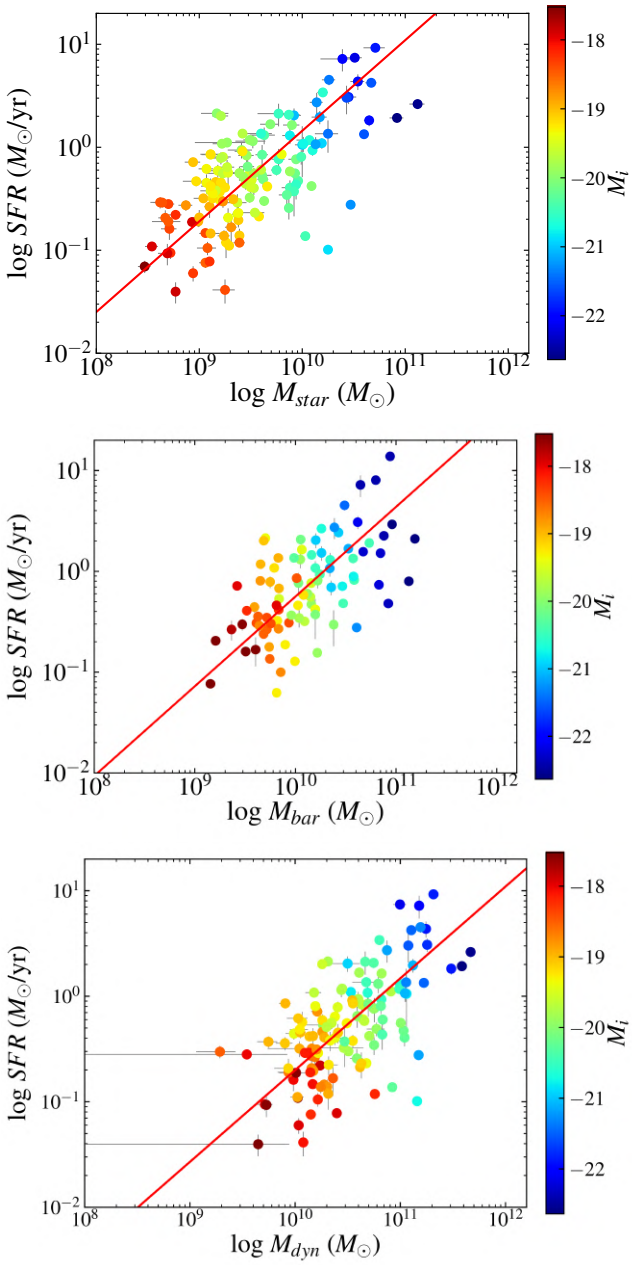

Fig. 14. Relationship between the SFR and M_{star} (top panel), M_{bar} (middle panel), and M_{dyn} (bottom panel). The OLS bisector regressions are represented with the solid red lines. The colors represent the $i-band$ magnitudes in logarithmic scale.

interesting to derive the main sequence using dynamical masses rather than with stellar masses.

The stellar main sequence relation has been derived and analysed for the HRS by Ciesla et al. (2014), Boselli et al. (2015) and Boselli et al. (2016). Thanks to the unique dataset in our hands, we can compare for the first time in the literature the main sequence relations derived using M_{star}, M_{bar}, and M_{dyn} (Fig. 14).

Consistently with Boselli et al. (2015), we use the whole HRS late-type sample but ignoring the HI-deficient galaxies. The SFR is studied considering the mean value derived using the three tracers M_{dyn}, M_{bar} and M_{star}. The number of galaxies

Galaxy mass	$\alpha \pm \sigma_\alpha$	$\beta \pm \sigma_\beta$	Scatter
Stellar mass	0.88 ± 0.10	-8.64 ± 0.67	0.29
Baryonic mass	0.89 ± 0.16	-9.05 ± 0.77	0.30
Dynamical mass	0.87 ± 0.19	-9.45 ± 0.56	0.29

Table 7. Stellar, baryonic and dynamical main sequence.

Coefficients obtained for the different main sequence relations $log\ SFR(M_\odot yr^{-1}) = (\beta \pm \sigma_\beta) + (\alpha \pm \sigma_\alpha)\ log\ M_{galaxy}(M_\odot)$ for the HRS star-forming sample. SFR are derived using a Chabrier IMF.

differs for the three cases according to the data available for each tracer. OLS bisector fits to the data have been computed. Fig. 14 and Table 7 show that the similar main sequence relations are present using the three different galaxy mass estimators. The slope and the scatter of the three relations are comparable. They obviously differ in their zero points given that $M_{dyn} > M_{bar} > M_{star}$. The best fit values can be taken for comparison with the predictions of models and simulations. We recall that these relations are valid within the mass range $3{\times}10^8 \lesssim M_{star} \lesssim 10^{11}$ $M_\odot$, or equivalently $3{\times}10^9 \lesssim M_{dyn} \lesssim 4{\times}10^{11}$ $M_\odot$. The correlation between the magnitudes (M_i), the three different mass tracers and the SFR is also pointed out on this figure with the expected scatters.

6. Conclusions

We present new high resolution Fabry-Perot observations gathered at the OHP of 152 star-forming galaxies belonging to the *Herschel* Reference Survey. Combined with those available in the literature (40 objects), previously collected with the same facility, an homogeneous set of kinematical data is now available for 192 objects (73.6% of the sample). By now, this is the first work presenting Hα high resolution spectroscopic data of the HRS, with a typical spatial sampling of ∼2 arcsec and a spectral resolution of R∼10,000. Using improved data reduction pipelines, we compute the Hα momenta, optimizing the spatial resolution given a signal-to-noise ratio through an adaptive binning method based on Voronoi tessellations. We also derive accurate kinematical models and parameters, residual velocity maps, and rotation curves.

i) We derive the *i*- and the 3.6 μm-band Tully-Fisher relations and compare them to those obtained for larger samples in the literature. Despite the difference in the kinematic data (Fabry-Perot Hα rotation curves in this work vs. HI line width profiles or long slit optical spectra in the literature), in the dynamical range of the sample, and in the statistics, the different TF relations are very consistent, suggesting that the HRS can be taken as a representative sample for these scaling relations in the local universe.

ii) Thanks to its unique multifrequency coverage, we use this dataset to derive the baryonic TF relation and the relation between the baryonic mass and the dynamical mass of galaxies. The baryonic mass is for the first time measured using direct estimates of the stellar, atomic, molecular, dust and metal mass of galaxies. The intrinsic scatter in the baryonic TF relation (∼0.16 dex) is in agreement with the predictions of cosmological simulations. The baryonic component is dominated by the stellar mass in massive objects and by the total gas mass (HI and H_2) in low mass systems. The dust content is just a very small fraction (∼0.2%) of the total baryonic mass, while the contribution of metals is fairly constant at ∼0.9%.

iv) We computed the baryonic and dynamical main sequence, finding relations with a similar slope and intrinsic scatter than the stellar mass main sequence.

The observations of the whole star-foming galaxy sample will be completed in forthcoming runs. Combined with those available at other frequencies, these 2D-spectroscopic data make the HRS a unique dataset for studying on strong statistical basis the role of gas kinematics on the process of star formation, a major step towards the understanding of the mechanisms that drive galaxy evolution.

Acknowledgements. Based on observations taken at the Observatoire de Haute Provence (OHP, France), operated by the French CNRS. The authors warmly thank Olivier Boissin from LAM and the OHP team for its technical assistance before and during the observations, namely the night team: Jean Balcaen, Stéphane Favard, Jean-Pierre Troncin, Didier Gravallon and the day team led by François Moreau as well as Dr. Auguste Le Van Suu, the Head of Observatoire de Haute Provence-Institut Pythéas. The authors thank the Mexican grants CONACYT-253085 and DGAPA-UNAM PAPIIT-IN109919 which have extensively supported this work. This work was supported by the Programme National Cosmology et Galaxies (PNCG) of CNRS/INSU with INP and IN2P3, co-funded by CEA and CNES. This research has made use of data from the HRS project. HRS is a Herschel Key Programme utilising guaranteed time from the SPIRE instrument team, ESAC scientists and a mission scientist. This research has also made use of the NASA/IPAC Extragalactic Database (NED) which is operated by the Jet Propulsion Laboratory, California Institute of Technology, under contract with the National Aeronautics and Space Administration. The authors have also made an extensive use of the HyperLeda Data base (`http://leda.univ-lyon1.fr`). The Digitized Sky Surveys were produced at the Space Telescope Science Institute under U.S. Government grant NAG W-2166. The images of these surveys are based on photographic data obtained using the Oschin Schmidt Telescope on Palomar Mountain and the UK Schmidt Telescope. The plates were processed into the present compressed digital form with the permission of these institutions. JAGL thanks the Consejo Nacional de Ciencia y Tecnologia (CONACYT) of Mexico for the scholarship awarded during the PhD studies at Aix-Marseille University. The authors are very grateful to the referee Dr. Octavio Valenzuela for the very constructive comments and suggestions.

References

Aquino-Ortíz, E., Valenzuela, O., Sánchez, S. F., et al. 2018, MNRAS, 479, 2133
Asplund, M., Grevesse, N., Sauval, A. J., & Scott, P. 2009, ARA&A, 47, 481
Bacon, R., Conseil, S., Mary, D., et al. 2017, A&A, 608, A1
Barnes, E. I. & Sellwood, J. A. 2003, AJ, 125, 1164
Bauer, A. E., Drory, N., Hill, G. J., & Feulner, G. 2005, ApJ, 621, L89
Bell, E. F. & de Jong, R. S. 2001, ApJ, 550, 212
Bell, E. F., McIntosh, D. H., Katz, N., & Weinberg, M. D. 2003, ApJS, 149, 289
Bell, E. F., Papovich, C., Wolf, C., et al. 2005, ApJ, 625, 23
Bendo, G. J., Galliano, F., & Madden, S. C. 2012, MNRAS, 423, 197
Boissier, S., Prantzos, N., Boselli, A., & Gavazzi, G. 2003, MNRAS, 346, 1215
Boselli, A. 2011, A Panchromatic View of Galaxies
Boselli, A., Boissier, S., Cortese, L., et al. 2009, ApJ, 706, 1527
Boselli, A., Boissier, S., Heinis, S., et al. 2011, A&A, 528, A107
Boselli, A., Cortese, L., & Boquien, M. 2014a, A&A, 564, A65
Boselli, A., Cortese, L., Boquien, M., et al. 2014b, A&A, 564, A67
Boselli, A., Eales, S., Cortese, L., et al. 2010, PASP, 122, 261
Boselli, A., Fossati, M., Consolandi, G., et al. 2018a, A&A, 620, A164
Boselli, A., Fossati, M., Ferrarese, L., et al. 2018b, A&A, 614, A56
Boselli, A., Fossati, M., Gavazzi, G., et al. 2015, A&A, 579, A102
Boselli, A. & Gavazzi, G. 2006, PASP, 118, 517
Boselli, A. & Gavazzi, G. 2014, A&A Rev., 22, 74
Boselli, A., Gavazzi, G., Donas, J., & Scodeggio, M. 2001, AJ, 121, 753
Boselli, A., Hughes, T. M., Cortese, L., Gavazzi, G., & Buat, V. 2013, A&A, 550, A114
Boselli, A., Lequeux, J., & Gavazzi, G. 2002, A&A, 384, 33
Boselli, A., Roehlly, Y., Fossati, M., et al. 2016, A&A, 596, A11
Brinchmann, J. & Ellis, R. S. 2000, ApJ, 536, L77
Brooks, A. M. & Zolotov, A. 2014, ApJ, 786, 87
Bryant, J. J., Owers, M. S., Robotham, A. S. G., et al. 2015, MNRAS, 447, 2857
Bundy, K., Bershady, M. A., Law, D. R., et al. 2015, ApJ, 798, 7
Cano-Díaz, M., Sánchez, S. F., Zibetti, S., et al. 2016, ApJ, 821, L26
Catinella, B., Giovanelli, R., & Haynes, M. P. 2006, ApJ, 640, 751
Catinella, B., Haynes, M. P., & Giovanelli, R. 2005, AJ, 130, 1037
Chemin, L., Balkowski, C., Cayatte, V., et al. 2006, MNRAS, 366, 812
Christensen, C. R., Governato, F., Quinn, T., et al. 2014, MNRAS, 440, 2843

Ciesla, L., Boquien, M., Boselli, A., et al. 2014, A&A, 565, A128
Ciesla, L., Boselli, A., Smith, M. W. L., et al. 2012, A&A, 543, A161
Corbelli, E. 2003, MNRAS, 342, 199
Cortese, L., Boissier, S., Boselli, A., et al. 2012, A&A, 544, A101
Cortese, L., Fogarty, L. M. R., Ho, I.-T., et al. 2014a, ApJ, 795, L37
Cortese, L., Fritz, J., Bianchi, S., et al. 2014b, MNRAS, 440, 942
Courteau, S. 1997, AJ, 114, 2402
Cowie, L. L., Songaila, A., Hu, E. M., & Cohen, J. G. 1996, AJ, 112, 839
Daddi, E., Dickinson, M., Morrison, G., et al. 2007, ApJ, 670, 156
Daigle, O., Carignan, C., Amram, P., et al. 2006a, MNRAS, 367, 469
Daigle, O., Carignan, C., Hernandez, O., Chemin, L., & Amram, P. 2006b, MNRAS, 368, 1016
Dicaire, I., Carignan, C., Amram, P., et al. 2008, MNRAS, 385, 553
Dutton, A. A. 2012, MNRAS, 424, 3123
Dutton, A. A. & Macciò, A. V. 2014, MNRAS, 441, 3359
Elbaz, D., Daddi, E., Le Borgne, D., et al. 2007, A&A, 468, 33
Elmegreen, B. G. 2015, ApJ, 814, L30
Epinat, B., Amram, P., & Marcelin, M. 2008a, MNRAS, 390, 466
Epinat, B., Amram, P., Marcelin, M., et al. 2008b, MNRAS, 388, 500
Ferrarese, L., Côté, P., Cuillandre, J.-C., et al. 2012, ApJS, 200, 4
Ferrero, I., Navarro, J. F., Abadi, M. G., et al. 2017, MNRAS, 464, 4736
Fossati, M., Gavazzi, G., Savorgnan, G., et al. 2013, A&A, 553, A91
Gach, J.-L., Hernandez, O., Boulesteix, J., et al. 2002, PASP, 114, 1043
Gallazzi, A., Brinchmann, J., Charlot, S., & White, S. D. M. 2008, MNRAS, 383, 1439
Garrido, O., Marcelin, M., & Amram, P. 2004, MNRAS, 349, 225
Garrido, O., Marcelin, M., Amram, P., et al. 2005, MNRAS, 362, 127
Garrido, O., Marcelin, M., Amram, P., & Boissin, O. 2003, A&A, 399, 51
Garrido, O., Marcelin, M., Amram, P., & Boulesteix, J. 2002, A&A, 387, 821
Gavazzi, G., Bonfanti, C., Sanvito, G., Boselli, A., & Scodeggio, M. 2002, ApJ, 576, 135
Gavazzi, G., Consolandi, G., Belladitta, S., Boselli, A., & Fossati, M. 2018, A&A, 615, A104
Gavazzi, G., Consolandi, G., Dotti, M., et al. 2015, A&A, 580, A116
Gavazzi, G., Pierini, D., & Boselli, A. 1996, A&A, 312, 397
Gavazzi, G., Zaccardo, A., Sanvito, G., Boselli, A., & Bonfanti, C. 2004, A&A, 417, 499
Giovanelli, R. & Haynes, M. P. 2002, ApJ, 571, L107
Giovanelli, R., Haynes, M. P., Herter, T., et al. 1997a, AJ, 113, 53
Giovanelli, R., Haynes, M. P., Herter, T., et al. 1997b, AJ, 113, 22
Gooch, R. 1996, in Astronomical Society of the Pacific Conference Series, Vol. 101, Astronomical Data Analysis Software and Systems V, ed. G. H. Jacoby & J. Barnes, 80
Governato, F., Zolotov, A., Pontzen, A., et al. 2012, MNRAS, 422, 1231
Guzmán, R., Gallego, J., Koo, D. C., et al. 1997, ApJ, 489, 559
Haynes, M. P. & Giovanelli, R. 1984, AJ, 89, 758
Hsieh, B. C., Lin, L., Lin, J. H., et al. 2017, ApJ, 851, L24
Hughes, T. M., Cortese, L., Boselli, A., Gavazzi, G., & Davies, J. I. 2013, A&A, 550, A115
Karim, A., Schinnerer, E., Martínez-Sansigre, A., et al. 2011, ApJ, 730, 61
Kennicutt, Jr., R. C. 1989, ApJ, 344, 685
Kennicutt, Jr., R. C. 1998a, ARA&A, 36, 189
Kennicutt, Jr., R. C. 1998b, ApJ, 498, 541
Korsaga, M., Amram, P., Carignan, C., & Epinat, B. 2019, MNRAS, 482, 154
Krumholz, M. R., Dekel, A., & McKee, C. F. 2012, ApJ, 745, 69
Krumholz, M. R. & McKee, C. F. 2005, ApJ, 630, 250
Larson, R. 1992, in Star Formation in Stellar Systems, ed. G. Tenorio-Tagle, M. Prieto, & F. Sanchez, 125
Lelli, F., McGaugh, S. S., & Schombert, J. M. 2016, ApJ, 816, L14
Lequeux, J. 1983, A&A, 125, 394
Leroy, A. K., Walter, F., Brinks, E., et al. 2008, AJ, 136, 2782
Marino, A., Plana, H., Rampazzo, R., et al. 2013, MNRAS, 428, 476
Masters, K. L., Mosleh, M., Romer, A. K., et al. 2010, MNRAS, 405, 783
Masters, K. L., Springob, C. M., Haynes, M. P., & Giovanelli, R. 2006, ApJ, 653, 861
McGaugh, S. S. 2005, ApJ, 632, 859
McGaugh, S. S. 2012, AJ, 143, 40
McGaugh, S. S. & Schombert, J. M. 2015, ApJ, 802, 18
McGaugh, S. S., Schombert, J. M., Bothun, G. D., & de Blok, W. J. G. 2000, ApJ, 533, L99
Medling, A. M., Cortese, L., Croom, S. M., et al. 2018, MNRAS, 475, 5194
Moster, B. P., Naab, T., & White, S. D. M. 2013, MNRAS, 428, 3121
Navarro, J. F., Frenk, C. S., & White, S. D. M. 1996, ApJ, 462, 563
Noeske, K. G., Weiner, B. J., Faber, S. M., et al. 2007, ApJ, 660, L43
Osterbrock, D. E., Fulbright, J. P., Martel, A. R., et al. 1996, PASP, 108, 277
Pagel, B. E. J. 2009, Nucleosynthesis and Chemical Evolution of Galaxies
Pannella, M., Gabasch, A., Goranova, Y., et al. 2009, ApJ, 701, 787
Papastergis, E., Adams, E. A. K., & van der Hulst, J. M. 2016, A&A, 593, A39
Papovich, C., Cool, R., Eisenstein, D., et al. 2006, AJ, 132, 231
Peng, Y.-j., Lilly, S. J., Kovač, K., et al. 2010, ApJ, 721, 193
Ponomareva, A. A., Verheijen, M. A. W., Papastergis, E., Bosma, A., & Peletier, R. F. 2018, MNRAS, 474, 4366
Ponomareva, A. A., Verheijen, M. A. W., Peletier, R. F., & Bosma, A. 2017, MNRAS, 469, 2387
Press, W. H., Teukolsky, S. A., Vetterling, W. T., & Flannery, B. P. 1992, Numerical Recipes in C: The Art of Scientific Computing. Second Edition
Randriamampandry, T. H., Combes, F., Carignan, C., & Deg, N. 2015, MNRAS, 454, 3743
Reddy, N. A., Steidel, C. C., Fadda, D., et al. 2006, ApJ, 644, 792
Renzini, A. & Peng, Y.-j. 2015, ApJ, 801, L29
Rodighiero, G., Cimatti, A., Gruppioni, C., et al. 2010, A&A, 518, L25
Sakai, S., Mould, J. R., Hughes, S. M. G., et al. 2000, ApJ, 529, 698
Salim, S., Rich, R. M., Charlot, S., et al. 2007, ApJS, 173, 267
Sánchez, S. F., Kennicutt, R. C., Gil de Paz, A., et al. 2012, A&A, 538, A8
Sandage, A. 1986, A&A, 161, 89
Schaye, J., Crain, R. A., Bower, R. G., et al. 2015, MNRAS, 446, 521
Schmidt, M. 1959, ApJ, 129, 243
Sheth, K., Regan, M., Hinz, J. L., et al. 2010, PASP, 122, 1397
Sorce, J. G., Tully, R. B., Courtois, H. M., et al. 2014, MNRAS, 444, 527
Sparre, M., Hayward, C. C., Springel, V., et al. 2015, MNRAS, 447, 3548
Speagle, J. S., Steinhardt, C. L., Capak, P. L., & Silverman, J. D. 2014, ApJS, 214, 15
Steinmetz, M. & Navarro, J. F. 1999, ApJ, 513, 555
Tan, J. C. 2000, ApJ, 536, 173
Toomre, A. 1964, ApJ, 139, 1217
Torres-Flores, S., Epinat, B., Amram, P., Plana, H., & Mendes de Oliveira, C. 2011, MNRAS, 416, 1936
Torrey, P., Vogelsberger, M., Genel, S., et al. 2014, MNRAS, 438, 1985
Tully, R. B. & Fisher, J. R. 1977, A&A, 54, 661
Tully, R. B. & Pierce, M. J. 2000, ApJ, 533, 744
van den Bosch, F. C. 2000, ApJ, 530, 177
van der Kruit, P. C. 1990, in The Milky Way as a Galaxy, ed. I. King, G. Gilmore, & P. C. van der Kruit, 185–226
van der Kruit, P. C. & Allen, R. J. 1978, ARA&A, 16, 103
Wang, B. & Silk, J. 1994, ApJ, 427, 759
Warner, P. J., Wright, M. C. H., & Baldwin, J. E. 1973, MNRAS, 163, 163
Whitaker, K. E., van Dokkum, P. G., Brammer, G., & Franx, M. 2012, ApJ, 754, L29
Wyse, R. F. G. 1986, ApJ, 311, L41
Zaritsky, D., Courtois, H., Muñoz-Mateos, J.-C., et al. 2014, AJ, 147, 134
Zibetti, S., Charlot, S., & Rix, H.-W. 2009, MNRAS, 400, 1181
Zu, Y. & Mandelbaum, R. 2015, MNRAS, 454, 1161

Appendix A: Quality Flags of the Rotation Curves

As described in the previous subsection 4.1.1, the maximum rotational velocity (V_{max}) per galaxy has been obtained by fitting a modified Courteau function to the rotation curve. We considered as V_{max} the maximum velocity value reached by the Courteau profile between $r = 0$ and the radius corresponding the last crown of the rotation curve. The estimated V_{max} per galaxy are shown in Table E.3, except for those galaxies for which no kinematical model was reached and therefore no rotation curve was obtained.

In order to quantify the quality of each rotation curve and to attribute a quality flag, we used an automatic classification method based on the next parameters:

i) The ratio between r_{RC} and r_{opt}. The extension of the rotation curve with respect to the optical radius is directly related to the S/N ratio of the data and the spatial coverage/distribution of Hα emission, resulting in an accurate or poor estimation of kinematics and thus influencing the quality of the rotation curve.

ii) The number of bins computed by the adaptive spatial binning when obtaining the different momenta (see Fig. A.1). High number of bins means good S/N and/or high spatial coverage of the galaxy, and vice versa, resulting in an accurate or poor estimation of kinematics and thus influencing the quality of the rotation curve.

iii) The mean velocity error of the rotation curve.

iv) The ratio between the radius of the receding and approaching side of the rotation curve. If one side is shorter than the other, its contribution to the Rotation curve will be smaller and the quality of the rotation curve will be affected.

v) We fitted a Spline function to both the receding and the approaching side in order to calculate the root mean square difference (RMSD) between both sides of the Rotation curves. The value of the RMSD is directly related to the symmetry of the velocity field from which we estimate the rotation curve and thus influencing its quality.

All these five quantities were normalized in order to be summed and to obtain a quality classification coefficient to flag the rotation curves (see Fig. A.2). These flags are given in the Table E.3:

Flag 1) Accurate estimation of the rotation curve and V_{max},

Flag 2) Reliable estimation of the rotation curve and V_{max},

Flag 3) Fairly reliable estimation of the rotation curve and V_{max} probably reached,

Flag 4) Poor estimation of the rotation curve and V_{max} probably not reached.

In addition to these 4 flags, we defined a supplementary quality classification flags called Flag “A" and Flag “B". The Flag “B" corresponds to those peculiar cases leading to a non-realistic kinematical fitting:

a) Galaxies for which $i \geq 70°$, since the absorption effects due to high inclination lead to velocity underestimations along the disc, and a little variation in i produces a very high variation in velocity determinations.

b) Objects for which $i \leq 25°$, because a little variation in i produces a very high variation in velocity determinations.

c) The difference between the morphological PA and the kinematical PA is bigger than 20°. A low S/N ratio or small spatial coverage lead to poor kinematical fittings and therefore a poor estimation of the PA. On the other hand, a velocity field supported by high velocity dispersion values related to big asymmetries, strong bars, strong defined spiral arms, among other non-circular motions, will influence the determination of the kinematical PA. Finally, morphological PAs have systematically higher uncertainties than kinematical ones, specially in galaxies with low inclination as showed in Epinat et al. (2008b).

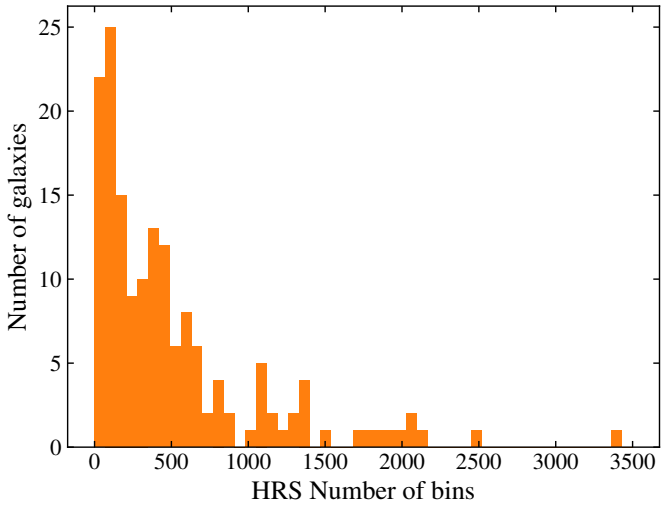

Fig. A.1. Histogram of the number of spatial bins used to compute the rotation curves. Galaxies with high spatial coverage and/or high S/N ratio have the highest number of bins.

d) the r_{RC}/r_{opt} ratio is lower than 0.6.

e) The number of bins of the adaptive spatial binning is less than 200. Poor S/N or small spatial coverage lead easily to non-realistic kinematical fittings.

f) the ratio between the Hα V_{max} of our Fabry-Perot dataset and the V_{max} of HI data (Boselli et al. 2015) is bigger than 1.5 or lower than 0.5. Since the rotation curve is derived from the velocity field, poor S/N or small Hα emission spatial coverage, in addition to asymmetries in the velocity field, could easily lead to an under/over estimation of the V_{max} of the galaxy.

g) the normalized RMSD between both sides of the RC is lower than 0.6.

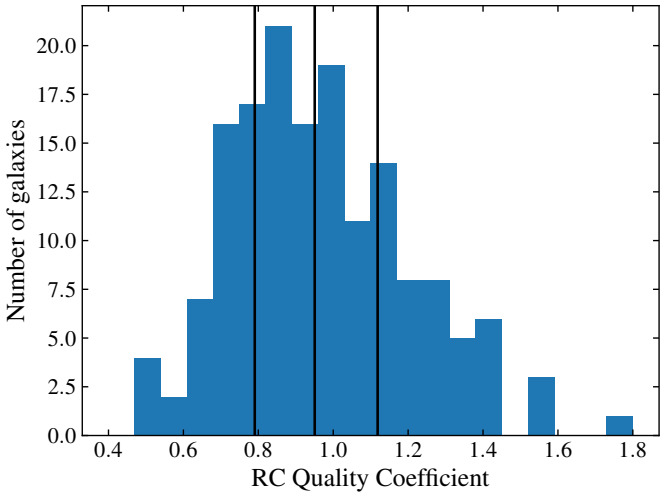

Fig. A.2. Histogram of the quality coefficient of the rotation curves. This distribution was divided in 4 quantiles with the same number of galaxies per quantil (35), in order to obtain four different Flag quality values indicated by the three vertical lines starting from the right to the left: Flag “1", Flag “2", Flag “3", Flag “4".

Appendix B: Notes on Individual Galaxies

HRS 1. Because this galaxy is not far from edge-on, the kinematical inclination was difficult to determine and we adopted the morphological value when computing the rotation curve. Otherwise the agreement between the kinematical and morphological PA of the major axis is very good. The rotation curve is fairly regular and symmetric but does not reach the r_{24} radius in *r*-band. Both models (Courteau and Zhao) suggest that it goes on rising beyond that radius.

HRS 2. There is a fairly good agreement for the PA of the major axis (4° difference only). Our rotation curve almost reaches the r_{24} radius in *r*-band for both sides. Courteau's model gives the best result since it extrapolates our rotation curve towards the HI V_{max} whereas Zhao's model suggests a declining curve beyond the r_{24} radius.

HRS 5. Because this galaxy is almost edge-on, the kinematical inclination was difficult to determine and we adopted the morphological value when computing our Hα rotation curve. Otherwise the agreement between the kinematical and morphological PA of the major axis is perfect. The rotation of the redshifted side appears more chaotic because of some faint Hα emission out of the disc which does not seem significant and could be ignored (N.B. It is not seen on the Hα + [NII] image from Boselli et al. 2015). Our curve exhibits a chaotic behavior of the redshifted side but the blueshifted side is fairly regular and both sides reach the effective radius in *r*-band where the velocity is close to the HI V_{max} for both.

HRS 6. For this edge-on galaxy we adopted the morphological values for the inclination, as well as for the PA of the major axis, when computing our Hα rotation curve. The rotation of the blueshifted side is more chaotic and the outermost part was not taken into account when tracing the rotation curve. Indeed, the residual velocity field shows exceedingly large values in the outer parts of that side. The Hα + [NII] image from Boselli et al. (2015) confirms that there is almost no emission of ionized gas beyond 30 arcsec from the nucleus on that side of the galaxy. Surprisingly, in spite of this deficiency, our Hα rotation velocity reaches much higher values than the HI V_{max} for both sides, redshifted as well as blueshifted. This is all the most surprising that our rotation curve barely reaches the effective radius in *r*-band and both models (but Zhao more than Courteau) suggest that the curve goes on rising beyond that radius.

HRS 9. The Hα emission is mainly seen on the southern and western part of the galaxy, where the Hα + [NII] image from Boselli et al. (2015) also shows bright spots. The velocity field is dominated by an almost constant value around 1410 km s^{-1} which could be due to a contamination of the observed velocities by an OH night-sky line (Osterbrock et al. (1996)). As a result, the residual velocity field exhibits strong values on both sides (north and south) of the galaxy and we did not take into account the corresponding velocities when tracing our Hα rotation curve. Also, this contamination of the velocity field could explain the difference observed between kinematical and morphological inclination (9°) as well as for the PA of the major axis (18°). The resulting rotation curve is quite chaotic for both sides and barely reaches the effective radius in *r*-band for the redshifted side. The velocity we find at this radius is close to the HI V_{max}.

HRS 10. We adopted the morphological value of the inclination for computing our Hα rotation curve. Otherwise there is an excellent agreement between the kinematical and morphological PA of the major axis (2° difference). The velocity field is regular and the resulting rotation curve is pretty good and symmetric, reaching a plateau slightly below the HI V_{max}. The curve almost reaches the r_{25} radius in B-band (quasi coincident here with the r_{24} radius in *r*-band).

HRS 11. There is an excellent agreement between the kinematical and morphological inclination (2° difference) as well as for the PA of the major axis (1° difference). The velocity field is regular, except for some high velocity points on the eastern edge of the disc (probably spurious since the Hα + [NII] image from Boselli et al. (2015) shows no significant emission at that place). Our Hα rotation curve is fairly regular and symmetric, it almost reaches the r_{25} radius in B-band for the redshifted side. Zhao's model suggests that the curve goes on rising towards a maximum reached at the r_{24} radius in *r*-band, whereas Courteau's model suggests a continuous rising beyond that radius. However, the velocity reached by our curve at the effective radius is already much higher than the HI V_{max}.

HRS 12. The Hα emission is limited to the inner disc of this galaxy and the outer parts of our velocity field are clearly not significant as suggested by the Hα + [NII] image from Boselli et al. (2015) (showing an abrupt fall of emission on the edge of the inner disc). This is confirmed by the residual velocity field where extreme values are seen all around the disc. This peculiar concentration of the ionized gas in the center of the galaxy probably explains the discrepancy observed between the kinematical and morphological inclination (9° difference) but, more specifically, that observed between the kinematical and morphological PA of the major axis (21° difference). Anyway the resulting rotation curve is fairly symmetric (when ignoring the outer parts of the velocity field) and steeply rising up to the effective radius in *r*-band where it reaches the HI V_{max}. Note however that Zhao's model exhibits a strange behavior while Courteau's model suggests that the curve reaches a plateau.

HRS 13. The Hα + [NII] image from Boselli et al. (2015) suggests that the southwestern extension of the disc, near the strong spiral arm, is spurious (which is confirmed by the extreme values of the residual velocity field) but the easternmost points, on the major axis, seem real. There is a fairly good agreement between the kinematical and morphological inclination (4° difference), also for the PA of the major axis (7° difference). The resulting rotation curve exhibits a slight asymmetry between redshifted and blueshifted side but the average is satisfying and reaches a plateau close to the HI V_{max} just after the effective radius in *r*-band.

HRS 17. We find an excellent agreement between the kinematical and morphological inclination (3° difference), also for the PA of the major axis (2° difference) when computing our Hα rotation curve. The resulting curve exhibits a perfect plateau (at the HI V_{max}) extending between the effective radius and the r_{24} radius in *r*-band.

HRS 18. Although the kinematical and morphological inclinations are in perfect agreement, we find a difference of 17° between the kinematical and morphological PA of the major axis. In fact the agreement is good for the inner part of the disc but the PA changes for the outermost isophotes of this almost face-on galaxy. Anyway the velocity field exhibits a clear gradient and the resulting Hα rotation curve is fairly symmetric but does not go very far beyond the effective radius in *r*-band. Also, the curve is continuously climbing and bends slightly after the effective radius in *r*-band, with the outermost points remaining below the HI V_{max}.

HRS 19. This galaxy has a nice spiral structure designed by many HII regions but it is almost face-on and exhibits a very faint velocity gradient, so that its Hα rotation curve is hard to draw. We adopted the morphological value of the inclination

when computing the rotation curve and found a huge difference (53°) between the kinematical and morphological PA of the major axis, likely to be explained by the shape of the outermost isophotes of the disc. The resulting rotation curve is quite chaotic and reaches a radius between the effective radius and the r_{24} radius in r-band. Also, the maximum of this curve is only half of the HI V_{max}.

HRS 21. For this edge-on galaxy, we adopted the morphological values for the inclination as well as for the PA of the major axis, when computing the Hα rotation curve. There is a marked velocity gradient and, athough it looks like a solid body rotation, the rotation curve probably reaches a plateau (as suggested by Courteau's model) beyond the effective radius in r-band since it reaches the HI maximum there.

HRS 23. Our continuum image is contaminated by many ghost images of field stars as well as by a ghost image of the galaxy itself (about 20 arcsec below the true image of HRS023) caused by a reflection of light between the Fabry-Perot interferometer and the interference filter. The extension of the Hα emission on the southwestern side of the disc is apparently linked with a ghost image of a field star, otherwise our monochromatic image seems clean when comparing with the Hα + [NII] image from Boselli et al. (2015). The velocity field is rather irregular as confirmed by the residual velocities, displaying extreme values on both sides. Nevertheless the Hα rotation curve is acceptable and continuously rising up to the r_{25} radius (at least for the blue side) where it reaches velocities 50% above the HI V_{max}. Moreover, the agreement between the kinematical and morphological inclination is perfect, as well as for the PA of the major axis.

HRS 25. This galaxy exhibits a nice velocity field and a fairly regular and symmetric Hα rotation curve, reaching a plateau at the same value as the HI V_{max} and almost extended up to the r_{24} radius in r-band (also not far from the r_{25} radius in B-band). We find an excellent agreement between the kinematical and morphological inclination (2° difference), as well as for the PA of the major axis (less than 1° difference). Both models (Zhao and Courteau) agree that our rotation curve reaches a plateau beyond the optical radius, with a rotation velocity slightly above the HI V_{max}.

HRS 26. For this almost edge-on galaxy, we adopted the morphological values for the inclination as well as for the PA of the major axis, when computing the Hα rotation curve. Although the Hα emission is limited to the inner disc of this galaxy, the rotation curve reaches the effective radius in r-band and climbs up to the HI V_{max}.

HRS 27. Despite its faint inclination (29° according to the morphology but 21° only according to the kinematics) this small galaxy exhibits a well marked velocity gradient. The kinematical PA of the major axis is slightly different from the morphological one. The resulting Hα rotation curve almost reaches the r_{24} radius in r-band (at least for the blueshifted side) and seems to climb up to a plateau at the level of the HI maximum velocity.

HRS 28. There is a good agreement between the kinematical and morphological inclination, also for the PA of the major axis, and the resulting Hα rotation curve (ignoring the northeastern extension) is fairly satisfying despite some kinks on the blueshifted side. This curve reaches the r_{25} radius for both sides and seems to approach a maximum value there, above the HI V_{max}.

HRS 32. This face-on galaxy, although it is of Sb type, has almost none Hα emission, as confirmed by the Hα + [NII] image from Boselli et al. (2015). Our Hα image and velocity field are mainly noise and we could not draw any Hα rotation curve for this galaxy.

HRS 35. As for HRS 32, this face-on galaxy has almost none Hα emission. Our Hα image and velocity field are mainly noise and we could not draw any Hα rotation curve for this galaxy.

HRS 37. Although there is 11° difference between the kinematical and morphological inclination and 16° difference between the kinematical and morphological PA of the major axis, our Hα velocity field produces a very nice and symmetric Hα rotation curve. It just reaches the r_{25} radius in B-band and probably stays flat afterwards but significantly below the HI V_{max} (150 km s^{-1} instead of 200 km s^{-1}).

HRS 38. There is a good agreement between the kinematical and morphological inclination and a perfect agreement between the kinematical and morphological PA of the major axis. Our Hα rotation curve is fairly satisfying and reaches the r_{24} radius in r-band for both sides. The maximum velocity reached there is the same as the HI V_{max} and the shape of the curve suggests that it is not far from reaching a plateau.

HRS 39. For this almost edge-on galaxy, we adopted the morphological values for the inclination as well as for the PA of the major axis, when computing the Hα rotation curve. Although our Hα rotation curve barely reaches the effective radius in r-band, it is not far from the HI V_{max} there. This is consistent with Courteau's model suggesting that it reaches a plateau just after, whereas Zhao's model suggests a continuous rising beyond.

HRS 40. The agreement between the kinematical and morphological inclination is good and it is perfect for the PA of the major axis. Our Hα rotation curve shows a solid body rotation up to the effective radius in r-band. The redshifted side suggests however that the curve reaches a plateau slightly after this radius, with a velocity matching the HI V_{max}. This is consistent with Courteau's model whereas Zhao's model suggests a decreasing curve in the outer parts.

HRS 44. This galaxy is almost face-on, hence a faint velocity gradient explaining the bad quality of the Hα rotation curve. We adopted the morphological value of the inclination for computing the Hα rotation curve and find a 38° difference between the kinematical and morphological PA of the major axis. Our Hα rotation curve is very chaotic for both sides (especially the blueshifted side) but almost reaches the r_{24} radius in r-band, with velocities greater than the HI V_{max} (100 km s^{-1} instead of 75 km s^{-1}). However, the outermost parts of our Hα map and velocity field are very noisy and must be considered with care.

HRS 47. Our Hα map and velocity field cover fairly well the optical extent of this galaxy. There is a good agreement between the kinematical and morphological inclination, also for the PA of the major axis. Despite some dispersion, our Hα rotation curve is fairly regular and symmetric; it reaches the r_{24} radius in r-band where the velocity is close to the HI V_{max} (150 km s^{-1}). Both models (Courteau and Zhao) suggest however that the curve must go on rising beyond.

HRS 48. The spiral pattern of this galaxy is well marked and our Hα map and velocity field follow this structure. The velocity gradient is well marked, despite a faint inclination of the disc. We adopted the morphological value of the inclination for computing our Hα rotation curve and find a 37° difference between the kinematical and morphological PA of the major axis. Our rotation curve is quite chaotic (especially the redshifted side) but seems to reach a plateau before the effective radius in r-band, with a velocity close to the HI V_{max} (around 120 km s^{-1}).

HRS 50. This galaxy has a nice velocity field and Hα rotation curve. We find a good agreement between kinematical and

morphological inclination, as well as for the PA of the major axis. The rotation curve is perfectly symmetric and almost reaches the r_{24} radius in r-band where the velocity is close to the HI V_{max}. Both models (Courteau and Zhao) suggest that it reaches a plateau just after.

HRS 52. The Hα + [NII] image of this galaxy from Boselli et al. (2015) shows many small HII regions dispersed in the disc that we miss here. Indeed our Hα map and velocity field only show the central part of the galaxy and none of these small regions. We find a fairly good agreement between the kinematical and morphological value of the PA of the major axis. Our rotation curve shows a steep rise and bends clearly before reaching the effective radius in r-band. The velocity almost reaches the HI V_{max} there and both models suggest that the rotation curve reaches its maximum there. However, Courteau's model suggests a plateau whereas Zhao's model suggests a decreasing curve beyond the effective radius.

HRS 56. The resulting curve is fairly symmetric and reaches a plateau between the effective radius and the r_{24} radius in r-band, with a velocity close to the HI V_{max} (around 190 km s^{-1}). Here again Courteau's model suggests a plateau whereas Zhao's model suggests a decreasing curve beyond the effective radius.

HRS 59. This galaxy is almost edge-on and the blueshifted side (west) on our Hα map seems brighter and more extended than the redshifted side (east), maybe because of dust absorption. We adopted the morphological values for the inclination as well as for the PA of the major axis, when computing our Hα rotation curve. Despite some dispersion, our curve is fairly symmetric up to the effective radius where, after a steep rising, it reaches the HI V_{max}. Beyond that radius, the curve is mainly traced by the blueshifted side which is quite chaotic. Anyway, the curve seems to follow a plateau at about 200 km s^{-1}, between the effective radius and the r_{24} radius in r-band (coincident here with the r_{25} radius in B-band).

HRS 60 (KPG 209B). The Hα emission is very faint on the redshifted side (south) of this barred galaxy, as can be seen also on the Hα + [NII] image from Boselli et al. (2015). As a result, our velocity field and Hα rotation curve mainly rely on the blueshifted side (north). The agreement between kinematical and morphological inclination is not very good (13° difference) but it is better for the PA of the major axis (5° difference). Our rotation curve is very chaotic, perhaps also because of the strong bar in the center. The curve barely reaches the effective radius in r-band where its velocity seems to stop rising although it is much smaller than the HI V_{max} (about 125 km s^{-1} compared with more than 300 km s^{-1}).

HRS 61. This galaxy is almost edge-on and the agreement between kinematical and morphological inclination is not very good (9° difference) but it is perfect for the PA of the major axis. The outermost extension to the north of our Hα map and velocity field is doubtful (there is no hint of any counterpart there on the Hα + [NII] image from Boselli et al. 2015). It gives large values on the residual velocity field and it was not taken into account when tracing our Hα rotation curve. Our curve is asymmetric, with a redshifted side rising steeper than the blueshifted side. The curve almost reaches the r_{25} radius in B-band where its velocity is slightly above the HI V_{max}. Both models (Courteau and Zhao) suggest that the rotation curve goes on rising beyond the r_{25} radius.

HRS 62. In spite of a slight disagreement between kinematical and morphological inclination (7° difference) as well as for the PA of the major axis (9° difference) our Hα rotation curve is fairly symmetric and regular. The curve reaches the r_{25} radius in B-band (coincident with the r_{24} radius in r-band for this galaxy) and its velocity there is slightly above the HI V_{max}. The curve extends beyond the r_{25} on the blueshifted side and both models (Courteau and Zhao) suggest that the plateau is not reached.

HRS 63. There is a good agreement between kinematical and morphological inclination, as well as for the PA of the major axis. Our Hα rotation curve is fairly symmetric and regular, almost reaching the r_{24} radius in r-band for both sides. The curve reaches its maximum there, with a velocity close to the HI V_{max} (around 160 km s^{-1}) although Courteau's model suggests that it goes on rising beyond that point.

HRS 64. This galaxy is almost edge-on and we adopted the morphological values for the inclination as well as for the PA of the major axis, when computing our Hα rotation curve. In spite of some dispersion, our curve is fairly symmetric and almost reaches the r_{24} radius in r-band for the blueshifted side. The maximum reached is not far from the HI V_{max} and both models (Courteau and Zhao) suggest that our curve reaches a plateau at the r_{24} radius (although slightly declining beyond that point for Zhao).

HRS 65. The Hα emission is rather patchy and very faint outside of the spiral pattern of the galaxy. Anyway, we find a fairly good agreement between kinematical and morphological inclination, as well as for the PA of the major axis. Our Hα rotation curve is quite chaotic and asymmetric but reaches the r_{25} radius in B-band (almost coincident here with the r_{24} radius in r-band). The velocity there is slightly below the HI V_{max} but both models (Courteau and Zhao) suggest that the curve, although clearly bending, is still rising beyond that radius.

HRS 66. We find a good agreement between kinematical and morphological inclination, as well as for the PA of the major axis. Our Hα rotation curve is fairly regular and symmetric, it almost reaches the r_{24} radius in r-band for both sides. The maximum velocity is slightly above the HI V_{max} and both models (but Courteau better than Zhao) suggest that the curve is about to reach a plateau after that radius.

HRS 67. The faint extension of our Hα map and velocity field, on the southern side of the galaxy, seems spurious (no counterpart can be seen on the Hα + [NII] image from Boselli et al. 2015). We adopted the morphological value of the inclination for computing our Hα rotation curve and find a 25° difference between the kinematical and morphological PA of the major axis. Anyway our Hα rotation curve, despite some dispersion, is fairly regular and symmetric. The curve barely reaches the effective radius in r-band, where the velocity is found to be close to the HI V_{max}. Both models (Courteau and Zhao) suggest that the curve goes on rising beyond the r_{24} radius in r-band but Courteau's model favors a plateau after that radius.

HRS 68. This galaxy is almost face-on and the Hα emission is concentrated in the center of the disc, as confirmed by the Hα + [NII] image from Boselli et al. (2015). As a result, the dispersion is very high in the outer parts of the velocity field, as can be seen also on the residual velocity field where extreme values are reached on both sides (blueshifted and redshifted). Furthermore, we adopted the morphological value of the inclination for computing our Hα rotation curve and find a huge 57° difference between the kinematical and morphological PA of the major axis. The resulting curve is quite chaotic and asymmetric, barely reaching a radius of 5 arcsec (about half the r_{25} radius in B-band). Also, the velocity remains below 100 km s^{-1} whereas the HI V_{max} is around 160 km s^{-1}.

HRS 70. We find an acceptable difference (12°) between the kinematical and morphological PA of the major axis. Despite this difference and some dispersion of the velocities in the very

center, our rotation curve is fairly regular and symmetric. It reaches the r_{24} radius in r-band for both sides, with a rotation velocity close to the HI V_{max}. Both models (but Courteau more than Zhao) suggest that the curve is about to reach a plateau beyond that radius.

HRS 72. Our Hα velocity field clearly suggests that this galaxy is not as inclined as suggested by its morphology (59° instead of 79°). Also, the kinematical PA of the major axis is found to be 28° different from that suggested by the outermost isophotes of the disc. The resulting Hα rotation curve is fairly regular and symmetric, revealing a pure solid body rotation up to the r_{24} radius in r-band. The rotation velocity at this radius is significantly higher than the HI V_{max} (about 160 km s^{-1} against 110 km s^{-1}).

HRS 74. Although this galaxy has a rather faint inclination, our Hα velocity field exhibits a marked velocity gradient. We find an acceptable difference (13°) between the kinematical and morphological PA of the major axis. Despite some lack of Hα emission in the very center (confirmed by the Hα + [NII] image from Boselli et al. 2015) the rotation curve can be traced with confidence and clearly shows that a maximum is reached for both sides at the effective radius in r-band. This maximum is significantly higher than the HI V_{max} (about 190 km s^{-1} instead of 165 km s^{-1}). Zhao's model suggests that the curve goes on declining beyond, whereas Courteau's model favors a plateau.

HRS 76. The lack of Hα emission on the northern side (redshifted) of this galaxy is confirmed by the Hα + [NII] image from Boselli et al. (2015). The high inclination of the disc led us to adopt the morphological values for the inclination and for the PA of the major axis when computing our Hα rotation curve. Despite a rather strong dispersion, the rotation curve is acceptable for the blueshifted side and seems to reach a plateau beyond the effective radius (but the redshifted side is difficult to exploit). Our maximum rotation velocity is close to the HI V_{max}.

HRS077. Our Hα image and velocity field covers at best the optical disc of this galaxy. The agreement between morphological and kinematical values is excellent for the inclination as well as for the PA of the major axis. Our Hα rotation curve is perfectly symmetric and, after a very steep rise, the velocity remains constant beyond the effective radius and close to the HI V_{max}. The plateau extends almost out to the r_{24} radius in r-band (close here to the r_{25} radius in B-band).

HRS 78. The agreement between morphological and kinematical values is rather good for the inclination as well as for the PA of the major axis. The Hα emission is brighter on the northern side (blueshifted) of this galaxy, as can be seen also on the Hα + [NII] image from Boselli et al. (2015). As a result, the rotation curve is better traced by the blueshifted side whereas the redshifted side is quite chaotic (also the residual velocity field shows some extreme values on the redshifted side). Our curve almost reaches the r_{24} radius in r-band and both models (Courteau and Zhao) suggest that it goes on rising for a while. Indeed the maximum rotation velocity reached by our curve is still much below the HI V_{max} (almost half).

HRS 79. This galaxy is almost edge-on and we adopted the morphological values for the inclination and for the PA of the major axis when computing our Hα rotation curve. The points surrounding the main body of the galaxy on our different maps are but noise and are not taken into account for tracing our Hα rotation curve. The Hα emission is more extended on the blueshifted side and the rotation curve is also more extended on that side, going beyond the r_{25} radius in B-band whereas it just outpasses the effective radius on the redshifted side. The maximum velocity rotation of our curve is clearly higher than the HI V_{max} (130 km s^{-1} instead of 100 km s^{-1}) and both models (but Zhao better than Courteau) suggest that the curve is not far from reaching a plateau beyond the r_{25} radius.

HRS 80. The Hα emission of this galaxy is very patchy and irregular, with only a few HII regions on the redshifted side (south). Furthermore its disc has a faint inclination and the velocity gradient is faint, leading us to adopt the morphological values for the inclination and for the PA of the major axis when computing our Hα rotation curve. Despite some dispersion, our rotation curve is fairly symmetric and both sides exhibit a strange behavior in the central part, with a clear bump within the 10 first arsec. Then the curve is mainly traced by the blueshifted side, rising up steeply before bending slightly. It extends halfway between the effective radius and the r_{24} radius in r-band where its velocity is close to the HI V_{max}. Zhao's model suggests that the rotation curve goes on rising whereas Courteau's model favors a plateau beyond the effective radius.

HRS 82 (KUG 1201+163). The Hα emission is concentrated in some bright spots in the very center of the disc of this galaxy. We find an excellent agreement between the kinematical and morphological PA of the major axis. The central part of our rotation curve rises steeply (steeper for the redshifted side) with a solid body rotation, almost out to the effective radius. Then the redshifted side goes on rising (up to the HI V_{max} of 80 km s^{-1}) whereas the blueshifted side reaches a plateau at 60 km s^{-1}. Courteau's model suggests that the rotation curve reaches a plateau at 75 km s^{-1} beyond the r_{24} radius in r-band whereas Zhao's model suggests that the curve reaches a maximum there before declining beyond.

HRS 83. The Hα emission is limited to the inner part of the disc of this galaxy. Because of the strong inclination, we adopted the morphological value of the inclination for computing our Hα rotation curve and find a perfect agreement between the kinematical and morphological PA of the major axis. Our rotation curve almost reaches the effective radius in r-band and exhibits a solid body rotation for both sides. Our maximum rotation velocity is close to the HI V_{max} and it is probable that we reach a plateau there (as suggested by Courteau's model) whereas Zhao's model suggests that it goes on rising beyond.

HRS 84. The Hα emission is much brighter on the southern part of the disc of this galaxy, as can be seen also on the Hα + [NII] image from Boselli et al. (2015). As a result, our Hα rotation curve is mainly traced by the blueshifted side (south). Also, there is some lack of emission in the very center of the disc, so that we have no points to trace the rising part of the rotation curve which is very steep here. The agreement between morphological and kinematical values is very good for the inclination as well as for the PA of the major axis. Our rotation curve almost reaches the r_{25} radius in B-band (here slightly shorter than the r_{24} radius in r-band). We find rotation velocities higher than the HI V_{max} beyond the effective radius and both models (Courteau and Zhao) suggest that it goes on rising beyond our last measured points.

HRS 86 (KPG 322A). The Hα emission covers fairly well the optical disc of this galaxy, although the Hα + [NII] image from Boselli et al. (2015) suggests that we miss some faint HII regions in the southern part of the disc. The agreement between morphological and kinematical values is not too bad for the inclination (10° difference) as well as for the PA of the major axis (7° difference). Our Hα rotation curve is fairly regular and symmetric, with a solid body rotation shape up to the r_{24} radius in r-band where it reaches a velocity close to the HI V_{max}. Despite some dispersion, the outermost points of both sides suggest that

the curve reaches its maximum there and the blueshifted side exhibits a plateau extending beyond the r_{25} radius in B-band.

HRS 88 (KPG 322B). Despite some holes, the Hα emission covers fairly well the optical disc of this galaxy. The agreement between morphological and kinematical values is not too bad for the inclination (13° difference) but rather bad for the PA of the major axis (31° difference). Our Hα rotation curve is quite chaotic in its central rising part, especially for the redshifted side (the residual velocity field shows extreme values on that side, in the inner part of the disc, and more generally all around the nucleus). The rotation curve is more quiet and symmetric beyond the effective radius and reaches the r_{24} radius in *r*-band for both sides. Altough we find a rotation velocity significantly higher than the HI V_{max}, even before reaching the effective radius, both models (Courteau and Zhao) suggest that our curve goes on rising much beyond our last measured points.

HRS 92. This galaxy is almost edge-on and we adopted the morphological values for the inclination and for the PA of the major axis when computing our Hα rotation curve. The signal to noise is rather faint, especially on the redshifted side (northwest) and our rotation curve is quite chaotic, barely reaching the effective radius. The curve exhibits a solid body rotation reaching a maximum velocity around 120 km s^{-1}. Courteau's model suggests a plateau slightly below the HI V_{max} (150 km s^{-1}) beyond the effective radius whereas Zhao's model favors a velocity peak at the effective radius.

HRS 95. The very thin stripe of Hα emission of this galaxy, as can be seen also on the Hα + [NII] image from Boselli et al. (2015), led to think that its disc is more inclined than suggested by the morphological value (56°). Anyway, we adopted that value when tracing our Hα rotation curve. We find a rather good agreement between morphological and kinematical values for the PA of the major axis (7° difference). Our rotation curve exhibits a solid body rotation for both sides, with a steep rise up to the effective radius in *r*-band. Then the curve bends clearly and reaches a maximum for both sides (around 85 km s^{-1} for the redshifted side and 110 km s^{-1} for the blueshifted side, slightly below the 115 km s^{-1} of the HI V_{max}). Courteau's model suggests that our curve reaches a plateau there, whereas Zhao's model favors a velocity peak at the effective radius.

HRS 98. This galaxy is almost edge-on and we adopted the morphological values for the inclination and for the PA of the major axis when computing our Hα rotation curve. The curve is fairly regular and symmetric but barely reaches the effective radius in *r*-band. Courteau's model suggests that the curve clearly bends after the effective radius, reaching a plateau close to the HI V_{max} at the optical radius, whereas Zhao's model suggests that it goes on rising much beyond.

HRS 104. This Sb type galaxy has no significant Hα emission, as confirmed by the Hα + [NII] image from Boselli et al. (2015). No Hα velocity field nor rotation curve could be extracted from our data. Note also that the isolated spot at about 30 arcsec north from the nucleus is probably but noise (maybe a ghost image).

HRS 106. The Hα emission covers fairly well the optical disc of this galaxy. Because of its faint inclination, we adopted the morphological value for the inclination when tracing our Hα rotation curve. We find a rather good agreement between morphological and kinematical values for the PA of the major axis (8° difference). Despite some chaotic behavior in the center (first 5 arcsec), our rotation curve is fairly regular and symmetric. The curve reaches the effective radius for both sides and the blueshifted side (south) extends out to the r_{24} radius in *r*-band. The rotation velocity reached there is close to the HI V_{max}. Anyway both models (Courteau as well as Zhao) suggest that the curve goes on rising beyond that radius.

HRS 107. This galaxy is almost edge-on and we adopted the morphological values for the inclination and for the PA of the major axis when computing our Hα rotation curve. The velocity gradient of the velocity field is well marked but the signal to noise is rather bad, so that our rotation curve suffers from dispersion. Our curve does not even reach the effective radius in *r*-band and the maximum velocity reached is between 100 km s^{-1} and 110 km s^{-1}, depending on the side, below the HI V_{max} (close to 130 km s^{-1}).

HRS 112. There is some diffuse Hα emission in the disc of this galaxy but its surface brightness is very faint, as can be seen also on the Hα + [NII] image from Boselli et al. (2015). As a result, the signal to noise ratio of our Hα map is also very faint and, despite the relatively high inclination of this galaxy, no velocity gradient can be guessed on our velocity field. We adopted the morphological values for the inclination and for the PA of the major axis when computing our Hα rotation curve, but no realistic curve could be obtained.

HRS 117. This galaxy is almost edge-on and we adopted the morphological values for the inclination and for the PA of the major axis when computing our Hα rotation curve. The Hα emission is limited to a few spots in the central part of the disc of this galaxy, mainly on the southwestern side, as can be seen also on the Hα + [NII] image from Boselli et al. (2015). As a result, our rotation curve is only traced by the blueshifted side (southwest) but nevertheless almost reaches the effective radius in *r*-band. The rotation velocity reached at this radius is close to the HI V_{max} and both models (Courteau and Zhao) suggest that the curve goes on rising beyond.

HRS 118. Apart a few bright spots in the center, the Hα emission of this galaxy is rather faint in this galaxy, as can be seen also on the Hα + [NII] image from Boselli et al. (2015). Nevertheless it covers fairly well the optical disc of the galaxy. We adopted the morphological value for the inclination and find an acceptable agreement between the morphological and kinematical values of the PA of the major axis (26° difference) when tracing our Hα rotation curve. The resulting curve is fairly regular and symmetric, almost reaching the r_{24} radius in *r*-band for both sides. The rotation velocity reached there is close to the HI V_{max}, however some patches of Hα emission northward of the disc enable to extend our Hα rotation curve much beyond the r_{25} radius in B-band on the redshifted side, suggesting that the rotation curve goes on rising beyond the optical disc. Note that Courteau's model fails to fit our data correctly, contrary to Zhao's model.

HRS 121. For this galaxy, when tracing our Hα rotation curve, we adopted the morphological values for the inclination as well as for the PA of the major axis. The resulting curve is fairly regular and symmetric, extending midway between the effective radius and the r_{24} radius in *r*-band (almost coincident here with the r_{25} radius in B-band). Both sides of the curve (although blueshifted better than redshifted) almost reach the HI V_{max}. Zhao's model suggests that the maximum of our Hα curve is almost reached by our outermost blue point whereas Courteau's model favors a continuous rising, even beyond the optical radius.

HRS 132. The Hα emission is mainly produced by some bright spots lying along the major axis. This galaxy is almost face-on. The rotation curve is quite chaotic for both sides, more especially the redshifted side (northeast) for which there is a counter rotation in the first 5 arcsec, with negative values, before the curve rises steeply. The residual velocity field exhibits high values there, but also extreme values all around the disc.

Anyway, both sides of the curve extend beyond the effective radius in *r*-band, with maximum values of the velocity rotation close to the HI V_{max}.

HRS 133. The comparison of our Hα map with the Hα + [NII] image from Boselli et al. (2015) show that we miss the outermost emission regions on the western side (redshifted) of the disc. This galaxy is almost edge-on and we adopted the morphological values for the inclination as well as for the PA of the major axis when tracing our rotation curve. Both sides of the curve are very chaotic in the central part (first 15 arcsec) then the trend is that of a solid body rotation. The curve barely reaches the effective radius in *r*-band, where its rotation velocity is clearly below the HI V_{max}. Indeed both models (Courteau and Zhao) suggest that our Hα curve goes on rising and reaches the HI V_{max} at the r_{24} radius in *r*-band.

HRS 134. Although this edge-on galaxy is classified as Sc type, its Hα emission is limited to two bright spots on each side of the nucleus, as confirmed by the Hα + [NII] image from Boselli et al. (2015). We adopted the morphological values for the inclination as well as for the PA of the major axis when tracing our Hα rotation curve. However, because of the lack of velocity points, no significant curve could be obtained.

HRS 136. This Sa type galaxy has no significant Hα emission, as confirmed by the Hα + [NII] image from Boselli et al. (2015). The spots on our maps are probably more noise than signal and no Hα rotation curve can be obtained for this galaxy.

HRS 139. When tracing the Hα rotation curve of this galaxy, we find a fairly good agreement between the morphological and kinematical values of the PA of the major axis (15° difference). The resulting rotation curve is fairly regular and symmetric, with both sides extending midway between the effective radius and the r_{24} radius in *r*-band. The rotation velocity reaches the HI V_{max} at the effective radius and the curve goes on rising beyond although with a smaller slope.

HRS 141. The Hα emission of this galaxy is rather faint and patchy but the velocity field is nice. We find a good agreement between the morphological and kinematical values of the inclination (6° difference) and a perfect agreement between the morphological and kinematical values of the PA of the major axis (less than 2° difference). The resulting Hα rotation curve is fairly regular and symmetric and reaches the effective radius in *r*-band for both sides. The rotation velocity reached there is slightly above the HI V_{max} and both models (Courteau and Zhao) suggest that it goes on rising beyond, although with a smaller slope.

HRS 142. There is a strong Hα emission in the inner disc of this Sa type galaxy but it is very faint beyond the effective radius, as can be seen also on the Hα + [NII] image from Boselli et al. (2015). Despite the relatively high inclination of the disc, the gradient of the Hα velocity is very faint, suggesting that the behavior of the ionized gas do not reflect that of the main body of the galaxy. Also, the outer parts of our velocity field have a very low signal to noise ratio and could be contaminated by a nightskyline. We adopted the morphological value for the inclination when tracing our rotation curve. The first 15 arcsec of the curve show a rising part fairly symmetric for both sides, almost out to the effective radius in *r*-band. Beyond that point the curve becomes quite chaotic but with a trend to decrease for both sides, casting doubts on the quality of our data in the outer parts of the disc of this galaxy. However, the fact that the rotation velocity reached at the effective radius is much below the HI V_{max} (20 km s^{-1} against 120 km s^{-1}) favors our hypothesis of a peculiar behavior of the ionized gas in the very center of this galaxy. Could it be the remnant of a merger?

HRS 143. This galaxy is almost edge-on and we adopted the morphological values for the inclination and for the PA of the major axis when computing our Hα rotation curve. The resulting rotation curve is fairly regular and symmetric, with both sides extending midway between the effective radius and the r_{24} radius in *r*-band. Courteau's model suggests that the curve goes on rising beyond and reaches the HI V_{max} between the r_{24} radius in *r*-band and the r_{25} radius in B-band, whereas Zhao's model favors a maximum reached at the r_{24} radius, with a rotation velocity slightly below the HI V_{max}.

HRS 145. We adopted the morphological value for the inclination of the disc of this galaxy and find a good agreement between the morphological and kinematical values of the PA of the major axis (4° difference) when computing our Hα rotation curve. The resulting curve is somewhat chaotic in the center (first 7 arcsec) where the Hα emission is less bright, otherwise it is fairly regular and symmetric, with both sides extending midway between the effective radius and the r_{24} radius in *r*-band. The rotation velocity reached at the effective radius is almost equal to the HI V_{max} but the curve goes on increasing beyond and none of the models (Courteau as well as Zhao) suggests any significant change in the slope beyond that radius.

HRS 146. This galaxy is almost edge-on and we adopted the morphological values for the inclination and for the PA of the major axis when computing our Hα rotation curve. Despite some dispersion, the resulting rotation curve is rather regular and symmetric, but barely reaches the effective radius in *r*-band. The rotation velocity reached there is around 70 km s^{-1} (against 90 km s^{-1} for the HI V_{max}). Courteau's model suggests that the rotation curve reaches a plateau beyond the optical radius (with a velocity close to the HI V_{max}) whereas Zhao's model favors a continuous increase beyond.

HRS 148. The disc of this almost edge-on galaxy appears more extended on the southeastern side (redshifted), both on continuum images and Hα images (also on the Hα + [NII] image from Boselli et al. 2015), maybe because of dust absorption. We adopted the morphological values for the inclination and for the PA of the major axis when computing our Hα rotation curve. The resulting rotation curve is fairly regular and symmetric, with both sides extending up to the effective radius in *r*-band, where the rotation velocity is equal to the HI V_{max}. The redshifted side enables to draw the curve up to the r_{25} radius in B-band (here almost coincident with the r_{24} radius in *r*-band). This side of the curve seems to reach a plateau at the effective radius but rises again shortly after, with a significant slope, although it seems to diminish when reaching the optical radius.

HRS 149. This galaxy is almost edge-on and we adopted the morphological values for the inclination and for the PA of the major axis when computing our Hα rotation curve. The resulting rotation curve is perfectly regular and symmetric, with both sides extending up to the effective radius in *r*-band, where the rotation velocity is slightly above the HI V_{max}. The shape of the curve suggests that it goes on rising beyond the effective radius, in agreement with both models (Courteau and Zhao).

HRS 151. We find a significant difference between the morphological and kinematical values of the PA of the major axis (21° difference) when computing our Hα rotation curve. The resulting curve is quite chaotic and asymmetric, anyway both sides extend slightly beyond the effective radius in *r*-band and bend slightly there, suggesting that the curve is about to reach a plateau, with a rotation velocity around the HI V_{max}. Both models

(Courteau as well as Zhao) suggest however that the curve goes on rising much beyond, even after the optical radius.

HRS 152. This galaxy is not far from face-on, we adopted the morphological value for the inclination of its disc and find a good agreement between the morphological and kinematical values of the PA of the major axis (6° difference) when computing our Hα rotation curve. The resulting rotation curve is fairly regular and symmetric, extending slightly beyond the effective radius in *r*-band (N.B. The redshifted side almost extends midway between the effective radius and the r_{24} radius in *r*-band). Courteau's model suggests that the rotation curve is not far from reaching a plateau beyond the optical radius (with a rotation velocity slightly above the HI V_{max}) whereas Zhao's model favors a continuous rising in the outer parts.

HRS 153. The disc of this galaxy is peppered with many HII regions covering its whole optical extent. It is faintly inclined and we adopted the morphological value for the inclination of the disc of this galaxy while finding a fairly good agreement between the morphological and kinematical values of the PA of the major axis (10° difference) when computing our Hα rotation curve. The resulting rotation curve is regular and symmetric, extending almost out to the r_{24} radius in *r*-band for both sides. Both models (but Courteau better than Zhao) suggest that the rotation curve reaches a plateau after the optical radius, with a rotation velocity close to the HI V_{max}.

HRS 154. This galaxy is not far from face-on, we adopted the morphological value for the inclination of its disc and find a large difference between the morphological and kinematical values of the PA of the major axis (56° difference) when computing our Hα rotation curve. Despite this disagreement, the resulting rotation curve is not so bad and, despite a strong dispersion in the central rising part (especially for the redshifted side) both sides exhibit the same trend and extend out to the r_{24} radius in *r*-band, almost reaching a plateau there, with a rotation velocity close to the HI V_{max}, as suggested by both models (Courteau and Zhao).

HRS 156. This galaxy is almost edge-on and we adopted the morphological values for the inclination and for the PA of the major axis when computing our Hα rotation curve. The resulting rotation curve is fairly regular and symmetric, with both sides extending up to the effective radius in *r*-band, where the rotation velocity is almost twice the HI V_{max}. Zhao's model suggests that the maximum of the Hα rotation curve is reached there, whereas Courteau's model suggests that it continuous rising after the effective radius and reaches a plateau beyond the optical radius.

HRS 157. The Hα emission is rich and perfectly covers the whole optical disc of this Sbc type galaxy. We find a perfect agreement between the morphological and kinematical values of the inclination and a rather good agreement between the morphological and kinematical values of the PA of the major axis (7° difference). The resulting Hα rotation curve is fairly regular and symmetric and reaches the r_{24} radius in *r*-band for both sides. The rotation velocity reached there is slightly above the HI V_{max} and both models (Courteau and Zhao) suggest that it goes on rising beyond, although with a smaller slope for Courteau's model, favoring a plateau beyond the optical radius.

HRS159. The Hα emission is limited to the inner disc of this Sa type galaxy, as can be seen also on the Hα + [NII] image from Boselli et al. (2015). Despite the relatively high inclination of the disc, the velocity gradient of the Hα velocity field of this galaxy is rather faint but, most strangely, it suggests that the PA of the major axis is almost at right angle with respect to the morphological value (92° difference). All of this suggests that the behavior of the ionized gas do not reflect that of the main body of the galaxy. Anyway, we traced our Hα rotation curve with the kinematical values suggested by our velocity field (85° for the inclination and 0° for the PA of the major axis, against 62° and 92° respectively for the morphological values). The resulting rotation curve is quite chaotic but suggests a solid body rotation for both sides of the central disc of ionized gas. The curve does not reach the effective radius but its maximum rotation velocity is close to the HI V_{max}. The strange behavior of the ionized gas in the center of this Sa galaxy leads to think that it could be the remnant of a merger (Boselli et al. 2018a).

HRS 160 (KPG 338A). We find a significant difference between the morphological and kinematical values of the inclination (17°) as well as for the PA of the major axis (17° difference) when computing our Hα rotation curve. Despite some chaotic behavior within the first 10 arcsec, the resulting curve is nevertheless fairly regular and symmetric, extending beyond the effective radius in the *r*-band. The maximum rotation velocity reached is however clearly below the HI V_{max}. Zhao's model suggests that the curve goes on rising with an almost constant slope, whereas Courteau's model suggests that we almost reach a plateau.

HRS 164. No significant Hα emission can be detected in this Sa type galaxy, as confirmed by the Hα + [NII] image from Boselli et al. (2015). We could not draw any velocity field nor rotation curve.

HRS 165. This galaxy is almost edge-on and we adopted the morphological values for the inclination and for the PA of the major axis when computing our Hα rotation curve. The resulting rotation curve is quite chaotic but reveals a solid body rotation for both sides, extending up to the effective radius in *r*-band, where the rotation velocity reaches the HI V_{max}. Zhao's model suggests that the rotation curve goes on rising beyond, whereas Courteau's model suggests that it reaches a plateau at this radius.

HRS 168. We find a fairly good agreement between the morphological and kinematical values of the PA of the major axis (9° difference) when computing our Hα rotation curve. The resulting curve is regular and symmetric, extending beyond the r_{24} radius in *r*-band for both sides. Both models (but Courteau better than Zhao) suggest that our curve reaches a plateau at the optical radius, with a rotation velocity slightly below the HI V_{max}.

HRS 169. We adopted the morphological value for the inclination of the disc of this galaxy and find a good agreement between the morphological and kinematical values of the PA of the major axis (6° difference) when computing our Hα rotation curve. Despite some dispersion for the redshifted side, the resulting curve is fairly regular and symmetric, extending beyond the effective radius in *r*-band for both sides and almost out to the r_{25} radius in B-band for the blueshifted side. The rotation velocity reaches the HI V_{max} at the effective radius but both models (Zhao more than Courteau) suggest that our curve goes on rising much beyond the optical radius.

HRS 171. The Hα emission of this Sbc galaxy is very bright but limited to the inner disc. The extension that can be seen on the northern side of the galaxy on our maps seems doubtful when comparing with the Hα + [NII] image from Boselli et al. (2015) and we did not take it into account when tracing our Hα rotation curve (indeed, this extension produces extreme values on the residual velocity field). We adopted the morphological value for the inclination of the disc of this galaxy and find a good agreement between the morphological and kinematical values of the PA of the major axis (6° difference) when computing our Hα rotation curve. The resulting curve is fairly regular and symmetric, it reaches the effective radius in *r*-band for both sides, with a rotation velocity close to the HI V_{max}. Zhao's model suggests that our curve reaches a maximum between the effective

radius and the r_{24} radius, whereas Courteau's model suggests that it goes on rising much beyond.

HRS 172. The Hα emission of this Sb galaxy is very bright but limited to the inner disc. We find a rather good agreement between the morphological and kinematical values of the inclination (10° difference) and a perfect agreement for the PA of the major axis (1° difference) when computing our Hα rotation curve. The resulting curve is fairly regular and symmetric but does not even reach the effective radius in r-band. The rotation velocity reached is close to the HI V_{max} but both models (Courteau and Zhao) suggest that the curve goes on rising much beyond.

HRS 177. This Sa type galaxy has a surprisingly rich Hα emission, covering almost all of its optical disc. We find a good agreement between the morphological and kinematical values of the inclination (5° difference) and a rather good agreement for the PA of the major axis (10° difference) when computing our Hα rotation curve. The resulting curve is fairly regular and symmetric, it extends midway between the effective radius and the r_{24} radius in r-band. The rotation velocity reached there is slightly below the HI V_{max}. Zhao's model suggests that the rotation curve goes on rising beyond the r_{24} radius, whereas Courteau's model suggests that it reaches a plateau at this radius, with a rotation velocity remaining below the HI V_{max}.

HRS 182. We find a good agreement between the morphological and kinematical values of the inclination (6° difference) and a perfect agreement for the PA of the major axis (1° difference) when computing our Hα rotation curve. The resulting curve is fairly regular and symmetric, it extends almost out to the r_{25} radius in B-band (close here from the r_{24} radius in B-band) at least for the blueshifted side. The rotation velocity reaches the HI V_{max} at the effective radius in r-band and both models (Zhao and Courteau) suggest that the Hα rotation curve reaches a plateau at the optical radius, with a rotation velocity slightly above the HI V_{max}.

HRS 184. There is but a small patch of Hα emission in the center of this Sa type galaxy, as confirmed by the Hα + [NII] image from Boselli et al. (2015). The other small spots on our maps are but noise or ghost image. We could not draw any realistic velocity field nor rotation curve.

HRS 185. The Hα emission of this Sa galaxy has a faint surface brightness and is mainly located in a central ring of about 10 arcsec radius, as can be seen also on the Hα + [NII] image from Boselli et al. (2015). Its disc is almost face-on and we adopted the morphological value for the inclination but find a significant difference between the morphological and kinematical values of the PA of the major axis (36° difference) when computing our H rotation curve. The resulting curve is poorly defined and quite chaotic, with only a few points between 5 and 20 arcsec from the center. It does not even reach the effective radius and the rotation velocity remains much below the HI V_{max} (about half).

HRS 187 (KPG 343A). Although this object is a pair of galaxies, both rich in Hα emission, the velocity field of the smaller one (NGC4496B, located about 1 arcmin southeast from NGC4496A) seems completely melted in the velocity field of the bigger one. As a result, we reduced the data as if it were a single galaxy. We find a good agreement between the morphological and kinematical values of the inclination (8° difference) as well as for the values of the PA of the major axis (7° difference) when computing our Hα rotation curve. The resulting curve is fairly regular and symmetric, it extends almost out to the r_{24} radius in r-band for both sides. The rotation velocity reaches the HI V_{max} at the effective radius in r-band and remains slightly above beyond, with an almost constant value. Both models (Zhao and Courteau) agree that the Hα rotation curve reaches its maximum at the r_{24} radius.

HRS 189. The Hα emission of this galaxy is asymmetric, with a very bright patch north of the nucleus, otherwise it is distributed rather uniformly in the central disc, as can be seen also on the Hα + [NII] image from Boselli et al. (2015). We find a rather good agreement between the morphological and kinematical values of the inclination (14° difference) and an excellent agreement between the values of the PA of the major axis (2° difference) when computing our Hα rotation curve. The resulting curve is quite chaotic, especially for the redshifted side (with extreme values on that side of the residual velocity field) and barely reaches the effective radius in r-band. The rotation velocity there is much below the HI V_{max}. Zhao's model suggests that the curve goes on rising beyond, whereas Courteau's model favors a plateau.

HRS 191. We find an excellent agreement between the morphological and kinematical values of the inclination (2° difference) as well as between the values of the PA of the major axis (1° difference) when computing our Hα rotation curve. The resulting curve is fairly regular and symmetric and extends midway between the effective radius and the r_{24} radius in r-band. Both models (Zhao and Courteau) suggest that it goes on rising, until it reaches the HI V_{max} at the r_{25} radius in B-band.

HRS 192. The Hα emission of this Sa type galaxy is limited to a few spots in the very center, as can be seen also on the Hα + [NII] image from Boselli et al. (2015). We nevertheless tried to draw the Hα rotation curve, using the morphological values of the inclination and PA of the major axis, but it gives nothing reliable.

HRS 193. We adopted the morphological value for the inclination but find a significant difference between the morphological and kinematical values of the PA of the major axis (21° difference) when computing our H rotation curve. Anyway, the resulting curve is fairly regular and symmetric and extends a bit after the effective radius in r-band for both sides (slightly more for the blueshifted side). The rotation velocity reaches the HI V_{max} after the effective radius and both models (Zhao and Courteau) suggest that it goes on rising much beyond.

HRS 195. No significant Hα emission can be seen in this Sab galaxy, as confirmed by the Hα + [NII] image from Boselli et al. (2015). The few spots seen on our maps are probably but noise. We could not draw any realistic velocity field nor rotation curve.

HRS 197. This galaxy is almost edge-on and we adopted the morphological value for the inclination. We then find an excellent agreement between the morphological and kinematical values of the PA of the major axis (2° difference) when computing our Hα rotation curve. The resulting rotation curve is fairly regular and symmetric and extends almost out to the effective radius in r-band for both sides. The rotation velocity reaches the HI V_{max} at the effective radius and both models (Zhao and Courteau) suggest that it goes on rising much beyond.

HRS 198. We find a good agreement between the morphological and kinematical values of the inclination (5° difference) as well as between the values of the PA of the major axis (5° difference) when computing our Hα rotation curve. The resulting curve is somewhat chaotic within the first 10 arcsec (for both sides) but becomes more regular and symmetric beyond. It extends almost midway between the effective radius and the r_{24} radius in r-band where the rotation velocity is close to the HI V_{max}. Zhao's model suggests that our Hα curve reaches its maximum there and declines afterwards, whereas Courteau's model favors a plateau slightly above the HI V_{max}.

HRS 199. The Hα emission of this Sb galaxy is very bright but limited to the inner disc as can be seen also on the Hα + [NII] image from Boselli et al. (2015). We find an acceptable agreement between the morphological and kinematical values of the inclination (16° difference) but a quite large difference between the morphological and kinematical values of the PA of the major axis (25° difference) when computing our Hα rotation curve. Despite some dispersion, the resulting curve shows a solid body rotation for both sides but, because of the small extension of the disc of ionized gas, it is far from reaching the effective radius in *r*-band. However, the maximum velocity rotation reached is above the HI V_{max}.

HRS 207. We find an excellent agreement between the morphological and kinematical values of the inclination (2° difference) but a quite large difference between the morphological and kinematical values of the PA of the major axis (31° difference) when computing our Hα rotation curve. The resulting curve is somewhat chaotic for the blueshifted side (especially within the 5 first arcsec) but much more regular for the redshifted side. The general shape for both sides is that of a solid body rotation, up to the effective radius in *r*-band. The blueshifted side of the curve extends a bit further, with a marked bending and a rotation velocity remaining slightly above the HI V_{max}. Zhao's model suggests that our Hα curve reaches its maximum there and declines afterwards, whereas Courteau's model favors a plateau above the HI V_{max}.

HRS 212 (KPG 346A). This galaxy has bright HII regions almost all over its optical disc. We adopted the morphological value for the inclination but find a significant difference between the morphological and kinematical values of the PA of the major axis (22° difference) when computing our Hα rotation curve. The shape of the isovelocity lines of our Hα velocity field suggests that the disc of this galaxy is warped, explaining such a difference. The velocity gradient is very faint in the center, so that our rotation curve is almost flat for both sides, up to a radius of 10 arcsec, then the curve rises very steeply and reaches a plateau at the effective radius in *r*-band, with different velocities depending on the side. The redshifted side exhibits a higher velocity than the blueshifted side (about 70 km s^{-1} against 50 km s^{-1}) but both remain much below the HI V_{max}.

HRS 225. The Hα emission of this Sb type galaxy is limited to a fuzzy patch on the southeastern side of the nucleus, as can be seen also on the Hα + [NII] image from Boselli et al. (2015). The faint northern spot seen on our Hα map is probably but noise. We nevertheless tried to draw the Hα rotation curve, using the morphological values of the inclination and PA of the major axis, but it gives nothing reliable.

HRS 226. We find an excellent agreement between the morphological and kinematical values of the inclination (1° difference) as well as between the morphological and kinematical values of the PA of the major axis (2° difference) when computing our Hα rotation curve. The resulting rotation curve is fairly regular and symmetric and extends out to the effective radius in *r*-band for both sides. Both models (Zhao and Courteau) agree that our curve reaches a plateau at the effective radius, with a rotation velocity slightly above the HI V_{max}.

HRS 230. We find an excellent agreement between the morphological and kinematical values of the inclination (less than 1° difference) as well as between the morphological and kinematical values of the PA of the major axis (1° difference) when computing our Hα rotation curve. The resulting rotation curve is fairly regular and symmetric and extends out to the effective radius in *r*-band for both sides. Both models (but Courteau better than Zhao) agree that our curve reaches a plateau slightly after the effective radius, with a rotation velocity remaining below the HI V_{max}.

HRS 237. Except in the very center, the Hα emission of this Im type galaxy has a faint surface brightness. We adopted the morphological value for the inclination when computing our Hα rotation curve. Despite some dispersion, the trend of the curve for both sides is that of a solid body rotation, albeit with a rather faint slope. Both sides extend a bit further than the effective radius in *r*-band and the rotation velocity remains below the HI V_{max}.

HRS 238. The Hα emission of this Sm galaxy is rather faint and patchy. The large extension bordering the whole northeastern side of the disc has a very faint surface brightness and seems doubtful (N.B. It was not imaged by Boselli et al. 2015). The fact that all this area appears with the same velocity (coded with blue color on our velocity field map) suggests that our data are polluted there by an OH night skyline insufficiently subtracted. We adopted the morphological value for the inclination but find a large difference between the morphological and kinematical values of the PA of the major axis (27° difference) when computing our Hα rotation curve. The resulting curve is rather poor, because of the faintness of the Hα emission, its trend is that of a solid body rotation for both sides. It reaches the effective radius in *r*-band, with a rotation velocity which is only half the HI V_{max}.

HRS 239 (KPG 351B). This galaxy is almost edge-on and we adopted the morphological values for the inclination and for the PA of the major axis when computing our Hα rotation curve. The resulting curve is fairly regular and symmetric up to a radius of 20 arcsec, showing a solid body rotation with a steep slope. Then the slope of the blueshifted side diminishes whereas the redshifted side stops for a while before climbing again with about the same slope as the blueshifted side. Both sides of the curve extend slightly after the effective radius in *r*-band and the models (Zhao as well as Courteau) suggest that our curve reaches a plateau at the optical radius, with a rotation velocity above the HI V_{max}.

HRS 249. The Hα emission of this Sb type galaxy is limited to a bright spot on the left of the nucleus and another (less bright) spot on its right. We could not draw any realistic velocity field nor rotation curve.

HRS 252. The disc of this Sd galaxy is peppered with many bright HII regions covering almost completely the southern part of its optical disc, but less numerous on the northern side (redshifted) as can be seen also on the Hα + [NII] image from Boselli et al. (2015). We find an excellent agreement between the morphological and kinematical values of the inclination (less than 1° difference) as well as between the morphological and kinematical values of the PA of the major axis (3° difference) when computing our Hα rotation curve. The resulting curve is fairly regular and symmetric up to the effective radius in *r*-band for both sides. The blueshifted side then enables to trace the curve up to the r_{24} radius in *r*-band (found here slightly beyond the r_{25} radius in B-band) where it reaches a rotation velocity higher than the HI V_{max}. Zhao's model suggests that our curve reaches a maximum there before declining, whereas Courteau's model favors a continuous rising, although with a smaller slope.

HRS 255. The spiral pattern of this Scd galaxy is underlined by many HII regions, as can be seen on the Hα + [NII] image from Boselli et al. (2015). This galaxy is not far from face-on, we adopted the morphological value for the inclination of its disc and find a large difference between the morphological and kinematical values of the PA of the major axis (55° difference) when computing our Hα rotation curve. The resulting curve

is quite chaotic, especially in the central part, but the general trend, for both sides, is that of a solid body rotation with a faint slope. Both sides extend beyond the r_{24} radius in r-band, where the rotation velocity is slightly above the HI V_{max}. The redshifted side enables to draw the rotation curve almost out to the r_{25} radius in B-band, keeping the same slope, but with a large uncertainty.

HRS 256. The Hα emission is bright but limited to the inner disc of this Sa type galaxy, as can be seen also on the Hα + [NII] image from Boselli et al. (2015). Despite the relatively high inclination of the disc, the velocity gradient of the Hα velocity field of this galaxy is rather faint but, most strangely, it suggests that the PA of the major axis is almost at right angle with respect to the morphological value (95° difference). All of this suggests that the behavior of the ionized gas do not reflect that of the main body of the galaxy. We adopted the morphological value for the inclination of its disc when computing our Hα rotation curve. The resulting curve is quite chaotic for the redshifted side while suggesting a solid body rotation for the blueshifted side of the central disc of ionized gas. The curve does not reach the effective radius and its maximum rotation velocity is very far from the HI V_{max}. The strange behavior of the ionized gas in the center of this Sa galaxy leads to think that it could be the remnant of a merger (as already seen for HRS142 and HRS159).

HRS 261. This galaxy is almost edge-on and we adopted the morphological values for the inclination and for the PA of the major axis when computing our Hα rotation curve. Except some strong dispersion around 10 arcsec radius for the redshifted side, the resulting curve is fairly regular and symmetric, rising up to the effective radius in r-band for both sides. The redshifted side enables to draw the curve a bit further (midway between the effective and r_{24} radius in r-band) where it reaches the HI V_{max}. Both models (Zhao as well as Courteau) suggest that our curve goes on rising beyond the optical radius, although with a smaller slope for Courteau's model.

HRS 264. This galaxy is almost edge-on and we adopted the morphological values for the inclination and for the PA of the major axis when computing our Hα rotation curve. The resulting curve is fairly regular and symmetric, almost reaching the effective in r-band for both sides. The rotation velocity at that radius is not far from the HI V_{max} but both models (Zhao as well as Courteau) suggest that our curve goes on rising beyond the optical radius.

HRS 267. The Hα emission of this almost edge-on Scd type galaxy is asymmetric, much brighter on the southwestern side (blueshifted), probably because of absorption by dust in the disc. We adopted the morphological values for the inclination and for the PA of the major axis when computing our Hα rotation curve. The resulting curve is quite chaotic, more especially for the redshifted side that exhibits a marked bump at about 10 arcsec radius before rising again. The curve do not even reach the effective radius in r-band and the rotation velocity remains much below the HI V_{max}.

HRS 268. We adopted the morphological values for the inclination and for the PA of the major axis when computing our Hα rotation curve. The resulting curve is fairly regular for the blueshifted side and extends out to the r_{25} radius in B-band (which is here slightly larger than the r_{24} radius in r-band). The redshifted side is shorter and more irregular, although with the same general trend. The rotation velocity reaches the HI V_{max} and the blueshifted side seems to mark a plateau at this value, although both models (Zhao and Courteau) favor a continuous rising of the rotation curve beyond the optical radius.

HRS 271. This galaxy is almost edge-on and we adopted the morphological values for the inclination and for the PA of the major axis when computing our Hα rotation curve. The resulting curve is quite irregular within 10 arcsec radius from the center but the general trend is the same for both sides, that of a solid body rotation with a diminishing slope when reaching the effective radius in r-band. The rotation velocity reached at that radius is equal to the HI V_{max}. Zhao's model suggests that our rotation curve reaches a maximum at the optical radius whereas Courteau's model favors a continuous rising beyond.

HRS 273. This galaxy is almost edge-on and we adopted the morphological values for the inclination when computing the rotation curve. We find an excellent agreement between the morphological and kinematical values of the PA of the major axis (less than 2° difference) and, despite some dispersion in the rising part, the resulting curve is fairly regular and symmetric. The curve extends midway between the effective radius and the r_{24} radius in r-band. The maximum rotation velocity reached is close to the HI V_{max} and both models (but Courteau better than Zhao) suggest that our rotation curve reaches a plateau at the optical radius.

HRS 275. The optical disc of this Sd type galaxy is peppered with many HII regions covering it completely. The inclination of the disc is rather faint and we adopted the morphological value when computing our Hα rotation curve. We find a rather large difference between the morphological and kinematical values of the PA of the major axis (35° difference) but the resulting rotation curve is quite regular and symmetric, despite some dispersion. Indeed both sides show the same trend, that of a solid body rotation, almost out to the r_{24} radius in r-band where the rotation velocity is about to reach the HI V_{max}. Zhao's model suggests that our curve reaches a maximum slightly after the r_{24} radius, whereas Courteau's model suggests a continuous rising beyond.

HRS 276. The Hα emission of this Sbc type galaxy covers fairly well the northeastern side of the optical disc but is patchy for the southwestern side (redshifted) as can be seen also on the Hα + [NII] image from Boselli et al. (2015). We adopted the morphological value for the inclination of the disc, when computing our Hα rotation curve, and find a rather good agreement between the morphological and kinematical values of the PA of the major axis (7° difference). The redshifted side of the curve is rather ill defined, because of the lack of velocity points, but the blueshifted side is quite regular and enables to trace the rotation curve much beyond the effective radius in r-band, after which it seems to reach a plateau. Indeed Courteau's model suggests that our curve reaches a plateau after the effective radius, with a velocity close to the HI V_{max}, whereas Zhao's model favors a continuous rising beyond that radius.

HRS 278. The Hα emission of this edge-on Sb type galaxy has a faint surface brightness and is limited to the inner disc as can be seen also on the Hα + [NII] image from Boselli et al. (2015). We adopted the morphological values for the inclination and for the PA of the major axis when computing our Hα rotation curve. Despite some dispersion, both sides of the curve show the same trend, that of a solid body rotation, and extend out to about 3/4 of the effective radius in r-band. The rotation velocity reached for both sides is clearly above the HI V_{max}.

HRS 279. The optical disc of this Sd type galaxy is peppered with many HII regions covering it completely. We find a fairly good agreement between the morphological and kinematical values of the inclination (7° difference) as well as between the morphological and kinematical values of the PA of the major axis (5° difference) when computing our Hα rotation

curve. Despite some dispersion within the first 20 arcsec, the resulting curve is fairly regular and symmetric, almost reaching the r_{24} radius in r-band (at least for the redshifted side) which is coincident here with the r_{25} radius in B-band. The rotation velocity reaches the HI V_{max} for both sides of the curve. Zhao's model suggests that our curve reaches a maximum before the optical radius and declines strongly beyond, whereas Courteau's model favors a continuous rising beyond the optical radius, although with a smaller slope.

HRS 280. The Hα emission of this Sb type galaxy shows a bright inner disc, with an extension of faint surface brightness on the western extremity of the disc (blueshifted side) as can be seen also on the Hα + [NII] image from Boselli et al. (2015). The inclination of the disc is rather strong and we adopted the morphological value when computing our Hα rotation curve. We find a rather good agreement between the morphological and kinematical values of the PA of the major axis (7° difference) and, despite the relative small number of velocity points, the resulting rotation curve is quite regular and symmetric. The curve extends out to the effective radius in r-band for both sides, reaching there a rotation velocity equal to the HI V_{max}. The blueshifted side enables to trace our rotation curve a bit further and seems to stop rising. Indeed both models (but Courteau better than Zhao) suggest that our curve reaches a plateau slightly above the HI V_{max} just after the effective radius.

HRS 282. We detected no significant Hα emission in this BCD type galaxy (N.B. It was not imaged by Boselli et al. 2015) and could not draw any reliable Hα velocity field nor rotation curve.

HRS 283. The disc of this galaxy is completely covered by Hα emission and we find an excellent agreement between the morphological and kinematical values of the inclination (1° difference only) as well as between the morphological and kinematical values of the PA of the major axis (2° difference only) when computing our Hα rotation curve. The resulting rotation curve is fairly regular and symmetric, despite some waves on the redshifted side, it extends out to the r_{24} radius in r-band (almost coincident here with the r_{25} radius in B-band) for both sides. The rotation velocity reached there is equal to the HI V_{max}, but both models (Zhao and Courteau) suggest that our curve goes on rising beyond the optical radius, although with a smaller slope for Courteau's model.

HRS 284. The disc of this galaxy is strongly inclined and we adopted the morphological values for the inclination and for the PA of the major axis when computing our rotation curve. The resulting curve is fairly regular and symmetric, with the same trend for both sides, that of a solid body rotation. The curve extends out to about 3/4 of the r_{24} radius in r-band and the rotation velocity reached is slightly above the HI V_{max}. Both models (Zhao and Courteau) suggest that our rotation curve reaches a plateau shortly after.

HRS 287. This Scd type galaxy has a thick bar and a strong spiral pattern, both underlined by bright HII regions. We adopted the morphological value for the inclination of the disc, when computing our Hα rotation curve, and find a significant difference between the morphological and kinematical values of the PA of the major axis (25° difference). Despite some distortions, the agreement between both sides of our curve is not so bad for the first 10 arcsec (about half the effective radius in r-band), but quite different beyond. The redshifted side then keeps an almost constant rotation velocity, equal to the HI V_{max}, out to the r_{24} radius in r-band (almost coincident here with the r_{25} radius in B-band). The blueshifted side is not so extended and its velocity, after a small pause, goes on rising continuously beyond the effective radius. Zhao's model suggests that our rotation curve reaches a maximum (close to the HI V_{max}) between the effective radius and r_{24} radius before declining very slowly, while Courteau's model suggests that it reaches a plateau with a rotation velocity close to the HI V_{max}.

HRS 289. This Sbc type galaxy has a nice spiral pattern, underlined by many bright HII regions. We find a reasonable agreement between the morphological and kinematical values of the inclination (10° difference) as well as between the morphological and kinematical values of the PA of the major axis (14° difference) when computing our Hα rotation curve. The resulting rotation curve is fairly regular and symmetric, extending almost out to the r_{24} radius in r-band (at least for the blueshifted side). The central part of the curve is ill defined, because of the lack of Hα emission there, and the velocity bump seen at about 10 arcsec from the center is likely to be explained by the strong central bulge. Both models (but Courteau better than Zhao) suggest that our curve rapidly reaches a plateau with a rotation velocity slightly above the HI V_{max}.

HRS 290. The Hα emission of this almost edge-on Sa type galaxy is concentrated in the inner disc. We adopted the morphological values for the inclination and for the PA of the major axis when computing our rotation curve. Despite the relatively small number of velocity points, the resulting curve is fairly regular and symmetric, almost reaching the effective radius in r-band. The redshifted side reaches a higher rotation velocity than the blueshifted side and both are clearly above the HI V_{max}.

HRS 291. The Hα emission of this Sab type galaxy is limited to a few faint spots around the nucleus. We cannot check if they are real or mere noise since it was not imaged by Boselli et al. (2015). We could not draw any reliable Hα velocity field nor rotation curve.

HRS 292. The Hα emission of this Sb type galaxy is very bright but limited to the inner disc, as can be seen also on the Hα + [NII] image from Boselli et al. (2015). We find an acceptable agreement between the morphological and kinematical values of the PA of the major axis (14° difference). The resulting curve is regular and symmetric, with both sides reaching the effective radius in r-band. The curve rises steeply up to a plateau at the HI V_{max} as confirmed by both models (Zhao and Courteau).

HRS293. The whole optical disc of this Sdm galaxy is well covered by HII regions. We find a reasonable agreement between the morphological and kinematical values of the inclination (7° difference) as well as between the morphological and kinematical values of the PA of the major axis (16° difference) when computing our Hα rotation curve. Despite some waves on the redshifted side, we find a fairly regular and symmetric curve, extending out to the optical radius (the r_{24} radius in r-band and r_{25} radius in B-band are coincident here). The rotation velocity reached there is the HI V_{max} but both models (Zhao and Courteau) suggest that our curve goes on rising beyond the optical radius.

HRS 294. Apart from a few bright spots, the Hα emission of this edge-on Sb type galaxy has a rather faint surface brightness, as can be seen also on the Hα + [NII] image from Boselli et al. (2015). We adopted the morphological values for the inclination and for the PA of the major axis when computing our rotation curve. Despite the relatively small number of velocity points, the resulting curve is fairly regular and symmetric but do not even reach the effective radius in r-band. Both sides show a solid body rotation that could reach the HI V_{max} at the effective radius if extrapolated keeping the same slope.

HRS 297. The whole optical disc of this Sbc type galaxy is peppered with bright HII regions. It is strongly inclined and we adopted the morphological values for the inclination as well as for the PA of the major axis when computing our rotation curve. Despite some waves on both sides, the resulting curve is fairly regular and symmetric, extending almost out to the r_{24} radius in r-band where the rotation velocity reaches the HI V_{max}. Zhaos's model suggests that our curve goes on rising beyond the optical radius, almost with the same slope, but Courteau's model apparently fails fitting our data correctly here.

HRS 298 (KPG 397A). The Hα emission of this peculiar galaxy is very bright but limited to the inner disc. The large and faint structure surrounding the northern and western side of the disc on our maps seems doubtful since nothing can be seen there on the Hα + [NII] image from Boselli et al. (2015). The fact that it pops out with the same velocity, color coded green on the map of our velocity field, strongly suggests that it is the remnant of an OH night skyline insufficiently subtracted (it also gives extreme values on the residual velocity field). Anyway, it was not taken into account when computing our Hα rotation curve. We adopted the morphological value for the inclination of the disc, when computing our Hα rotation curve, and find a rather good agreement between the morphological and kinematical values of the PA of the major axis (9° difference). The resulting rotation curve is very regular and symmetric, extending almost out to the r_{25} radius in B-band where it reaches a rotation velocity higher than the HI V_{max}. Zhao's model suggests that our curve goes on rising beyond the optical radius but Courteau's model favors a plateau shortly after.

HRS 300. There is no significant Hα emission in this Sab type galaxy, as confirmed by the Hα + [NII] image from Boselli et al. (2015) that shows only a very faint fuzzy spot in the center. The spots on our maps are probably more noise than signal and we could not draw any reliable Hα velocity field nor rotation curve.

HRS 301. The whole optical disc of this Sc type galaxy is peppered with numerous HII regions as can be seen also on the Hα + [NII] image from Boselli et al. (2015). We find a good agreement between the morphological and kinematical values of the inclination (8° difference) as well as between the morphological and kinematical values of the PA of the major axis (6° difference) when computing our Hα rotation curve. The resulting rotation curve is fairly regular and symmetric, except some dispersion (for both sides) around the 10 arcsec radius. The curve extends out to the r_{24} radius in r-band and reaches a rotation velocity higher than the HI V_{max}. Both models (Zhao and Courteau) suggest that our curve goes on rising beyond the optical radius but with a diminishing slope.

HRS 303. The Hα emission of this Sb type galaxy is very bright but limited to the inner disc. We find a rather good agreement between the morphological and kinematical values of the inclination (10° difference) and an excellent agreement between the morphological and kinematical values of the PA of the major axis (2° difference) when computing our Hα rotation curve. The resulting curve is fairly regular and symmetric, with both sides extending a bit further than the effective radius in r-band. Courteau's model suggests that our rotation curve reaches a plateau at the optical radius with a rotation velocity around 120 km s^{-1} whereas Zhao's model favors a continuous rising curve.

HRS 304. The disc is strongly inclined and we adopted the morphological values for the inclination as well as for the PA of the major axis when computing our rotation curve. The resulting curve is fairly regular and symmetric, with both sides extending a bit further than the effective radius in r-band. The curve reaches the HI V_{max} there but both models (Zhao and Courteau) suggest that it goes on rising beyond that radius, although with a smaller slope for Courteau's model.

HRS 305. The Hα emission of this peculiar galaxy is limited to two relatively bright spots on each side of the nucleus, as can be seen also on the Hα + [NII] image from Boselli et al. (2015). Some velocity gradient can be seen anyway on our velocity field and we adopted the morphological values for the inclination as well as for the PA of the major axis when computing our rotation curve. The resulting curve is quite chaotic and limited to one third of the effective radius in r-band. The blueshifted side is less dispersed than the redshifted side but no more extended and its rotation velocity remains much below the HI V_{max}.

HRS 308. The Hα emission of this Sb type galaxy is limited to a faint fuzzy central patch as can be seen also on the Hα + [NII] image from Boselli et al. (2015). Anyway, our velocity field shows some gradient and we tried to draw the rotation curve. The disc is strongly inclined and we adopted the morphological values for the inclination as well as for the PA of the major axis in order to compute our rotation curve. The result is however quite disappointing and not reliable.

HRS 309. The optical disc of this Sm type galaxy is peppered with many bright HII regions. We find a rather good agreement between the morphological and kinematical values of the inclination (11° difference) and an excellent agreement between the morphological and kinematical values of the PA of the major axis (3° difference) when computing our Hα rotation curve. Despite a rather faint spatial sampling, the resulting curve is fairly regular and symmetric, with both sides extending a bit further than the r_{24} radius in r-band. Our curve remains clearly below the HI V_{max} but both models (Zhao and Courteau) suggest that it goes on rising beyond the optical radius, although with a smaller slope for Courteau's model.

HRS 313. The disc of this Sbc type galaxy is peppered with many bright HII regions. The disc is strongly inclined and we adopted the morphological values for the inclination as well as for the PA of the major axis in order to compute our rotation curve. Despite some dispersion, the resulting curve is fairly regular and symmetric, with both sides extending out halfway between the effective radius and the r_{24} radius in r-band. Our curve just reaches the HI V_{max} but both models (Zhao and Courteau) suggest that it goes on rising beyond the optical radius, although with a smaller slope for Courteau's model which is almost flat in the outer part.

HRS 314. The Hα emission of this Sd type galaxy is asymmetric, with brighter HII regions on the northern side (blueshifted) as can be also on the Hα + [NII] image from Boselli et al. (2015). The whole optical disc is nevertheless well covered on both sides by ionized gas. We find a good agreement between the morphological and kinematical values of the inclination (6° difference) and an acceptable agreement between the morphological and kinematical values of the PA of the major axis (13° difference) when computing our Hα rotation curve. The resulting curve is quite chaotic, with a larger dispersion on the redshifted side for which the Hα emission is the less bright. Nevertheless, both sides of the curve exhibit the same general trend, steeply rising up to the effective radius in r-band where the rotation velocity reaches the HI V_{max}. Beyond that radius, the rotation velocity remains almost constant for both sides, out to the r_{25} radius in B-band for the redshifted side. Zhao's model suggests that the curve reaches a maximum (with a rotation velocity close to the HI V_{max}) before the optical radius and declines beyond, whereas Courteau's model favors a plateau

beyond the optical radius (with a rotation velocity close to the HI V_{max}).

HRS 317. This galaxy is almost edge-on and we adopted the morphological value for the inclination. We then find an excellent agreement between the morphological and kinematical values of the PA of the major axis (less than 1° difference) when computing our Hα rotation curve. Despite the faint sampling and some dispersion, the resulting rotation curve is fairly regular and symmetric and extends almost out to the r_{25} radius in B-band for both sides. The rotation velocity just reaches the HI V_{max} but both models (Zhao and Courteau) suggest that it goes on rising beyond the optical radius.

HRS318. The faint extension seen on our maps, on the northeastern side of the disc, is doubtful since nothing can be seen there on the Hα + [NII] image from Boselli et al. (2015). We adopted the morphological value for the inclination and find an acceptable agreement between the morphological and kinematical values of the PA of the major axis (16° difference) when computing our Hα rotation curve. The resulting curve is fairly regular and symmetric, despite some waves in the outer part of the redshifted side. The curve extends out to the r_{25} radius in B-band (almost coincident here with the r_{24} radius in *r*-band). Both models (Zhao and Courteau) suggest that our curve goes on rising beyond the optical radius, athough with a lower slope for Courteau's model.

HRS 319. The spiral pattern of this Scd galaxy is underlined by bright HII regions. We find an excellent agreement between the morphological and kinematical values of the inclination (1° difference) as well as between the morphological and kinematical values of the PA of the major axis (3° difference) when computing our Hα rotation curve. However, although the rising part of our curve is fairly regular and symmetric, it becomes quite chaotic and asymmetric beyond the effective radius in *r*-band. The blueshifted side of the curve rises up to the HI V_{max}, extending midway between the effective radius and the r_{24} radius in *r*-band. The redshifted side extends out to the r_{25} radius in B-band with velocities remaining clearly below the HI V_{max}. Zhao's model suggests a declining curve beyond the effective radius, whereas Courteau's model favors a plateau after that radius.

HRS 321. The Hα emission of this Sb type galaxy is very bright but limited to the inner disc as can be seen also on the Hα + [NII] image from Boselli et al. (2015). We adopted the morphological value for the inclination and find a good agreement between the morphological and kinematical values of the PA of the major axis (4° difference) when computing our Hα rotation curve. The resulting curve is fairly regular and symmetric but extends out only midway between the effective radius in *r*-band and the r_{25} radius in B-band (at least for the redshifted side). The rotation velocity remains much below the HI V_{max} and both models (Zhao and Courteau) suggest that it stops rising beyond the effective radius in *r*-band. Zhao's model suggests that our curve declines beyond that radius, whereas Courteau's model favors a plateau.

HRS 322. The spiral pattern of this almost face-on Sa type galaxy is underlined by HII regions tracing a ring with about 1.5 arcmin radius. Because of this peculiar distribution of the H alpha emission, our rotation curve has no points in its rising part and it is difficult to optimize the kinematical parameters. We adopted the morphological value of the inclination and choose the value of the PA of the major axis by eye-estimate from the gradient of the velocity field. The resulting curve shows a plateau at about 210 km s^{-1}, above the HI V_{max}.

HRS 323. The Hα emission of this almost edge-on Sb galaxy is asymmetric, much brighter on the northern side (blueshifted), as can be seen also on the Hα + [NII] image from Boselli et al. (2015). We adopted the morphological values for the inclination as well as for the PA of the major axis when computing our rotation curve. The resulting curve is quite chaotic in the central part, out to a radius of 10 arcsec radius, but more regular and symmetric beyond. The blueshifted side (which is the brighter) is better defined than the redshifted side but both sides have about the same slope in their outer part, extending a bit further than the effective radius in *r*-band. Both models (Zhao and Courteau) suggest that our curve goes on rising with about the same slope and reaches the HI V_{max} at the r_{24} radius in *r*-band.

Appendix C: Hα profiles

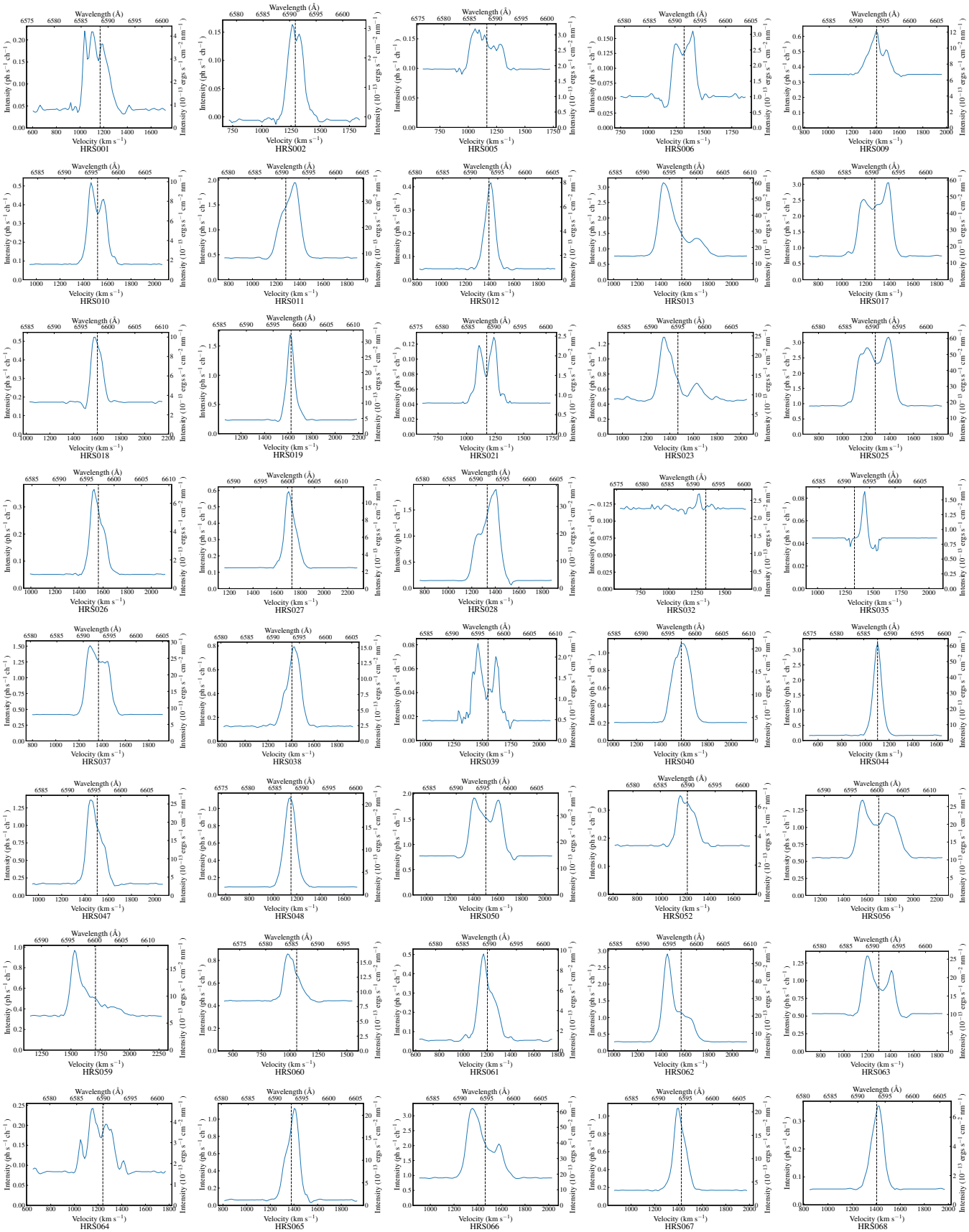

Fig. C.1. Integrated Hα profiles for the 152 HRS galaxies concerning this work. The profiles are displayed over three times the free spectral range (~25Å top label, 1100 km s^{-1} bottom label). The calibrated intensity in erg seg^{-1} cm^{-2} nm^{-1} appears on the right side of the Y-axis. The black dashed vertical line represents the systemic velocity computed by the kinematical models; in the cases where a kinematical modelling was not possible, the corresponding systemic velocity taken from Boselli et al. (2010) is plotted instead.

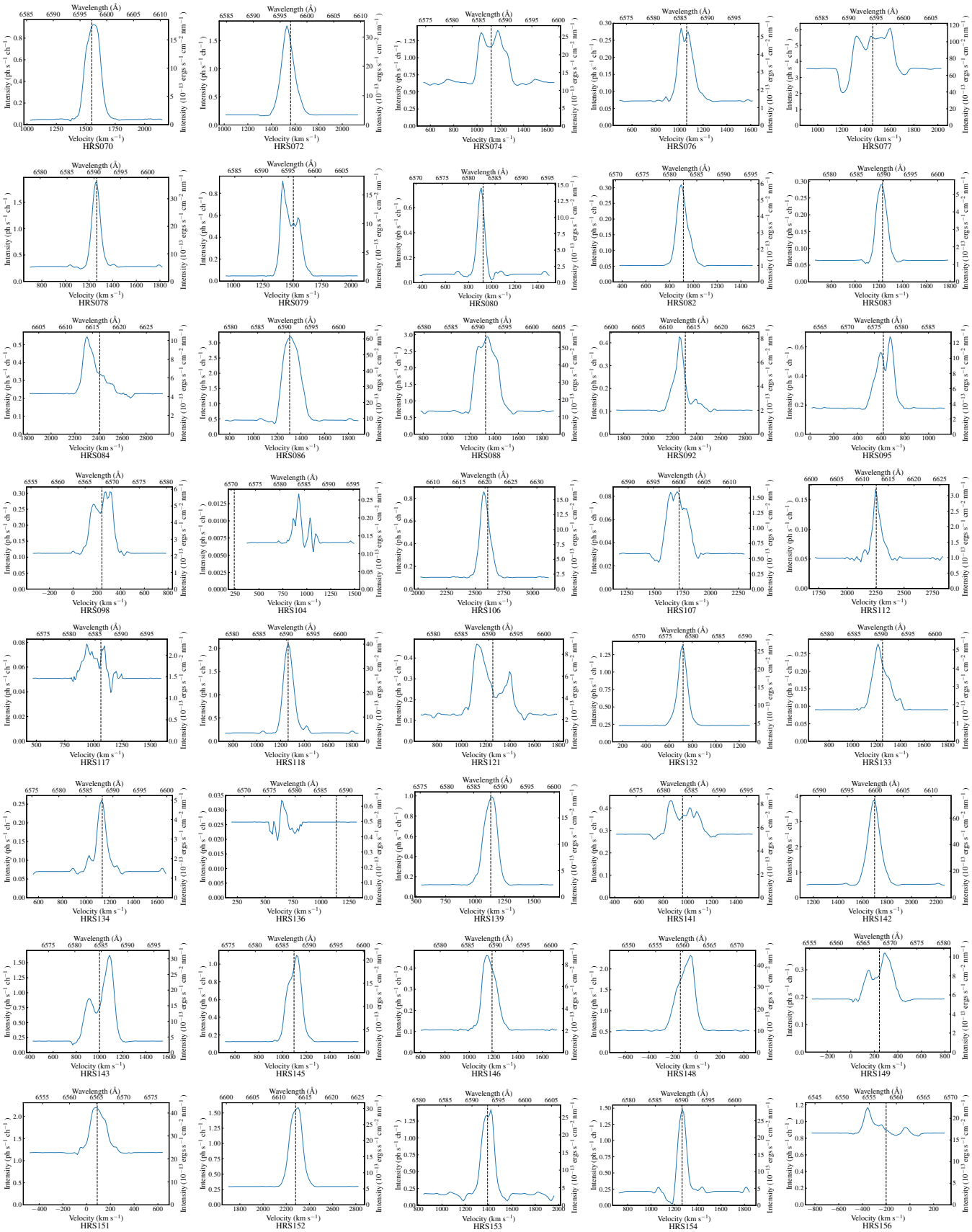
Wavelength (Å)
Intensity (ph s^{-1} ch^{-1})
Intensity (10^{-13} ergs s^{-1} cm^{-2} nm^{-1})
Velocity (km s^{-1})
HRS070
HRS072
HRS074
HRS076
HRS077
HRS078
HRS079
HRS080
HRS082
HRS083
HRS084
HRS086
HRS088
HRS092
HRS095
HRS098
HRS104
HRS106
HRS107
HRS112
HRS117
HRS118
HRS121
HRS132
HRS133
HRS134
HRS136
HRS139
HRS141
HRS142
HRS143
HRS145
HRS146
HRS148
HRS149
HRS151
HRS152
HRS153
HRS154
HRS156

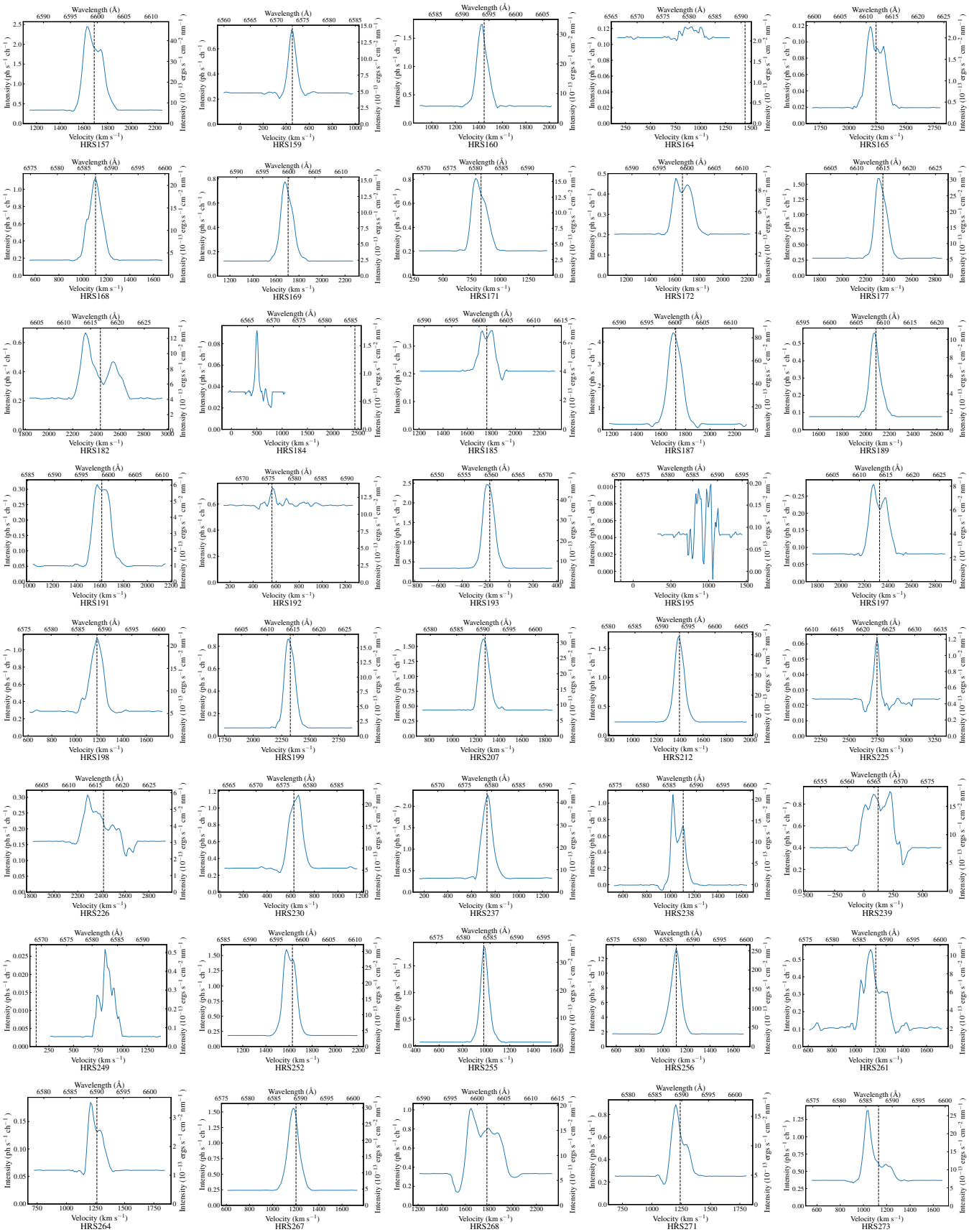
Wavelength (Å)
Velocity (km s^{-1})
Intensity (ph s^{-1} ch^{-1})
Intensity (10^{-13} ergs s^{-1} cm^{-2} nm^{-1})
HRS157
HRS159
HRS160
HRS164
HRS165
HRS168
HRS169
HRS171
HRS172
HRS177
HRS182
HRS184
HRS185
HRS187
HRS189
HRS191
HRS192
HRS193
HRS195
HRS197
HRS198
HRS199
HRS207
HRS212
HRS225
HRS226
HRS230
HRS237
HRS238
HRS239
HRS249
HRS252
HRS255
HRS256
HRS261
HRS264
HRS267
HRS268
HRS271
HRS273

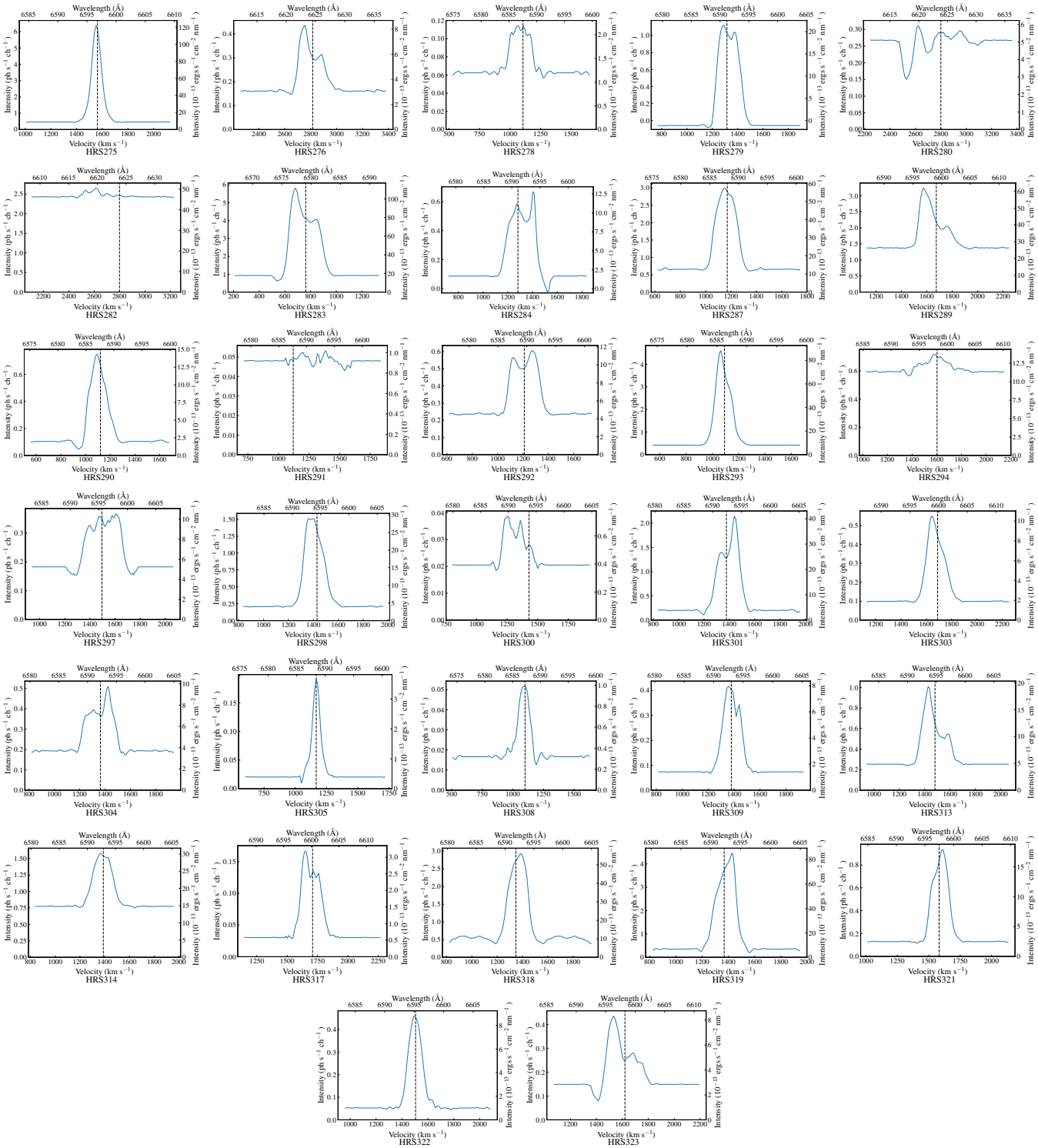
Wavelength (Å)
Intensity (ph s^{-1} ch^{-1})
Intensity (10^{-13} ergs s^{-1} cm^{-2} nm^{-1})
Velocity (km s^{-1})
HRS275
HRS276
HRS278
HRS279
HRS280
HRS282
HRS283
HRS284
HRS287
HRS289
HRS290
HRS291
HRS292
HRS293
HRS294
HRS297
HRS298
HRS300
HRS301
HRS303
HRS304
HRS305
HRS308
HRS309
HRS313
HRS314
HRS317
HRS318
HRS319
HRS321
HRS322
HRS323

Appendix D: Individual Maps

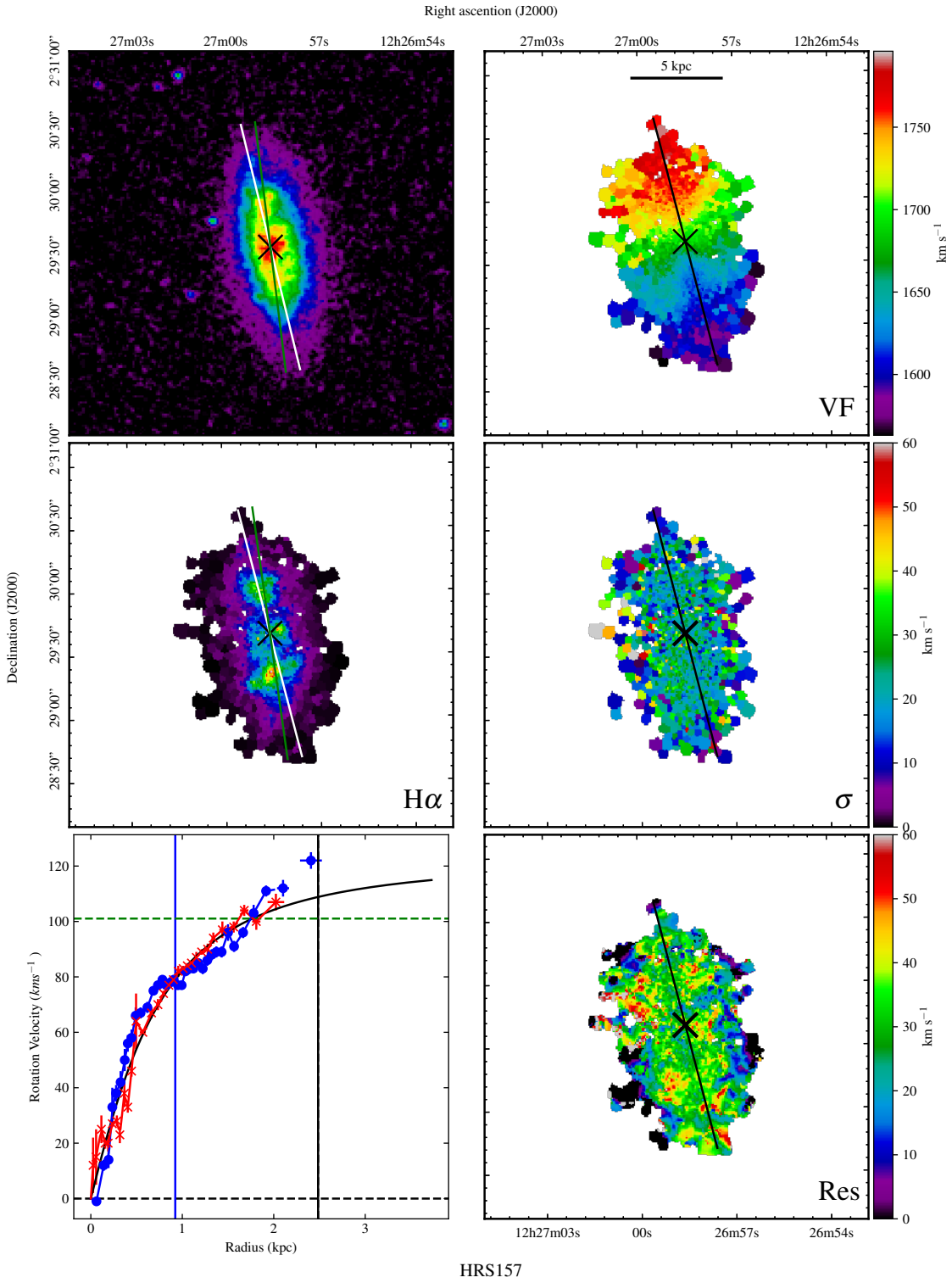

Fig. D.1. Galaxy HRS 157. Top left: XDSS *R*-band image. Top right: Hα velocity field. Middle left: Hα monochromatic image. Middle right: Hα velocity dispersion field. Bottom left: rotation curve (if computed). Bottom right: residual velocity field (if computed).The black cross is the kinematical center. In the maps, the green line is the morphological major axis, while the black/white line is the estimated kinematical major axis, its length represents the $2 \times r_{opt}$. In the rotation curve, blue dots indicate the approaching side while red crosses the receding side, the black solid vertical line represents the r_{opt}, and the black dashed line represents the r_{25}; the blue solid line the r_{eff} (if available in Cortese et al. 2012) and the green horizontal line the HI V_{max} (if available in Boselli et al. 2014a); the solid black curve is the best fit Courteau function to the rotation curve.

Appendix E: Tables

Table E.1. Herschel Reference Survey.

HRS	CGCG	VCC	UGC	NGC	IC	RA(2000) (h m s)	Dec(2000) (° ' ")	D Mpc	Type	r_{eff} kpc	D_{24} kpc	D_{25} kpc	i mag	IRAC1 mag	log M_{star} $M_\odot$	E(B-V)	Virgo D °	Memb	HI_{Def}
(1)	(2)	(3)	(4)	(5)	(6)	(7)	(8)	(9)	(10)	(11)	(12)	(13)	(14)	(15)	(16)	(17)	(18)	(19)	(20)
1	123-035	-	-	-	-	10 17 39.66	+22 48 35.9	16.79	Pec	0.45	2.32	2.44	13.899	-	8.72	0.0311	34.88	Leo Cl.	-
2	124-004	-	5588	-	-	10 20 57.13	+25 21 53.4	18.44	S?	0.39	1.96	1.39	13.259	-	8.77	0.023	34.96	Leo Cl.	0.07
5	94-052	-	-	-	610	10 26 28.37	+20 13 41.5	16.71	Sc	1.07	4.91	4.52	12.59	12.253	9.62	0.0203	32.06	Leo Cl.	0.66
6	154-016	-	5662	-	-	10 27 01.16	+28 38 21.9	18.89	SB(s)b	1.80	6.32	9.09	13.545	14.206	8.94	0.0267	34.96	Leo Cl.	0.62
9	154-026	-	5731	3277	-	10 32 55.45	+28 30 42.2	20.21	SA(r)ab;HII	1.40	8.20	5.73	11.037	11.46	10.08	0.0266	33.6	Leo Cl.	0.49
10	183-028	-	5738	-	-	10 34 29.82	+35 15 24.4	21.66	S?	0.53	2.77	2.87	13.47	-	8.71	0.0271	36.99	Leo Cl.	0.12
11	124-038	-	5742	3287	-	10 34 47.31	+21 38 54.0	18.93	SB(s)d	1.56	6.75	5.75	11.85	12.282	9.45	0.023	30.45	Leo Cl.	0.24
12	124-041	-	-	-	-	10 35 42.07	+26 07 33.7	19.89	cI	0.43	2.17	1.71	14.088	-	8.47	0.023	31.89	Leo Cl.	0.06
13	183-030	-	5753	3294	-	10 36 16.25	+37 19 28.9	22.47	SA(s)c	2.45	11.86	11.6	10.71	10.829	10.17	0.0195	37.97	Leo Cl.	0.25
17	95-019	-	5887	3370	-	10 47 04.05	+17 16 25.3	18.3	SA(s)c	1.22	6.95	8.41	11.57	11.747	9.46	0.0308	26.39	Leo Cl.	-0.09
18	155-015	-	5906	3380	-	10 48 12.17	+28 36 06.5	22.91	(R')SBa?	0.84	5.20	5.66	12.014	12.428	9.77	0.0248	30.35	Leo Cl.	0.59
19	184-016	-	5909	3381	-	10 48 24.82	+34 42 41.1	23.29	SB pec	1.32	6.00	6.91	12.123	12.553	9.39	0.0204	33.97	Leo Cl.	-0.18
21	155-028	-	5958	-	-	10 51 15.81	+27 50 54.9	16.89	Sbc	0.95	3.93	3.56	13.838	14.14	8.82	0.0238	29.3	Leo Cl.	0.72
23	184-028	-	5972	3424	-	10 51 46.33	+32 54 02.7	21.44	SB(s)b:?;HII	1.73	9.23	8.79	11.761	11.418	9.9	0.0234	32.15	Leo Cl.	0.32
25	125-013	-	5995	3437	-	10 52 35.75	+22 56 02.9	18.24	SAB(rs)c:	1.08	6.26	6.66	11.41	11.264	9.69	0.0186	26.72	Leo Cl.	-0.08
26	184-031	-	5990	-	-	10 52 38.34	+34 28 59.3	22.41	Sab	0.89	4.30	4.40	13.755	14.169	8.94	0.0193	33.02	Leo Cl.	0.44
27	184-034	-	6001	3442	-	10 53 08.11	+33 54 37.3	24.77	Sa?	0.43	2.52	2.23	13.043	-	8.94	0.0183	32.55	Leo Cl.	0.03
28	155-035	-	6023	3451	-	10 54 20.86	+27 14 22.9	19.03	Sd	0.98	4.59	4.71	12.441	12.898	9.16	0.0218	28.32	Leo Cl.	0.05
32	95-065	-	6030	3457	-	10 54 48.63	+17 37 16.3	16.54	S?	0.45	2.65	2.19	12.069	-	9.46	0.0308	24.57	Leo Cl.	0.82
35	267-037	-	6115	3499	-	11 03 11.03	+56 13 18.2	21.74	I0	0.41	2.72	2.56	12.651	-	9.69	0.0087	49	Ursa Maj. SS	-
37	155-051	-	6128	3512	-	11 04 02.98	+28 02 12.5	19.61	SAB(rs)c	0.84	4.39	4.62	11.935	12.185	9.53	0.0282	26.75	Leo Cl.	0.04
38	38-129	-	6167	3526	-	11 06 56.63	+07 10 26.1	20.27	SAc pec sp	1.61	7.13	5.63	12.745	13.253	9.1	0.0334	20.73	Leo Cl.	0.03
39	66-115	-	6169	-	-	11 07 03.35	+12 03 36.2	22.24	Sb:	1.01	4.66	6.02	13.367	13.636	9.08	0.0155	20.94	Leo Cl.	0.16
40	67-019	-	6209	3547	-	11 09 55.94	+10 43 15.0	22.63	Sb:	1.00	5.30	6.29	12.476	12.874	9.18	0.0241	20.15	Leo Cl.	0.3
44	69-058	-	7117	4124	-	12 08 09.64	+10 22 43.4	17	S?	2.10	11.03	10.14	10.751	-	8.7	0.0279	19.25	Leo Cl.	0.34
47	96-029	-	6343	3626	-	11 20 03.80	+18 21 24.5	21.34	SA(s)cd:	1.46	9.34	8.35	10.624	10.762	9.11	0.0194	22.83	Leo Cl.	-0.15
48	156-064	-	6352	3629	-	11 20 31.82	+26 57 48.2	21.53	SA(s)c	1.45	5.82	7.17	12.334	13.122	9.92	0.0184	44.35	Ursa Major Cl.	0.09
50	39-130	-	6368	3640	-	11 21 06.85	+03 14 05.4	17.87	SA(s)c:;HII	1.27	10.89	10.34	9.753	-	9.87	0.0422	17.49	Leo Cl.	-0.32
52	96-038	-	6405	3659	-	11 23 45.49	+17 49 06.8	18.56	SAB(rs)c pec	0.91	4.75	5.64	12.244	12.563	9.11	0.0193	43.84	Ursa Major Cl.	-0.65
56	96-047	-	6453	3684	-	11 27 11.18	+17 01 49.0	16.54	SB(s)c?;HII	1.12	5.63	6.95	-	11.749	10.2	0.0259	47.22	Ursa Major Cl.	0.09
59	96-050	-	6464	3691	-	11 28 09.41	+16 55 13.7	15.24	Sb;LINER;HII	0.69	3.01	2.99	12.472	13.07	9.96	0.0261	15.41	Leo Cl.	0.38
60	67-084	-	6474	3692	-	11 28 24.01	+09 24 27.5	24.53	SB(r)a pec	1.85	11.2	11.27	11.751	11.81	9.93	0.0321	43.16	Ursa Major Cl.	-0.29
61	268-051	-	6547	3729	-	11 33 49.34	+53 07 31.8	15.14	Scd:;HII	1.25	6.30	6.21	10.845	11.116	8.54	0.0114	47.78	Ursa Major Cl.	-0.08
62	292-009	-	6575	-	-	11 36 26.47	+58 11 29.0	17.39	SAB(rs)c pec	1.01	4.25	4.93	13.379	14.123	9.11	0.0154	27.59	Ursa Maj. SS	-0.17
63	186-012	-	6577	3755	-	11 36 33.37	+36 24 37.2	22.44	SAB(rs)bc	2.40	10.15	10.31	12.408	12.975	9.94	0.0251	44.03	Ursa Major Cl.	0.27
64	268-063	-	6579	3756	-	11 36 48.02	+54 17 36.8	18.41	Sc;HII	2.23	10.09	11.17	10.888	11.266	9.06	0.0114	47.93	Ursa Major Cl.	0.24
65	292-017	-	6629	3795	-	11 40 06.84	+58 36 47.2	17.33	SAB(s)d	0.98	4.74	5.39	12.787	13.165	9.04	0.0144	45.55	Ursa Major Cl.	-0.18
66	292-019	-	6640	3794	-	11 40 53.42	+56 12 07.3	19.76	SA(rs)b:	1.44	6.27	6.44	12.566	13.347	9.77	0.0132	27.14	Ursa Maj. SS	-0.05
67	186-024	-	6651	3813	-	11 41 18.65	+36 32 48.3	20.97	SB(s)m:	1.44	7.78	6.83	11.235	11.222	8.99	0.019	44.21	Ursa Major Cl.	0.06
68	268-076	-	6706	-	-	11 44 14.83	+55 02 05.9	20.51	S?	1.37	5.70	5.70	12.744	13.585	8.93	0.0135	25.05	Ursa Maj. SS	0.27
70	268-088	-	6787	3898	-	11 49 15.37	+56 05 03.7	16.73	SB(r)bc?;HII	1.35	10.61	10.63	9.985	10.371	9.01a	0.0209	15.09	Crater Cl.	0.16
72	292-042	-	6860	3945	-	11 53 13.73	+60 40 32.0	17.99	IBm: sp;HII	1.40	13.08	13.74	9.957	-	8.85a	0.0287	15.01	Crater Cl.	-0.27
74	269-013	-	6870	3953	-	11 53 48.92	+52 19 36.4	15	SAB(r)b:;HII;Sy2	2.75	13.85	15.1	9.477	9.58	9.52	0.03	43.59	Ursa Major Cl.	0.1

The general properties of the 152 HRS galaxies observed at OHP with GHASP instrument. (1) HRS galaxy number. (2)(3)(4)(5)(6) Name of the galaxy in the CGCG/VCC/UGC/NGC/IC catalogs when available. (7)(8) Coordinates (in J2000) of the photometric center of the galaxy (Boselli et al. (2010)). (9) Distance to the galaxy in Mpc from Boselli et al. (2015). (10) Morphological type according to Boselli et al. (2010) . (11)(12) Effective radius (r_eff) and D_{24} in r-band when available in Cortese et al. (2012) converted to kpc. (13) D_{25} in B-band from Boselli et al. (2010) converted to kpc. (14)(15) Apparent asymptotic magnitude in the i-band and in the IRAC1 3.6μm from Cortese et al. (2012) and Sheth et al. (2010) respectively and if available. (16) Stellar mass from Cortese et al. (2012) and Boselli et al. (2015), determined using the prescription given in Zibetti et al. (2009) based on the i-band luminosity and $g-i$ mass-to-light ratio. For those objects without SDSS g and i-band data (11 objects, marked with "a" in Table E.1), the stellar masses were calculated as in Boselli et al. (2009) based on the H-band luminosity and $B-H$ mass-to-light ratio. (17) Color index from Cortese et al. (2012). (18)(19)(20) Distance from Virgo cluster (Virgo A or Virgo B) in degrees, name of the cloud where the galaxy is member, and HI-deficiency parameter from Boselli et al. (2015).

HRS	CGCG	VCC	UGC	NGC	IC	RA(2000) (h m s)	Dec(2000) (° ' ")	D Mpc	Type	r_{eff} kpc	D_{24} kpc	D_{25} kpc	i mag	IRAC1 mag	log M_{star} $M_\odot$	E(B-V)	Virgo D °	Memb	Def_{HI}
(1)	(2)	(3)	(4)	(5)	(6)	(7)	(8)	(9)	(10)	(11)	(12)	(13)	(14)	(15)	(16)	(17)	(18)	(19)	(20)
76	269-020	-	6919	-	-	11 56 37.51	+55 37 59.5	18.33	Im:	0.97	3.71	3.87	13.681	-	8.72	0.0144	41.65	Ursa Major Cl.	0.24
77	269-022	-	6923	-	-	11 56 49.43	+53 09 37.3	15.27	SA(s)bc;HII	1.11	4.20	4.44	12.815	-	10.54	0.026	11.7	Crater Cl.	-0.14
78	13-033	-	6993	4030	-	12 00 23.64	-01 06 00.0	20.83	Im:	1.76	12.00	12.63	9.8	9.835	9.2	0.0266	10.79	Coma I Cl.	-0.3
79	98-019	-	6995	4032	-	12 00 32.82	+20 04 26.0	18.13	SBb? sp	0.87	4.32	4.90	12.103	12.838	8.62	0.0347	7.608	Virgo Out.	0.28
80	69-024	-	7001	4019	755	12 01 10.39	+14 06 16.2	21.54	SB(rs)b:	1.17	5.92	7.52	13.363	13.976	9.51	0.0317	7.426	Virgo Out.	0.77
82	13-046	-	7021	4045	-	12 02 42.26	+01 58 36.4	17	Sab	1.21	7.07	7.42	11.184	11.24	8.69	0.0225	7.73	Virgo Out.	0.37
83	98-037	-	-	-	-	12 03 35.94	+16 03 20.0	17	SB(r)a:;HII	0.45	2.15	1.48	13.379	-	8.53	0.03	8.446	Crater Cl.	0.68
84	41-031	-	7035	-	-	12 03 40.14	+02 38 28.4	17.6	SA(s)b:	0.75	3.58	2.82	13.559	14.181	9.39	0.027	6.833	Virgo Out.	0.38
86	243-044	-	7095	4100	-	12 06 08.60	+49 34 56.3	15.31	SB(rs)dm	2.17	10.91	11.96	10.444	10.483	9.23	0.0231	7.673	Virgo Out.	-0.21
88	41-042	-	7116	4123	-	12 08 11.11	+02 52 41.8	17	SB(r)c;Sbrst;HII	2.41	8.65	12.36	10.941	11.299	9.63	0.0201	7.442	Virgo Out.	0.05
92	69-101	131	7255	-	3061	12 15 04.44	+14 01 44.3	17	SBc? sp	1.09	4.72	6.43	13.06	13.243	9.1	0.0371	4.265	Virgo N Cl.	0.28
95	69-107	152	7268	4207	-	12 15 30.50	+09 35 05.6	17	Scd	0.82	4.33	4.85	12.002	11.871	9.66	0.0173	3.904	Virgo N Cl.	0.27
98	69-119	187	7291	4222	-	12 16 22.52	+13 18 25.5	17	Sc	1.92	7.91	8.70	12.529	12.56	9.31	0.0313	3.726	Virgo N Cl.	0.25
104	99-015	-	7366	-	-	12 19 28.66	+17 13 49.4	17	Spiral	0.80	2.72	2.97	13.682	-	8.8	0.0242	5.609	Virgo Out.	-
106	42-032	393	7385	4276	-	12 20 07.50	+07 41 31.2	23	S(s)c II	1.28	5.42	7.02	12.479	13.004	9.37	0.0292	2.433	Virgo B	0.4
107	42-033	404	7387	-	-	12 20 17.35	+04 12 05.1	17	Sd(f)	1.24	4.67	4.67	13.48	13.53	8.98	0.0224	4.479	Virgo S Cl.	0.46
112	42-044	492	7413	4300	-	12 21 41.47	+05 23 05.4	23	Sa	1.18	6.36	7.23	11.851	-	10.04	0.0216	3.306	Virgo B	0.94
117	70-029	524	7431	4307	-	12 22 05.63	+09 02 36.8	23	Sb	2.22	11.11	13.21	11.188	11.232	10.35	0.0228	2.187	Virgo B	1.5
118	42-053	552	7439	-	-	12 22 27.25	+04 33 58.7	17	SAB(s)cd	1.02	3.88	4.67	12.808	13.68	8.67	0.0242	3.892	Virgo S Cl.	-0.26
121	70-035	576	7447	4316	-	12 22 42.24	+09 19 56.9	23	Sbc	1.63	8.63	8.30	11.945	11.762	10.09	0.0221	2.214	Virgo B	0.37
132	42-080	699	7477	-	3268	12 24 07.44	+06 36 26.9	23	Sm/Im	0.76	3.95	6.52	12.76	13.551	9.13	0.0247	1.985	Virgo B	0.16
133	158-099	-	7483	4359	-	12 24 11.06	+31 31 17.8	17.9	SB(rs)c? sp	1.78	6.85	9.37	12.205	12.816	9.26	0.0247	19.2	Coma I Cl.	0.19
134	70-048	713	7482	4356	-	12 24 14.53	+08 32 08.9	23	Sc	2.47	10.91	10.7	11.958	12.227	9.96	0.0269	1.484	Virgo B	1.46
136	42-089	758	7492	4370	-	12 24 54.93	+07 26 40.4	23	Sa	1.15	6.05	5.89	11.8	11.822	10.14	0.0237	1.337	Virgo B	1.2
139	42-093	787	7498	4376	-	12 25 18.06	+05 44 28.3	23	Im	1.27	5.25	6.16	12.938	13.534	9	0.023	2.521	Virgo B	0.18
141	70-061	792	7503	4380	-	12 25 22.17	+10 01 00.5	23	SA(rs)b:?	2.94	12.61	11.78	10.893	11.148	10.32	0.0236	2.299	Virgo B	1.14
142	99-044	801	7507	4383	-	12 25 25.50	+16 28 12.0	17	Sa? pec;HII	0.69	5.51	6.43	11.577	11.768	9.42	0.0237	4.296	Virgo A	-0.28
143	42-095	827	7513	-	-	12 25 42.63	+07 13 00.1	23	SB(s)cd: sp	2.43	9.53	12.04	12.277	12.112	9.6	0.0256	1.284	Virgo B	-0.06
145	70-067	849	7519	4390	-	12 25 50.67	+10 27 32.6	23	Sbc(s) II	1.50	5.92	7.29	12.359	12.939	9.31	0.031	2.298	Virgo B	0.42
146	42-098	851	7518	-	3322	12 25 54.12	+07 33 17.4	23	SAB(s)cd: sp	1.90	7.69	7.23	12.835	13.085	9.38	0.0293	1.067	Virgo B	0.4
148	99-049	865	7526	4396	-	12 25 58.80	+15 40 17.3	17	SAd: sp	2.27	8.65	8.31	12.075	12.414	9.25	0.0261	3.496	Virgo A	0.2
149	70-071	873	7528	4402	-	12 26 07.56	+13 06 46.0	17	Sb	2.35	10.48	9.77	11.057	10.837	10.04	0.029	1.379	Virgo A	0.83
151	70-076	912	7538	4413	-	12 26 32.25	+12 36 39.5	17	(R')SB(rs)ab:	1.37	6.08	7.22	11.537	12.097	9.68	0.0322	1.094	Virgo A	0.92
152	42-104	921	7536	4412	-	12 26 36.10	+03 57 52.7	17	SB(r)b? pec;LINER	0.86	4.08	4.67	11.924	12.146	9.3	0.018	4.112	Virgo S Cl.	0.75
153	42-105	938	7541	4416	-	12 26 46.72	+07 55 08.4	17	SB(rs)cd:;Sbrst	0.98	4.25	5.39	12.058	12.514	9.34	0.0253	0.7544	Virgo S Cl.	0.53
154	70-082	939	7546	-	-	12 26 47.23	+08 53 04.6	23	SAB(s)cd	2.39	8.10	11.54	12.021	12.882	9.49	0.0293	1.159	Virgo B	0.03
156	99-054	958	7551	4419	-	12 26 56.43	+15 02 50.7	17	SB(s)a;LINER;HII	1.31	8.48	8.70	10.563	10.389	10.24	0.033	2.828	Virgo A	1.36
157	42-106	957	7549	4420	-	12 26 58.48	+02 29 39.7	17	SB(r)bc:	0.92	4.97	4.97	11.801	12.053	9.28	0.0178	5.55	Virgo S Cl.	0.28
159	70-090	979	7561	4424	-	12 27 11.59	+09 25 14.0	23	SB(s)a:;HII	2.59	12.28	14.48	10.899	11.506	10.17	0.0207	1.561	Virgo B	0.98
160	42-111	1002	7566	4430	-	12 27 26.41	+06 15 46.0	23	SB(rs)b:	1.91	8.30	10.10	11.506	12.022	9.83	0.0186	1.833	Virgo B	0.65
164	70-099	1047	7581	4440	-	12 27 53.57	+12 17 35.6	17	SB(rs)a	0.74	4.80	4.97	11.287	-	9.91	0.027	0.7393	Virgo A	1.1
165	42-117	1048	7579	-	-	12 27 55.39	+05 43 16.4	23	Sdm:	1.06	4.62	6.32	13.776	14.069	8.86	0.0197	2.326	Virgo B	0.68
168	70-108	1091	7590	-	-	12 28 18.77	+08 43 46.1	23	Sbc	0.83	3.95	5.89	13.499	14.218	8.64	0.0215	0.816	Virgo B	-0.03
169	99-063	-	7595	-	3391	12 28 27.28	+18 24 55.1	24.3	Scd:	1.42	5.87	3.89	12.679	13.195	9.28	0.0323	6.053	Coma I Cl.	0.31
171	70-111	1118	7600	4451	-	12 28 40.55	+09 15 32.2	23	Sbc:	0.89	5.55	6.56	12.04	12.386	9.69	0.0188	1.289	Virgo B	0.78
172	99-065	1126	7602	-	3392	12 28 43.26	+14 59 58.2	17	SAb:	1.31	6.63	7.22	11.563	11.829	9.77	0.0369	2.66	Virgo A	1.48
177	42-132	1205	7627	4470	-	12 29 37.78	+07 49 27.1	17	Sa?;HII	0.73	3.78	4.55	12.052	12.474	9.2	0.0241	0.1799	Virgo S Cl.	0.32
182	42-139	1290	7647	4480	-	12 30 26.78	+04 14 47.3	17	SAB(s)c	1.17	5.14	4.97	11.943	12.297	9.38	0.0242	3.757	Virgo S Cl.	0.05
184	70-140	1326	7657	4491	-	12 30 57.13	+11 29 00.8	17	SB(s)a:	1.01	5.12	4.67	11.989	12.512	9.55	0.0416	0.9077	Virgo A	1.27
185	42-141	1330	7656	4492	-	12 30 59.74	+08 04 40.6	17	SA(s)a?	1.46	6.68	4.85	11.045	11.611	10.06	0.0254	0.314	Virgo S Cl.	1.43
187	42-144	1375	7668	4505	-	12 31 39.21	+03 56 22.1	17	SB(rs)m	1.93	7.94	11.77	11.352	11.774	9.41	0.0245	4.088	Virgo S Cl.	-0.01
189	99-077	1393	7676	-	797	12 31 54.76	+15 07 26.2	17	SB(s)c II.5	1.10	4.33	4.18	12.507	13.063	8.94	0.0307	2.746	Virgo A	0.42
191	99-078	1410	7677	4502	-	12 32 03.35	+16 41 15.8	17	Scd:	0.64	2.74	3.66	13.559	14.273	8.56	0.0291	4.308	Virgo A	0.55
192	70-152	1419	7682	4506	-	12 32 10.53	+13 25 10.6	17	Sa pec?	0.96	4.38	5.34	12.288	12.91	9.39	0.0287	1.083	Virgo A	1.31

HRS	CGCG	VCC	UGC	NGC	IC	RA(2000)	Dec(2000)	D	Type	r_{eff}	D_{24}	D_{25}	i	IRAC1	log M_{star}	E(B-V)	Virgo D	Memb	Def_{HI}
						(h m s)	(° ’ ”)	Mpc		kpc	kpc	kpc	mag	mag	$M_\odot$		°		
(1)	(2)	(3)	(4)	(5)	(6)	(7)	(8)	(9)	(10)	(11)	(12)	(13)	(14)	(15)	(16)	(17)	(18)	(19)	(20)
193	70-157	1450	7695	-	3476	12 32 41.88	+14 03 01.8	17	IB(s)m:	1.27	5.32	6.43	12.319	12.929	9.03	0.0358	1.724	Virgo A	0.66
195	99-087	1479	7703	4516	-	12 33 07.56	+14 34 29.8	17	SB(rs)ab?	1.11	5.14	5.34	11.98	-	9.66	0.036	2.258	Virgo A	0.71
197	70-168	1516	7711	4522	-	12 33 39.66	+09 10 29.5	17	SB(s)cd: sp	2.06	8.78	9.99	11.817	12.034	9.38	0.0207	1.524	Virgo S Cl.	0.68
198	159-016	-	7714	4525	-	12 33 51.19	+30 16 39.1	16.77	Scd:	1.35	5.73	7.32	12.074	12.69	9.29	0.0229	17.9	Coma I Cl.	0.36
199	99-090	1532	7716	-	800	12 33 56.66	+15 21 17.4	17	SB(rs)c pec?	1.21	4.30	4.85	12.587	13.169	9.07	0.0377	3.065	Virgo A	1
207	99-093	1588	7742	4540	-	12 34 50.87	+15 33 05.2	17	SAB(rs)cd;LINER;Sy1	1.20	5.91	6.43	11.354	11.788	9.69	0.0349	3.316	Virgo A	0.6
212	99-098	-	7768	4561	-	12 36 08.14	+19 19 21.4	20.14	SB(rs)dm	1.18	4.86	4.42	12.262	13.094	9.14	0.0263	7.058	Coma I Cl.	-0.53
225	70-202	1778	7817	-	3611	12 39 04.14	+13 21 48.7	17	S?	0.87	3.78	4.35	13.25	13.988	8.72	0.0358	2.279	Virgo E Cl.	1.28
226	42-191	1780	7821	4591	-	12 39 12.44	+06 00 44.3	17	Sb	0.69	3.93	4.85	12.52	12.808	9.31	0.0216	3.083	Virgo S Cl.	0.79
230	99-106	1811	7826	4595	-	12 39 51.91	+15 17 52.1	17	SAB(rs)b?	0.99	4.80	5.34	12.008	12.524	9.15	0.0367	3.682	Virgo E Cl.	0.54
237	42-208	1923	7871	4630	-	12 42 31.15	+03 57 37.3	17	IB(s)m?	1.05	4.99	5.71	11.792	12.221	9.51	0.0298	5.145	Virgo S Cl.	0.31
238	14-109	-	7869	4629	-	12 42 32.67	-01 21 02.4	15.94	SAB(s)m pec	0.77	2.81	3.2	13.286	14.179	8.46	0.0371	9.881	Virgo Out.	-0.57
239	99-112	1932	7875	4634	-	12 42 40.96	+14 17 45.0	17	SBcd: sp	1.80	8.95	7.22	11.825	11.609	9.57	0.0278	3.524	Virgo E Cl.	0.45
249	71-026	2006	7920	-	3718	12 44 45.99	+12 21 05.2	17	S	1.45	5.54	6.43	12.854	13.635	9.01	0.0293	3.486	Virgo E Cl.	1.49
252	15-016	-	7931	4668	-	12 45 32.14	-00 32 05.0	23.13	SB(s)d:;NLAGN	1.16	5.21	4.64	12.634	13.31	9.13	0.0246	9.4	Virgo Out.	-0.28
255	43-028	-	7961	4688	-	12 47 46.46	+04 20 09.9	17	SB(s)cd	1.83	5.39	10.88	12.092	12.791	8.97	0.0305	5.802	Virgo Out.	0.08
256	15-023	-	-	4691	-	12 48 13.63	-03 19 57.8	15.99	(R)SB(s)0/a pec;HII	1.33	8.28	6.56	10.381	10.805	9.98	0.0276	12.24	Virgo Out.	0.75
261	43-040	-	7982	-	-	12 49 50.19	+02 51 10.4	16.54	Sd(f)	1.76	7.14	8.16	12.37	12.675	9.42	0.0347	7.186	Virgo Out.	0.52
264	15-027	-	7991	-	-	12 50 38.96	+01 27 52.3	18.17	Sd(f)	1.43	5.66	4.49	13.309	13.667	9.06	0.0247	8.363	Virgo Out.	0.48
267	129-028	-	8005	4747	-	12 51 45.96	+25 46 38.3	16.84	SBcd? pec sp	2.67	10.04	9.67	11.676	12.095	9.5	0.0104	14.37	Coma I Cl.	0.06
268	71-060	-	8007	4746	-	12 51 55.37	+12 04 58.9	17	Sb: sp	0.98	4.87	5.44	12.065	11.783	9.42	0.0358	5.284	Virgo Out.	0.15
271	100-015	-	8014	4758	-	12 52 44.04	+15 50 55.9	17	Im:;HII	2.11	8.95	7.42	12.234	12.535	9.33	0.0261	6.478	Virgo Out.	0.23
273	15-031	-	8020	4771	-	12 53 21.27	+01 16 09.0	17	SAd? sp;NLAGN	1.80	9.00	9.89	11.338	11.576	9.88	0.0197	8.947	Virgo Out.	0.42
275	-	-	-	4775	-	12 53 45.70	-06 37 19.8	22.37	SA(s)d	-	-	6.96	-	11.835	9.61a	0.035	15.8	Virgo Out.	-0.49
276	71-068	-	8022	4779	-	12 53 50.86	+09 42 35.7	17	SB(rs)bc;Sbrst	1.04	4.80	5.19	11.962	12.288	9.35	0.0219	6.255	Virgo Out.	0.42
278	71-071	-	8032	-	-	12 54 44.19	+13 14 14.2	16.01	S	1.30	5.87	6.4	12.621	-	9.31	0.0359	6.038	Virgo Out.	1.67
279	15-037	-	8041	-	-	12 55 12.68	+00 07 00.0	17	SB(s)d	2.17	7.54	7.66	11.936	12.623	9.24	0.0221	10.13	Virgo Out.	-0.01
280	43-066	-	8043	4799	-	12 55 15.53	+02 53 47.9	17	S?	0.56	3.63	3.96	12.322	12.412	9.48	0.034	8.162	Virgo Out.	0.44
282	43-069	-	-	4803	-	12 55 33.67	+08 14 25.8	17	Comp	0.32	2.35	1.24	12.949	-	9.3	0.0306	6.45	Virgo Out.	-0.3
283	43-071	-	8054	4808	-	12 55 48.94	+04 18 14.7	17	SA(s)cd:;HII	1.21	6.08	6.43	11.369	11.435	9.49	0.0368	7.485	Virgo Out.	-0.58
284	-	-	-	-	3908	12 56 40.62	-07 33 46.1	18.51	SB(s)d?;HII	-	-	4.90	-	11.425	9.71a	0.0349	16.95	Virgo Out.	0
287	15-055	-	8121	4904	-	13 00 58.67	-00 01 38.8	17	SB(s)cd;Sbrst	1.20	5.61	5.93	11.487	11.885	9.53	0.0306	11.19	Virgo Out.	0.05
289	-	-	-	4981	-	13 08 48.74	-06 46 39.1	23.97	SAB(r)bc;LINER	-	-	9.59	-	11.141	10.31a	0.0422	17.71	Virgo Out.	-0.16
290	189-037	-	8271	5014	-	13 11 31.16	+36 16 54.9	16.23	Sa? sp	0.57	3.64	4.01	12.335	12.606	9.23	0.0078	25.97	Canes Ven. Spur	0.37
291	217-031	-	8388	5103	-	13 20 30.08	+43 05 02.3	18.53	Sab	0.53	4.55	3.91	11.673	12.136	9.86	0.0178	33.11	Canes Ven. Spur	0.51
292	218-010	-	8439	5145	-	13 25 13.92	+43 16 02.2	17.5	S?;HII;Sbrst	0.51	3.49	5.09	11.958	11.719	9.8	0.0121	33.74	Canes Ven. Spur	0.17
293	16-069	-	8443	5147	-	13 26 19.71	+02 06 02.7	15.6	SB(s)dm	1.03	4.36	4.33	11.786	12.144	9.07	0.0271	15.32	Virgo Out.	-0.1
294	246-017	-	8593	-	902	13 36 01.22	+49 57 39.0	22.97	Sb	1.55	7.12	7.32	12.74	12.775	9.56	0.0108	40.95	Canes Ven. Spur	0.5
297	246-023	-	8711	5301	-	13 46 24.61	+46 06 26.7	21.54	SA(s)bc: sp	2.66	11.69	13.06	11.373	11.446	9.99	0.0173	38.65	Canes Ven. Spur	0.13
298	218-047	-	8725	5303	-	13 47 44.97	+38 18 16.4	20.27	Pec	0.55	3.07	2.68	12.431	-	9.11	0.0139	32.27	Canes Ven. Spur	-0.41
300	218-058	-	8756	-	-	13 50 35.89	+42 32 29.5	19.34	Sab	0.79	4.47	4.78	12.77	13.022	9.47	0.0142	36.15	Canes Ven. Spur	0.65
301	17-088	-	8790	5334	4338	13 52 54.46	-01 06 52.7	19.71	SB(rs)c:	2.74	10.15	11.95	11.239	11.886	9.75	0.0459	22.69	Virgo-Libra Cl.	0.12
303	295-024	-	8843	5372	-	13 54 46.01	+58 39 59.4	24.53	S?	0.49	2.89	2.32	12.833	-	9.23	0.0098	50.81	Canes Ven-Came. Cl.	-
304	46-001	-	8831	5356	-	13 54 58.46	+05 20 01.4	19.57	SABbc: sp;HII	2.08	9.17	8.80	11.719	11.897	10.01	0.0251	21.47	Virgo-Libra Cl.	0.84
305	46-003	-	8838	5360	958	13 55 38.75	+04 59 06.2	16.73	I0	1.16	4.36	5.33	13.051	13.566	9.13	0.0288	21.68	Virgo-Libra Cl.	1.38
308	46-011	-	8857	-	-	13 56 26.61	+04 23 48.0	15.59	Sb(f)	0.52	2.40	2.06	13.968	-	8.61	0.0326	21.96	Virgo-Libra Cl.	0.39
309	272-031	-	9036	5486	-	14 07 24.97	+55 06 11.1	19.76	SA(s)m:	1.14	4.51	5.35	13.135	14.041	8.7	0.0203	49.07	Canes Ven-Came. Cl.	-0.1
313	47-022	-	9187	5577	-	14 21 13.11	+03 26 08.8	21.29	SA(rs)bc:	2.27	9.82	10.5	11.98	12.306	9.64	0.0404	28.23	Virgo-Libra Cl.	0.52
314	19-012	-	9215	-	-	14 23 27.12	+01 43 34.7	19.84	SB(s)d	1.72	7.30	6.32	12.299	12.969	9.07	0.0322	29.1	Virgo-Libra Cl.	-0.18
317	47-066	-	9311	-	1022	14 30 01.85	+03 46 22.3	24.51	S?	0.96	4.35	3.92	13.803	-	8.94	0.033	30.36	Virgo-Libra Cl.	0.23
318	47-070	-	9328	5645	-	14 30 39.35	+07 16 30.3	19.57	SB(s)d	1.53	7.23	6.83	11.698	12.298	9.43	0.0272	30.23	Virgo-Libra Cl.	-0.15
319	75-064	-	9353	5669	-	14 32 43.88	+09 53 30.5	19.54	SAB(rs)cd	2.35	8.98	11.31	11.444	11.981	9.47	0.0272	30.58	Virgo-Libra Cl.	-0.1
321	47-123	-	9427	5692	-	14 38 18.12	+03 24 37.2	22.59	S?	0.58	3.35	2.92	12.687	-	9.11	0.0371	32.46	Virgo-Libra Cl.	0.24
322	47-127	-	9436	5701	-	14 39 11.06	+05 21 48.8	21.5	(R)SB(rs)0/a;LINER	1.77	12.88	13.35	10.412	10.757	10.45	0.0378	32.46	Virgo-Libra Cl.	-0.27
323	48-004	-	9483	-	1048	14 42 57.88	+04 53 24.5	23.43	S	1.56	7.63	7.63	12.134	12.101	9.88	0.037	33.44	Virgo-Libra Cl.	0.06

Table E.2. Log of the observations.

HRS	λ_c	date	exp time	Filter tilt
	Å	dd/mm/yy	s	°
(1)	(2)	(3)	(4)	(5)
1	6595	24/02/17	7360	2.5
2	6595	23/02/17	7360	2.5
5	6595	21/02/17	8960	2.5
6	6595	19/02/17	7360	0
9	6595	01/03/16	9720	0
10	6595	20/02/17	5760	0
11	6595	04/02/17	7380	0
12	6595	25/02/17	7200	0
13	6605	07/02/16	7380	5
17	6595	04/02/16	7020	0
18	6605	02/03/16	7530	5
19	6605	10/02/16	7380	5
21	6585	22/02/17	7040	0
23	6595	18/02/17	7360	0
25	6595	04/02/16	7020	0
26	6605	28/02/17	6340	3
27	6605	26/02/17	5760	3
28	6595	03/02/16	10440	0
32	6595	18/04/17	7039	5
35	6595	08/02/18	5440	0
37	6595	05/03/16	6000	0
38	6595	25/02/17	6400	0
39	6605	15/03/08	8160*	4
40	6605	06/03/16	7380	5
44	6595	22/05/17	6080	4
47	6595	05/02/16	7380	0
48	6595	02/02/16	10794	4
50	6595	15/02/18	6400	1
52	6595	20/05/17	6720	4
56	6605	08/03/16	7380	3
59	6605	24/02/17	7040	2.5
60	6585	11/02/16	7380	0
61	6595	19/04/17	6340	4
62	6605	19/02/17	7360	4
63	6595	05/02/16	10744	0
64	6595	02/05/17	7040	2.5
65	6595	16/02/16	6000	0
66	6595	07/02/16	7380	0
67	6595	12/03/16	7380	0
68	6595	15/02/18	7040	1
70	6605	27/04/17	6400	5
72	6605	10/03/16	8100	5
74	6585	14/02/16	7020	0
76	6585	07/03/16	7620	0
77	6595	10/02/16	6060	0
78	6595	11/03/16	7380	2.5
79	6595	19/03/2018	6720	0
80	6585	15/02/16	7080	0
82	6585	10/02-12/02/2018	8320	0
83	6595	22/03/18	6400	4
84	6615	28/05/17	6720	0
86	6595	03/02/16	7800	0
88	6595	07/02/16	6741	0
92	6615	20/03/18	6400	0
95	6575	22/04/17	6400	0
98	6575	21/03/2018	6400	4
104	6585	15/02-22/02-22/03/18	6320	0
106	6625	28/04/17	6720	1.5
107	6605	08/02/18	7040	2.3
112	6615	24/04/17	7380	0
117	6585	17/03/18	5760*	0
118	6595	10/02/16	7380	1.7
121	6595	23/04/17	6400	4
132	6585	06/03/16	7380	5
133	6595	18/03/18	7040	4
134	6595	23/04/17	6720	4
136	6585	02/05/17	8000	5
139	6595	21/05/17	6080	5
141	6585	12/02/16	8616	0
142	6605	28/02/17	5900	3
143	6595	20/03/2018	6080	0
145	6595	24/04/17	7380	4
146	6595	24/05/17	6400	4
148	6565	25/02/17	6000	3
149	6575	13-15/03/18	17280*	4
151	6565	28/04/17	6720	0
152	6615	19/04/17	8639	0
153	6595	18/02/17	7360	0
154	6595	03/02/16	7800	0
156	6565	21/02/17	7040	5
157	6605	19/02/17	5760	4
159	6575	21/04/17	14400	0
160	6595	14/02/16	7380	0
164	6585	24/02/17	6080	4
165	6615	20/03/18	4160	0
168	6595	22/03/18	6400	4
169	6605	12/02/18	7380	3
171	6585	22/03/18	5760	0
172	6605	08/03/16	7380	3
177	6615	26/05/17	5760	0
182	6615	25/05/17	6400	0
184	6575	13/03/16	9180	0
185	6605	19/03/18	6400	0
187	6605	15/02/16	7080	1
189	6615	22/03/18	5300	4
191	6605	23/05/17	5760	5
192	6585	24/05/17	6400	5
193	6565	26/05/17	4800	4
195	6585	31/05/17	3000	0
197	6615	13/03/18	7680*	0
198	6595	22/02/17	7040	5

Log of the Fabry-Perot observations carried out so far at OHP and presented in this work. (1) HRS galaxy number. (2) Central wavelength of the interference filter used (FWHM = 15Å). (3) Date of the observations. (4) Total exposure time in second; observations scanned with 48 instead of 32 channels are marked with a star. (5) Filter tiltination when the case.

HRS	λ_c	date	exp time	Filter tilt
	Å	dd/mm/yy	s	°
(1)	(2)	(3)	(4)	(5)
199	6625	28/05/17	5120	5
207	6595	04/02/16	5420	0
212	6595	12/03/18	7680*	0
225	6625	08/02/18	7040	0
226	6615	27/05/17	6400	0
230	6585	20/05/17	6400	5
237	6585	01/05/17	7040	3.5
238	6595	23/05/17	7040	4
239	6565	28/04/17	5440	0
249	6585	30/04/17	7680	3.5
252	6605	13/02/18	7040	3
255	6585	16/02/16	7380	0
256	6595	28/02/17	3520	5
261	6595	20/04/17	3520	4
264	6595	15/02/18	7040	1
267	6595	19/03/18	6080	4
268	6605	19/03/18	6400	0
271	6595	24/02/17	6080	2.5
273	6595	21/03/18	6700	4
275	6605	11/03/16	7380	5
276	6625	12/03/16	7380	0
278	6595	22/05/17	5760	4
279	6595	20/02/17	7360	0
280	6625	11/02/18	7040	0
282	6625	08/02-11/02/18	6080	0
283	6585	22/02/17	3420	0
284	6595	22/04/17	6400	4
287	6595	22/02/17	6710	2.5
289	6605	25/02/17	7040	4
290	6595	18/04/17	5439	5
291	6595	20/04/17	7040	4
292	6595	19/04/17	5439	4
293	6585	21/02/17	7040	0
294	6605	22/04/17	6720	4
297	6595	12/03-15/03/18	14480*	2
298	6595	27/02/17	6400	2
300	6595	18/02/17	8640	0
301	6595	10/02/16	6480	0
303	6605	27/02/2017	6600	3
304	6595	25/02/17	6760	0
305	6595	20/04/17	7320	4
308	6595	21/05/17	5760	4
309	6595	10/03/16	6231	1.5
313	6595	26/02/17	7040	0
314	6595	12/03/16	8346	0
317	6605	18/04/17	6420	2.5
318	6595	28/02/17	6720	0
319	6595	15/02/16	6420	0
321	6605	22/04/17	6080	4
322	6595	16/02/16	7080	0
323	6605	21/04/17	6079	4

Table E.3. Galaxy parameters.

HRS	ϵ	χ^2_{red} model	i_{morph} °	i_{kin} °	V_{sys} km s^{-1}	$V_{sys_{FP}}$ km s^{-1}	PA_{morph} °	PA_{kin} °	V_{max} km s^{-1}	V_{max} flag	$\overline{res}$ km s^{-1}	σ_{res} km s^{-1}	f (Hα) 10^{-13} erg s^{-1} cm^{-2}	r_{RC}/r_{eff}	N_{beams}
(1)	(2)	(3)	(4)	(5)	(6)	(7)	(8)	(9)	(10)	(11)	(12)	(13)	(14)	(15)	(16)
1	0.60	2.8	67	67*	1175	1170 ± 1	175	177 ± 2	103*	2-B	0.17	10.04	1.58	2.58	450
2	0.28	1.32	45	28 ± 9	1291	1287 ± 1	35	39 ± 1	101*	3-B	0.22	7.05	1.22	2.50	159
5	0.76	2.25	77	77*	1170	1164 ± 1	29	30±3	145*	4-B	-0.10	9.50	0.10	2.30	536
6	0.85	4.01	85	85*	1322	1321± 3	330	330*	130*	4-B	-0.55	12.00	1.00	1.75	1013
9	0.28	4.75	45	54 ± 9	1415	1409 ± 3	216	198 ± 2	159*	4-B	0.76	10.68	0.25	2.93	3054
10	0.30	0.97	47	47*	1516	1518 ± 1	32	30 ± 2	100*	2-A	-0.22	6.37	2.57	2.60	467
11	0.53	0.93	63	61 ± 6	1325	1282 ± 1	20	19 ± 1	136	1-B	0.03	6.59	9.58	2.61	1843
12	0.34	0.59	49	58 ± 16	1392	1393 ± 1	30	51 ± 3	50	2-B	0.35	4.48	1.82	2.16	250
13	0.54	2.74	63	59± 3	1573	1576 ± 2	116	119 ± 1	213*	1-A	1.00	11.54	14.01	2.54	5815
17	0.47	1.31	58	55 ± 2	1281	1277 ± 1	323	325 ± 1	160	1-A	0.75	7.91	19.7	2.41	5062
18	0.05	0.74	19	19*	1604	1601 ± 1	61	44 ± 2	147*	4-B	0.03	5.32	1.78	2.86	2066
19	0.07	1.37	22	22*	1630	1625 ± 1	38	165 ± 7	34*	3-B	0.21	7.68	4.98	3.11	3415
21	0.78	1.97	80	80*	1182	1176 ± 1	0	0*	92*	4-B	0.30	8.62	0.06	2.29	365
23	0.74	1.6	79	79 ± 2	1501	1469± 2	109	109 ± 1	139	3-B	-0.68	8.57	7.78	2.08	1929
25	0.62	1.87	68	66 ± 1	1277	1277 ± 2	300	299 ± 1	168	1-A	0.24	9.39	21.62	2.68	1830
26	0.71	1.31	78	78*	1569	1561 ± 2	194	194*	90*	4-B	0.08	7.51	1.55	2.90	413
27	0.12	1.26	29	21 ± 13	1734	1729 ± 1	24	15 ± 2	112*	4-B	0.70	7.20	0.86	2.44	262
28	0.50	2.24	61	63 ± 5	1332	1331 ± 2	46	50 ± 2	137	1-A	-0.52	9.66	5.68	2.92	1239
32	0.05	-	18	-	1158	-	5	-	-	-	-	-	0.30	-	-
35	0.14	-	31	-	1522	-	4	-	-	-	-	-	0.01	-	-
37	0.12	1.13	29	39 ± 4	1373	1368 ± 1	144	128 ± 1	155	1-A	0.17	7.06	1.8	3.30	2203
38	0.76	1.84	77	82 ± 2	1419	1407 ± 5	234	234± 1	96	2-B	0.85	8.80	4.26	2.61	756
39	0.66	3.26	73	73*	1557	1550± 2	2	2*	113*	3-B	-0.50	11.18	0.05	2.21	536
40	0.48	1.15	60	55 ± 5	1584	1578 ± 1	9	10 ± 1	114*	2-A	-0.82	7.20	2.38	2.29	1616
44	0.05	1.07	18	18*	1121	1102 ± 2	57	95 ± 4	101	4-B	0.70	6.95	11.57	2.65	681
47	0.23	1.55	40	36 ± 11	1507	1506 ± 1	30	31 ± 1	150	2-A	-0.49	8.24	7.87	2.43	3339
48	0.10	2.51	26	26*	1155	1152 ± 1	310	337 ± 1	115*	2-B	-0.02	10.27	0.63	2.01	21553
50	0.34	1.07	49	47 ± 2	1500	1500 ± 1	210	207 ± 1	177	1-A	0.20	7.03	5.55	2.04	1443
52	0.15	1.83	32	32 ± 1	1204	1216 ± 2	160	163 ± 2	157*	4-B	0.30	8.42	1.07	3.23	1683
56	0.50	2.45	61	64 ± 3	1708	1702 ± 2	304	303 ± 2	190*	1-A	2.03	10.61	8.57	3.01	1155
59	0.78	13.28	82	82 ± 2	1717	1709 ± 6	93*	93*	213	3-B	-0.24	34.51	3.19	3.10	2019
60	0.30	3.71	47	60 ± 4	991	1060 ± 3	173	169 ± 2	120*	4-B	0.76	12.76	2.24	3.03	4848
61	0.68	2.85	72	81 ± 7	1217	1205 ± 2	171	169 ± 2	133	3-B	1.10	11.32	2.58	2.53	737
62	0.65	1.42	70	63 ± 2	1571	1569 ± 1	305	296 ± 1	165	1-A	-0.54	8.10	13.36	2.10	3925
63	0.50	2.08	61	58 ± 2	1289	1299 ± 1	3	179 ± 1	168	1-A	-0.40	9.52	0.95	2.12	7844
64	0.68	2.22	72	72*	1213	1240 ± 2	54	54*	105	3-B	1.09	10.01	1.28	2.27	1059

Kinematical parameters computed from the models for the 152 HRS galaxies concerning this work. (1) HRS galaxy number. (2) Elipticity from Cortese et al. (2012). (3) χ^2_{red} of the kinematical model. (4) Morphological inclination calculated with the elipticity value as in Masters et al. (2010). (5) Inclination calculated by our kinematical model (6) Systemic velocity from Boselli et al. (2010). (7) Systemic velocity computed by our kinematical models (8) Morphological PA taken from Cortese et al. (2012); if necessary, the value of the PA has been transformed in order to be able to compare with the kinematical PA easily. (9) PA calculated by our kinematical models (The case of galaxy HRS 322 is very explained in Appendix B). (10) V_{max} derived from the Courteau function fitted to the rotation curve, marked with a star when extrapolated. (11) Flag of the rotation curve. (12) Mean residual velocity dispersion of the residual velocity fields. (13) Mean velocity dispersion of the residual velocity fields. (14) Integrated flux deduced from our comparison to Boselli et al. (2014a) data. (15) r_{RC} normalised to r_{eff}. (16) Number of resolution elements per galaxy spatial coverage.

HRS	ϵ	χ^2_{red} model	i_{morph} °	i_{kin} °	V_{sys} km s^{-1}	$V_{sys_{FP}}$ km s^{-1}	PA_{morph} °	PA_{kin} °	V_{max} km s^{-1}	V_{max} flag	$\overline{res}$ km s^{-1}	σ_{res} km s^{-1}	f (Hα) 10^{-13} erg s^{-1} cm^{-2}	r_{RC}/r_{eff}	N_{beams}
(1)	(2)	(3)	(4)	(5)	(6)	(7)	(8)	(9)	(10)	(11)	(12)	(13)	(14)	(15)	(16)
65	0.45	1.92	57	59 ± 6	1383	1378 ± 1	115	123 ± 2	87	2-A	-0.73	9.10	6.15	2.42	2923
66	0.55	1.35	65	63 ± 2	1468	1464 ± 2	87	85 ± 1	169	1-A	-1.07	7.96	18.6	2.19	2220
67	0.36	1.06	51	51*	1436	1424 ± 1	40	65 ± 3	85*	3-A	0.07	6.69	4.61	2.70	2664
68	0.05	1.65	18	18*	1412	1405 ± 1	0	57 ± 5	89*	4-B	-0.84	7.59	0.88	2.08	66
70	0.36	1.19	51	40 ± 12	1617	1552 ± 1	280	268 ± 1	96	1-A	0.03	6.90	5.05	-	863
72	0.48	2.06	59	79 ± 15	1577	1562 ± 2	80	52 ± 2	161	2-B	0.81	9.76	5.13	-	953
74	0.17	2.78	35	24 ± 10	1108	1122 ± 2	200	187 ± 1	189*	2-A	-2.02	11.43	8.10	-	4293
76	0.60	2.23	67	67*	1069	1061 ± 2	353	353*	72*	3-B	-0.98	9.85	1.28	2.91	1494
77	0.23	1.96	40	40 ± 2	1458	1458 ± 1	31	36 ± 1	246	1-A	-0.05	9.81	11.22	1.90	11334
78	0.16	0.96	33	39 ± 16	1269	1265. ± 1	178	174 ± 3	56*	2-B	0.52	6.49	5.86	3.40	3047
79	0.80	3.83	84	84*	1508	1510 ± 6	144	144*	133	2-B	1.40	13.51	1.53	2.48	691
80	0.12	1.25	29	29*	932	925 ± 1	161	161*	81*	3-B	-0.37	7.25	3.52	2.54	4608
82	0.35	1.35	51	37 ± 16	931	916 ± 2	102	103 ± 4	71*	3-B	1.55	7.15	0.39	1.78	216
83	0.66	0.83	75	75*	1232	1231 ± 1	327	326 ± 2	61*	4-B	0.46	5.92	0.28	2.39	307
84	0.22	1.38	39	42 ± 3	2424	2410 ± 1	40	42 ± 1	194*	2-A	0.27	5.34	0.32	2.39	961
86	0.41	1.28	54	65 ± 7	1309	1305 ± 1	337	344 ± 2	132	1-A	0.63	7.71	18.11	2.78	8208
88	0.32	2.13	47	35 ± 8	1326	1324 ± 1	307	338 ± 1	210	1-B	0.79	9.72	19.49	1.98	17460
92	0.76	5.97	77	77*	2316	2307 ± 3	301	301*	124*	4-B	1.11	12.59	0.11	1.80	655
95	0.43	2.25	56	56*	596	618 ± 2	125	118 ± 3	101*	3-B	-1.65	11.04	3.13	2.17	1570
98	0.82	3.13	81	81*	229	242 ± 3	58	58*	94*	3-B	-1.25	12.3	0.14	2.66	1584
104	0.41	-	55	-	925	-	-55	-	-	-	-	-	0.01	-	-
106	0.12	1.95	29	29*	2617	2609 ± 1	6	14 ± 2	123	3-B	-0.67	9.98	3.85	2.11	3969
107	0.80	3.01	80	80*	1733	1718 ± 2	196	196*	99*	4-B	0.52	12.44	0.03	1.89	391
112	0.48	7.09	61	61*	2310	2256 ± 3	220	220*	8*	4-B	0.30	13.79	0.82	2.69	1380
117	0.69	1.77	75	75*	1035	1066 ± 5	24	24*	144*	2-B	-0.04	5.47	0.01	2.50	2560
118	0.30	0.89	46	46*	1296	1264 ± 1	13	347 ± 3	52	2-B	1.02	6.45	8.17	1.90	2432
121	0.73	1.65	77	77*	1250	1258 ± 1	113	113*	154*	1-B	0.35	8.07	3.08	2.64	1116
132	0.07	1.65	22	22*	727	718 ± 2	46	62 ± 10	98*	3-B	0.78	12.61	4.66	2.59	2422
133	0.62	2.84	68	68*	1253	1250 ± 2	286	286*	88*	4-A	-0.01	11.79	0.07	1.93	3208
134	0.75	3.33	77	77*	1137	1137 ± 5	39	39*	0*	4-B	-2.68	15.65	0.78	2.21	1440
136	0.32	-	49	-	784	-	85	-	-	-	-	-	0.01	-	-
139	0.4	1.01	54	40 ± 13	1136	1133 ± 1	341	356 ± 2	107*	1-A	-0.34	6.84	4.95	2.07	1772
141	0.47	2.2	59	53 ± 3	963	959 ± 1	335	337 ± 1	170*	3-B	-0.11	9.47	0.09	2.15	5544
142	0.41	1.52	56	56*	1710	1700 ± 2	200	180 ± 10	14*	3-B	-0.55	7.29	14.12	4.02	3019
143	0.76	1	77	77*	992	1001 ± 1	338	338*	122*	1-B	0.02	7.45	3.95	1.97	1393
145	0.30	1.11	46	46*	1101	1097± 1	272	276 ± 1	99*	2-A	0.99	7.64	1.10	1.97	3571
146	0.73	1.38	75	75*	1195	1188 ± 2	156	156*	78*	4-B	1.18	8.82	2.16	2.02	972
148	0.73	1.75	75	75*	-122	-136 ± 4	125	125*	130	1-B	0.52	10.95	12.32	1.91	3024
149	0.70	1.38	76	76*	230	243 ± 1	89	89*	137*	1-B	-0.07	8.85	0.36	1.91	4124
151	0.34	3.97	50	53 ± 23	103	89 ± 3	237	258 ± 4	110*	3-B	3.42	17.05	2.21	2.23	4599
152	0.08	0.97	23	23*	2289	2281 ± 1	267	273 ± 1	128*	2-B	0.44	8.60	1.99	2.38	2671
153	0.11	1.35	27	27*	1395	1391 ± 1	283	277 ± 2	120	1-B	0.40	10.11	6.16	2.17	4003
154	0.05	0.96	18	18*	1272	1266 ± 1	176	232 ± 1	104	2-B	0.13	9.68	6.47	1.69	2671

HRS	ϵ	χ^2_{red} model	i_{morph} °	i_{kin} °	V_{sys} km s^{-1}	$V_{sys_{FP}}$ km s^{-1}	PA_{morph} °	PA_{kin} °	V_{max} km s^{-1}	V_{max} flag	$\overline{res}$ km s^{-1}	σ_{res} km s^{-1}	f (Hα) 10^{-13} erg s^{-1} cm^{-2}	r_{RC}/r_{eff}	N_{beams}
(1)	(2)	(3)	(4)	(5)	(6)	(7)	(8)	(9)	(10)	(11)	(12)	(13)	(14)	(15)	(16)
156	0.65	4.69	74	74*	-275	-200 ± 2	314	314*	186*	3-B	-0.49	10.42	0.22	3.23	4002
157	0.51	1.27	61	62 ± 4	1695	1687 ± 2	8	15 ± 2	108	1-A	-0.69	9.03	4.10	2.69	10712
159	0.49	1.49	62	85 ± 24	437	453 ± 3	92	92*	21*	4-B	0.54	6.93	1.02	2.37	4404
160	0.11	1.16	28	45 ± 9	1450	1445 ± 1	60	77 ± 2	95	3-A	-0.04	8.52	7.57	2.18	1538
164	0.10	-	27	-	724	-	-0.68	-	-	-	-	-	0.15	-	-
165	0.72	1.81	75	75*	2252	2238 ± 1	312	312*	88*	4-B	0.32	8.72	0.06	3.24	8418
168	0.50	1.63	61	48 ± 15	1120	1110 ± 1	174	165 ± 3	86	1-A	0.08	9.03	1.04	2.38	3093
169	0.28	0.98	44	44*	1701	1706 ± 1	239	245 ± 2	88	2-A	0.08	8.67	0.66	2.07	442
171	0.34	1.25	49	49*	858	834 ± 2	170	176 ± 2	124*	2-B	1.27	9.52	1.14	3.11	824
172	0.56	1.29	66	56 ± 8	1668	1665 ± 1	40	39 ± 2	106*	4-B	0.20	10.57	0.38	2.52	813
177	0.34	0.75	51	55 ± 7	2341	2349 ± 1	1	171 ± 2	72*	2-A	-0.73	6.77	2.33	2.58	1711
182	0.48	2.16	59	54 ± 2	2438	2434 ± 1	175	174 ± 1	189	2-A	-0.50	11.51	4.04	2.20	3049
184	0.48	-	61	-	497	-	-30	-	-	-	-	-	0.2	-	-
185	0.05	2.11	18	18*	1777	1763 ± 1	250	213 ± 2	176*	3-B	-0.35	8.86	0.05	2.28	1936
187	0.21	0.95	38	30 ± 6	1732	1721 ± 1	42	49 ± 1	135	1-A	-0.25	7.56	21.49	2.10	1600
189	0.36	1.36	51	65 ± 17	2096	2086 ± 1	107	109 ± 3	51*	4-B	0.31	8.72	0.26	2.32	3457
191	0.40	0.59	54	56 ± 4	1629	1615 ± 1	46	45 ± 1	89*	2-B	-0.09	4.87	1.95	2.13	16151
192	0.24	2.32	42	42*	737	564 ± 4	116	116*	0*	4-B	-0.21	6.51	0.20	2.12	1688
193	0.35	0.87	50	50*	-170	-166 ± 1	38	59 ± 3	85*	1-A	0.22	9.18	4.16	1.79	1039
195	0.51	-	63	-	958	-	7	-	-	-	-	-	0.01	-	-
197	0.72	1.9	75	75*	2329	2327 ± 1	215	213 ± 1	106*	3-B	-0.09	14.90	0.27	2.46	4703
198	0.46	1.37	58	52 ± 16	1174	1182 ± 1	231	226 ± 2	88*	2-A	-0.04	8.81	5.14	2.18	1944
199	0.30	0.98	46	30 ± 13	2349	2326 ± 1	153	183 ± 3	97*	4-B	0.38	7.34	0.62	2.86	3636
207	0.14	1.35	31	29 ± 17	1288	1280 ± 1	43	12 ± 3	121*	3-B	0.71	9.89	0.97	2.42	4320
212	0.21	1.17	38	38*	1410	1397 ± 1	221	243 ± 4	56	2-B	0.64	10.61	3.67	2.38	2505
225	0.52	0.39	63	63*	2737	2745 ± 1	137	137*	3*	4-B	0.36	2.83	0.01	1.83	4376
226	0.47	2.56	59	58 ± 3	2424	2418 ± 1	220	218 ± 1	175*	3-B	-0.35	18.12	0.13	2.49	1753
230	0.38	1.15	53	52 ± 5	630	626 ± 1	290	291 ± 2	71*	3-A	-0.04	8.62	5.24	1.91	3326
237	0.25	0.97	42	42*	742	731 ± 2	194	188± 4	81*	2-A	0.92	6.88	8.92	2.26	1528
238	0.22	1.47	39	39*	1116	1107 ± 2	284	311 ± 5	56	3-B	-0.63	5.95	6.25	1.47	2286
239	0.80	4.16	80	80*	119	120 ± 3	336	336*	146*	3-B	-0.49	21.67	1.65	3.11	1661
249	0.66	-	73	-	849	-	71	-	-	-	-	-	0.01	-	-
252	0.43	0.9	56	56 ± 8	1619	1629 ± 1	2	359 ± 1	89	2-A	-0.09	9.4	2.03	2.00	16276
255	0.10	0.87	26	26*	984	980 ± 1	320	13 ± 3	61	4-B	0.28	4.45	3.01	1.47	981
256	0.22	1.15	40	40*	1119	1113 ± 1	251	336 ± 7	24*	3-B	-0.74	12.66	34.69	3.11	16276
261	0.79	2.02	79	79*	1158	1170 ± 1	181	181*	107*	3-B	0.06	9.74	3.67	2.03	5812
264	0.80	0.59	80	80*	1272	1262 ± 1	171	171*	77*	3-B	-0.27	6.42	0.07	1.98	2258
267	0.67	2.83	72	72*	1179	1202 ± 3	30	30*	51*	3-B	-2.75	17.19	2.44	1.89	367
268	0.62	3.57	70	70*	1779	1782 ± 3	119	119*	191	2-A	0.63	19.82	2.27	2.49	6435
271	0.78	1.45	79	79*	1240	1242 ± 2	338	338*	88*	3-B	1.05	14.00	0.71	2.13	1208
273	0.74	3.28	76	76*	1119	1130 ± 2	313	315 ± 1	142	3-B	0.60	15.52	0.47	2.50	2241
275	0.08	1.01	23	23*	1566	1562 ± 1	216	251 ± 2	101	1-B	0.51	7.87	20.67	-	3708

HRS	ϵ	χ^2_{red} model	i_{morph} °	i_{kin} °	V_{sys} km s^{-1}	$V_{sys_{FP}}$ km s^{-1}	PA_{morph} °	PA_{kin} °	V_{max} km s^{-1}	V_{max} flag	$\overline{res}$ km s^{-1}	σ_{res} km s^{-1}	f (Hα) 10^{-13} erg s^{-1} cm^{-2}	r_{RC}/r_{eff}	N_{beams}
(1)	(2)	(3)	(4)	(5)	(6)	(7)	(8)	(9)	(10)	(11)	(12)	(13)	(14)	(15)	(16)
276	0.2	4.15	37	37*	2832	2816 ± 2	244	237 ± 2	165*	4-B	1.33	17.06	2.12	2.13	3852
278	0.77	2.58	81	81*	1121	1106 ± 2	347	347*	90*	4-B	0.67	8.75	0.53	2.25	3459
279	0.51	1.63	61	54 ± 3	1321	1315 ± 1	340	345 ± 1	116	1-A	0.21	10.53	1.68	1.74	1757
280	0.52	2.06	63	63*	2802	2800 ± 2	92	89± 1	220*	2-B	-0.27	16.40	0.26	3.23	5031
282	0.3	-	46	-	2664	-	5	-	-	-	-	-	0.68	-	-
283	0.57	1.78	65	66 ± 2	760	762 ± 2	309	311 ± 1	143	1-A	-0.49	17.65	14.16	3.64	135
284	0.63	2.41	69	69*	1296	1282 ± 3	348	348*	150*	2-A	1.56	18.69	1.36	2.50	2855
287	0.29	2.53	45	45*	1174	1171 ± 2	202	227 ± 2	140	2-A	-1.01	14.40	16.42	-	1114
289	0.39	1.43	53	43 ± 3	1678	1675 ± 1	155	142 ± 1	168	2-A	0.55	16.4	11.43	2.34	3672
290	0.6	1.89	70	70*	1136	1120 ± 3	281	281*	90*	4-B	1.02	11.32	4.16	-	5049
291	0.27	-	44	-	1297	-	-39	-	-	-	-	-	0.01	-	-
292	0.24	1.45	41	32 ± 9	1225	1210 ± 1	74	88 ± 1	159*	1-B	-0.53	13.32	3.32	3.22	1240
293	0.19	0.95	36	44 ± 12	1092	1092 ± 1	290	306 ± 2	124	1-A	-1.11	14.93	9.83	4.26	3204
294	0.75	4.01	80	80*	1608	1602 ± 3	259	159*	98*	4-B	-0.84	11.13	0.30	3.43	2664
297	0.73	2.67	77	77*	1508	1496 ± 1	150	150*	114	2-B	0.24	14.98	0.56	2.30	828
298	0.35	0.97	50	50*	1419	1429 ± 1	261	270 ± 2	127	1-A	-0.38	11.25	9.07	2.20	3190
300	0.7	-	77	-	1354	-	83	-	-	-	-	-	0.01	-	-
301	0.3	1.32	46	38 ± 4	1380	1377 ± 1	12	6 ± 1	173	1-A	0.00	7.54	13.56	2.78	11334
303	0.2	1.12	38	47 ± 10	1717	1689 ± 1	309	307 ± 2	115*	3-B	0.62	2.65	1.42	2.84	210
304	0.72	2.27	76	76*	1370	1363 ± 2	16	16*	137*	2-B	-0.55	11.45	2.77	1.85	2363
305	0.59	0.82	66	66*	1171	1167 ± 1	67	67*	15*	4-B	0.33	14.38	0.10	2.94	1959
308	0.65	2.56	72	72*	1091	1099 ± 4	128	128*	63*	4-B	0.15	15.46	0.19	2.21	3051
309	0.39	0.84	53	64 ± 3	1383	1378 ± 1	253	250 ± 1	98	2-A	-0.28	7.61	0.51	1.88	2484
313	0.71	2.7	75	75 ± 2	1490	1481 ± 2	55	55*	126*	2-B	-0.07	10.93	0.55	2.33	3051
314	0.54	3.94	63	57 ± 7	1389	1389 ± 2	159	172 ± 2	119	3-A	-1.27	14.67	1.88	1.98	2483
317	0.65	2.24	72	72*	1716	1709 ± 7	340	340 ± 2	105	2-B	0.55	17.02	0.09	2.15	366
318	0.43	1.62	56	56*	1370	1348 ± 2	80	64 ± 2	114	1-A	1.82	12.44	15.68	2.13	3262
319	0.26	2.58	43	44 ± 7	1368	1368 ± 1	63	66 ± 1	114	1-A	-0.34	16.09	25.69	2.29	10101
321	0.33	0.87	49	49*	1581	1582 ± 2	38	34 ± 1	90*	2-A	-0.42	15.18	4.78	2.89	449
322	0.05	0.67	18	19*	1505	1505 ± 1	84	45*	211*	3-B	-0.18	4.68	3.11	2.64	15641
323	0.65	5.3	72	72*	1640	1620 ± 6	163	163*	131*	4-B	0.11	14.39	0.29	2.46	1452

Table E.4. HRS 157 Rotation curve

r	σ_r	r	σ_r	v	σ_v	N bins	side
kpc	kpc	"	"	km s^{-1}	km s^{-1}		
(1)	(2)	(3)	(4)	(5)	(6)	(7)	(8)
0.05	0.00	0.6	0.0	12	10	1	r
0.12	0.00	1.4	0.0	15	10	1	r
0.13	0.01	1.5	0.2	-1	0	2	a
0.23	0.02	2.8	0.2	25	5	2	r
0.28	0.02	3.4	0.3	12	2	4	a
0.31	0.01	3.8	0.1	20	2	3	r
0.38	0.02	4.6	0.3	20	3	5	r
0.39	0.02	4.7	0.3	14	3	2	a
0.47	0.02	5.7	0.2	33	7	4	a
0.47	0.02	5.7	0.3	27	1	3	r
0.56	0.03	6.7	0.3	38	3	6	a
0.57	0.02	6.9	0.2	28	2	7	r
0.63	0.02	7.7	0.2	23	3	2	r
0.65	0.02	7.9	0.3	42	4	7	a
0.73	0.02	8.9	0.2	38	5	4	r
0.74	0.02	9.0	0.3	50	4	5	a
0.81	0.02	9.8	0.2	56	3	7	a
0.81	0.00	9.8	0.0	33	2	2	r
0.89	0.02	10.8	0.2	46	2	11	r
0.89	0.02	10.8	0.2	58	3	9	a
0.98	0.02	11.9	0.3	66	3	11	a
0.99	0.03	12.0	0.4	64	10	3	r
1.08	0.05	13.2	0.6	67	2	23	a
1.13	0.07	13.8	0.8	60	1	23	r
1.24	0.05	15.0	0.6	69	2	23	a
1.33	0.04	16.1	0.5	67	2	23	r
1.37	0.03	16.6	0.4	75	1	23	a
1.47	0.04	17.8	0.5	70	2	23	r
1.47	0.03	17.8	0.3	77	1	23	a
1.56	0.03	19.0	0.3	79	1	23	a
1.59	0.03	19.3	0.4	74	1	23	r
1.65	0.02	20.0	0.3	77	1	23	a
1.71	0.03	20.7	0.4	77	1	23	r
1.74	0.02	21.1	0.3	78	2	23	a
1.80	0.03	21.9	0.4	79	1	23	r
1.82	0.02	22.0	0.3	79	1	23	a
1.91	0.03	23.1	0.4	77	1	23	a
1.92	0.03	23.2	0.4	82	2	23	r
1.99	0.02	24.1	0.2	77	1	23	a
2.02	0.03	24.5	0.3	83	1	23	r
2.07	0.02	25.1	0.3	82	1	23	a
2.11	0.02	25.6	0.3	84	1	23	r
2.16	0.03	26.1	0.3	83	2	23	a
2.20	0.03	26.7	0.4	85	1	23	r
2.24	0.04	27.2	0.4	83	1	23	a
2.31	0.03	28.0	0.3	87	2	23	r
2.35	0.03	28.5	0.4	85	1	23	a
2.42	0.04	29.4	0.5	89	1	23	r
2.45	0.03	29.7	0.4	83	2	23	a
2.55	0.03	30.9	0.3	86	2	23	a
2.55	0.03	31.0	0.4	90	2	23	r
2.65	0.03	32.1	0.3	88	2	23	a
2.68	0.04	32.5	0.5	94	2	23	r
2.74	0.03	33.3	0.4	89	2	23	a
2.86	0.03	34.7	0.4	89	2	23	a
2.88	0.07	34.9	0.8	97	3	23	r
3.00	0.04	36.4	0.5	96	3	23	a
3.12	0.08	37.9	0.9	98	2	23	r
3.13	0.04	38.0	0.5	91	2	23	a
3.33	0.07	40.4	0.8	96	2	23	a
3.35	0.09	40.7	1.1	104	2	23	r
3.56	0.07	43.2	0.9	103	3	23	a
3.62	0.09	43.9	1.1	100	3	23	r
3.83	0.09	46.5	1.1	111	2	23	a
4.04	0.18	49.1	2.2	107	3	20	r
4.20	0.14	51.0	1.6	112	3	23	a
4.82	0.24	58.4	2.9	122	3	16	a
2.55	0.03	31.0	0.4	90	2	23	r
2.65	0.03	32.1	0.3	88	2	23	a
2.68	0.04	32.5	0.5	94	2	23	r
2.74	0.03	33.3	0.4	89	2	23	a
2.86	0.03	34.7	0.4	89	2	23	a
2.88	0.07	34.9	0.8	97	3	23	r
3.00	0.04	36.4	0.5	96	3	23	a
3.12	0.08	37.9	0.9	98	2	23	r
3.13	0.04	38.0	0.5	91	2	23	a
3.33	0.07	40.4	0.8	96	2	23	a
3.35	0.09	40.7	1.1	104	2	23	r
3.56	0.07	43.2	0.9	103	3	23	a
3.62	0.09	43.9	1.1	100	3	23	r
3.83	0.09	46.5	1.1	111	2	23	a
4.04	0.18	49.1	2.2	107	3	20	r
4.20	0.14	51.0	1.6	112	3	23	a
4.82	0.24	58.4	2.9	122	3	16	a

Numerical table of the rotation curve for the galaxy HRS 157. (1)(3) Galactic radius. (2), (4) Dispersion around the galactic radius (if zero, it is because only one bin was used). (5) Rotation velocity. (6) Dispersion on the rotation velocity. (7) Number of velocity bins. (8) Receding – r – or approaching – a – side.

4.2 HRS galaxies observed at SPM

4.2.1 Paper II (in prep.): An Hα kinematic survey of the *Herschel* Reference Survey – II. Fabry-Perot observations with the 2.12m telescope at SPM and the 1.93m telescope at OHP

This is the second of a serie of publications called "An Hα kinematic survey of the *Herschel* Reference Survey–". This paper is still in preparation and presents the observations and data reduction for the 69 late-type galaxies observed at SPM and OHP. Different kinematical parameters, momenta, integrated fluxes, individual comments, as well as the rotation curves were obtained/computed/done/written for these galaxies.

Astronomy & Astrophysics manuscript no. JAGL_aa_SPM_onecolumn ©ESO 2019
August 22, 2019

An Hα kinematic survey of the *Herschel* Reference Survey – II. Fabry-Perot observations with the 2.12m telescope at SPM and the 1.93m telescope at OHP*.

Gómez-López, J. A.[1]**et al.

Aix Marseille Univ, CNRS, CNES, LAM, Marseille, France. e-mail: jesus.gomez-lopez@lam.fr

Received September 15, 1996; accepted March 16, 1997

ABSTRACT

Aims. We present new 2D high resolution Fabry-Perot spectroscopic observations of 69 star-forming galaxies which are part of the *Herschel* Reference Survey (HRS), a complete *K*-band selected, volume-limited sample of nearby galaxies, spanning a wide range in stellar mass and morphological type.

Methods. Using improved data reduction techniques that provide adaptive binning based on Voronoi tessellation, we derive Hα datacubes from which we compute Hα maps and radial 2D velocity fields. A robust method based on such fields allows us to accurately compute rotation curves and kinematical parameters, for which uncertainties are calculated using a method based on the power spectrum of the residual velocity fields.

Results. We check the consistency of the rotation curves by comparing our maximum rotational velocities to those derived from HI data, and computing the *i*-band, NIR, stellar and baryonic Tully-Fisher relations. We use this set of kinematical data combined to those available at other frequencies to study for the first time...

Key words. Galaxies: fundamental parameters – Galaxies: kinematics and dynamics – Galaxies: spiral – Galaxies: general – Galaxies: statistics – Galaxies: evolution.

* Based on observations collected at the Observatorio Astronómico Nacional de San Pedro Mártir (SPM) in Mexico and the Observatoire de Haute Provence (OHP) in France.
** Alternative e-mail: jagl.c06@gmail.com

1. Introduction

The *Herschel* Reference Survey (HRS, Boselli et al. 2010) is a complete sample of 323 nearby galaxies defined with the purpose of studying the relation between the star formation process and the different components of the interstellar medium (ISM).

This is the second of a serie of papers devoted to collect HRS Fabry-Perot observations in order to construct a spectroscopic HRS late-type survey. This paper presents new Fabry-Perot data for 69 HRS star-forming galaxies gathered during 9 observing runs at SPM and 1 run at OHP. These data are used to derive the kinematical properties of the ionised gas at high spatial and spectral resolution. Combining this new set of data with other Fabry-Perot data available in the literature we study the relation between the dynamical and the baryonic mass, this last directly measured using multifrequency observations.

The paper is organised as follows. Section 2 describes the HRS sample, section 3 the observations and data reduction. In section 4 we derive the kinematical parameters. The summary and conclusions are given in Section 6. All the data products, including comments on individual objects, are given in the different Appendices.

Consistently with our previous works, all the Fabry-Perot data will be made available on the HRS dedicated database HeDAM (`https://hedam.lam.fr/`), and on the Fabry-Perot database (`https://cesam.lam.fr/fabryperot`).

2. The Sample

The *Herschel* Reference Survey (HRS) is a K-band-selected (where the K-band is a proxy of stellar mass, Gavazzi et al. 1996), volume-limited ($15 < D < 25$ Mpc) complete sample of 323 galaxies spanning a wide range in morphological type (from ellipticals to late-type spirals and irregulars) and stellar mass ($10^8 < M_{star} < 10^{11}$ $M_\odot$). The sample, which has been extensively presented in Boselli et al. (2010), includes galaxies belonging to different environments, from the Virgo cluster to isolated systems in the field. Thanks to its statistical completeness, the HRS is becoming the ideal reference for local and high-redshift studies as well as for models and simulations.

In this work we present new Fabry-Perot data for 69 star forming galaxies observed at the SPM and OHP observatories (see Table **??**). So far, Fabry-Perot data are finally available for all the 261 star-forming galaxies of the sample.

3. Observations and Data Reduction

Fabry-Perot observations scanning the Hα emission line of 45 late-type galaxies have been obtained along 91 nights at the OHP (9 runs from February 2016 to April 2018) and for 24 galaxies at the OHP along 14 nights in April 2019. The observations have been carried out in good photometric

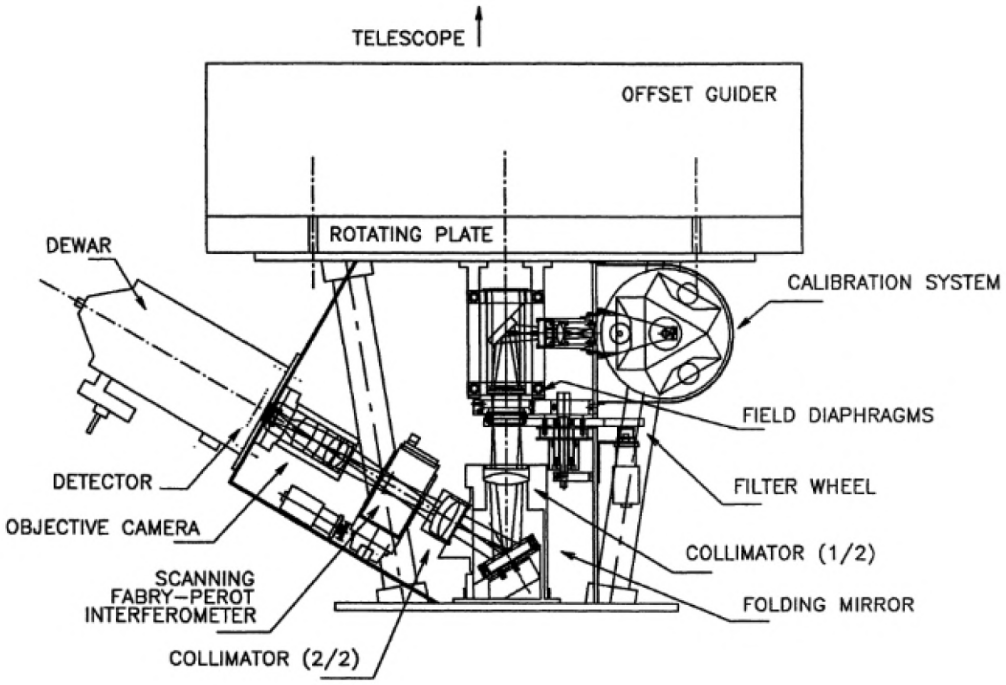

Fig. 1. The optical-mechanical design of the PUMA instrument (Rosado et al. 1995).

conditions and with a typical integration time of 2 hours per galaxy. The journal of the observations is given in Table **??**.

3.1. PUMA Instrumental setup

The instrument we use at SPM is PUMA, a focal reducer containing a scanning Fabry-Perot interferometer attached at the SPM 2.1m telescope. The principles and characteristics of the PUMA instrument are extensively explained in Rosado et al. (1995).

Briefly, PUMA (Fig. 3.1 is composed by a focal reducer (collimator + camera) coupled to a scanning Fabry-Perot interferometer with a QueensGate constant of 10.74, which can be taken out of the optical path to obtain direct imaging. The instrument is constantly bathed by dry nitrogen in order to avoid humidity into the piezoelectric control. PUMA covers a Field of View (FoV) of 10'×10' (ideal to cover the whole spatial coverage of the largest galaxies of the survey) with a pixelsize of 0.295"×0.295" for a CCD of 2048×2048 pixels. The interference order of the instrument is 330Å for Hα with a FSR of 19.98Å (916 km s^{-1}) and a spectral resolution of 0.83Å (19 km s^{-1}); the effective finesse is 24. A typical exposure for a galaxy is ∼2 hours scanning 47 or 48 channels, with a detection limit of ∼2.5×10^{-17} erg s^{-1} cm^{-2} arcsec^{-2} (Rosado et al. 1995).

The instrument is controlled by a UNIX-based software, in order to indicate the number of channels to be scanned, the exposure time, spatial pixel binning (usually 4×4 pixels = 1.19"×1.19" for a FoV=512×512 pix) and the automatic parallelisation of the interferometer plates.

Table 1. Interference filters used for SPM observations

Object filter (Å)	Calibration filter (Å)	Calibration lamp
6563/30	6562	H
	6563/30	H
	6570/30	H
6583/30	6583/30	Ne
	6589/20	Ne
6590/30	6590/30	Ne
6598/30	6598/30	Ne
6607/89	6607/89	Ne
	6720/20	Ne

Different interference filters used for the observations of the HRS galaxies with PUMA at SPM. First column: the centroid/FWHM of the filter used to get the observed object datacube. Second column: the centroid/FWHM of the filter used to get the calibration cube. Third column: Lamp used to do the calibration cube.

3.2. Data reduction

Fabry-Perot observations were carried out from 2015 to 2019 for 44 objects (16.86% of the HRS star-forming sample) at SPM using PUMA instrument. 9 different narrow and wide band filters (listed in Table 1) were used to cover a spectral range from 6555Å to 6655Å.All the galaxies were observed in general in good photometrical conditions, with a seeing of ∼1".

The softwares *computeeverything* and *reducWizard* can be used as well to reduce CDD Fabry-Perot data. Nevertheless, such software was in principle designed to reduce IPCS data. On the other hand, output CCD data got by PUMA are in CIGALE format; because of that, the corrections from telescope drift, subtraction of cosmic rays and bias were done first using the windows based *Analyse et Depouillement Homogene des Observations Cigale windows* (ADHOCw) software, developed by J. Boulesteix. Once these corrections done, a "neb.ad3" object cube and a "calibration.ad3" cube are obtained per galaxy, ready to continue the data reduction using *computeeverything* just before computing the phase maps and the lambda cube.

The different momenta of the data were computed, as well as the integrated Hα profiles, kinematical models and rotation curves for each galaxy. We also removed the LSF instrument contribution as done in Gomez-Lopez et al. (2019) for the SPM Fabry-Perot data.

3.3. Flux Calibration and Hα profiles

During the SPM runs, in order to maximize the observing time on the galaxies themselves, we do not observe flux calibration sources but we use instead the high quality Hα photometry, available for the whole HRS sample (Boselli et al. 2015). Thus we perform an indirect calibration of the total Hα flux for the 44 datacubes using the calibrated fluxes from Boselli et al. (2015). We correct their Hα + [NII] fluxes for [NII] contamination (6584 and 6548 Å) using the [NII]/Hα ratio derived from spectroscopic observations (Boselli et al. 2013); for galaxies where there is no available [NII]/Hα ratio, we calculate it according to the $[NII]/H\alpha$ *vs* M_{star} relation in the B-band given in Boselli et al. (2009).

For each galaxy, the total Hα emission is computed by integrating the flux for each spatial element of the datacubes as described in Epinat et al. (2008), taking into account:

i) the response of the instrument,

ii) the aperture of the instrument,

iii) the exposure time (given in Table **??**),

iv) using the velocity field to disentangle the FSR overlaps when necessary.

v) the shift of the interference filter spectral range due to the tilt (if any) and the temperature,

vi) the subtraction of the continuum contribution.

To minimize the foreground sky contamination, we only consider the spatial elements not masked in the final momenta maps (shown in Appendix C). The integrated Hα profiles per galaxy are shown in Appendix B.1.

4. Data Analysis

5. Main Discussion and Analysis

6. Conclusions

We present new high resolution Fabry-Perot observations gathered at the SPM of 44 star-forming galaxies belonging to the *Herschel* Reference Survey. Combined with those available in the literature (217 objects), previously collected with the same facility, an homogeneous set of kinematical data is now available for the whole sample. Using improved data reduction pipelines, we compute the Hα momenta, optimizing the spatial resolution given a S/N ratio through an adaptive binning method based on Voronoi tessellations. We also derive accurate kinematical models and parameters, residual velocity maps, and rotation curves.

Combined with those available at other frequencies, these 2D-spectroscopic data make the HRS a unique dataset for studying on strong statistical basis the role of gas kinematics on the process of star formation, a major step towards the understanding of the mechanisms that drive galaxy evolution.

Acknowledgements. The authors thank the Mexican grants CONACYT-253085 and DGAPA-UNAM PAPIIT-IN109919 which have extensively supported this work. This research has made use of data from the HRS project. HRS is a Herschel Key Programme utilising guaranteed time from the SPIRE instrument team, ESAC scientists and a mission scientist. This research has also made use of the NASA/IPAC Extragalactic Database (NED) which is operated by the Jet Propulsion Laboratory, California Institute of Technology, under contract with the National Aeronautics and Space Administration. The authors have also made an extensive use of the HyperLeda Data base (`http://leda.univ-lyon1.fr`). The Digitized Sky Surveys were produced at the Space Telescope Science Institute under U.S. Government grant NAG W-2166. The images of these surveys are based on photographic data obtained using the Oschin Schmidt Telescope on Palomar Mountain and the UK Schmidt Telescope. The plates were processed into the present compressed digital form with the permission of these institutions. JAGL thanks the Consejo Nacional de Ciencia y Tecnologia (CONACYT) of Mexico for the scholarship awarded during the PhD studies at Aix-Marseille University.

References

Boselli, A., Boissier, S., Cortese, L., et al. 2009, ApJ, 706, 1527

Boselli, A., Cortese, L., & Boquien, M. 2014, A&A, 564, A65

Boselli, A., Eales, S., Cortese, L., et al. 2010, PASP, 122, 261

Boselli, A., Fossati, M., Gavazzi, G., et al. 2015, A&A, 579, A102

Boselli, A., Hughes, T. M., Cortese, L., Gavazzi, G., & Buat, V. 2013, A&A, 550, A114

Cortese, L., Boissier, S., Boselli, A., et al. 2012, A&A, 544, A101

Epinat, B., Amram, P., & Marcelin, M. 2008, MNRAS, 390, 466

Gavazzi, G., Pierini, D., & Boselli, A. 1996, A&A, 312, 397

Rosado, M., Langarica, R., Bernal, A., et al. 1995, in Revista Mexicana de Astronomia y Astrofisica, vol. 27, Vol. 3, Revista Mexicana de Astronomia y Astrofisica Conference Series, ed. M. Pena & S. Kurtz, 263

Appendix A: Notes on individual galaxies

HRS 62. In spite of a slight disagreement between kinematical and morphological inclination (7° difference) as well as for the PA of the major axis (9° difference) our Hα rotation curve is fairly symmetric and regular. The curve reaches the r_{25} radius in B-band (coincident with the r_{24} radius in r-band for this galaxy) and its velocity there is slightly above the HI V_{max}. The curve extends beyond the r_{25} on the blueshifted side and both models (Courteau and Zhao) suggest that the plateau is not reached.

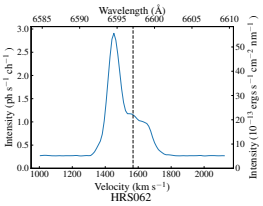

Fig. B.1. Integrated Hα profiles for the 44 HRS galaxies concerning this work. The profiles are displayed over three times the free spectral range (∼25Å top label, 1100 km s^{-1} bottom label). The calibrated intensity in erg seg^{-1} cm^{-2} nm^{-1} appears on the right side of the Y-axis. The black dashed vertical line represents the systemic velocity computed by the kinematical models; in the cases where a kinematical modelling was not possible, the corresponding systemic velocity taken from Boselli et al. (2010) is plotted instead.

Appendix B: Hα profiles

Appendix C: Individual maps

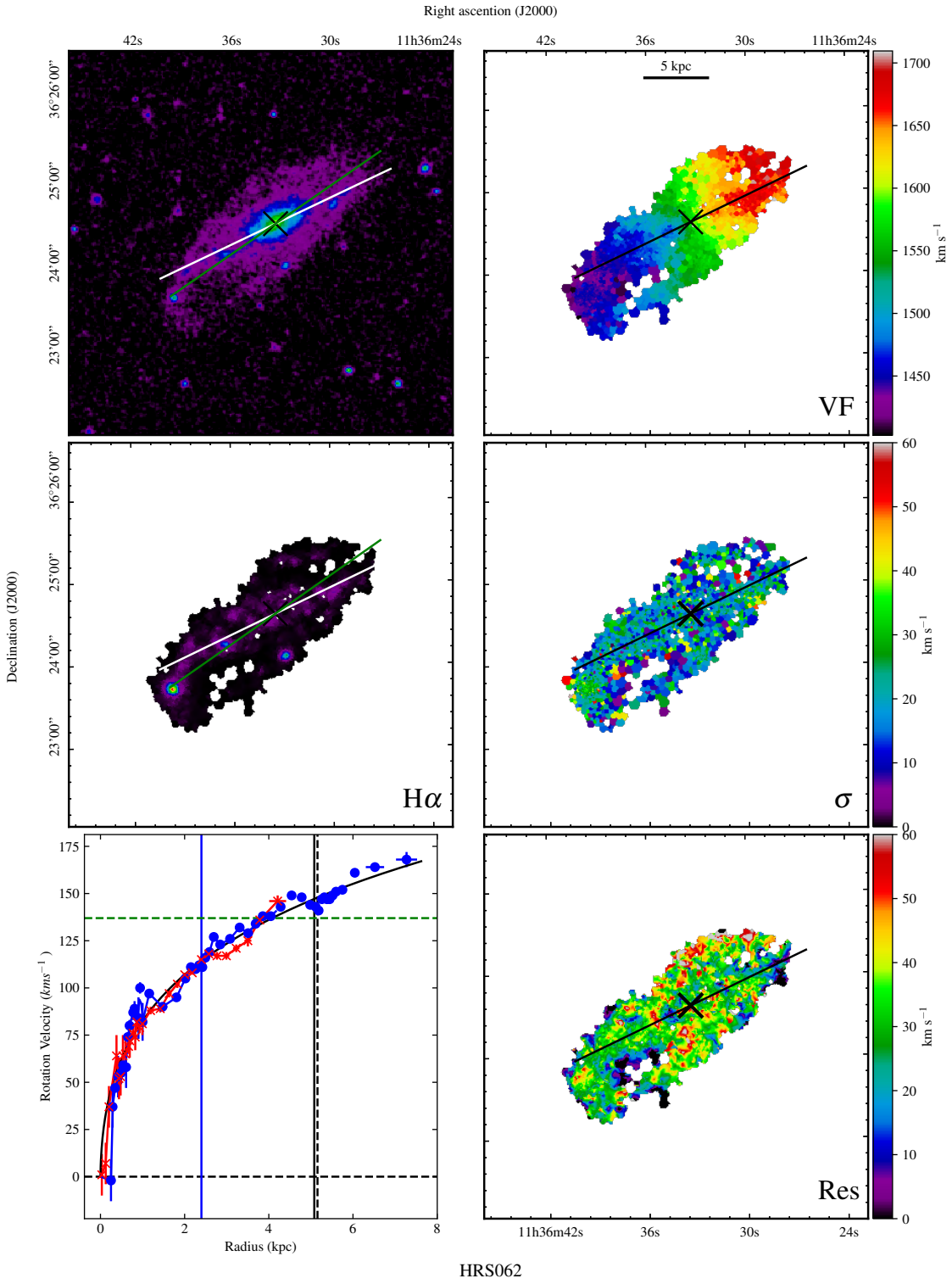

Fig. C.1. Galaxy HRS 62. Top left: XDSS *R*-band image. Top right: Hα velocity field. Middle left: Hα monochromatic image. Middle right: Hα velocity dispersion field. Bottom left: rotation curve (if computed). Bottom right: residual velocity field (if computed).The black cross is the kinematical center. In the maps, the green line is the morphological major axis, while the black/white line is the estimated kinematical major axis, its length represents the $2 \times r_{opt}$. In the rotation curve, blue dots indicate the approaching side while red crosses the receding side, the black solid vertical line represents the r_{opt}, and the black dashed line represents the r_{25}; the blue solid line the r_{eff} (if available in Cortese et al. 2012) and the green horizontal line the HI V_{max} (if available in Boselli et al. 2014); the solid black curve is the best fit Courteau function to the rotation curve.

Appendix D: Tables

5 The role of kinematics on the star formation process in local galaxies

Although it is not a "'law" properly since it is an empirical relation, in late-type galaxies, the star formation is tightly correlated to the gas column density according to the Kennicutt-Schmidt law (Schmidt, 1959; Kennicutt, 1998b, reflecting the fact that gas is the input driver for star formation, which is often parametrized with a power law:

$$\Sigma_{SFR} \propto \Sigma_{gas}^{n}. \tag{5.1}$$

The precise form of this relation depends on assumptions about how Σ_{SFR} and Σ_{gas}^{n} are derived from the observations. For instance, the form of this integrated Law appears to be surprisingly insensitive to SFR environment and parameters such as the atomic versus molecular fraction, but some metal-poor galaxies (defined as $Z < 0.3\ Z_{\odot}$) deviate systematically from the main relation, reflecting a breakdown in the application of a constant X_{CO} factor. Indeed, the interpretation of the results in this law is strongly dependent on the assumptions made about X_{CO} in late-type systems (Boselli et al., 2002b; Leroy et al., 2011; Boselli et al., 2014a,c).

Over the past few years major progress has been made in characterizing the spatially-resolved star formation law within individual galaxies. This work has been enabled by large multi-wavelength surveys of nearby galaxies such as SINGS (Kennicutt et al., 2003), the GALEX Nearby Galaxies Survey (Gil de Paz et al., 2007), the Spitzer/GALEX Local Volume Legacy survey (LVL; Dale et al., 2009; (Lee et al., 2011)), and the Herschel KINGFISH Survey (Kennicutt et al., 2011). The resulting datasets provide the means to measure spatially-resolved and dust-corrected SFRs across a wide range of galaxy properties. The study of the Kennicut-Schmidt Law has been recently improved thanks to those surveys in order to accurately trace the relation between SFR and gas column density (HI + H_2, Fig. 5.1, Kennicutt et al., 2007; Bigiel et al., 2008, 2010, 2011; Leroy et al., 2008; Blanc et al., 2009; Eales et al., 2010; Verley et al., 2010; Rahman et al., 2011, 2012; Schruba et al., 2011; Kennicutt & Evans, 2012). However, these studies just consider the Σ_{SFR} vs Σ_{gas} relation, and only explore occasionally on limited samples the role of disc kinematics on the star formation process (Kennicutt, 1998b; Boissier et al., 2003; Bigiel et al., 2008; Leroy et al., 2008).

The Toomre parameter Q (Toomre, 1964) defines the stability of stellar disks:

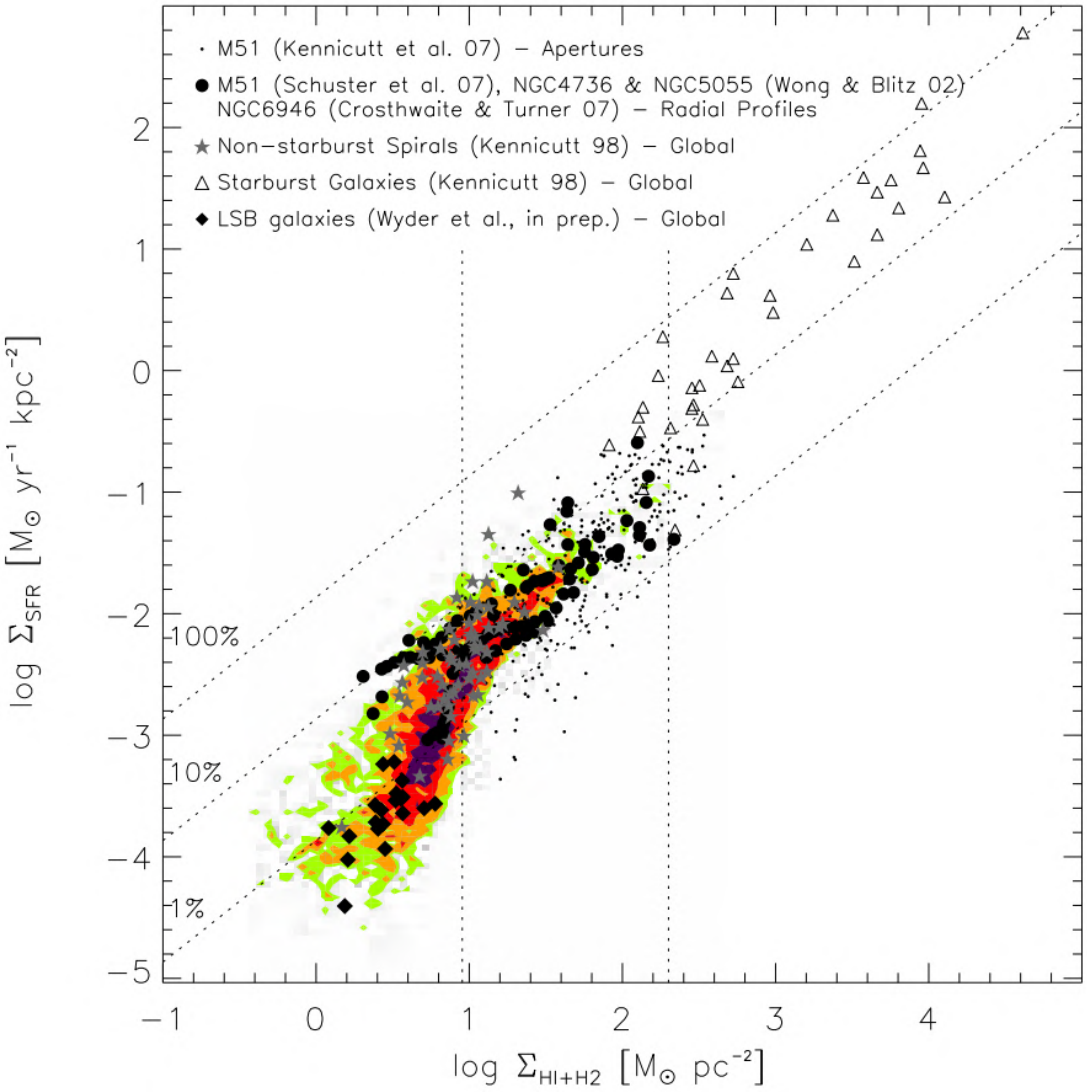

Figure 5.1 – Relation between SFR surface densities and total (atomic and molecular) gas surface densities for various sets of measurements, from Bigiel et al. (2008). Colored contours show the distribution of values from measurements of sub-regions of SINGS galaxies. Overplotted as black dots are data from measurements in individual apertures in M51 (Kennicutt et al., 2007). Data from radial profiles from M51 (Schuster et al., 2007), NGC 4736, and NGC 5055 (Wong & Blitz, 2002), and NGC 6946 (Crosthwaite & Turner, 2007) are shown as black filled circles. The disk-averaged measurements from 61 normal spiral galaxies (filled gray stars) and 36 starburst galaxies (triangles) from Kennicutt (1998b) are also shown. The black filled diamonds show global measurements from 20 low surface brightness galaxies (Wyder et al., 2009). The three lines extending from lower left to upper right show lines of constant global star formation efficiency.

$$Q = \frac{\sigma_{gas}\kappa_{gas}}{\pi G \Sigma_{gas}} \tag{5.2}$$

where $\kappa = \sqrt{2}\Omega_{gas}$ is the epicyclic frequency. A rotating stellar disk is unstable when $Q < 1$.

Indeed, assuming $\Sigma_{SFR} \propto \Sigma_{gas}/\tau$, where τ is the cloud-collapse timescale, there are theoretical indications that the Kennicutt-Schmidt Law is probably modulated at large scales by the differential rotation of the disc, as well as by the compression of the gas in the density waves associated to spiral arms, while at smaller scales by non-circular motions through the instability of the gas in GMC (Wyse, 1986; Larson, 1992; Kennicutt, 1998b; Boissier & Prantzos, 1999; Tan, 2000; Kennicutt & Evans, 2012):

$$\text{if } \; Q{=}1 \;\; \Rightarrow \;\; \tau \propto \kappa^{-1} \;\; \Rightarrow \;\; \Sigma_{\rm SFR} \propto \Sigma_{\rm gas}\, \kappa, \tag{5.3}$$

$$\text{if } \; \tau \propto \frac{\sigma_{\rm gas}}{\pi {\rm G} \Sigma_{\rm gas}} \;\; \Rightarrow \;\; \Sigma_{\rm SFR} \propto \Sigma^2_{\rm gas}/\sigma_{\rm gas}. \tag{5.4}$$

Equations 5.3 and 5.4 consider "gravitation versus dispersion" and "self-regulated star formation" mechanisms, respectively. These processes must favour cloud-cloud collisions and can directly participate in star formation.

The aim of this chapter is to study the role of the kinematics (κ and σ) on the Kennicutt-Schmidt Law at GMCs scales in the HRS nearby galaxies, taking advantage of the unique dataset available in our hands. However, we will across the next subsections that the role of technical (spatial and spectral resolution) and physical problems (conversion factors, energy transfer, dust attenuation, etc.) must be analysed and traited/corrected carefully in order to perform a correct study of the role of kinematics on the Kennicutt-Schmidt Law. It is thus worth to study carefully such technical and physical effects, taking first a one representative star-forming late-type galaxy with medium inclination, not strongly perturbed and with high spatial coverage, and for which data are available in all the resolved bands necessary to perform our tests (as showed across Chapter 1): the galaxy NGC 4254. We make a first attempt for our study proceeding as follows:

1) We must see first if the resolution plays an important role for the original Kennicutt-Schmidt Law,.

2) The CO emission lines can also be used to accurately trace the kinematics, the disadvantage is that we need very big and demanded instruments such as the ALMA interferometer in order to get CO datacubes with enough angular resolution (and thus the reason that ALMA data is available only for a few HRS galaxies); in addition, ALMA covers only certain spatial coverage that is often much smaller than the major axis in

nearby objects. Because of the latter, once quantified the role of spatial resolution, and since we are quantifying the gas content using CO data, we will see if the kinematics of cold gas (CO, tracer of the molecular component) is comparable to the kinematics of warm gas (Hα, tracer of HII regions) computed with Fabry-Perot techniques.

3) We will quantify the influence of kinematics on the Kennicutt-Schmidt Law in the case of NGC 4254, testing different theoretical relations existing in the literature.

IMPORTANT: Due to the spatial coverage of the ALMA data (3.5×4.5') of the galaxy NGC4254, we will consider hereafter the area contained within that coverage (Fig. 5.2).

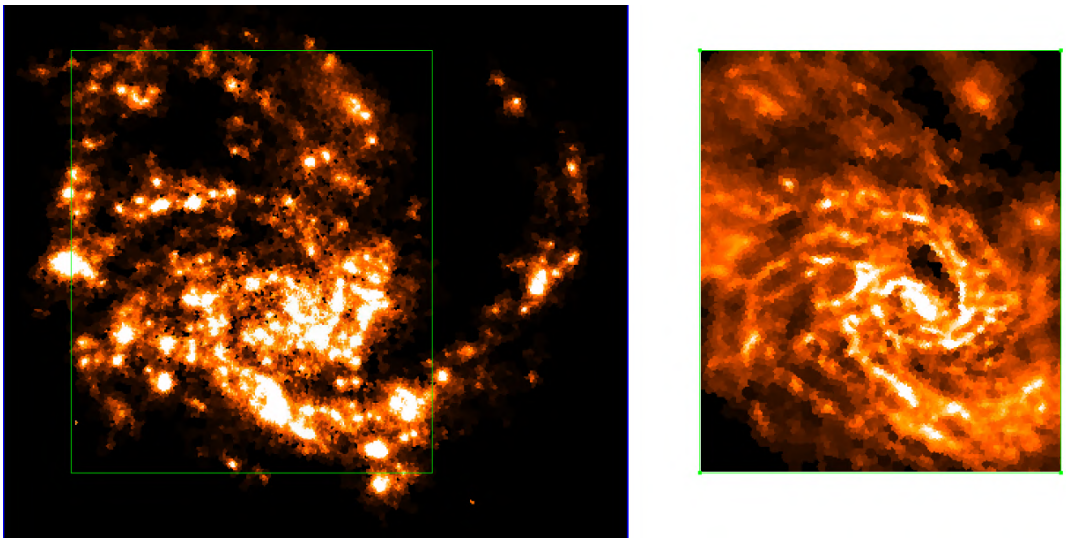

Figure 5.2 – The galaxy NGC 4254 has an diameter of ~ 6' (left panel, Hα image), while the ALMA+IRAM30m data only cover a 3.5'×4.5' box of the galaxy (right panel, CO(2-1) image).

5.1 The galaxy NGC 4254

The spiral galaxy NGC 4254 (HRS 102, M99) is located at the northern periphery of the Virgo cluster at a D = 16.5 Mpc, and at ≃ 1.0 Mpc from M87. It was discovered by Pierre Méchain on March 17, 1781. The discovery was then reported to Charles Messier, who included the object in the Messier Catalogue of comet-like objects. Messier 99 was one of the first galaxies in which a spiral pattern was seen. This pattern was first identified by Lord Rosse in the spring of 1846.

This galaxy has a morphological classification of SA(s)c, indicating a pure spiral shape with loosely wound arms. It has a peculiar shape with one normal looking arm and an extended arm that is less tightly wound. The galaxy is inclined by 42° to the line-of-sight with a major axis $PA \sim 68°$.

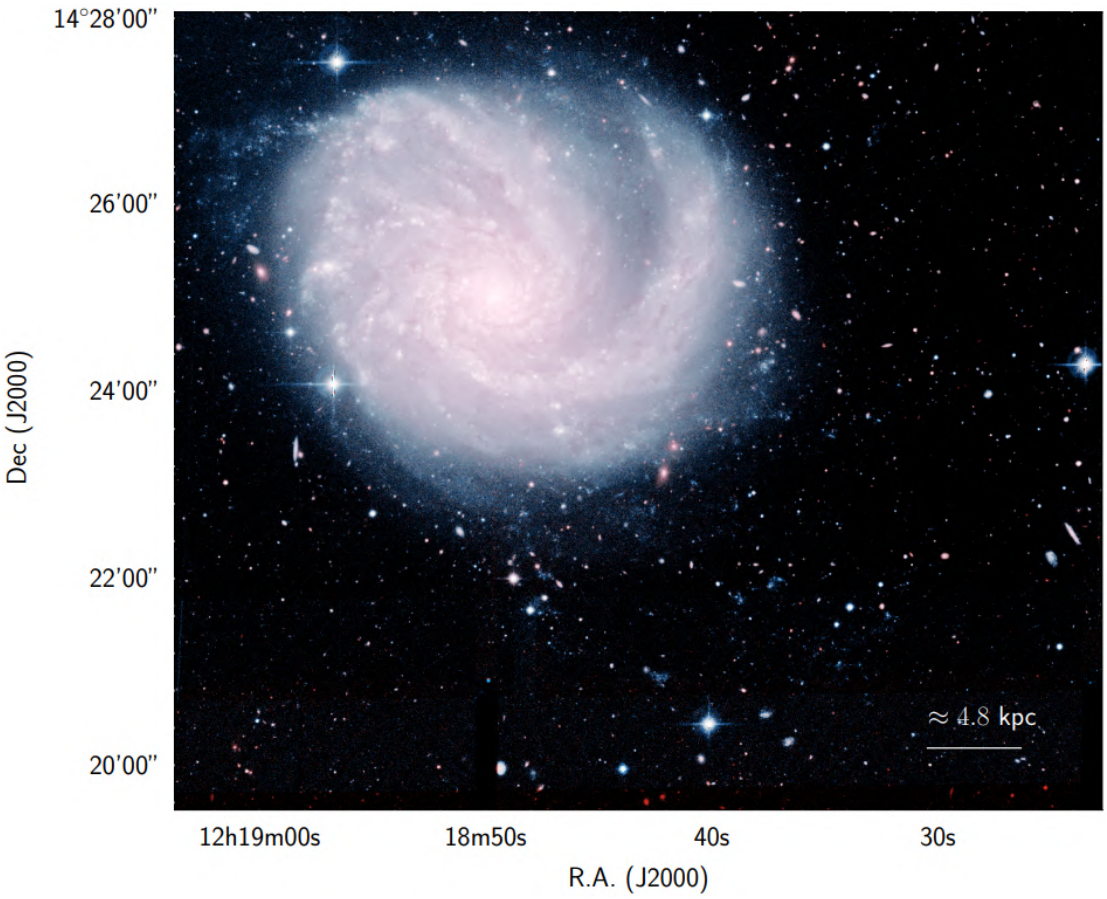

Figure 5.3 – Colour *ugi* RGB image of the galaxy NGC 4254 obtained using the NGVS data (Ferrarese et al., 2012). At the distance of the galaxy (16.5 Mpc), 1 arcmin = 4.8 kpc. Taken from Boselli et al. (2018b).

The presence of a ~250 kpc long tail of HI gas indicates that the galaxy has been gravitationally perturbed after a rapid encounter with another Virgo cluster member (Haynes et al., 2007; Boselli et al., 2018b). The interaction is thought to be responsible for the creation of a free floating HI cloud of gas not associated to any stellar component, the so called dark galaxy Virgo HI21 (Minchin et al., 2005). While not classified as a starburst galaxy, M99 has a star formation activity three times larger than other galaxies of similar Hubble type that may have been triggered by the encounter.

The galaxy is undergoing ram-pressure stripping as it moves through the intracluster medium. Because of that, and because of the availability of spatially resolved multifrequency imagerie and high resolution spectroscopic data for NGC 4254 (Presented in Chapter 1 and 3), this galaxy is thus an ideal target for studying the star formation process, and another candidate to extend previous studies to different environments.

5.2 Kennicutt-Schmidt Law at different resolutions

Nowadays, in the era of large spatially resolved surveys, we are studying the Kennicutt-Schmidt Law at GMCs scales by deriving the star formation from VESTIGE Hα imaging, and at kpc scales by deriving the star formation from SED-fitting. We will explain in detail why we do this in order to compare both methods and the influence of resolution on the Kennicutt-Schmidt Law.

5.2.1 SFR

5.2.1.1 Hα imaging

Hα fluxes should be corrected by Galactic extinction, [NII] contamination (VESTIGE observations at the CFHT made use of a filter with λ_c = 6590Å; and $\delta\lambda$ = 104Å, thus including the Hα line and the two [NII] lines λ=6548, 6584Å), as well as dust attenuation before converting them into SFR densities.

We correct each pixel for Galactic extinction using the Schlegel et al. (1998) extinction map combined with the Galactic extinction curve of Fitzpatrick & Massa (2007):

$$A_G(H\alpha) = 2.517 \times E(B-V)_G. \tag{5.5}$$

Concerning [NII] contamination, its is well known that [NII]6548~0.33×[NII]6584Å (Boselli et al., 2015). In order to do a proper correction of both emission lines, we made a radial approximation taking into account 9 HII regions for which the $f_{[NII]}$(6584Å) value is available (Fig. 5.4, Shields et al., 1991):

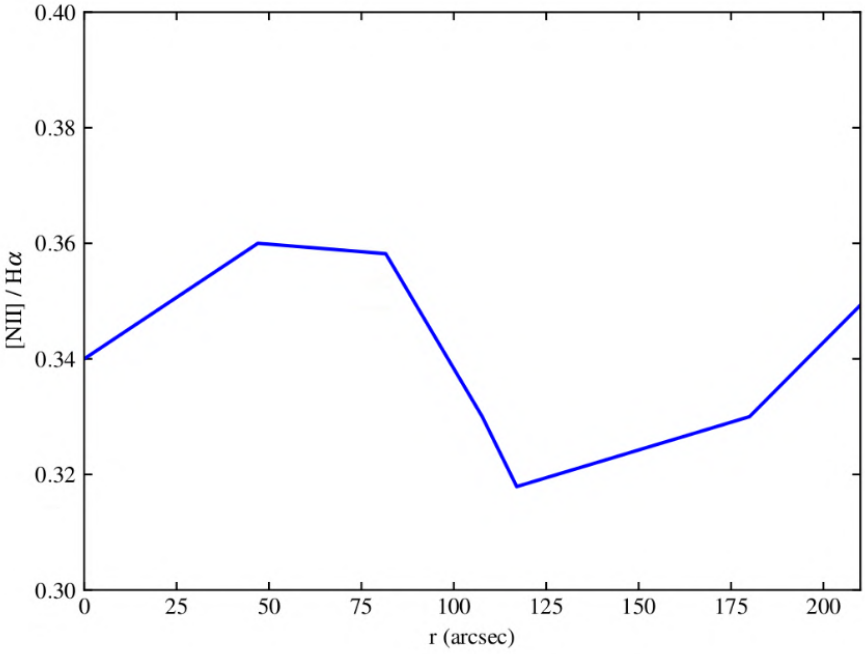

Figure 5.4 – [NII]/Hα radial correction factor based on 9 HII regions of the galaxy NGC 4254 (Shields et al. 1991).

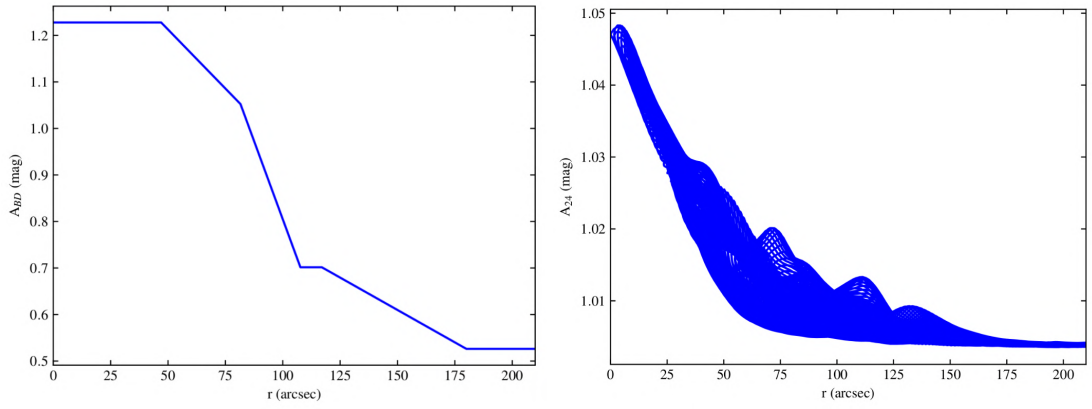

Figure 5.5 – Attenuation factor based on Balmer decrement (A_{BD}, left panel) and on 24μm flux (A_{24}, right panel) as a function of the radius of the galaxy NGC 4254.

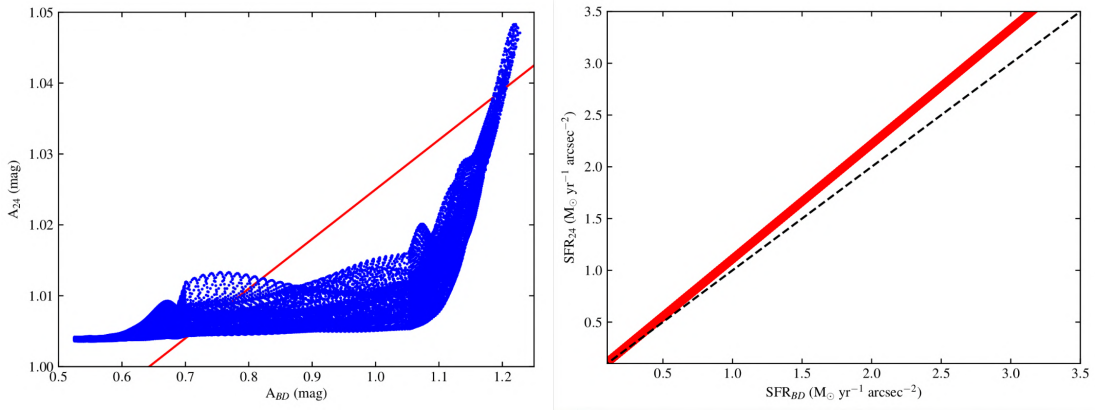

Figure 5.6 – Top panel: Comparison between $A_{BD}(r)$ and $A_{24}(r)$ dust attenuations; red line is the bisector regression. Bottom panel: SFRs of the galaxy NGC 4254, derived from Hα luminosities corrected by Balmer Decrement (X-axis) and by 24μm luminosities (Y-axis).

$$f_{NII}(r) = 1.33 \times f_{[NII]}(6584)\,(r). \tag{5.6}$$

Equally, since there is no way to correct dust attenuation at GMCs scales, we did a radial approximation A_λ(r) considering two different ways (Fig. 5.5):

a) The Balmer Decrement (BD) considering the same 9 HII regions from Shields et al. (1991) for which the BD $C(H\beta)$ coefficient is available:

$$A_{BD}(r) = 1.754 \times C(H\beta)\,(r), \tag{5.7}$$

b) The correction based on the 24μm flux. For this purpose, we took the WISE 22μm image and converted the luminosities per pixel to 24μm multiplying by a factor 1.22 (Ciesla et al., 2014) and then correcting the Hα luminosities per pixel as follows (Boselli et al., 2015):

$$log\ L(H\alpha)_{corr} = log\ L(H\alpha)_{obs} + 0.020 \times log\ L(24\mu m). \tag{5.8}$$

In Fig. 5.5 we can see that both radial dust attenuations $A_{24}(r)$ and $A_{BD}(r)$ are stronger close to the galaxy center and weaker at bigger radius. Nevertheless, $A_{24}(r) = 0.12 \times A_{BD}(r) + 0.92$ (Fig 5.6, left panel); the latter relation is expected since, in general, for integrated galaxy luminosities, $A_{24} < A_{BD}$ according toBoselli et al. (2015); indeed, their average A_{BD} value for the galaxy NGC 4254 is 1.09, while our $A_{24}(r)$ goes from $\sim$ 0.98 to $\sim$ 1.048. Finally, in order to see the impact of each radial dust attenuation factor on the SFR, we computed the SFR from the Hα image at GMCs

scales considering each A_λ(r) separately (Fig 5.6, right panel) and following the recipe:

$$SFR_{H\alpha}(M_\odot\ yr^{-1}) = K_{H\alpha} \times L(H\alpha)_{corr}(erg\ s^{-1}), \tag{5.9}$$

where $K_{H\alpha} = 8.79 \times 10^{-42}$ assuming an IMF of Salpeter (1955), obtaining a slope of:

$$SFR(H\alpha)_{24} = (1.09\pm\ 0.05) \times SFR(H\alpha)_{BD} + (0.01\pm0.01\ ). \tag{5.10}$$

That means that the radial dust attenuation $A_{24}(r)$ is ~9% stronger than $A_{BD}(r)$, in very good agreement with Boselli et al. (2015) for Hα integrated fluxes of the HRS.

We averaged both attenuation factors $A_{BD}(r)$ and $A_{24\mu m}(r)$ in order to consider a more accurate radial dust attenuation, before recalculating the SFR using Eq. 5.9 on the VESTIGE image.

5.2.1.2 SED-fitting

CIGALE code fits the SED of galaxies simultaneously from the UV to the FIR. It has been used with success on nearby galaxies ((Noll et al., 2009); Buat et al., 2011a, Boselli et al., 2016) and high redshift objects (Giovannoli et al., 2011; Buat et al., 2011b; Burgarella et al., 2011) bringing new constraints on the physical properties of galaxies and on the attenuation laws at play.

Briefly, CIGALE models the SED of galaxies by combining several old and young stellar populations based on Bruzual & Charlot (2003) or Maraston (2005), including nebular emission. The UV–optical domain is reddened by an attenuation law modified from the Calzetti et al. (1994, 2000) curve. This energy is re-emitted in the mid- and FIR which is fitted by the Dale & Helou (2002) templates. The absorption and the dust emission are constrained through an energy balance.

In order to study to the SED at GMCs scales on the galaxy NGC4254, we corrected the whole resolved imaging dataset, from FUV to FIR, by Galactic extinction using Eq. 5.5.

Processing all images to a similar Point Spread Function (PSF) is crucial to study the SED at GMCs scales without being affected by resolution effects. To retain as many resolution elements as possible while keeping strong constraints on the emission of the dust, we have convolved the GALEX, NGVS, Hα, S4G, WISE, and MIPS images to the PSF of the PACS 100μm resolution (~9") using the the large set of convolution kernels presented by Aniano et al. (2011).

To allow for a direct pixel-by-pixel comparison, all images need to be projected on the same grid. All images were then registered on the same reference frame making use of the *wregister* procedure in IRAF.

Once the multifrequency dataset degraded, to extract the physical parameters from

Table 5.1 – List of CIGALE parameters.

Parameter	Unit	Range
Metallicity	Z	0.02
Age of the old population	Gyr	13
Quenching age	Gyr	from 0.70 to 0.00
Quenching factor		from -1.00 to 1.00
Initial Mass Function		Salpeter (1955)
Slope modifying parameter δ		from -0.40 to 0.00
V–band attenuation of the young population	mag	from 0.05 to 1.50
Reduction of the attenuation for the old population	mag	from 0.25 to 0.75
IR power–law slope α (Dale & Helou, 2002)		from 1.00 to 4.00

the observations, we fitted the SED of each pixel using CIGALE.

We selected the input parameters given in Table 5.1 following the prescription of Boquien et al. (2013). Concerning the Star Formation History (SFH), we tested the delayed, two-exponential and Buat et al. (2008) SFHs, as well as a SFH derived from 2D chemo-spectrophotometric models of galaxy evolution (Boissier et al., 2003). We selected the last SFH because it matched the most to the Hα-derived SFR, as we will see in the next subsection.

5.2.1.3 Hα vs SED-fitting SFR

The very first test we must do is to compare the Σ_{SFR} derived from Hα to those coming from SED-fitting. For this purpose, since the Σ_{SFR} image derived from Hα is at high resolution (~0.6" or ~80 pc), we must degrade it to the resolution of the Σ_{SFR} image derived from SED-fitting which is ~9" or ~1 kpc.

Both Σ_{SFR} maps are presented in Fig. 5.7 (left and middle panels) at the PACS-100 angular resolution. Applying an OLS bisector fitting, we obtained (Fig. 5.8):

$$log\,\Sigma_{SFR}(H\alpha)\,(M_\odot\ yr^{-1}) = (0.96 \pm 0.11) \times log\,\Sigma_{SFR}(SED)\,(M_\odot\ yr^{-1}) + (-0.18 \pm 0.03), \quad (5.11)$$

with a intrinsic scatter of $\sigma = 0.18$, thus observing that both SFR values are equivalent, despite the technical and physical problems in both methods we had to deal with.

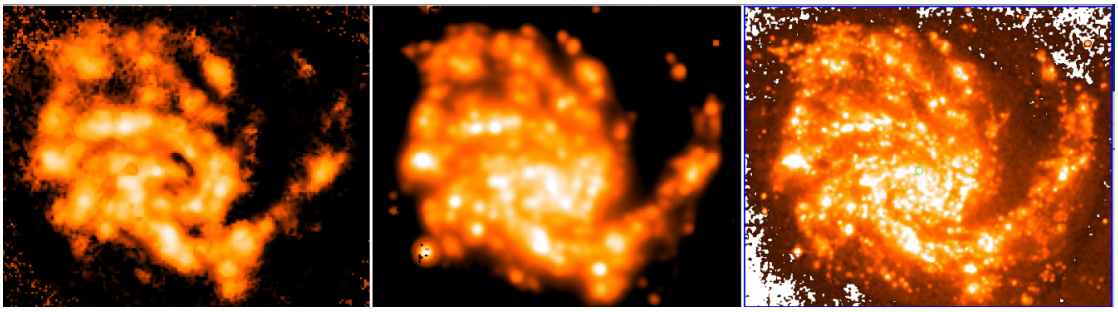

Figure 5.7 – SFR maps of the galaxy NGC4254. Left panel: SFR map at low resolution computed from SED-fitting. Middle panel: SFR map computed from the Hα image degraded to low resolution. Right panel: SFR map, computed from the Hα image, at the original high resolution.

5.2.2 Gas column density at GMCs scales

We may use both HI and H_2 to compute the gas content of a galaxy. Nevertheless, our aim is to compute such content at GMCs scales, thus the HI data angular resolution (~15") is insufficient. Since there is lack of correlation of the SFR with HI column density and a strong correlation with H_2 column density (Boselli et al., 2014c), we only used high resolution CO data to compute the gas column density and then trace the Kennicutt-Schmidt Law at GMCs scales.

The PHANGS collaboration (Leroy et al. 2018; Sun et al., 2018; Utomo et al., 2018, making use of the ALMA three configuration arrays (Main Array, ACA, and TP), mapped the cold gas of 74 nearby systems, gathering CO(2-1)@230GHz datacubes with an angular resolution ~1" and a spectral resolution ~ 5 km s^{-1}.

Unfortunately, the PHANGS collaboration informed us that the TP observations for the galaxy NGC 4254 are corrupted. However, we can recover the diffuse emission and well cover the UV Fourier space using the single dish observations carried out at IRAM-30m telescope for our galaxy.

During an internship in Grenoble in 2018, I learned from the IRAM's team how to combine the high resolution ALMA Main Array datacube with the low resolution IRAM-30m datacube (~12", Leroy et al., 2009) with a very small loss of angular resolution, using the Python/C++ based CASA and GILDAS softwares. Before merging both datacubes, the ALMA's presented poor CO emission distributed in thin filaments along the spiral arms; after merging the data, we recovered several emission across the galaxy (Fig. 5.9).

In order to convert the CO fluxes per pixel into H_2 gas column densities, we followed the prescription given in Boselli et al. (2014):

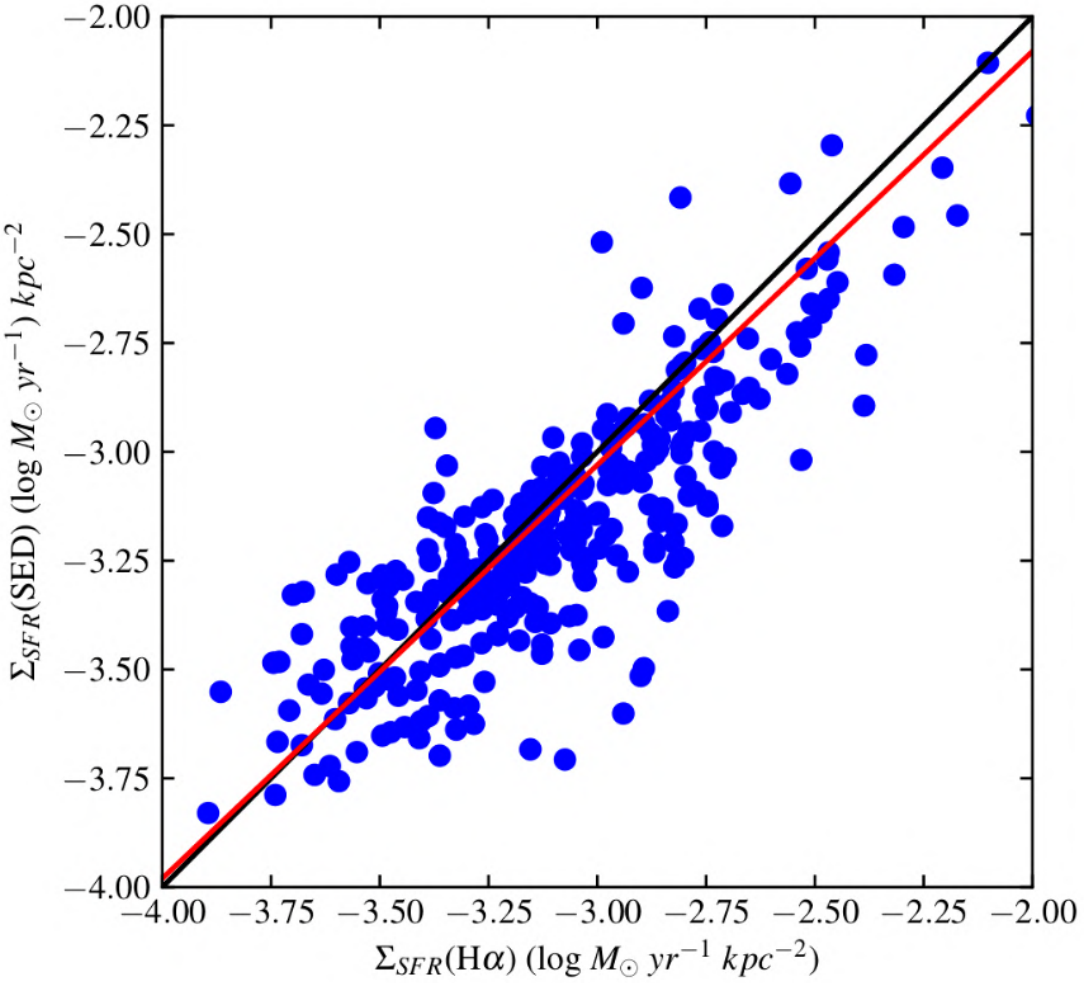

Figure 5.8 – Comparison between the ∼1-kpc SFRs for the galaxy NGC4254, computed at low resolution from Hα image and with SED-fitting. Black solid line represents the 1-1 relation, while red solid line represents the OLS bisector fit.

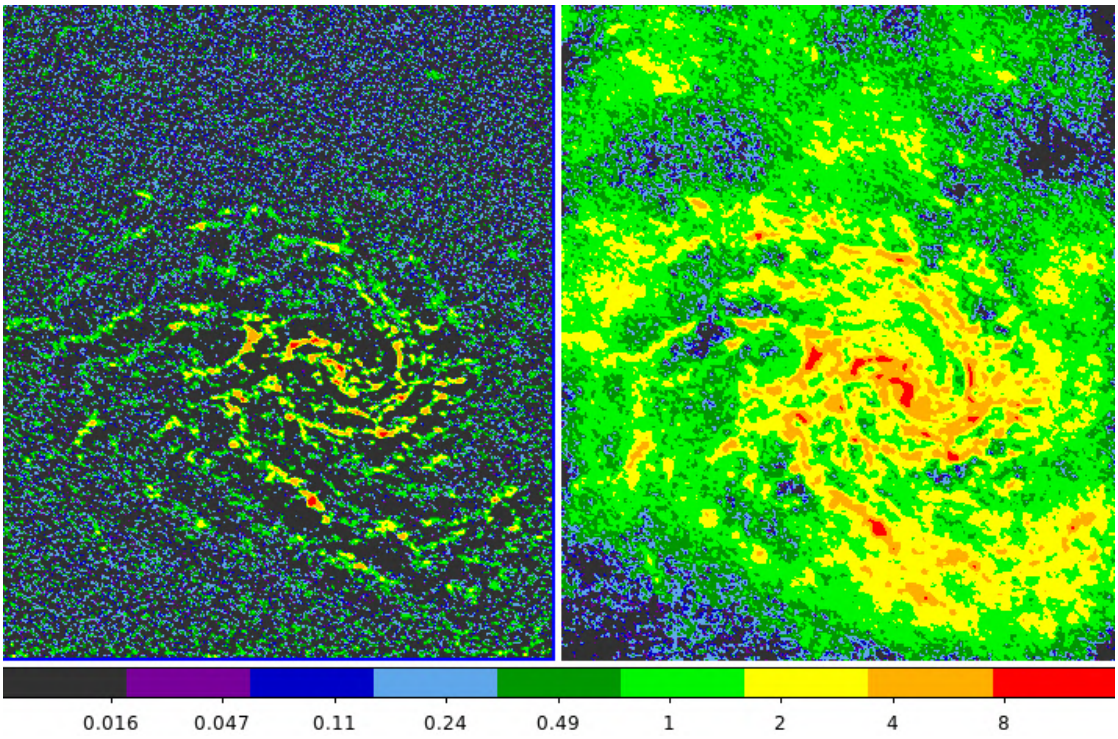

Figure 5.9 – Galaxy NGC 4254 in CO(2-1) emission. Left panel: ALMA-arr12m. Right panel: ALMA-arr12m + IRAM30m image. Recover the diffuse emission of the cold gas is important to well compute the gas column density among many other properties. Colorbar indicates units in log ($M_{\odot}$ kpc^{-2}).

$$M(H_2)(M_\odot) = 3.90 \times 10^{-17} \times X_{CO} \times f_{CO}(K\ km\ s^{-1}) \times D^2(Mpc), \tag{5.12}$$

where we used the metallicity dependent conversion factor X_{CO} prescribed in Boselli et al. (2002b), but in a radial way since we are working at GMCs scales:

$$log\ X_{CO}\,(r)\ (cm^{-2}/(K\ km\ s^{-1}) = 26.43 \pm 0.86 - 0.67 \pm 0.10 \times (12 + log\ O/H)(r). \tag{5.13}$$

taking the metallicity values from the same 9 HII regions used across this section taken from Shields et al. (1991).

5.2.3 Kennicutt-Schmidt Law at low and high resolution.

The Kennicutt-Schmidt Law at high resolution (ALMA+IRAM angular resolution data ~120 pc, top panel of Fig. 5.10), presents the next coefficients through an OLS bisector fit:

$$log\ \Sigma_{SFR,H\alpha} = (-2.62 \pm 0.37) \times log\ \Sigma_{H_2} + (0.90 \pm 0.15), \tag{5.14}$$

with an intrinsic scatter $\sigma = 0.08$ and a correlation coefficient $R^2 = 0.60$, while the Schmidt Law at low resolution (spatial resolution ~1 kpc, bottom panel of Fig. 5.10), for which we have much less points than the previous case, presents the next coefficients through an OLS bisector fit:

$$log\ \Sigma_{SFR,SED} = (-2.75 \pm 0.45) \times log\ \Sigma_{H_2} + (0.90 \pm 0.12), \tag{5.15}$$

with an intrinsic scatter $\sigma = 0.12$ and $R^2 = 0.72$, which is in agreement at 1σ with Bigiel et al. 2008.

The Kennicutt-Schmidt relationships found for the galaxy NGC 4254 are similar in both low (~1 kpc scales) and high (GMCs scales) angular resolution concerning slope and intercept, and 12% of the variance gives advantage to the fit at low angular resolution using SED-fitting (fit computed with much less number of points), meaning that angular resolution has not an important effect on this Law.

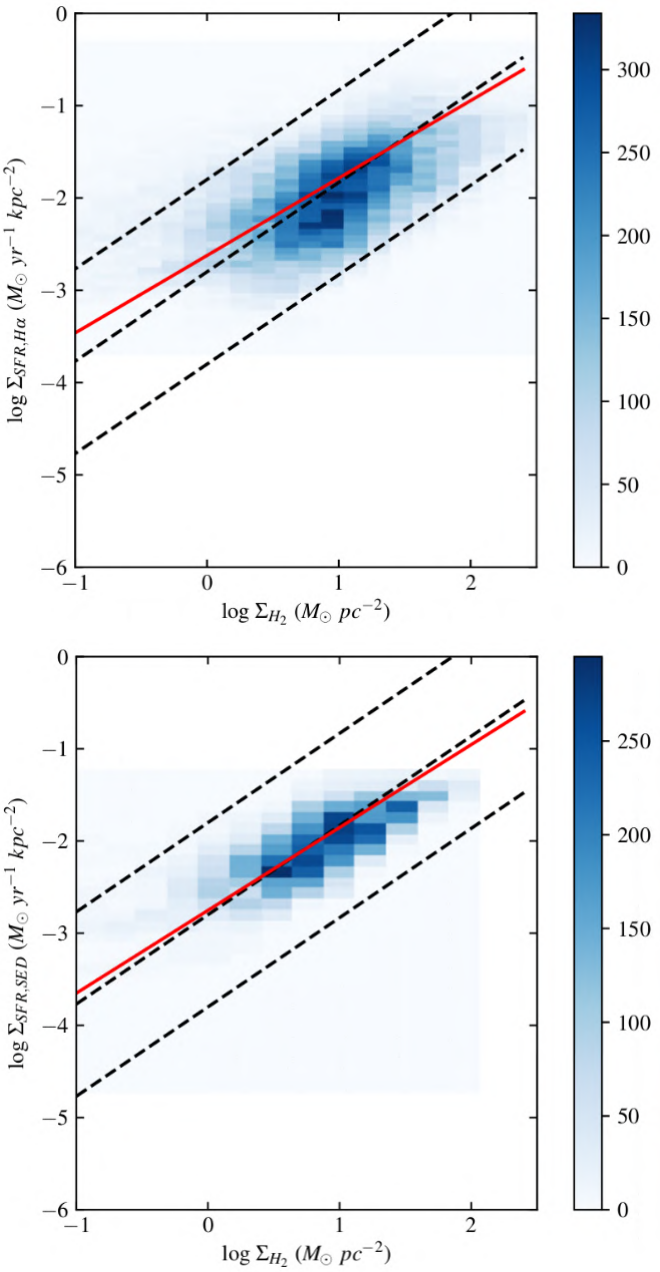

Figure 5.10 – Schmidt Law for the galaxy NGC4254. Top panel: high angular resolution, where Σ_{SFR} have been computed from Hα imaging. Bottom panel: low resolution, where Σ_{SFR} have been computed using SED-fitting. The red solid lines are the OLS bisector regressions, the dotted black lines indicate, from bottom to top, the SFE at 1 Myr, 10 Myr and 100 Myr. The scale bar indicates the number of pixels per bin.

5.3 Modified Kennicutt-Schmidt Law

5.3.1 Kinematics of the warm gas vs cold gas

As previously mentioned, the Hα emission line is ideal to trace the kinematics of gas, but actually it is well possible to trace kinematics using either warm (Hα) or cold gas (through CO emission line).

In order to see if the kinematics of warm and cold gas of the galaxy NGC 4254 are similar, we computed the moment 1 and 2 of the Hα and CO(2-1) datacubes using the IDL-based *compuveeverything* and *reducWizard* codes for consistency (Fig. 5.11), and then we compared each moment.

For the moment 1, there is an almost 1-1 relation between the rotation velocity of the warm and cold gas. An OLS bisector fit gave the following relation (Fig 5.12, top panel):

$$V_{rot_{H\alpha}} = (0.96 \pm 0.25) * V_{rot_{CO}} + (0.42 \pm 9.52), \tag{5.16}$$

with an intrinsic scatter $\sigma = 8$ km s^{-1}.

For the moment 2, an OLS bisector fit gave the following relation (Fig 5.12, bottom panel):

$$\sigma_{H\alpha} = (0.95 \pm 0.13) * \sigma_{CO} + (0.44 \pm 0.32), \tag{5.17}$$

with an intrinsic scatter $\sigma = 3$ km s^{-1}.

Since visual inspection is also a strong tool to test statistical relations, we compared in Fig. 5.13 some line profiles belonging to randomly selected pixels of Hα and CO datacubes, not observing an important difference between the velocity and σ of such profiles.

Now one can say that the moment 1 and 2 of the kinematics of the warm and cold gas for the galaxy NGC 4254 are equivalent. Since the Hα emission line is directly linked to star forming regions, hereafter we will use the kinematics traced with Hα Fabry-Perot observations (Fig. 5.14) for the following analyses.

5.3.2 Role of rotation velocity and velocity dispersion on the Kennicutt-Schmidt Law

For the Eq. 5.3, if we asume [1] that $\Omega = V_{rot} r^{-1}$, applying an OLS bisector fit, we obtained the relation (Fig. 5.15, top panel):

$$log\, \Sigma_{SFR} = (-2.45 \pm 0.39) \times log\, (\Sigma_{H_2}\, \Omega) + (0.66 \pm 0.33), \tag{5.18}$$

1. $V_{rot}(r)$ is measured according to the the modeled rotation curve.

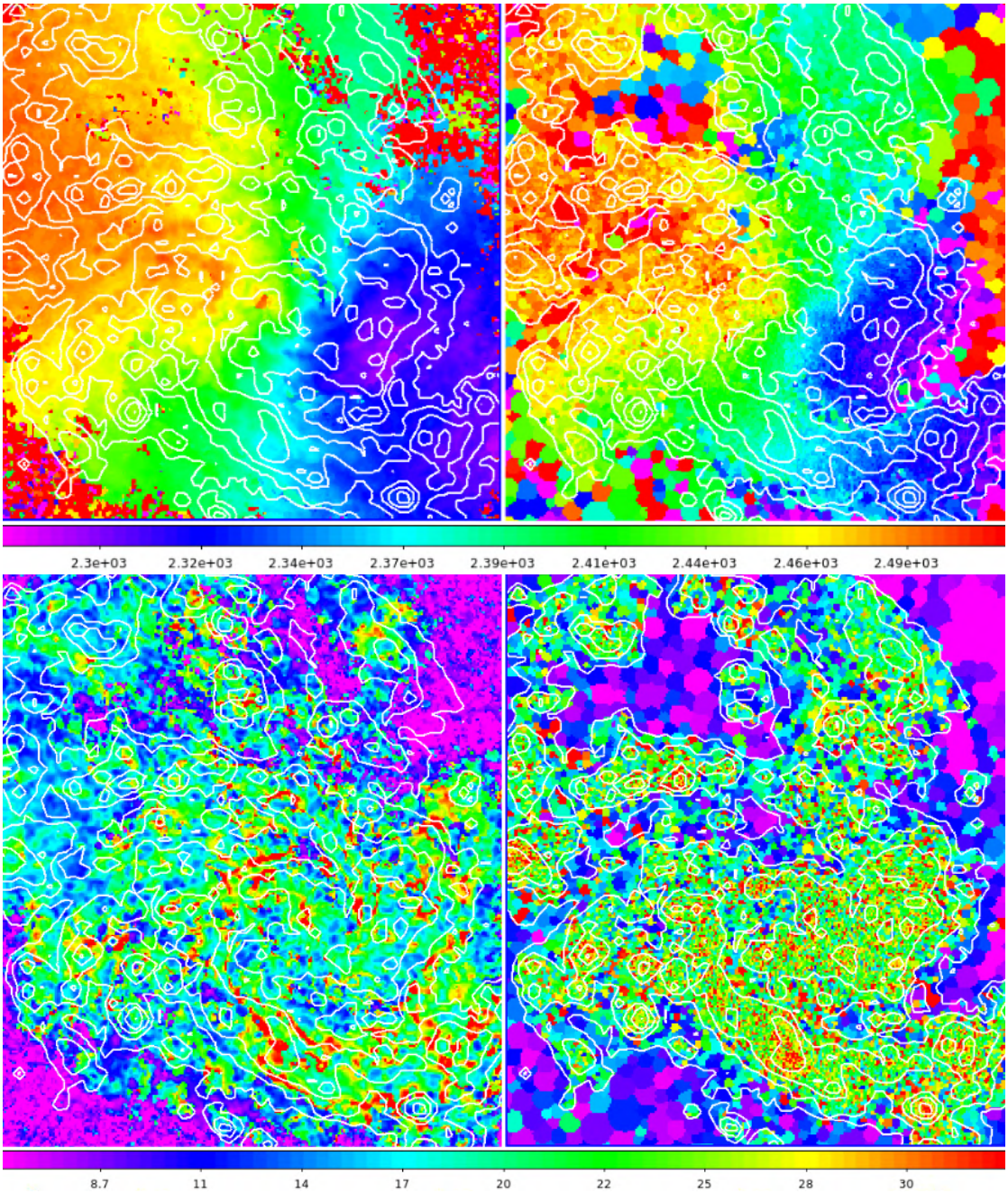

Figure 5.11 – Kinematical maps of CO (left panels) versus Hα (right panels) for the galaxy NGC 4254. Top panel: rotation velocity maps. Bottom panel: Velocity dispersion maps. The colorbar indicates the scale in km s^{-1}. Hα flux isophotes are pictured in white.

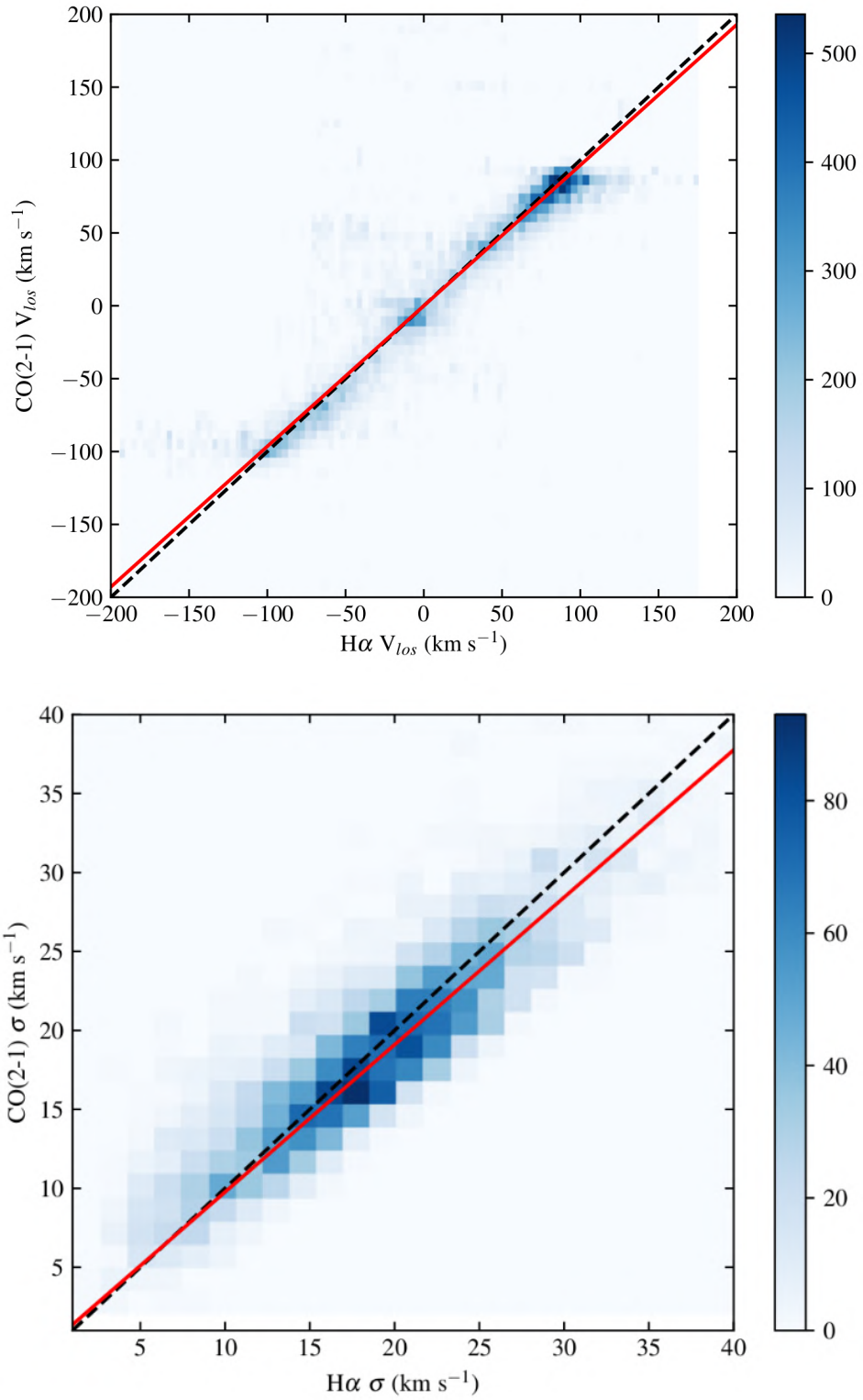

Figure 5.12 – Kinematics of CO versus Hα for the galaxy NGC 4254. Top panel: line-of-sight rotation velocity. Bottom panel: Velocity dispersion. The colorbar indicates number of pixels per bin. The red solid line is the OLS bisector fit.

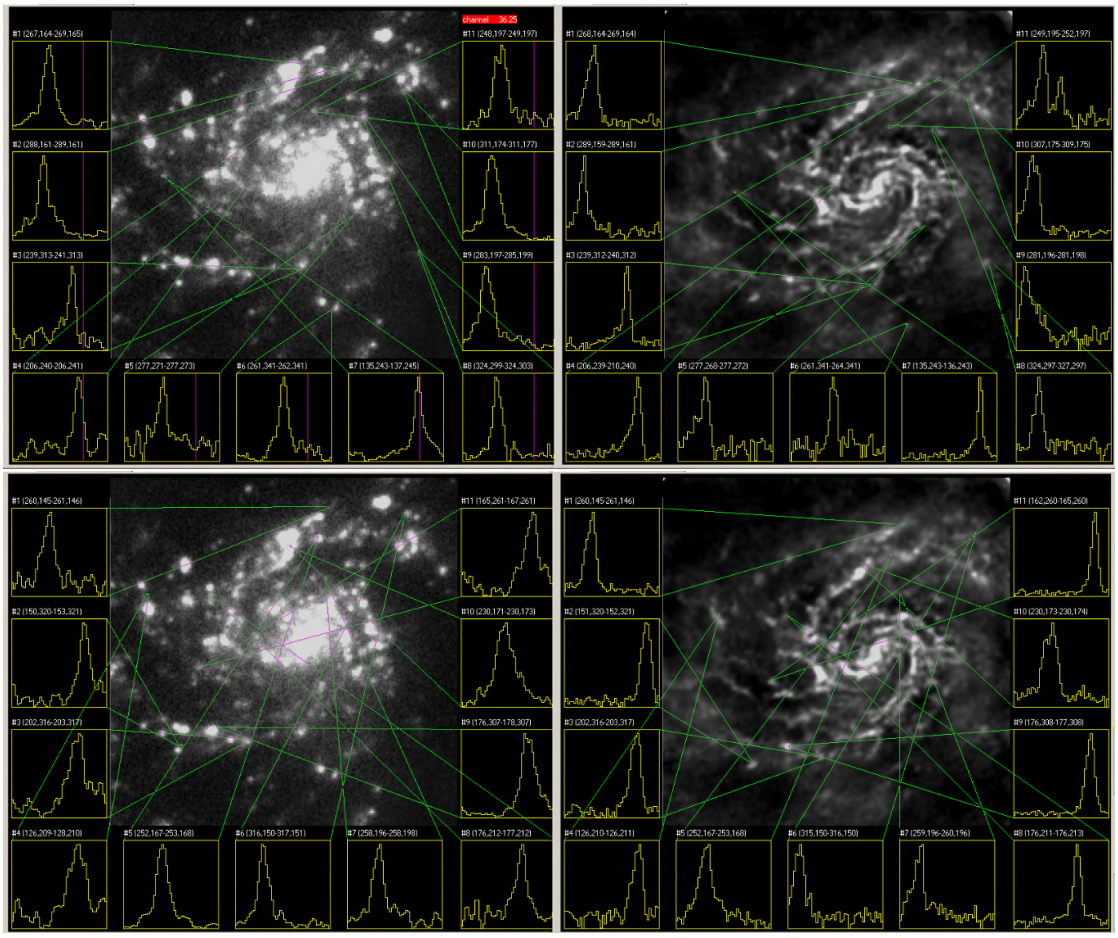

Figure 5.13 – Concerning the Eq. 5.17, we compared, for the Hα datacube (left panel) and the CO(2-1) datacube (right panel), line profiles of random pixels situated within 0.5σ limits (top panel) and outside the 2σ limits (bottom panel). We do not see a significant difference between Hα and CO profiles.

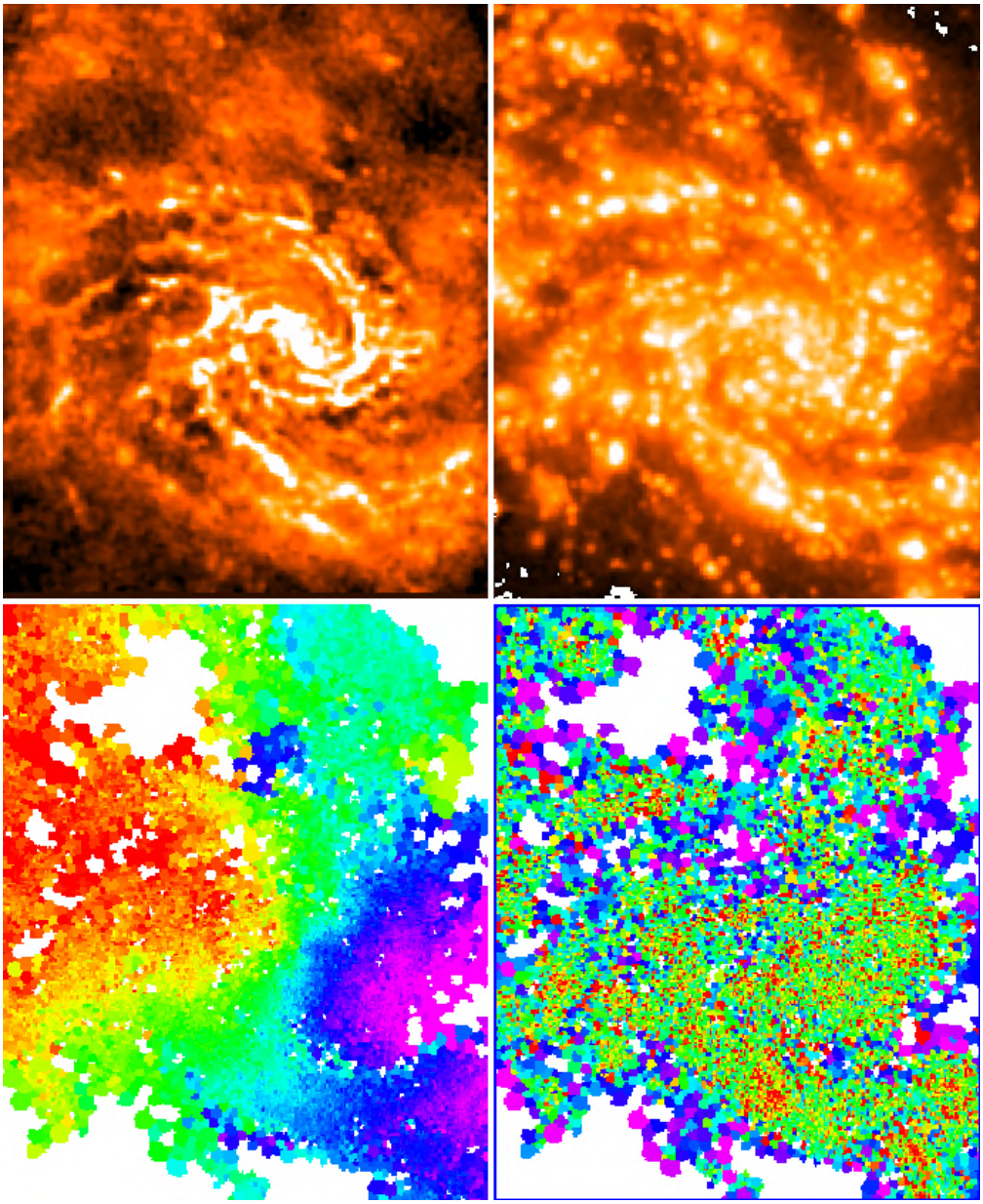

Figure 5.14 – The dataset convolved to the Fabry-Perot resolution (GMCs scales). Top left panel: molecular gas mass map computed from ALMA+IRAM CO(2-1) image. Top rigth panel: SFR map computed from VESTIGE Hα image. Bottom left panel: Fabry-Perot velocity map. Bottom right panel: Fabry-Perot velocity dispersion map.

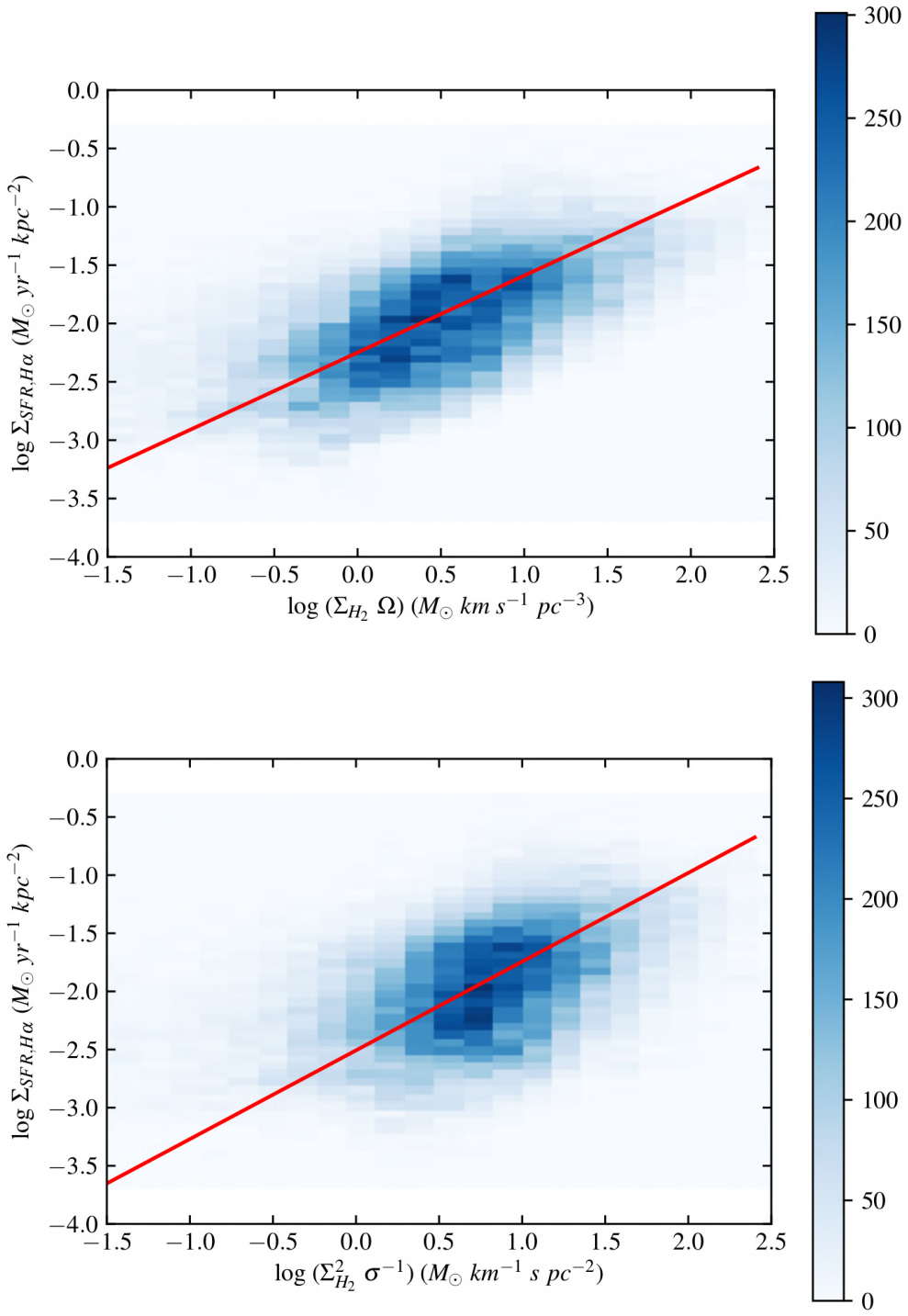

Figure 5.15 – Density plot of the Kennicutt-Schmidt law at GMC scales modulated by rotational velocity (top panel) and velocity dispersion (bottom panel) for the galaxy NGC4254. The colorbar indicates pixels per bin. Red solid lines are the OLS bisector fits.

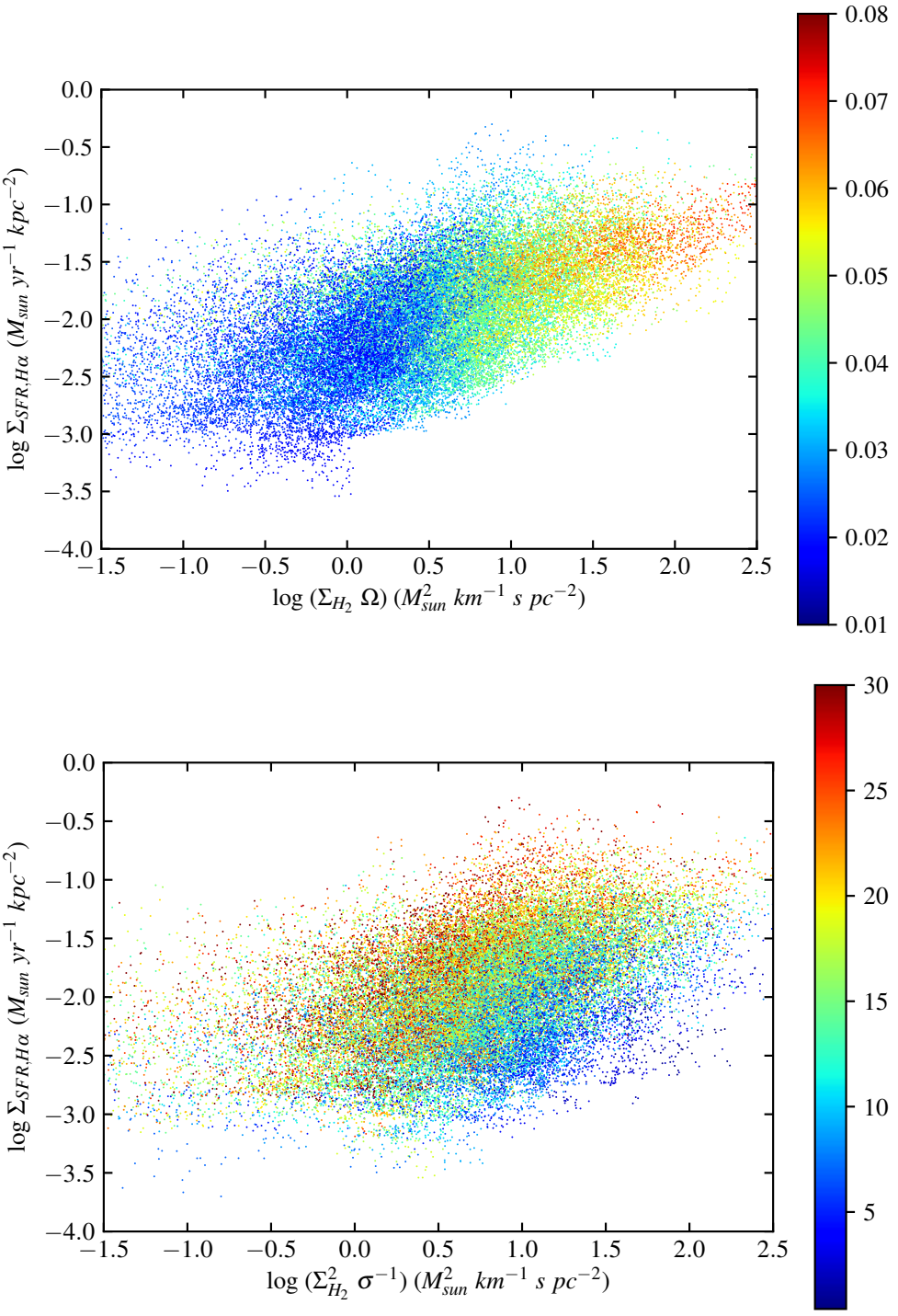

Figure 5.16 – Kennicutt-Schmidt law at GMC scales modulated by rotational velocity (top panel) and velocity dispersion (bottom panel) for the galaxy NGC4254. Each point represents a pixel. The colorbar indicates km s^{-1}.

with a intrinsic scatter $\sigma = 0.09$ and $R^2 = 0.61$, in good agreement with Kennicutt (1998b) who found $\Sigma_{SFR} = 0.017\,\Sigma_{gas}\,\Omega$, thus rotation velocity values must self-regulates star formation across the disc of NGC 4254. As discussed by Larson (1992) and Elmegreen (1994), a large-scale Schmidt law would be expected for self-gravitating discs assisted by Ω if the SFR scales as the ratio of the gas density (ρ_{gas}) to the free-fall time scale ($\propto \rho_{gas}^{-0.5}$) and the average gas scale height is roughly constant ($\Sigma_{gas} \propto \rho_{gas}$). Elmegreen (1997) and Silk (1997) have suggested that the SFR might scale with the ratio of the gas density to the average orbital time scale; this is equivalent to postulating that discs process a fixed fraction of their gas into stars in each orbit around the galactic center: τ is defined as one disc orbit time, measured at half of the outer radius of the star-forming disc, in units of years (see Kennicutt, 1998a for details).This means that:

a) when star formation occurs, it may dynamically heat the gaseous disc, what will also increase the Toomre parameter Q;

b) the disc may then become stable, and star formation stops;

c) the gas can then cool down and Q goes down, and the process starts again,

everything in a timescale to turn gas into stars $\tau = \kappa^{-1} \sim 50$ Myr: SFR does depend on the density of gas and the rotation velocity for the galaxy NGC 4254 (Fig 5.16; higher Ω reflects higher $\Sigma_{SFR,H\alpha}$).

For the Eq. 5.4, applying an OLS bisector fit, we obtained the following relation (Fig. 5.15, bottom panel):

$$log\,\Sigma_{SFR} = (-2.50 \pm 0.42) \times log\,(\Sigma^2_{H_2}/\sigma) + (0.76 \pm 0.37), \tag{5.19}$$

with a intrinsic scatter $\sigma = 0.06$ and $R^2 = 0.45$, indicating that for the galaxy NGC 4254, the local turbulences/instabilities have a clear correlation with the star formation process, in agreement with theoretical predictions (Krumholz et al., 2018: in the models, the gas is in vertical pressure and energy balance; star formation feedback injects energy and momentum, and non-axisymmetric torques prevent the gas from becoming more than marginally gravitationally unstable), meaning that either the star formation process heat the gas dinamically (via feedback and reflecting strong σ) or the local instabilities powered by gravity move and transport the molecular gas producing a $Q \sim 1$ and thus fueling star formation, both of them being possible at the same time and happening during certain $\tau = \sigma_{gas}/(\pi\,G\,\Sigma_{gas})$ (Larson, 1992). The lower value obtained for R^2 with respect to that obtained for Eq. 5.18 could be due, for instance, to the fact that we are considering squared Σ_{H_2} and dividing it by σ in this case, and if we consider $\Sigma^2_{H_2}/\sigma$ as a single dependent variable, that may bias the correlation but not meaning that such relationship is weak (not implying causality), because we see a clear correlation in

Fig. 5.15 (bottom panel) and Fig 5.16 (bottom panel: higher σ reflects higher $\Sigma_{SFR,H\alpha}$). On the other hand, this τ equivalence is only valid down to kpc scales because the gravitational aggregation proceeds on these scales according to Larson (1992): the time required to collect the molecular gas into large clouds and convert into stars is expected to be comparable to the growth time of the above instabilities, in other words, $10 < \tau < 50$ Myr.

6 Conclusions

The study of the universe is important to understand how it was formed and evolved until the current stage of matter distribution that is observed at our epoch. The objective of any realistic cosmological model is to propose a scenario which allows the prediction of the observations from CMB (z∼1100) to z∼0, reproducing the primordial cosmology and the observed evolution of the universe at different redshifts, from the homogeneous structure observed in the CMB to the current observed anisotropies and large scale structures across the local cosmic web.

Nearby galaxies represent the last scenario of the galaxy evolution that the cosmological and semi-analytical models must predict, and current observing facilities give us the opportunity to study and robustly constrain the statistical properties of galaxies situated in different environments in an extremely accurate and detailed way. On the other hand, nearby objects are spatially resolved enough to accurately study and understand the impact of the environment on the galaxy properties.

Galaxy evolution strongly depends on mass and environment, which affect the physical and kinematical properties of galaxies. A robust statistical study of these properties requires a well representative sample of galaxies, with a complete multi-wavelength spatially resolved dataset, from FUV to radio. However, in order to perform a complete study it is mandatory to obtain 2D high-resolution kinematic data, which is fundamental to understand the kinematic perturbations and determine its influence on physical properties such as star formation and gas content.

One of the main processes regulating galaxy evolution and the matter cycle in galaxies is the star formation. The Kennicutt-Schmidt Law relates the SFR with the gas column density in late-type galaxies. In addition, there are theoretical indications that the Kennicutt-Schmidt Law is modulated at large scales by the differential rotation of the disc and the compression of the gas in the density waves associated to spiral arms, while at smaller scales such relation is driven by non-circular motions through the instability of the gas in GMCs.

The Virgo cluster and the surrounding clouds are the ideal laboratory to study galaxy evolution, contaning systems situated in different environments. Located at a distance of 16.5 Mpc, Virgo is the closest concentration of galaxies to the Milky Way. Thanks to its proximity, all galaxies in Virgo and surrounding clouds, including those objects down to the dwarf population, can be easily resolved at different frequencies.

In this context, the *Herschel* Reference Survey (HRS), is a complete sample defined with the purpose of studying the relationship between the star formation process

and the different components of the interstellar medium (ISM), as well as the main drivers of galaxy formation and evolution. The HRS is a complete K-band-selected, volume-limited ($15 < D < 25$ Mpc) sample of 323 nearby galaxies spanning a wide range in morphological type (from E to Sd-Im-BC) and stellar mass ($10^8 < M_{star} < 10^{11}$ $M_\odot$), out of which 261 are star-forming late-type systems. It has been the target of pointed imaging and spectroscopic observations at several other wavelengths, from the UV to the radio centimetric. Thanks to its complete nature, the HRS is now becoming the reference for several nearby and high redshift studies of galaxies.

The HRS is perfectly suited to study the relation between star formation, gas column density and kinematics of galaxies. Since spatially resolved 2D spectroscopic observations lacked in order to trace the kinematics of the HRS, we constructed an Hα kinematic survey for the HRS star-forming sample.

During my PhD we have gathered and analysed Hα Fabry-Perot spectroscopic observations for the HRS at OHP and SPM observatories. This technique has a fundamental advantage: gathering high spatial (~1"-3" or GMC/HII regions scales) and spectral (R~10000 or 5-10 km/s) resolution observations using relatively small telescopes (diameter of ~2m). We have derived Hα datacubes from which, using improved data reduction pipelines, we computed the Hα momenta, optimizing the spatial resolution given a S/N ratio through an adaptive binning method based on Voronoi tessellations. We also derived accurate kinematical models and parameters, residual velocity maps, and rotation curves, obtaining the following results:

i) We derived the *i*- and the 3.6 μm-band Tully-Fisher relations and compared them to those obtained for larger samples in the literature. Despite the difference in the kinematic data (Fabry-Perot Hα rotation curve in this work vs. HI line width profiles or long slit optical spectra in the literature), in the dynamical range of the sample, and in the statistics, the different TF relations are very consistent, suggesting that the HRS can be taken as a representative sample of other larger samples for these scaling relations in the local universe.

ii) Thanks to its unique multifrequency coverage, we used this dataset to derive the baryonic TF relation and the relation between the baryonic mass and the dynamical mass of galaxies. The baryonic mass was for the first time measured using direct estimates of the stellar, atomic, molecular, dust and metal mass of galaxies. The intrinsic scatter in the baryonic TF relation is in agreement with the predictions of cosmological simulations. The baryonic component is dominated by the stellar mass in massive objects and by the total gas mass (HI and H_2) in low mass systems. The dust content is just a very small fraction (~0.2 %) of the total baryonic mass, while the contribution of metals is fairly constant at ~0.9%.

iii) We computed the baryonic and dynamical main sequence, finding relations with a similar slope and intrinsic scatter than the stellar mass main sequence.

By now, this is the first work presenting Hα high resolution spectroscopic data for the

HRS [1].

A detailed study of the relation between star formation, gas column density and kinematics of nearby galaxies requires to derive four properties of each galaxy of the sample:

a) The SFR density Σ_{SFR}, computed from Hα luminosities (~GMC scales) and by SED-fitting (~1 kpc scales).
b) The gas column density Σ_{CO} computed from CO data in our case (further details below).
c) rotation velocity V_{rot} and velocity dispersion σ from Fabry-Perot data.

Since the role of technical (spatial and spectral resolution) and physical problems (conversion factors, energy transfer, dust attenuation, etc.) had to be analysed and traited/corrected carefully in order to perform the most possible unbiased study, we analysed such technical and physical effects on the galaxy NGC 4254 (HRS 102) as follows:

i) We first verified whether the spatial resolution played an important role on the Kennicutt-Schmidt Law. We did not found an important difference, thus the best is to perform the study at GMCs scales in order to disentangle HII individual regions and their corresponding turbulences; such study at GMC scales is in agreement with the literature.

ii) Then we verified whether the kinematics of cold gas are comparable to the warm gas computed with Fabry-Perot techniques, since both emission data have enought spatial and spectral resolution to accurately trace the kinematics. The test was positive. Nevertheless, Hα is directly linked to HII star-forming regions, thus we continued our analyses using Hα Fabry-Perot data.

iii) We quantified the influence of kinematics on the Kennicutt-Schmidt Law, testing two different theoretical relations existing in the literature that involved V_{rot} (self-regulated star formation, where $\tau \propto \kappa^{-1}$) and σ (gravitation versus dispersion, where $\tau \propto \sigma^{-0.5}$). The intrinsic scatter and R^2 obtained respectively were: 0.09 and 0.61, 0.06 and 0.45. Kinematics do have a direct relation on the star formation process in late-type galaxies.

These results on NGC 4254 are preliminary, and this is an ongoing work to fully define the methodology to study the role of kinematics on the Kennicutt-Schmidt Law.

1. The HRS Fabry-Perot dataset will be made available to the community on the HRS dedicated database HeDAM (https://hedam.lam.fr/), and on the Fabry-Perot database (https://cesam.lam.fr/fabryperot) in fall 2019.

7 Perspectives

The high resolution kinematical data for the HRS star-forming sample is ready. A further kinematical analysis of the whole HRS could be done:

1) Mass distribution in field and dense environments. The mass determination of a galaxy has always been a complicated issue. The use of rotation curves to determine the dynamical mass is now widely accepted in HI and optical domains. On the other hand, Current CDM simulations tend to create too compact structures with many dwarf galaxies halos and a dark halo density profile too steep. Even if the dark matter halo is difficult to estimate due to its unknown nature, the stellar mass is not as straightforward estimative. Therefore, rotation curves derived from 2D velocity fields and near IR photometry could be used to determine the dark matter and stellar disk contribution in a sample of galaxies located in dense and field environments. It is worth to perform a similar analysis as the developed by Spano et al. (2008). This analysis will significantly improve our understanding of mass distribution in HRS galaxies located in different environments.

2) A detailed study of the non-circular motions. Circular motions should dominate the kinematics of an isolated galaxy. However, in practice, streaming and non-circular motions are typically found in external galaxies, and these motions should provide useful information regarding some structural parameters of the galaxies. Additionally, these non-circular motions can provide clues regarding past galaxy-galaxy interactions. In this context, previous authors have studied the link that exists between structural parameters and non-circular motions. Therefore, there is an unique opportunity to determine the influence of the environment and from the morphological components in the kinematic of galaxies, by analyzing the non-circular motions which can be derived from the residual velocity fields. This information is already available for the HRS sample. We note that the spectral resolution allow us to detect differences in velocities of the order of 10 km/s (in the residual maps), which is much better than other surveys. We will determine the influence of the environment in the formation of non circular-motions.

3) The data allow to qualify the dynamical support and quantify the angular momentum of the HRS galaxies, and also explore the possibility to fit an Universal Rotation Curve for the HRS.

On the other hand, once ended the analyses on the galaxy NGC 4254 (and a well defined methodology as well) to study the influence of kinematics on the Kennicutt-Schmidt Law is defined, we will publish the results, and:

1) The PHANGS collaboration will release high resolution (∼1") CO(2-1) data for dozens of Virgo cluster objects during 2019, providing the HRS with resolved H_2 data for dozens of cluster galaxies. This will allow us to extend our study to a larger sample of galaxies situated in different environments, where GMCs scale regions can be resolved, so that the star formation process can be studied at small scales. Using the CO emission, we will estimate the H_2 mass for the different star-forming regions present in these systems and we will determine their position in the Kennicutt-Schmidt plane, so we can quantify the role of kinematics at GMCs scales and in a statistical way. Here, the Fabry-Perot kinematic information will be extremely useful to determine if non-circular motions triggered by the galaxy-galaxy interactions play a significant role in the star formation processes.

2) We must increase the CO dataset available for the HRS in order to extend the analysis to the largest possible sample of galaxies. We will submit observing proposals both for ALMA and for NOEMA array + IRAM-30m telescopes during 2020, in order to well cover the UV-space, recover the diffuse emission and preserving high angular resolution at the same time. If these observing proposals are successful, that means we will gather CO(2-1) complementary data.

Bibliography

Abazajian, K. N., Adelman-McCarthy, J. K., Agüeros, M. A., et al. 2009, APJS, 182, 543

Amram, P. 1991, Etude cinematique du gaz ionise dans les galaxies spirales. Importance de l'environment: galaxies binaires et galaxies d'amas

Amram, P. & Georgelin, Y. 2000, Physica Scripta Volume T, 86, 76

Aniano, G., Draine, B. T., Gordon, K. D., & Sandstrom, K. 2011, PASP, 123, 1218

Atherton, P. D., Taylor, K., Pike, C. D., et al. 1982, MNRAS, 201, 661

Bacon, R., Conseil, S., Mary, D., et al. 2017, AAP, 608, A1

Bendo, G. J., Galliano, F., & Madden, S. C. 2012, MNRAS, 423, 197

Bigiel, F., Leroy, A., Walter, F., et al. 2010, AJ, 140, 1194

Bigiel, F., Leroy, A., Walter, F., et al. 2008, AJ, 136, 2846

Bigiel, F., Leroy, A. K., Walter, F., et al. 2011, APJL, 730, L13

Blanc, G. A., Heiderman, A., Gebhardt, K., Evans, II, N. J., & Adams, J. 2009, APJ, 704, 842

Bland, J., Taylor, K., & Atherton, P. D. 1987, MNRAS, 228, 595

Bland, J. & Tully, R. B. 1989, AJ, 98, 723

Boissier, S. 2013, Star Formation in Galaxies, ed. T. D. Oswalt & W. C. Keel, 141

Boissier, S. & Prantzos, N. 1999, MNRAS, 307, 857

Boissier, S., Prantzos, N., Boselli, A., & Gavazzi, G. 2003, MNRAS, 346, 1215

Boquien, M., Boselli, A., Buat, V., et al. 2013, AAP, 554, A14

Boquien, M., Buat, V., & Perret, V. 2014, AAP, 571, A72

Boselli, A. 2011, A Panchromatic View of Galaxies

Boselli, A., Boissier, S., Cortese, L., et al. 2009, APJ, 706, 1527

Boselli, A., Boissier, S., Heinis, S., et al. 2011, AAP, 528, A107

Boselli, A., Ciesla, L., Cortese, L., et al. 2012, AAP, 540, A54

Boselli, A., Cortese, L., & Boquien, M. 2014a, AAP, 564, A65

Boselli, A., Cortese, L., Boquien, M., et al. 2014b, AAP, 564, A67

Boselli, A., Cortese, L., Boquien, M., et al. 2014c, AAP, 564, A66

Boselli, A., Eales, S., Cortese, L., et al. 2010, PASP, 122, 261

Boselli, A., Fossati, M., Consolandi, G., et al. 2018a, AAP, 620, A164

Boselli, A., Fossati, M., Cuillandre, J. C., et al. 2018b, AAP, 615, A114

Boselli, A., Fossati, M., Ferrarese, L., et al. 2018c, AAP, 614, A56

Boselli, A., Fossati, M., Ferrarese, L., et al. 2018d, AAP, 614, A56

Boselli, A., Fossati, M., Gavazzi, G., et al. 2015, AAP, 579, A102

Boselli, A. & Gavazzi, G. 2006, PASP, 118, 517

Boselli, A. & Gavazzi, G. 2014, A&A, 22, 74

Boselli, A., Gavazzi, G., Donas, J., & Scodeggio, M. 2001, AJ, 121, 753

Boselli, A., Hughes, T. M., Cortese, L., Gavazzi, G., & Buat, V. 2013, AAP, 550, A114

Boselli, A., Iglesias-Páramo, J., Vílchez, J. M., & Gavazzi, G. 2002a, AAP, 386, 134

Boselli, A., Lequeux, J., & Gavazzi, G. 2002b, AAP, 384, 33

Boselli, A., Roehlly, Y., Fossati, M., et al. 2016, AAP, 596, A11

Boulesteix, J., Georgelin, Y., Marcelin, M., & Monnet, G. 1984, in , Vol. 445, Instrumentation in astronomy V, ed. A. Boksenberg & D. L. Crawford, 37–41

Boulesteix, J., Georgelin, Y. P., Lecoarer, E., Marcelin, M., & Monnet, G. 1987, AAP, 178, 91

Brooks, A. M. & Zolotov, A. 2014, APJ, 786, 87

Bruzual, G. & Charlot, S. 1993, APJ, 405, 538

Bruzual, G. & Charlot, S. 2003, MNRAS, 344, 1000

Bryant, J. J., Owers, M. S., Robotham, A. S. G., et al. 2015, MNRAS, 447, 2857

Buat, V., Boissier, S., Burgarella, D., et al. 2008, AAP, 483, 107

Buat, V., Giovannoli, E., Heinis, S., et al. 2011a, AAP, 533, A93

Buat, V., Giovannoli, E., Takeuchi, T. T., et al. 2011b, AAP, 529, A22

Buisson, H., Fabry, C., & Bourget, H. 1914, APJ, 40

Bundy, K., Bershady, M. A., Law, D. R., et al. 2015, APJ, 798, 7

Burgarella, D., Heinis, S., Magdis, G., et al. 2011, APJL, 734, L12

Calzetti, D., Armus, L., Bohlin, R. C., et al. 2000, APJ, 533, 682

Calzetti, D., Kinney, A. L., & Storchi-Bergmann, T. 1994, APJ, 429, 582

Chemin, L., Balkowski, C., Cayatte, V., et al. 2006, MNRAS, 366, 812

Christensen, C. R., Governato, F., Quinn, T., et al. 2014, MNRAS, 440, 2843

Chung, A., van Gorkom, J. H., Kenney, J. D. P., Crowl, H., & Vollmer, B. 2009, AJ, 138, 1741

Ciesla, L., Boquien, M., Boselli, A., et al. 2014, AAP, 565, A128

Ciesla, L., Boselli, A., Smith, M. W. L., et al. 2012, AAP, 543, A161

Cole, S., Norberg, P., Baugh, C. M., et al. 2001, MNRAS, 326, 255

Condon, J. J., Cotton, W. D., Greisen, E. W., et al. 1998, AJ, 115, 1693

Cortese, L., Boissier, S., Boselli, A., et al. 2012, AAP, 544, A101

Cortese, L., Fritz, J., Bianchi, S., et al. 2014, MNRAS, 440, 942

Courtès, G. 1972, Vistas in Astronomy, 14, 81

Cowie, L. L., Songaila, A., Hu, E. M., & Cohen, J. G. 1996, AJ, 112, 839

Crosthwaite, L. P. & Turner, J. L. 2007, AJ, 134, 1827

Daigle, O., Carignan, C., Amram, P., et al. 2006a, MNRAS, 367, 469

Daigle, O., Carignan, C., Hernandez, O., Chemin, L., & Amram, P. 2006b, MNRAS, 368, 1016

Dale, D. A., Cohen, S. A., Johnson, L. C., et al. 2009, APJ, 703, 517

Dale, D. A. & Helou, G. 2002, APJ, 576, 159

Dressler, A. 1980, APJ, 236, 351

Drissen, L., Martin, T., Rousseau-Nepton, L., et al. 2019, MNRAS, 485, 3930

Eales, S. A., Raymond, G., Roseboom, I. G., et al. 2010, AAP, 518, L23

Elmegreen, B. G. 1994, APJL, 425, L73

Elmegreen, B. G. 1997, APJ, 486, 944

Epinat, B., Amram, P., & Marcelin, M. 2008a, MNRAS, 390, 466

Epinat, B., Amram, P., Marcelin, M., et al. 2008b, MNRAS, 388, 500

Fazio, G. G., Hora, J. L., Allen, L. E., et al. 2004, APJS, 154, 10

Ferrarese, L., Côté, P., Cuillandre, J.-C., et al. 2012, APJS, 200, 4

Fitzpatrick, E. L. & Massa, D. 2007, APJ, 663, 320

Fowles, G. 1989, Introduction to Modern Optics, Dover Books on Physics Series (Dover Publications)

Freeman, K. C. 1970, APJ, 160, 811

Fuentes-Carrera, I., Rosado, M., & Amram, P. 2003, in Revista Mexicana de Astronomia y Astrofisica Conference Series, Vol. 17, Revista Mexicana de Astronomia y Astrofisica Conference Series, ed. V. Avila-Reese, C. Firmani, C. S. Frenk, & C. Allen, 44–44

Fuentes-Carrera, I., Rosado, M., Amram, P., et al. 2001, in Revista Mexicana de Astronomia y Astrofisica Conference Series, Vol. 10, Revista Mexicana de Astronomia y Astrofisica Conference Series, ed. J. Cantó & L. F. Rodríguez, 134–137

Fumagalli, M., Fossati, M., Hau, G. K. T., et al. 2014, MNRAS, 445, 4335

Gach, J.-L., Hernandez, O., Boulesteix, J., et al. 2002, PASP, 114, 1043

Garrido, O., Marcelin, M., Amram, P., et al. 2005, MNRAS, 362, 127

Garrido, O., Marcelin, M., Amram, P., & Boissin, O. 2003, AAP, 399, 51

Gavazzi, G., Bonfanti, C., Sanvito, G., Boselli, A., & Scodeggio, M. 2002, APJ, 576, 135

Gavazzi, G., Boselli, A., Cortese, L., et al. 2006, AAP, 446, 839

Gavazzi, G., Boselli, A., Scodeggio, M., Pierini, D., & Belsole, E. 1999, MNRAS, 304, 595

Gavazzi, G., Consolandi, G., Belladitta, S., Boselli, A., & Fossati, M. 2018, AAP, 615, A104

Gavazzi, G., Pierini, D., & Boselli, A. 1996, AAP, 312, 397

Georgelin, Y. M., Boulesteix, J., Georgelin, Y. P., Laval, A., & Marcelin, M. 1987, AAP, 174, 257

Giavalisco, M., Ferguson, H. C., Koekemoer, A. M., et al. 2004, APJL, 600, L93

Gil de Paz, A., Boissier, S., Madore, B. F., et al. 2007, APJS, 173, 185

Giovannoli, E., Buat, V., Noll, S., Burgarella, D., & Magnelli, B. 2011, AAP, 525, A150

Governato, F., Zolotov, A., Pontzen, A., et al. 2012, MNRAS, 422, 1231

Haynes, M. P. & Giovanelli, R. 1984, AJ, 89, 758

Haynes, M. P., Giovanelli, R., & Kent, B. R. 2007, APJL, 665, L19

Helfer, T. T., Thornley, M. D., Regan, M. W., et al. 2003, APJS, 145, 259

Hicks, T. R., Reay, N. K., & Stephens, C. L. 1976, AAP, 51, 367

Hubble, E. P. 1936, Realm of the Nebulae

Hughes, T. M., Cortese, L., Boselli, A., Gavazzi, G., & Davies, J. I. 2013, AAP, 550, A115

Hunter, D. 1997, PASP, 109, 937

Jarosik, N., Bennett, C. L., Dunkley, J., et al. 2011, APJS, 192, 14

Jarrett, T. H., Chester, T., Cutri, R., Schneider, S. E., & Huchra, J. P. 2003, AJ, 125, 525

Kennicutt, R. C., Calzetti, D., Aniano, G., et al. 2011, PASP, 123, 1347

Kennicutt, R. C. & Evans, N. J. 2012, ARAA, 50, 531

Kennicutt, Jr., R. C. 1989, APJ, 344, 685

Kennicutt, Jr., R. C. 1998a, ARAA, 36, 189

Kennicutt, Jr., R. C. 1998b, APJ, 498, 541

Kennicutt, Jr., R. C., Armus, L., Bendo, G., et al. 2003, PASP, 115, 928

Kennicutt, Jr., R. C., Calzetti, D., Walter, F., et al. 2007, APJ, 671, 333

Kewley, L. J. & Ellison, S. L. 2008, APJ, 681, 1183

Kochanek, C. S., Pahre, M. A., Falco, E. E., et al. 2001, APJ, 560, 566

Krumholz, M. R., Burkhart, B., Forbes, J. C., & Crocker, R. M. 2018, MNRAS, 477, 2716

Kuno, N., Sato, N., Nakanishi, H., et al. 2007, PASJ, 59, 117

Larson, R. 1992, in Star Formation in Stellar Systems, ed. G. Tenorio-Tagle, M. Prieto, & F. Sanchez, 125

Laval, A., Boulesteix, J., Georgelin, Y. P., Georgelin, Y. M., & Marcelin, M. 1987, AAP, 175, 199

Le Coarer, E., Amram, P., Boulesteix, J., et al. 1992, AAP, 257, 389

Lee, J. C., Gil de Paz, A., Kennicutt, Jr., R. C., et al. 2011, APJS, 192, 6

Lequeux, J. 2005, The Interstellar Medium

Leroy, A. K., Bolatto, A., Gordon, K., et al. 2011, APJ, 737, 12

Leroy, A. K., Walter, F., Bigiel, F., et al. 2009, AJ, 137, 4670

Leroy, A. K., Walter, F., Brinks, E., et al. 2008, AJ, 136, 2782

Liller, M. H. 1966, APJ, 146, 28

Maraston, C. 2005, MNRAS, 362, 799

Marcelin, M., Lecoarer, E., Boulesteix, J., Georgelin, Y., & Monnet, G. 1987, AAP, 179, 101

Marino, A., Plana, H., Rampazzo, R., et al. 2013, MNRAS, 428, 476

Mei, S., Blakeslee, J. P., Côté, P., et al. 2007, APJ, 655, 144

Minchin, R., Davies, J., Disney, M., et al. 2005, APJL, 622, L21

Moshir, M. & et al. 1990, in IRAS Faint Source Catalogue, version 2.0 (1990)

Neugebauer, G., Habing, H. J., van Duinen, R., et al. 1984, APJL, 278, L1

Noll, S., Burgarella, D., Giovannoli, E., et al. 2009, AAP, 507, 1793

Perlmutter, S. 1999, in Lepton and Photon Interactions at High Energies, ed. J. A. Janos & M. E. Peskin, 715

Plana, H. 1996, Etude du gaz ionise dans les galaxies elliptiques avec un Perot-Fabry a balayage

Planck Collaboration, Ade, P. A. R., Aghanim, N., et al. 2016, AAP, 594, A13

Press, W. H., Teukolsky, S. A., Vetterling, W. T., & Flannery, B. P. 1992, Numerical Recipes in C: The Art of Scientific Computing. Second Edition

Rahman, N., Bolatto, A. D., Wong, T., et al. 2011, APJ, 730, 72

Rahman, N., Bolatto, A. D., Xue, R., et al. 2012, APJ, 745, 183

Riess, A. G., Filippenko, A. V., Challis, P., et al. 1998, AJ, 116, 1009

Rosado, M., Langarica, R., Bernal, A., et al. 1995, in Revista Mexicana de Astronomia y Astrofisica, vol. 27, Vol. 3, Revista Mexicana de Astronomia y Astrofisica Conference Series, ed. M. Pena & S. Kurtz, 263

Russeil, D. 1998, PhD thesis, , Univ. Provence, (1998)

Russeil, D., Adami, C., Amram, P., et al. 2005, AAP, 429, 497

Salpeter, E. E. 1955, APJ, 121, 161

Sánchez, S. F., Kennicutt, R. C., Gil de Paz, A., et al. 2012, AAP, 538, A8

Sanders, D. B., Mazzarella, J. M., Kim, D.-C., Surace, J. A., & Soifer, B. T. 2003, AJ, 126, 1607

Sauvage, M. & Thuan, T. X. 1994, APJ, 429, 153

Schaye, J., Crain, R. A., Bower, R. G., et al. 2015, MNRAS, 446, 521

Schlegel, D. J., Finkbeiner, D. P., & Davis, M. 1998, APJ, 500, 525

Schmidt, M. 1959, APJ, 129, 243

Schruba, A., Leroy, A. K., Walter, F., et al. 2011, AJ, 142, 37

Schuster, K. F., Kramer, C., Hitschfeld, M., Garcia-Burillo, S., & Mookerjea, B. 2007, AAP, 461, 143

Scoville, N., Aussel, H., Brusa, M., et al. 2007, APJS, 172, 1

Sheth, K., Regan, M., Hinz, J. L., et al. 2010, PASP, 122, 1397

Shields, G. A., Skillman, E. D., & Kennicutt, Jr., R. C. 1991, APJ, 371, 82

Silk, J. 1997, APJ, 481, 703

Skrutskie, M. F., Cutri, R. M., Stiening, R., et al. 2006, AJ, 131, 1163

Soifer, B. T., Boehmer, L., Neugebauer, G., & Sanders, D. B. 1989, AJ, 98, 766

Spano, M., Marcelin, M., Amram, P., et al. 2008, MNRAS, 383, 297

Sun, J., Leroy, A. K., Schruba, A., et al. 2018, APJ, 860, 172

Tan, J. C. 2000, APJ, 536, 173

Thuan, T. X. & Sauvage, M. 1992, AAPS, 92, 749

Tully, R. B. 1988, Nearby galaxies catalog

Tully, R. B. & Fisher, J. R. 1977, AAP, 54, 661

Utomo, D., Sun, J., Leroy, A. K., et al. 2018, APJL, 861, L18

Verley, S., Corbelli, E., Giovanardi, C., & Hunt, L. K. 2010, AAP, 510, A64

Whitmore, B. C., Gilmore, D. M., & Jones, C. 1993, APJ, 407, 489

Wilson, C. D. 1995, APJL, 448, L97

Wong, T. & Blitz, L. 2002, APJ, 569, 157

Wright, E. L., Eisenhardt, P. R. M., Mainzer, A. K., et al. 2010, AJ, 140, 1868

Wyder, T. K., Martin, D. C., Barlow, T. A., et al. 2009, APJ, 696, 1834

Wyse, R. F. G. 1986, APJL, 311, L41

Young, J. S., Allen, L., Kenney, J. D. P., Lesser, A., & Rownd, B. 1996, AJ, 112, 1903

Young, L. M., Bureau, M., Davis, T. A., et al. 2011, MNRAS, 414, 940

Appendix

Figure D of Paper I: 152 Plots

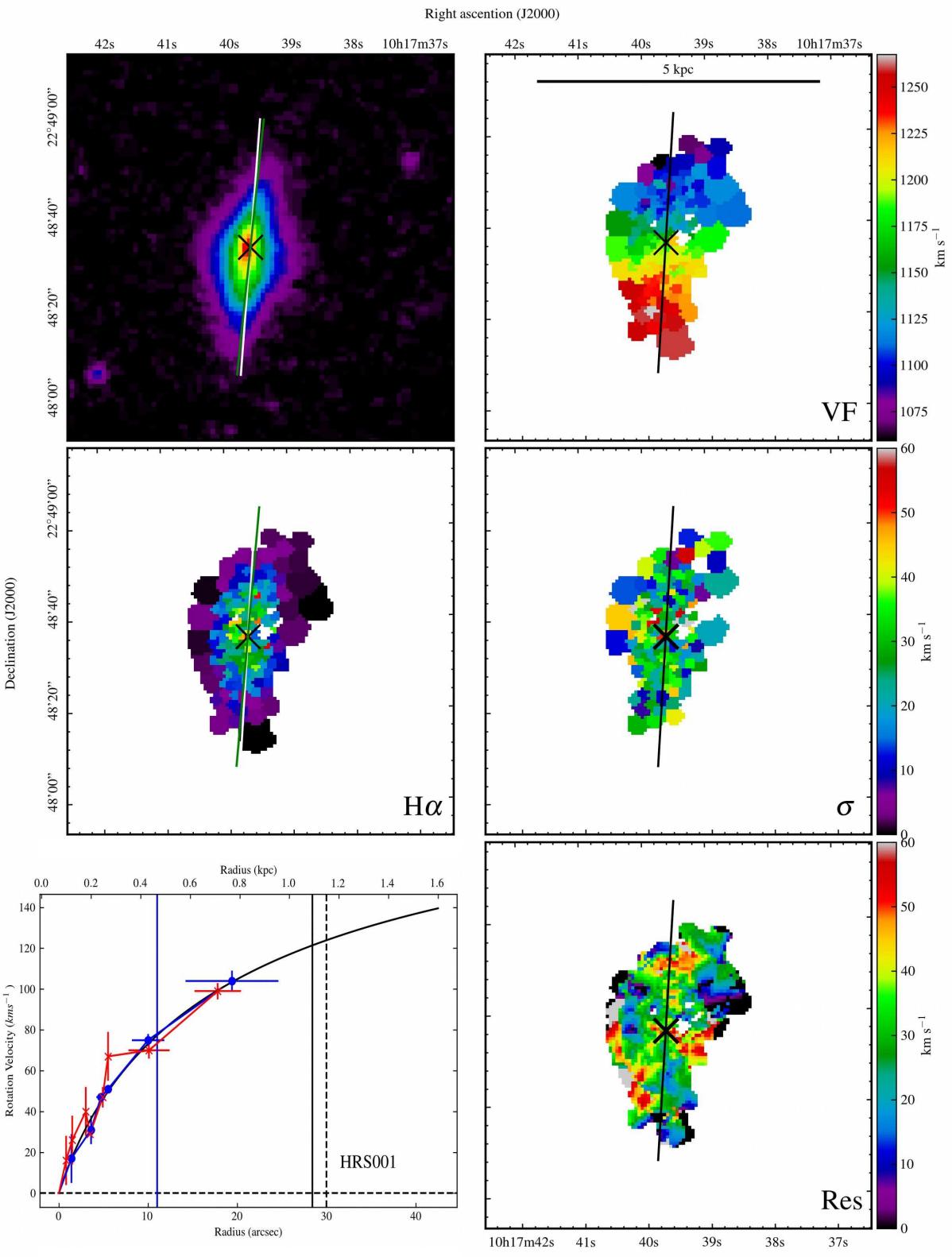
Right ascention (J2000)
42s
41s
40s
39s
38s
10h17m37s
10h17m42s
37s
Declination (J2000)
22°49'00"
48'40"
48'20"
48'00"
5 kpc
VF
Hα
σ
Res
km s⁻¹
1250
1225
1200
1175
1150
1125
1100
1075
60
50
40
30
20
10
0
Radius (kpc)
0.0
0.2
0.4
0.6
0.8
1.0
1.2
1.4
1.6
Rotation Velocity (kms⁻¹)
140
120
100
80
60
40
20
0
Radius (arcsec)
HRS001

HRS001

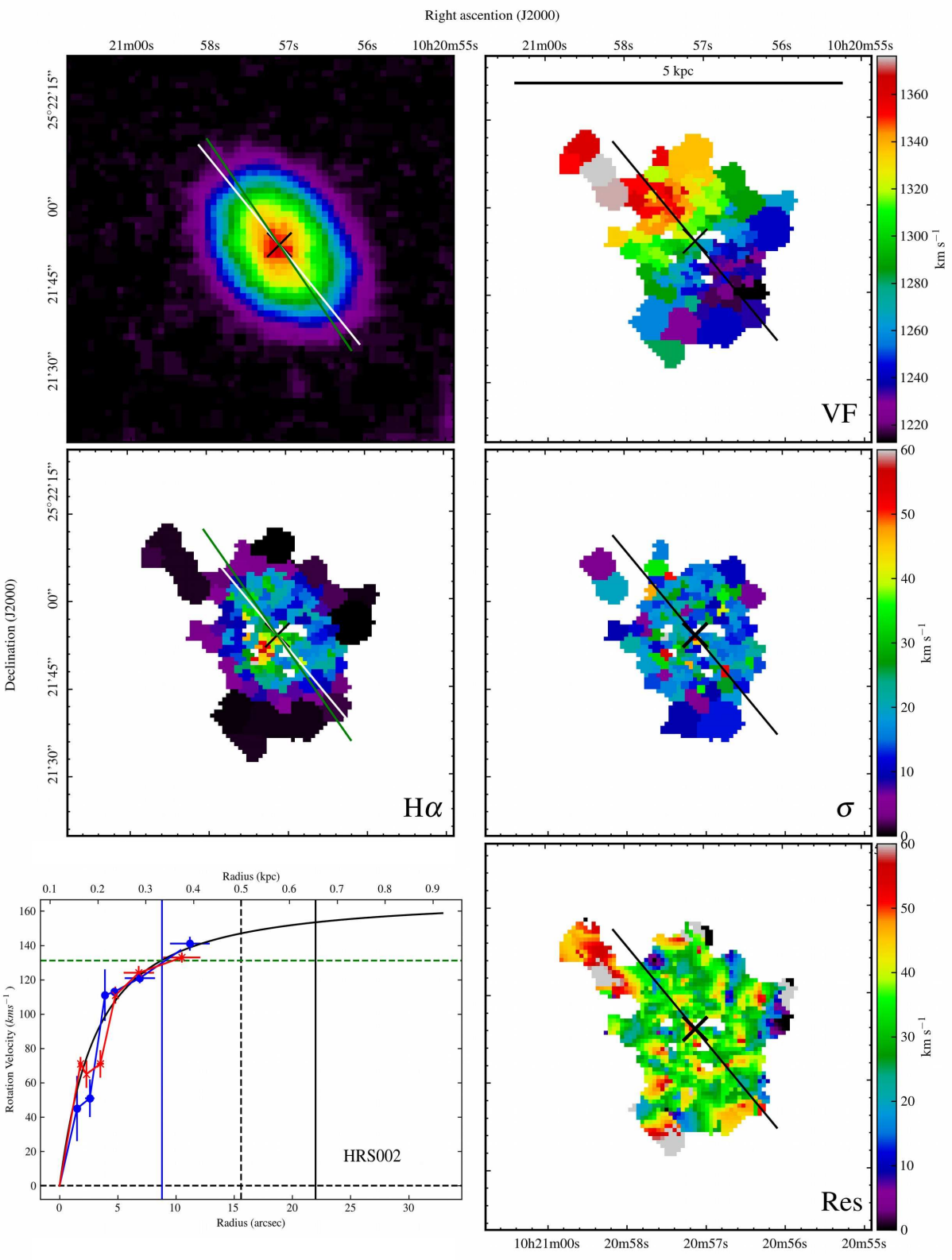
Right ascention (J2000)
21m00s
58s
57s
56s
10h20m55s
Declination (J2000)
25°22'15"
00"
21'45"
21'30"
5 kpc
VF
Hα
σ
Res
km s⁻¹
Radius (kpc)
Rotation Velocity (kms⁻¹)
Radius (arcsec)
HRS002
10h21m00s
20m58s
20m57s
20m56s
20m55s

HRS002

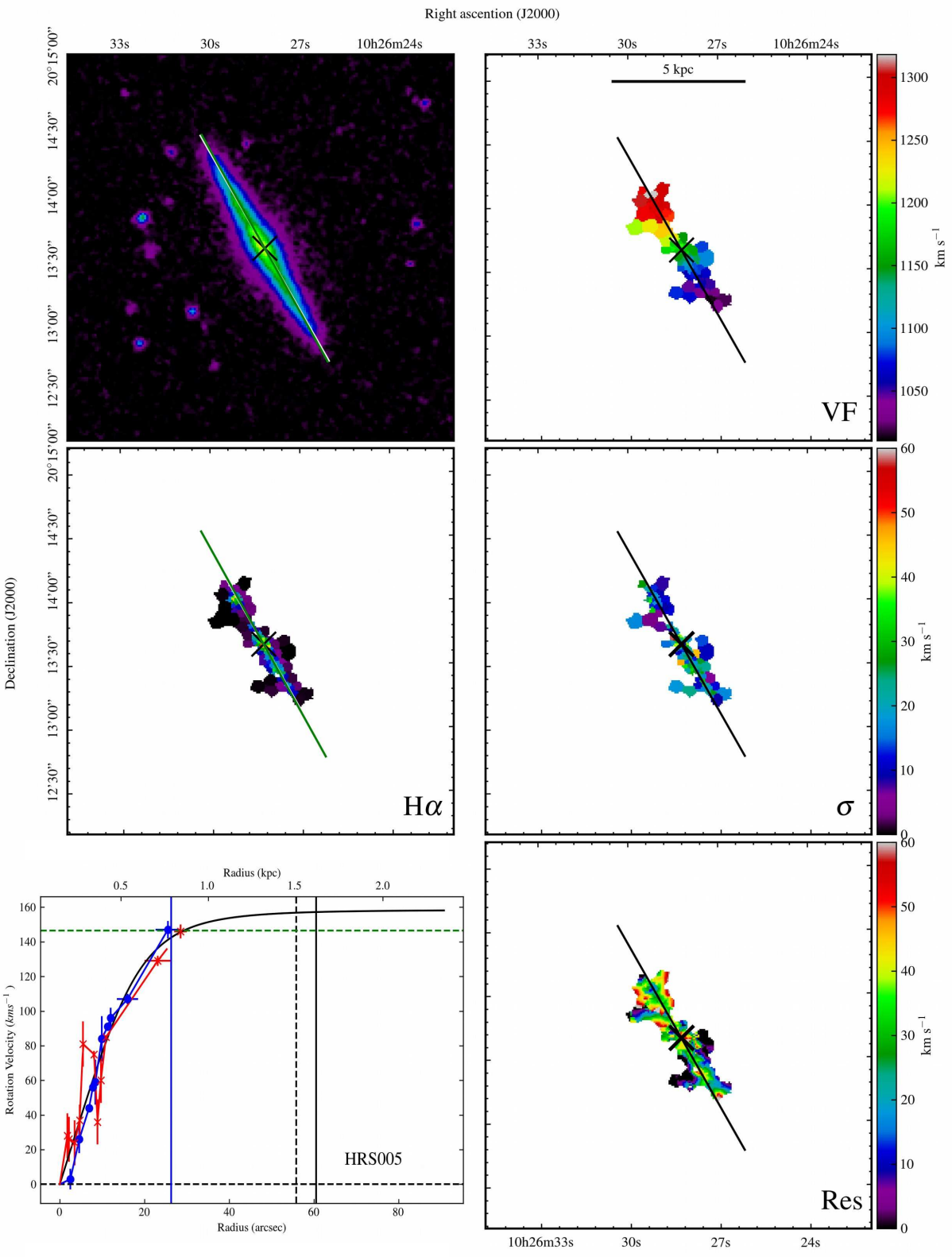
Right ascention (J2000)
Declination (J2000)
33s
30s
27s
10h26m24s
20°15'00"
14'30"
14'00"
13'30"
13'00"
12'30"
5 kpc
VF
Hα
σ
Res
km s⁻¹
Radius (kpc)
0.5
1.0
1.5
2.0
Rotation Velocity (kms⁻¹)
Radius (arcsec)
HRS005
10h26m33s
24s

HRS005

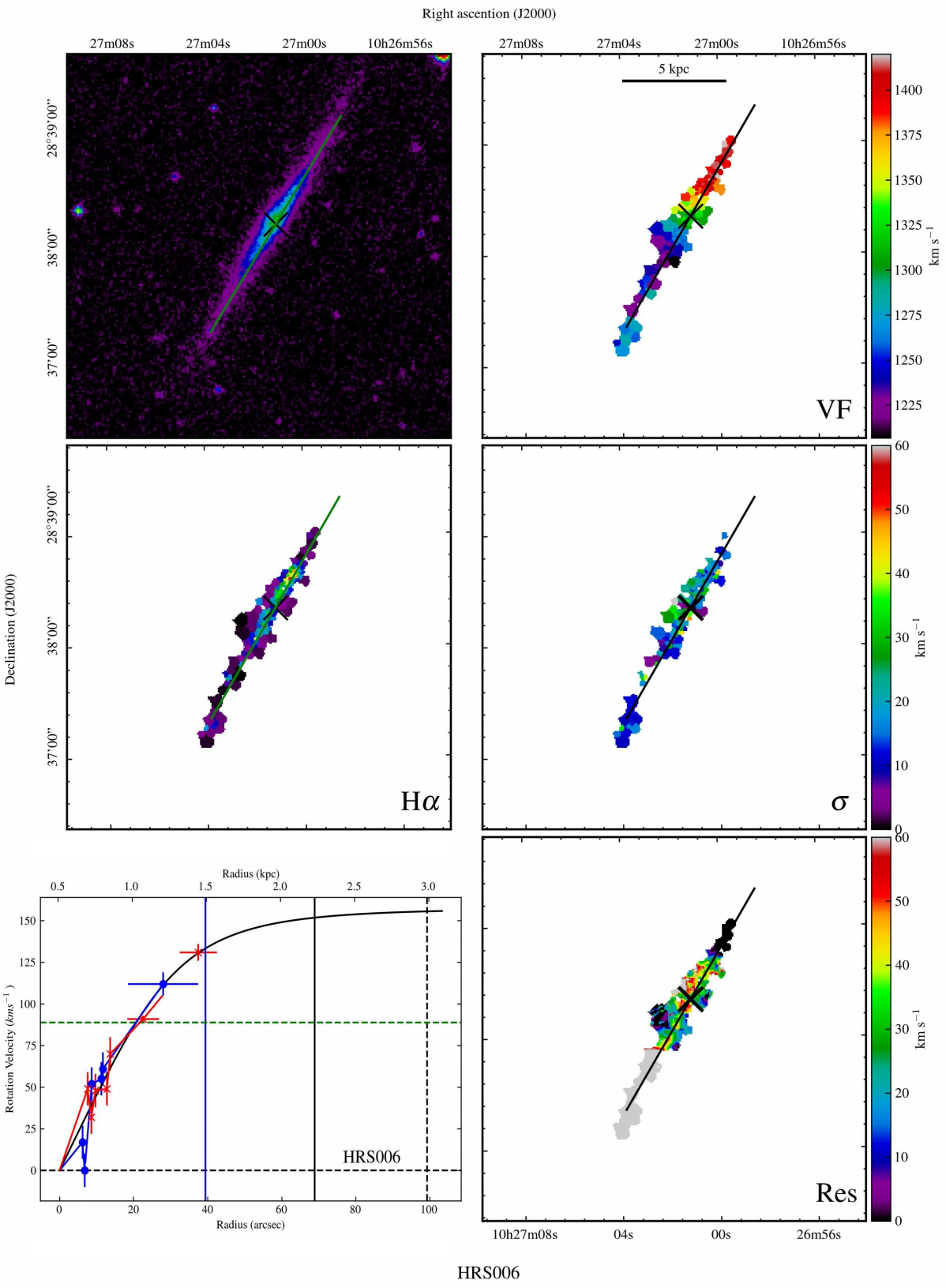
Right ascention (J2000)
27m08s
27m04s
27m00s
10h26m56s
Declination (J2000)
28°39'00"
38'00"
37'00"
5 kpc
VF
Hα
σ
Res
km s⁻¹
Radius (kpc)
Radius (arcsec)
Rotation Velocity (kms⁻¹)
HRS006
10h27m08s
04s
00s
26m56s

HRS006

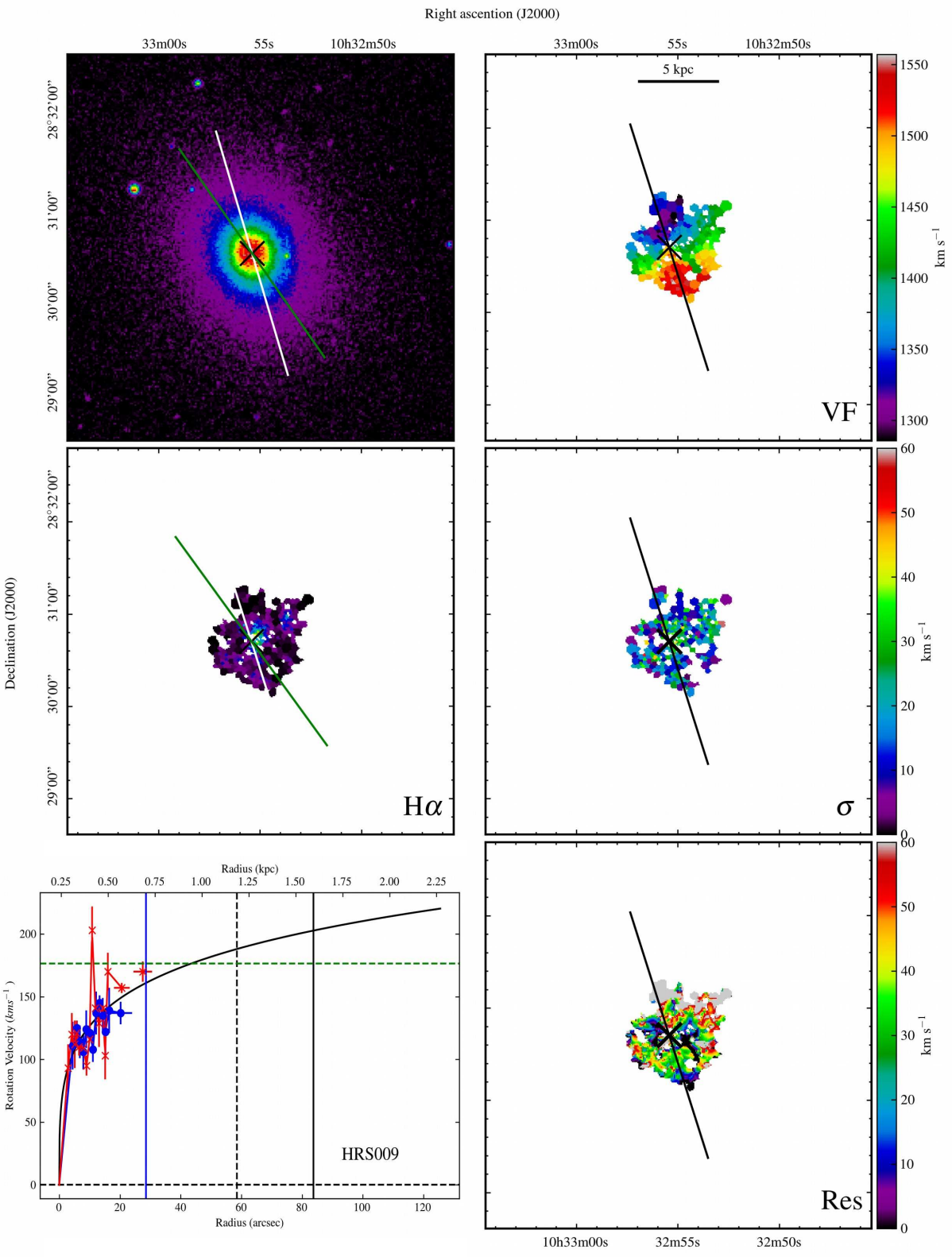
Right ascention (J2000)
33m00s
55s
10h32m50s
28°32'00"
31'00"
30'00"
29'00"
Declination (J2000)
5 kpc
VF
Hα
σ
Res
km s⁻¹
1550
1500
1450
1400
1350
1300
60
50
40
30
20
10
0
Radius (kpc)
0.25
0.50
0.75
1.00
1.25
1.50
1.75
2.00
2.25
Rotation Velocity (kms⁻¹)
200
150
100
50
0
HRS009
Radius (arcsec)
0
20
40
60
80
100
120
10h33m00s
32m55s
32m50s

HRS009

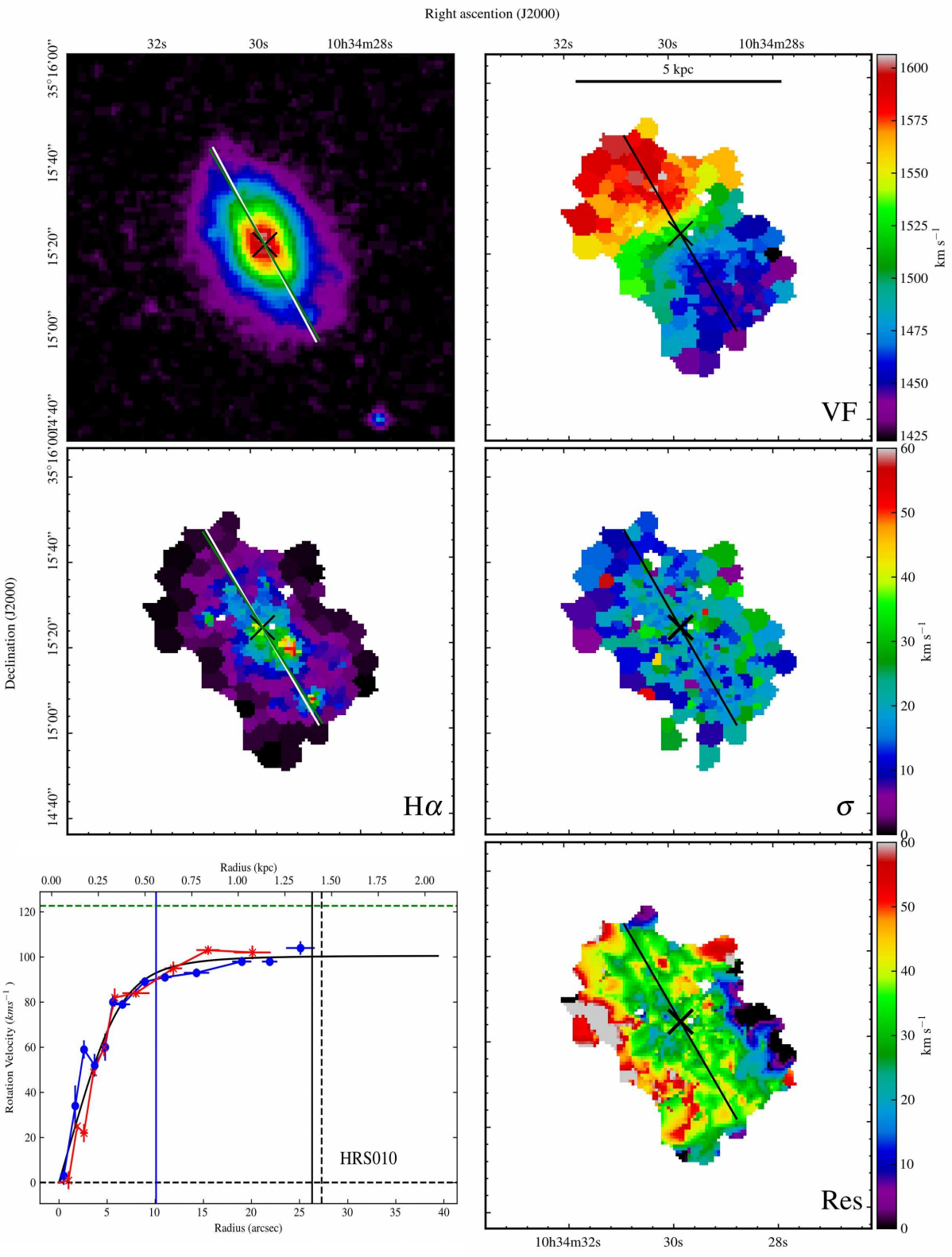
Right ascention (J2000)
32s
30s
10h34m28s
35°16'00"
15'40"
15'20"
15'00"
14'40"
Declination (J2000)
5 kpc
VF
Hα
σ
Res
km s⁻¹
Radius (kpc)
0.00
0.25
0.50
0.75
1.00
1.25
1.50
1.75
2.00
Rotation Velocity (kms⁻¹)
Radius (arcsec)
HRS010
10h34m32s

HRS010

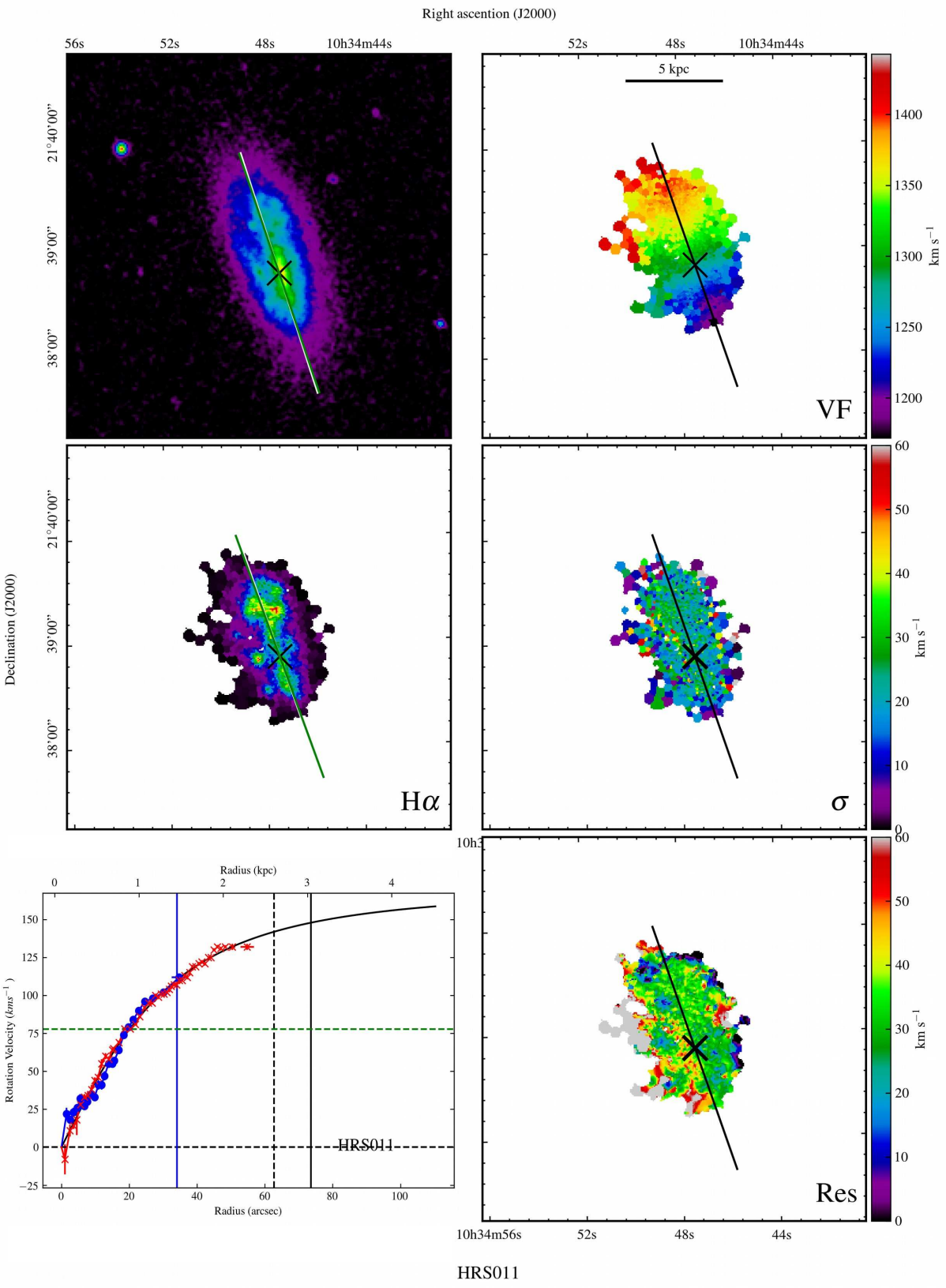
Right ascention (J2000)
56s
52s
48s
10h34m44s
21°40'00"
39'00"
38'00"
Declination (J2000)
5 kpc
VF
Hα
σ
Res
km s⁻¹
1400
1350
1300
1250
1200
60
50
40
30
20
10
0
10h34m56s
52s
48s
44s
Radius (kpc)
0
1
2
3
4
Rotation Velocity (kms⁻¹)
150
125
100
75
50
25
0
−25
Radius (arcsec)
0
20
40
60
80
100
HRS011

HRS011

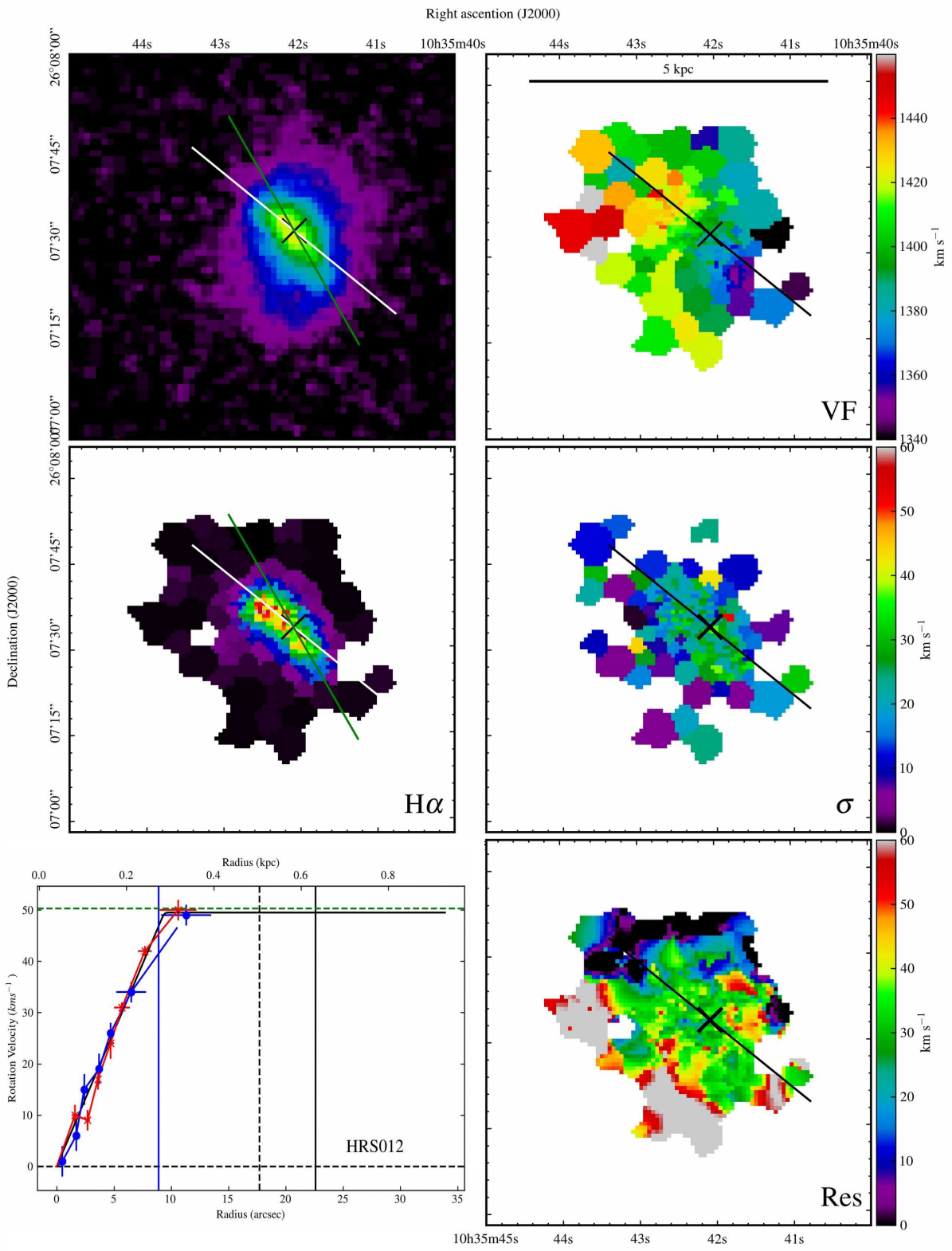
Right ascention (J2000)
Declination (J2000)
5 kpc
VF
Hα
σ
Res
km s^{-1}
Radius (kpc)
Radius (arcsec)
Rotation Velocity (kms^{-1})
HRS012

HRS012

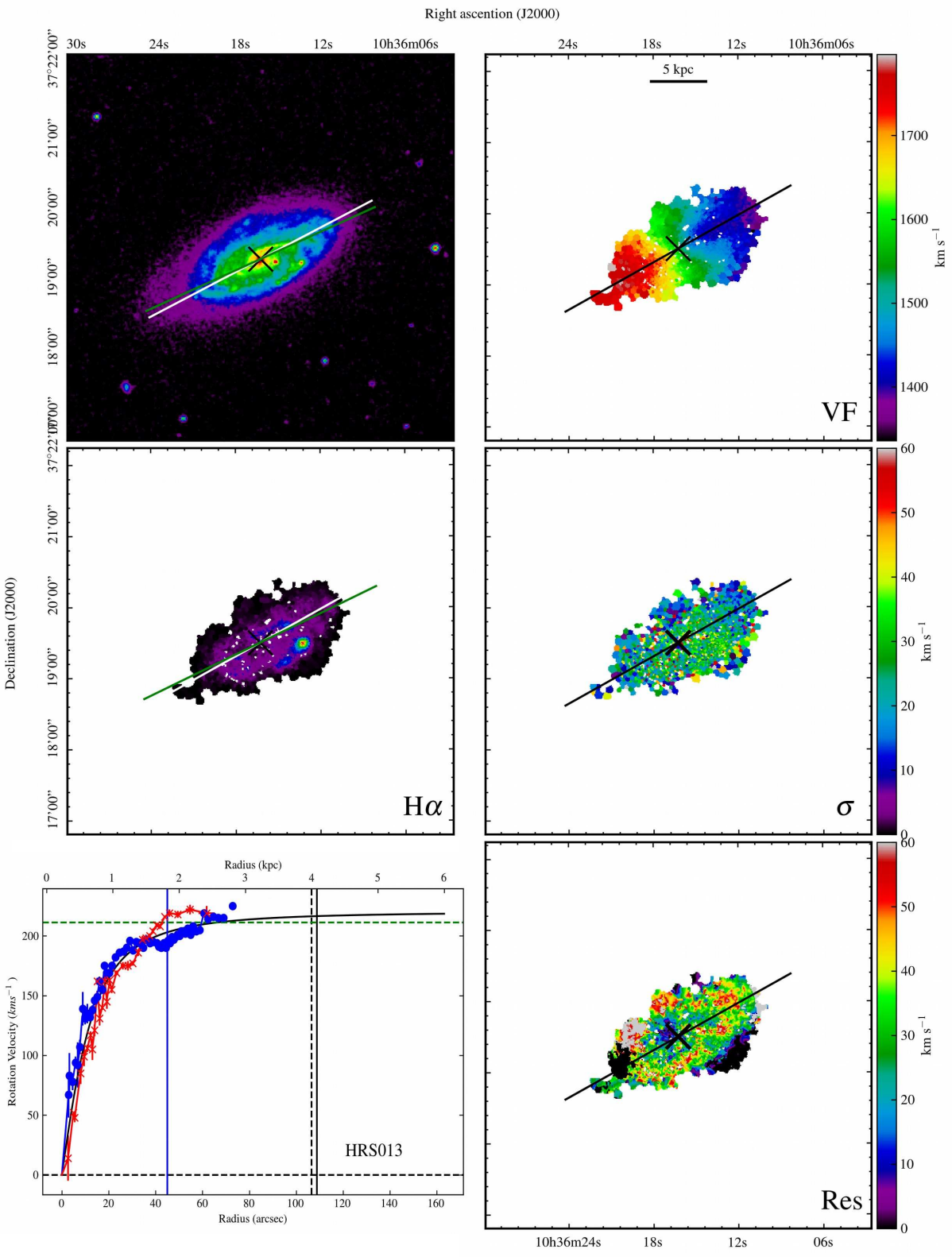
Right ascention (J2000)
Declination (J2000)
30s
24s
18s
12s
10h36m06s
37°22'00"
21'00"
20'00"
19'00"
18'00"
17'00"
5 kpc
VF
Hα
σ
Res
km s⁻¹
1700
1600
1500
1400
60
50
40
30
20
10
0
10h36m24s
06s
Radius (kpc)
Rotation Velocity (kms⁻¹)
Radius (arcsec)
HRS013

HRS013

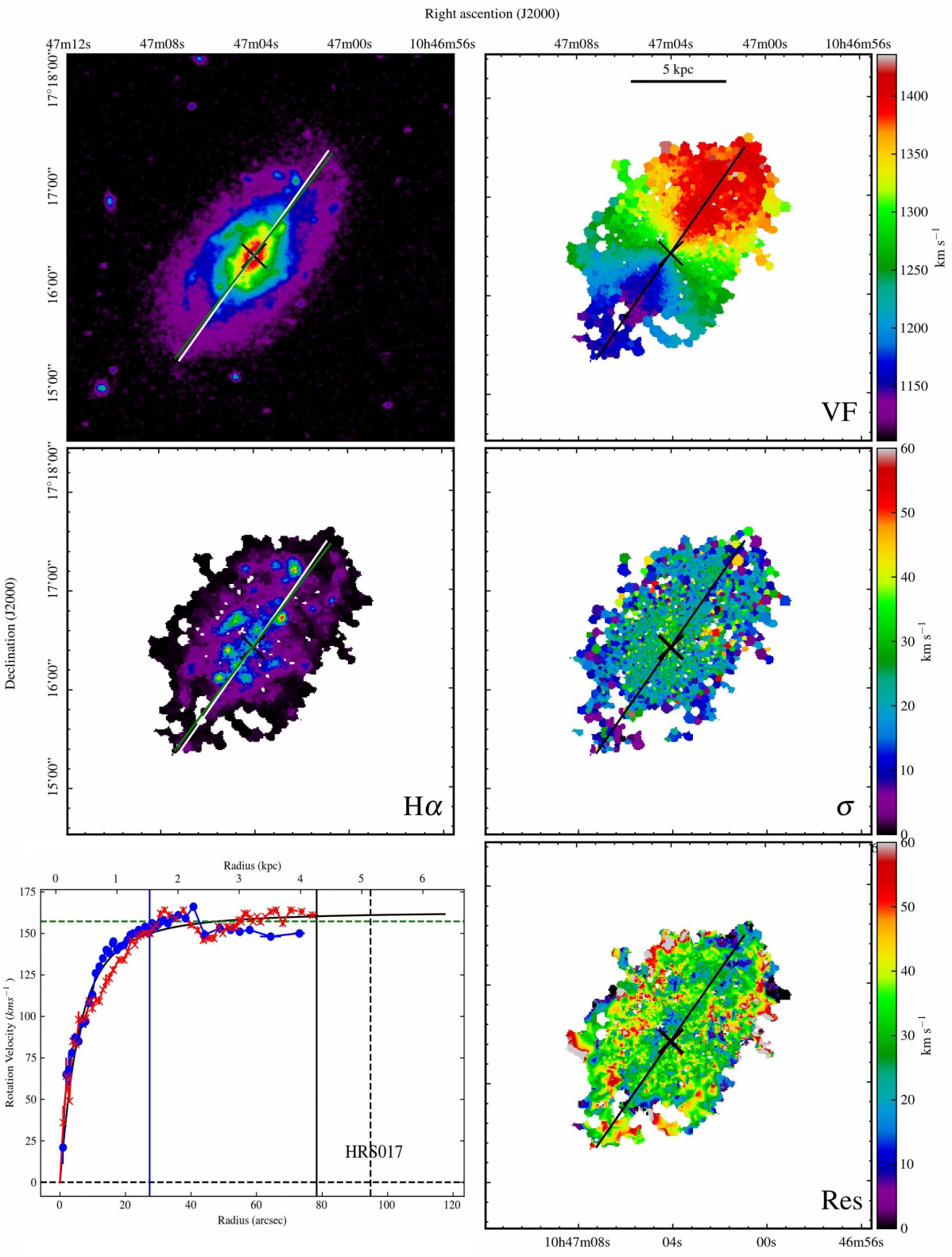
Right ascention (J2000)
47m12s
47m08s
47m04s
47m00s
10h46m56s
17°18'00"
17'00"
16'00"
15'00"
Declination (J2000)
5 kpc
VF
Hα
σ
Res
km s⁻¹
Radius (kpc)
Rotation Velocity (kms⁻¹)
Radius (arcsec)
HRS017
10h47m08s
04s
00s
46m56s

HRS017

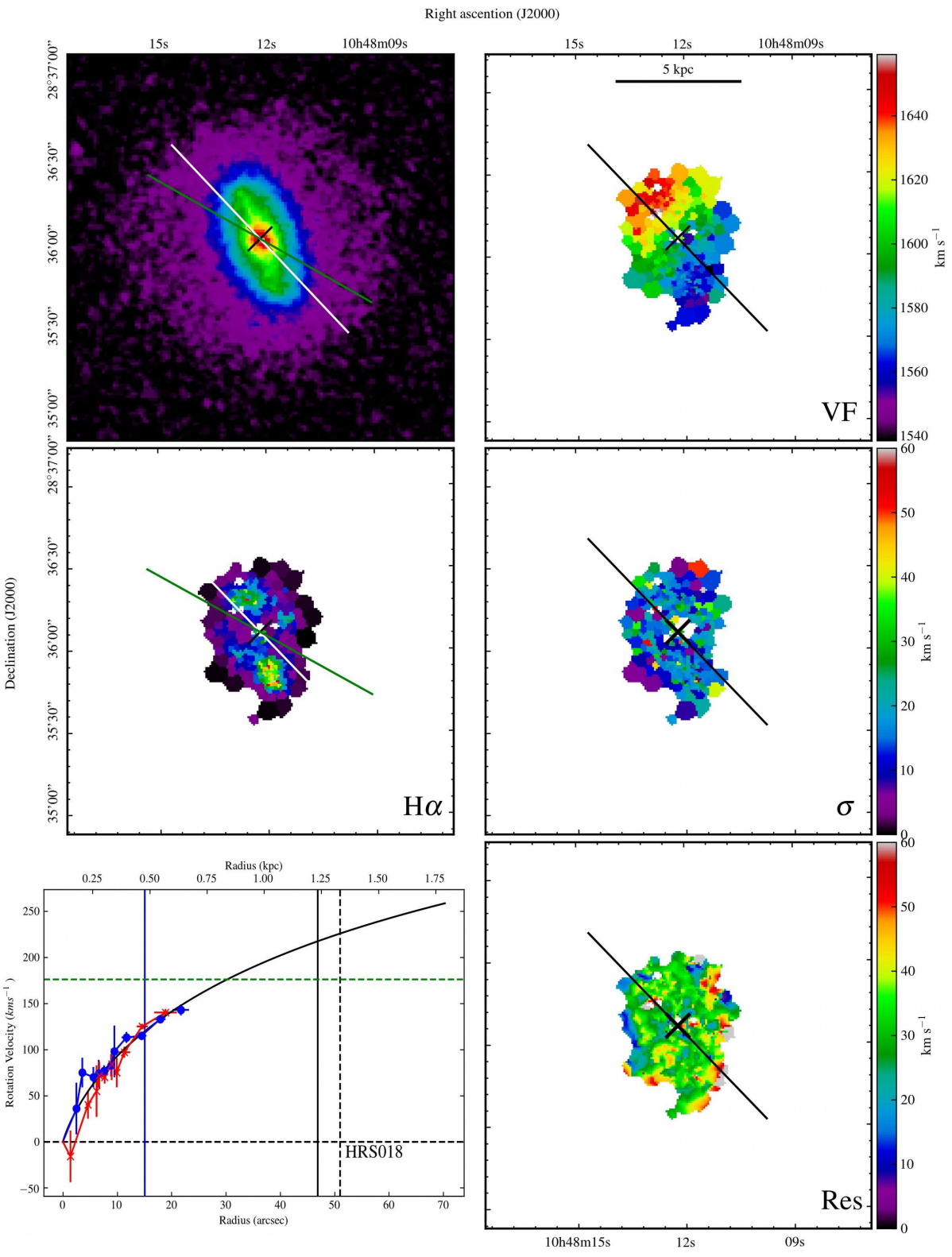
Right ascention (J2000)
15s
12s
10h48m09s
28°37'00"
36'30"
36'00"
35'30"
35'00"
Declination (J2000)
5 kpc
VF
Hα
σ
Res
km s⁻¹
1640
1620
1600
1580
1560
1540
60
50
40
30
20
10
0
Radius (kpc)
0.25
0.50
0.75
1.00
1.25
1.50
1.75
Rotation Velocity (kms⁻¹)
250
200
150
100
50
0
−50
HRS018
Radius (arcsec)
0
10
20
30
40
50
60
70
10h48m15s
09s

HRS018

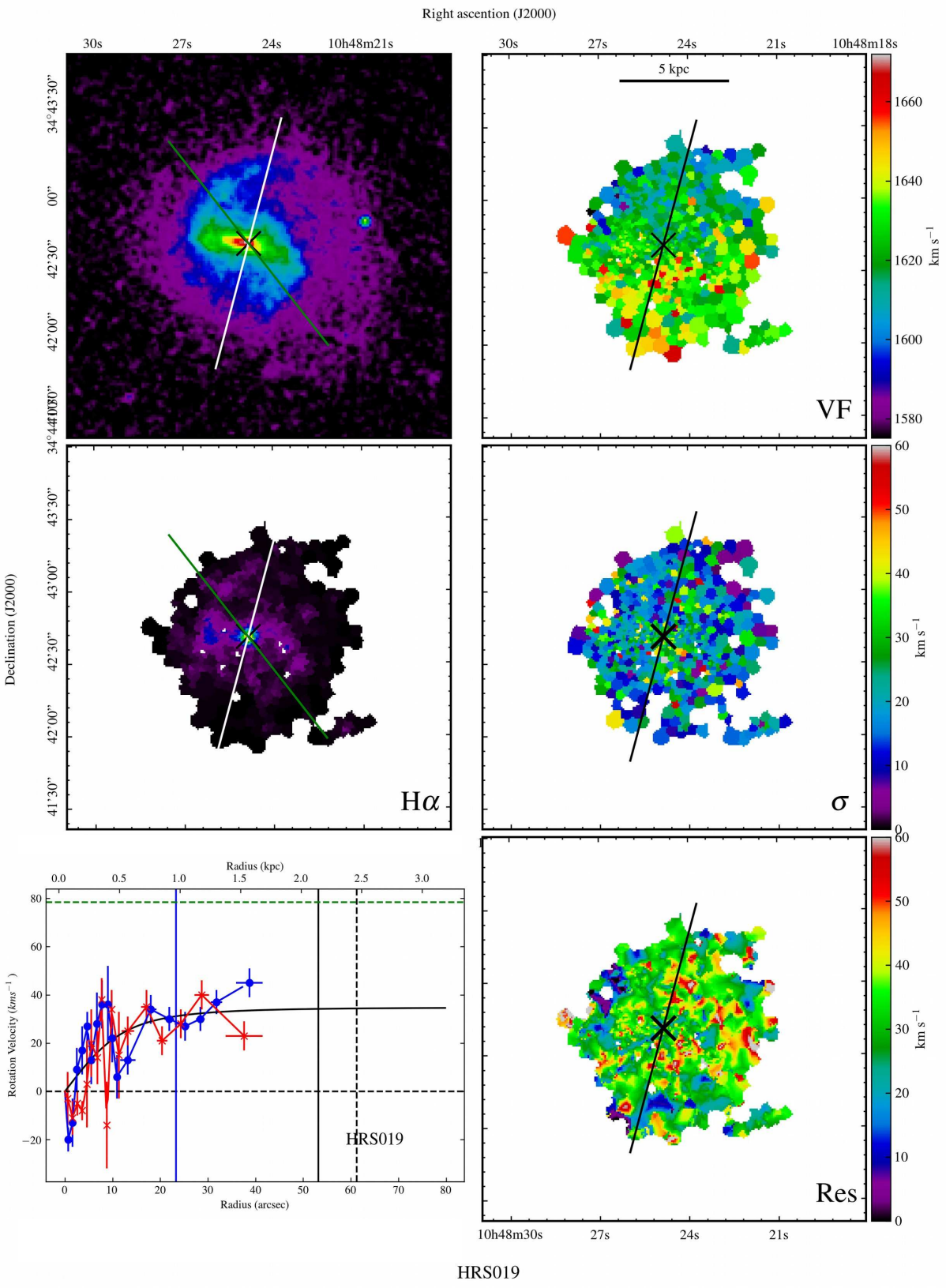
Right ascention (J2000)
30s
27s
24s
10h48m21s
10h48m18s
21s
5 kpc
VF
Hα
σ
Res
km s⁻¹
Declination (J2000)
34°43'30"
00"
42'30"
42'00"
43'30"
43'00"
41'30"
Radius (kpc)
Radius (arcsec)
Rotation Velocity (kms⁻¹)
HRS019
10h48m30s

HRS019

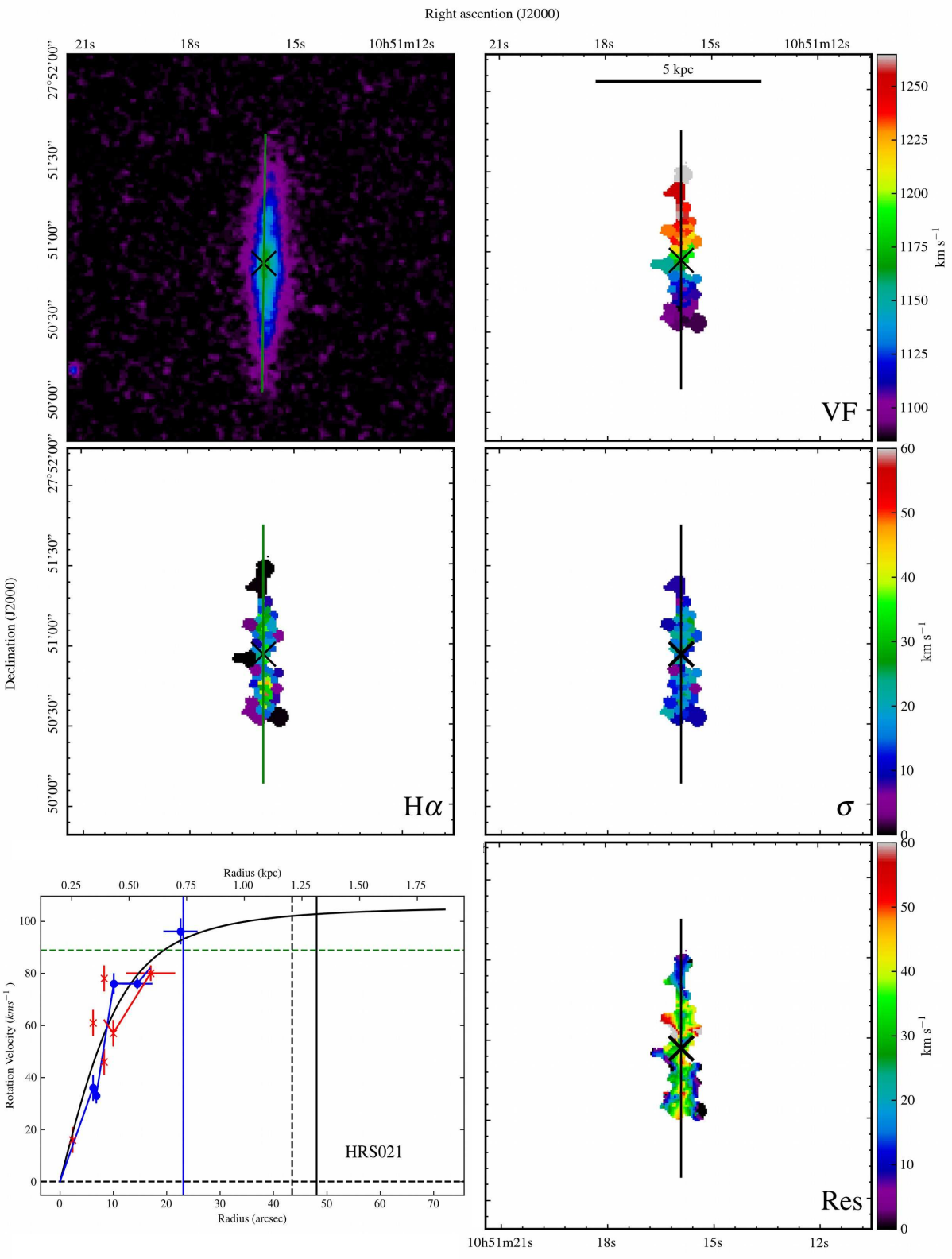
Right ascention (J2000)
Declination (J2000)
21s
18s
15s
10h51m12s
10h51m21s
12s
27°52'00"
51'30"
51'00"
50'30"
50'00"
5 kpc
VF
Hα
σ
Res
km s⁻¹
Radius (kpc)
Radius (arcsec)
Rotation Velocity (kms⁻¹)
HRS021

HRS021

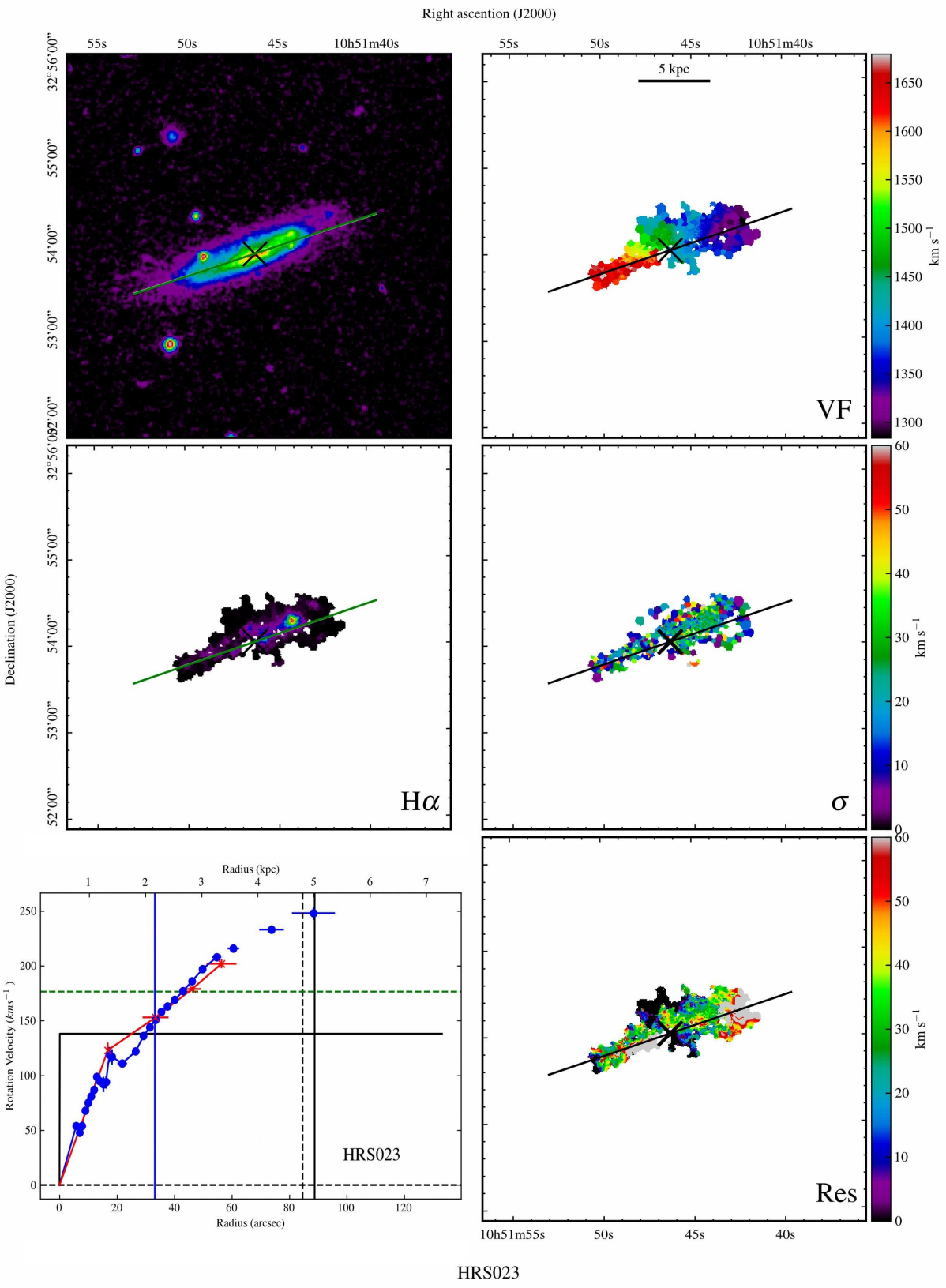
Right ascention (J2000)
55s
50s
45s
10h51m40s
10h51m55s
40s
Declination (J2000)
32°56'00"
55'00"
54'00"
53'00"
52'00"
5 kpc
VF
Hα
σ
Res
km s⁻¹
1650
1600
1550
1500
1450
1400
1350
1300
60
50
40
30
20
10
0
Radius (kpc)
1
2
3
4
5
6
7
Rotation Velocity (kms⁻¹)
250
200
150
100
50
0
Radius (arcsec)
0
20
40
60
80
100
120
HRS023

HRS023

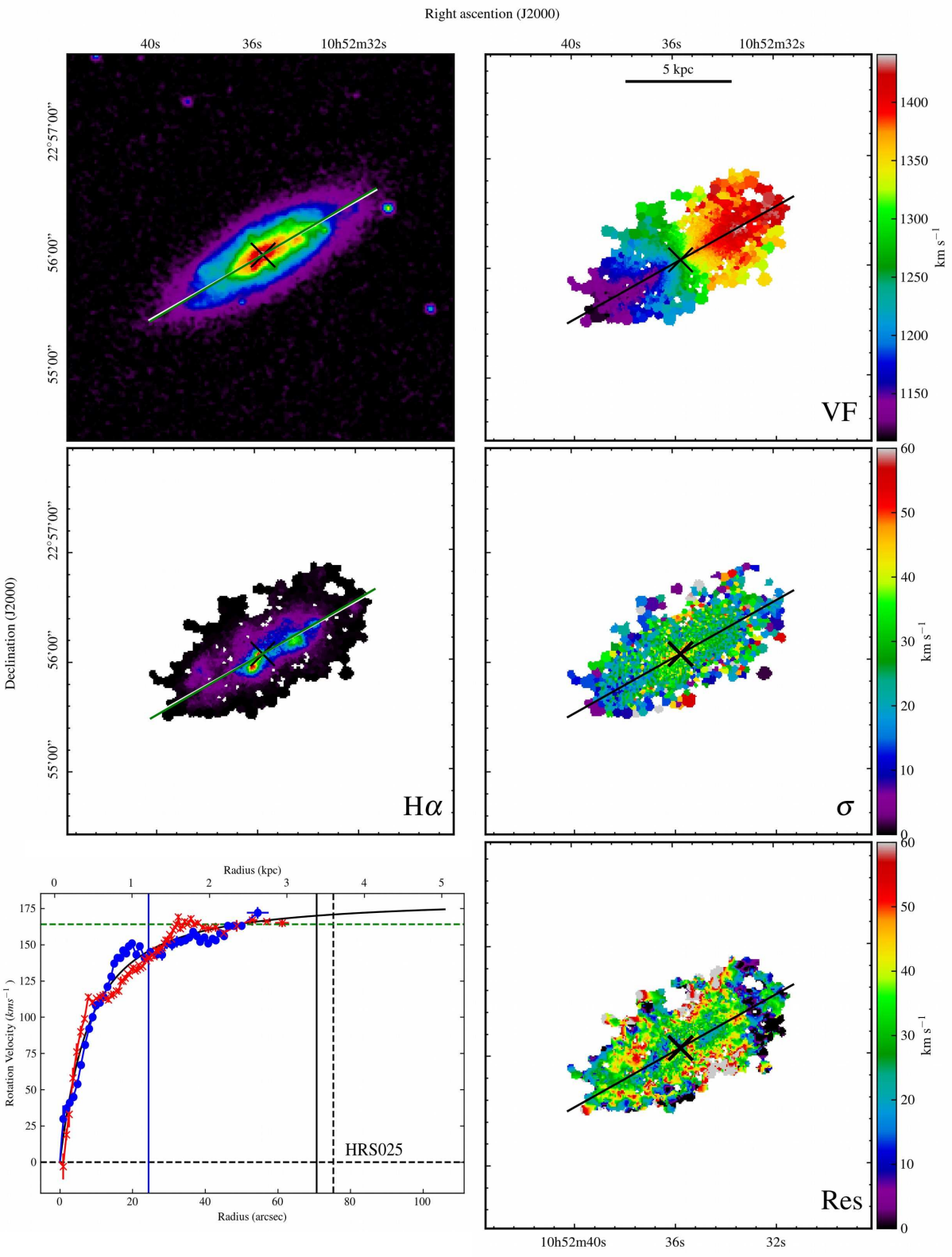
Right ascention (J2000)
40s
36s
10h52m32s
5 kpc
VF
Hα
σ
Res
Declination (J2000)
22°57'00"
56'00"
55'00"
km s⁻¹
Radius (kpc)
Rotation Velocity (kms⁻¹)
Radius (arcsec)
HRS025
10h52m40s
32s

HRS025

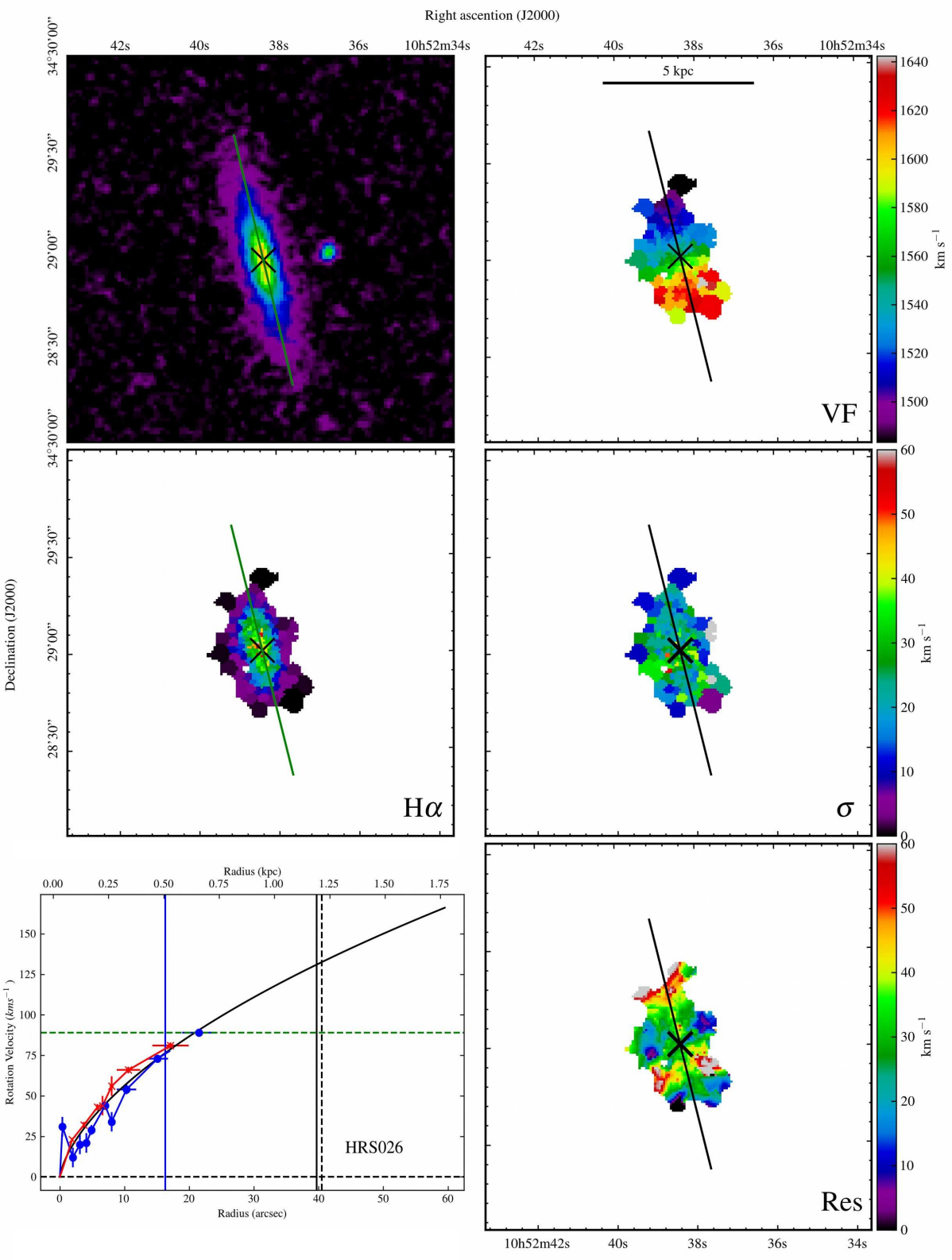
Right ascention (J2000)
42s
40s
38s
36s
10h52m34s
34°30'00"
29'30"
29'00"
28'30"
Declination (J2000)
5 kpc
VF
Hα
σ
Res
km s⁻¹
Radius (kpc)
0.00
0.25
0.50
0.75
1.00
1.25
1.50
1.75
Rotation Velocity (kms⁻¹)
Radius (arcsec)
HRS026
10h52m42s
34s

HRS026

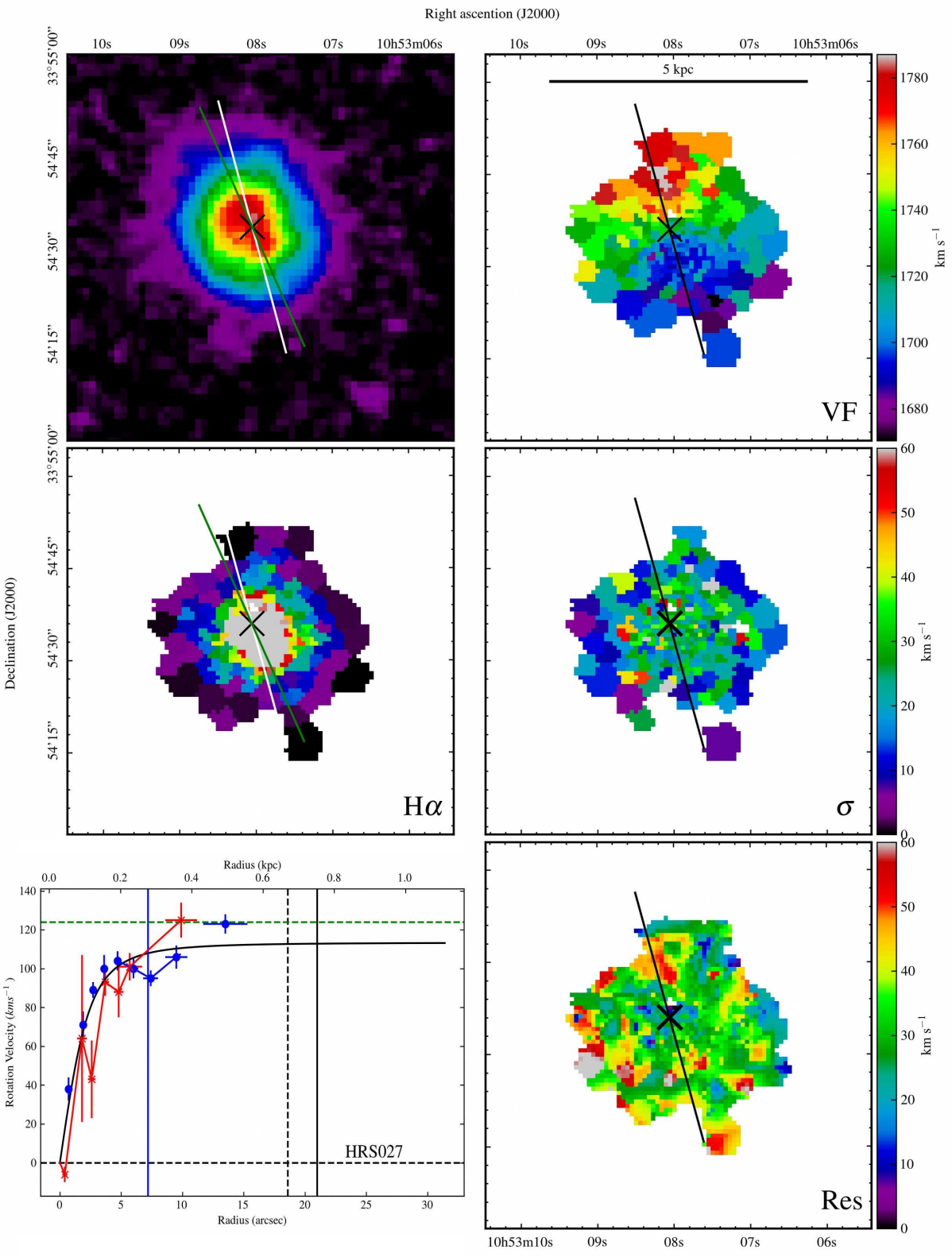
Right ascention (J2000)
Declination (J2000)
10s
09s
08s
07s
10h53m06s
10h53m10s
06s
33°55'00"
54'45"
54'30"
54'15"
5 kpc
VF
Hα
σ
Res
km s⁻¹
1780
1760
1740
1720
1700
1680
60
50
40
30
20
10
0
Radius (kpc)
0.0
0.2
0.4
0.6
0.8
1.0
Rotation Velocity (kms⁻¹)
140
120
100
80
60
40
20
0
Radius (arcsec)
0
5
10
15
20
25
30
HRS027

HRS027

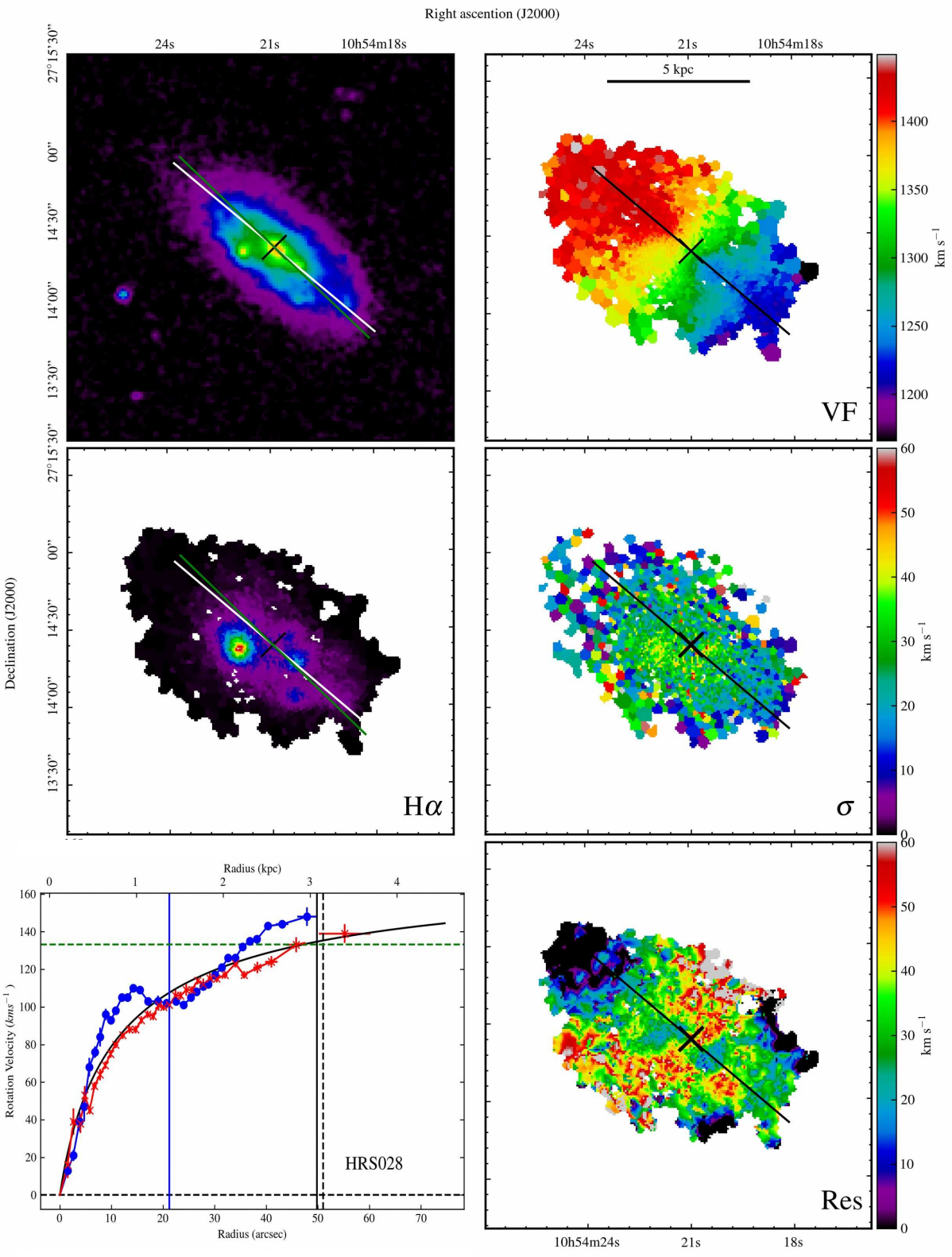
Right ascention (J2000)
24s
21s
10h54m18s
27°15'30"
00"
14'30"
14'00"
13'30"
Declination (J2000)
5 kpc
VF
Hα
σ
Res
km s⁻¹
Radius (kpc)
Rotation Velocity (kms⁻¹)
Radius (arcsec)
HRS028
10h54m24s
21s
18s

HRS028

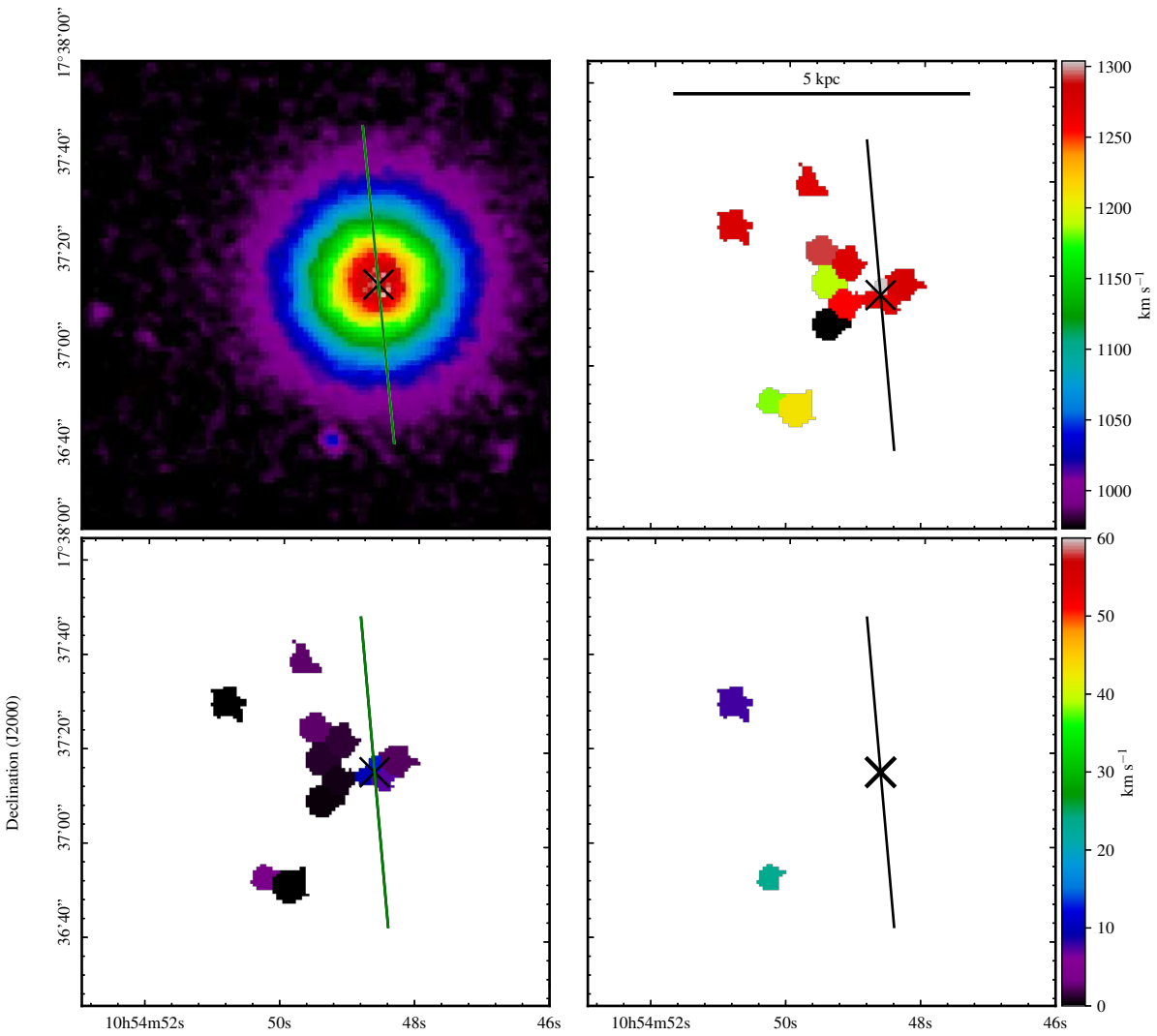
17°38'00"
37'40"
37'20"
37'00"
36'40"
5 kpc
1300
1250
1200
1150
1100
1050
1000
km s^{-1}
60
50
40
30
20
10
0
10h54m52s
50s
48s
46s
Declination (J2000)
Right ascention (J2000)
HRS032

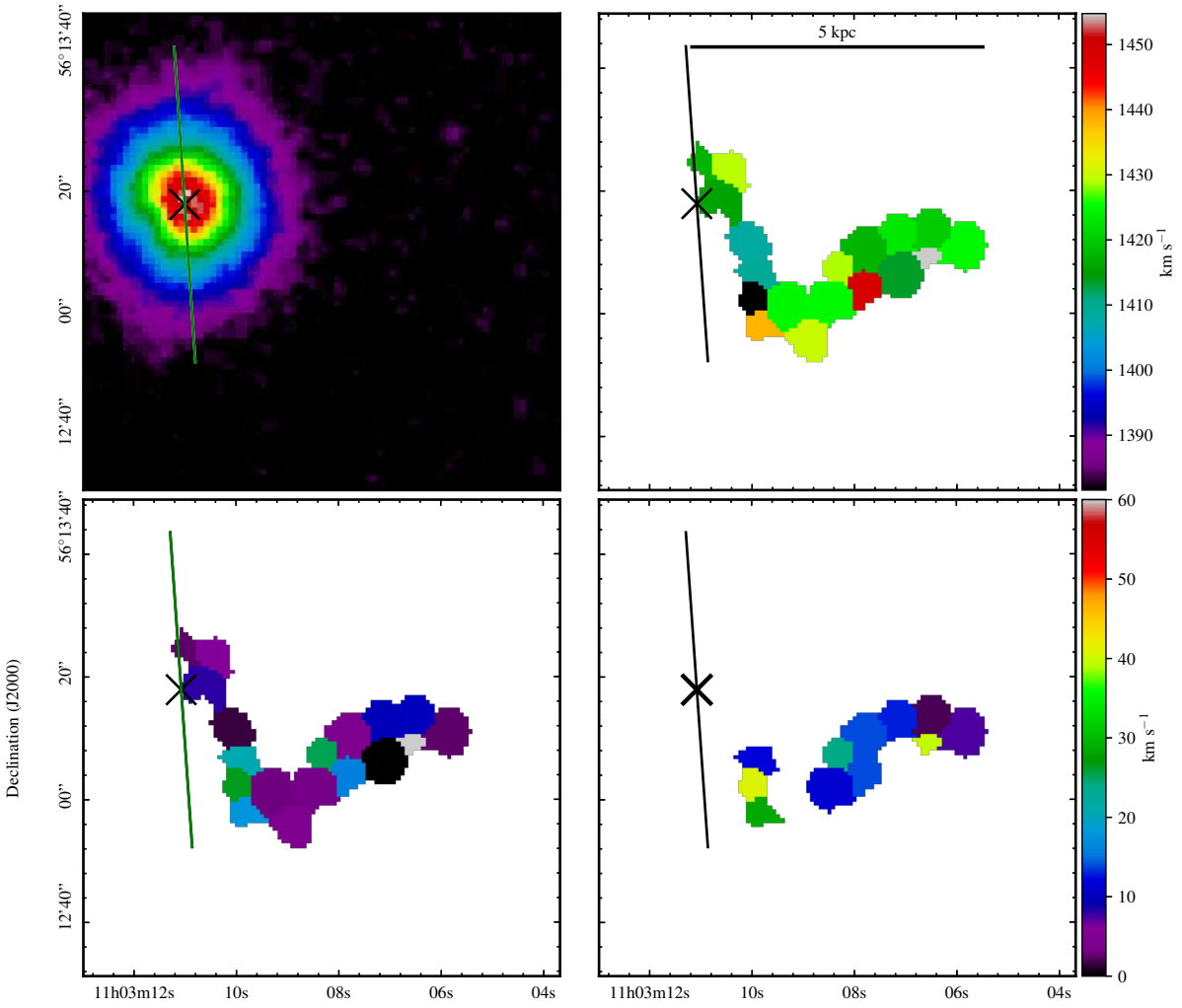
5 kpc
1450
1440
1430
1420
1410
1400
1390
km s^{-1}
60
50
40
30
20
10
0
km s^{-1}
56°13'40"
20"
00"
12'40"
Declination (J2000)
11h03m12s
10s
08s
06s
04s
Right ascention (J2000)
HRS035

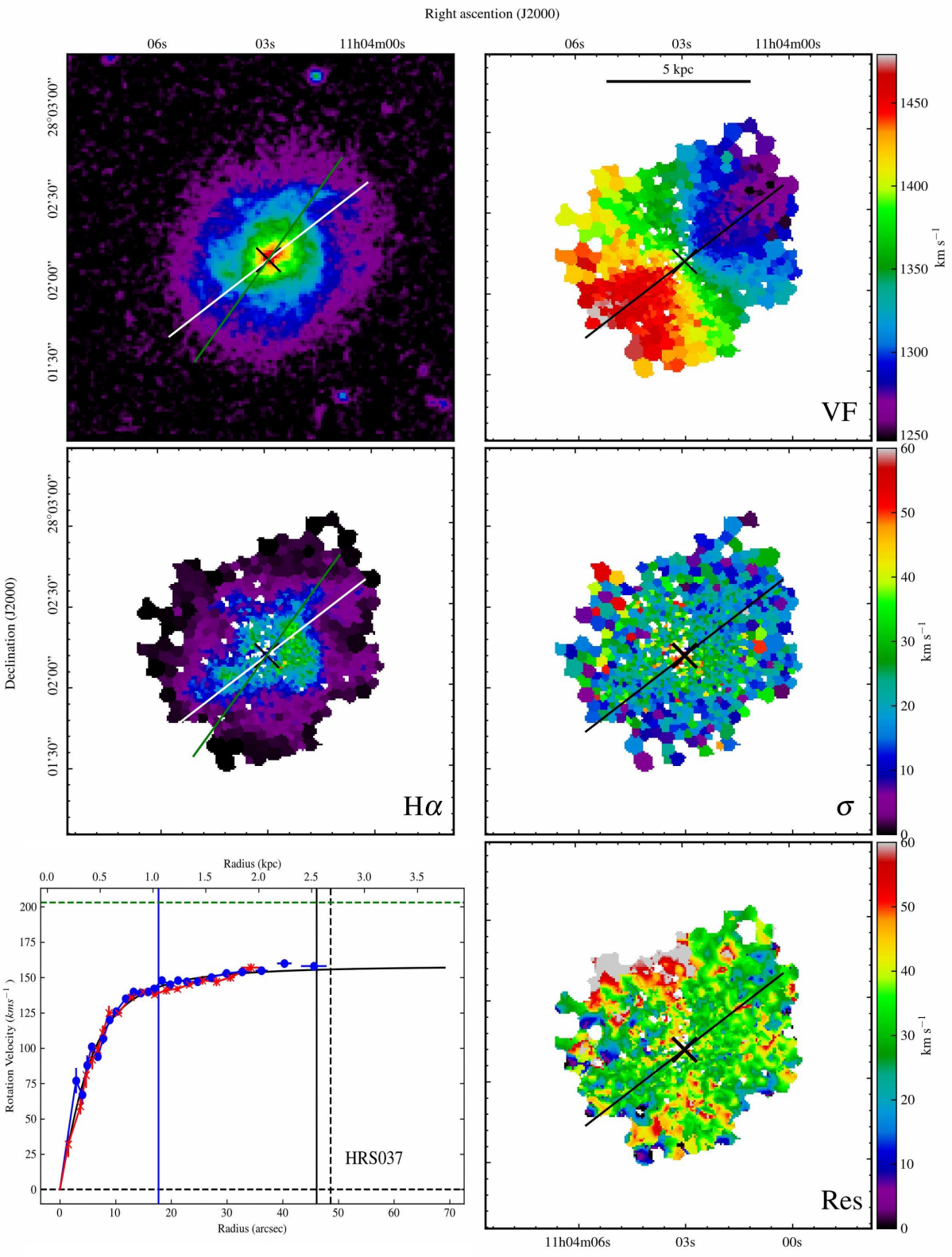
Right ascention (J2000)
06s
03s
11h04m00s
Declination (J2000)
28°03'00"
02'30"
02'00"
01'30"
5 kpc
VF
Hα
σ
Res
km s⁻¹
1450
1400
1350
1300
1250
60
50
40
30
20
10
0
Radius (kpc)
0.0
0.5
1.0
1.5
2.0
2.5
3.0
3.5
Rotation Velocity (kms⁻¹)
200
175
150
125
100
75
50
25
0
Radius (arcsec)
HRS037
11h04m06s
00s

HRS037

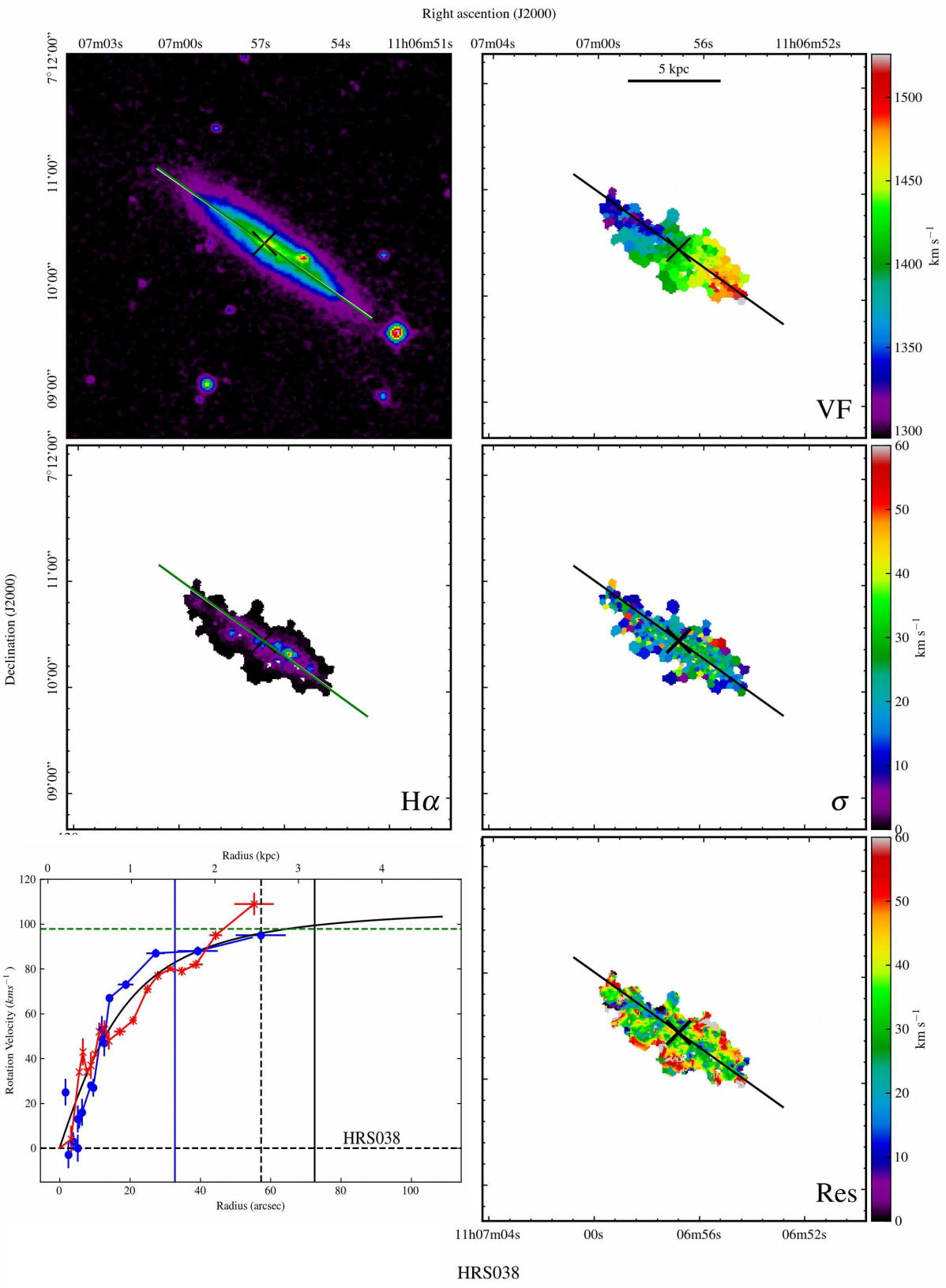
Right ascention (J2000)
07m03s
07m00s
57s
54s
11h06m51s
07m04s
07m00s
56s
11h06m52s
7°12'00"
11'00"
10'00"
09'00"
Declination (J2000)
5 kpc
VF
Hα
σ
Res
km s⁻¹
Radius (kpc)
Rotation Velocity (kms⁻¹)
Radius (arcsec)
HRS038
11h07m04s
00s
06m56s
06m52s

HRS038

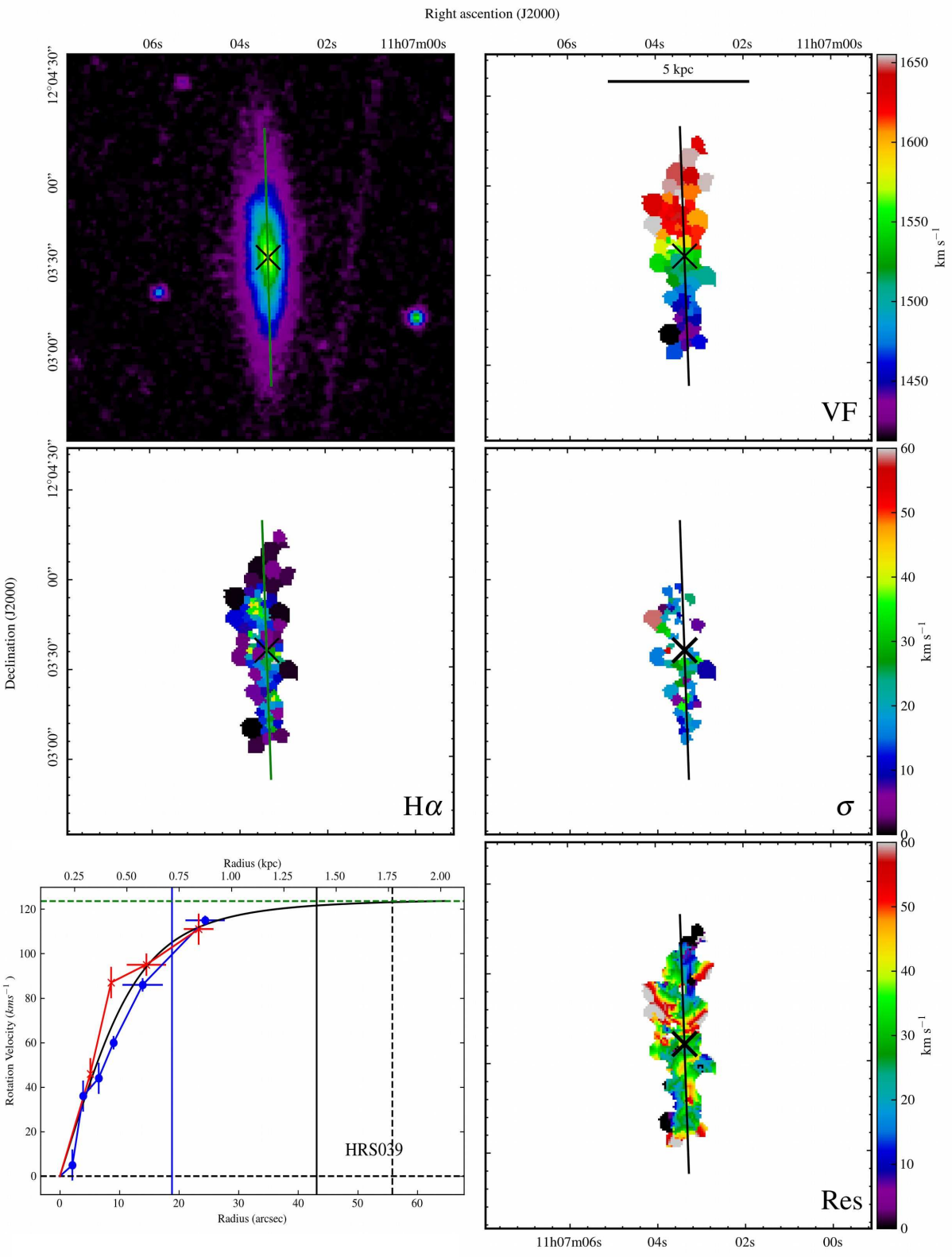
Right ascention (J2000)
06s
04s
02s
11h07m00s
12°04'30"
00"
03'30"
03'00"
Declination (J2000)
5 kpc
VF
Hα
σ
Res
km s⁻¹
1650
1600
1550
1500
1450
60
50
40
30
20
10
0
11h07m06s
04s
02s
00s
Radius (kpc)
0.25
0.50
0.75
1.00
1.25
1.50
1.75
2.00
Rotation Velocity (kms⁻¹)
120
100
80
60
40
20
0
Radius (arcsec)
HRS039

HRS039

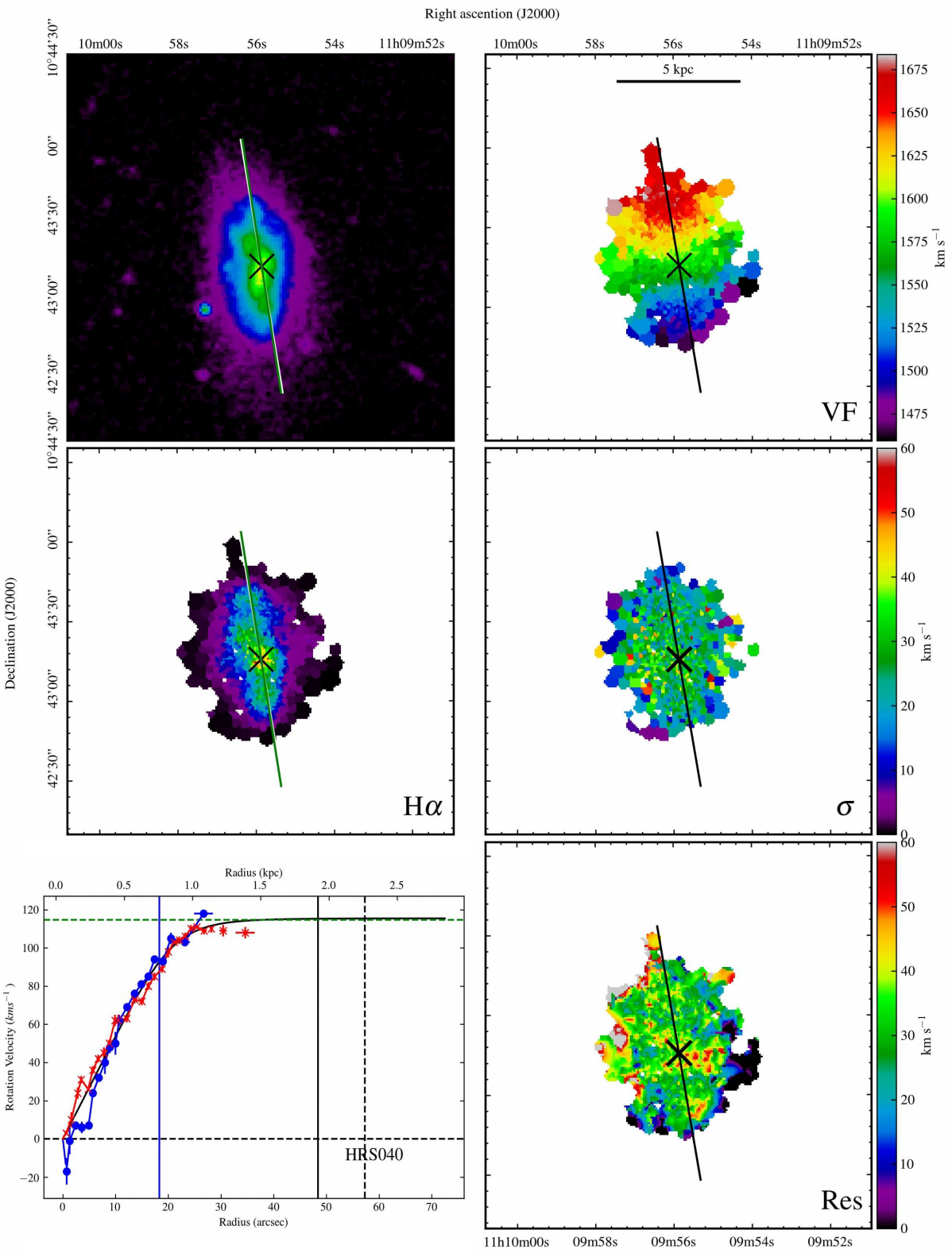
Right ascention (J2000)
10m00s
58s
56s
54s
11h09m52s
10°44'30"
00"
43'30"
43'00"
42'30"
Declination (J2000)
5 kpc
VF
Hα
σ
Res
km s⁻¹
Radius (kpc)
Rotation Velocity (kms⁻¹)
Radius (arcsec)
HRS040
11h10m00s
09m58s
09m56s
09m54s
09m52s

HRS040

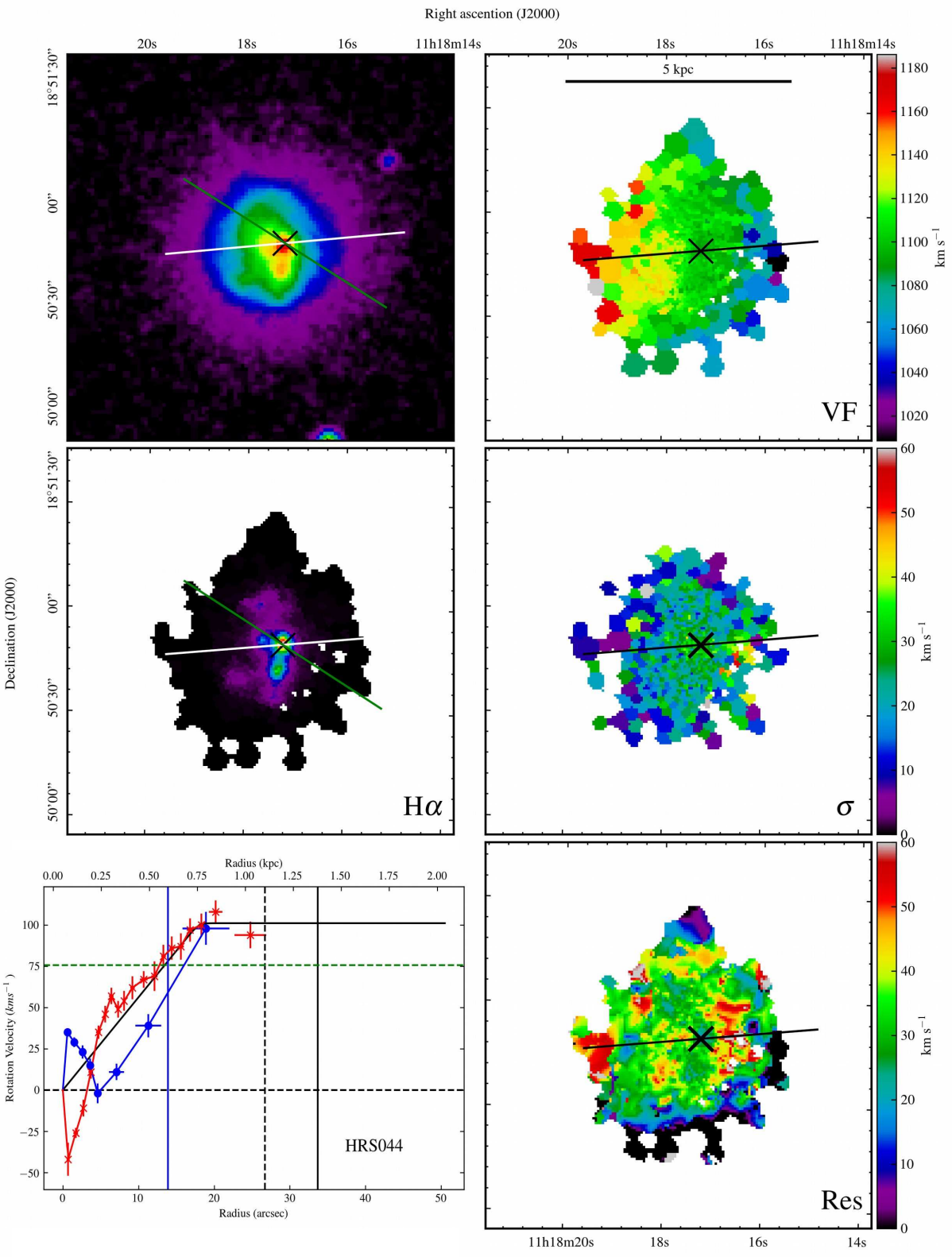
Right ascention (J2000)
Declination (J2000)
20s
18s
16s
11h18m14s
18°51'30"
00"
50'30"
50'00"
5 kpc
VF
Hα
σ
Res
km s⁻¹
Radius (kpc)
Radius (arcsec)
Rotation Velocity (kms⁻¹)
HRS044
11h18m20s
14s

HRS044

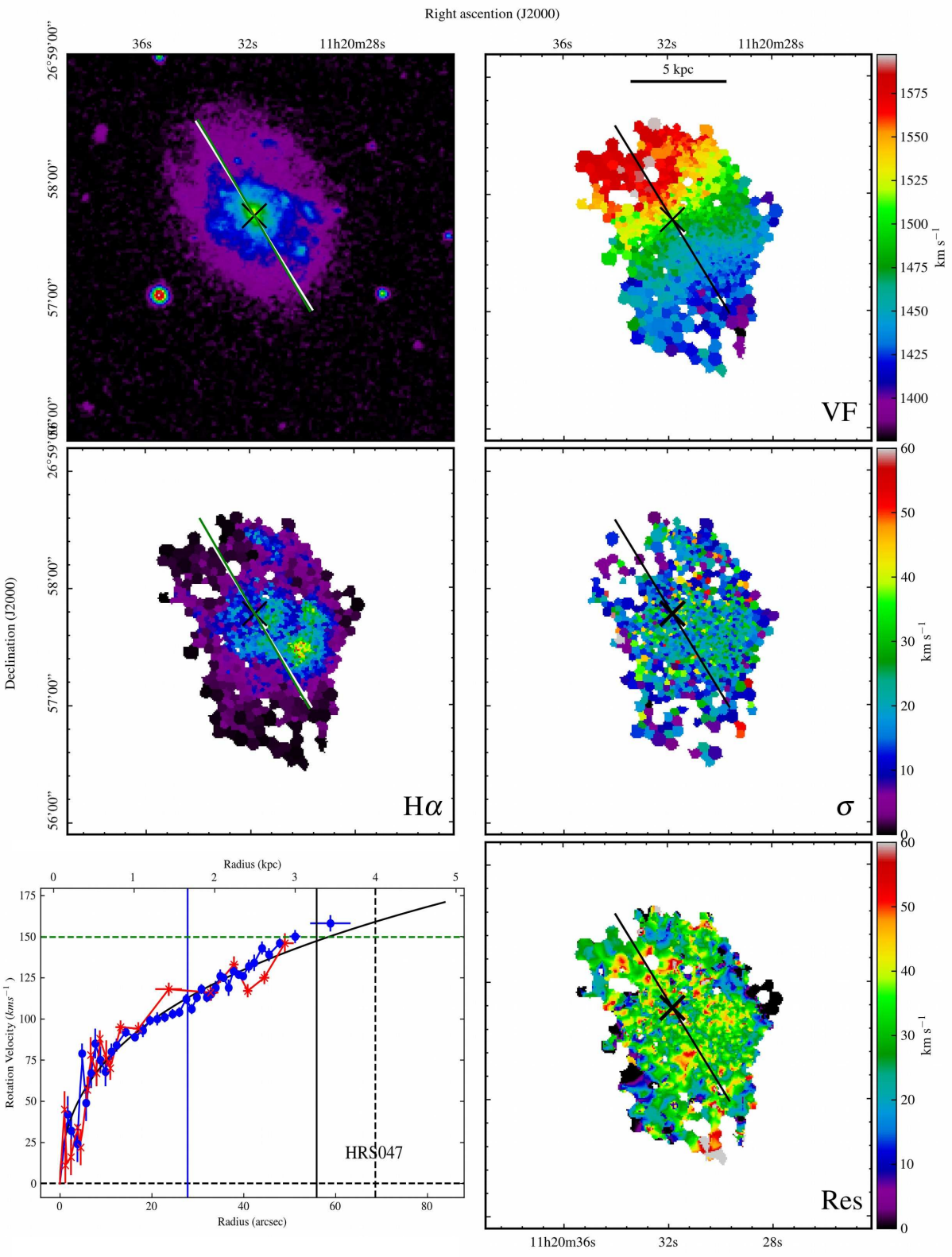
Right ascention (J2000)
Declination (J2000)
36s
32s
11h20m28s
11h20m36s
28s
26°59'00"
58'00"
57'00"
56'00"
5 kpc
VF
Hα
σ
Res
km s⁻¹
Radius (kpc)
Radius (arcsec)
Rotation Velocity (kms⁻¹)
HRS047

HRS047

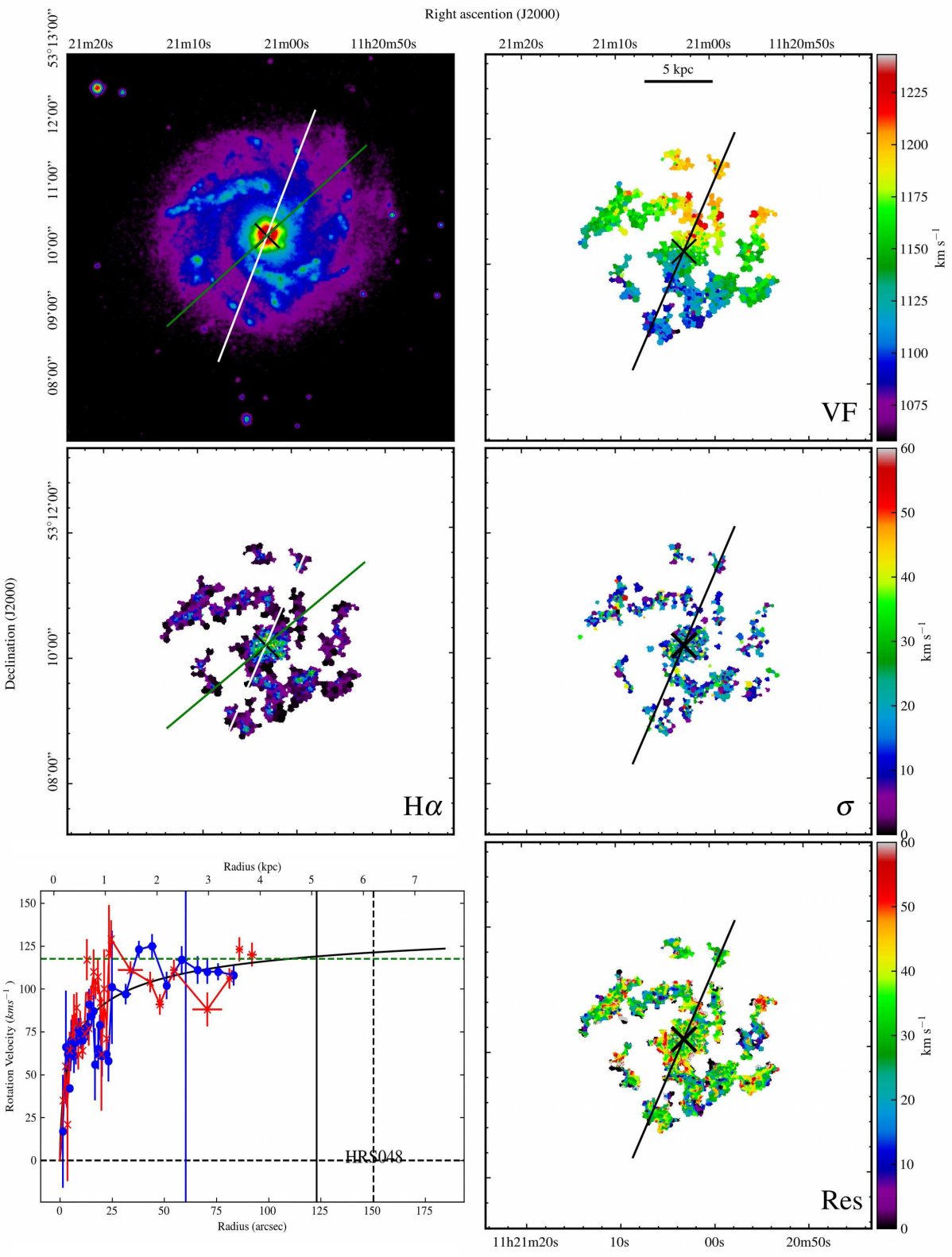
Right ascention (J2000)
Declination (J2000)
21m20s
21m10s
21m00s
11h20m50s
53°13'00"
12'00"
11'00"
10'00"
09'00"
08'00"
5 kpc
VF
Hα
σ
Res
km s−1
Radius (kpc)
Rotation Velocity (kms−1)
Radius (arcsec)
HRS048

HRS048

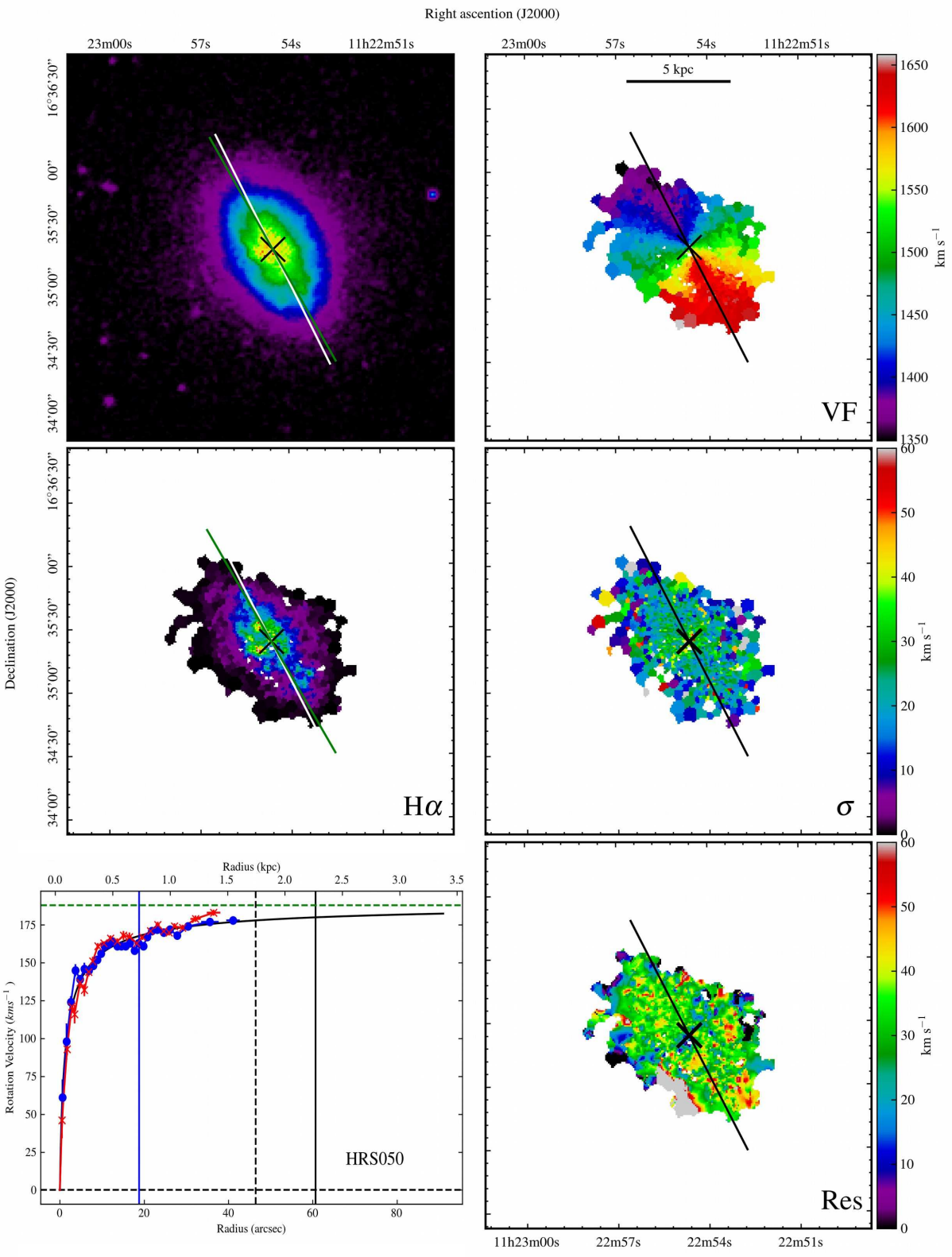
Right ascention (J2000)
23m00s
57s
54s
11h22m51s
Declination (J2000)
16°36'30"
00"
35'30"
35'00"
34'30"
34'00"
5 kpc
VF
Hα
σ
Res
km s⁻¹
1650
1600
1550
1500
1450
1400
1350
60
50
40
30
20
10
0
Radius (kpc)
0.0
0.5
1.0
1.5
2.0
2.5
3.0
3.5
Rotation Velocity (kms⁻¹)
175
150
125
100
75
50
25
0
Radius (arcsec)
0
20
40
60
80
HRS050
11h23m00s
22m57s
22m54s
22m51s

HRS050

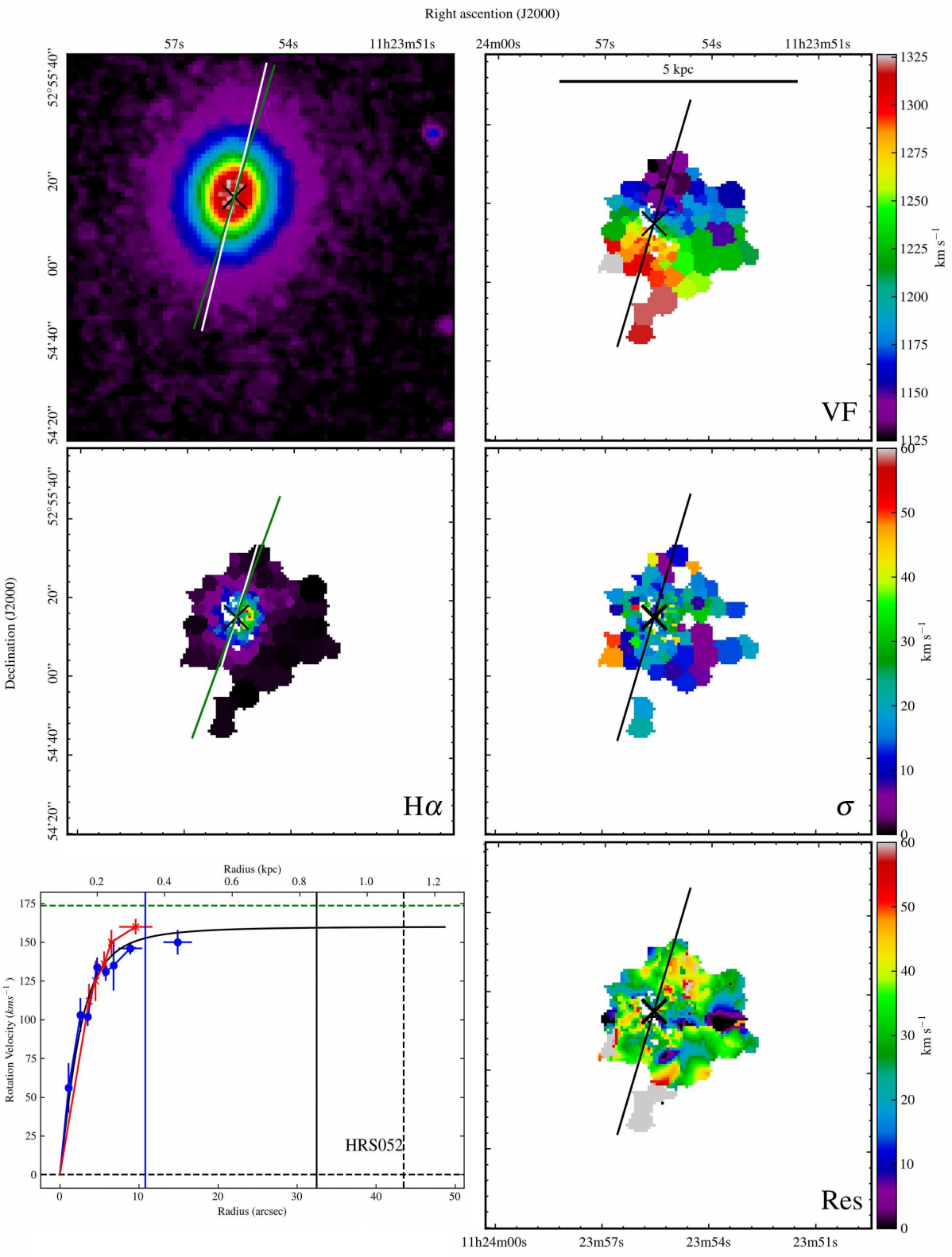
Right ascention (J2000)
Declination (J2000)
5 kpc
VF
Hα
σ
Res
km s⁻¹
Radius (kpc)
Radius (arcsec)
Rotation Velocity (kms⁻¹)
HRS052

HRS052

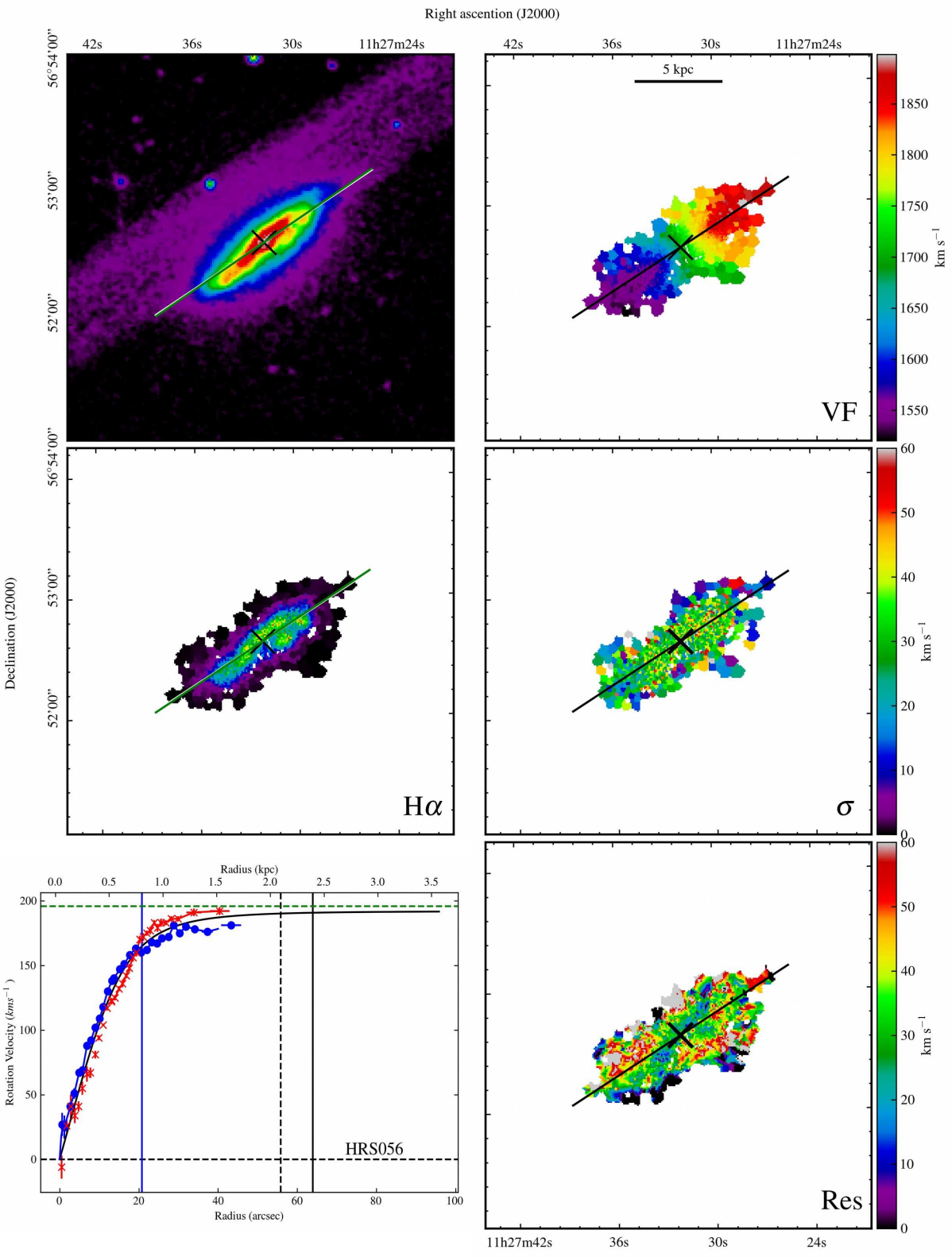
Right ascention (J2000)
42s
36s
30s
11h27m24s
56°54'00"
53'00"
52'00"
Declination (J2000)
5 kpc
VF
Hα
σ
Res
km s⁻¹
1850
1800
1750
1700
1650
1600
1550
60
50
40
30
20
10
0
Radius (kpc)
0.0
0.5
1.0
1.5
2.0
2.5
3.0
3.5
Rotation Velocity (kms⁻¹)
200
150
100
50
0
HRS056
Radius (arcsec)
0
20
40
60
80
100
11h27m42s
36s
30s
24s

HRS056

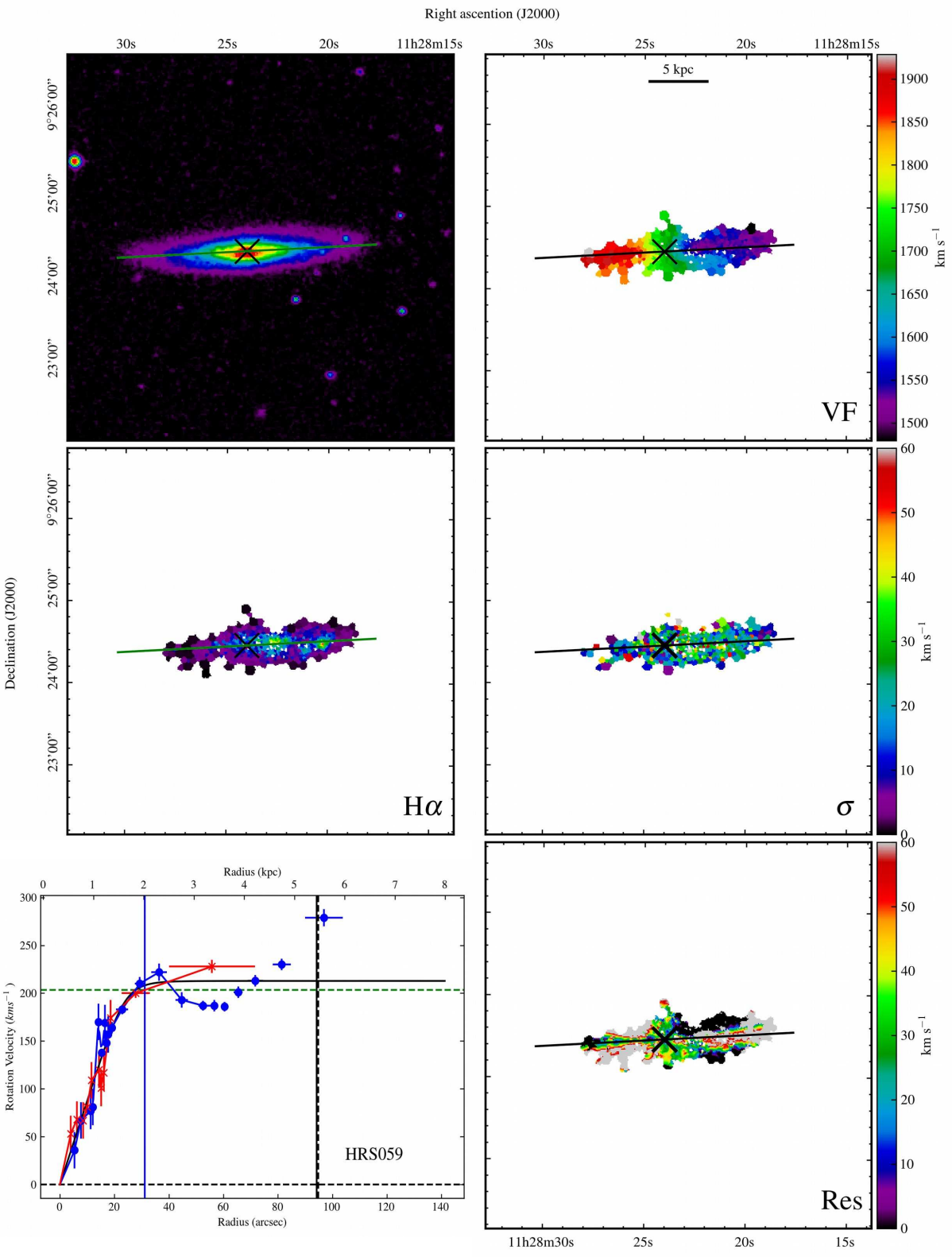
Right ascention (J2000)
30s
25s
20s
11h28m15s
Declination (J2000)
9°26'00"
25'00"
24'00"
23'00"
5 kpc
VF
Hα
σ
Res
km s⁻¹
Radius (kpc)
Rotation Velocity (kms⁻¹)
Radius (arcsec)
HRS059
11h28m30s
15s

HRS059

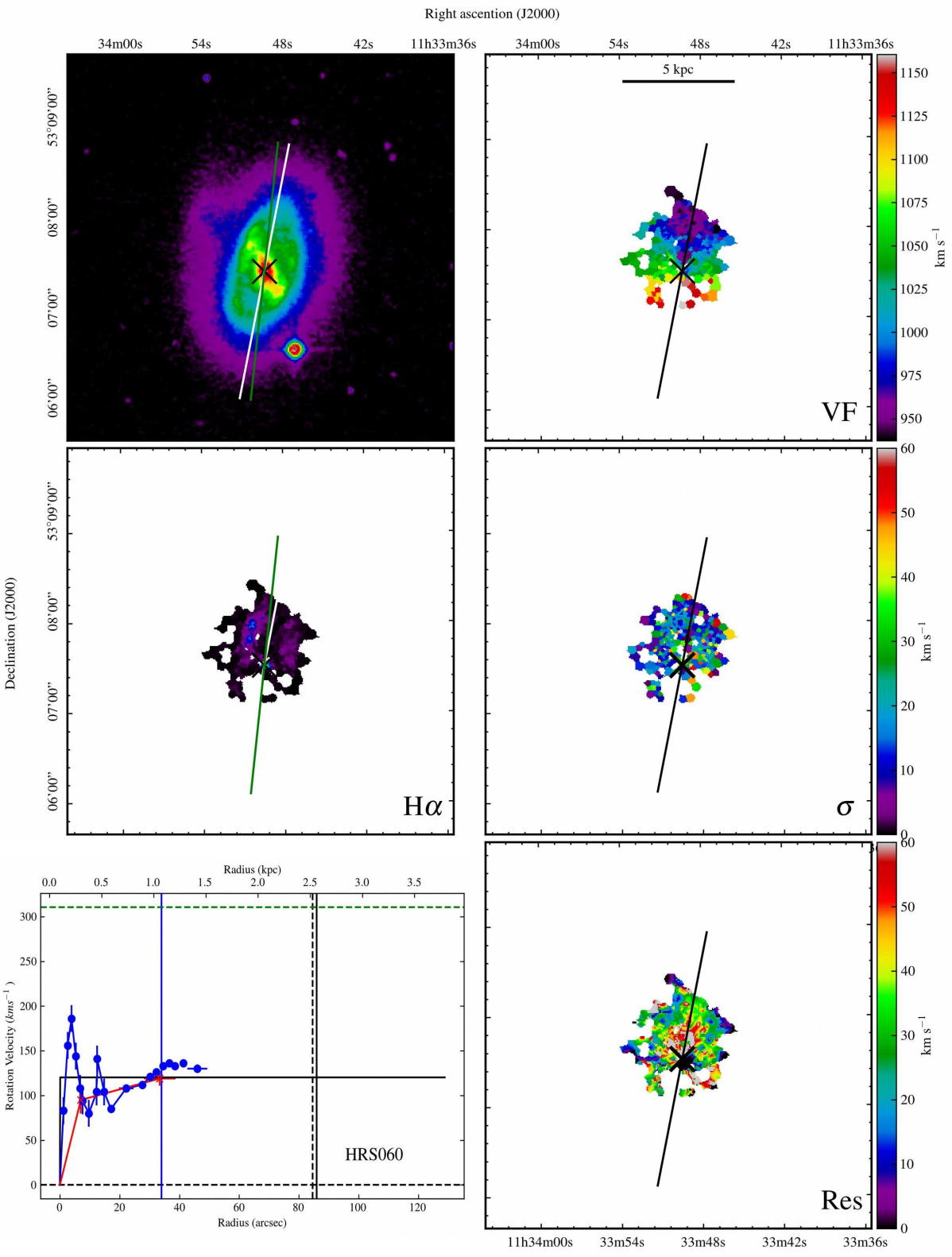
Right ascention (J2000)
34m00s
54s
48s
42s
11h33m36s
53°09'00"
08'00"
07'00"
06'00"
Declination (J2000)
5 kpc
VF
Hα
σ
Res
km s⁻¹
Radius (kpc)
Rotation Velocity (kms⁻¹)
Radius (arcsec)
HRS060
11h34m00s
33m54s
33m48s
33m42s
33m36s

HRS060

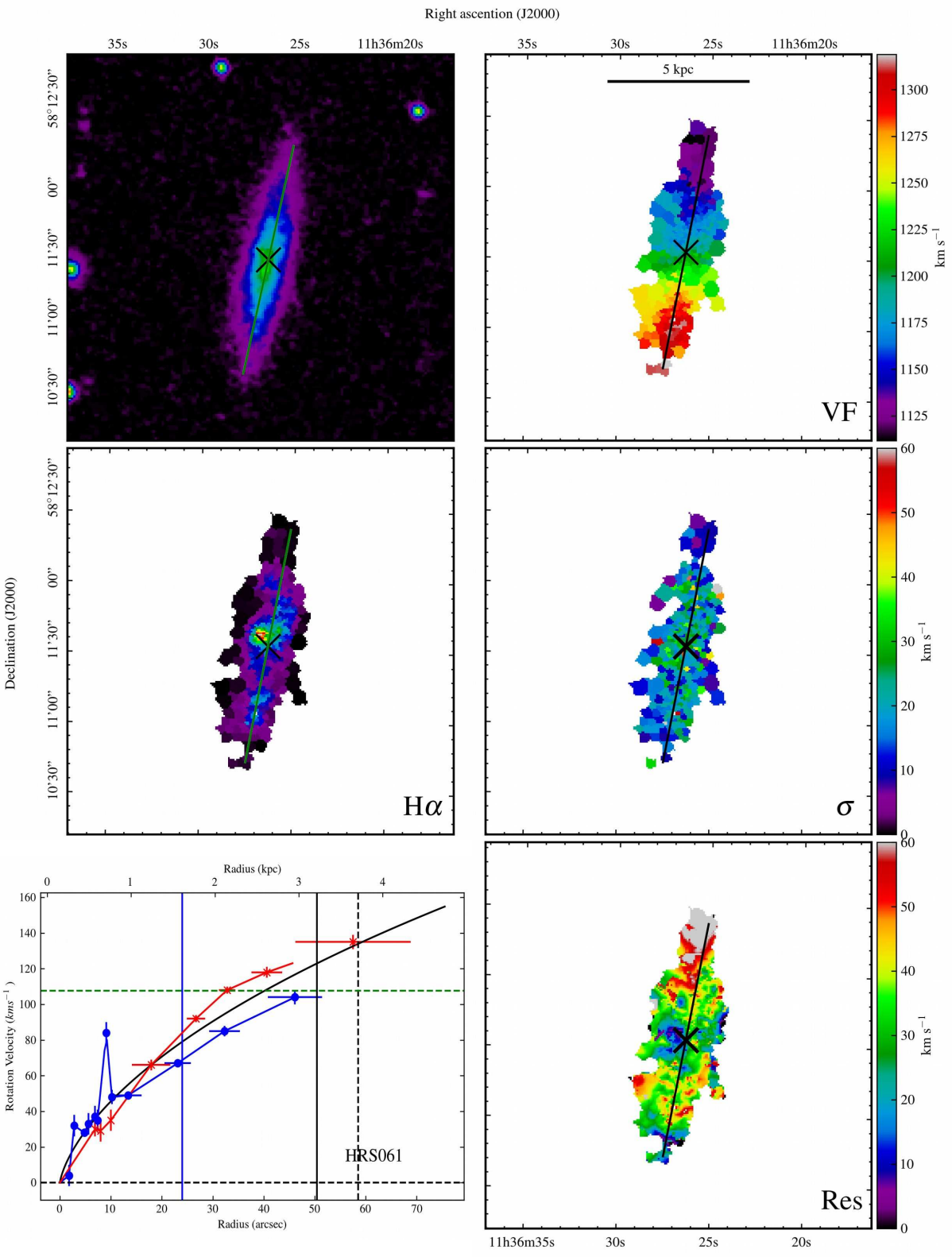
Right ascention (J2000)
35s
30s
25s
11h36m20s
58°12'30"
00"
11'30"
11'00"
10'30"
Declination (J2000)
5 kpc
VF
Hα
σ
Res
km s⁻¹
1300
1275
1250
1225
1200
1175
1150
1125
60
50
40
30
20
10
0
11h36m35s
30s
25s
20s
Radius (kpc)
0
1
2
3
4
Rotation Velocity (kms⁻¹)
160
140
120
100
80
60
40
20
0
0
10
20
30
40
50
60
70
Radius (arcsec)
HRS061

HRS061

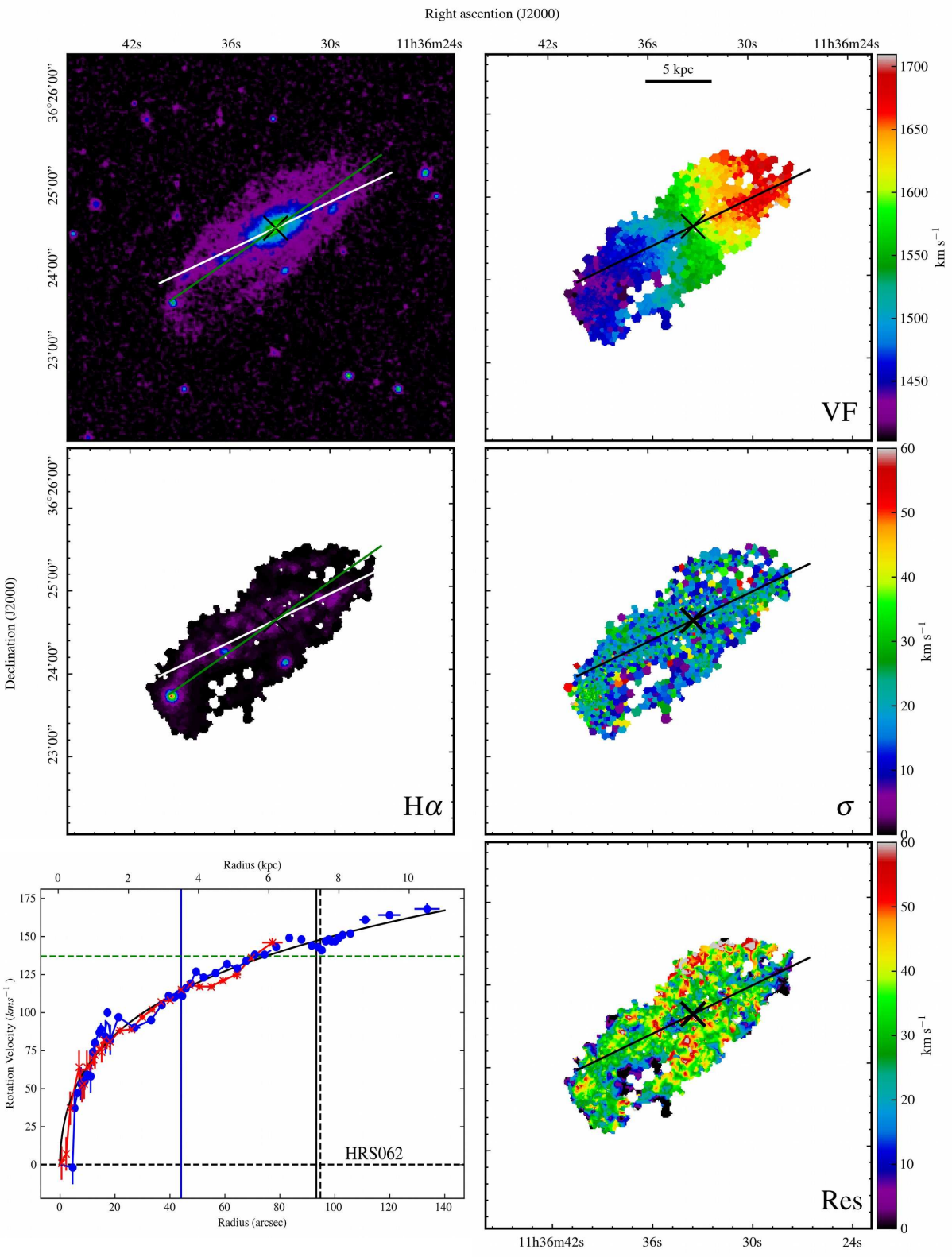
Right ascention (J2000)
42s
36s
30s
11h36m24s
Declination (J2000)
36°26'00"
25'00"
24'00"
23'00"
5 kpc
VF
Hα
σ
Res
km s⁻¹
Radius (kpc)
Rotation Velocity (kms⁻¹)
Radius (arcsec)
HRS062
11h36m42s
24s

HRS062

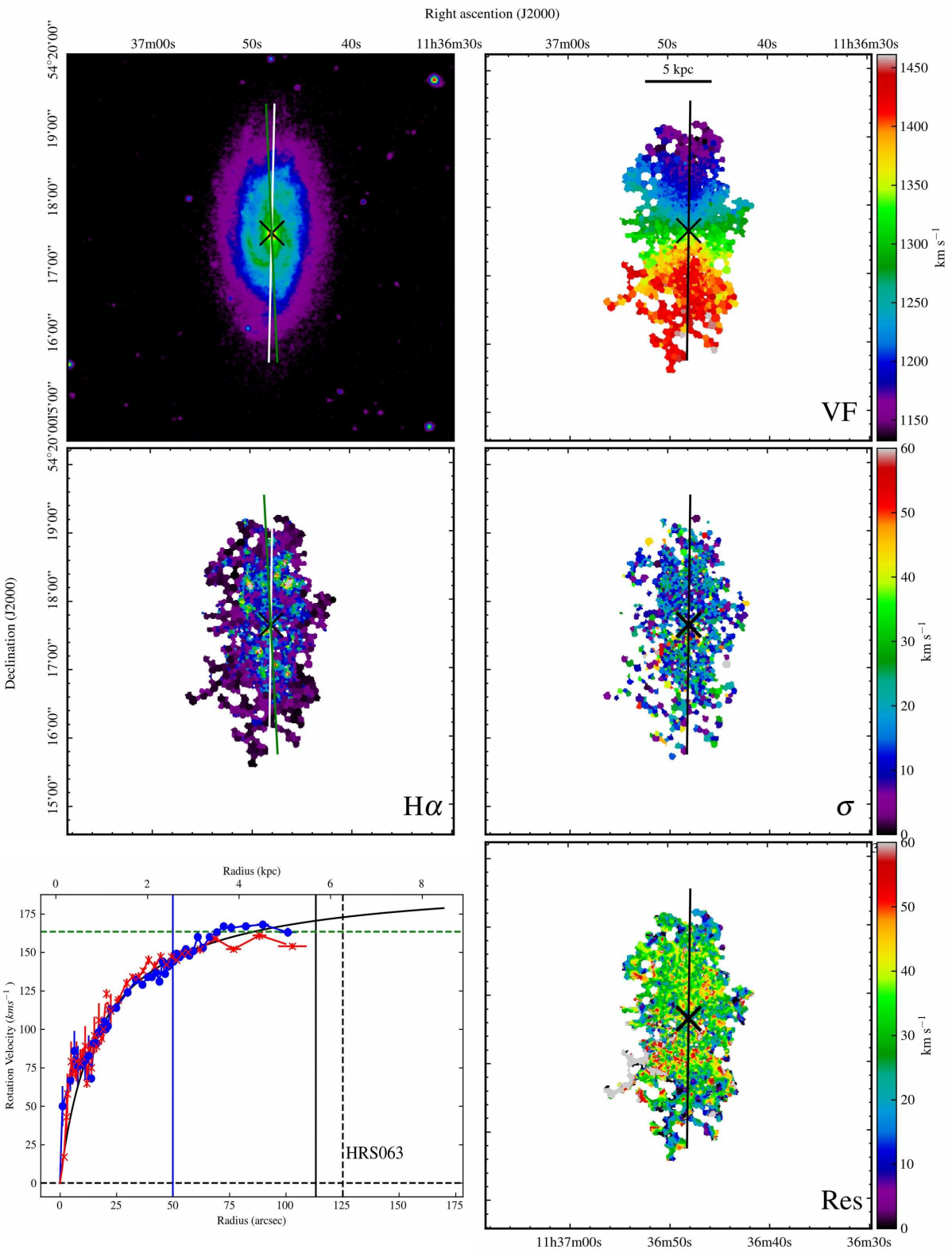
Right ascention (J2000)
37m00s
50s
40s
11h36m30s
54°20'00"
19'00"
18'00"
17'00"
16'00"
15'00"
Declination (J2000)
5 kpc
VF
Hα
σ
Res
km s⁻¹
1450
1400
1350
1300
1250
1200
1150
60
50
40
30
20
10
0
11h37m00s
36m50s
36m40s
36m30s
Radius (kpc)
0
2
4
6
8
Rotation Velocity (kms⁻¹)
175
150
125
100
75
50
25
0
HRS063
Radius (arcsec)
0
25
50
75
100
125
150
175

HRS063

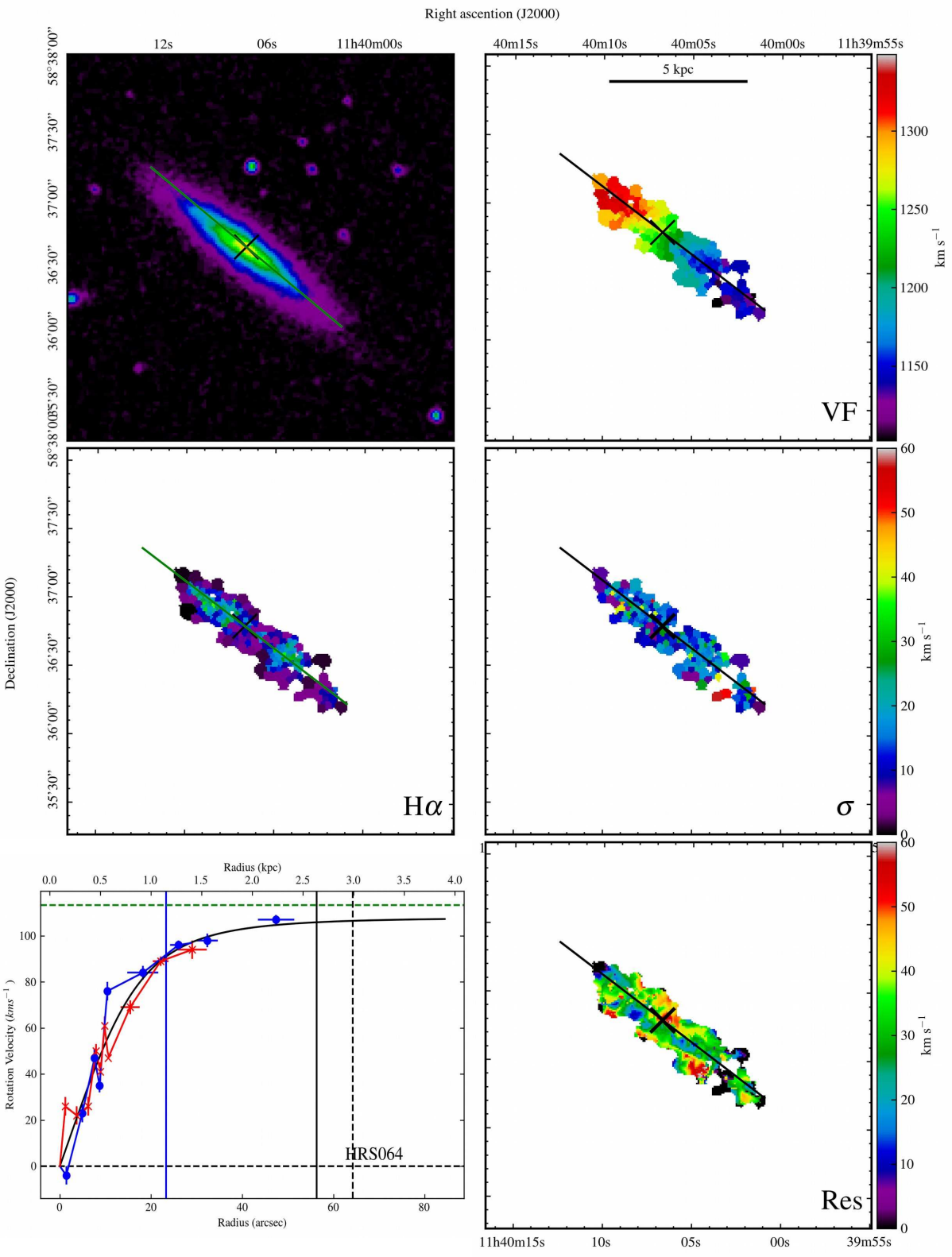
Right ascention (J2000)
12s
06s
11h40m00s
40m15s
40m10s
40m05s
40m00s
11h39m55s
5 kpc
VF
Hα
σ
Res
Declination (J2000)
km s^{-1}
Radius (kpc)
Rotation Velocity (kms^{-1})
Radius (arcsec)
HRS064
11h40m15s
10s
05s
00s
39m55s

HRS064

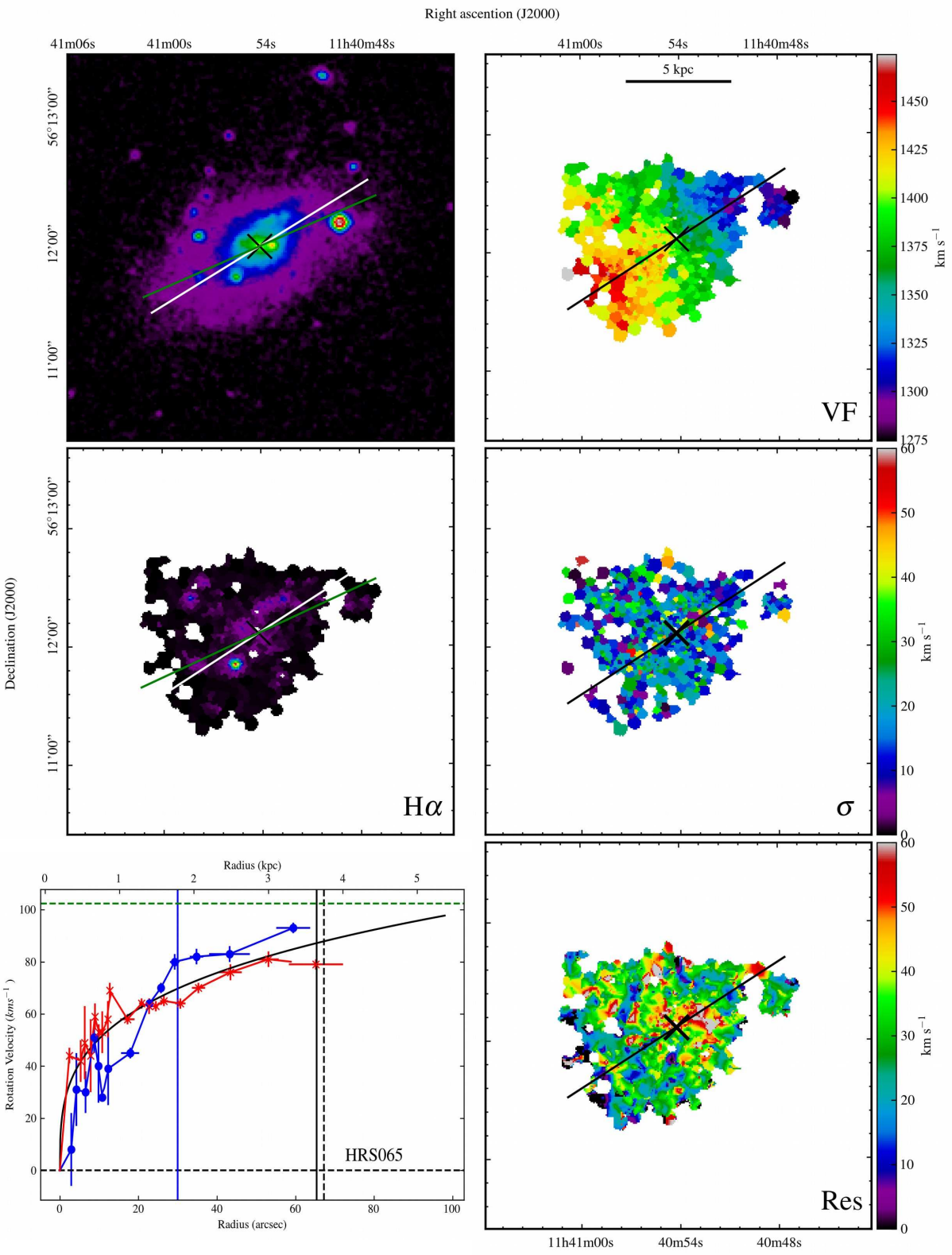
Right ascention (J2000)
41m06s
41m00s
54s
11h40m48s
56°13'00"
12'00"
11'00"
Declination (J2000)
5 kpc
VF
Hα
σ
Res
km s⁻¹
Radius (kpc)
Rotation Velocity (kms⁻¹)
Radius (arcsec)
HRS065
11h41m00s
40m54s
40m48s

HRS065

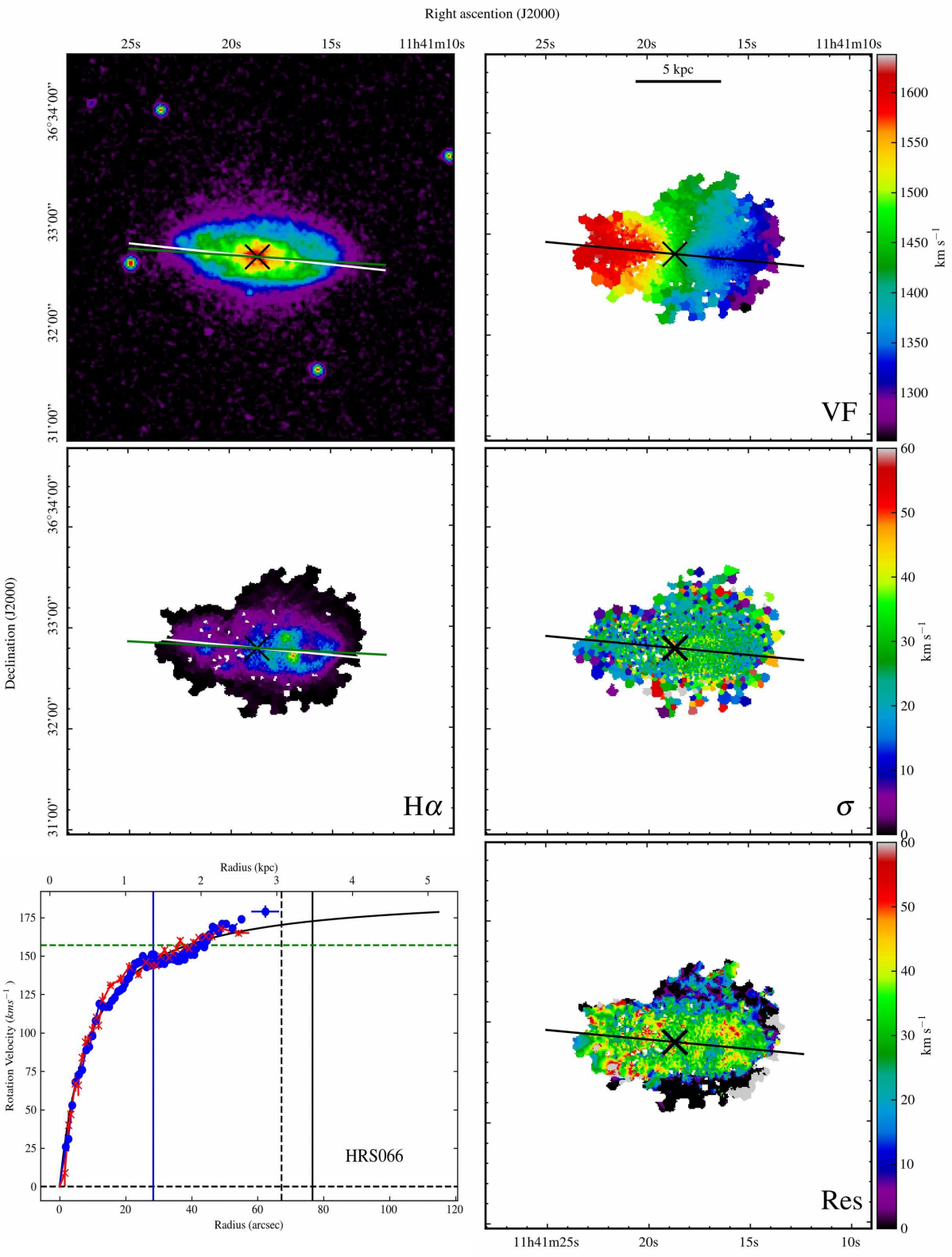
Right ascention (J2000)
25s
20s
15s
11h41m10s
Declination (J2000)
36°34'00"
33'00"
32'00"
31'00"
5 kpc
VF
Hα
σ
Res
km s⁻¹
Radius (kpc)
Rotation Velocity (kms⁻¹)
Radius (arcsec)
HRS066
11h41m25s
10s

HRS066

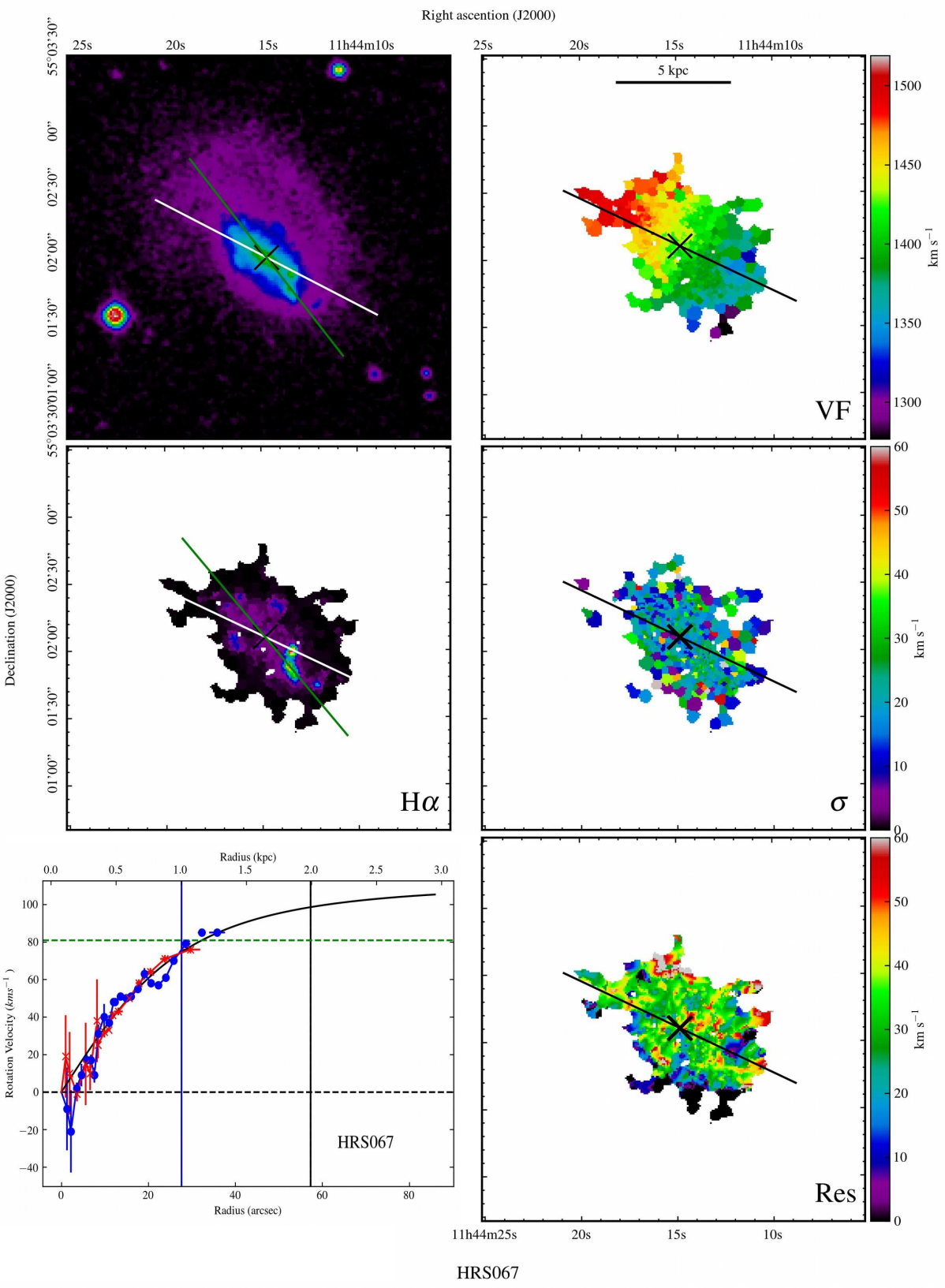
Right ascention (J2000)
25s
20s
15s
11h44m10s
55°03'30"
00"
02'30"
02'00"
01'30"
01'00"
Declination (J2000)
5 kpc
VF
Hα
σ
Res
km s⁻¹
1500
1450
1400
1350
1300
60
50
40
30
20
10
0
11h44m25s
10s
Radius (kpc)
0.0
0.5
1.0
1.5
2.0
2.5
3.0
Rotation Velocity (kms⁻¹)
100
80
60
40
20
0
−20
−40
Radius (arcsec)
HRS067

HRS067

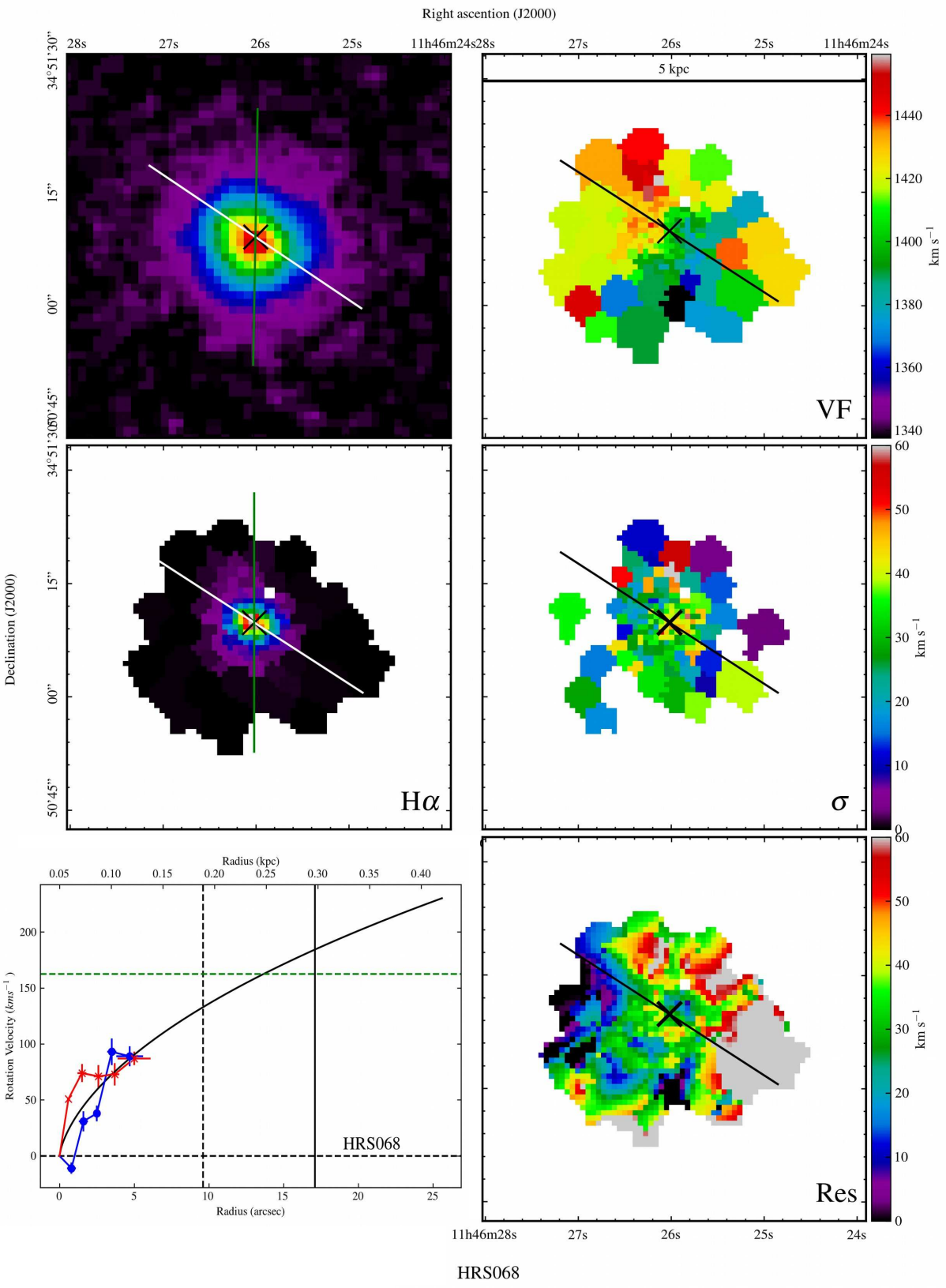
Right ascention (J2000)
Declination (J2000)
5 kpc
VF
Hα
σ
Res
km s−1
Radius (kpc)
Radius (arcsec)
Rotation Velocity (kms−1)
HRS068

HRS068

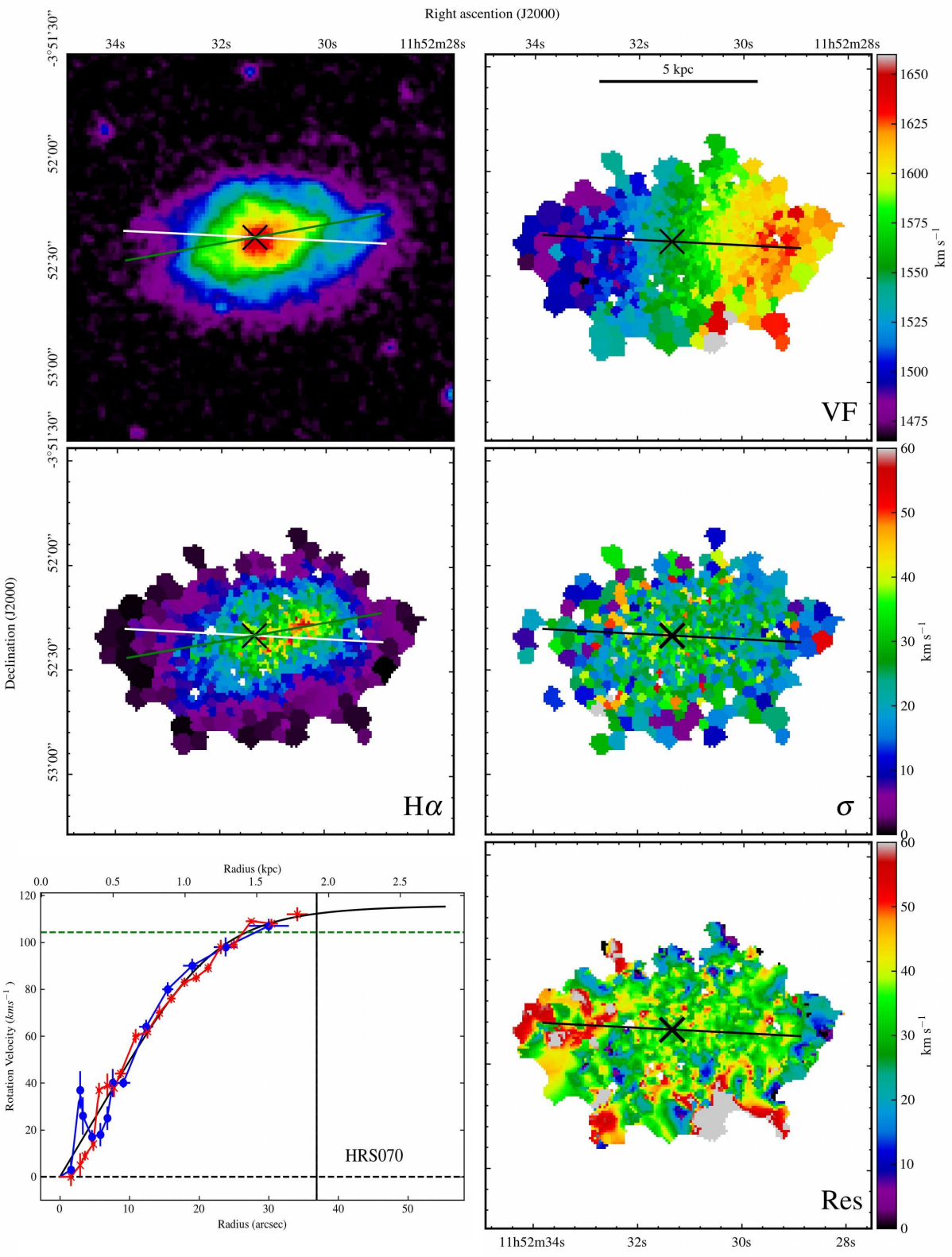
Right ascention (J2000)
Declination (J2000)
34s
32s
30s
11h52m28s
-3°51'30"
52'00"
52'30"
53'00"
5 kpc
VF
Hα
σ
Res
km s⁻¹
Radius (kpc)
Rotation Velocity (kms⁻¹)
Radius (arcsec)
HRS070
11h52m34s
28s

HRS070

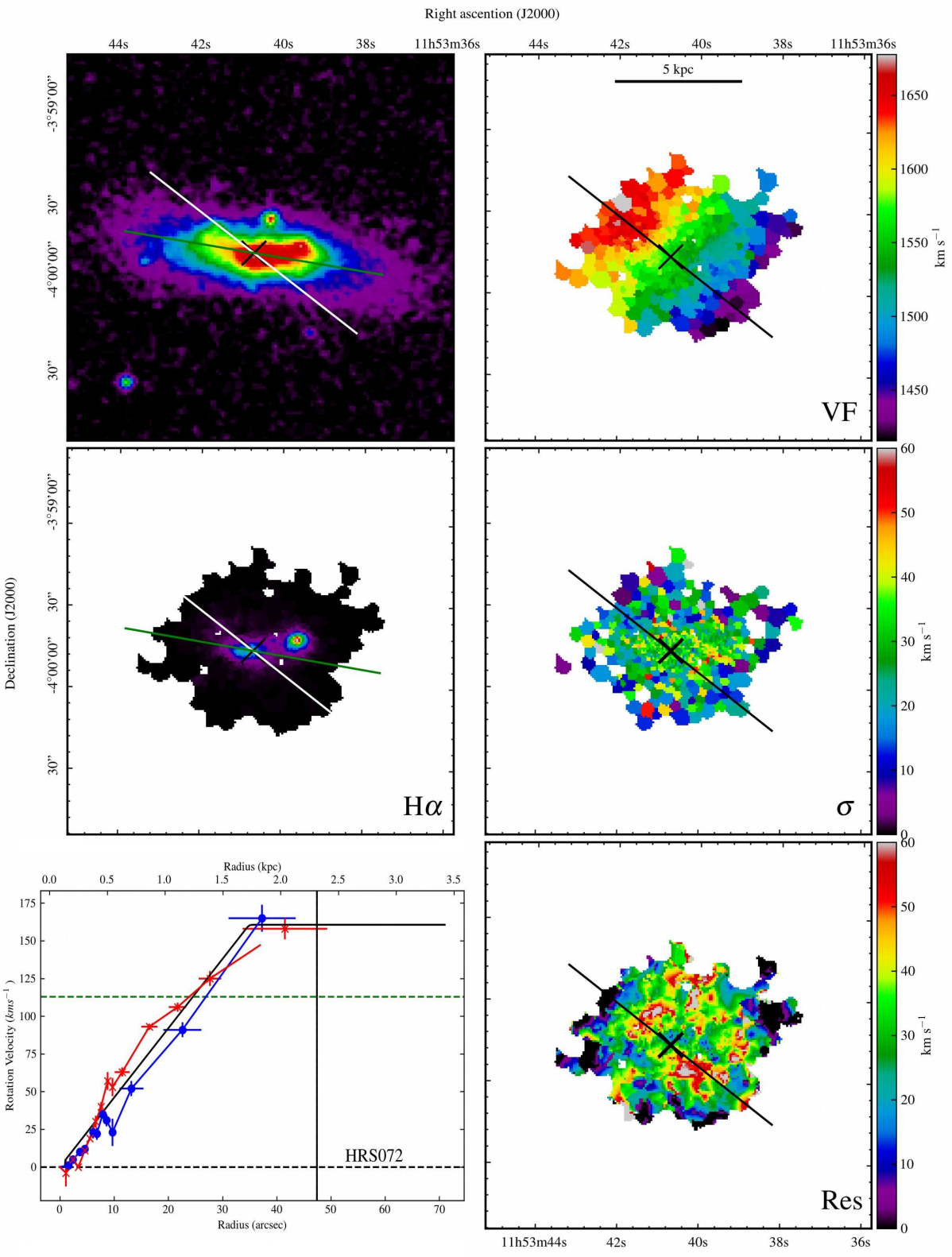
Right ascention (J2000)
44s
42s
40s
38s
11h53m36s
Declination (J2000)
-3°59'00"
-4°00'00"
30"
5 kpc
VF
Hα
σ
Res
km s^{-1}
1650
1600
1550
1500
1450
60
50
40
30
20
10
0
11h53m44s
36s
Radius (kpc)
Rotation Velocity (kms^{-1})
Radius (arcsec)
HRS072

HRS072

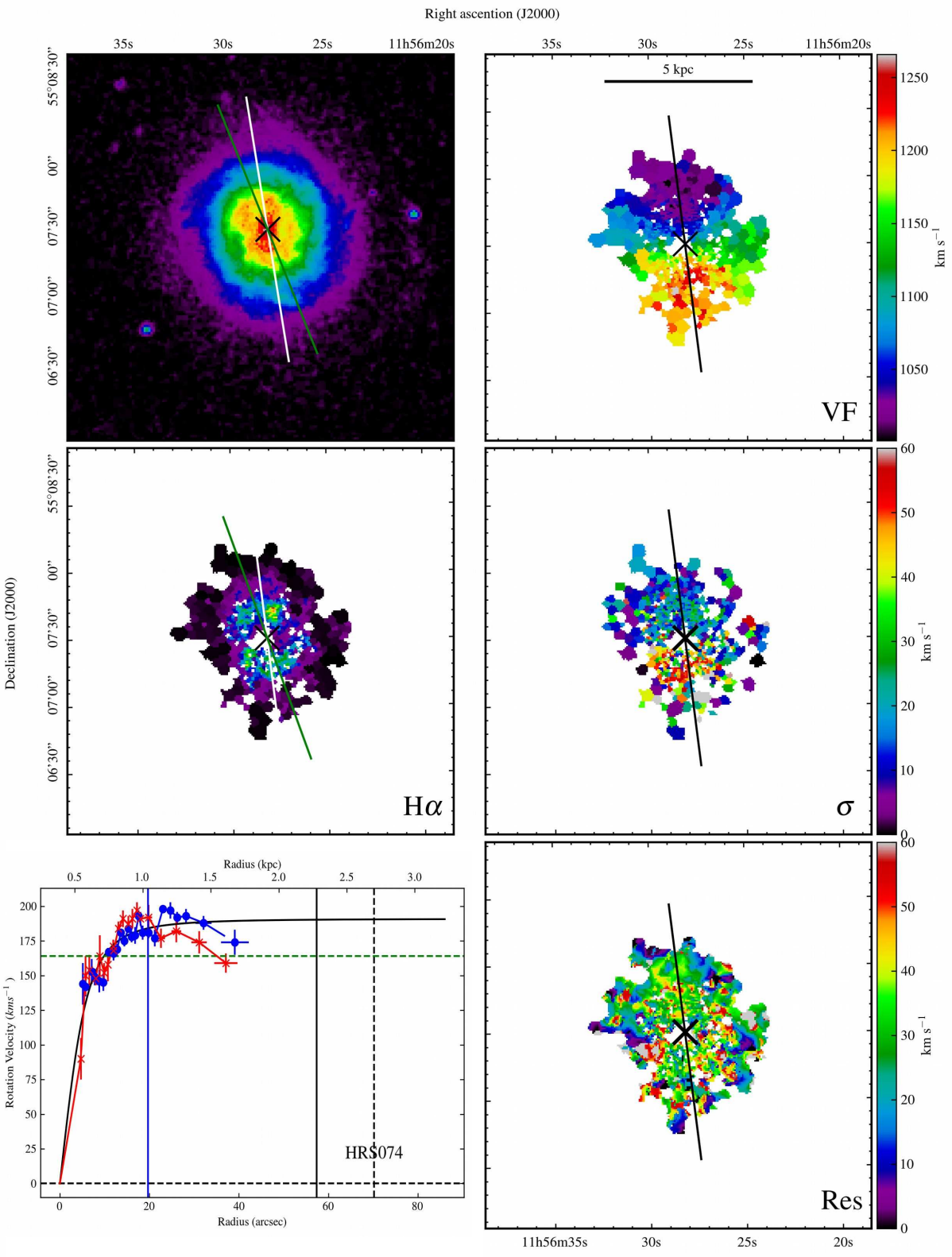
Right ascention (J2000)
35s
30s
25s
11h56m20s
55°08'30"
00"
07'30"
07'00"
06'30"
Declination (J2000)
5 kpc
VF
Hα
σ
Res
km s⁻¹
Radius (kpc)
Rotation Velocity (kms⁻¹)
Radius (arcsec)
HRS074
11h56m35s
20s

HRS074

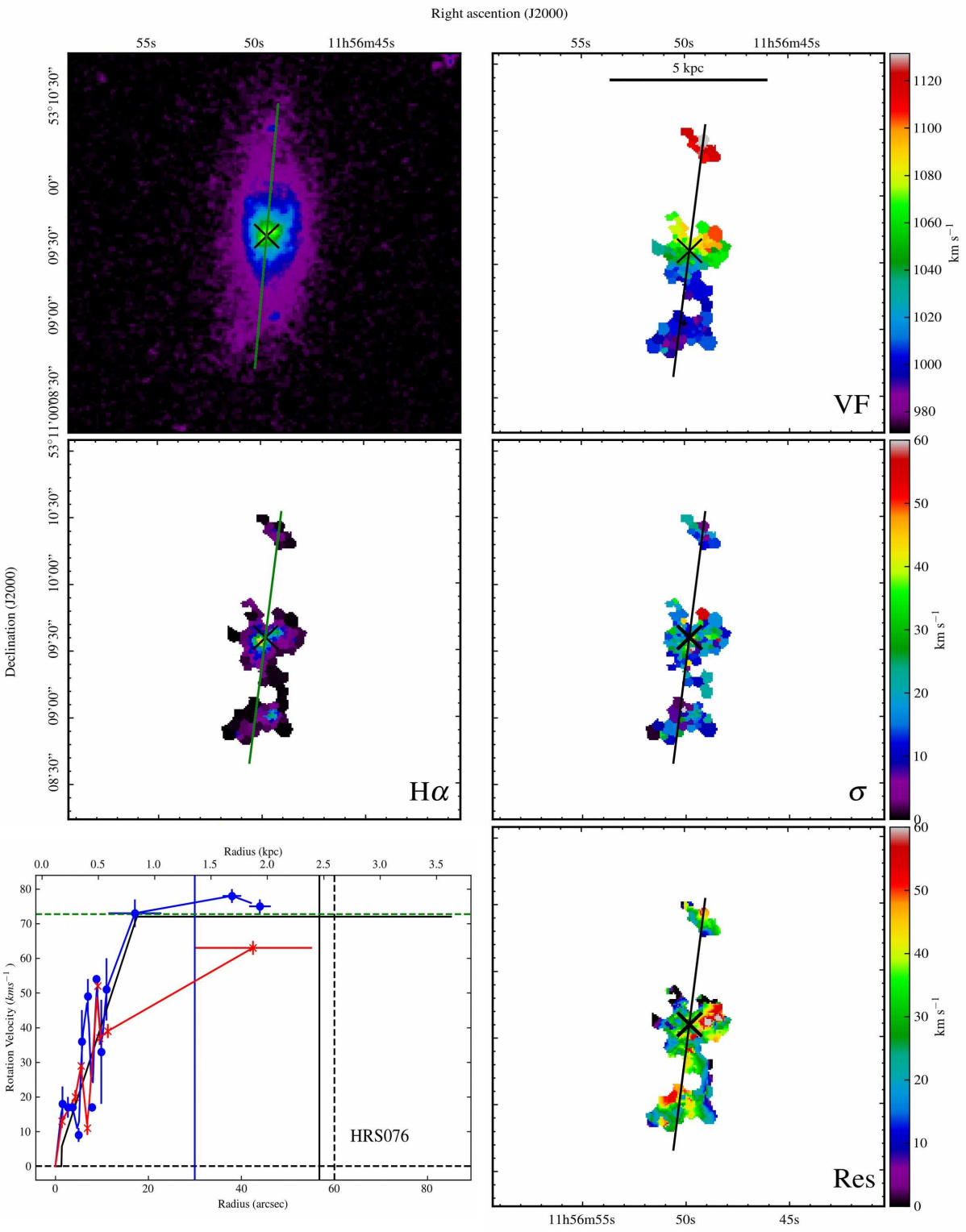
Right ascention (J2000)
55s
50s
11h56m45s
Declination (J2000)
53°10'30"
00"
09'30"
09'00"
08'30"
53°11'00"
10'30"
10'00"
09'30"
09'00"
08'30"
5 kpc
VF
Hα
σ
Res
km s−1
1120
1100
1080
1060
1040
1020
1000
980
60
50
40
30
20
10
0
11h56m55s
50s
45s
Radius (kpc)
0.0
0.5
1.0
1.5
2.0
2.5
3.0
3.5
Rotation Velocity (kms−1)
80
70
60
50
40
30
20
10
0
Radius (arcsec)
0
20
40
60
80
HRS076

HRS076

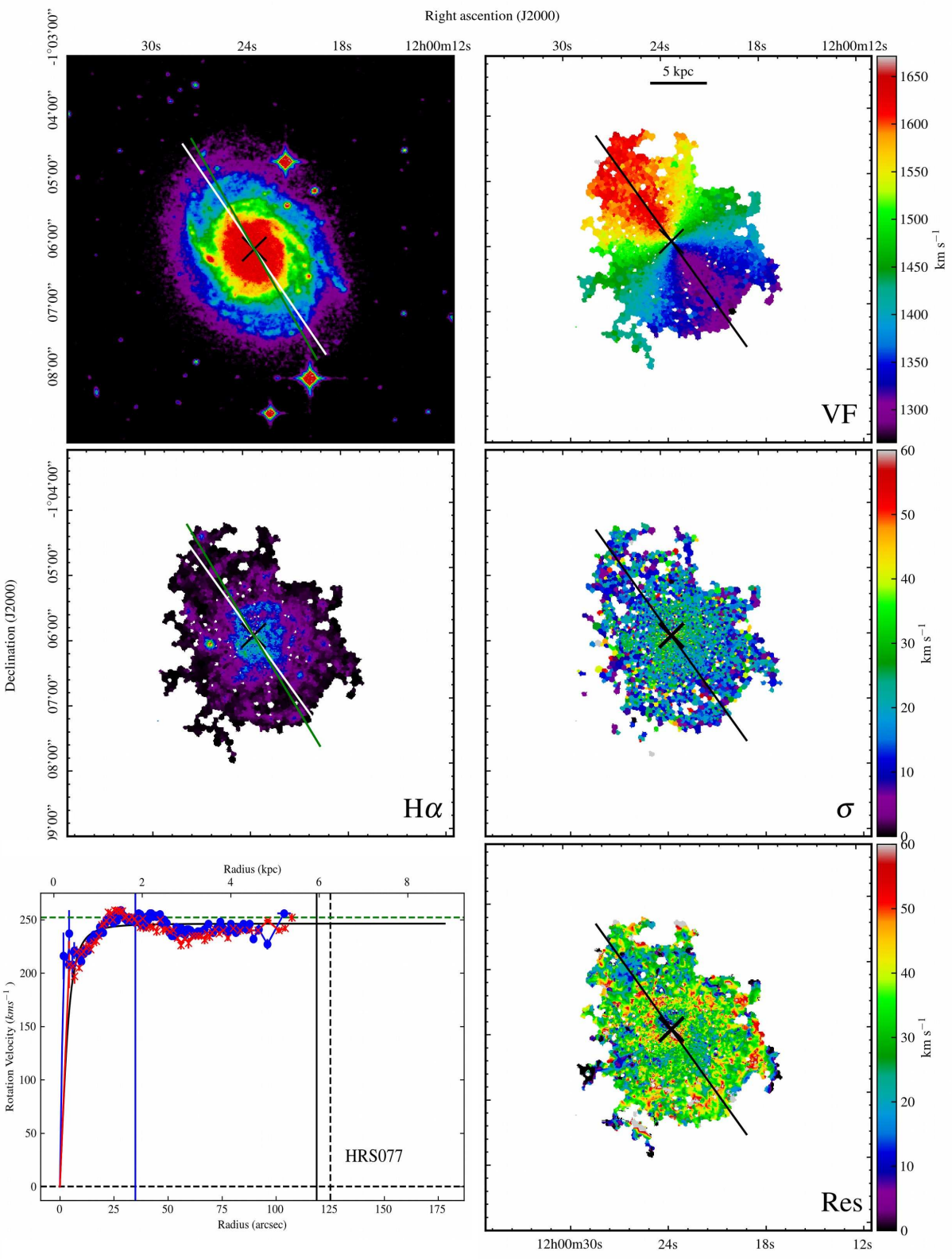
Right ascention (J2000)
Declination (J2000)
5 kpc
VF
Hα
σ
Res
km s⁻¹
Radius (kpc)
Rotation Velocity (kms⁻¹)
Radius (arcsec)
HRS077

HRS077

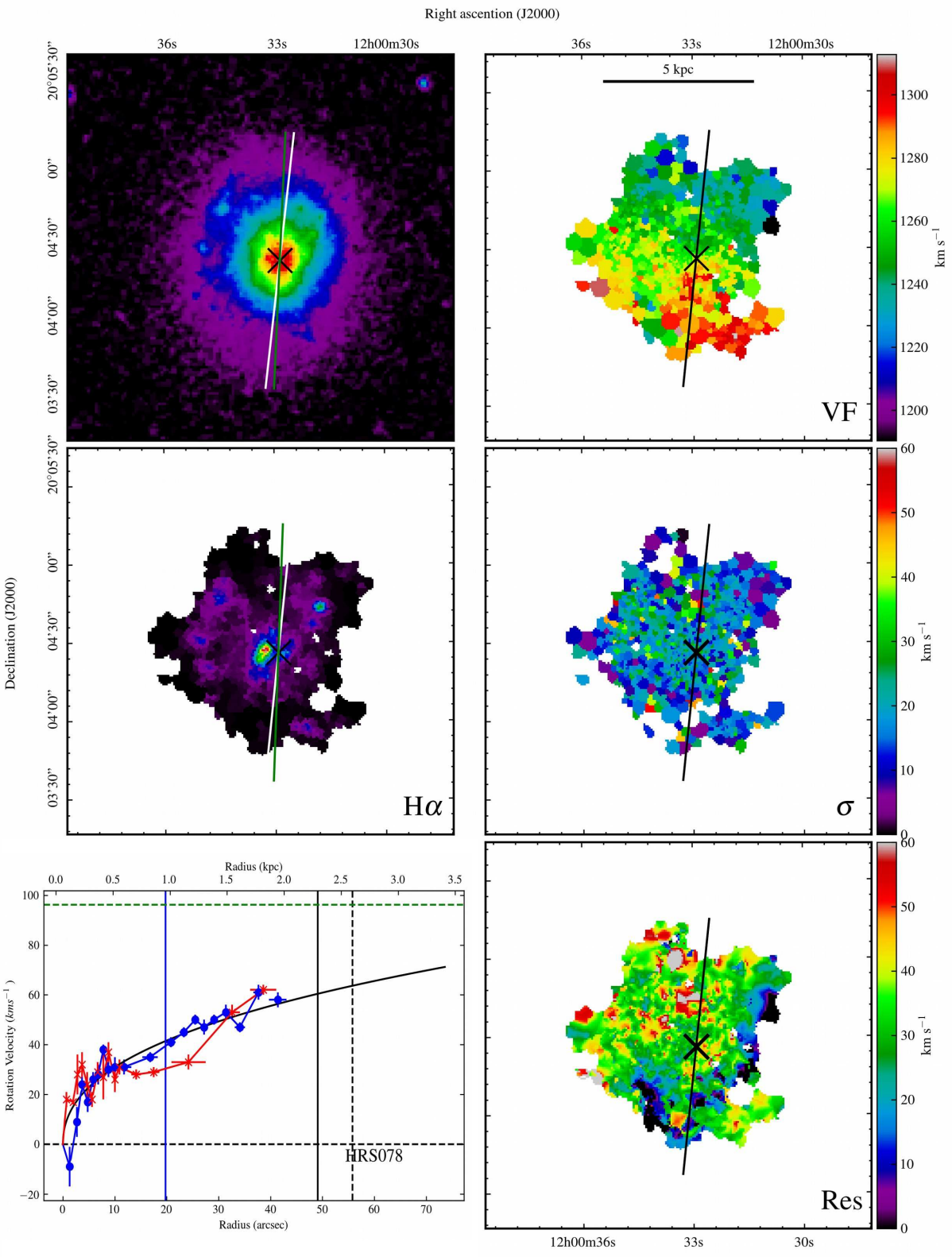
Right ascention (J2000)
36s
33s
12h00m30s
20°05'30"
00"
04'30"
04'00"
03'30"
Declination (J2000)
5 kpc
VF
Hα
σ
Res
km s⁻¹
1300
1280
1260
1240
1220
1200
60
50
40
30
20
10
0
Radius (kpc)
0.0
0.5
1.0
1.5
2.0
2.5
3.0
3.5
Rotation Velocity (kms⁻¹)
100
80
60
40
20
0
−20
HRS078
Radius (arcsec)
0
10
20
30
40
50
60
70
12h00m36s
33s
30s

HRS078

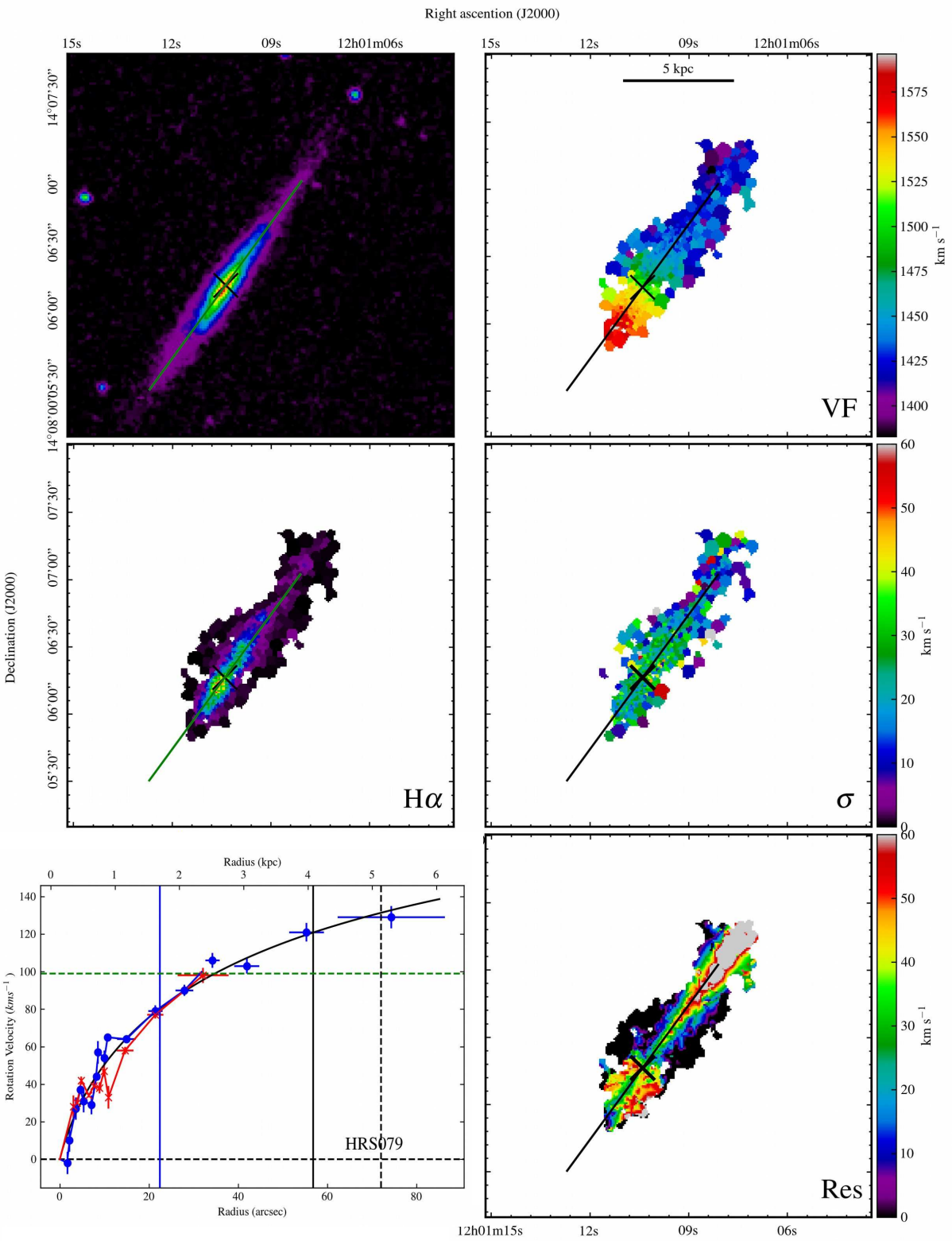
Right ascention (J2000)
15s
12s
09s
12h01m06s
12h01m15s
06s
Declination (J2000)
14°07'30"
00"
06'30"
06'00"
05'30"
14°08'00"
07'30"
07'00"
06'30"
06'00"
05'30"
5 kpc
VF
Hα
σ
Res
km s^{-1}
1575
1550
1525
1500
1475
1450
1425
1400
60
50
40
30
20
10
0
Radius (kpc)
0
1
2
3
4
5
6
Rotation Velocity (kms^{-1})
140
120
100
80
60
40
20
0
Radius (arcsec)
0
20
40
60
80
HRS079

HRS079

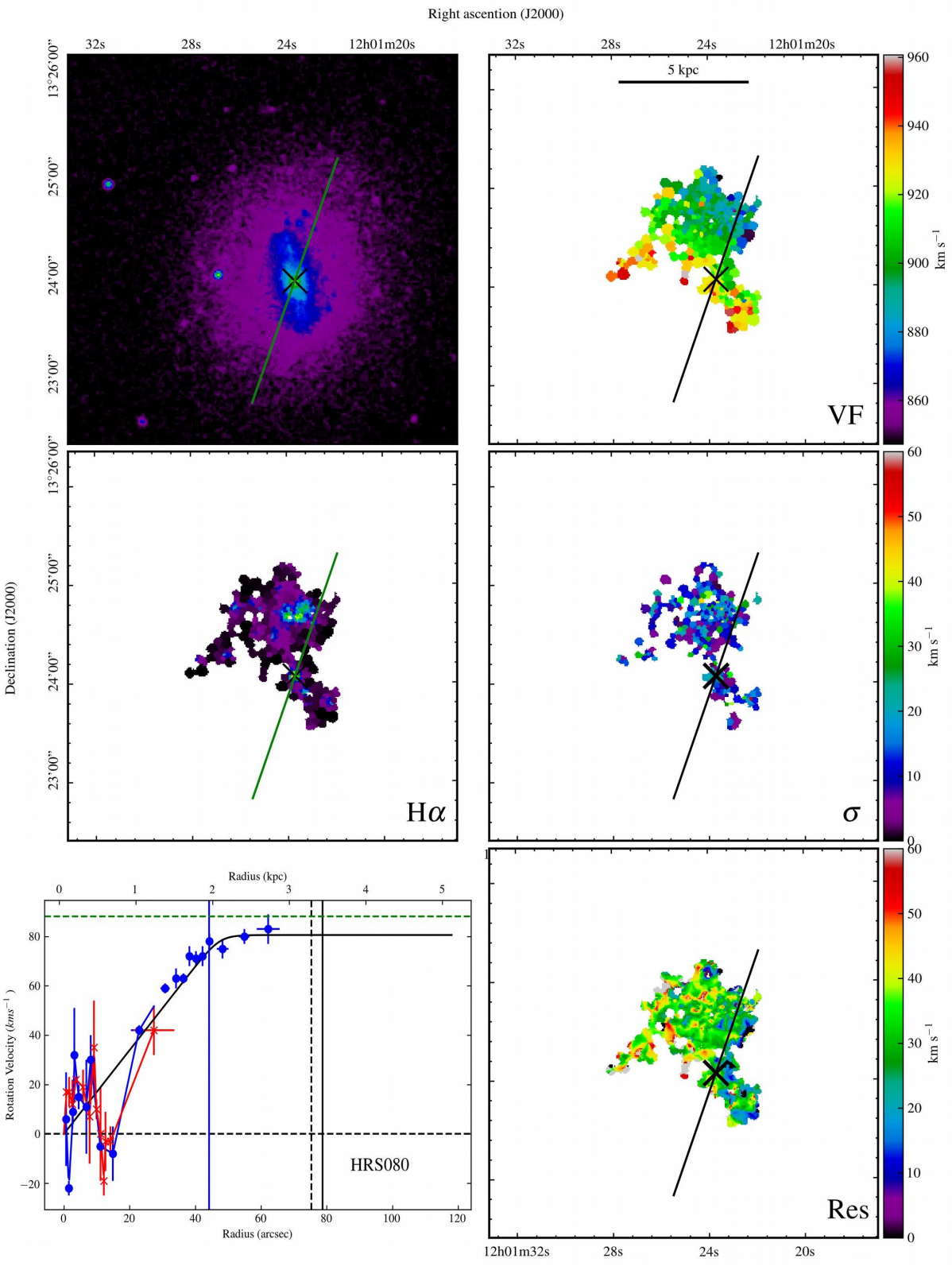
Right ascention (J2000)
32s
28s
24s
12h01m20s
13°26'00"
25'00"
24'00"
23'00"
Declination (J2000)
5 kpc
VF
Hα
σ
Res
km s−1
960
940
920
900
880
860
60
50
40
30
20
10
0
12h01m32s
28s
24s
20s
Radius (kpc)
0
1
2
3
4
5
Rotation Velocity (kms−1)
80
60
40
20
0
−20
HRS080
Radius (arcsec)
0
20
40
60
80
100
120

HRS080

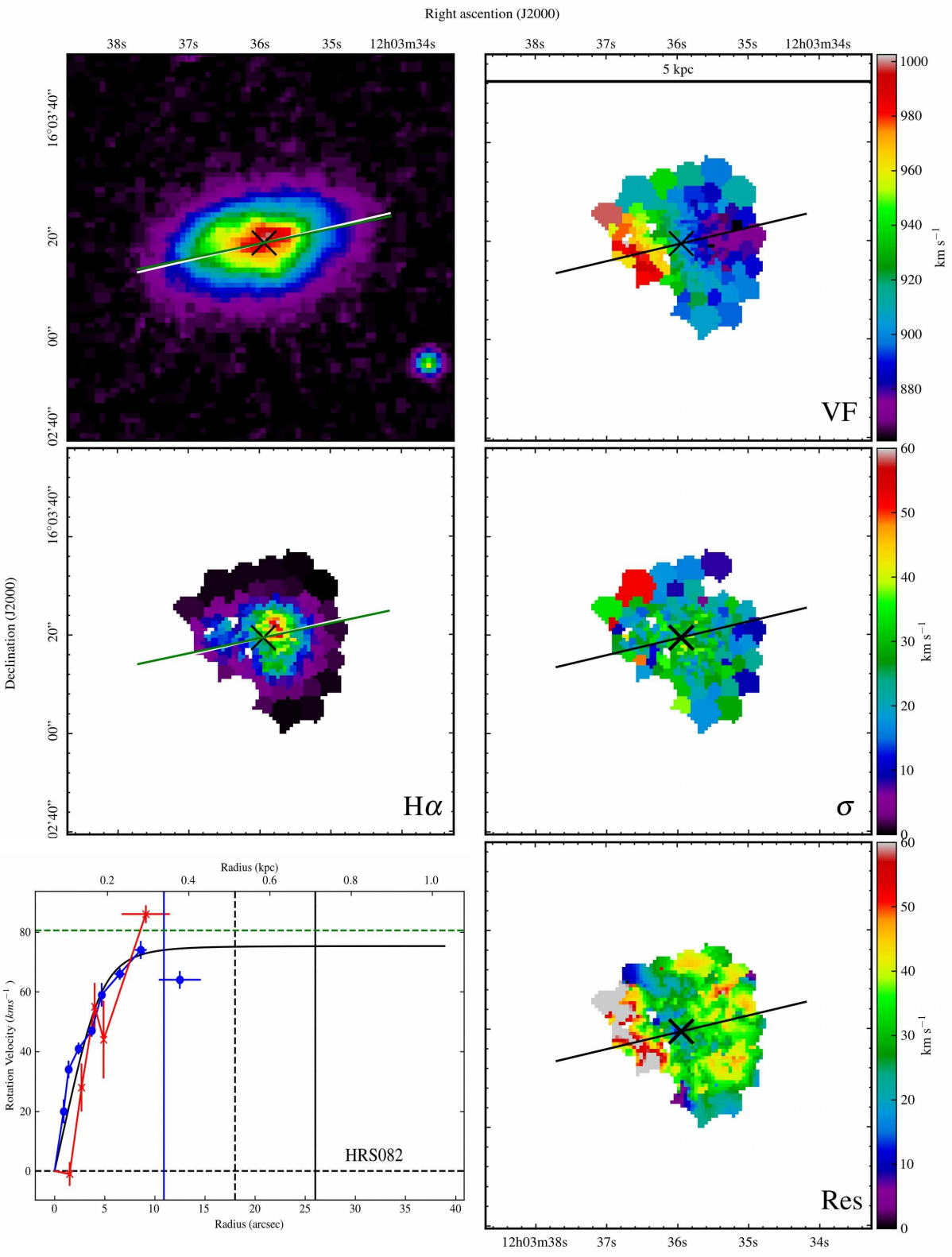
Right ascention (J2000)
Declination (J2000)
38s
37s
36s
35s
12h03m34s
16°03'40"
20"
00"
02'40"
5 kpc
1000
980
960
940
920
900
880
km s^{-1}
VF
Hα
σ
Res
60
50
40
30
20
10
0
12h03m38s
34s
Radius (kpc)
0.2
0.4
0.6
0.8
1.0
Rotation Velocity (kms^{-1})
80
60
40
20
0
HRS082
5
10
15
20
25
30
35
40
Radius (arcsec)

HRS082

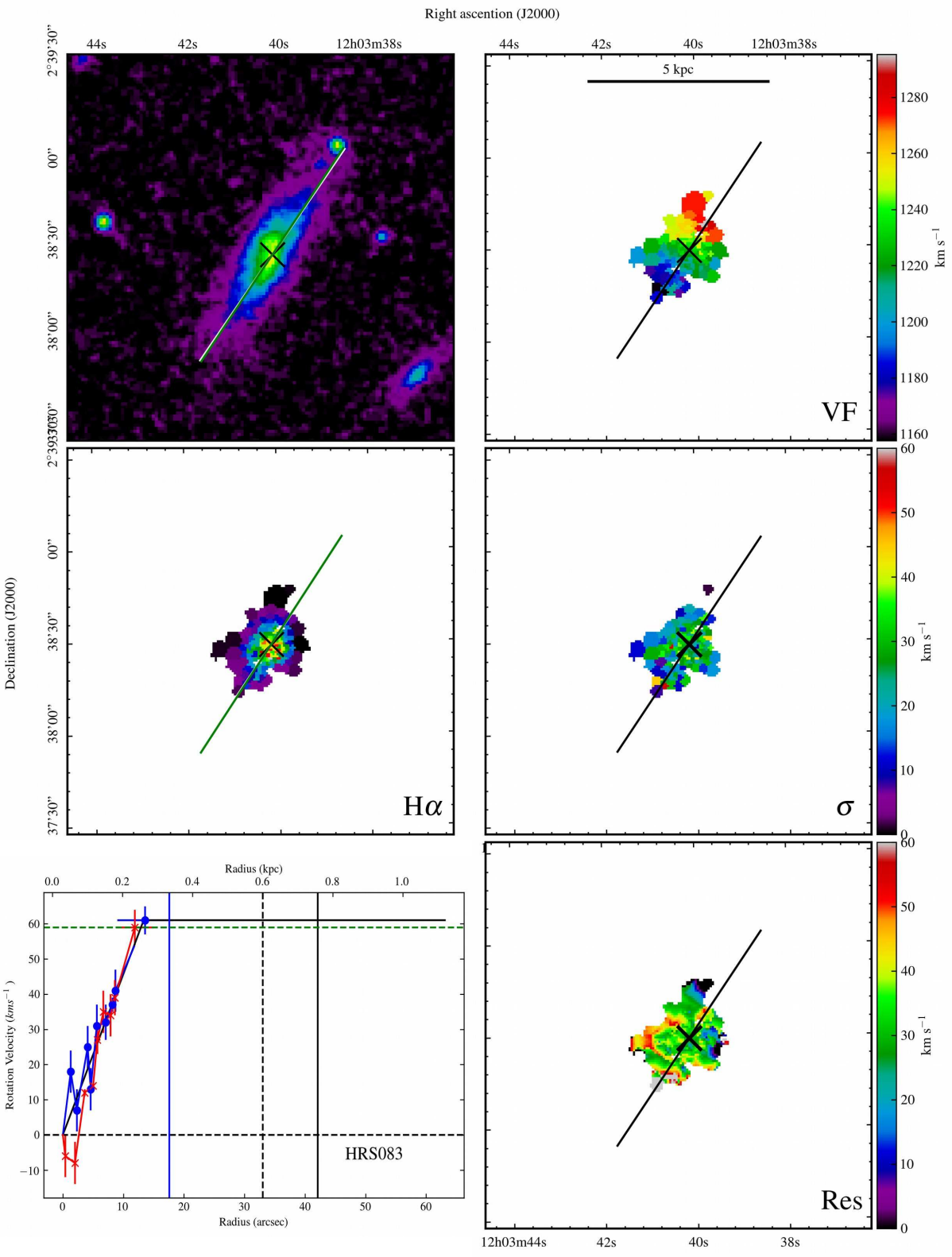
Right ascention (J2000)
44s
42s
40s
12h03m38s
2°39'30"
00"
38'30"
38'00"
37'30"
Declination (J2000)
5 kpc
VF
Hα
σ
Res
km s⁻¹
1280
1260
1240
1220
1200
1180
1160
60
50
40
30
20
10
0
12h03m44s
42s
40s
38s
Radius (kpc)
0.0
0.2
0.4
0.6
0.8
1.0
Rotation Velocity (kms⁻¹)
HRS083
Radius (arcsec)

HRS083

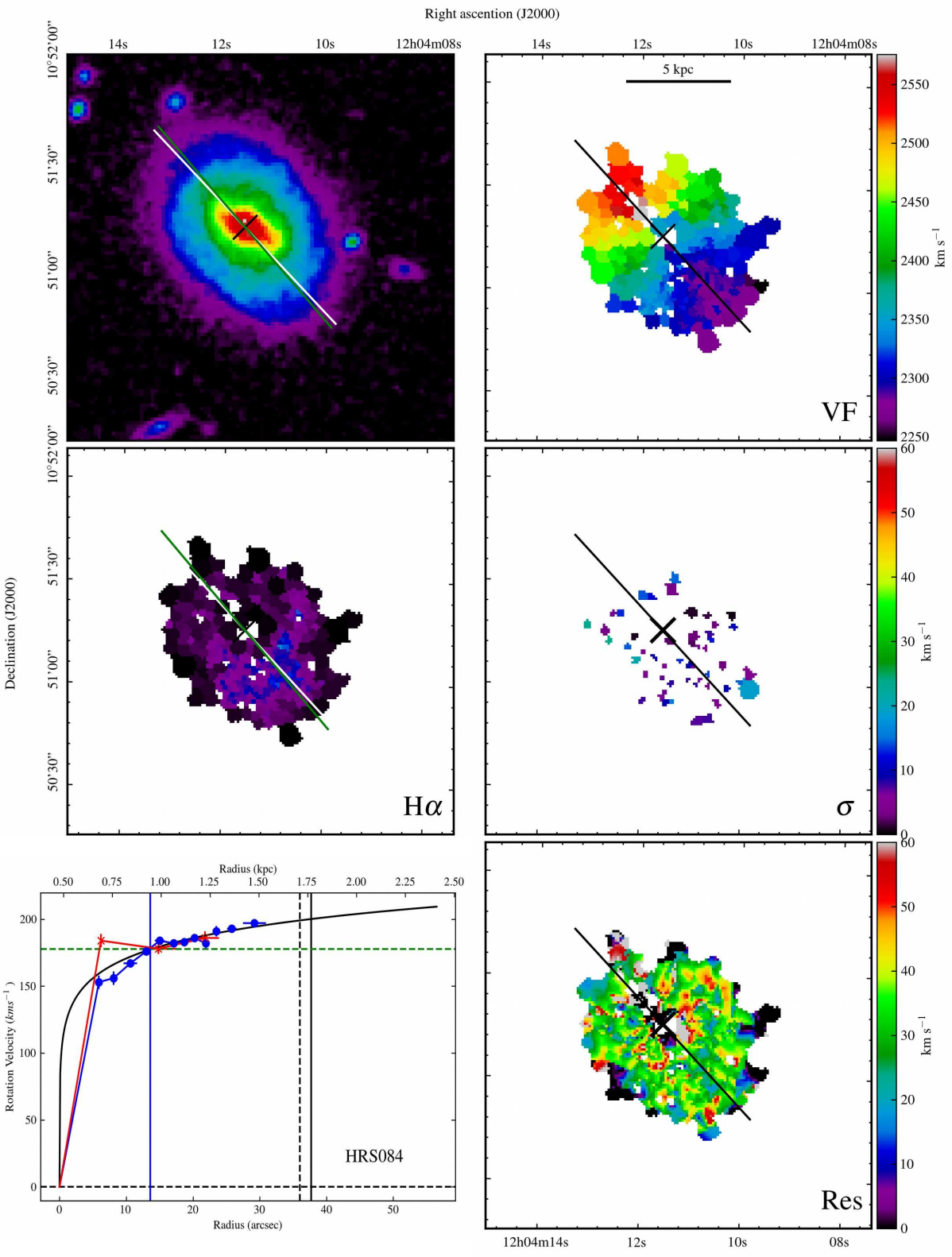
Right ascention (J2000)
Declination (J2000)
14s
12s
10s
12h04m08s
10°52'00"
51'30"
51'00"
50'30"
5 kpc
VF
Hα
σ
Res
km s⁻¹
Radius (kpc)
Radius (arcsec)
Rotation Velocity (kms⁻¹)
HRS084
12h04m14s
08s

HRS084

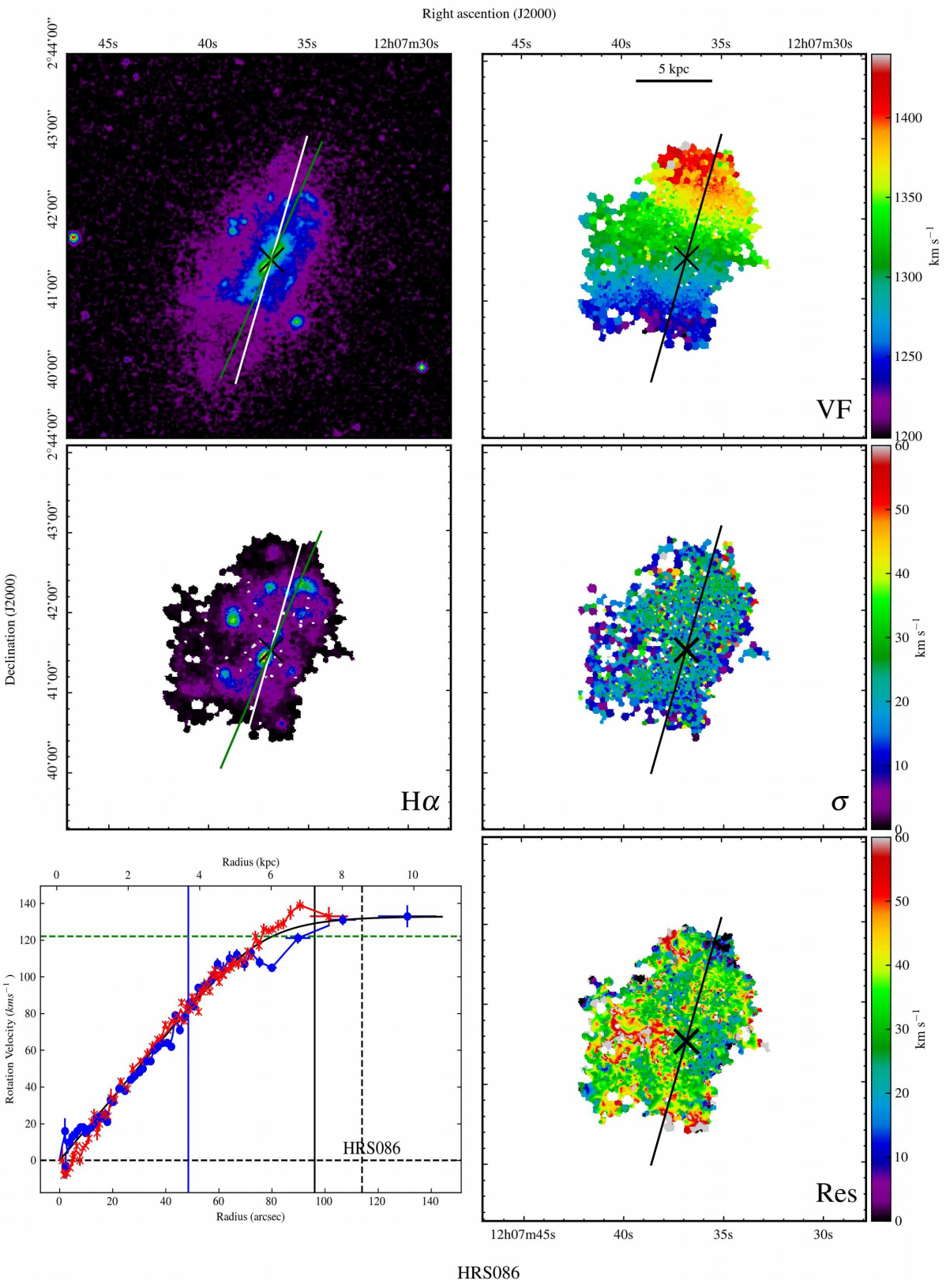
Right ascention (J2000)
45s
40s
35s
12h07m30s
2°44'00"
43'00"
42'00"
41'00"
40'00"
Declination (J2000)
5 kpc
VF
Hα
σ
Res
km s⁻¹
1400
1350
1300
1250
1200
60
50
40
30
20
10
0
12h07m45s
40s
35s
30s
Radius (kpc)
0
2
4
6
8
10
Rotation Velocity (kms⁻¹)
140
120
100
80
60
40
20
0
HRS086
Radius (arcsec)
0
20
40
60
80
100
120
140

HRS086

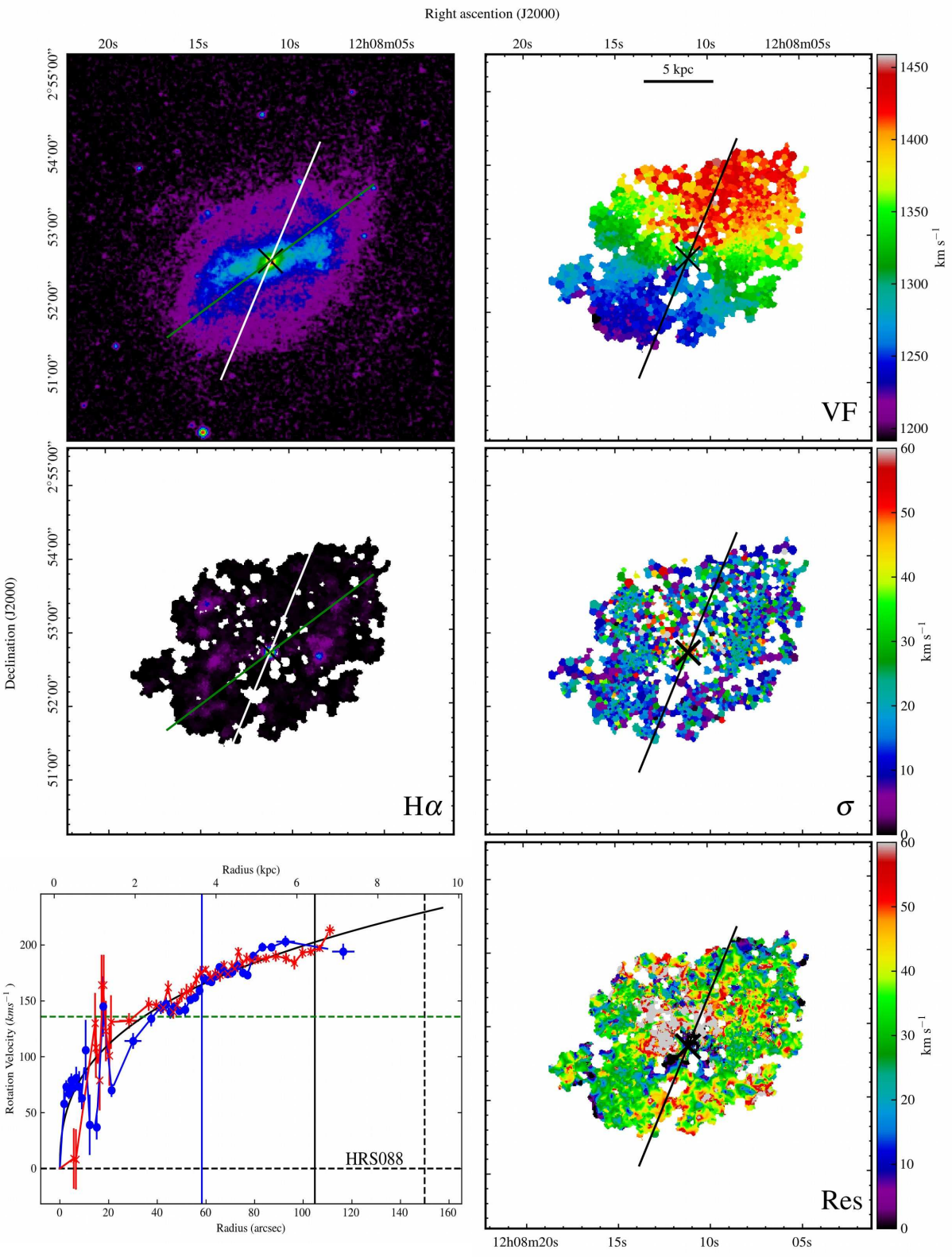
Right ascention (J2000)
Declination (J2000)
20s
15s
10s
12h08m05s
2°55'00"
54'00"
53'00"
52'00"
51'00"
5 kpc
VF
Hα
σ
Res
km s⁻¹
1450
1400
1350
1300
1250
1200
60
50
40
30
20
10
0
Radius (kpc)
Rotation Velocity (kms⁻¹)
Radius (arcsec)
HRS088
12h08m20s
05s

HRS088

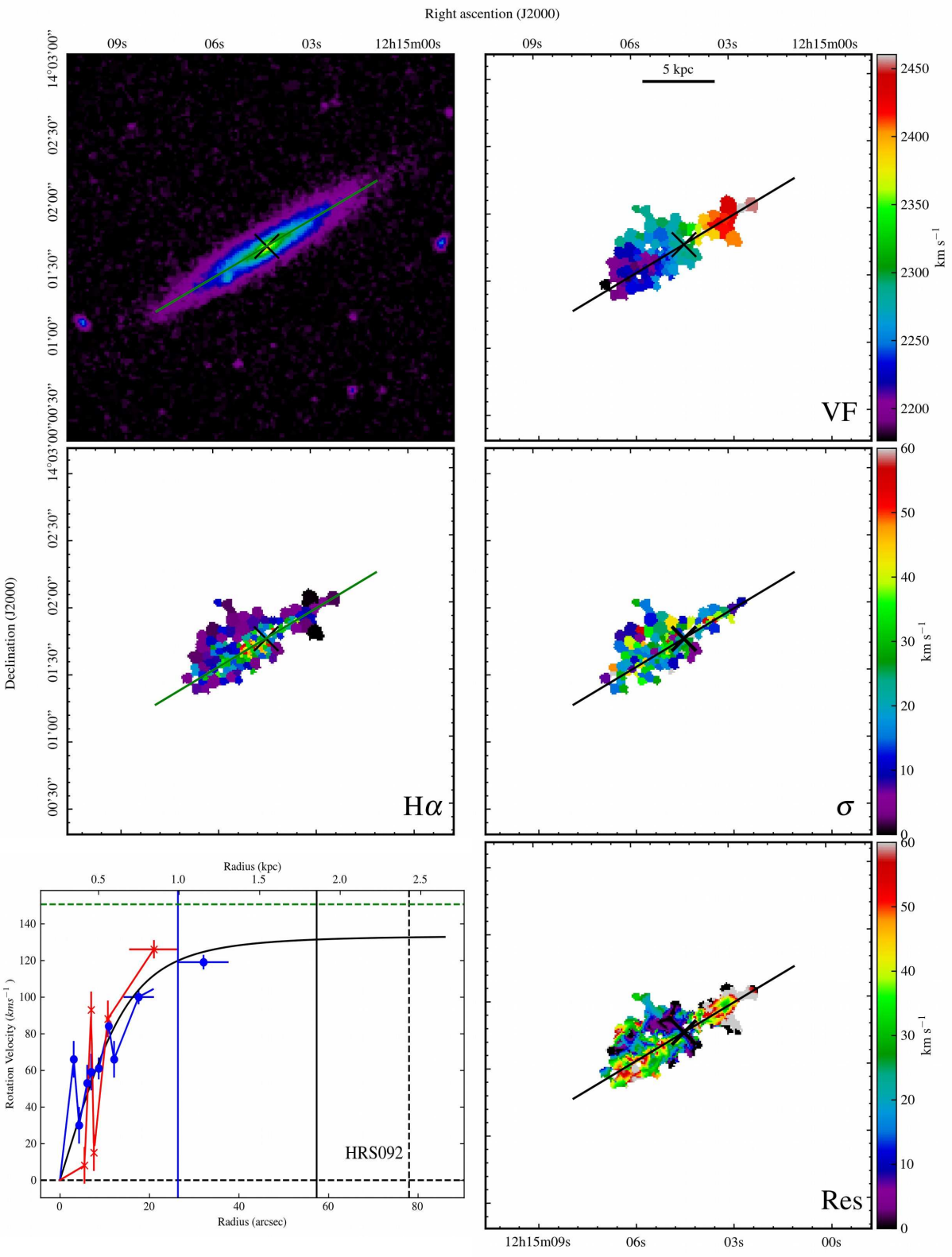
Right ascention (J2000)
09s
06s
03s
12h15m00s
Declination (J2000)
14°03'00"
02'30"
02'00"
01'30"
01'00"
00'30"
5 kpc
VF
Hα
σ
Res
km s⁻¹
Radius (kpc)
0.5
1.0
1.5
2.0
2.5
Rotation Velocity (kms⁻¹)
Radius (arcsec)
HRS092
12h15m09s
00s

HRS092

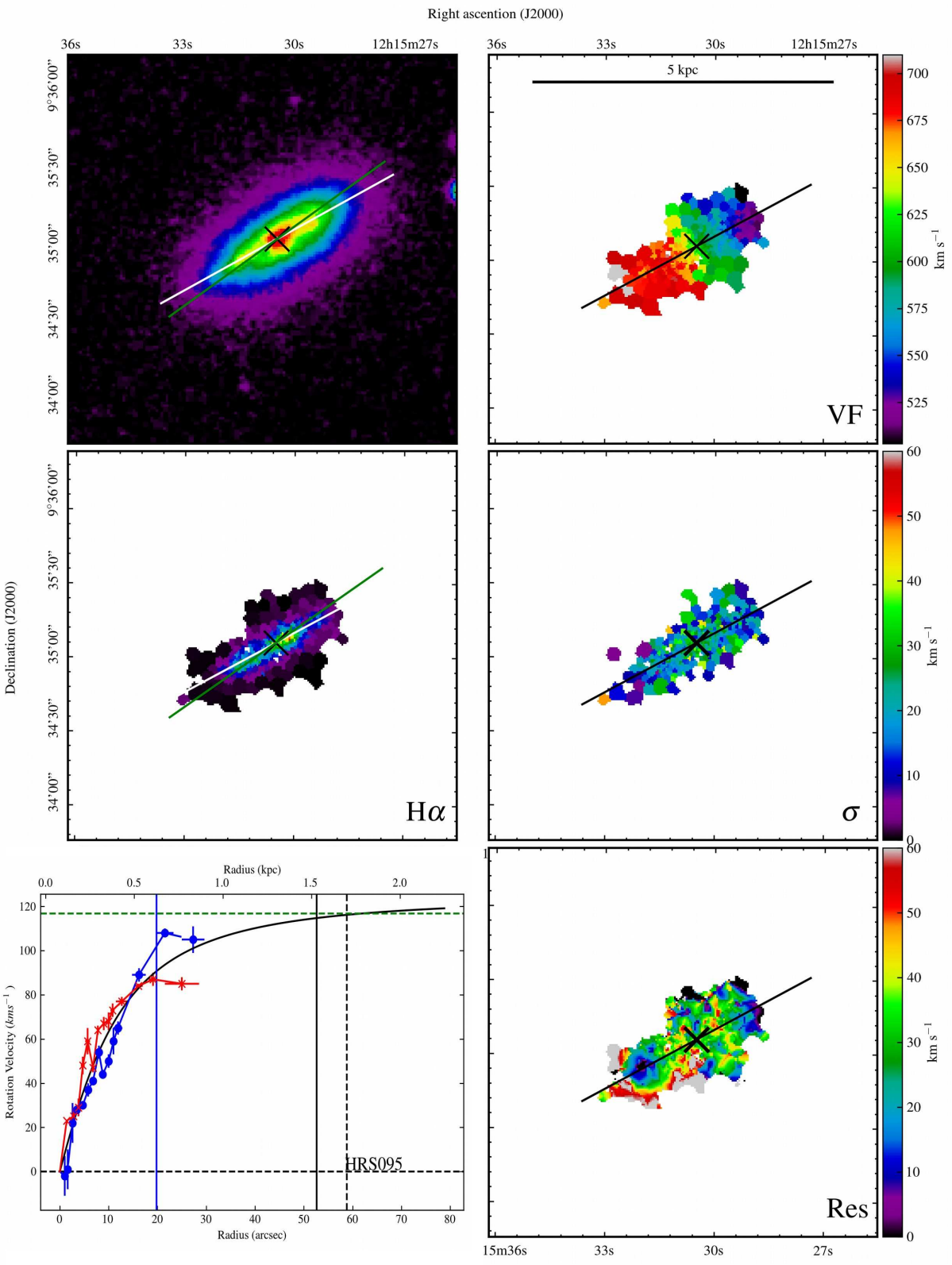
Right ascention (J2000)
36s
33s
30s
12h15m27s
9°36'00"
35'30"
35'00"
34'30"
34'00"
Declination (J2000)
5 kpc
VF
Hα
σ
Res
km s−1
700
675
650
625
600
575
550
525
60
50
40
30
20
10
0
15m36s
33s
30s
27s
Radius (kpc)
0.0
0.5
1.0
1.5
2.0
Rotation Velocity (kms−1)
120
100
80
60
40
20
0
HRS095
Radius (arcsec)
0
10
20
30
40
50
60
70
80

HRS095

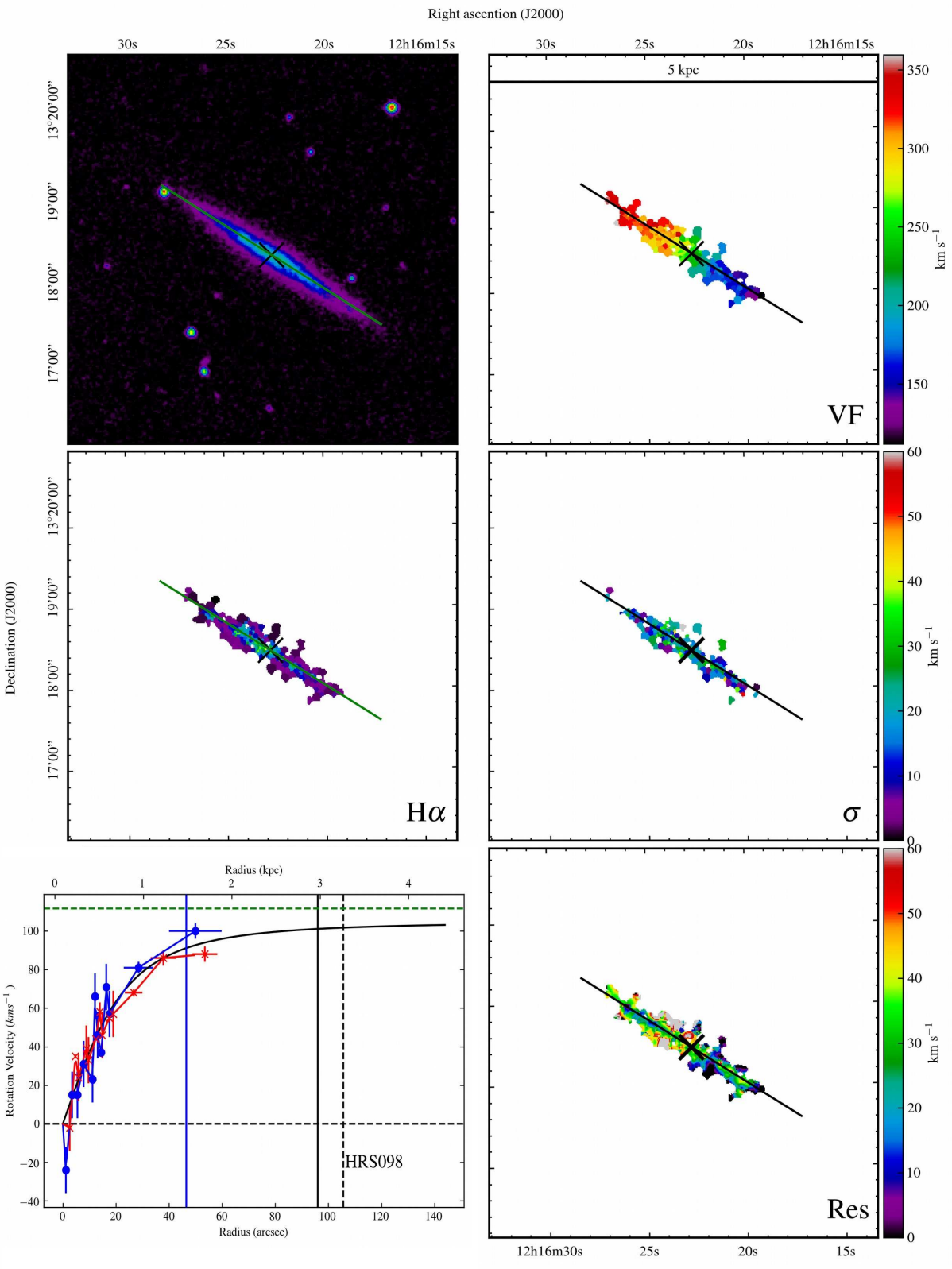
Right ascention (J2000)
30s
25s
20s
12h16m15s
Declination (J2000)
13°20'00"
19'00"
18'00"
17'00"
5 kpc
VF
Hα
σ
Res
km s−1
Radius (kpc)
Rotation Velocity (kms−1)
Radius (arcsec)
HRS098
12h16m30s
15s

HRS098

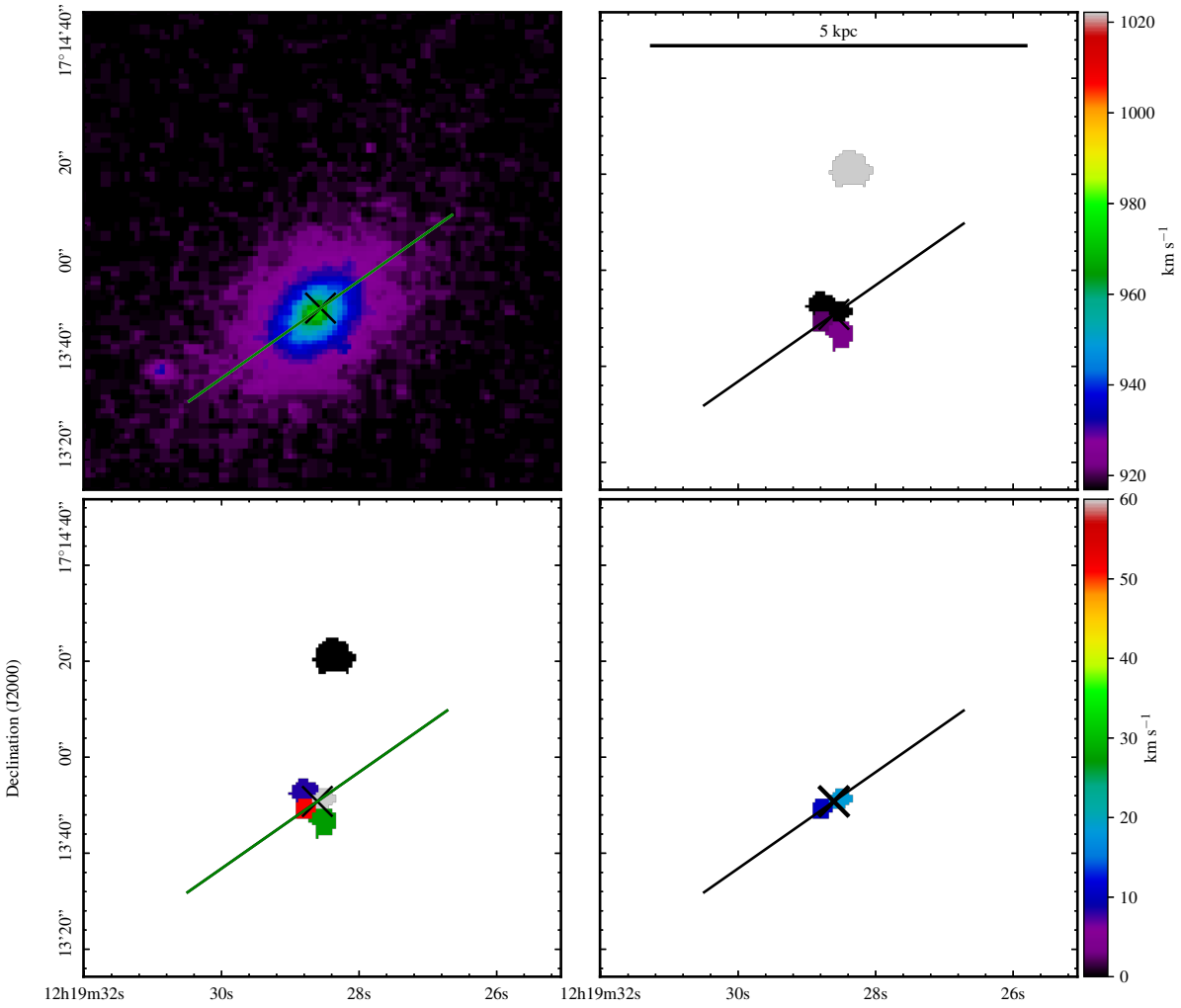
5 kpc
1020
1000
980
960
940
920
km s^{-1}
60
50
40
30
20
10
0
km s^{-1}
17°14'40"
20"
00"
13'40"
13'20"
Declination (J2000)
12h19m32s
30s
28s
26s
Right ascention (J2000)

HRS104

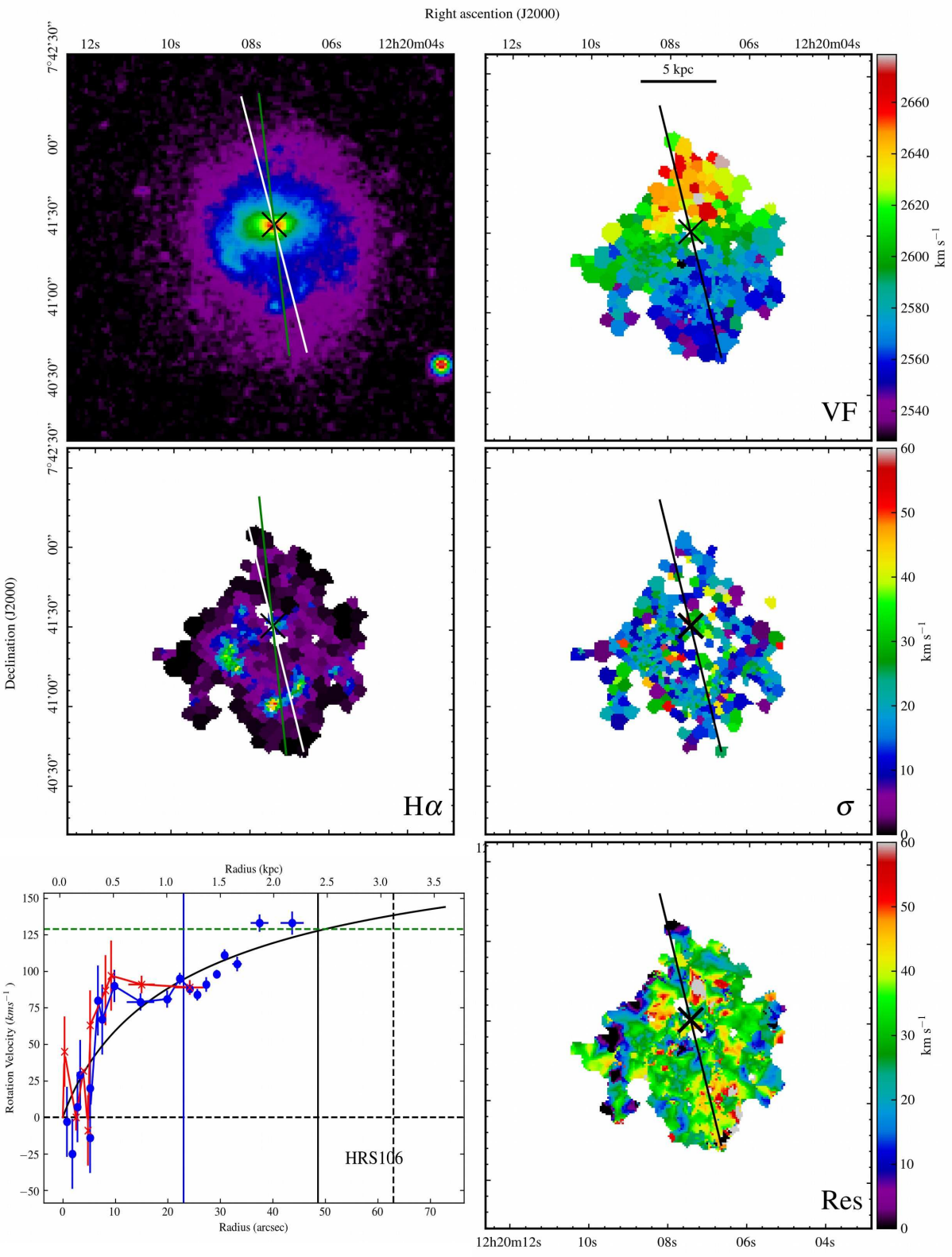
Right ascention (J2000)
Declination (J2000)
12s
10s
08s
06s
12h20m04s
7°42'30"
00"
41'30"
41'00"
40'30"
5 kpc
VF
Hα
σ
Res
km s⁻¹
2660
2640
2620
2600
2580
2560
2540
60
50
40
30
20
10
0
Radius (kpc)
0.0
0.5
1.0
1.5
2.0
2.5
3.0
3.5
Rotation Velocity (kms⁻¹)
150
125
100
75
50
25
0
−25
−50
Radius (arcsec)
0
10
20
30
40
50
60
70
HRS106
12h20m12s
04s

HRS106

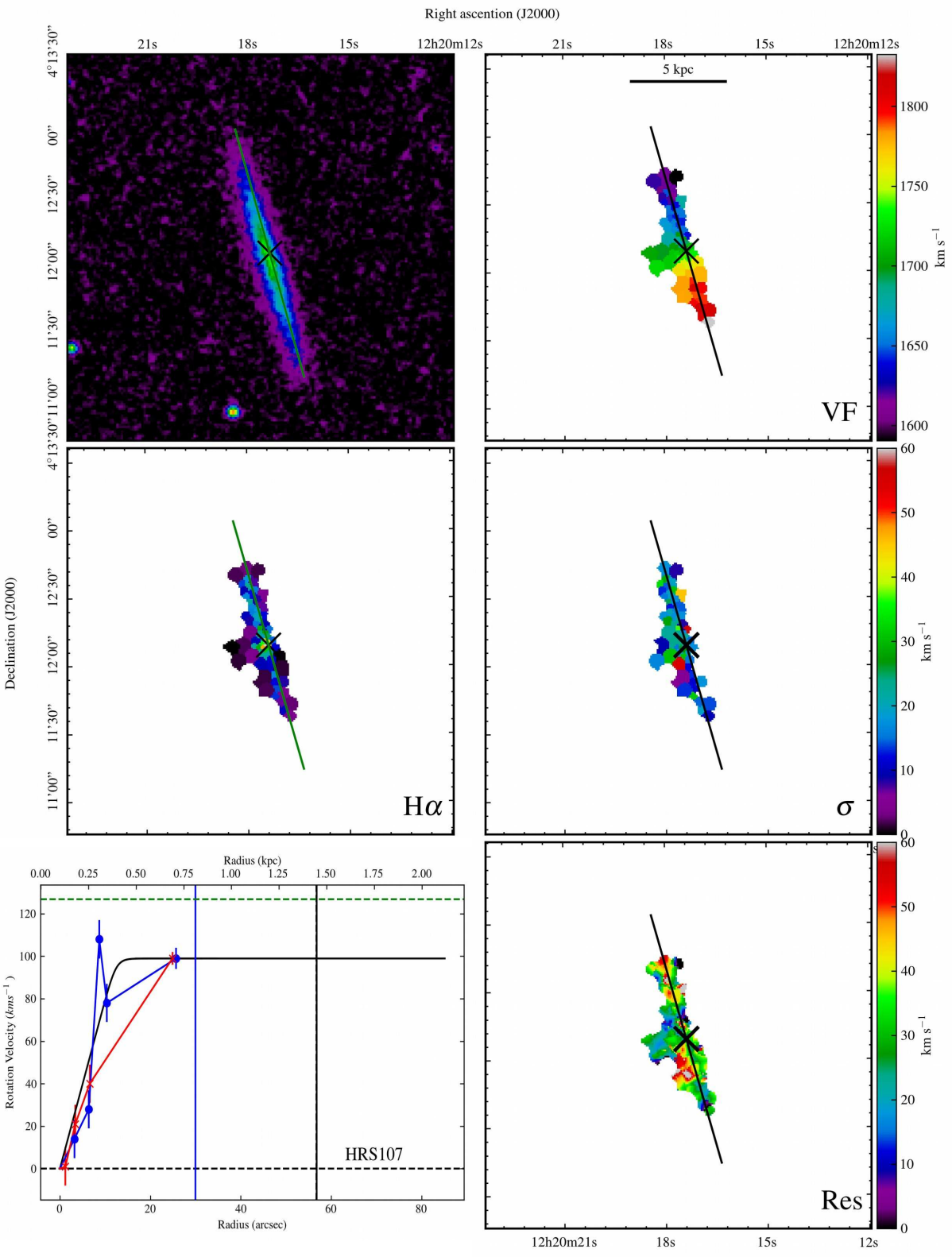
Right ascention (J2000)
Declination (J2000)
5 kpc
VF
Hα
σ
Res
km s−1
Radius (kpc)
Radius (arcsec)
Rotation Velocity (kms−1)
HRS107

HRS107

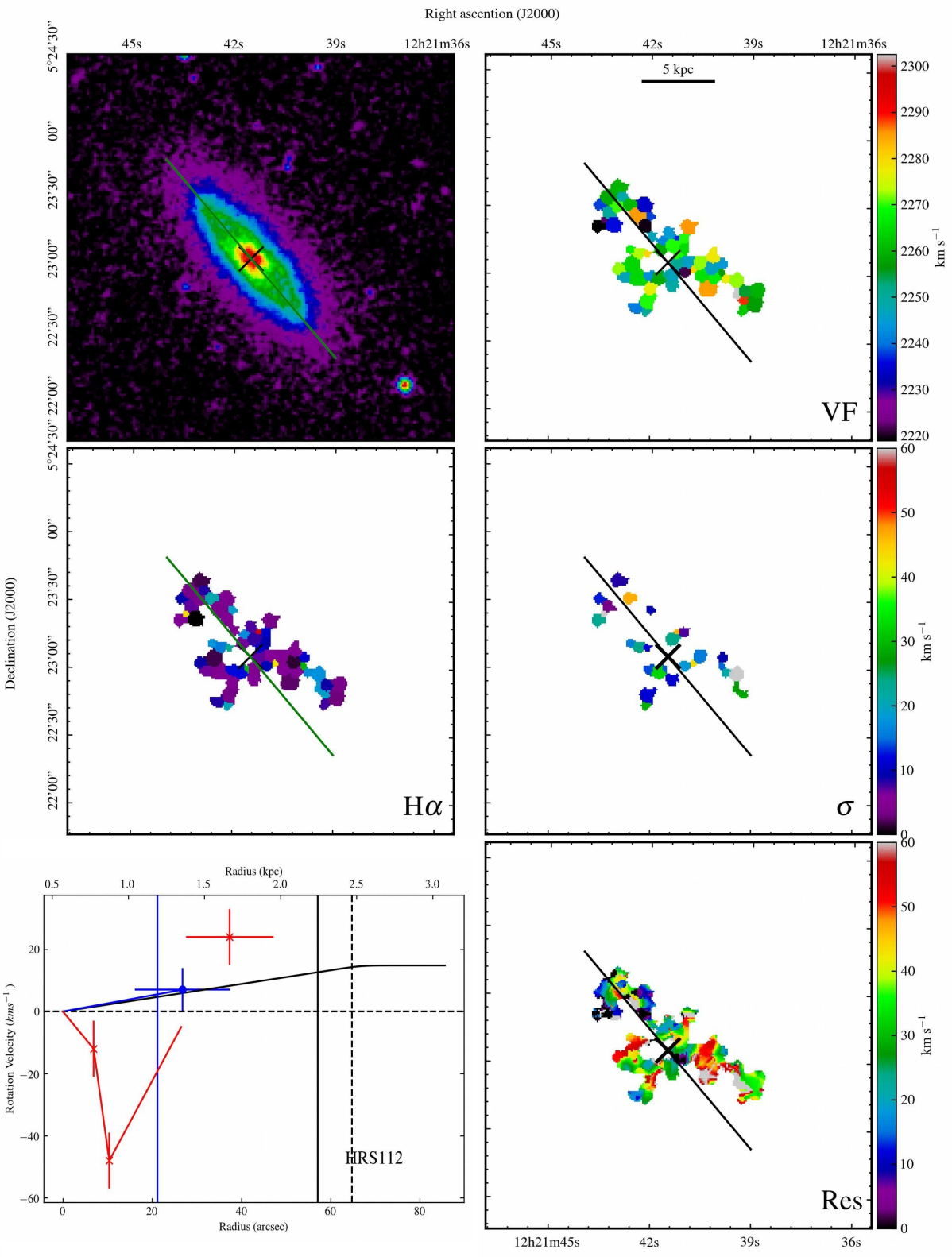
Right ascention (J2000)
45s
42s
39s
12h21m36s
5°24'30"
00"
23'30"
23'00"
22'30"
22'00"
Declination (J2000)
5 kpc
VF
Hα
σ
Res
km s⁻¹
2300
2290
2280
2270
2260
2250
2240
2230
2220
60
50
40
30
20
10
0
12h21m45s
42s
39s
36s
Radius (kpc)
0.5
1.0
1.5
2.0
2.5
3.0
Rotation Velocity (kms⁻¹)
20
0
−20
−40
−60
HRS112
0
20
40
60
80
Radius (arcsec)

HRS112

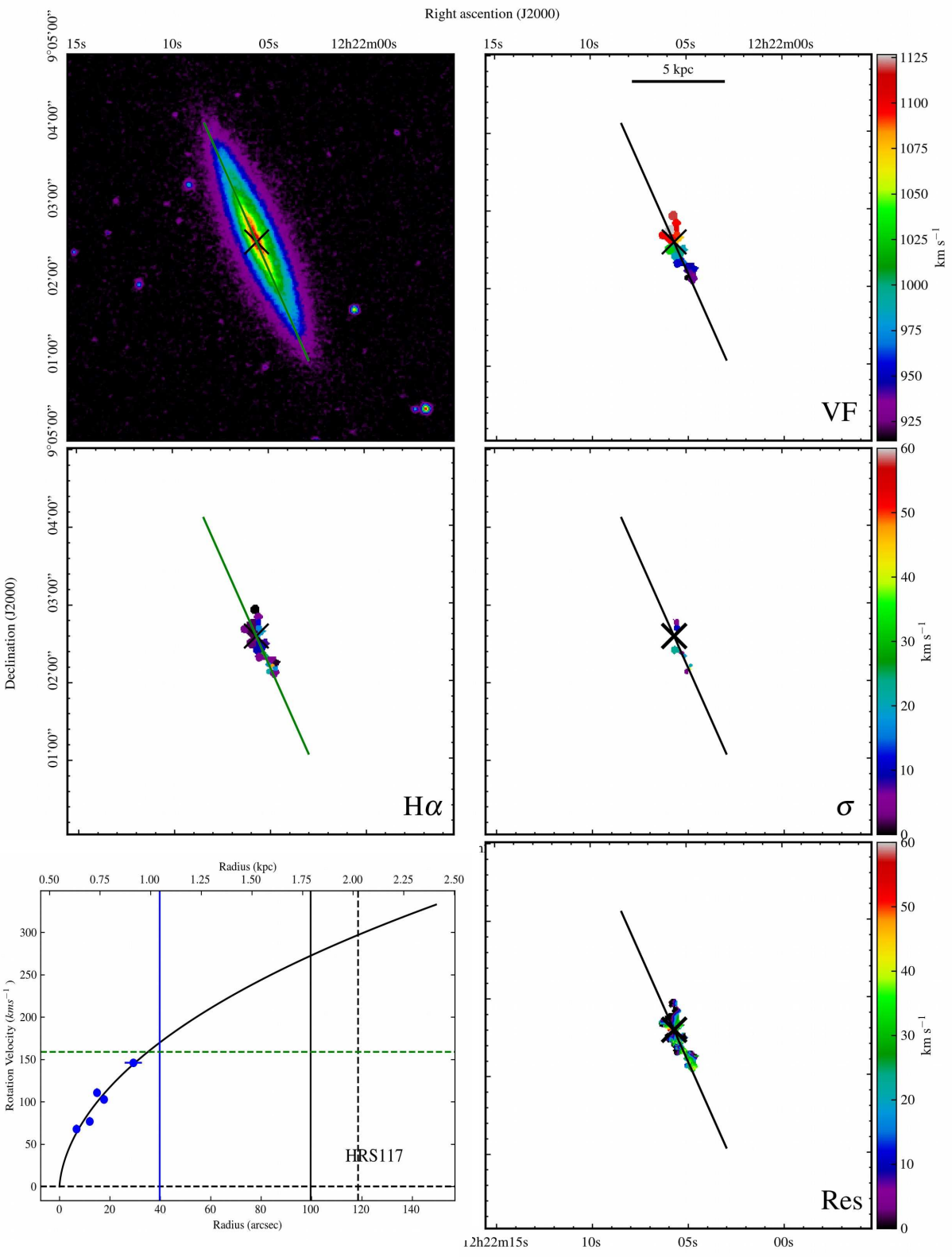
Right ascention (J2000)
Declination (J2000)
15s
10s
05s
12h22m00s
9°05'00"
04'00"
03'00"
02'00"
01'00"
5 kpc
VF
Hα
σ
Res
km s^{-1}
Radius (kpc)
Radius (arcsec)
Rotation Velocity (kms^{-1})
HRS117
12h22m15s
00s

HRS117

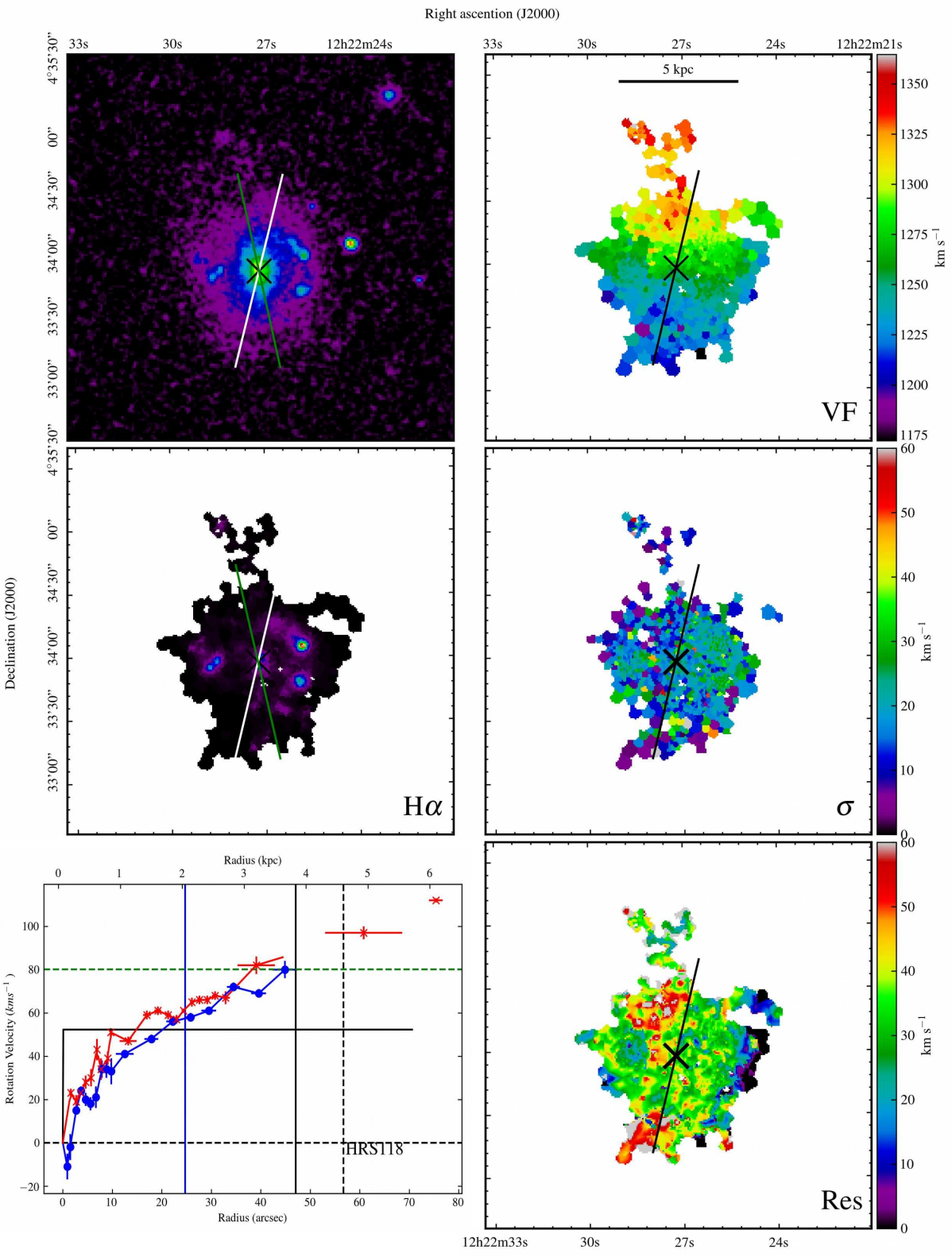
Right ascention (J2000)
Declination (J2000)
33s
30s
27s
12h22m24s
24s
12h22m21s
12h22m33s
4°35'30"
00"
34'30"
34'00"
33'30"
33'00"
5 kpc
VF
Hα
σ
Res
km s⁻¹
Radius (kpc)
Radius (arcsec)
Rotation Velocity (kms⁻¹)
HRS118

HRS118

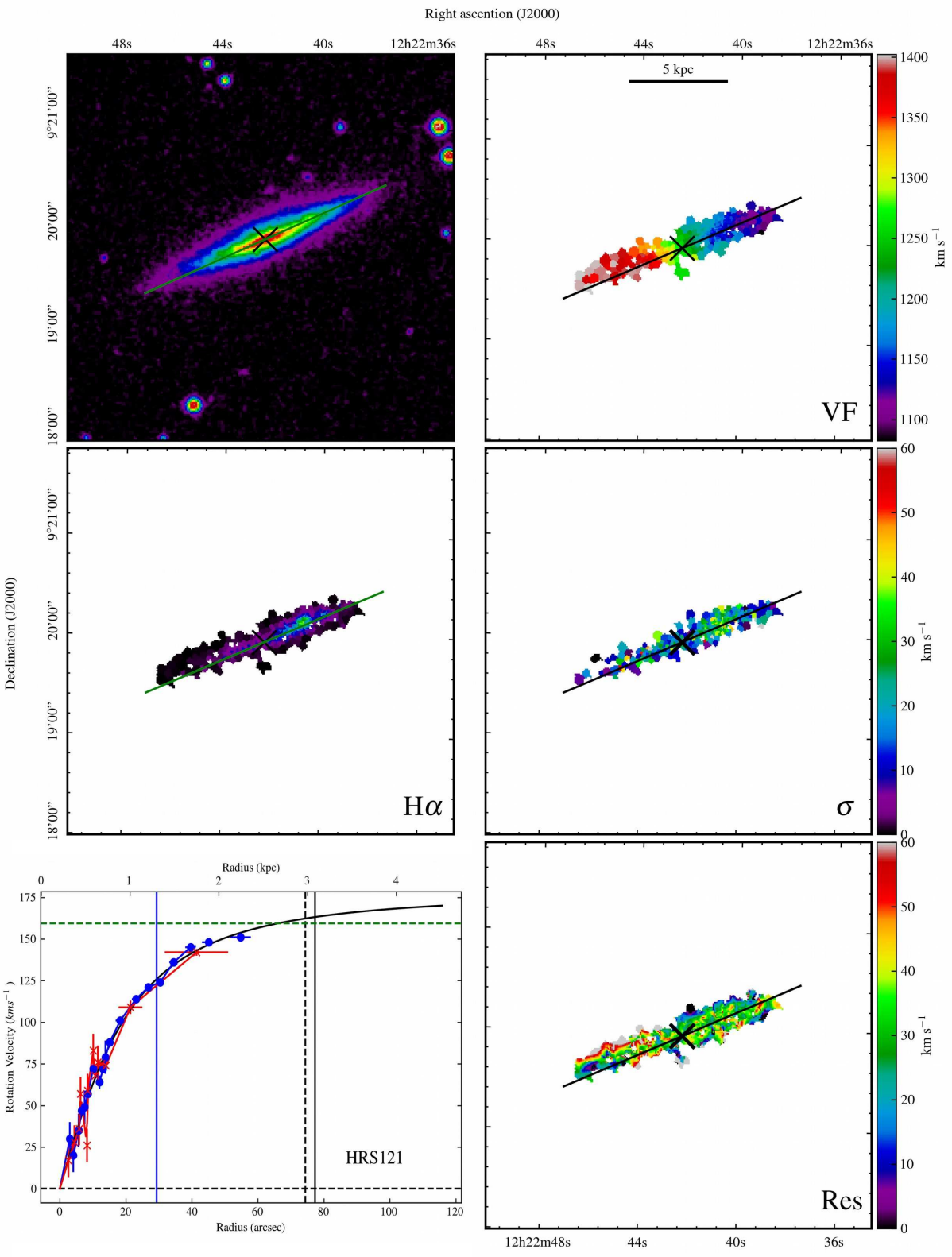
Right ascention (J2000)
48s
44s
40s
12h22m36s
9°21'00"
20'00"
19'00"
18'00"
Declination (J2000)
5 kpc
VF
Hα
σ
Res
km s⁻¹
Radius (kpc)
Rotation Velocity (kms⁻¹)
Radius (arcsec)
HRS121
12h22m48s
36s

HRS121

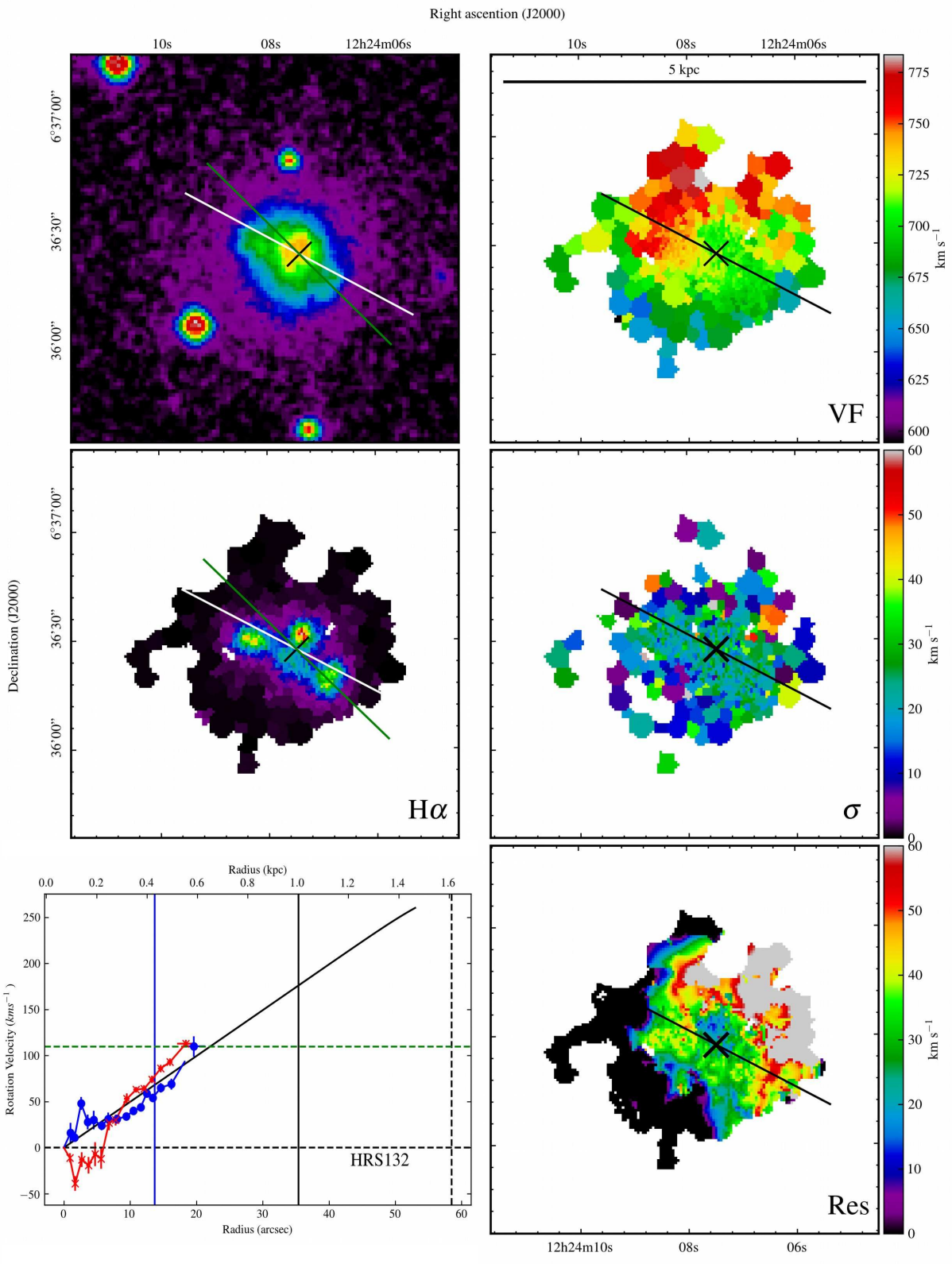
Right ascention (J2000)
10s
08s
12h24m06s
12h24m10s
06s
Declination (J2000)
6°37'00"
36'30"
36'00"
5 kpc
VF
Hα
σ
Res
km s−1
Radius (kpc)
Rotation Velocity (kms−1)
Radius (arcsec)
HRS132

HRS132

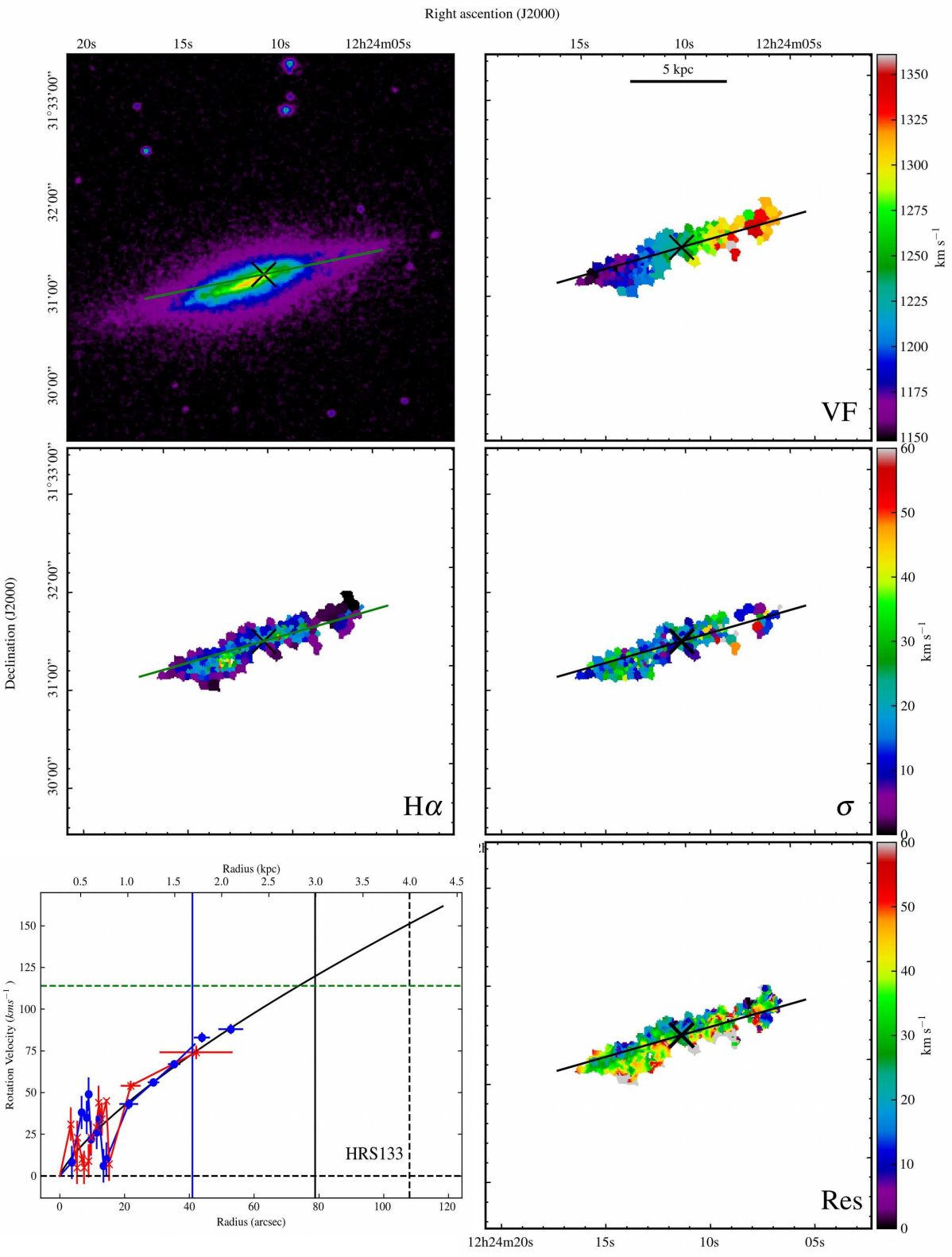
Right ascention (J2000)
20s
15s
10s
12h24m05s
15s
10s
12h24m05s
5 kpc
31°33'00"
32'00"
31'00"
30'00"
Declination (J2000)
VF
Hα
σ
Res
km s⁻¹
1350
1325
1300
1275
1250
1225
1200
1175
1150
60
50
40
30
20
10
0
Radius (kpc)
0.5
1.0
1.5
2.0
2.5
3.0
3.5
4.0
4.5
Rotation Velocity (kms⁻¹)
150
125
100
75
50
25
0
HRS133
0
20
40
60
80
100
120
Radius (arcsec)
12h24m20s
15s
10s
05s

HRS133

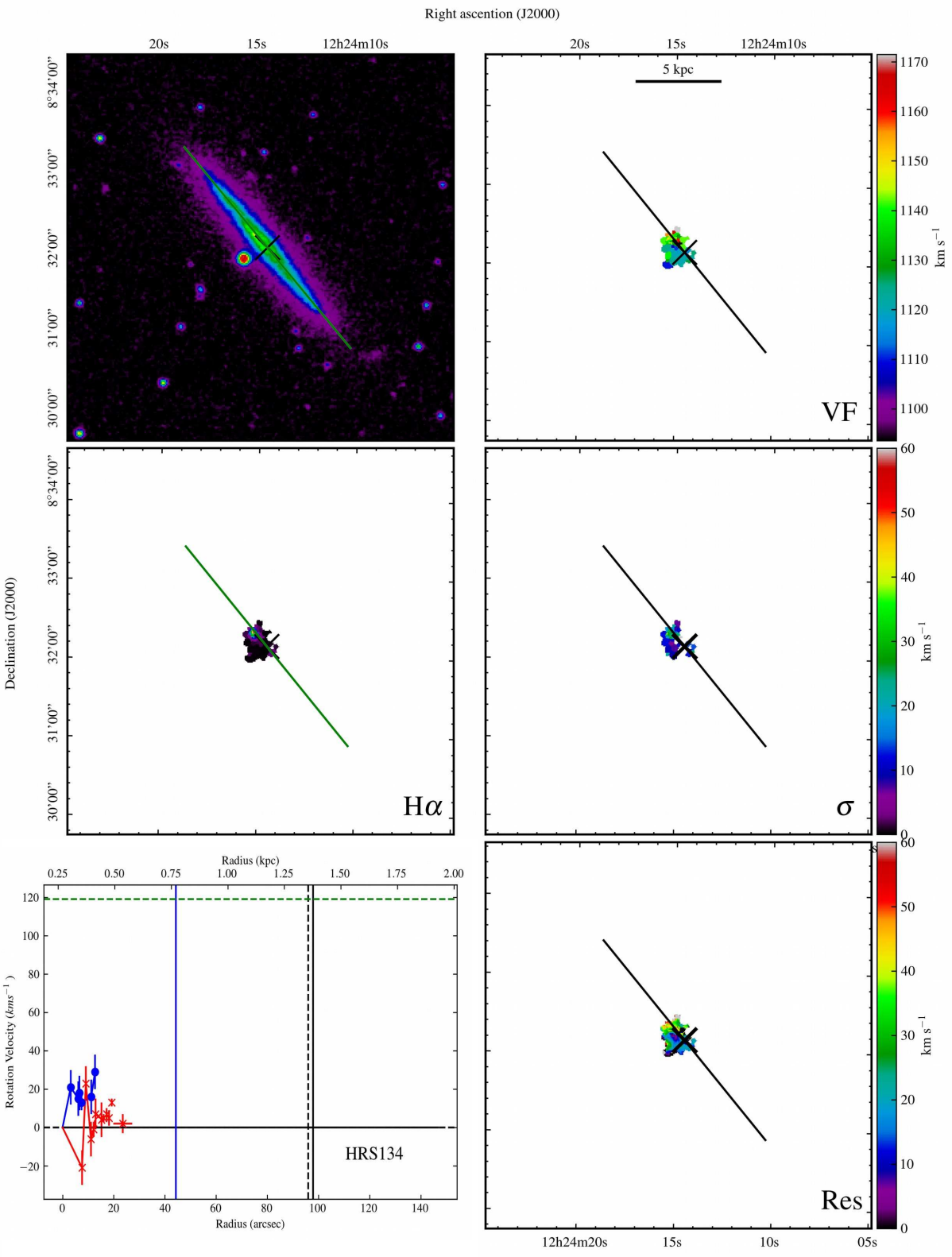
Right ascention (J2000)
20s
15s
12h24m10s
8°34'00"
33'00"
32'00"
31'00"
30'00"
Declination (J2000)
5 kpc
VF
Hα
σ
Res
km s⁻¹
1170
1160
1150
1140
1130
1120
1110
1100
60
50
40
30
20
10
0
Radius (kpc)
0.25
0.50
0.75
1.00
1.25
1.50
1.75
2.00
Rotation Velocity (kms⁻¹)
120
100
80
60
40
20
0
−20
HRS134
Radius (arcsec)
0
20
40
60
80
100
120
140
12h24m20s
10s
05s

HRS134

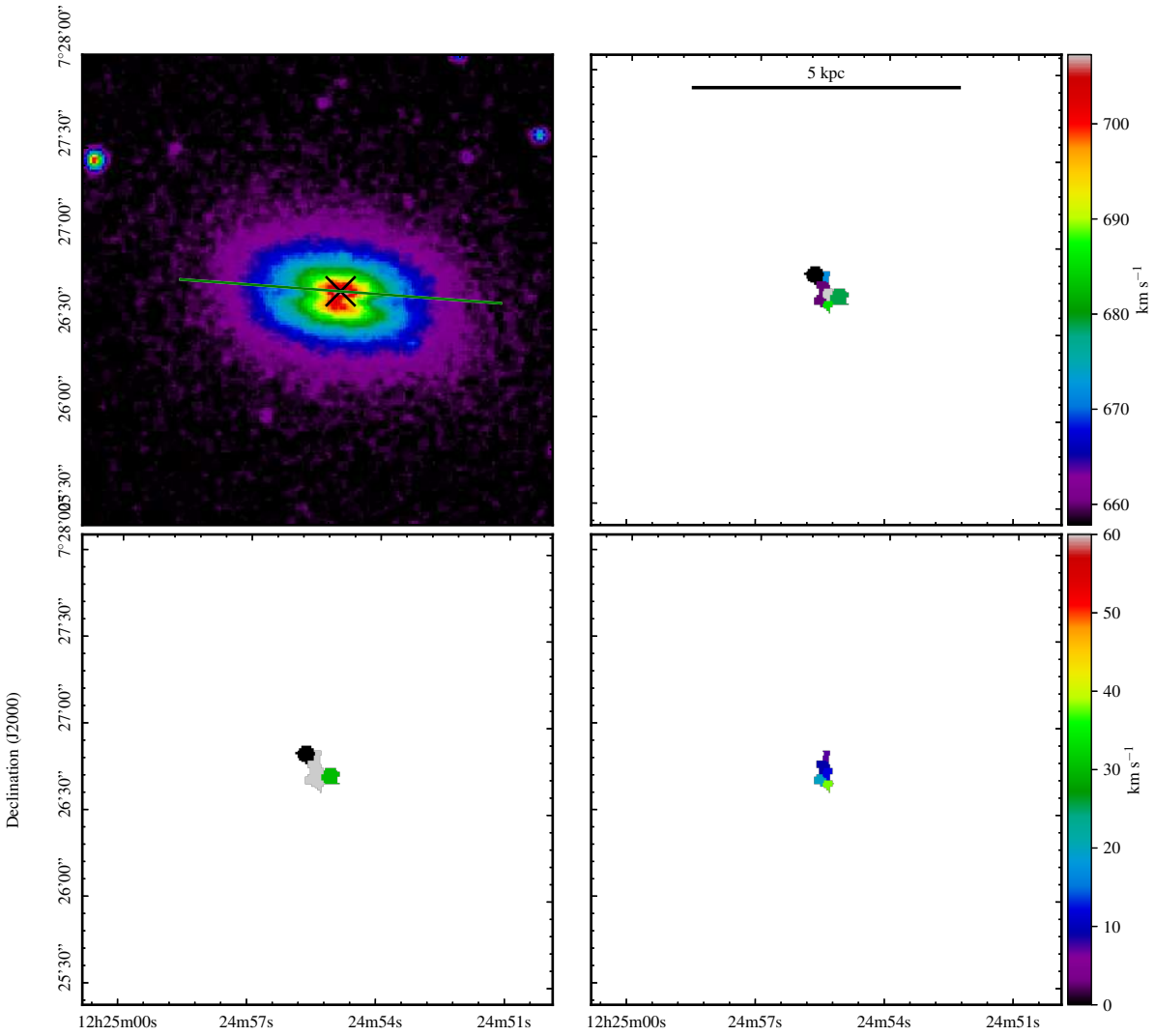

Right ascention (J2000)
HRS136

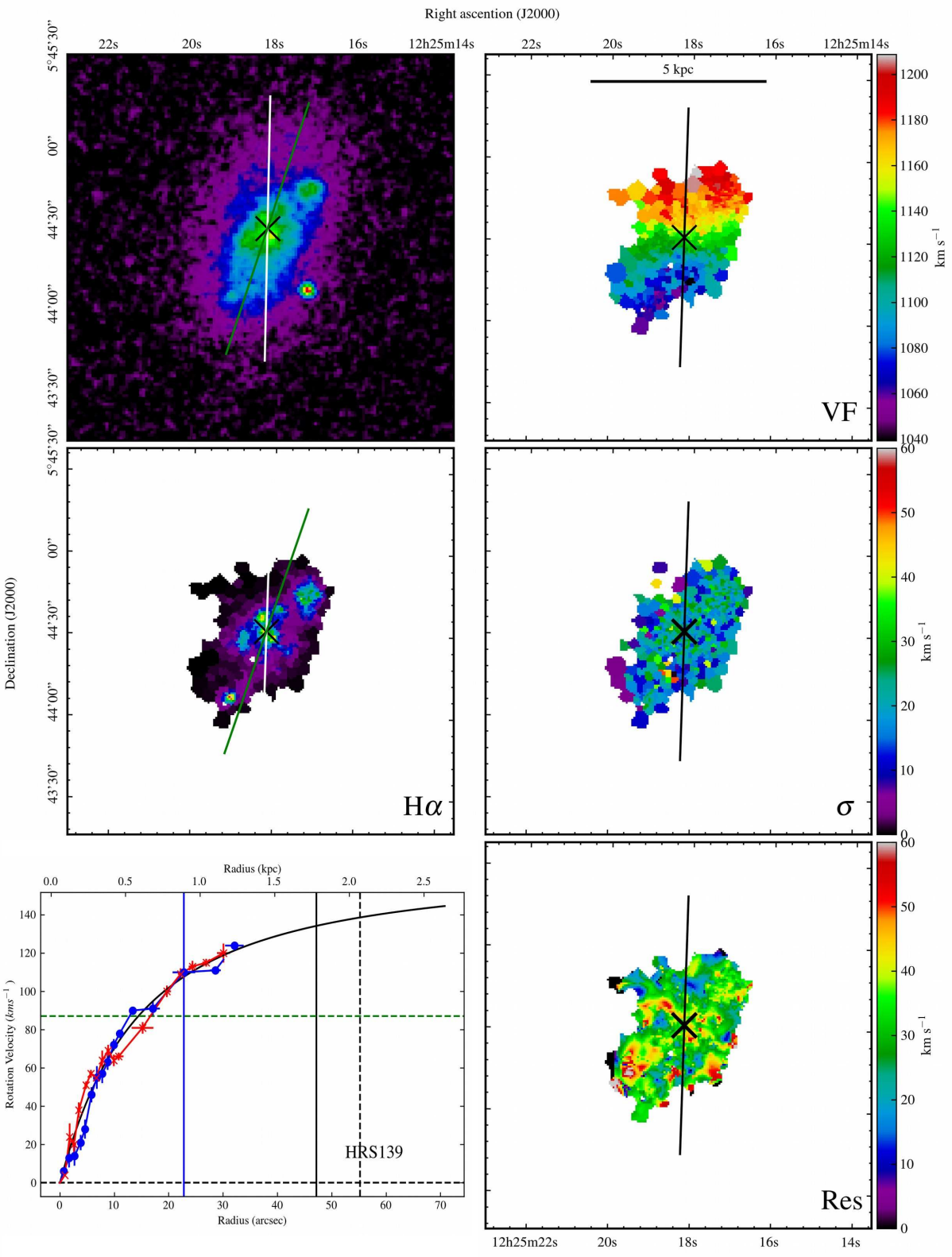
Right ascention (J2000)
Declination (J2000)
5 kpc
VF
Hα
σ
Res
km s−1
Radius (kpc)
Radius (arcsec)
Rotation Velocity (kms−1)
HRS139

HRS139

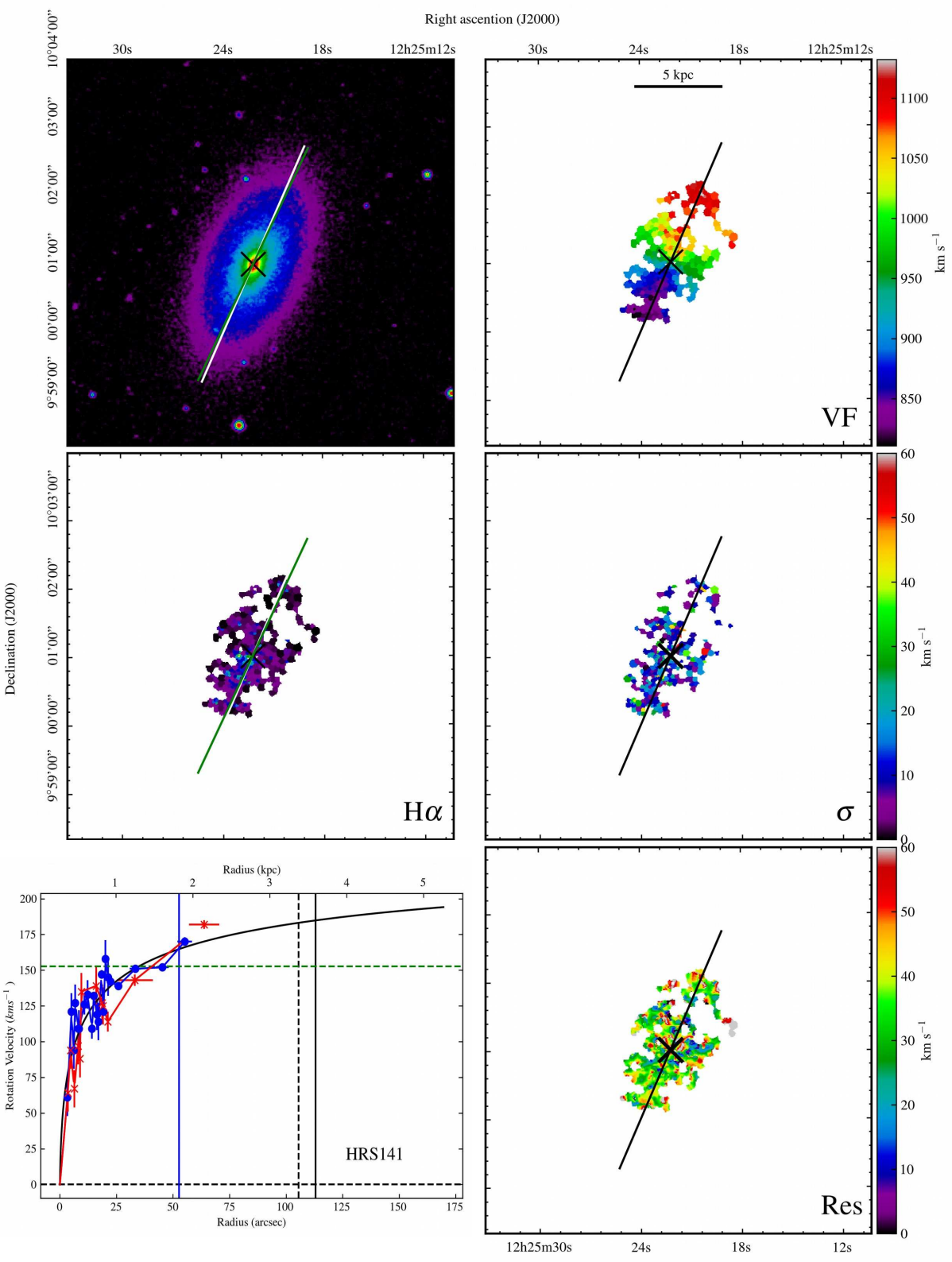
Right ascention (J2000)
Declination (J2000)
30s
24s
18s
12h25m12s
12h25m30s
12s
10°04'00"
03'00"
02'00"
01'00"
00'00"
9°59'00"
10°03'00"
5 kpc
VF
Hα
σ
Res
km s^{-1}
1100
1050
1000
950
900
850
60
50
40
30
20
10
0
Radius (kpc)
1
2
3
4
5
Rotation Velocity (kms^{-1})
200
175
150
125
100
75
50
25
0
Radius (arcsec)
HRS141

HRS141

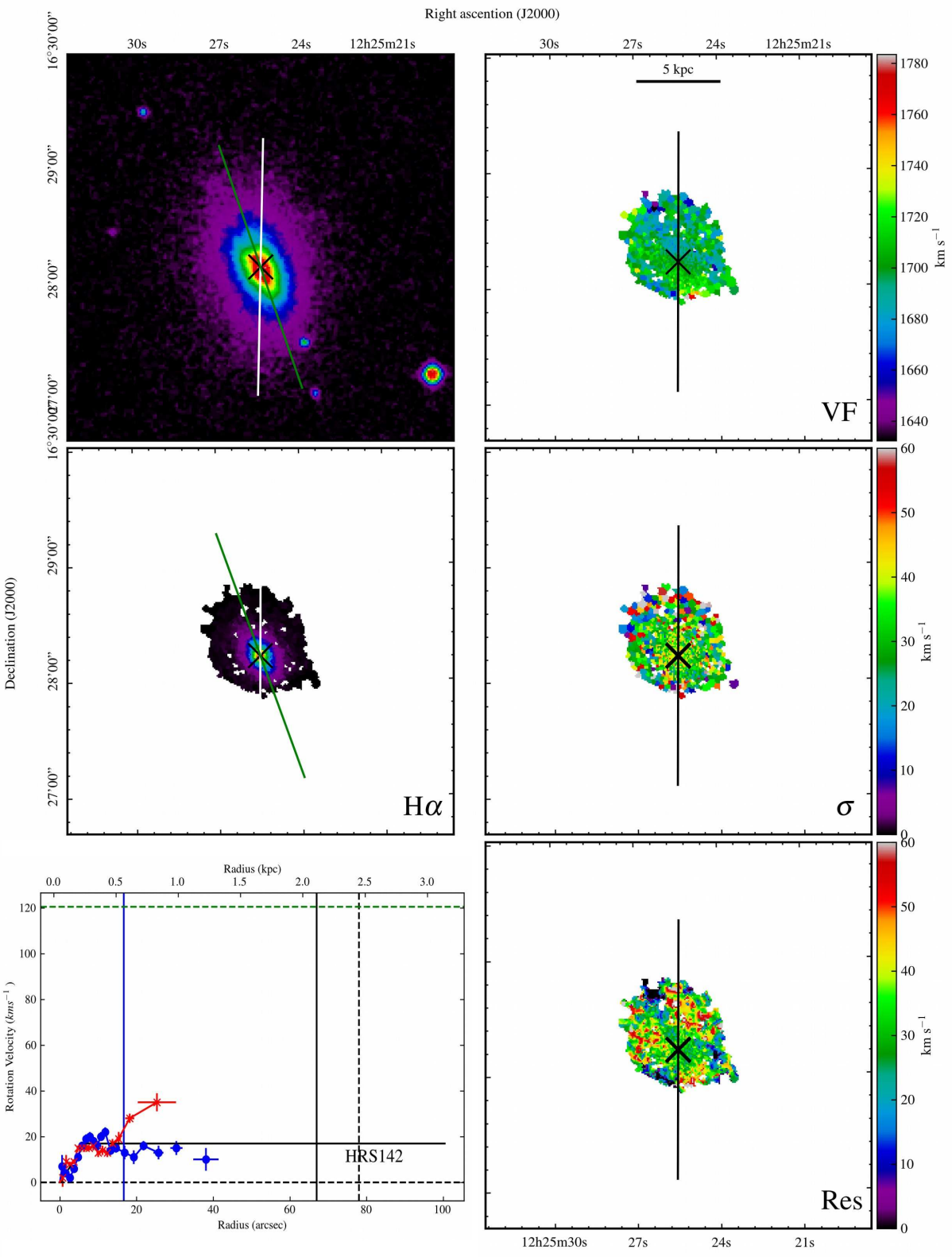
Right ascention (J2000)
Declination (J2000)
5 kpc
VF
Hα
σ
Res
km s⁻¹
Radius (kpc)
Radius (arcsec)
Rotation Velocity (kms⁻¹)
HRS142

HRS142

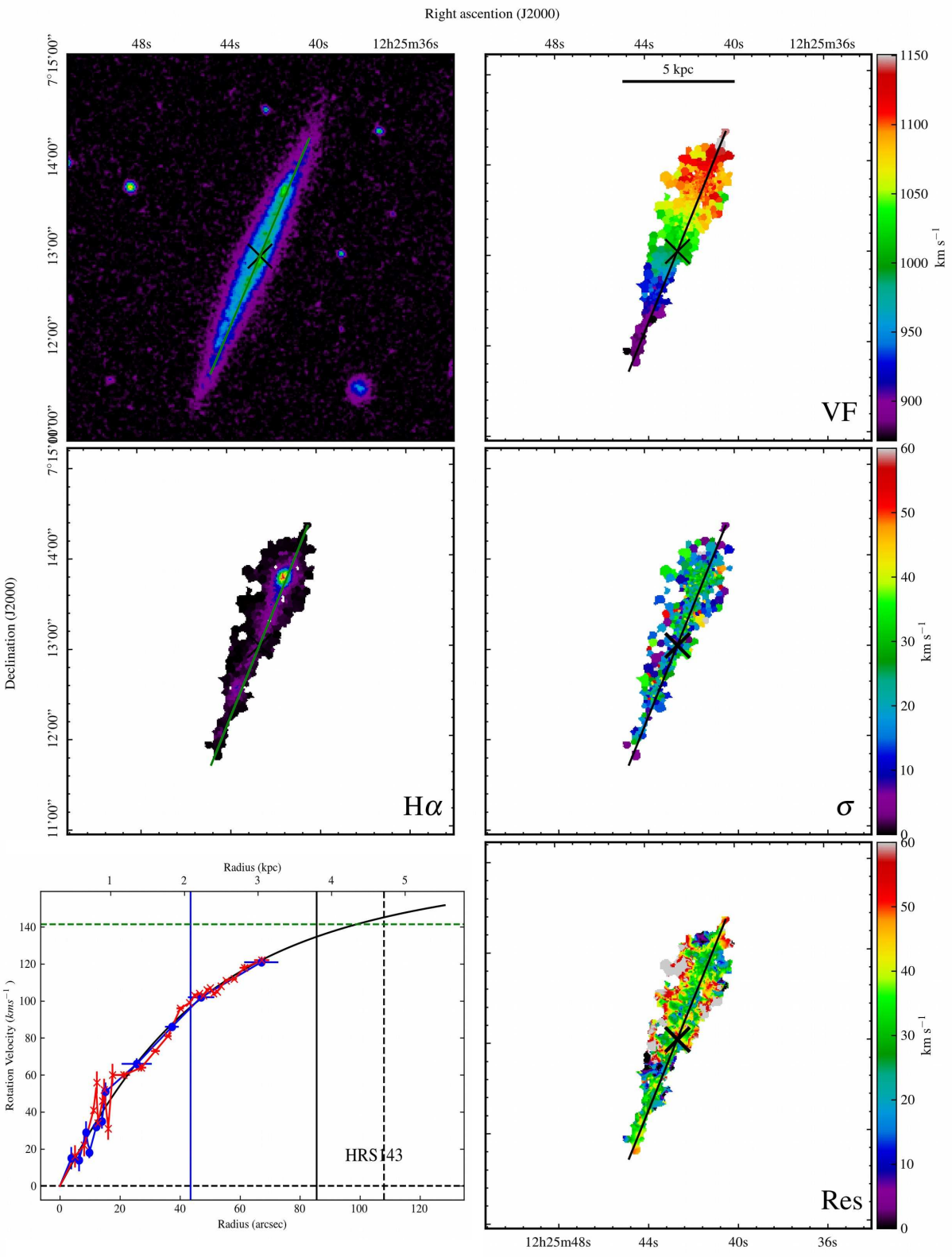
Right ascention (J2000)
Declination (J2000)
48s
44s
40s
12h25m36s
7°15'00"
14'00"
13'00"
12'00"
11'00"
5 kpc
VF
Hα
σ
Res
km s⁻¹
Radius (kpc)
Rotation Velocity (kms⁻¹)
Radius (arcsec)
HRS143
12h25m48s
36s

HRS143

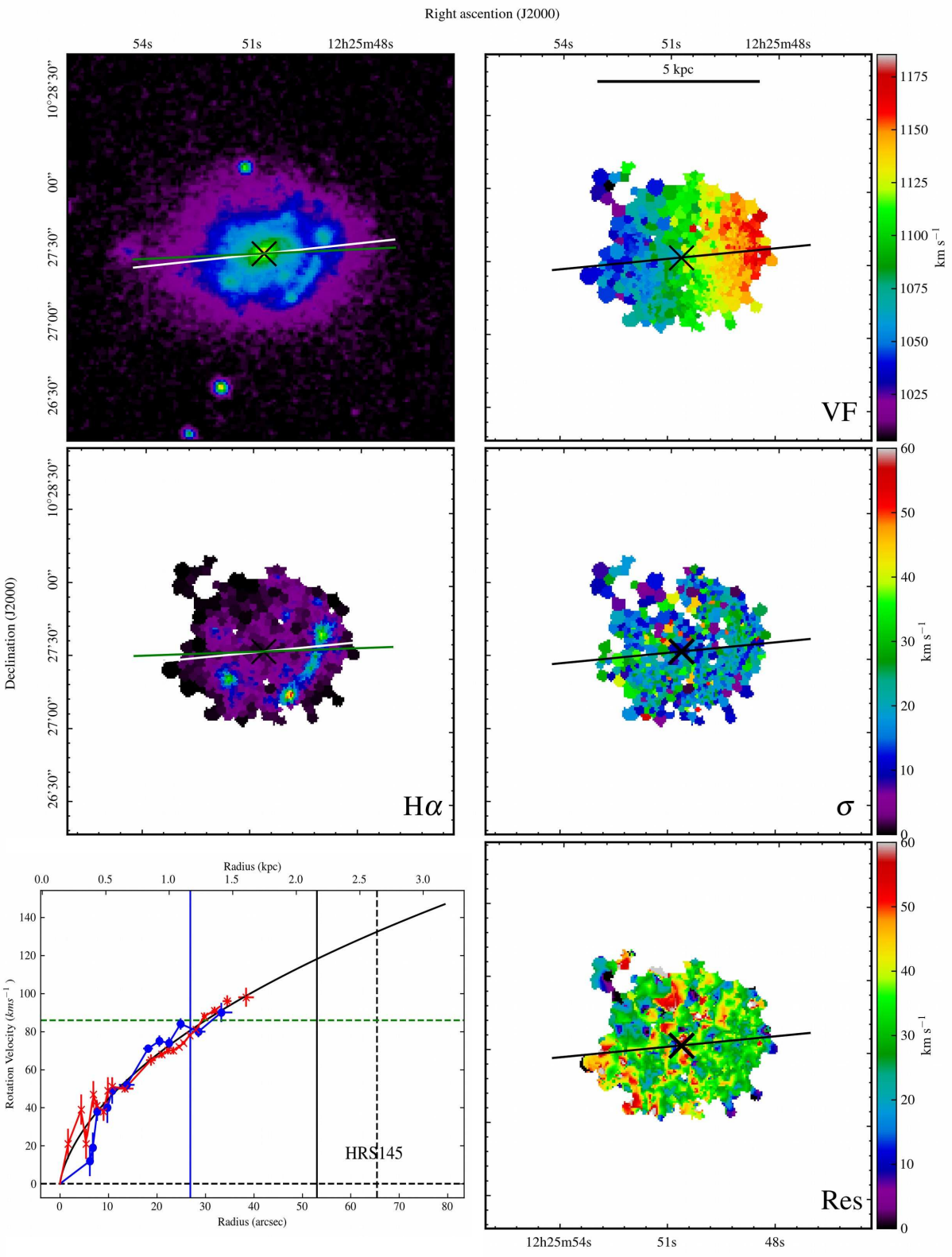
Right ascention (J2000)
54s
51s
12h25m48s
Declination (J2000)
10°28'30"
00"
27'30"
27'00"
26'30"
5 kpc
VF
Hα
σ
Res
km s^{-1}
Radius (kpc)
Rotation Velocity (kms^{-1})
Radius (arcsec)
HRS145
12h25m54s
48s

HRS145

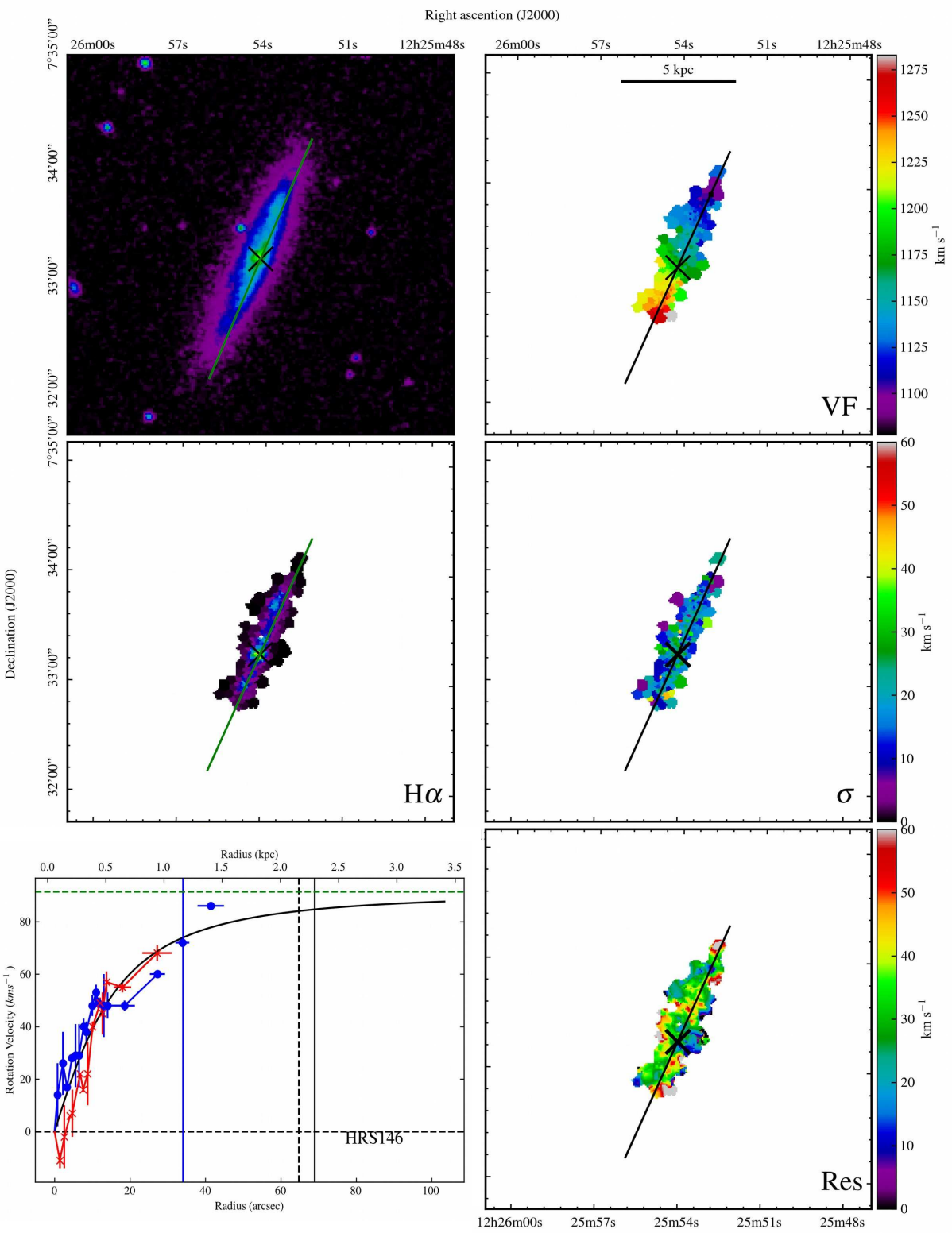
Right ascention (J2000)
Declination (J2000)
26m00s
57s
54s
51s
12h25m48s
7°35'00"
34'00"
33'00"
32'00"
5 kpc
VF
Hα
σ
Res
km s−1
Radius (kpc)
Radius (arcsec)
Rotation Velocity (kms−1)
HRS146
12h26m00s
25m57s
25m54s
25m51s
25m48s

HRS146

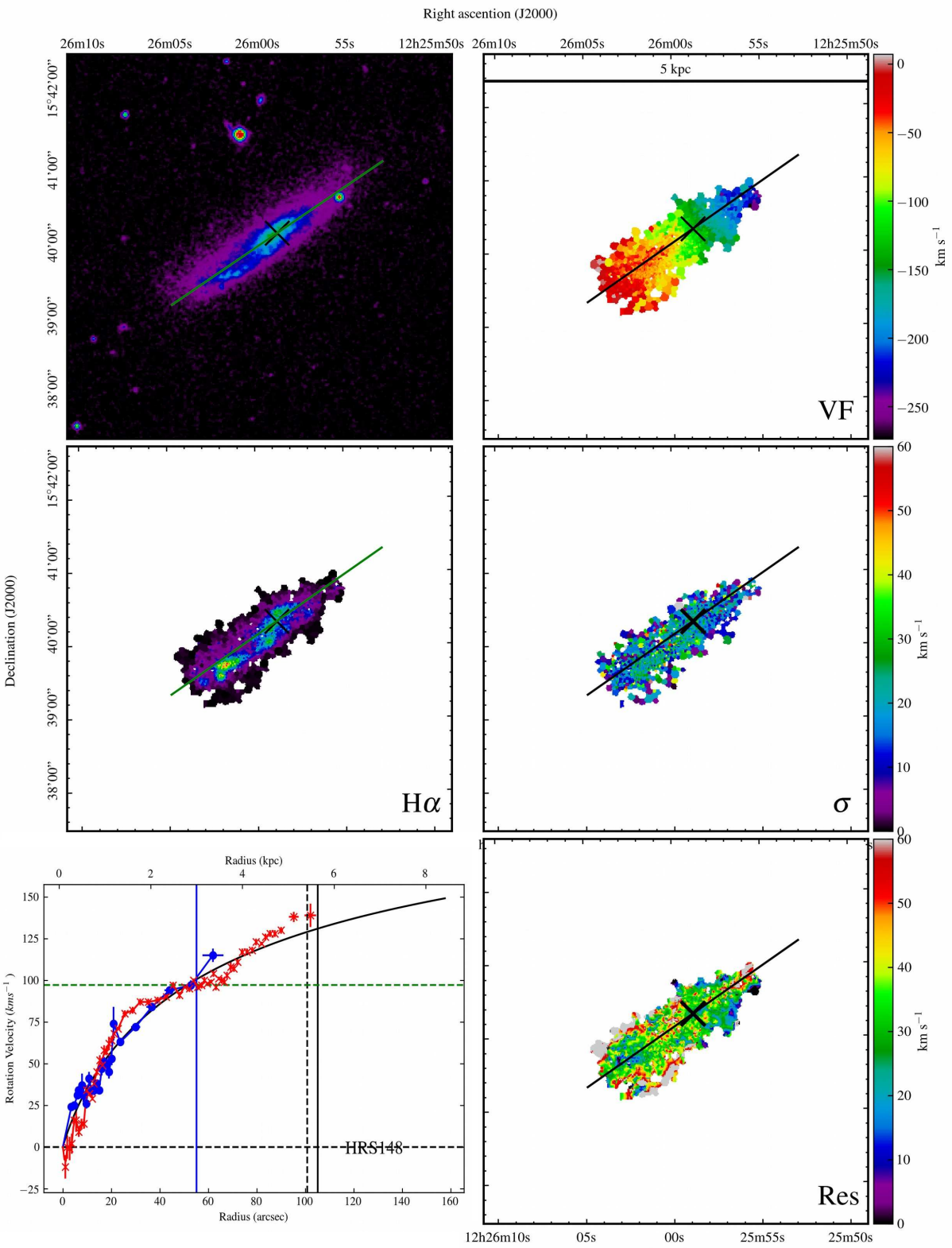
Right ascention (J2000)
26m10s
26m05s
26m00s
55s
12h25m50s
Declination (J2000)
15°42'00"
41'00"
40'00"
39'00"
38'00"
5 kpc
VF
Hα
σ
Res
km s−1
Radius (kpc)
Rotation Velocity (kms−1)
Radius (arcsec)
HRS148
12h26m10s
05s
00s
25m55s
25m50s

HRS148

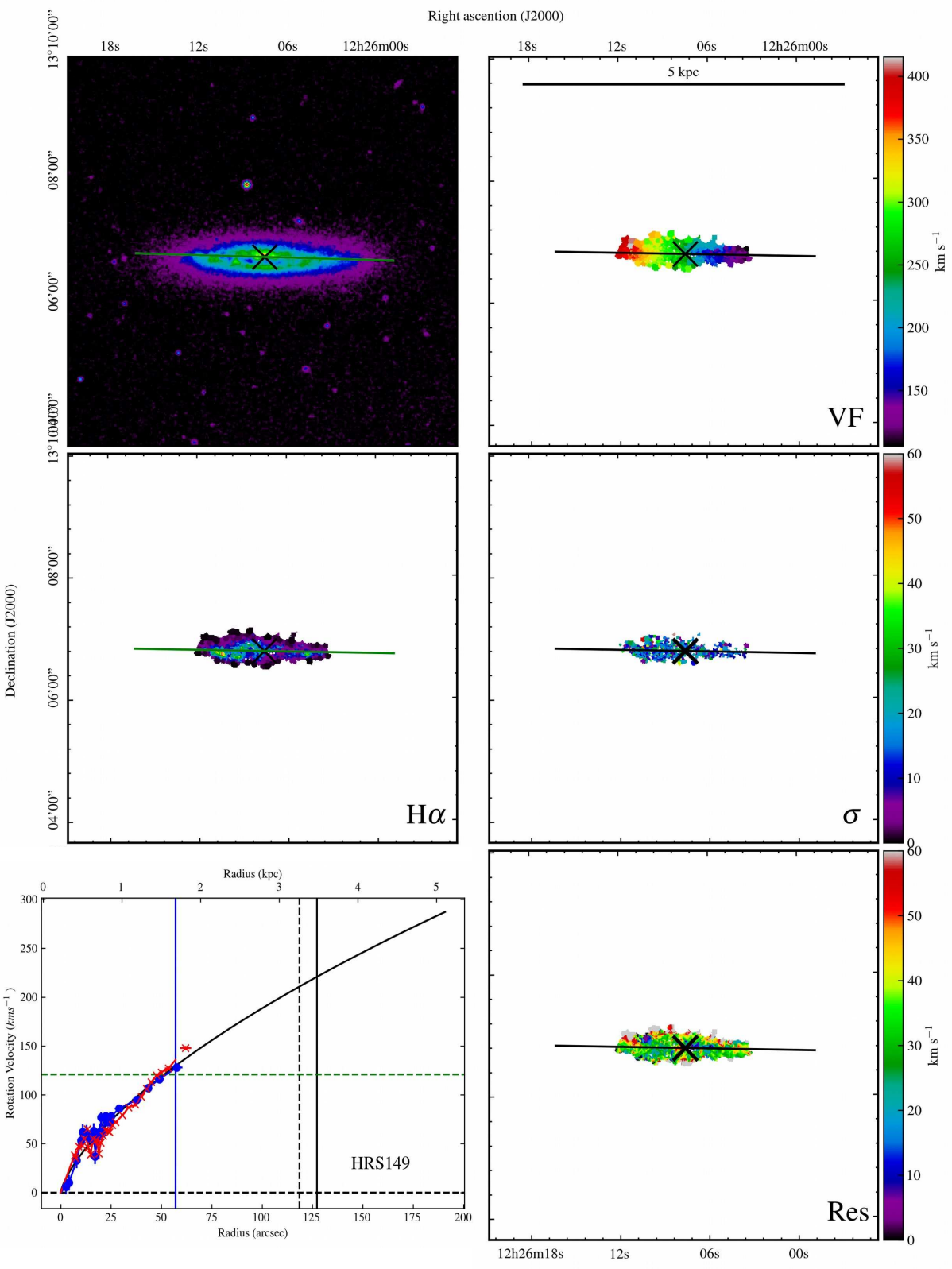
Right ascention (J2000)
Declination (J2000)
18s
12s
06s
12h26m00s
12h26m18s
00s
5 kpc
VF
Hα
σ
Res
km s−1
Radius (kpc)
Rotation Velocity (kms−1)
Radius (arcsec)
HRS149

HRS149

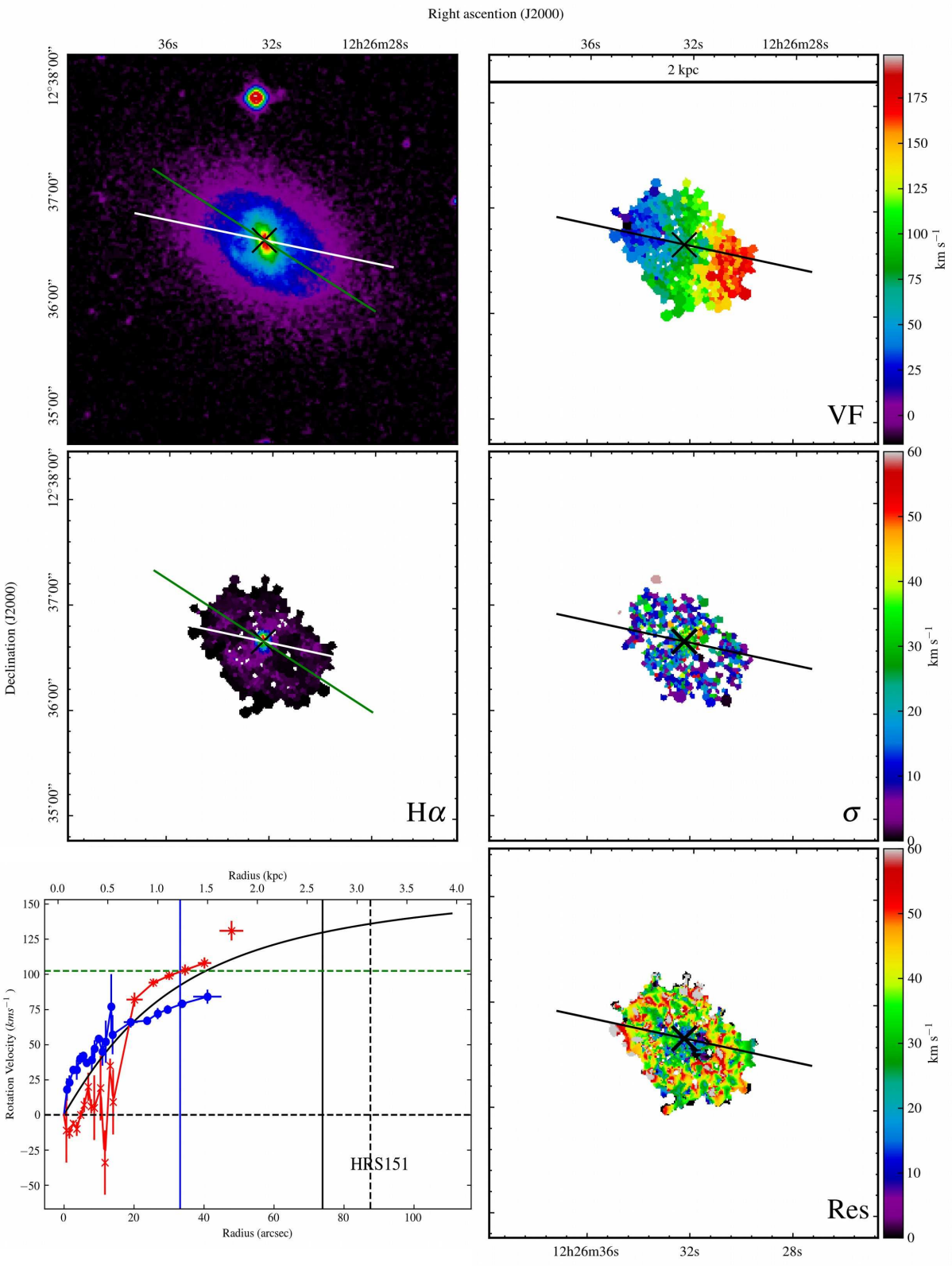
Right ascention (J2000)
36s
32s
12h26m28s
12°38'00"
37'00"
36'00"
35'00"
Declination (J2000)
2 kpc
VF
Hα
σ
Res
km s⁻¹
Radius (kpc)
Rotation Velocity (kms⁻¹)
Radius (arcsec)
HRS151
12h26m36s
28s

HRS151

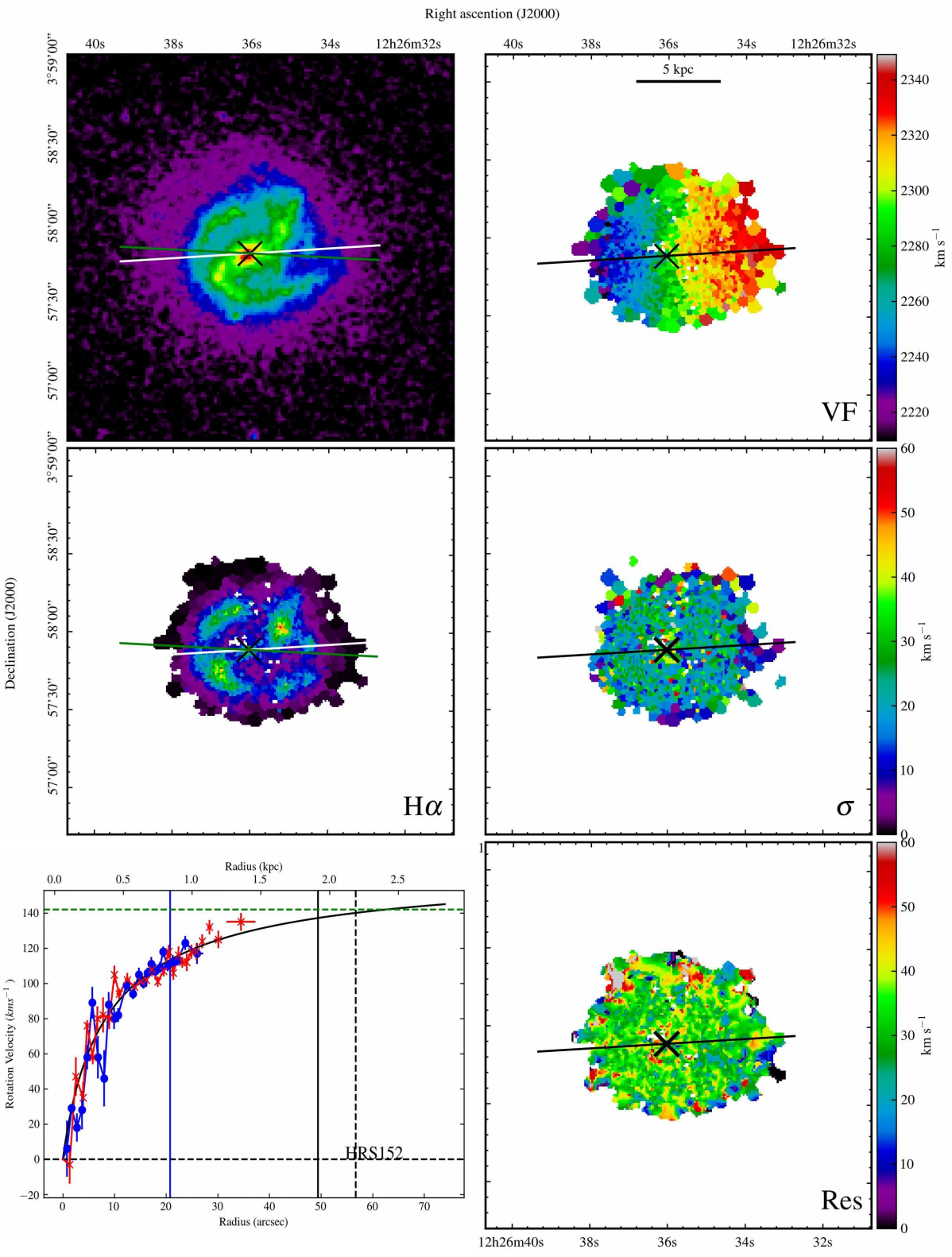
Right ascention (J2000)
Declination (J2000)
40s
38s
36s
34s
12h26m32s
3°59'00"
58'30"
58'00"
57'30"
57'00"
5 kpc
VF
Hα
σ
Res
km s⁻¹
2340
2320
2300
2280
2260
2240
2220
60
50
40
30
20
10
0
12h26m40s
32s
Radius (kpc)
0.0
0.5
1.0
1.5
2.0
2.5
Rotation Velocity (kms⁻¹)
140
120
100
80
60
40
20
0
−20
Radius (arcsec)
10
20
30
40
50
60
70
HRS152

HRS152

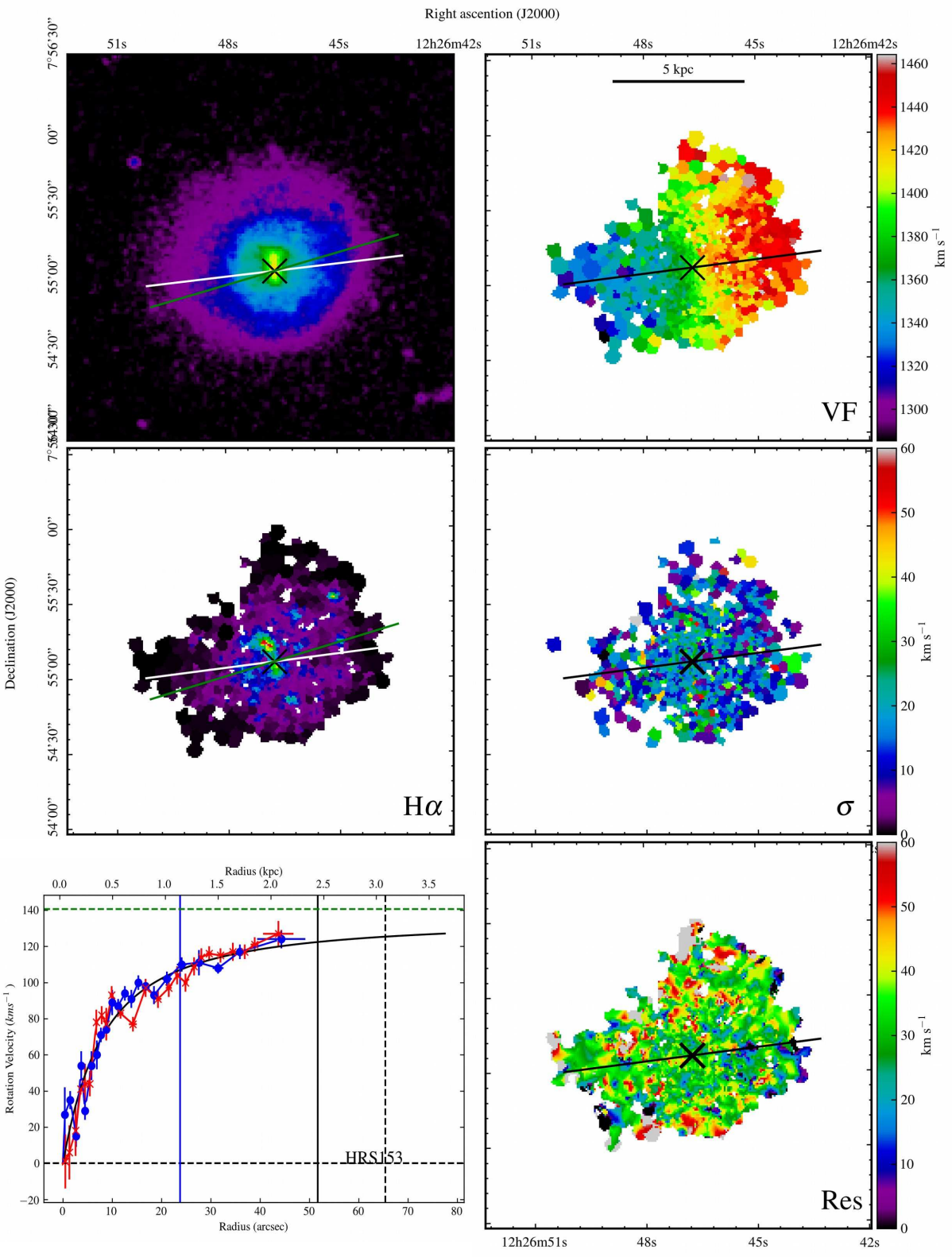
Right ascention (J2000)
Declination (J2000)
5 kpc
VF
Hα
σ
Res
km s⁻¹
Radius (kpc)
Radius (arcsec)
Rotation Velocity (kms⁻¹)
HRS153

HRS153

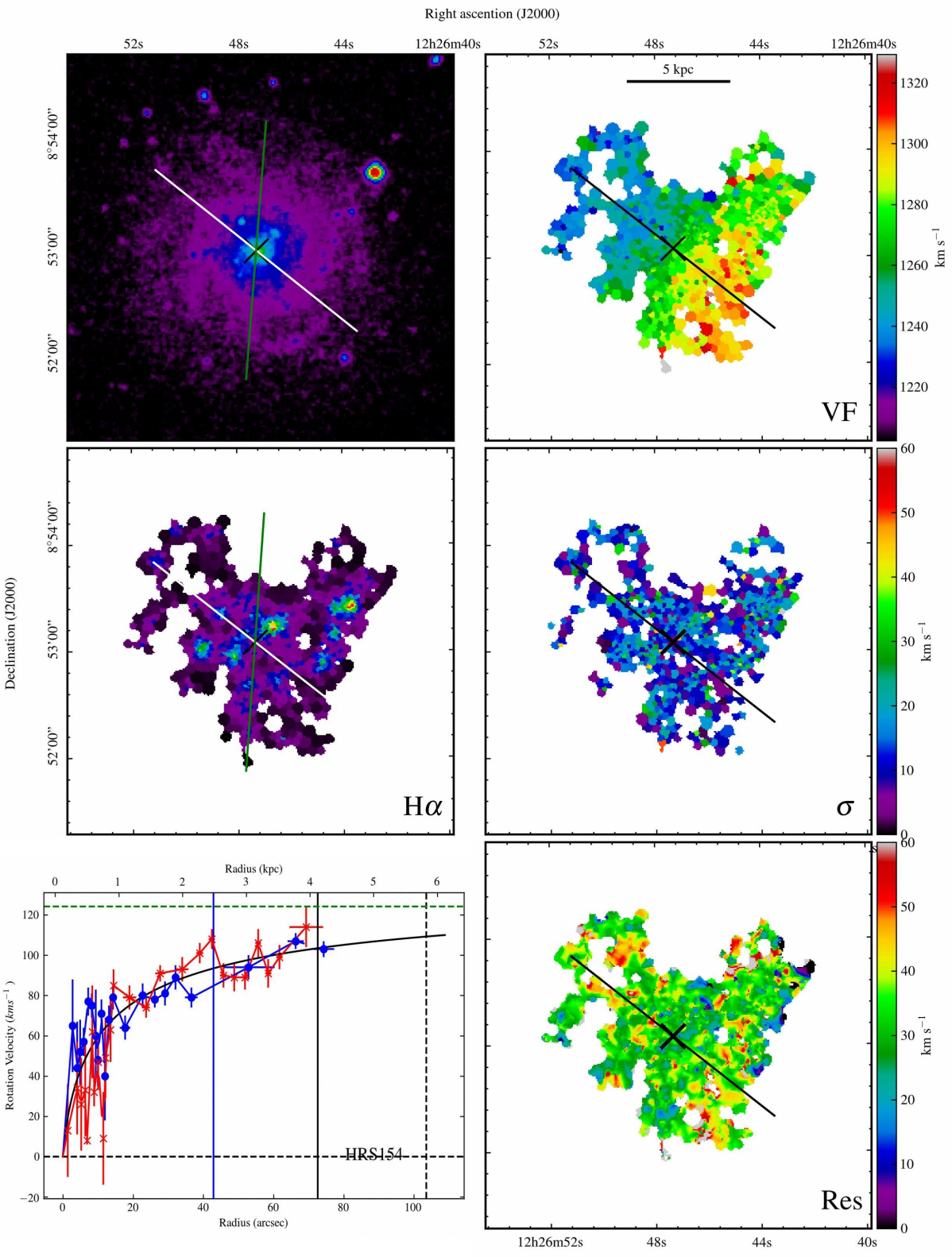
Right ascention (J2000)
52s
48s
44s
12h26m40s
52s
48s
44s
12h26m40s
Declination (J2000)
8°54'00"
53'00"
52'00"
8°54'00"
53'00"
52'00"
5 kpc
VF
Hα
σ
Res
km s⁻¹
1320
1300
1280
1260
1240
1220
60
50
40
30
20
10
0
Radius (kpc)
0
1
2
3
4
5
6
Rotation Velocity (kms⁻¹)
120
100
80
60
40
20
0
−20
HRS154
Radius (arcsec)
0
20
40
60
80
100
12h26m52s
48s
44s
40s

HRS154

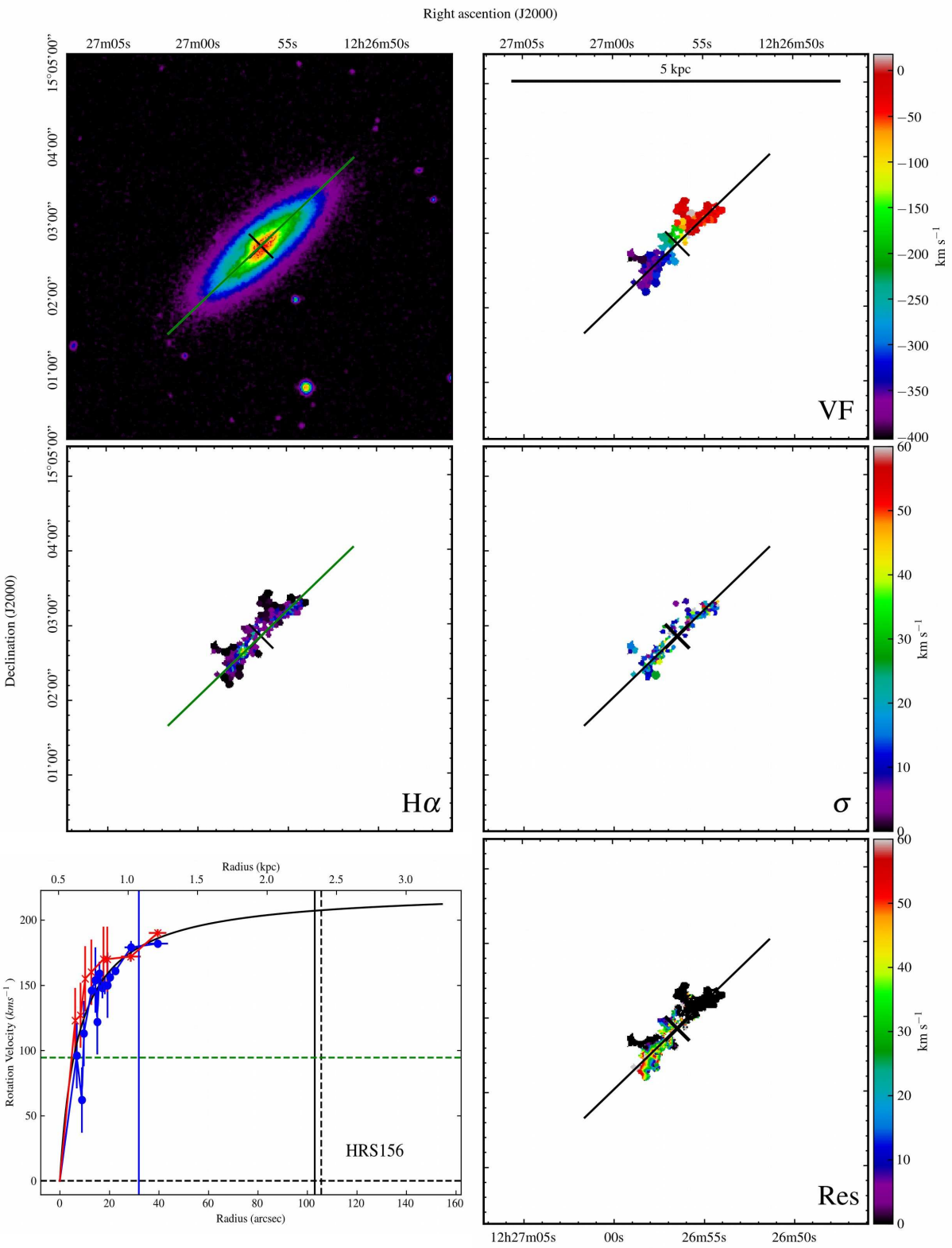
Right ascention (J2000)
27m05s
27m00s
55s
12h26m50s
Declination (J2000)
15°05'00"
04'00"
03'00"
02'00"
01'00"
5 kpc
VF
Hα
σ
Res
km s−1
Radius (kpc)
Rotation Velocity (kms−1)
Radius (arcsec)
HRS156
12h27m05s
00s
26m55s
26m50s

HRS156

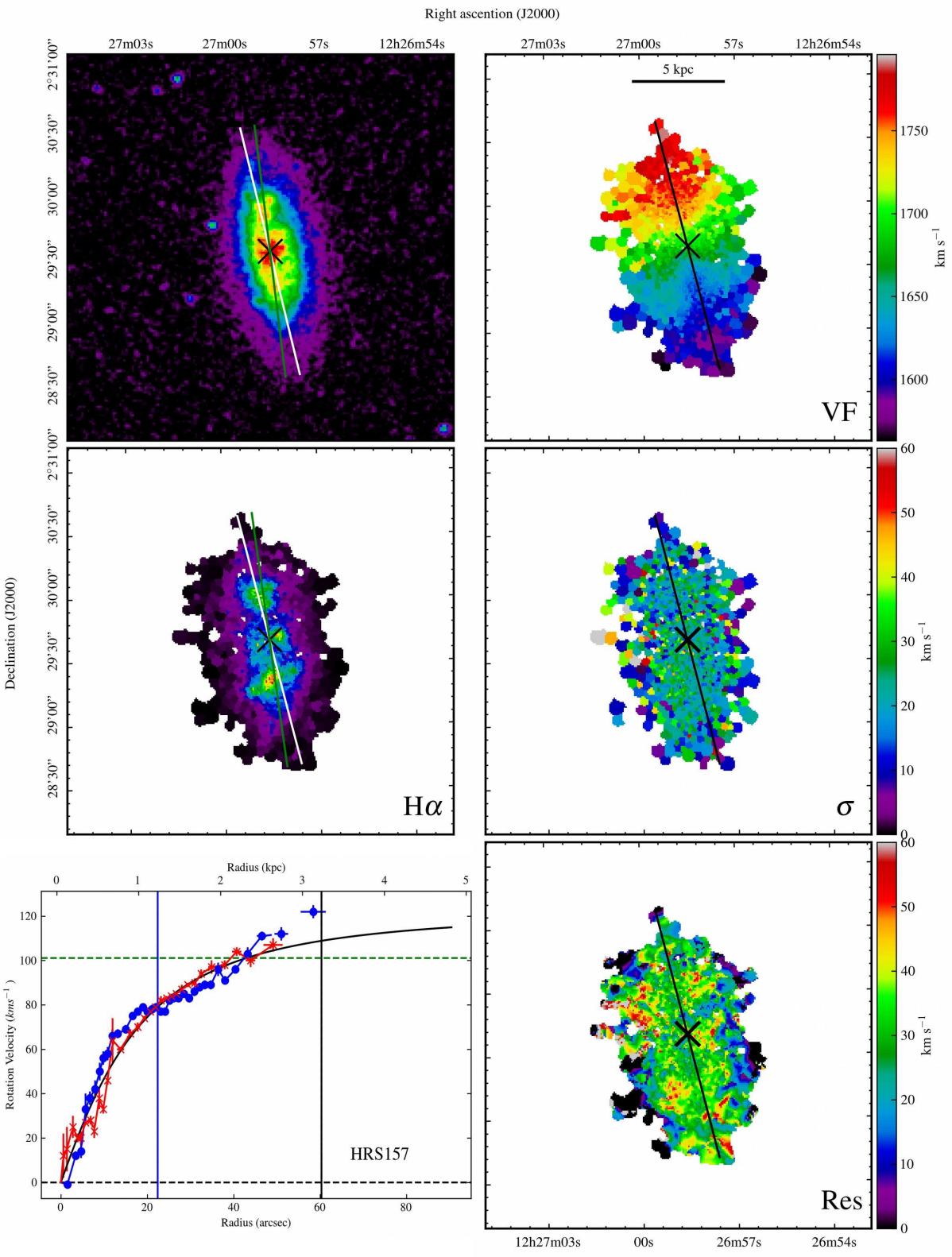
Right ascention (J2000)
Declination (J2000)
27m03s
27m00s
57s
12h26m54s
2°31'00"
30'30"
30'00"
29'30"
29'00"
28'30"
5 kpc
VF
Hα
σ
Res
km s⁻¹
1750
1700
1650
1600
60
50
40
30
20
10
0
12h27m03s
00s
26m57s
26m54s
Radius (kpc)
Rotation Velocity (kms⁻¹)
Radius (arcsec)
HRS157

HRS157

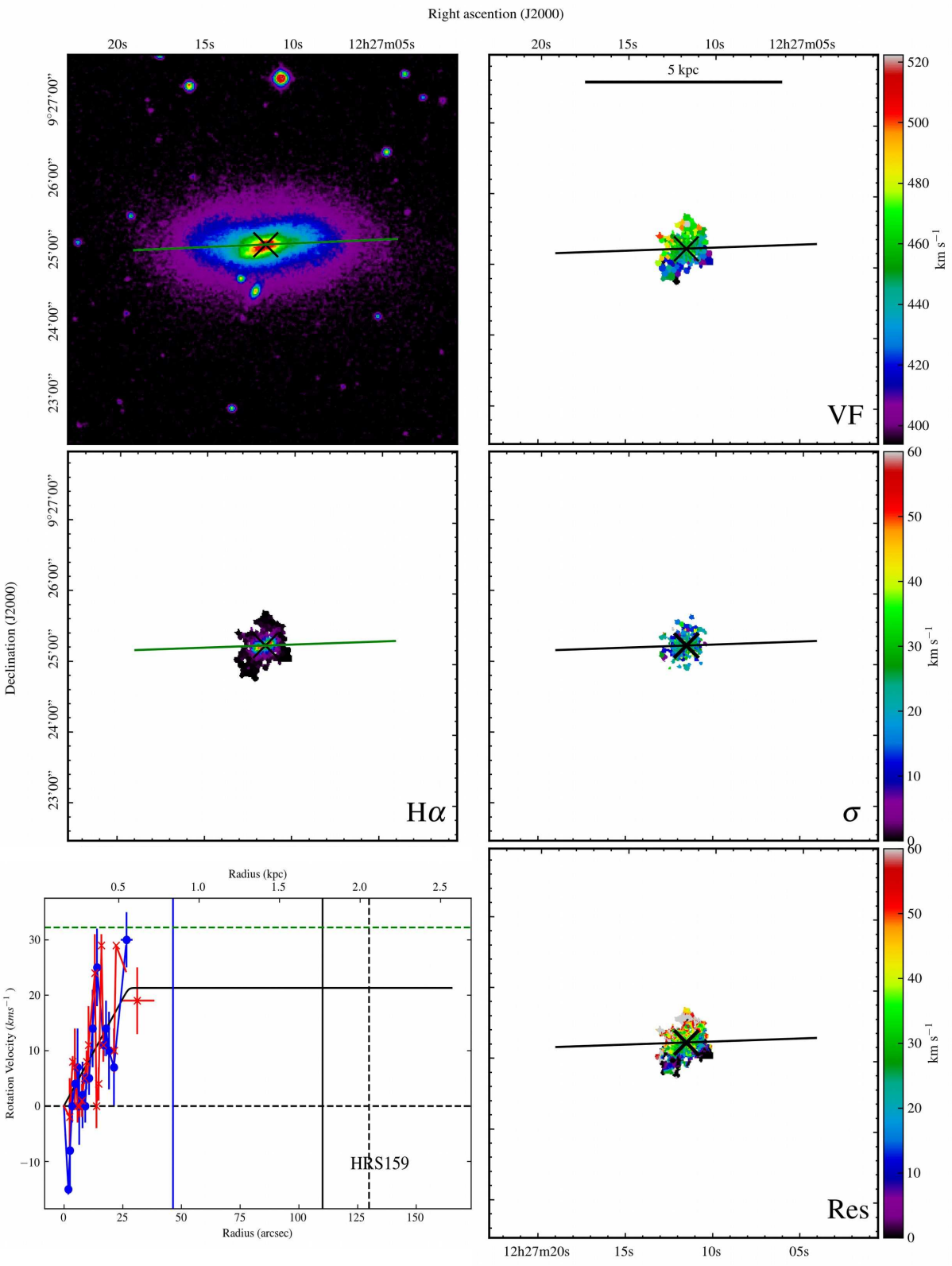
Right ascention (J2000)
20s
15s
10s
12h27m05s
9°27'00"
26'00"
25'00"
24'00"
23'00"
Declination (J2000)
5 kpc
VF
Hα
σ
Res
km s−1
520
500
480
460
440
420
400
60
50
40
30
20
10
0
Radius (kpc)
0.5
1.0
1.5
2.0
2.5
Rotation Velocity (kms−1)
HRS159
Radius (arcsec)
0
25
50
75
100
125
150
12h27m20s
05s

HRS159

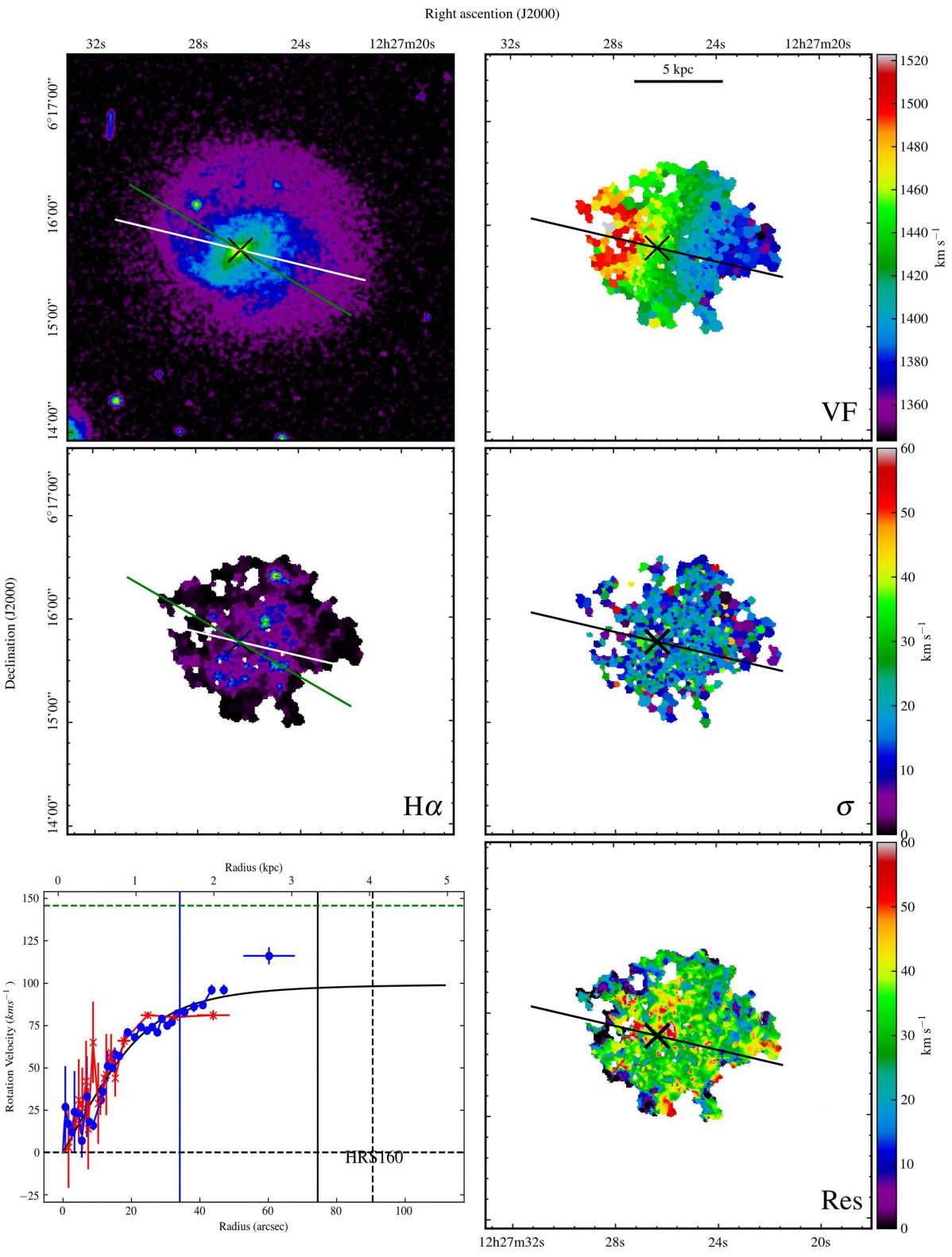
Right ascention (J2000)
Declination (J2000)
32s
28s
24s
12h27m20s
6°17'00"
16'00"
15'00"
14'00"
5 kpc
VF
Hα
σ
Res
km s⁻¹
Radius (kpc)
Rotation Velocity (kms⁻¹)
Radius (arcsec)
HRS160
12h27m32s
20s

HRS160

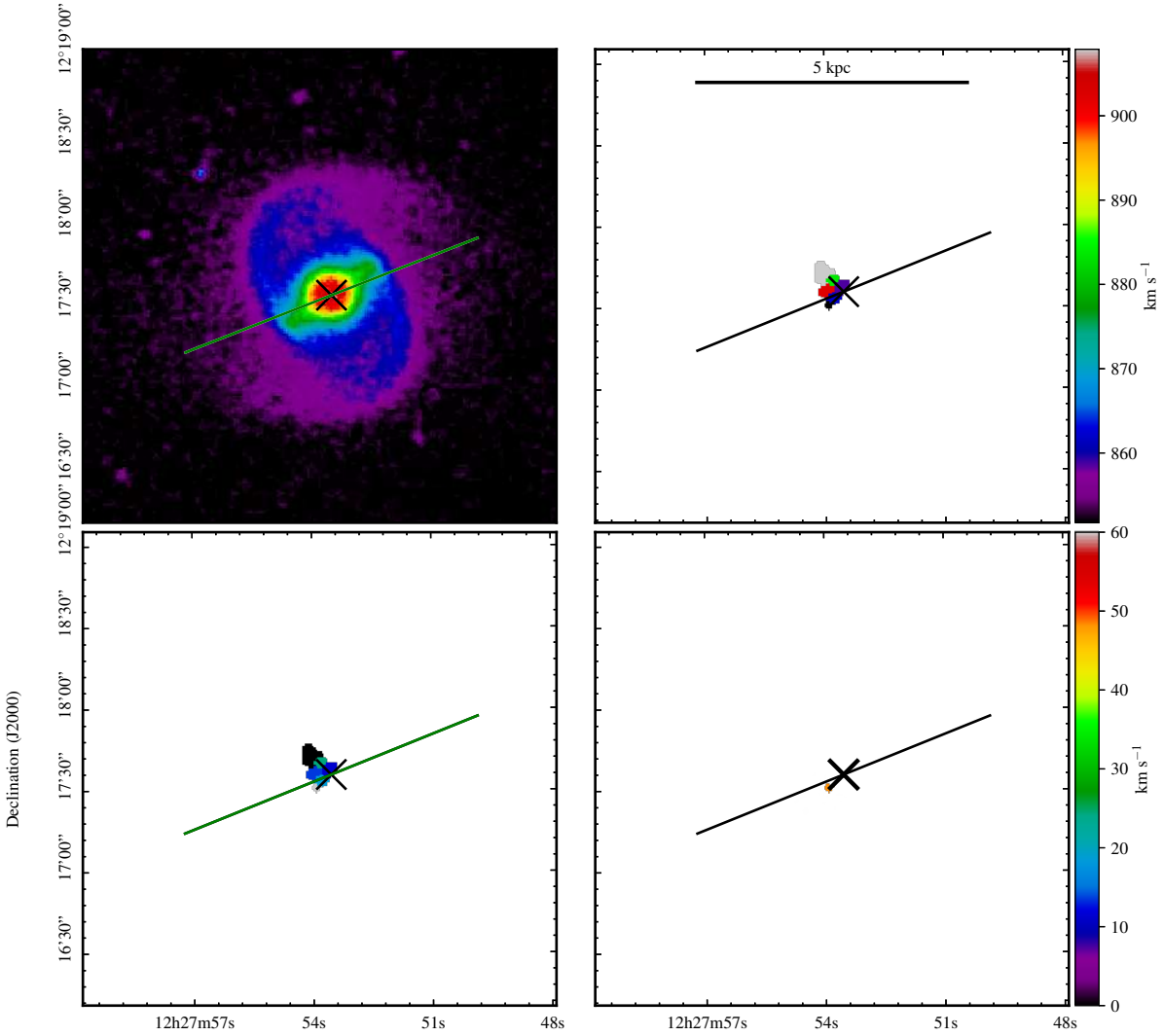

Right ascention (J2000)
HRS164

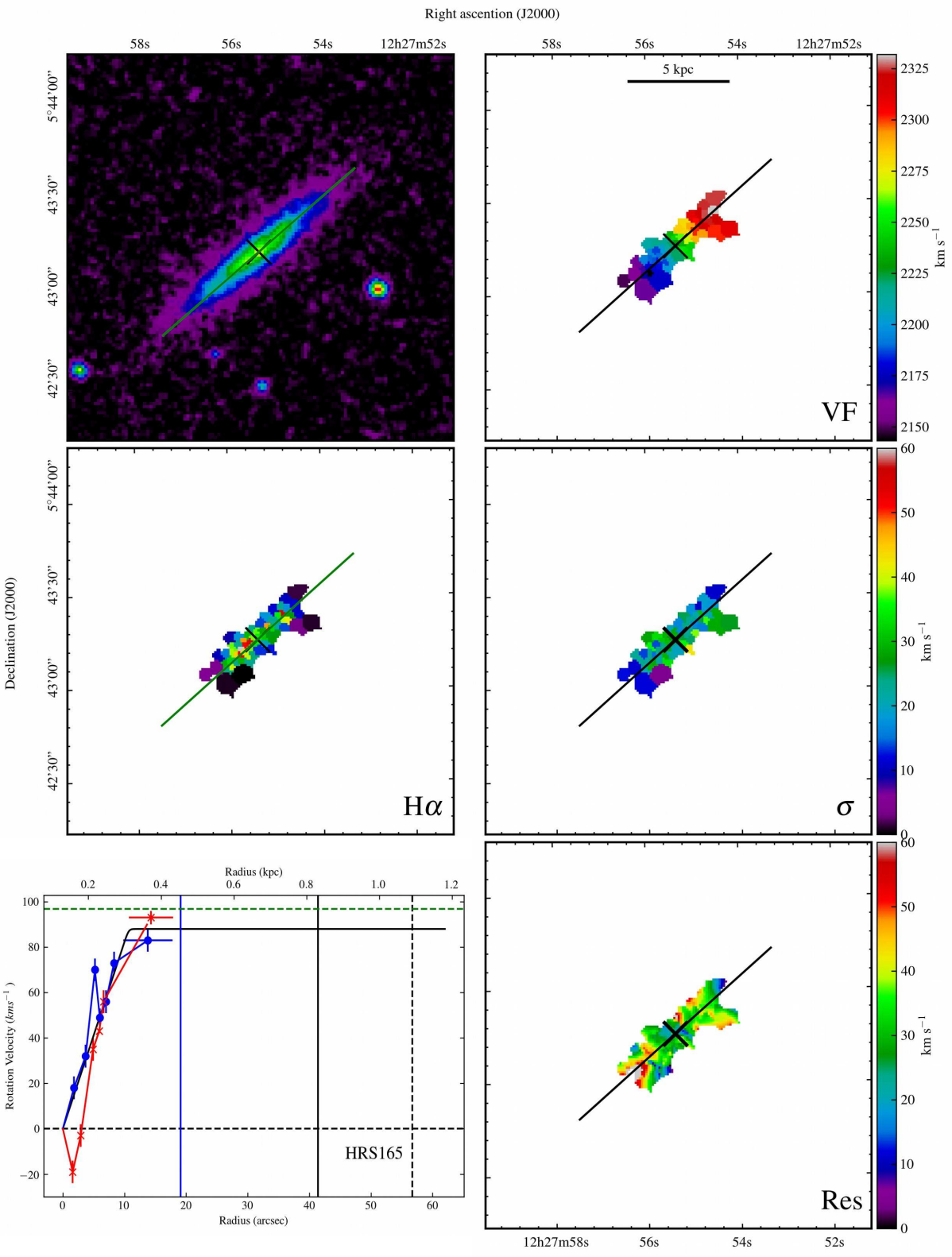
Right ascention (J2000)
58s
56s
54s
12h27m52s
5°44'00"
43'30"
43'00"
42'30"
Declination (J2000)
5 kpc
VF
Hα
σ
Res
km s⁻¹
Radius (kpc)
Rotation Velocity (kms⁻¹)
Radius (arcsec)
HRS165
12h27m58s
52s

HRS165

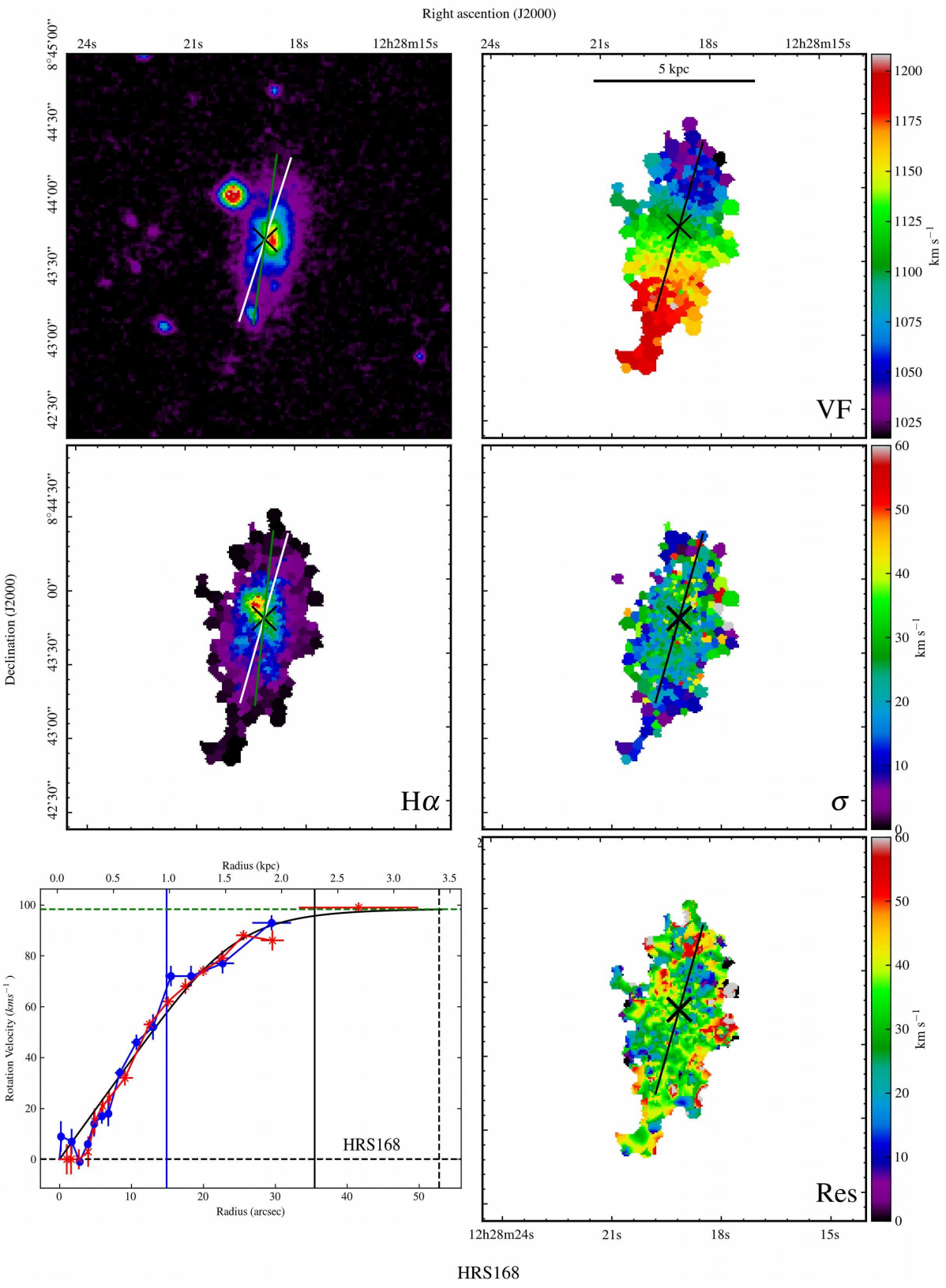
Right ascention (J2000)
Declination (J2000)
24s
21s
18s
12h28m15s
12h28m24s
15s
8°45'00"
44'30"
44'00"
43'30"
43'00"
42'30"
8°44'30"
00"
5 kpc
VF
Hα
σ
Res
km s⁻¹
Radius (kpc)
Radius (arcsec)
Rotation Velocity (kms⁻¹)
HRS168

HRS168

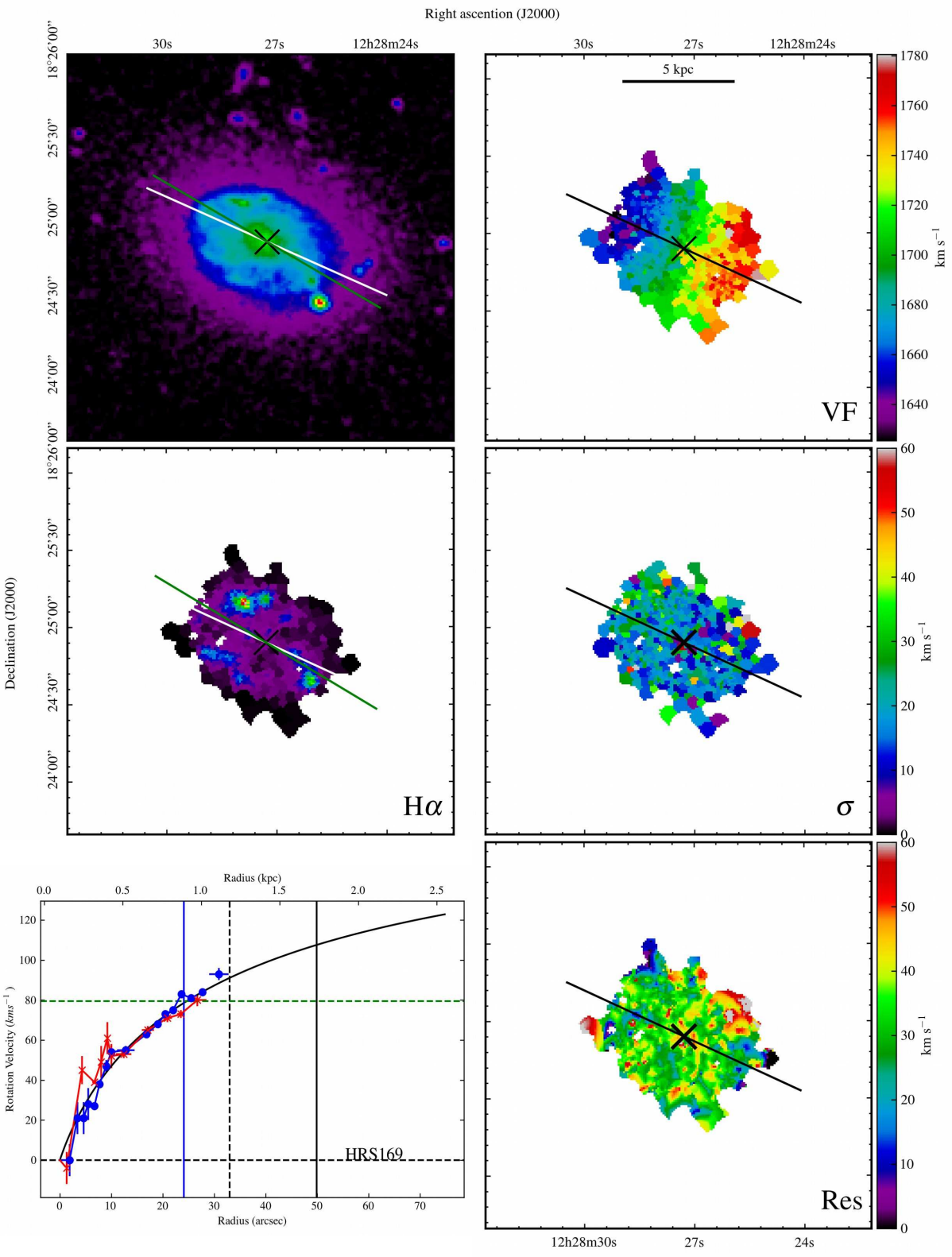
Right ascention (J2000)
Declination (J2000)
30s
27s
12h28m24s
18°26'00"
25'30"
25'00"
24'30"
24'00"
5 kpc
VF
Hα
σ
Res
km s⁻¹
1780
1760
1740
1720
1700
1680
1660
1640
60
50
40
30
20
10
0
12h28m30s
24s
Radius (kpc)
0.0
0.5
1.0
1.5
2.0
2.5
Rotation Velocity (kms⁻¹)
120
100
80
60
40
20
0
HRS169
Radius (arcsec)
0
10
20
30
40
50
60
70

HRS169

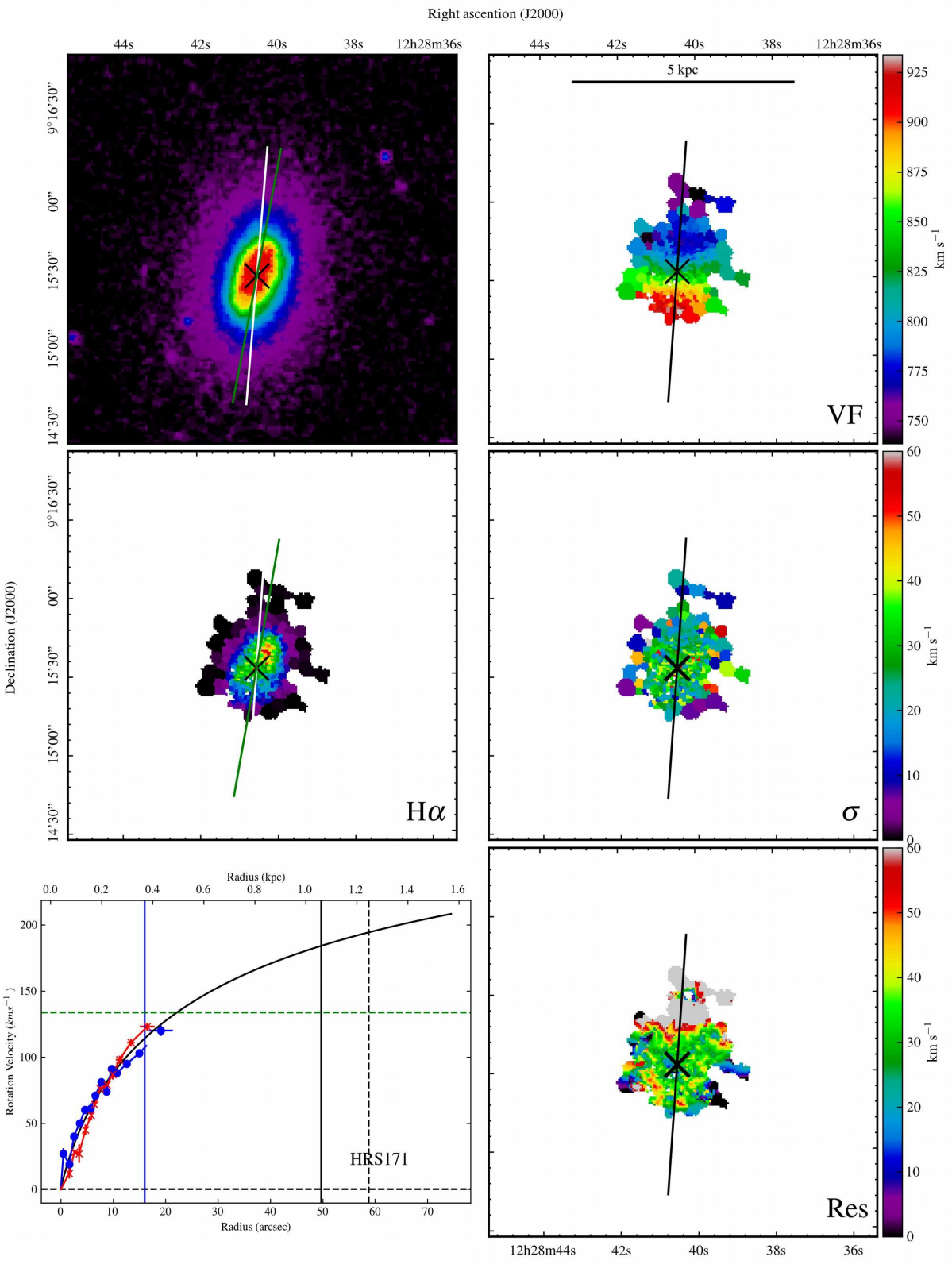
Right ascention (J2000)
44s
42s
40s
38s
12h28m36s
Declination (J2000)
9°16'30"
00"
15'30"
15'00"
14'30"
5 kpc
VF
Hα
σ
Res
km s−1
925
900
875
850
825
800
775
750
60
50
40
30
20
10
0
Radius (kpc)
0.0
0.2
0.4
0.6
0.8
1.0
1.2
1.4
1.6
Rotation Velocity (kms−1)
200
150
100
50
0
Radius (arcsec)
0
10
20
30
40
50
60
70
HRS171
12h28m44s
36s

HRS171

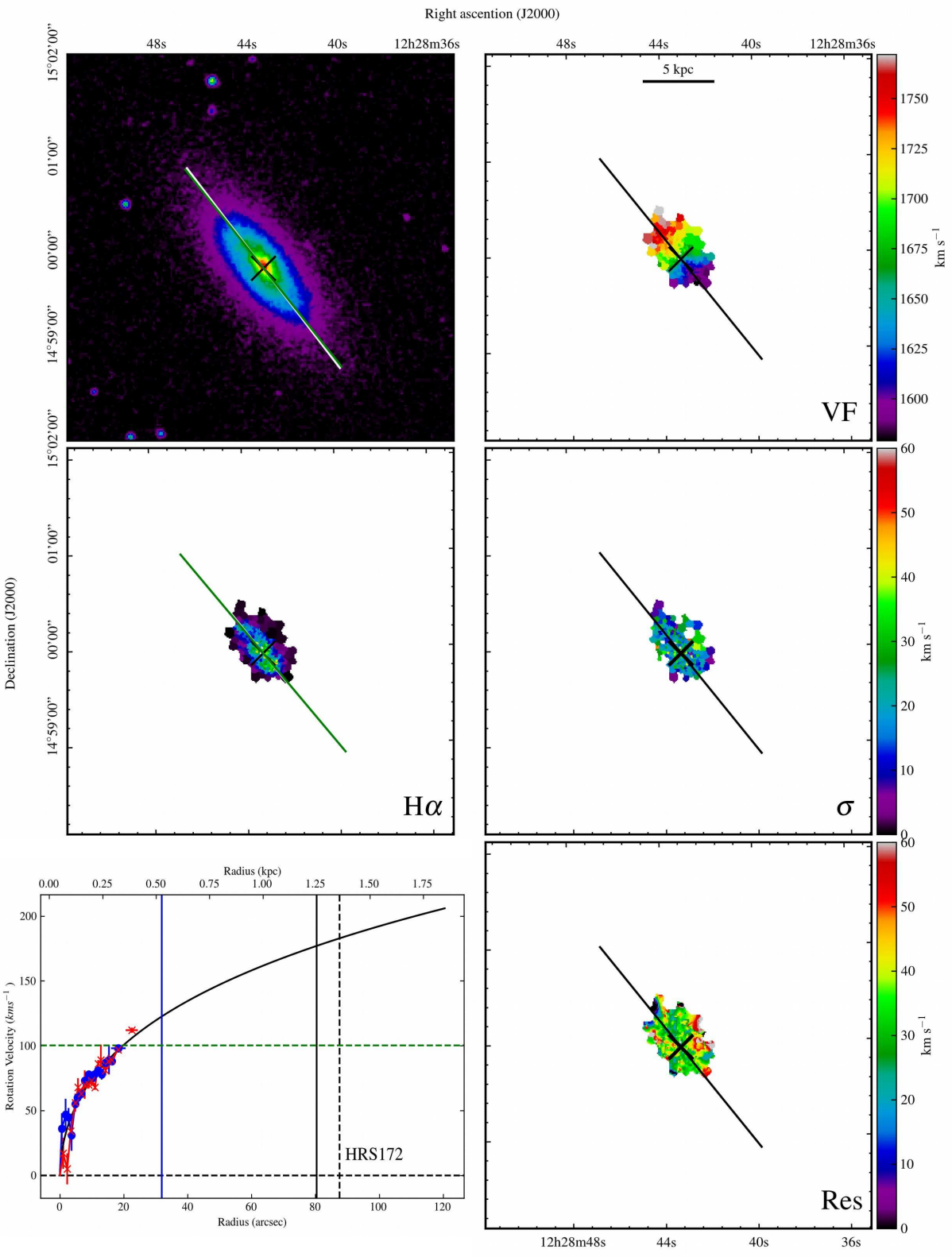
Right ascention (J2000)
Declination (J2000)
48s
44s
40s
12h28m36s
15°02'00"
01'00"
00'00"
14°59'00"
5 kpc
VF
Hα
σ
Res
km s⁻¹
Radius (kpc)
Radius (arcsec)
Rotation Velocity (kms⁻¹)
HRS172
12h28m48s
36s

HRS172

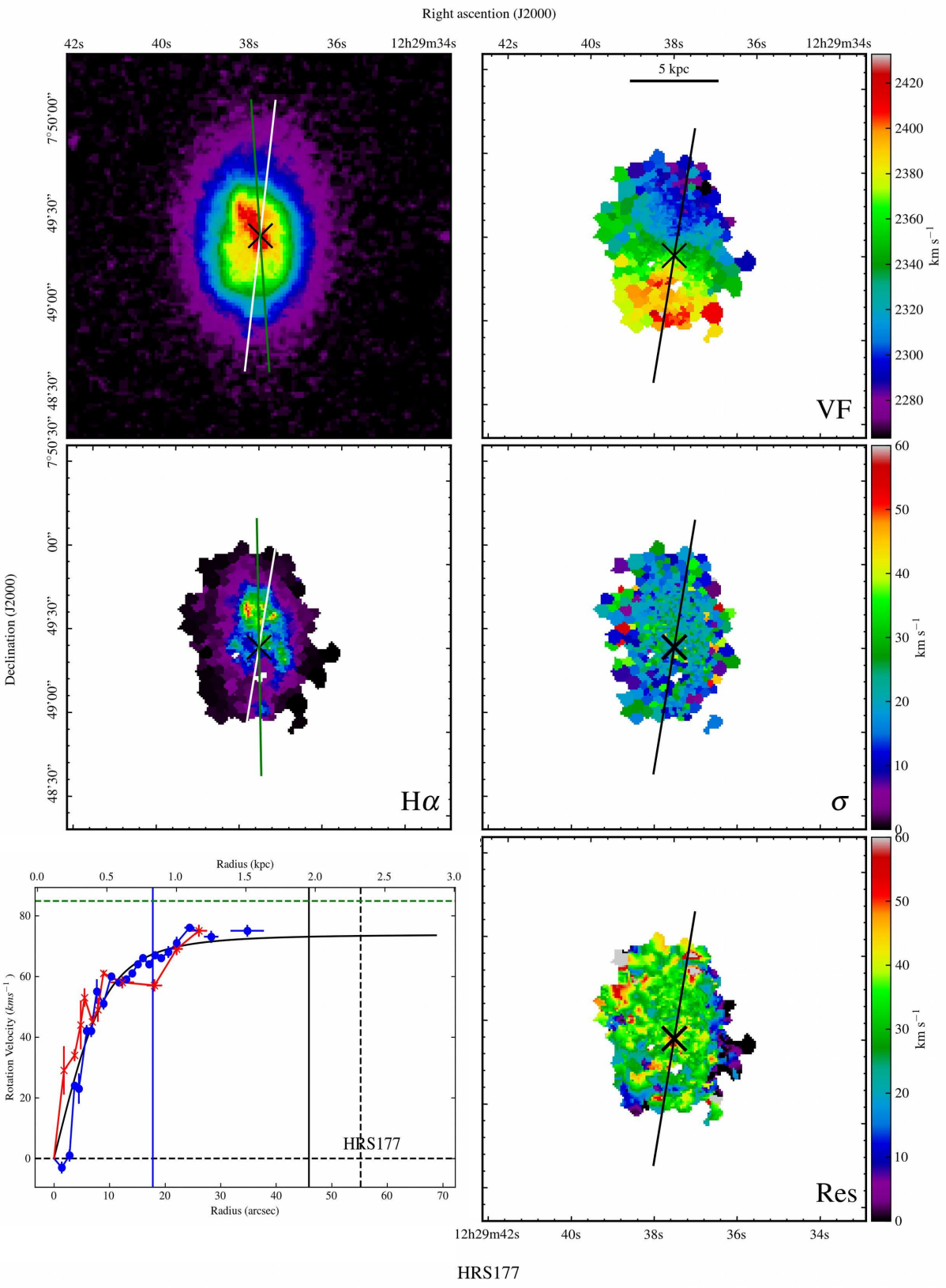
Right ascention (J2000)
42s
40s
38s
36s
12h29m34s
12h29m42s
34s
Declination (J2000)
7°50'00"
49'30"
49'00"
48'30"
00"
5 kpc
VF
Hα
σ
Res
km s⁻¹
2420
2400
2380
2360
2340
2320
2300
2280
60
50
40
30
20
10
0
Radius (kpc)
0.0
0.5
1.0
1.5
2.0
2.5
3.0
Rotation Velocity (kms⁻¹)
80
60
40
20
0
Radius (arcsec)
0
10
20
30
40
50
60
70
HRS177

HRS177

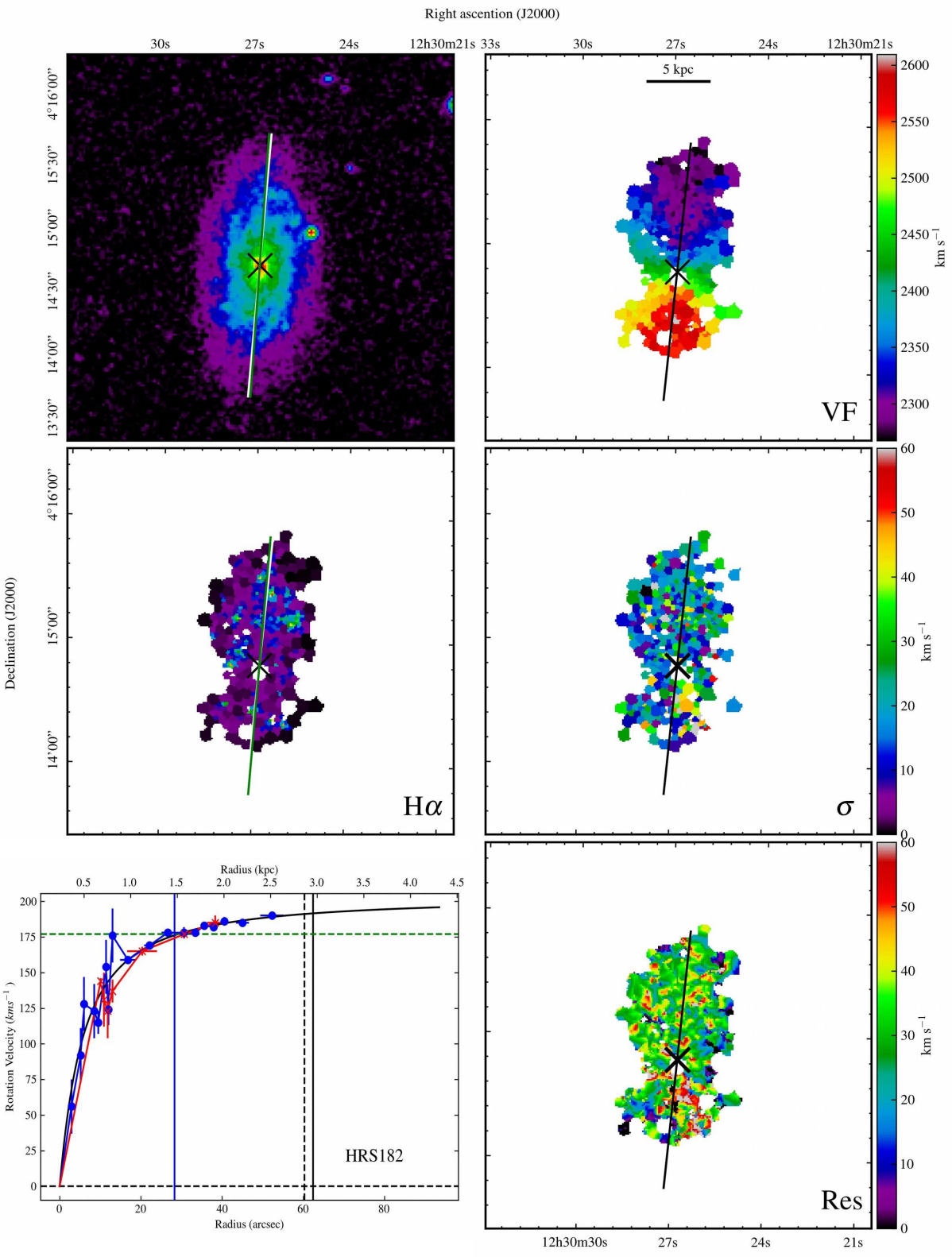
Right ascention (J2000)
30s
27s
24s
12h30m21s
33s
Declination (J2000)
4°16'00"
15'30"
15'00"
14'30"
14'00"
13'30"
5 kpc
VF
Hα
σ
Res
km s⁻¹
2600
2550
2500
2450
2400
2350
2300
60
50
40
30
20
10
0
12h30m30s
21s
Radius (kpc)
0.5
1.0
1.5
2.0
2.5
3.0
3.5
4.0
4.5
Rotation Velocity (kms⁻¹)
200
175
150
125
100
75
50
25
0
Radius (arcsec)
20
40
60
80
HRS182

HRS182

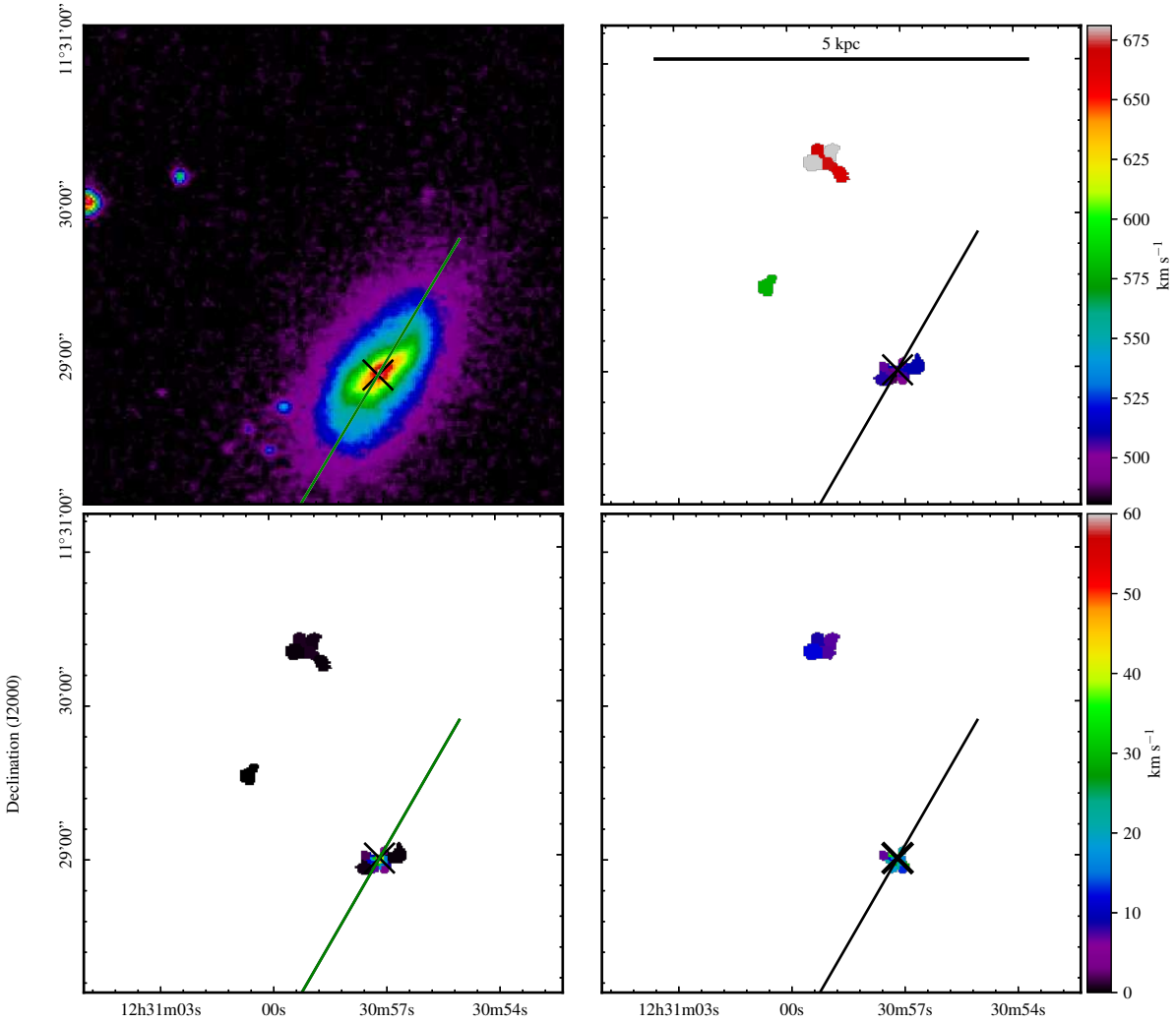

Right ascention (J2000)
HRS184

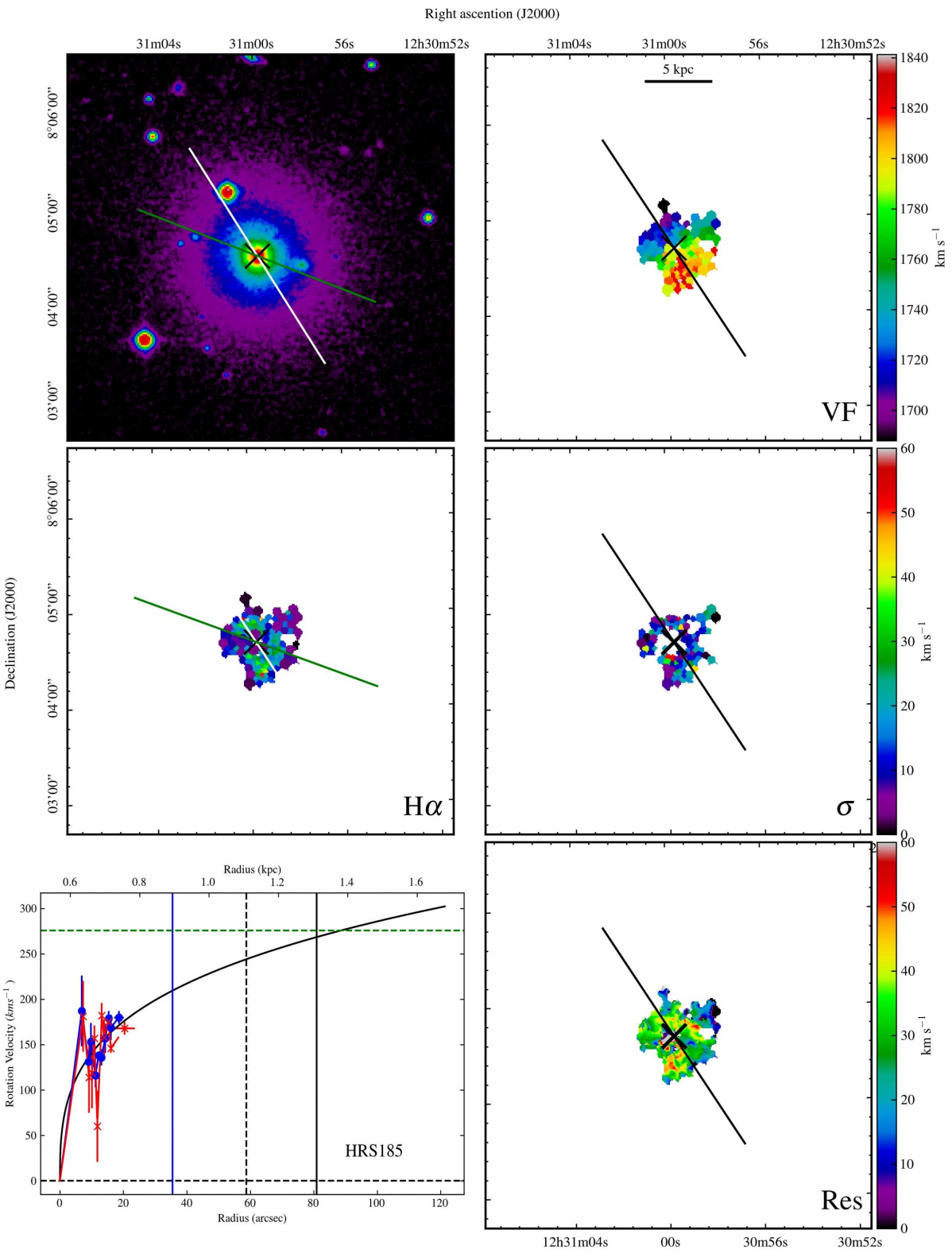
Right ascention (J2000)
31m04s
31m00s
56s
12h30m52s
Declination (J2000)
8°06'00"
05'00"
04'00"
03'00"
5 kpc
VF
Hα
σ
Res
km s−1
1840
1820
1800
1780
1760
1740
1720
1700
60
50
40
30
20
10
0
12h31m04s
00s
30m56s
30m52s
Radius (kpc)
0.6
0.8
1.0
1.2
1.4
1.6
Rotation Velocity (kms−1)
300
250
200
150
100
50
0
Radius (arcsec)
0
20
40
60
80
100
120
HRS185

HRS185

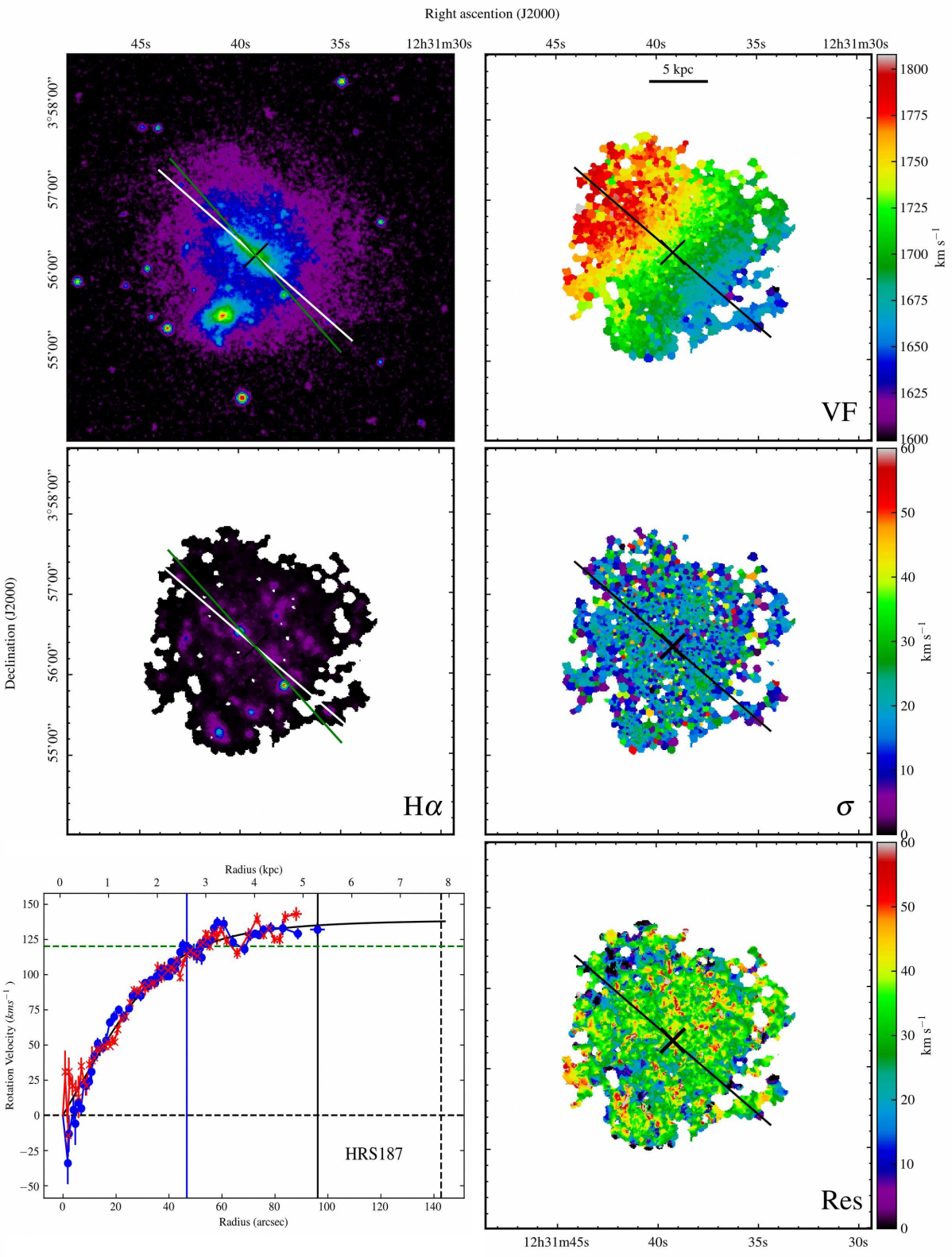
Right ascention (J2000)
45s
40s
35s
12h31m30s
Declination (J2000)
3°58'00"
57'00"
56'00"
55'00"
5 kpc
VF
Hα
σ
Res
km s⁻¹
Radius (kpc)
Rotation Velocity (kms⁻¹)
Radius (arcsec)
HRS187
12h31m45s
30s

HRS187

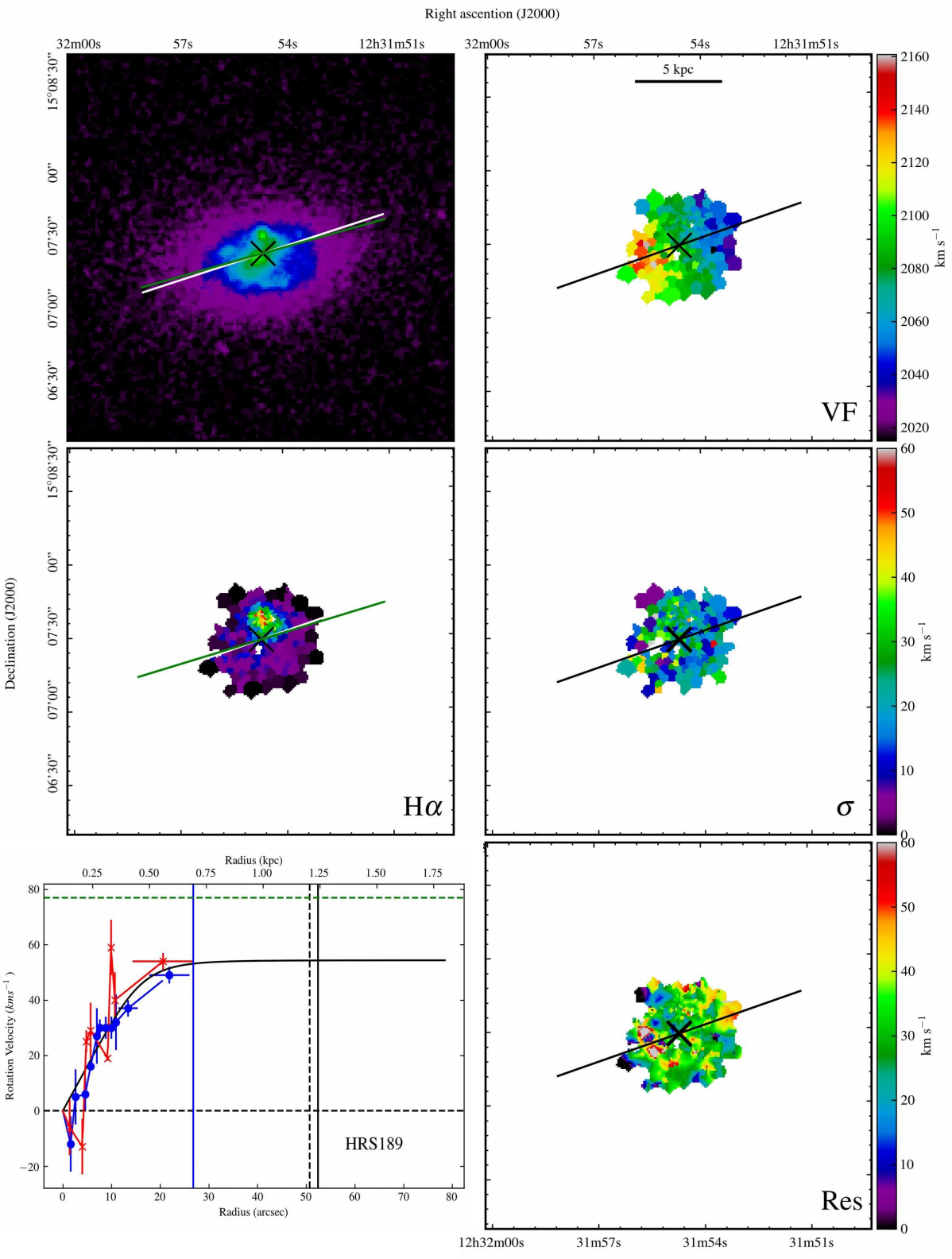
Right ascention (J2000)
32m00s
57s
54s
12h31m51s
15°08'30"
00"
07'30"
07'00"
06'30"
Declination (J2000)
5 kpc
VF
Hα
σ
Res
km s⁻¹
Radius (kpc)
0.25
0.50
0.75
1.00
1.25
1.50
1.75
Rotation Velocity (kms⁻¹)
HRS189
Radius (arcsec)
12h32m00s
31m57s
31m54s
31m51s

HRS189

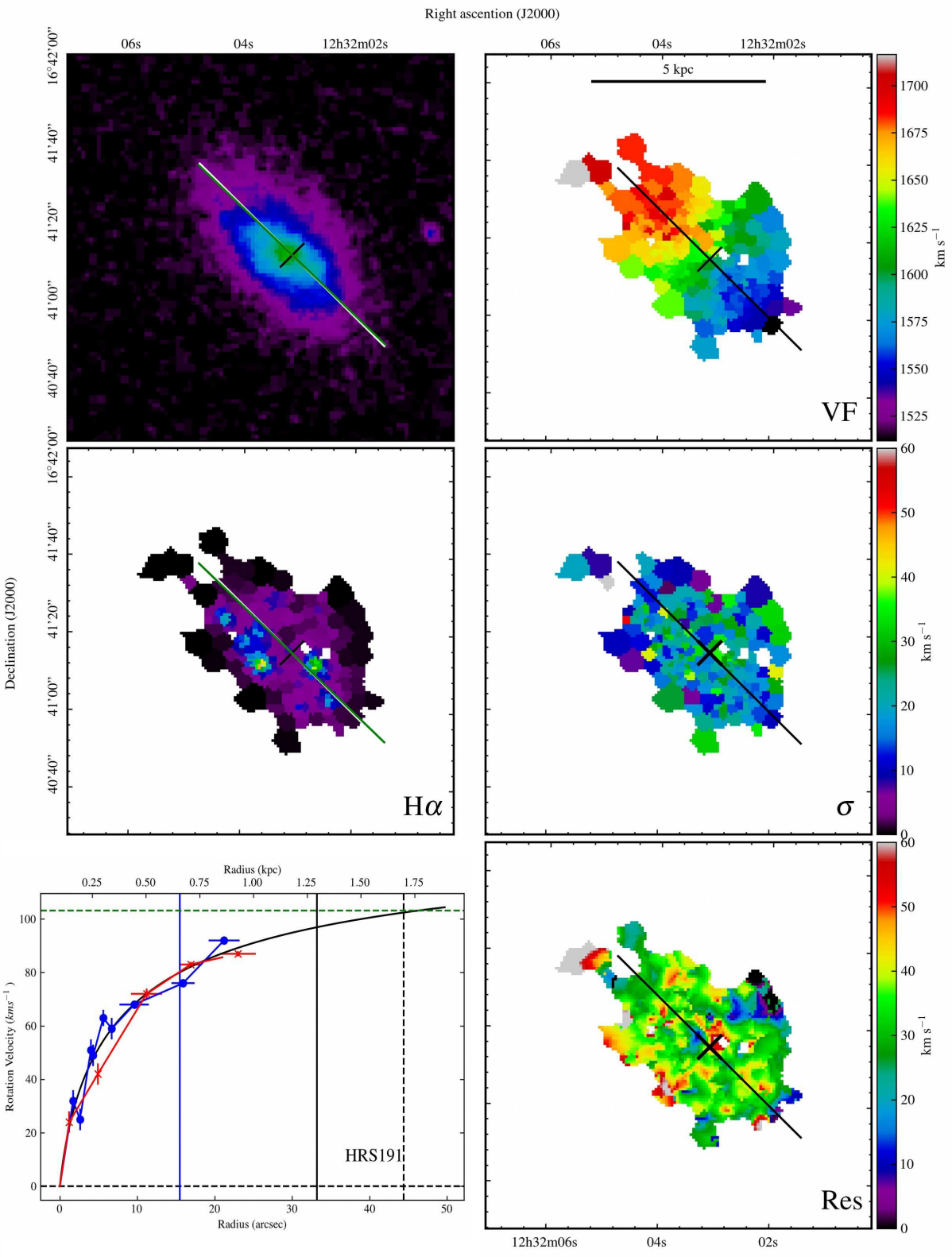
Right ascention (J2000)
06s
04s
12h32m02s
16°42'00"
41'40"
41'20"
41'00"
40'40"
Declination (J2000)
5 kpc
VF
Hα
σ
Res
km s⁻¹
Radius (kpc)
0.25
0.50
0.75
1.00
1.25
1.50
1.75
Rotation Velocity (kms⁻¹)
Radius (arcsec)
HRS191
12h32m06s
02s

HRS191

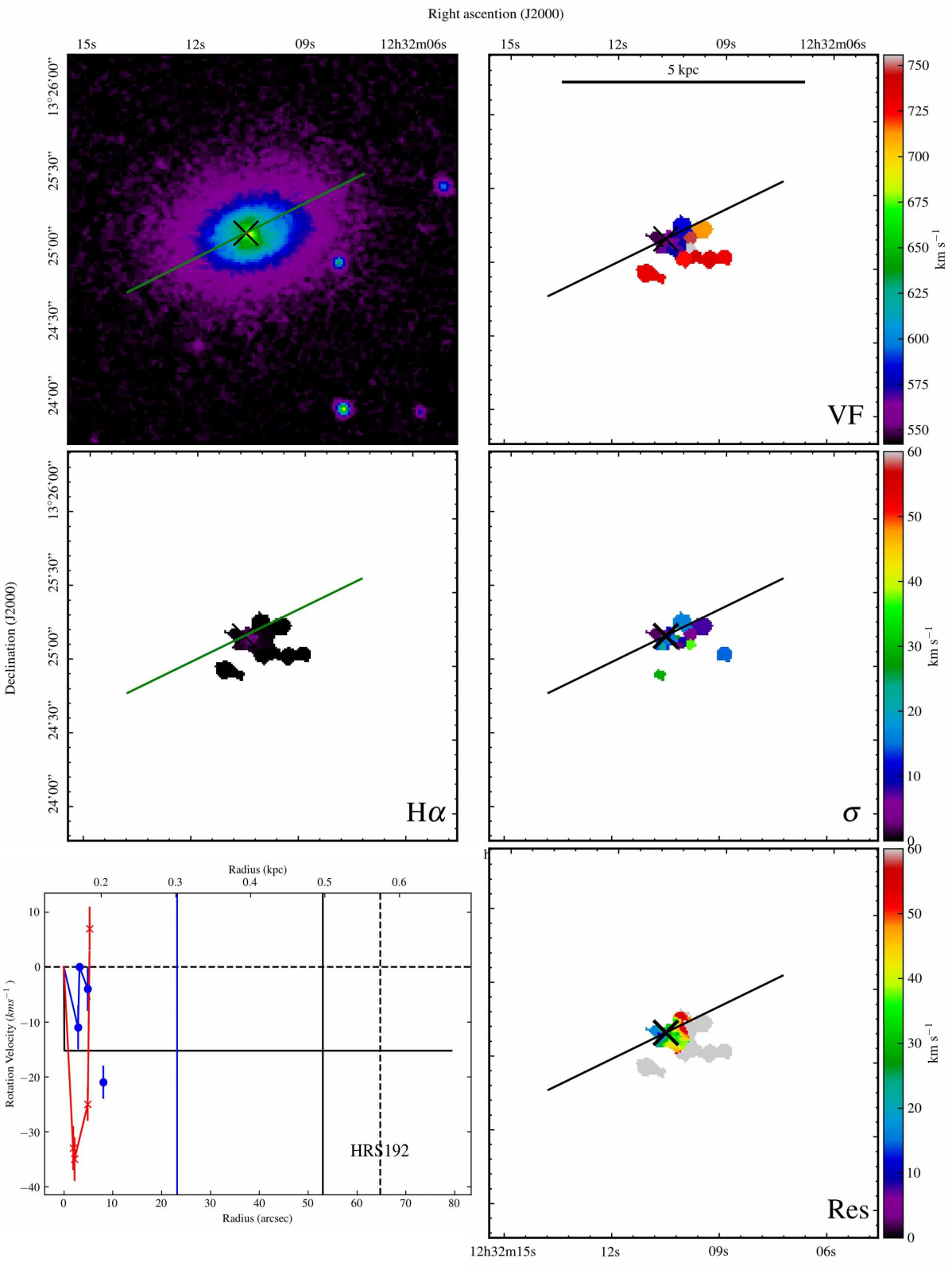
Right ascention (J2000)
15s
12s
09s
12h32m06s
Declination (J2000)
13°26'00"
25'30"
25'00"
24'30"
24'00"
5 kpc
VF
Hα
σ
Res
km s−1
Radius (kpc)
Rotation Velocity (kms−1)
Radius (arcsec)
HRS192
12h32m15s
06s

HRS192

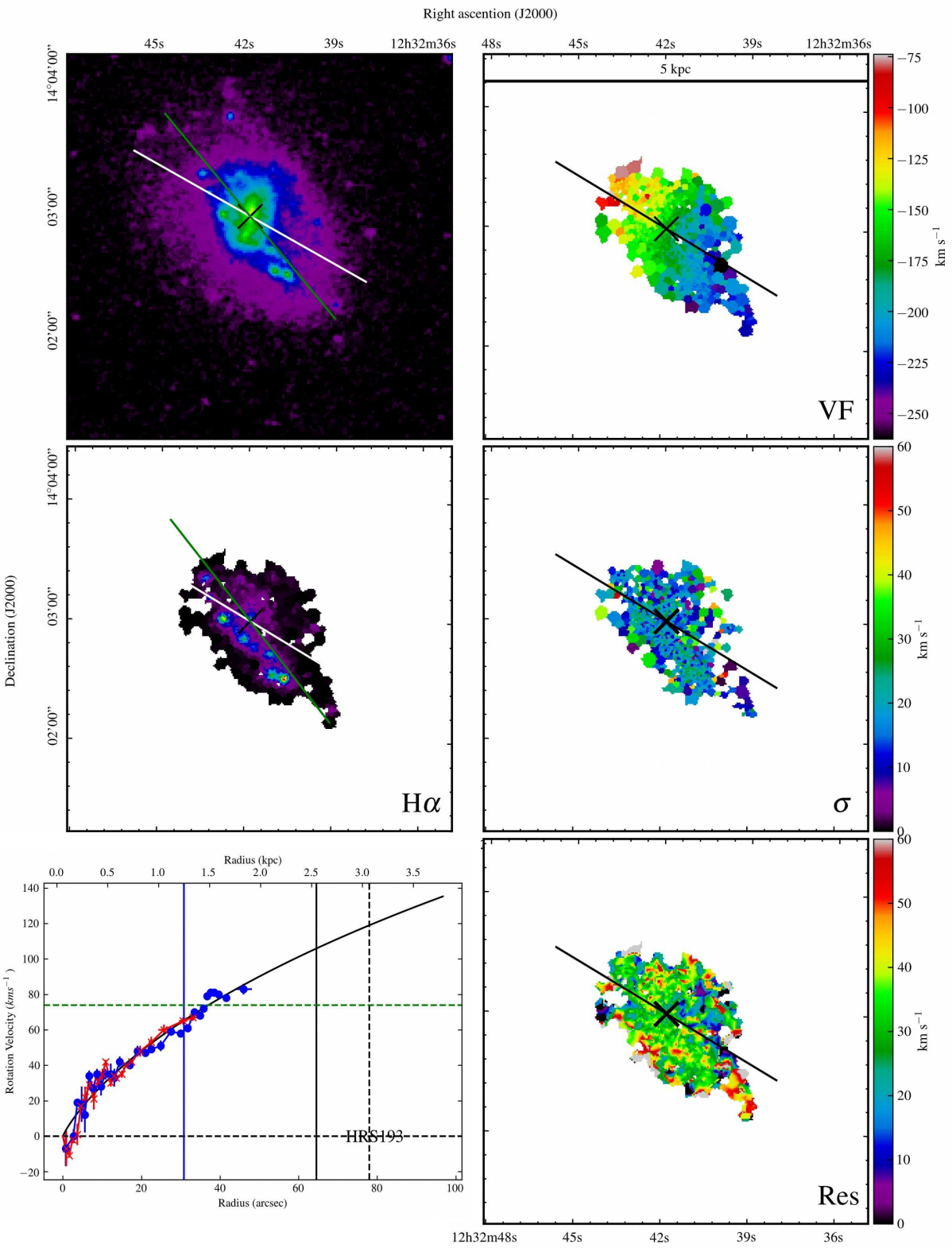
Right ascention (J2000)
45s
42s
39s
12h32m36s
48s
14°04'00"
03'00"
02'00"
5 kpc
VF
Hα
σ
Res
Declination (J2000)
km s−1
Radius (kpc)
Rotation Velocity (kms−1)
Radius (arcsec)
HRS193
12h32m48s
36s

HRS193

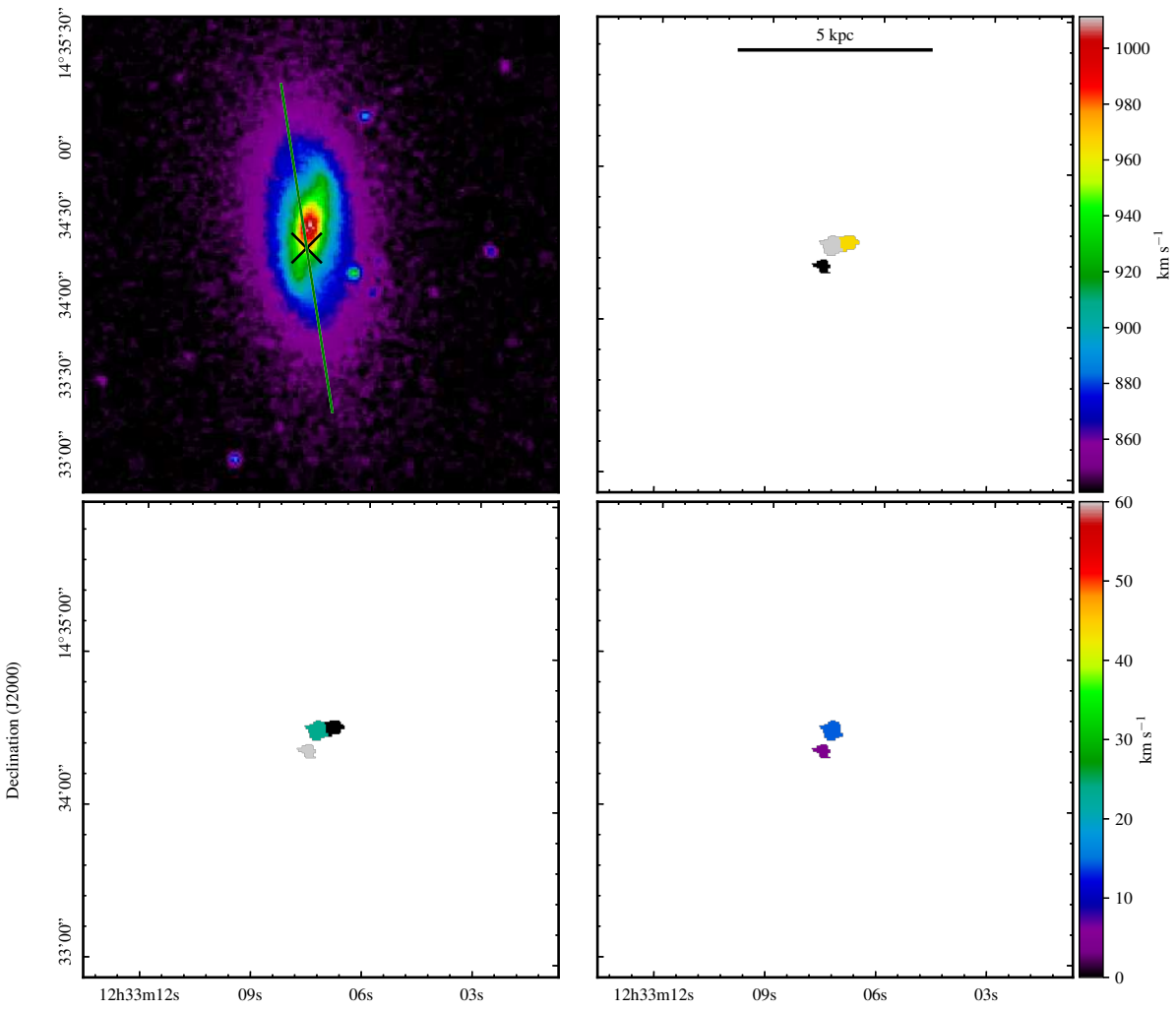
5 kpc
1000
980
960
940
920
900
880
860
km s^{-1}
60
50
40
30
20
10
0
km s^{-1}
14°35'30"
00"
34'30"
34'00"
33'30"
33'00"
14°35'00"
34'00"
33'00"
Declination (J2000)
12h33m12s
09s
06s
03s
12h33m12s
09s
06s
03s
Right ascention (J2000)
HRS195

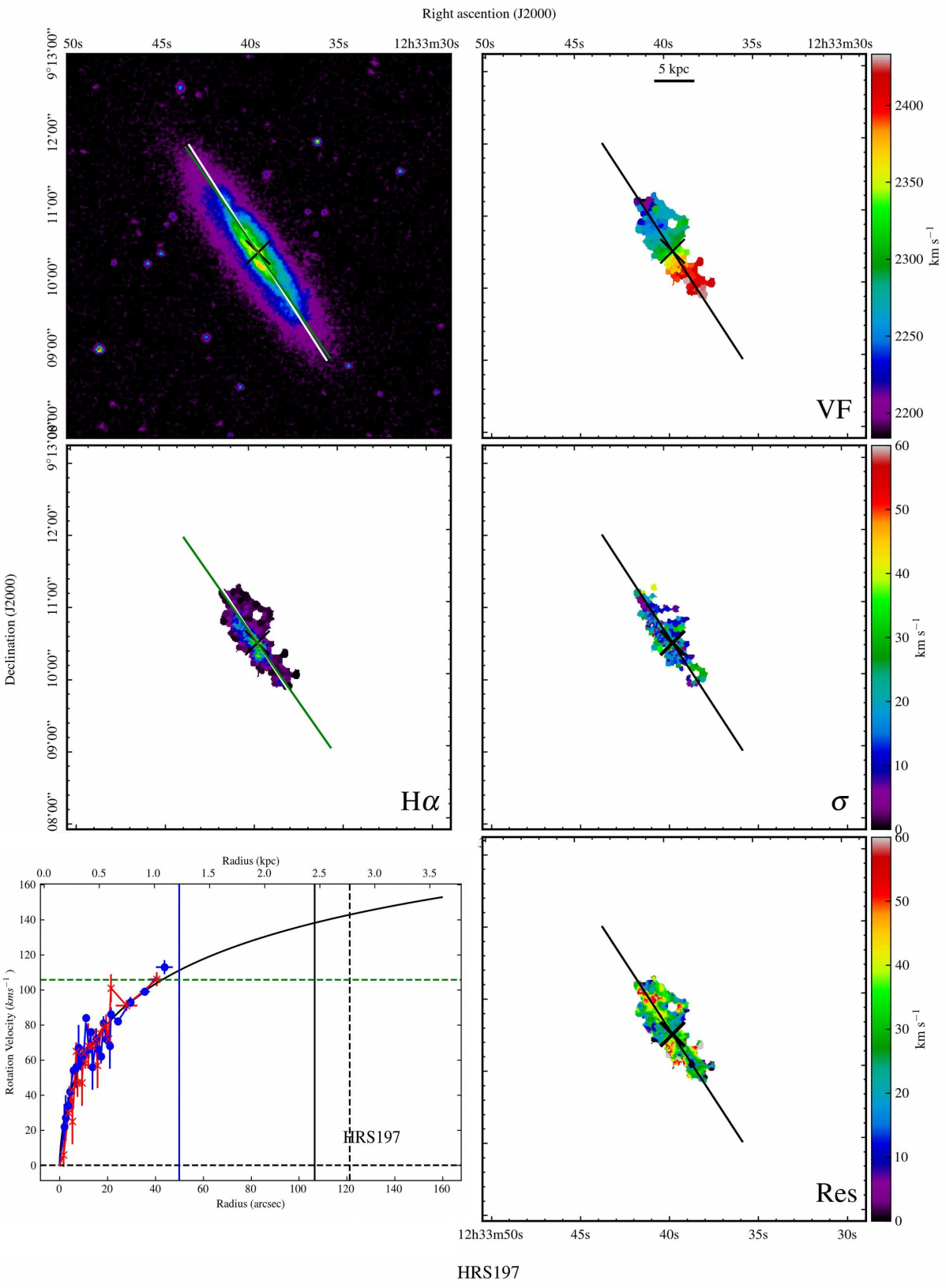
Right ascention (J2000)
Declination (J2000)
5 kpc
VF
Hα
σ
Res
km s−1
Radius (kpc)
Radius (arcsec)
Rotation Velocity (kms−1)
HRS197

HRS197

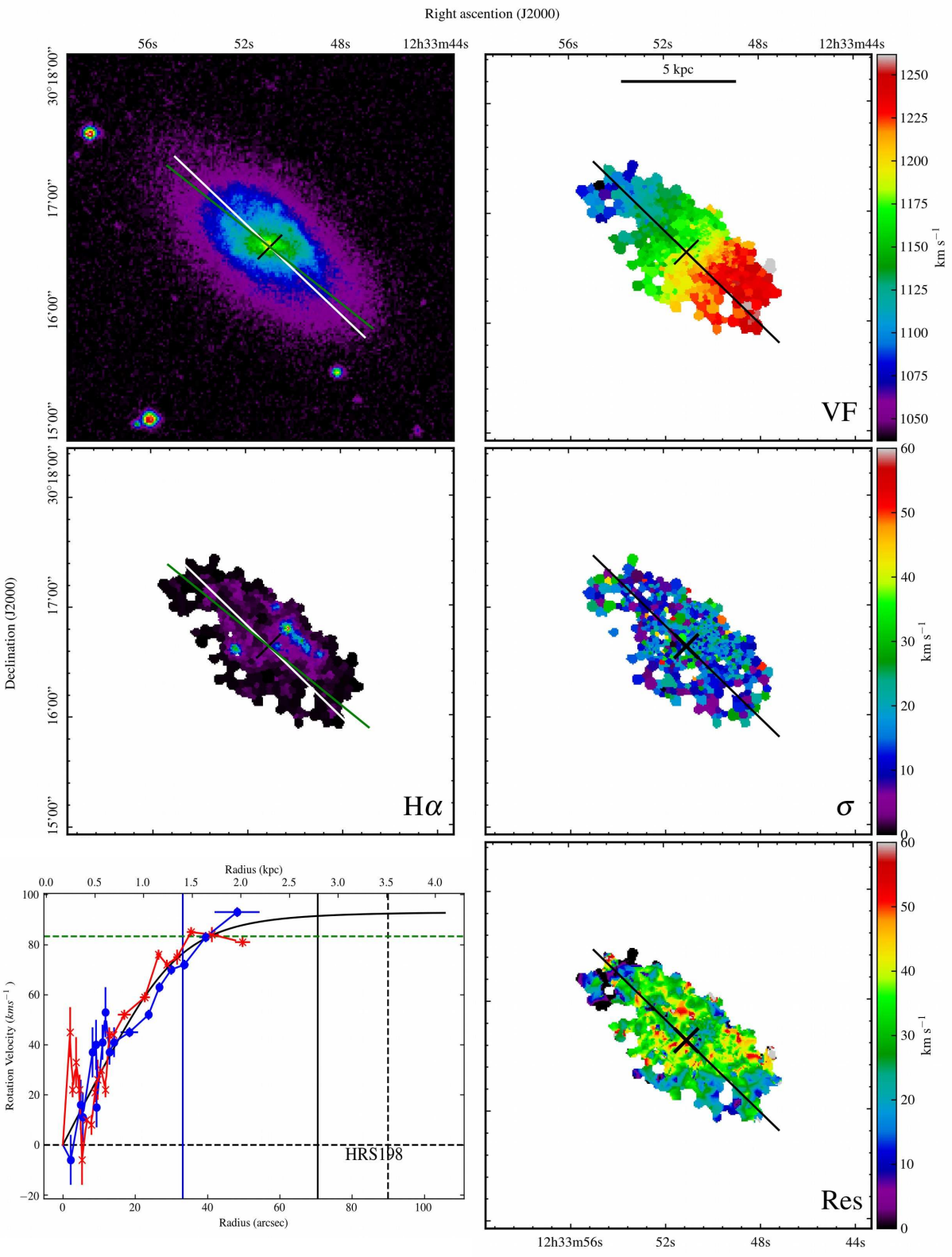
Right ascention (J2000)
56s
52s
48s
12h33m44s
30°18'00"
17'00"
16'00"
15'00"
Declination (J2000)
5 kpc
VF
Hα
σ
Res
km s⁻¹
Radius (kpc)
Rotation Velocity (kms⁻¹)
Radius (arcsec)
HRS198
12h33m56s
44s

HRS198

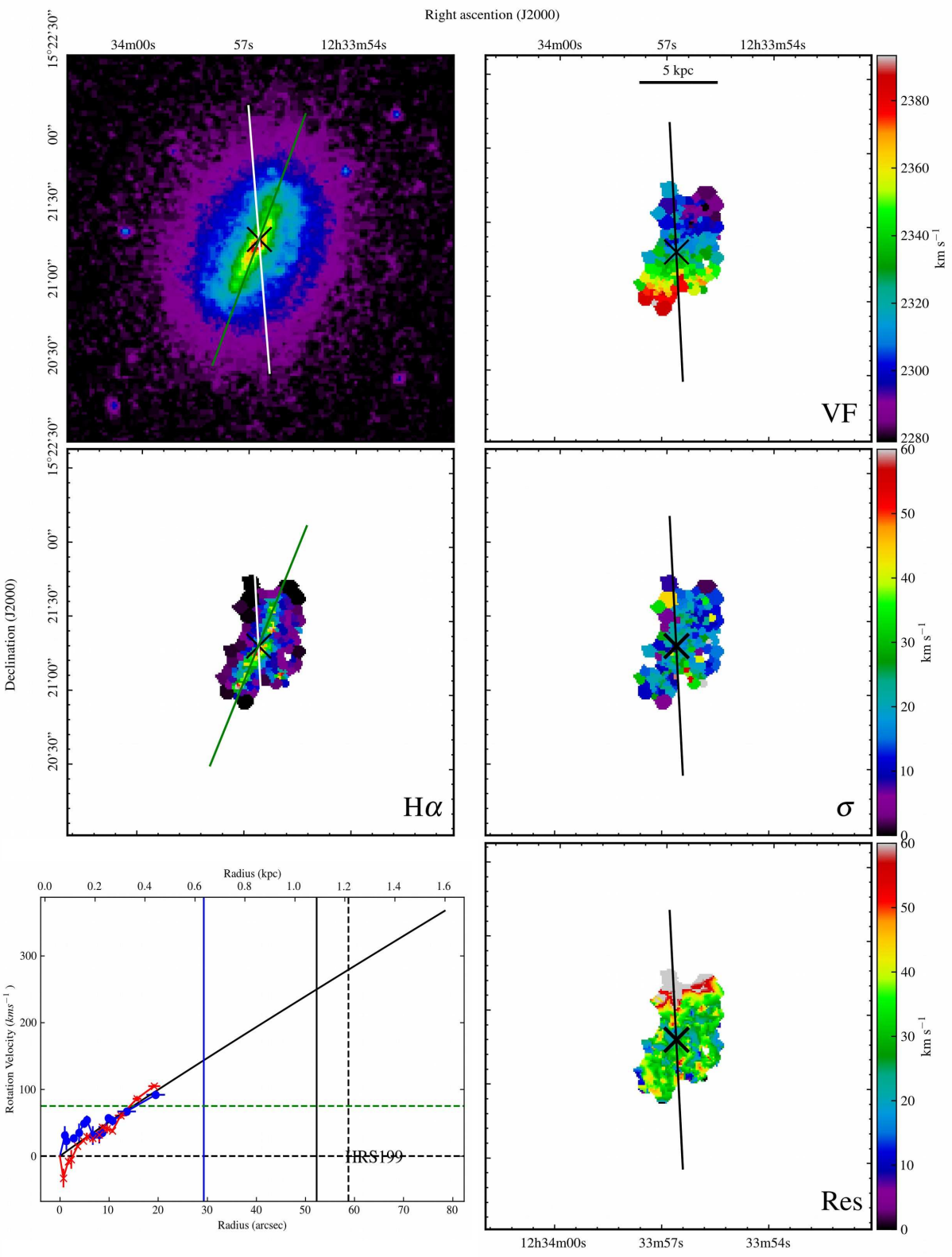
Right ascention (J2000)
34m00s
57s
12h33m54s
15°22'30"
00"
21'30"
21'00"
20'30"
Declination (J2000)
5 kpc
VF
Hα
σ
Res
km s⁻¹
2380
2360
2340
2320
2300
2280
60
50
40
30
20
10
0
12h34m00s
33m57s
33m54s
Radius (kpc)
0.0
0.2
0.4
0.6
0.8
1.0
1.2
1.4
1.6
Rotation Velocity (kms⁻¹)
300
200
100
0
HRS199
Radius (arcsec)
0
10
20
30
40
50
60
70
80

HRS199

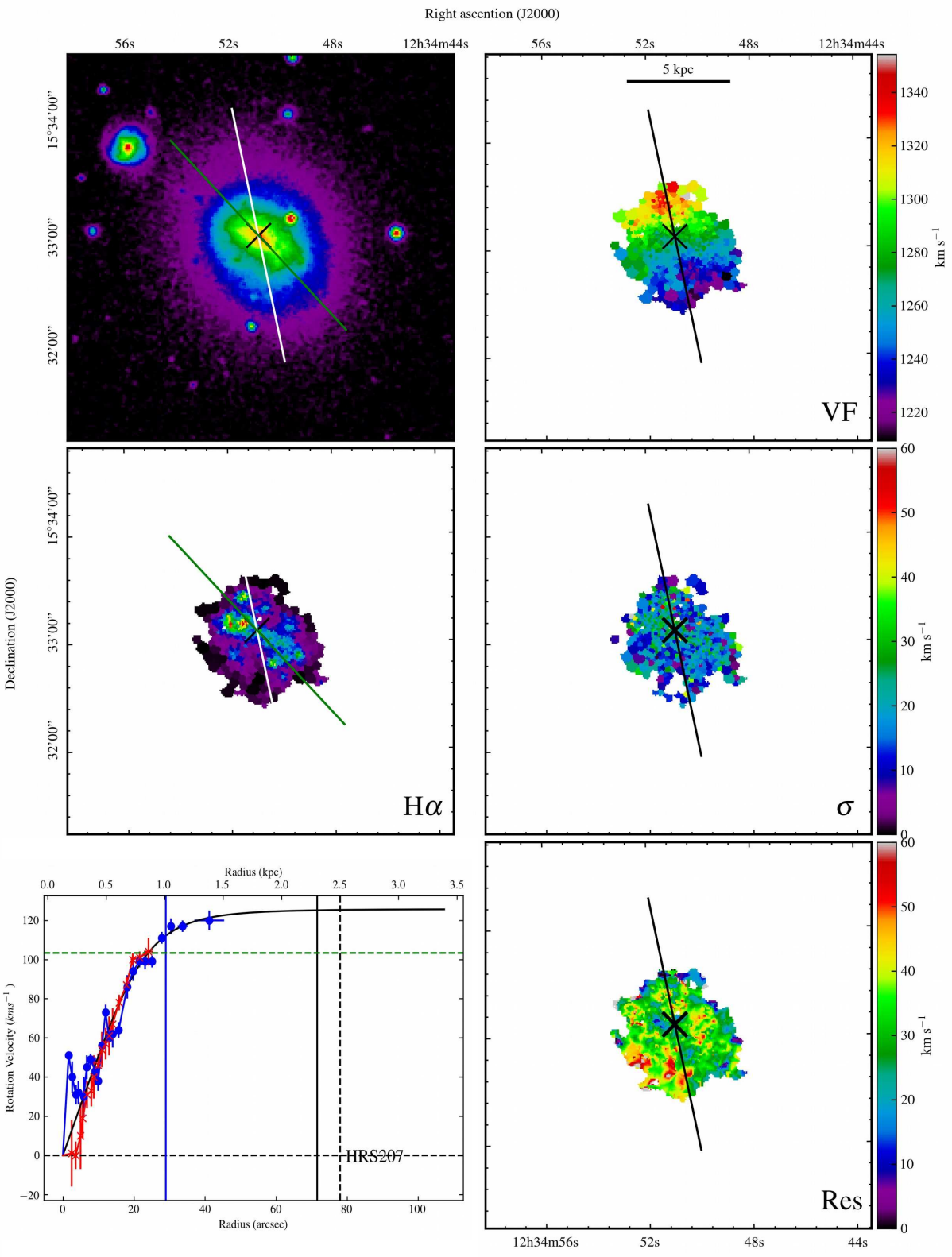
Right ascention (J2000)
56s
52s
48s
12h34m44s
Declination (J2000)
15°34'00"
33'00"
32'00"
5 kpc
VF
Hα
σ
Res
km s⁻¹
Radius (kpc)
Rotation Velocity (kms⁻¹)
Radius (arcsec)
HRS207
12h34m56s
44s

HRS207

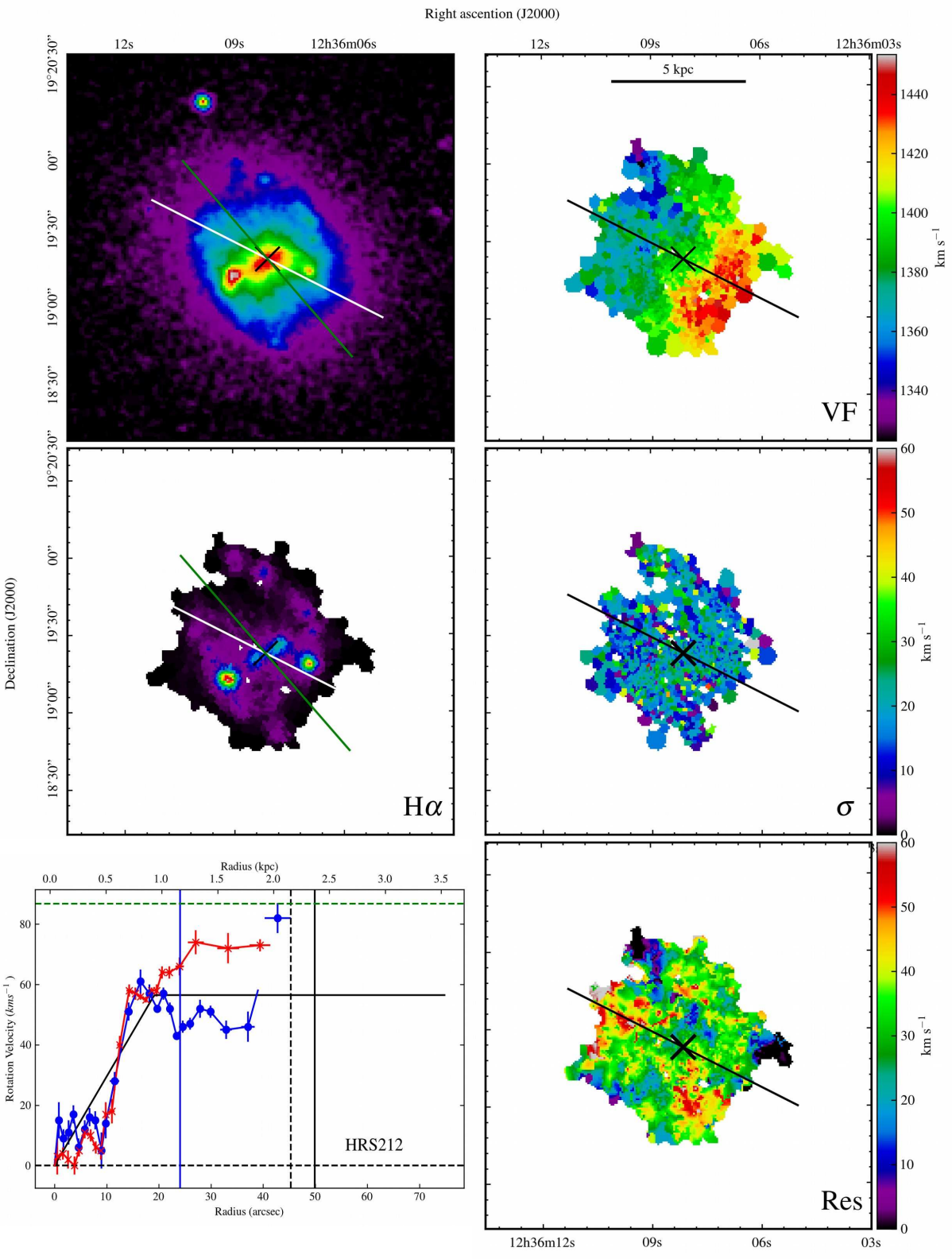
Right ascention (J2000)
12s
09s
12h36m06s
12h36m03s
06s
Declination (J2000)
19°20'30"
00"
19'30"
19'00"
18'30"
5 kpc
VF
Hα
σ
Res
km s⁻¹
1440
1420
1400
1380
1360
1340
60
50
40
30
20
10
0
Radius (kpc)
0.0
0.5
1.0
1.5
2.0
2.5
3.0
3.5
Rotation Velocity (kms⁻¹)
80
60
40
20
0
HRS212
Radius (arcsec)
10
20
30
40
50
60
70
12h36m12s

HRS212

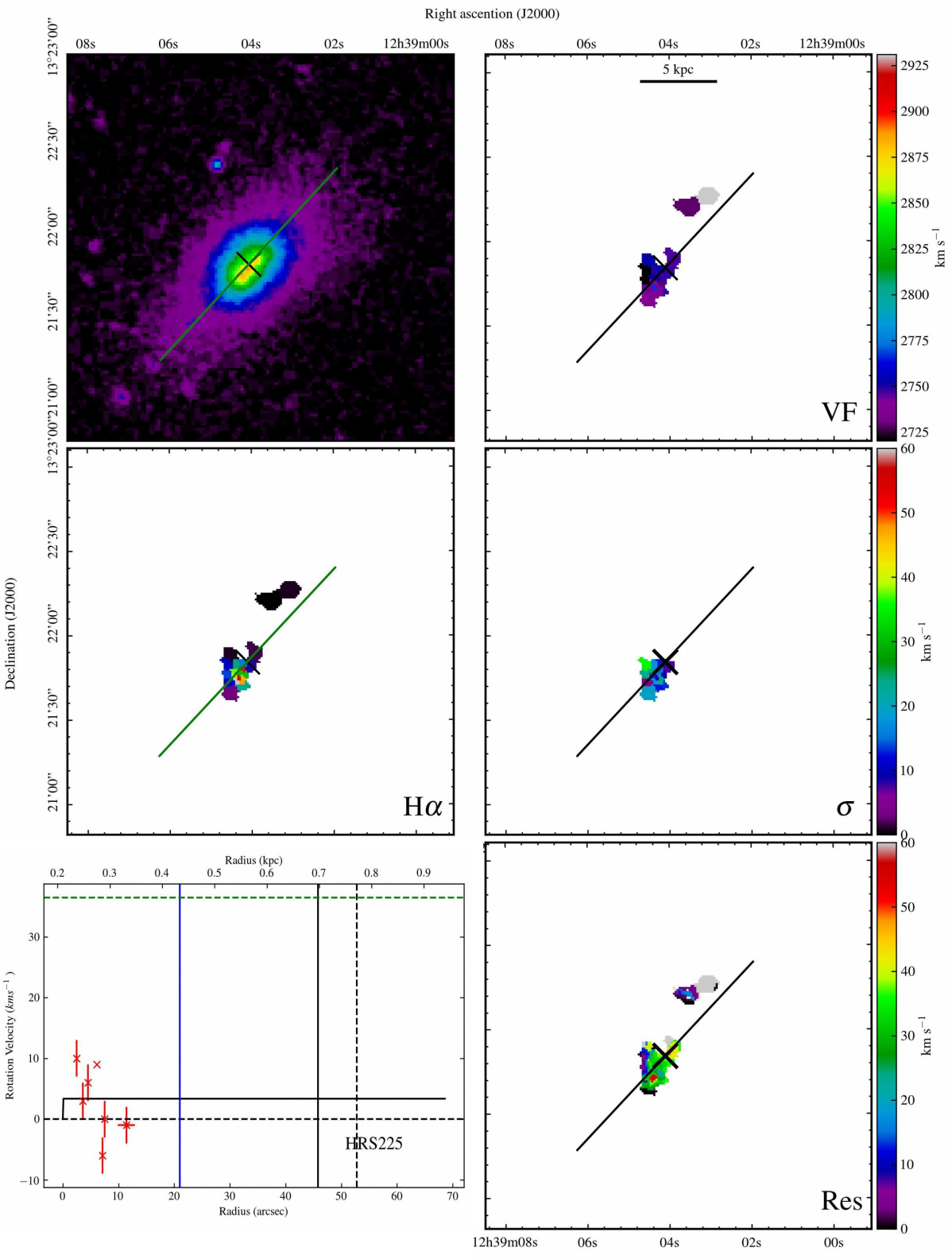
Right ascention (J2000)
Declination (J2000)
5 kpc
VF
Hα
σ
Res
km s−1
Radius (kpc)
Radius (arcsec)
Rotation Velocity (kms−1)
HRS225

HRS225

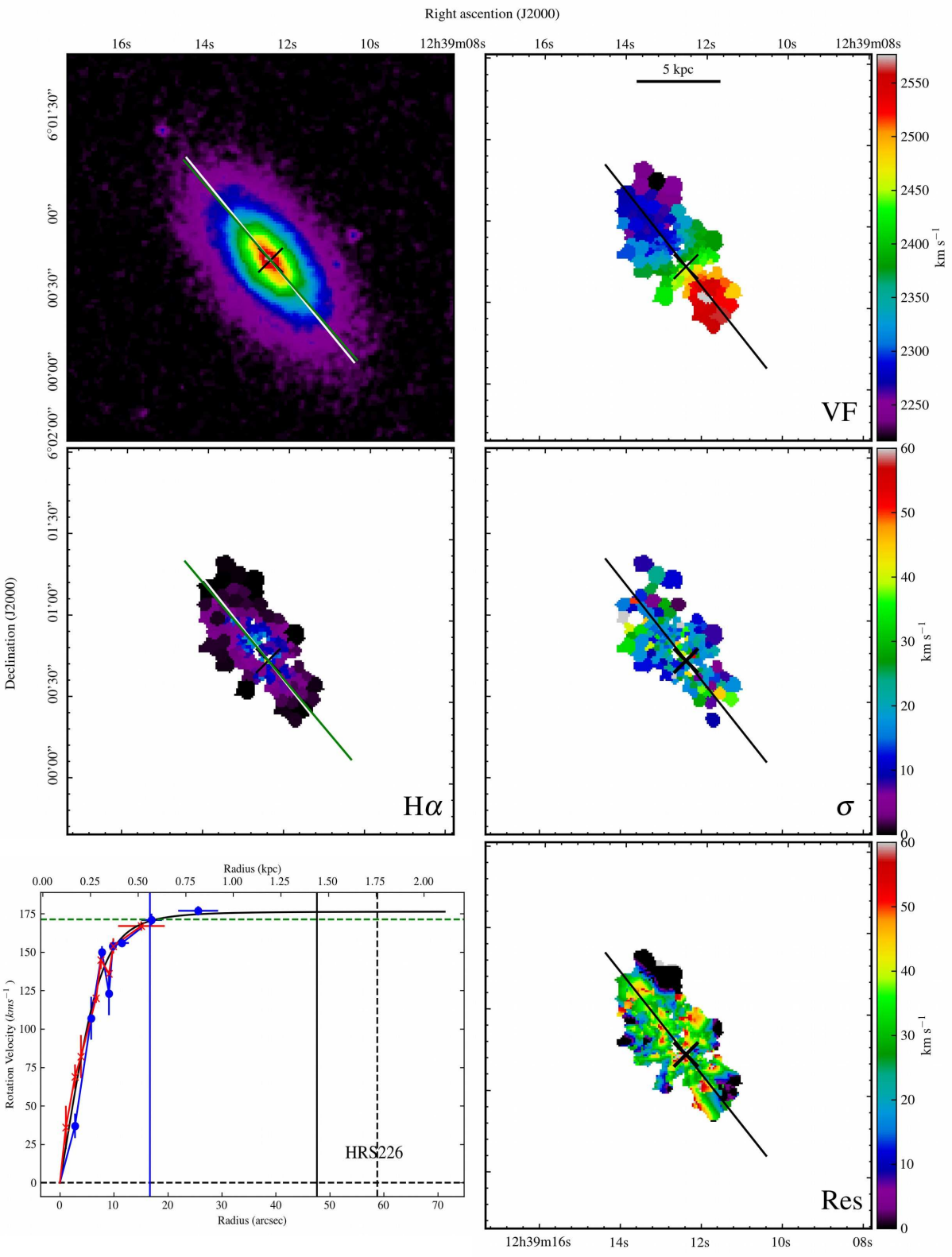
Right ascention (J2000)
16s
14s
12s
10s
12h39m08s
Declination (J2000)
6°01'30"
00"
00'30"
00'00"
6°02'00"
01'30"
01'00"
00'30"
00'00"
5 kpc
VF
Hα
σ
Res
km s⁻¹
2550
2500
2450
2400
2350
2300
2250
60
50
40
30
20
10
0
Radius (kpc)
0.00
0.25
0.50
0.75
1.00
1.25
1.50
1.75
2.00
Rotation Velocity (kms⁻¹)
175
150
125
100
75
50
25
0
Radius (arcsec)
0
10
20
30
40
50
60
70
HRS226
12h39m16s
08s

HRS226

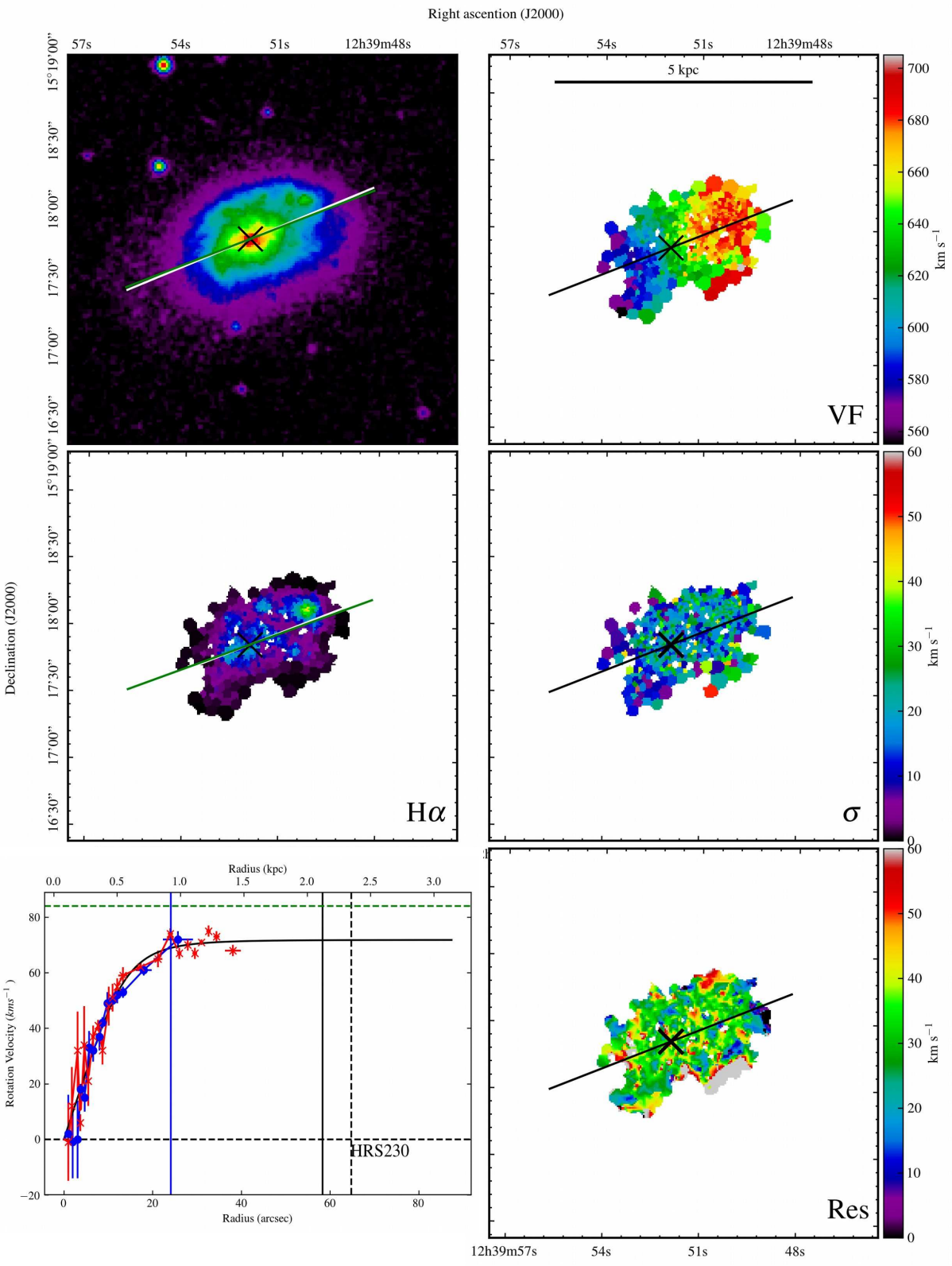
Right ascention (J2000)
57s
54s
51s
12h39m48s
15°19'00"
18'30"
18'00"
17'30"
17'00"
16'30"
Declination (J2000)
5 kpc
VF
Hα
σ
Res
km s−1
700
680
660
640
620
600
580
560
60
50
40
30
20
10
0
Radius (kpc)
0.0
0.5
1.0
1.5
2.0
2.5
3.0
Rotation Velocity (kms−1)
80
60
40
20
0
−20
HRS230
Radius (arcsec)
0
20
40
60
80
12h39m57s
54s
51s
48s

HRS230

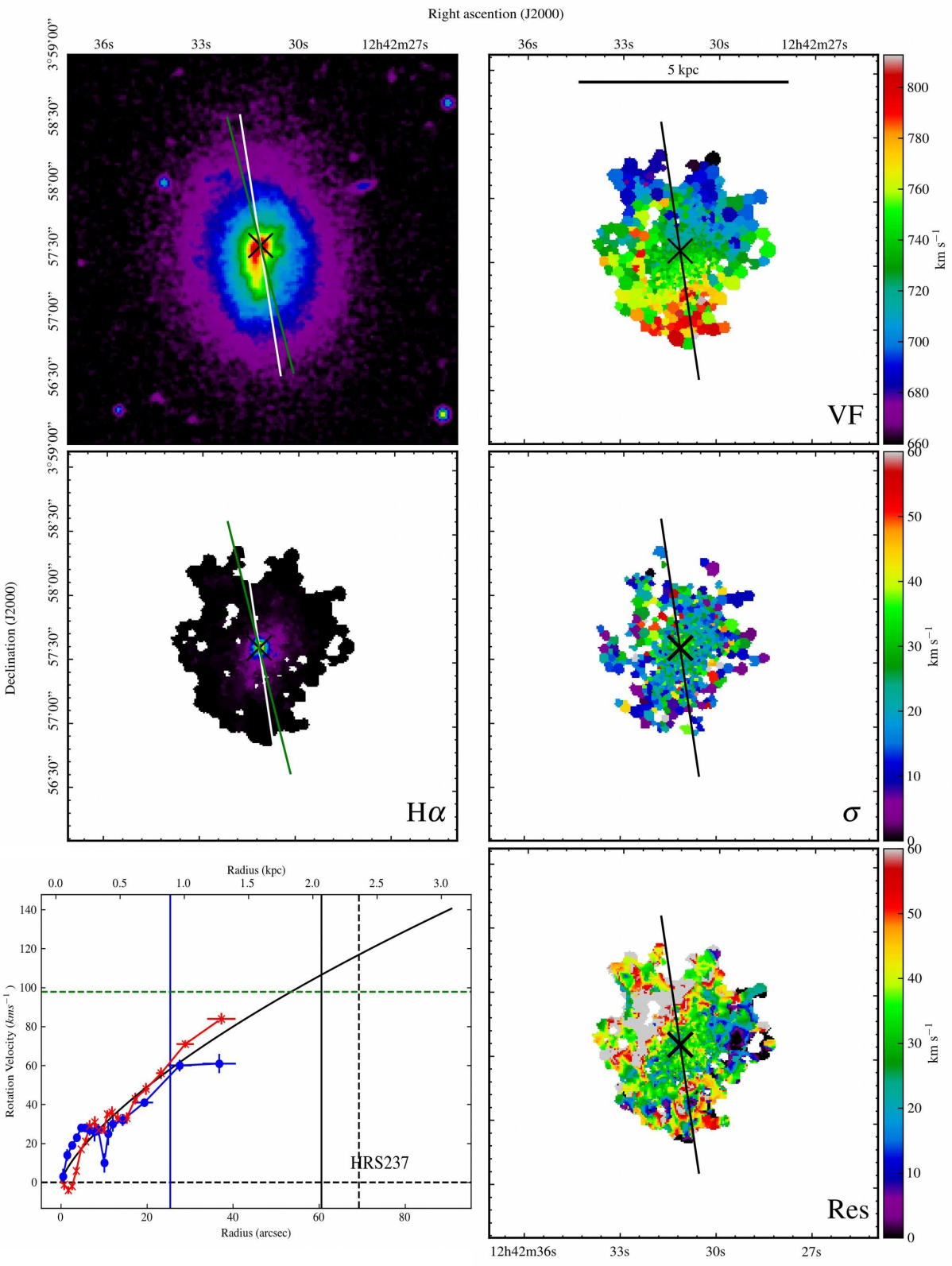
Right ascention (J2000)
36s
33s
30s
12h42m27s
3°59'00"
58'30"
58'00"
57'30"
57'00"
56'30"
Declination (J2000)
5 kpc
VF
Hα
σ
Res
km s^{-1}
Radius (kpc)
Rotation Velocity (kms^{-1})
Radius (arcsec)
HRS237
12h42m36s

HRS237

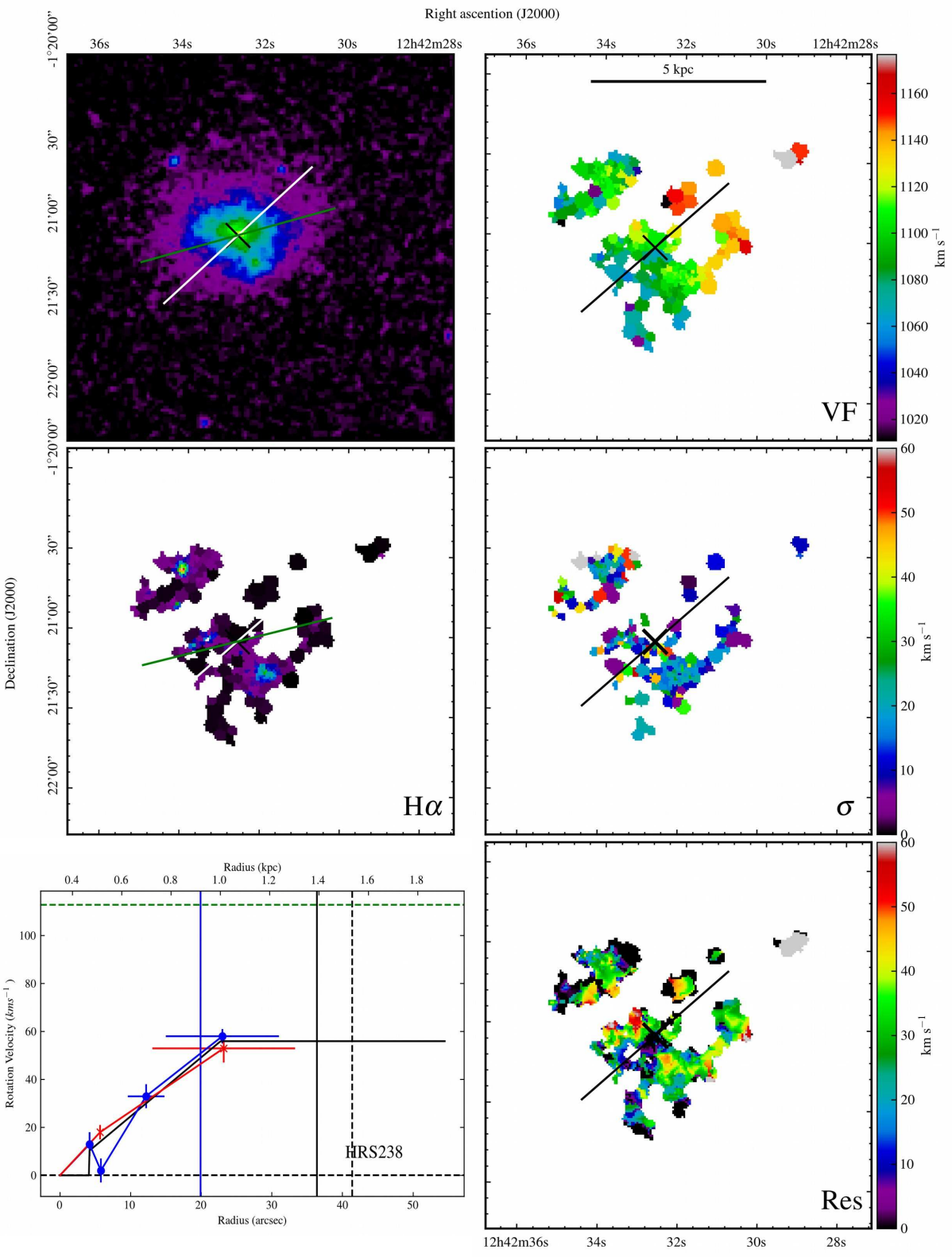
Right ascention (J2000)
Declination (J2000)
36s
34s
32s
30s
12h42m28s
12h42m36s
28s
-1°20'00"
30"
21'00"
21'30"
22'00"
5 kpc
VF
Hα
σ
Res
km s⁻¹
1160
1140
1120
1100
1080
1060
1040
1020
60
50
40
30
20
10
0
Radius (kpc)
0.4
0.6
0.8
1.0
1.2
1.4
1.6
1.8
Rotation Velocity (kms⁻¹)
100
80
60
40
20
0
Radius (arcsec)
0
10
20
30
40
50
HRS238

HRS238

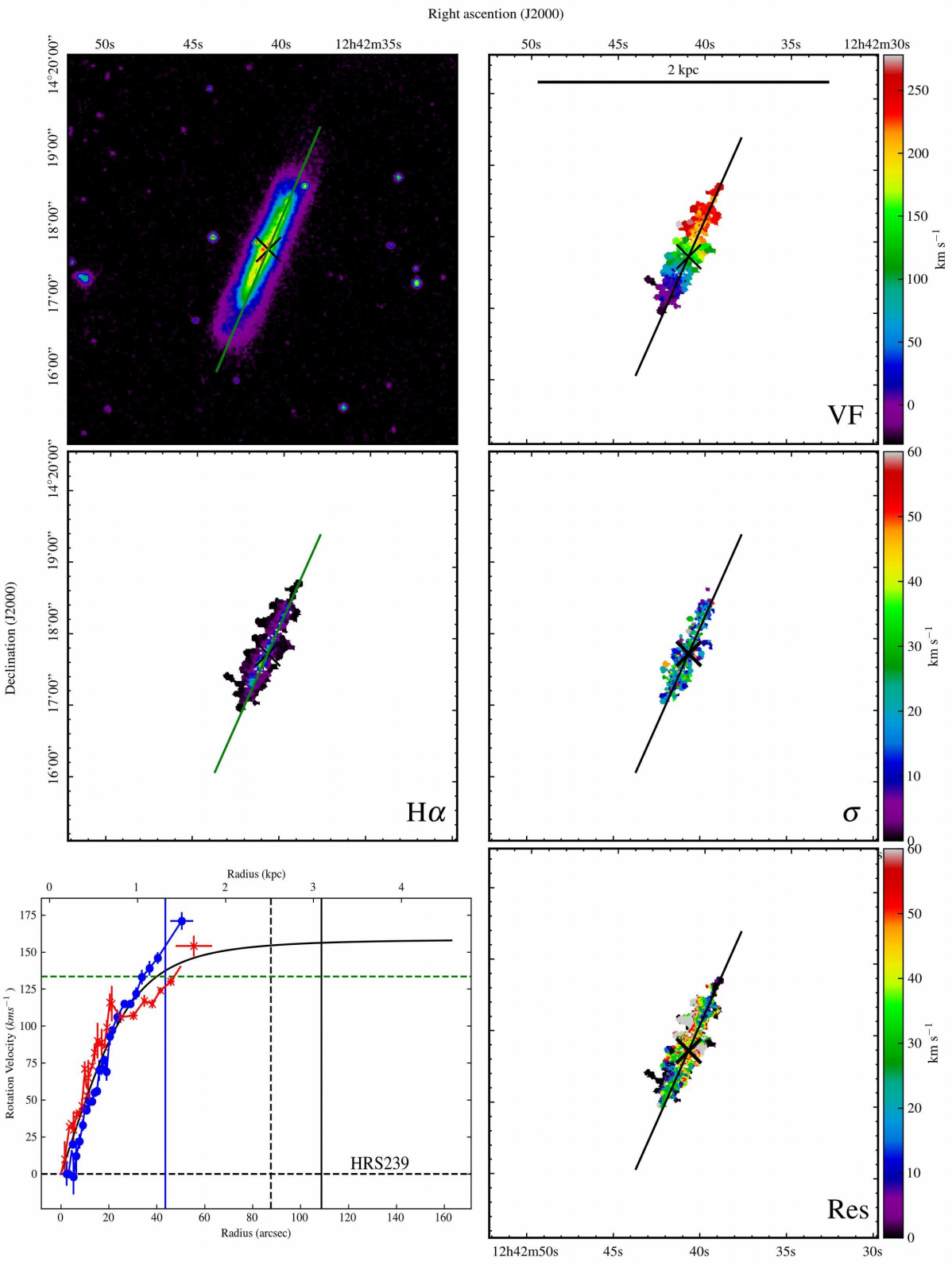
Right ascention (J2000)
Declination (J2000)
50s
45s
40s
35s
12h42m35s
12h42m30s
12h42m50s
30s
14°20'00"
19'00"
18'00"
17'00"
16'00"
2 kpc
VF
Hα
σ
Res
km s−1
Radius (kpc)
Rotation Velocity (kms−1)
Radius (arcsec)
HRS239

HRS239

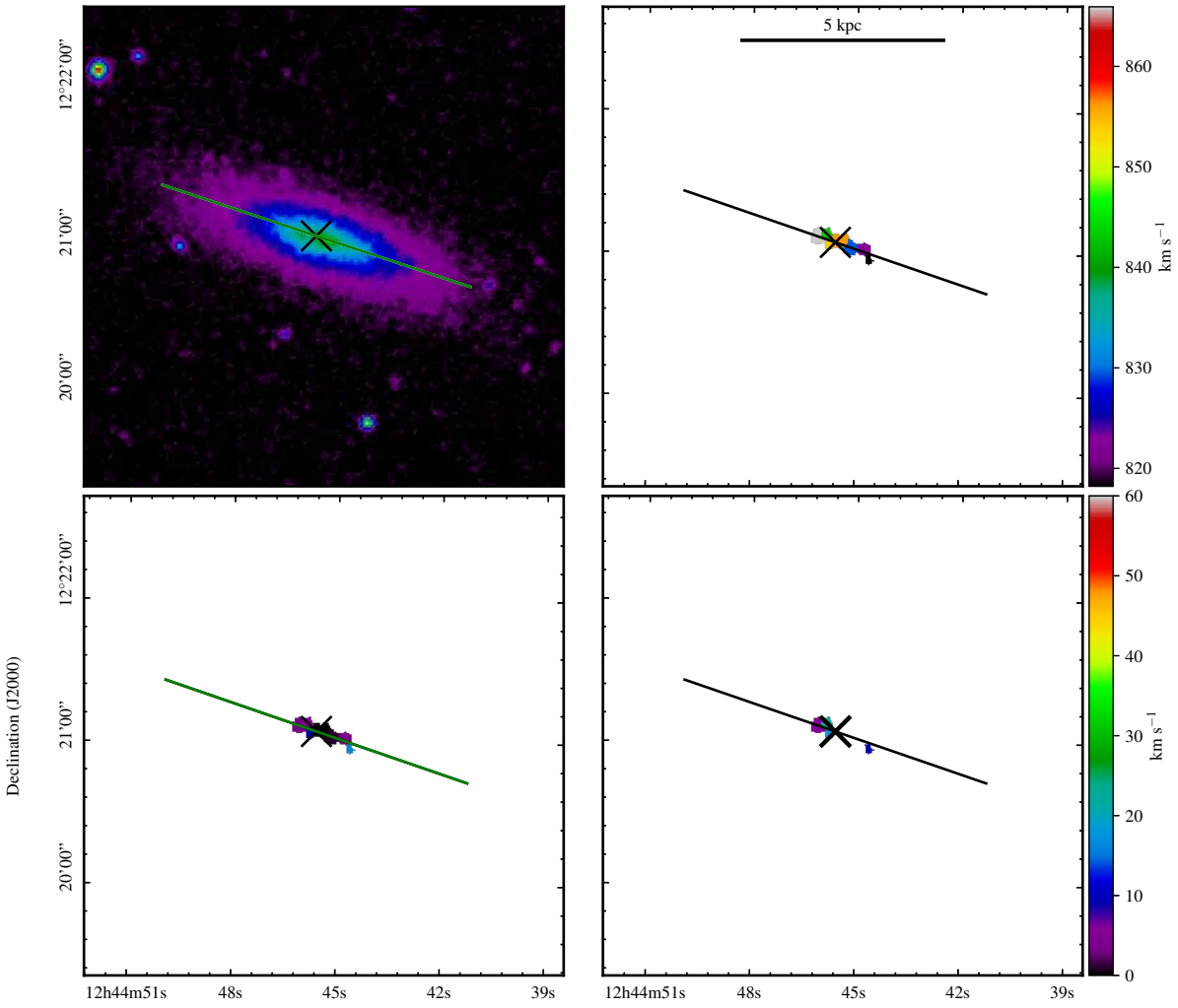
5 kpc
860
850
840
830
820
km s^{-1}
60
50
40
30
20
10
0
km s^{-1}
12°22'00"
21'00"
20'00"
Declination (J2000)
12h44m51s
48s
45s
42s
39s
Right ascention (J2000)
HRS249

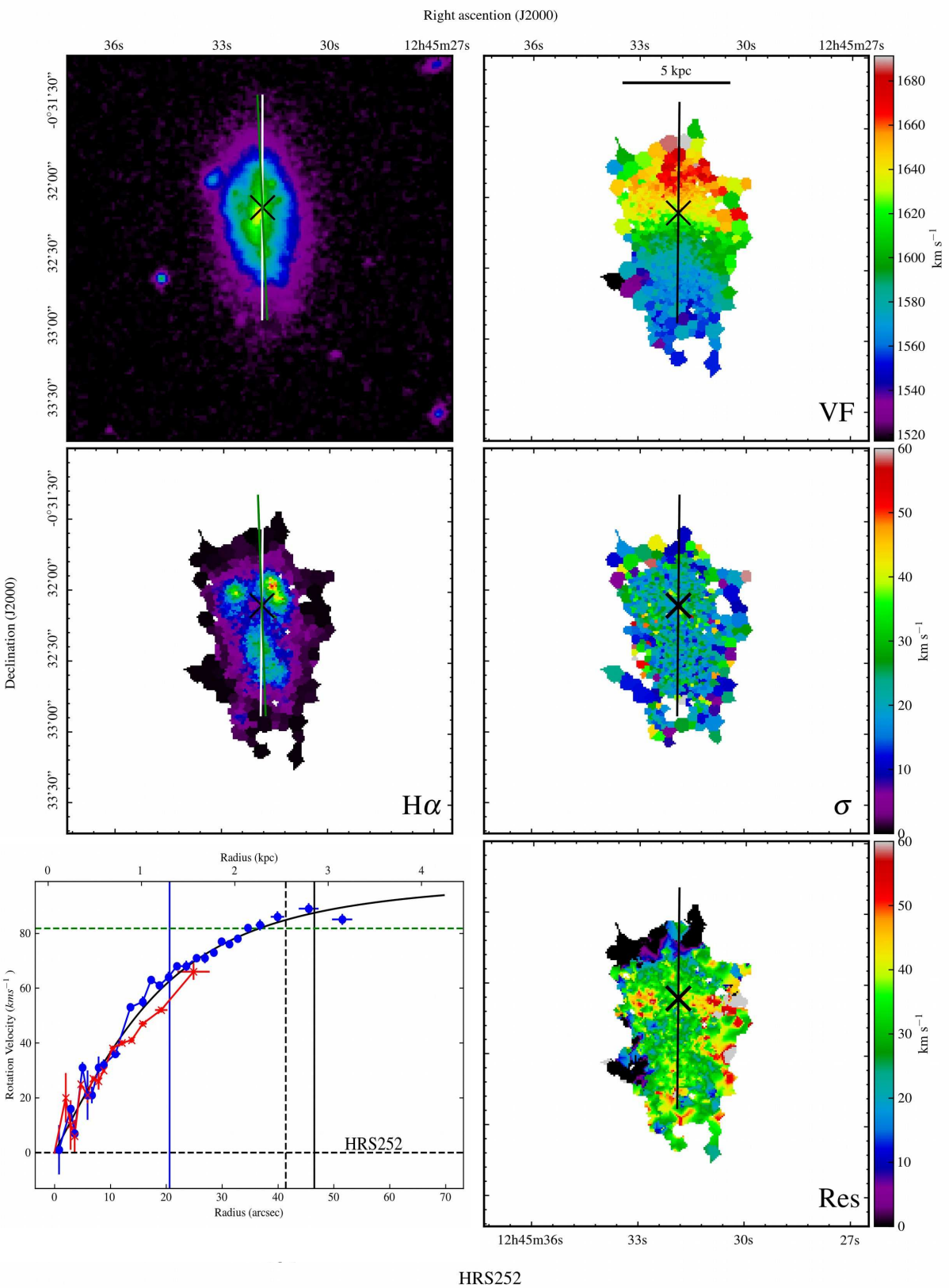
Right ascention (J2000)
36s
33s
30s
12h45m27s
Declination (J2000)
-0°31'30"
32'00"
32'30"
33'00"
33'30"
5 kpc
VF
Hα
σ
Res
km s⁻¹
Radius (kpc)
Rotation Velocity (kms⁻¹)
Radius (arcsec)
HRS252
12h45m36s
27s

HRS252

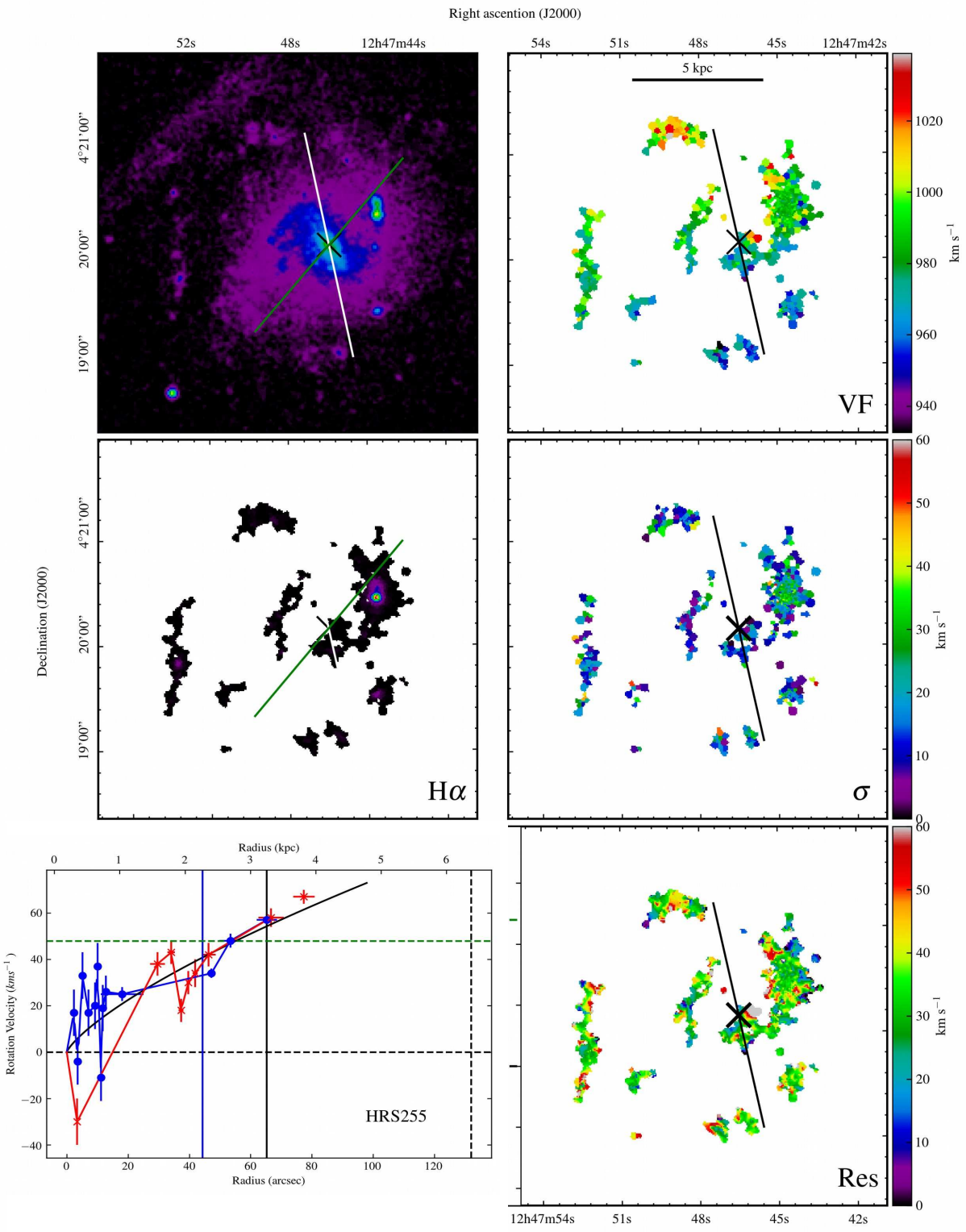
Right ascention (J2000)
52s
48s
12h47m44s
54s
51s
48s
45s
12h47m42s
5 kpc
4°21'00"
20'00"
19'00"
Declination (J2000)
VF
Hα
σ
Res
km s^{-1}
1020
1000
980
960
940
60
50
40
30
20
10
0
Radius (kpc)
0
1
2
3
4
5
6
Rotation Velocity (kms^{-1})
60
40
20
0
−20
−40
HRS255
Radius (arcsec)
0
20
40
60
80
100
120
12h47m54s
51s
48s
45s
42s

HRS255

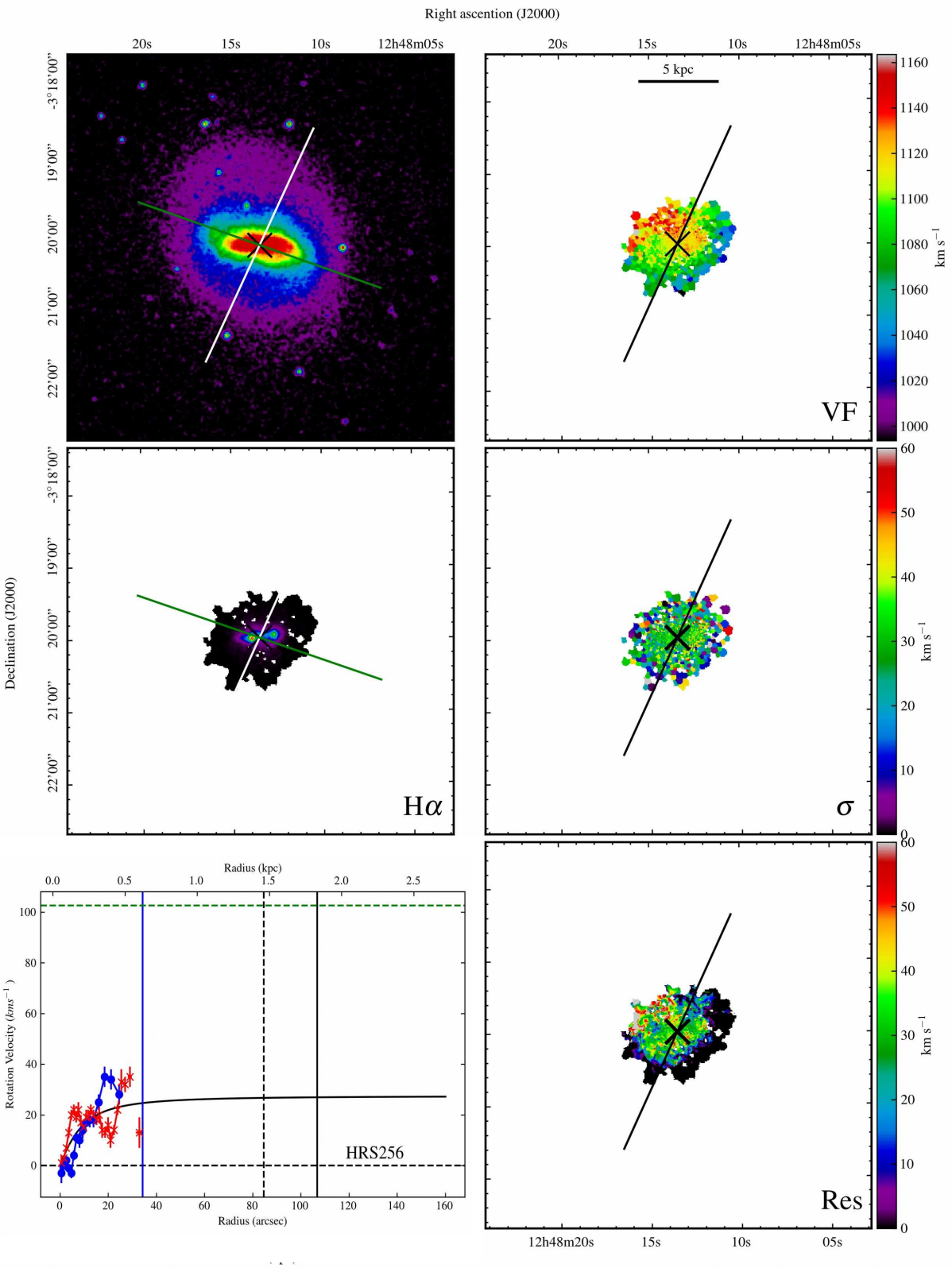
Right ascention (J2000)
20s
15s
10s
12h48m05s
Declination (J2000)
-3°18'00"
19'00"
20'00"
21'00"
22'00"
5 kpc
VF
Hα
σ
Res
km s⁻¹
Radius (kpc)
Rotation Velocity (kms⁻¹)
Radius (arcsec)
HRS256
12h48m20s
05s

HRS256

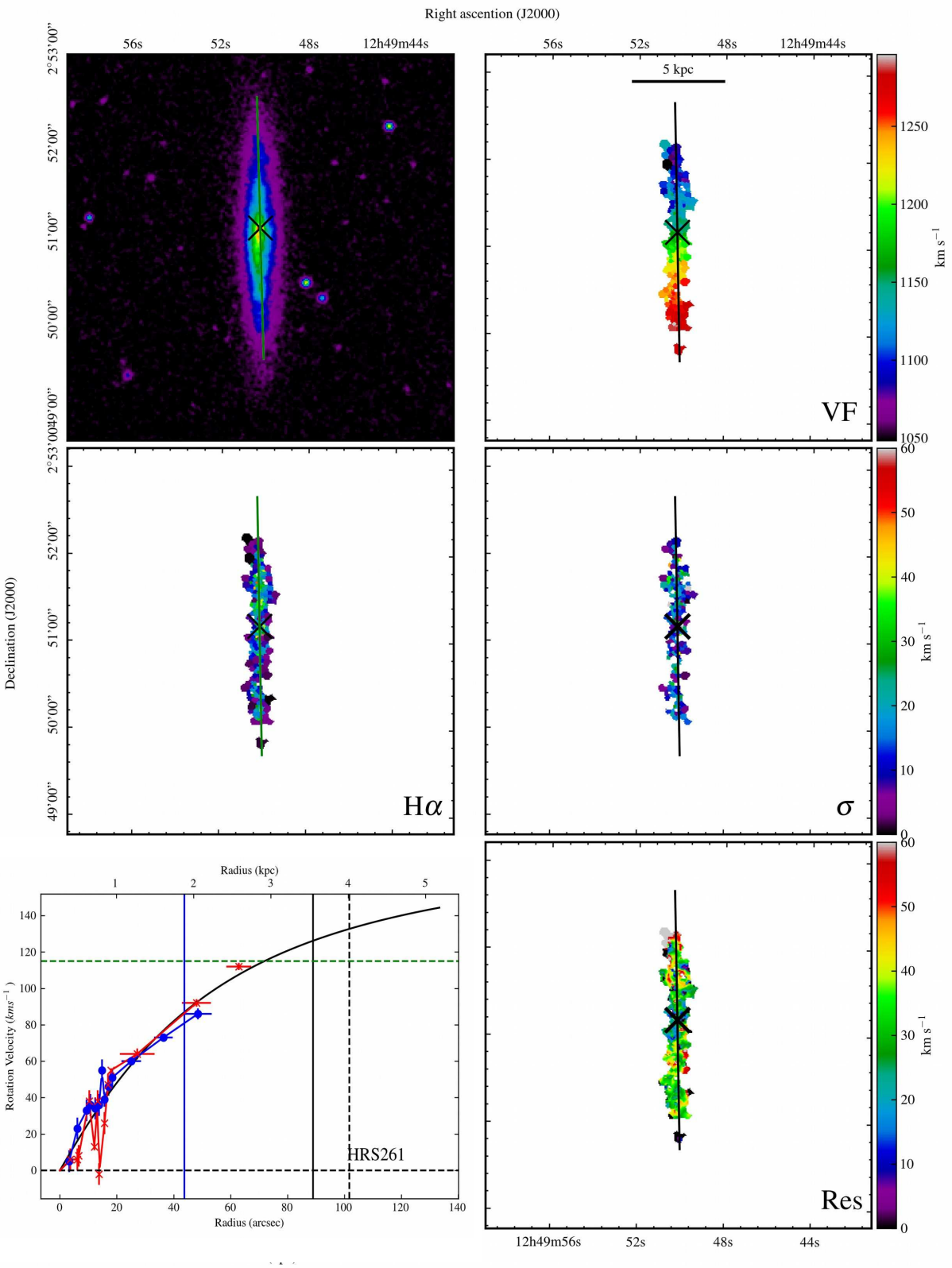
Right ascention (J2000)
Declination (J2000)
56s
52s
48s
12h49m44s
12h49m56s
44s
2°53'00"
52'00"
51'00"
50'00"
49'00"
5 kpc
VF
Hα
σ
Res
km s⁻¹
1250
1200
1150
1100
1050
60
50
40
30
20
10
0
Radius (kpc)
1
2
3
4
5
Rotation Velocity (kms⁻¹)
Radius (arcsec)
0
20
40
60
80
100
120
140
HRS261

HRS261

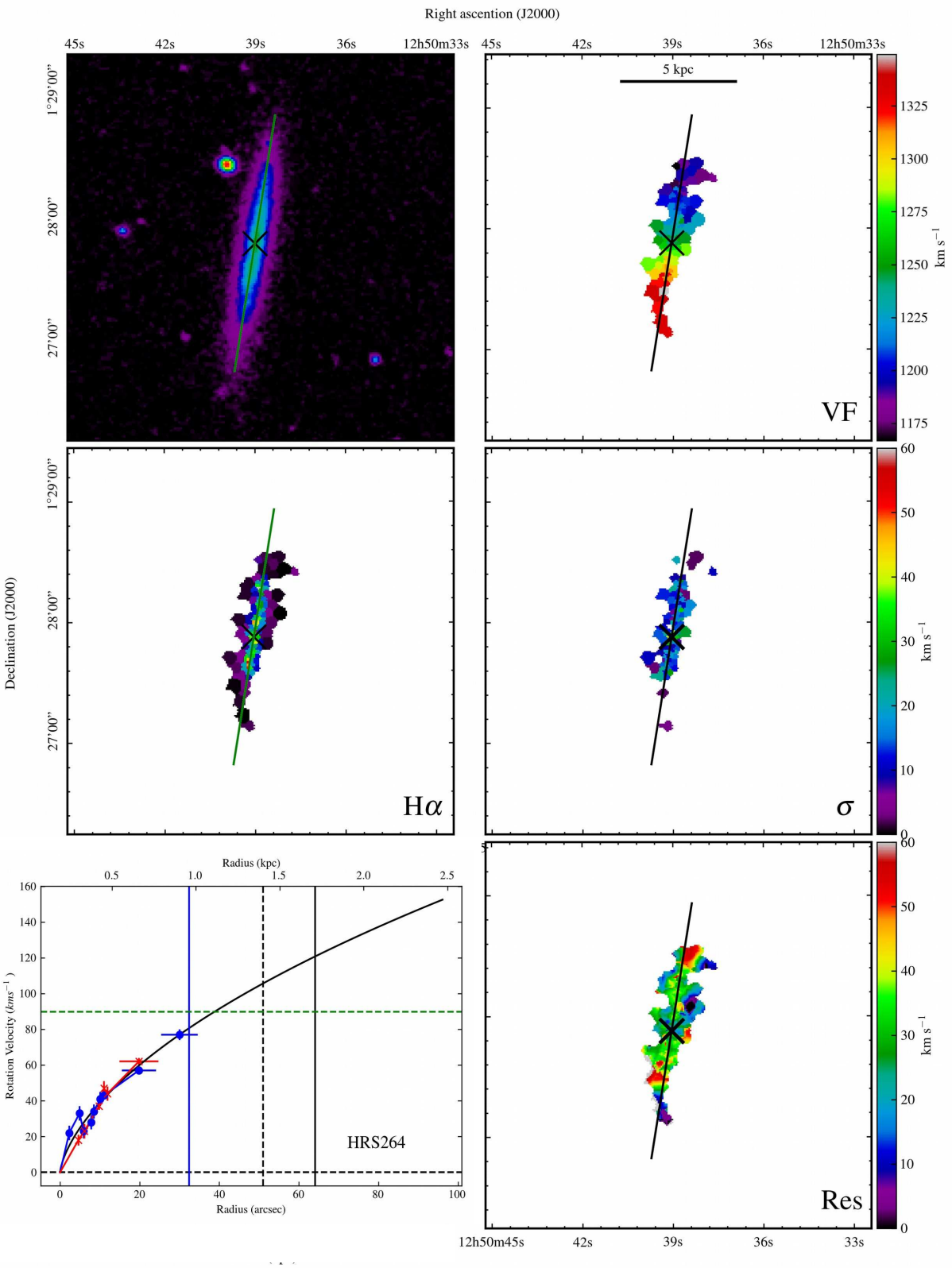
Right ascention (J2000)
45s
42s
39s
36s
12h50m33s
1°29'00"
28'00"
27'00"
Declination (J2000)
5 kpc
VF
Hα
σ
Res
km s⁻¹
1325
1300
1275
1250
1225
1200
1175
60
50
40
30
20
10
0
Radius (kpc)
0.5
1.0
1.5
2.0
2.5
Rotation Velocity (kms⁻¹)
160
140
120
100
80
60
40
20
0
Radius (arcsec)
HRS264
12h50m45s
33s

HRS264

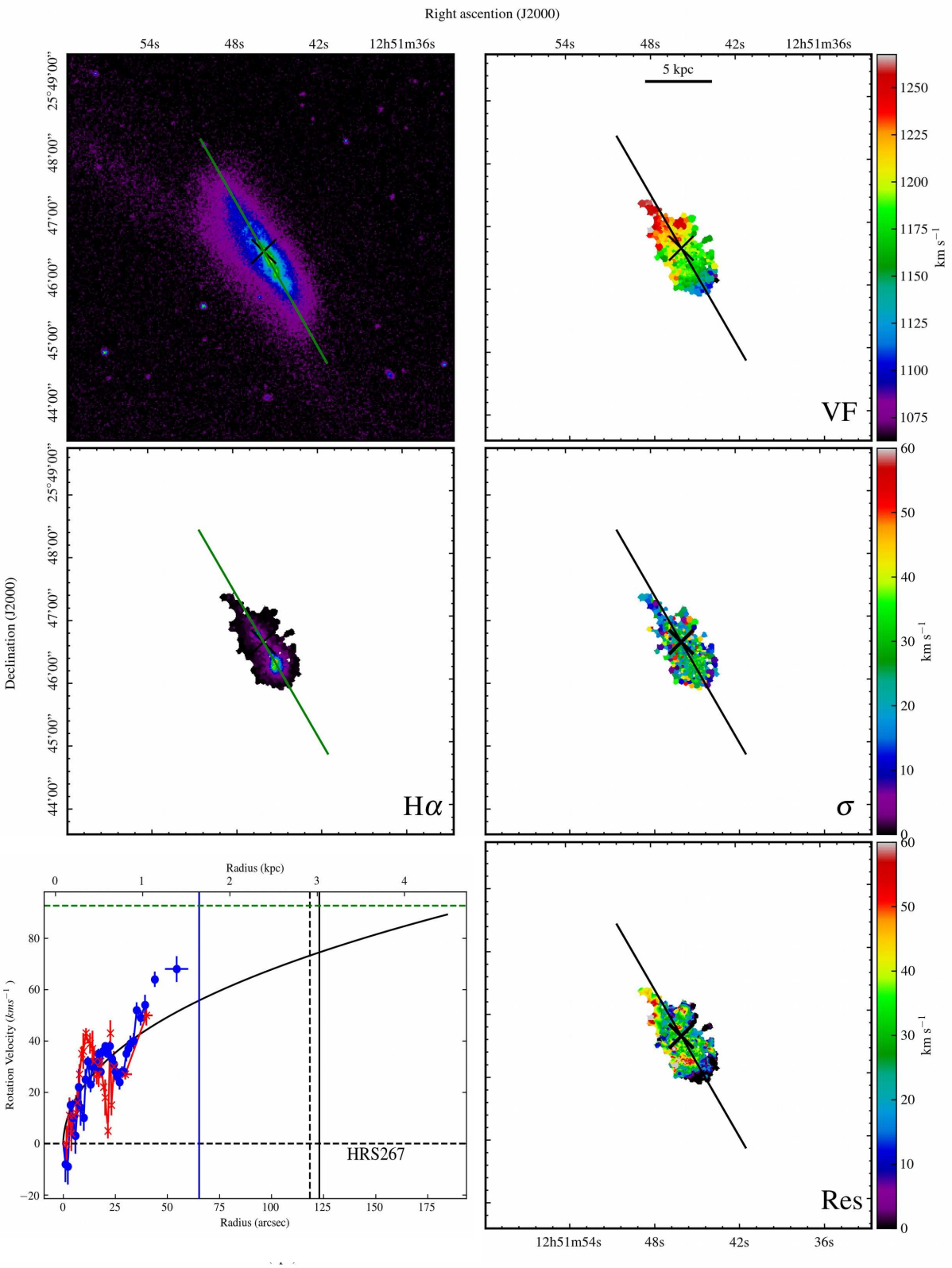
Right ascention (J2000)
54s
48s
42s
12h51m36s
25°49'00"
48'00"
47'00"
46'00"
45'00"
44'00"
Declination (J2000)
5 kpc
VF
Hα
σ
Res
km s−1
1250
1225
1200
1175
1150
1125
1100
1075
60
50
40
30
20
10
0
Radius (kpc)
0
1
2
3
4
Rotation Velocity (kms−1)
80
60
40
20
0
−20
HRS267
Radius (arcsec)
0
25
50
75
100
125
150
175
12h51m54s
48s
42s
36s

HRS267

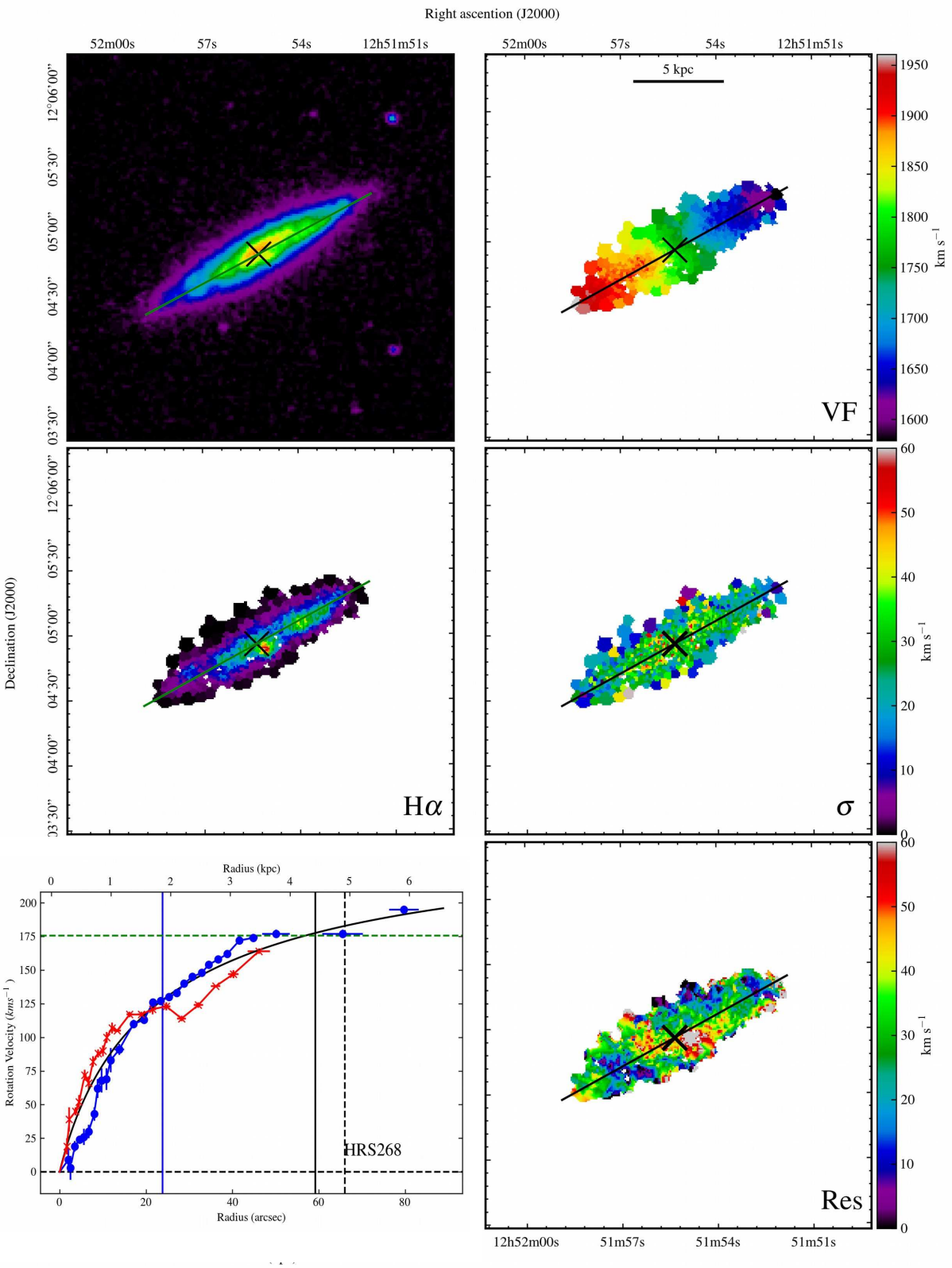
Right ascention (J2000)
52m00s
57s
54s
12h51m51s
Declination (J2000)
12°06'00"
05'30"
05'00"
04'30"
04'00"
03'30"
5 kpc
VF
Hα
σ
Res
km s⁻¹
Radius (kpc)
Rotation Velocity (kms⁻¹)
Radius (arcsec)
HRS268
12h52m00s
51m57s
51m54s
51m51s

HRS268

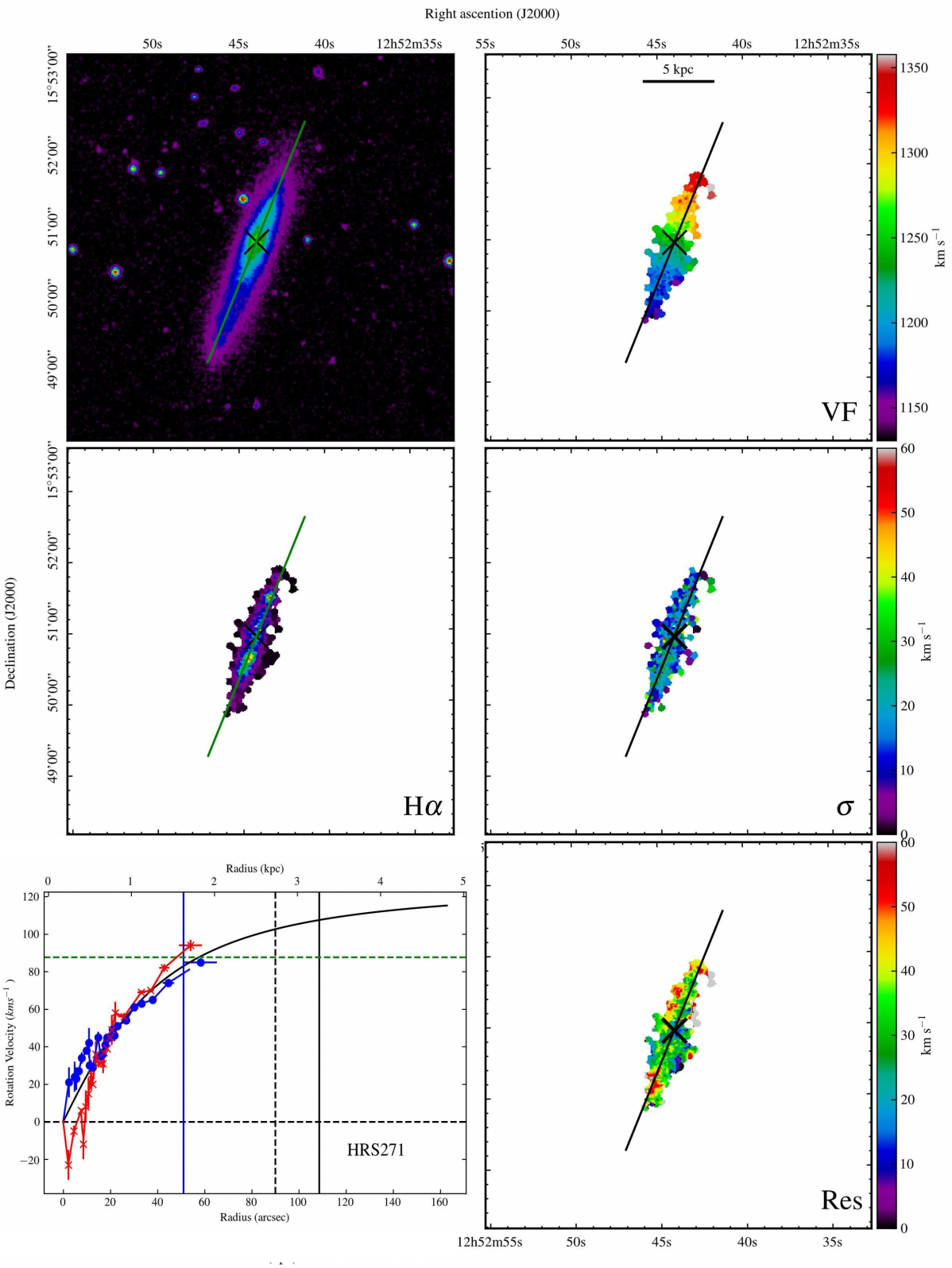
Right ascention (J2000)
Declination (J2000)
5 kpc
VF
Hα
σ
Res
km s−1
Radius (kpc)
Radius (arcsec)
Rotation Velocity (kms−1)
HRS271

HRS271

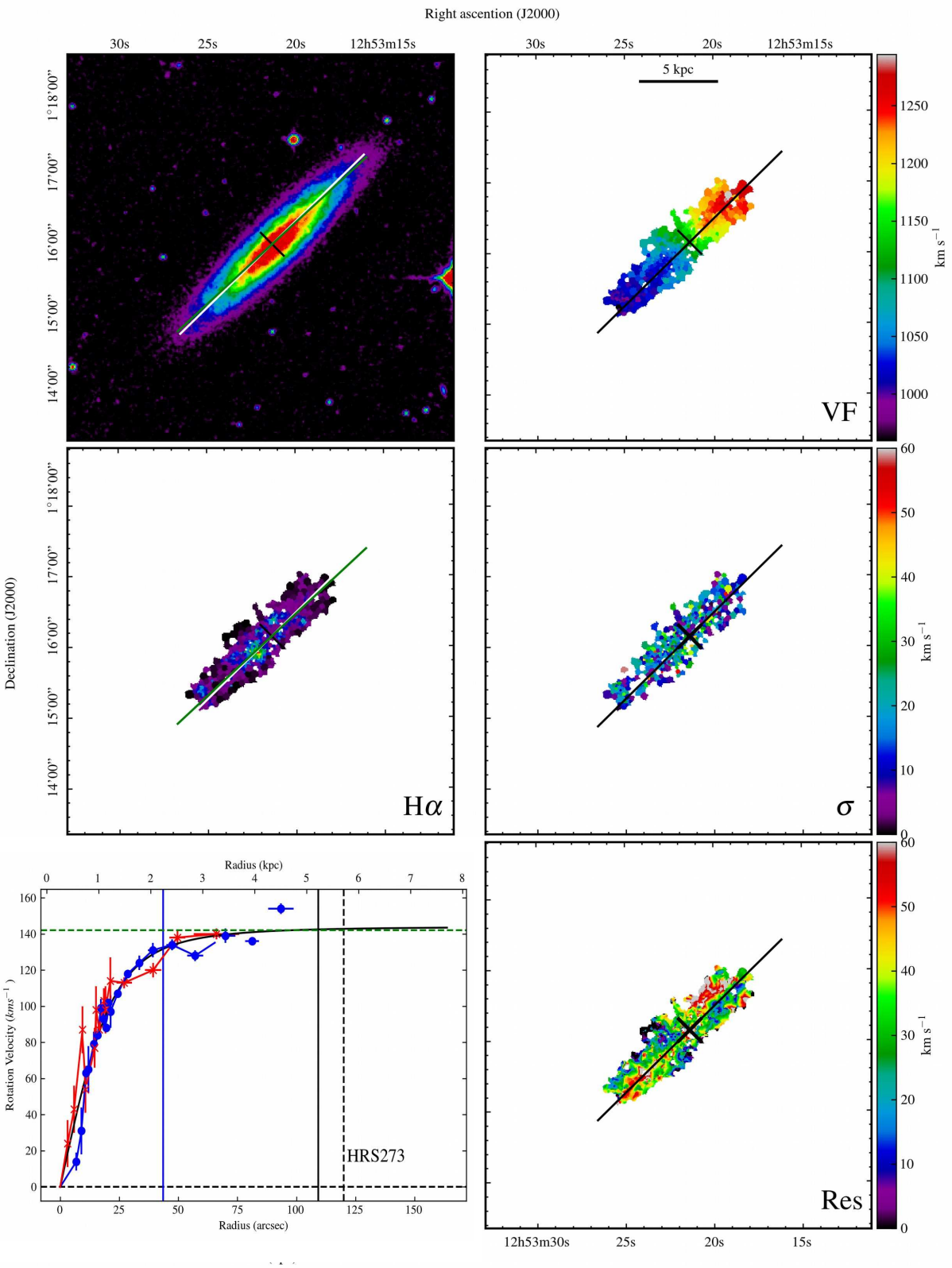
Right ascention (J2000)
30s
25s
20s
12h53m15s
1°18'00"
17'00"
16'00"
15'00"
14'00"
Declination (J2000)
5 kpc
VF
Hα
σ
Res
km s⁻¹
Radius (kpc)
Rotation Velocity (kms⁻¹)
Radius (arcsec)
HRS273
12h53m30s
15s

HRS273

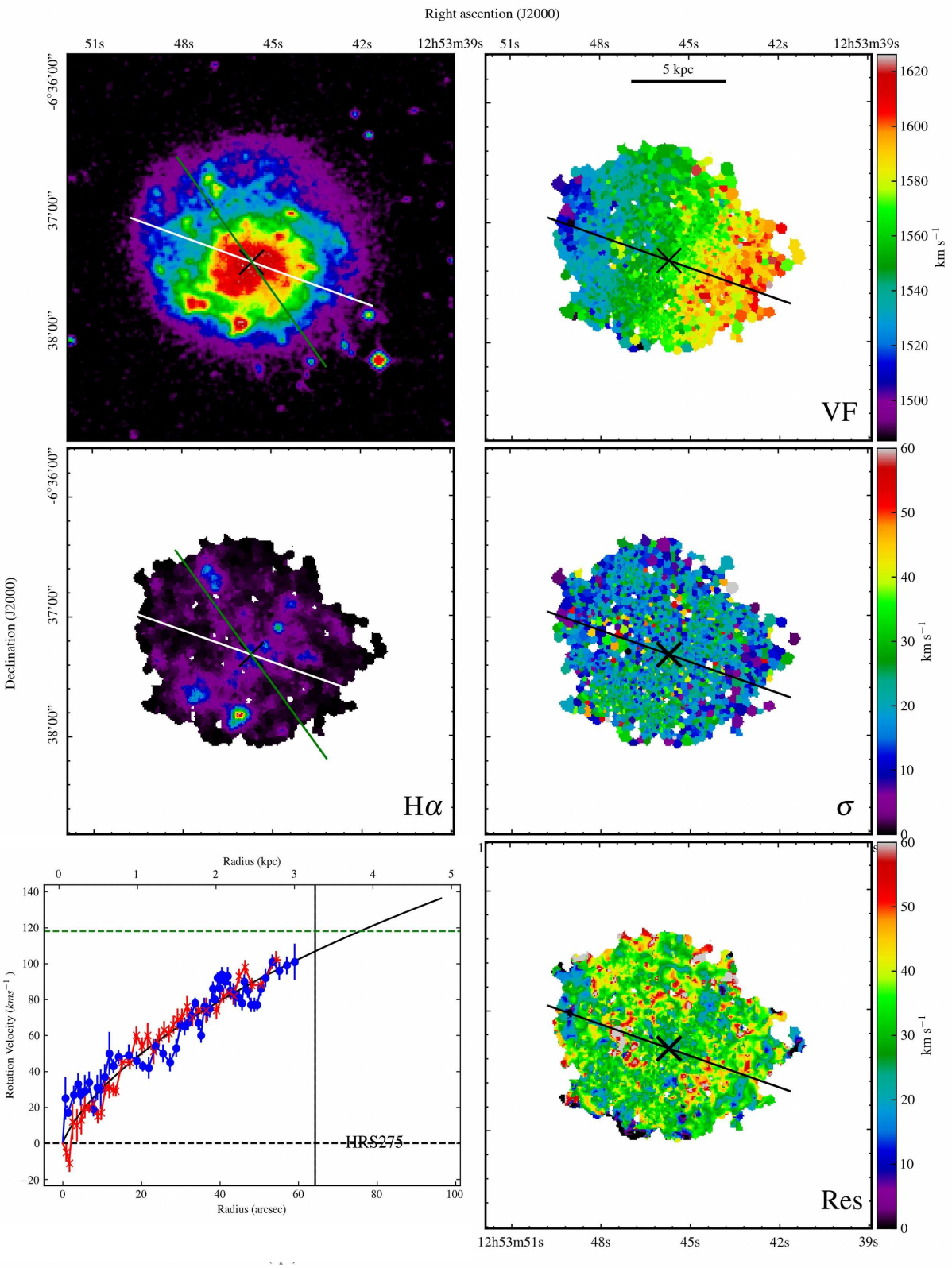
Right ascention (J2000)
51s
48s
45s
42s
12h53m39s
-6°36'00"
37'00"
38'00"
Declination (J2000)
5 kpc
VF
Hα
σ
Res
km s⁻¹
1620
1600
1580
1560
1540
1520
1500
60
50
40
30
20
10
0
12h53m51s
39s
Radius (kpc)
Rotation Velocity (kms⁻¹)
Radius (arcsec)
HRS275

HRS275

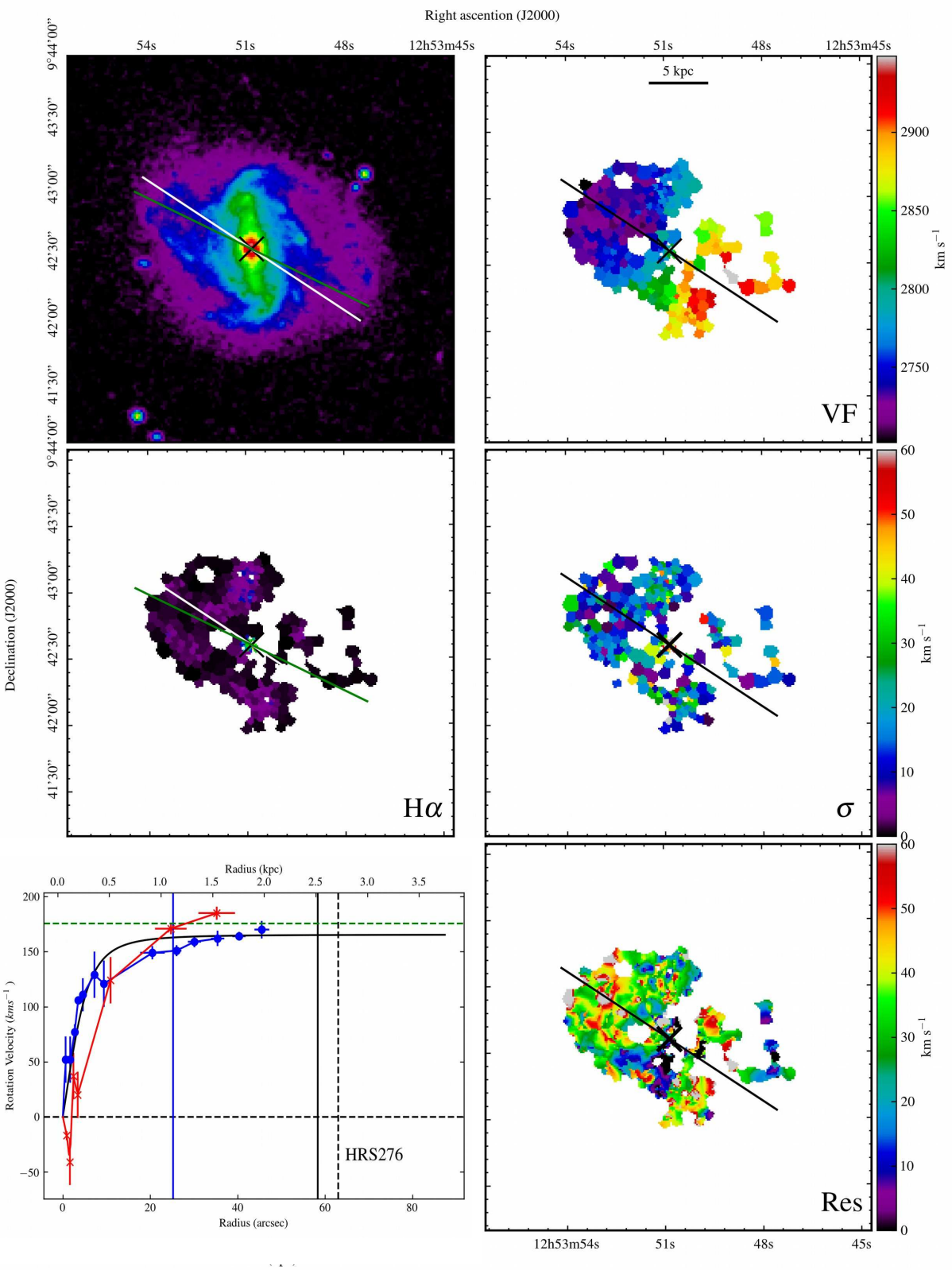
Right ascention (J2000)
54s
51s
48s
12h53m45s
Declination (J2000)
9°44'00"
43'30"
43'00"
42'30"
42'00"
41'30"
5 kpc
VF
Hα
σ
Res
km s⁻¹
Radius (kpc)
Rotation Velocity (kms⁻¹)
Radius (arcsec)
HRS276

HRS276

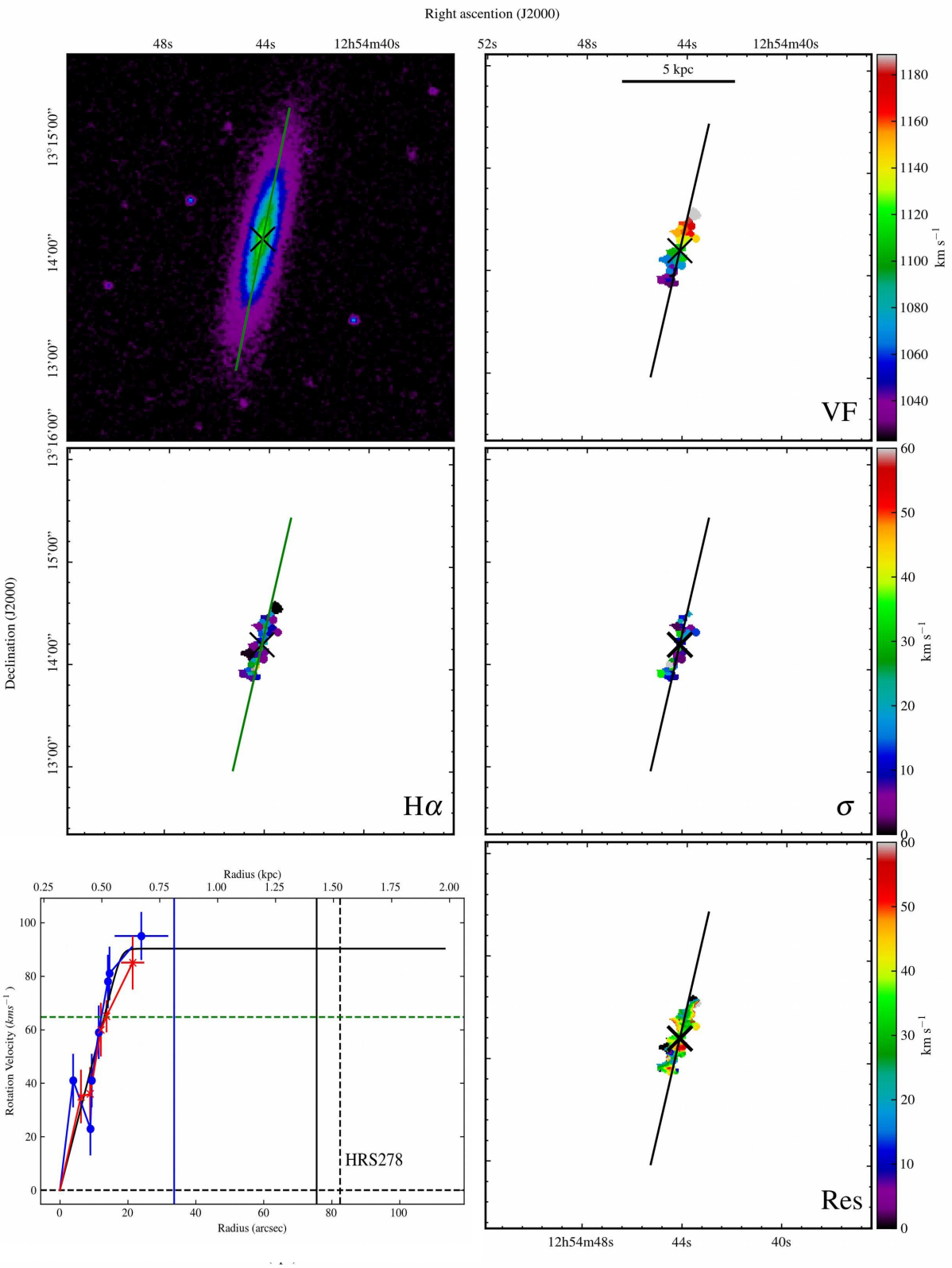
Right ascention (J2000)
48s
44s
12h54m40s
52s
48s
44s
12h54m40s
5 kpc
13°15'00"
14'00"
13'00"
13°16'00"
15'00"
14'00"
13'00"
Declination (J2000)
VF
Hα
σ
Res
km s⁻¹
1180
1160
1140
1120
1100
1080
1060
1040
60
50
40
30
20
10
0
Radius (kpc)
0.25
0.50
0.75
1.00
1.25
1.50
1.75
2.00
Rotation Velocity (kms⁻¹)
100
80
60
40
20
0
HRS278
Radius (arcsec)
0
20
40
60
80
100
12h54m48s
44s
40s

HRS278

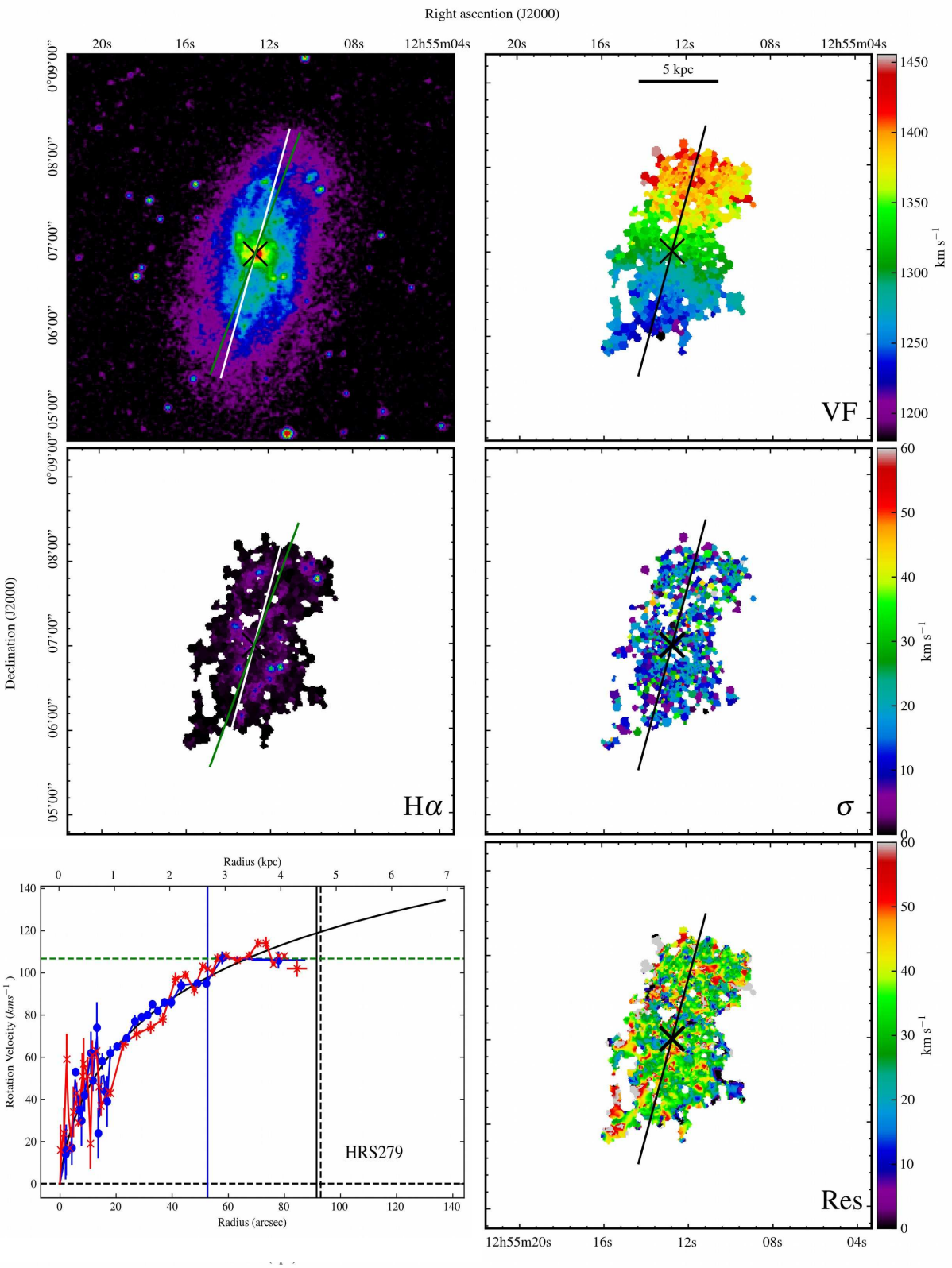
Right ascention (J2000)
20s
16s
12s
08s
12h55m04s
Declination (J2000)
0°09'00"
08'00"
07'00"
06'00"
05'00"
5 kpc
VF
Hα
σ
Res
km s⁻¹
1450
1400
1350
1300
1250
1200
60
50
40
30
20
10
0
Radius (kpc)
Rotation Velocity (kms⁻¹)
Radius (arcsec)
HRS279
12h55m20s
04s

HRS279

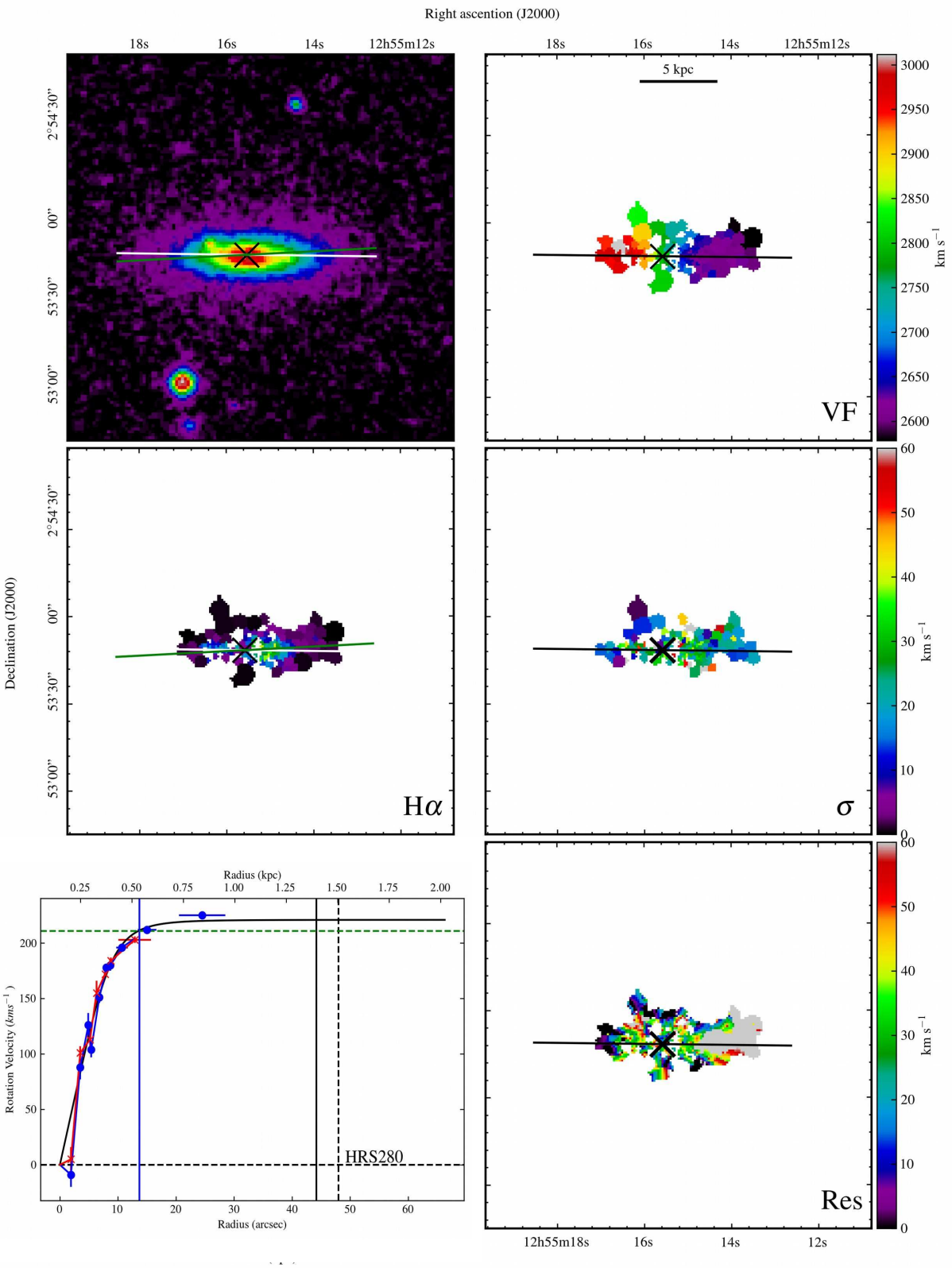
Right ascention (J2000)
18s
16s
14s
12h55m12s
2°54'30"
00"
53'30"
53'00"
Declination (J2000)
5 kpc
VF
Hα
σ
Res
km s⁻¹
3000
2950
2900
2850
2800
2750
2700
2650
2600
60
50
40
30
20
10
0
Radius (kpc)
0.25
0.50
0.75
1.00
1.25
1.50
1.75
2.00
Rotation Velocity (kms⁻¹)
200
150
100
50
0
HRS280
Radius (arcsec)
0
10
20
30
40
50
60
12h55m18s
12s

HRS280

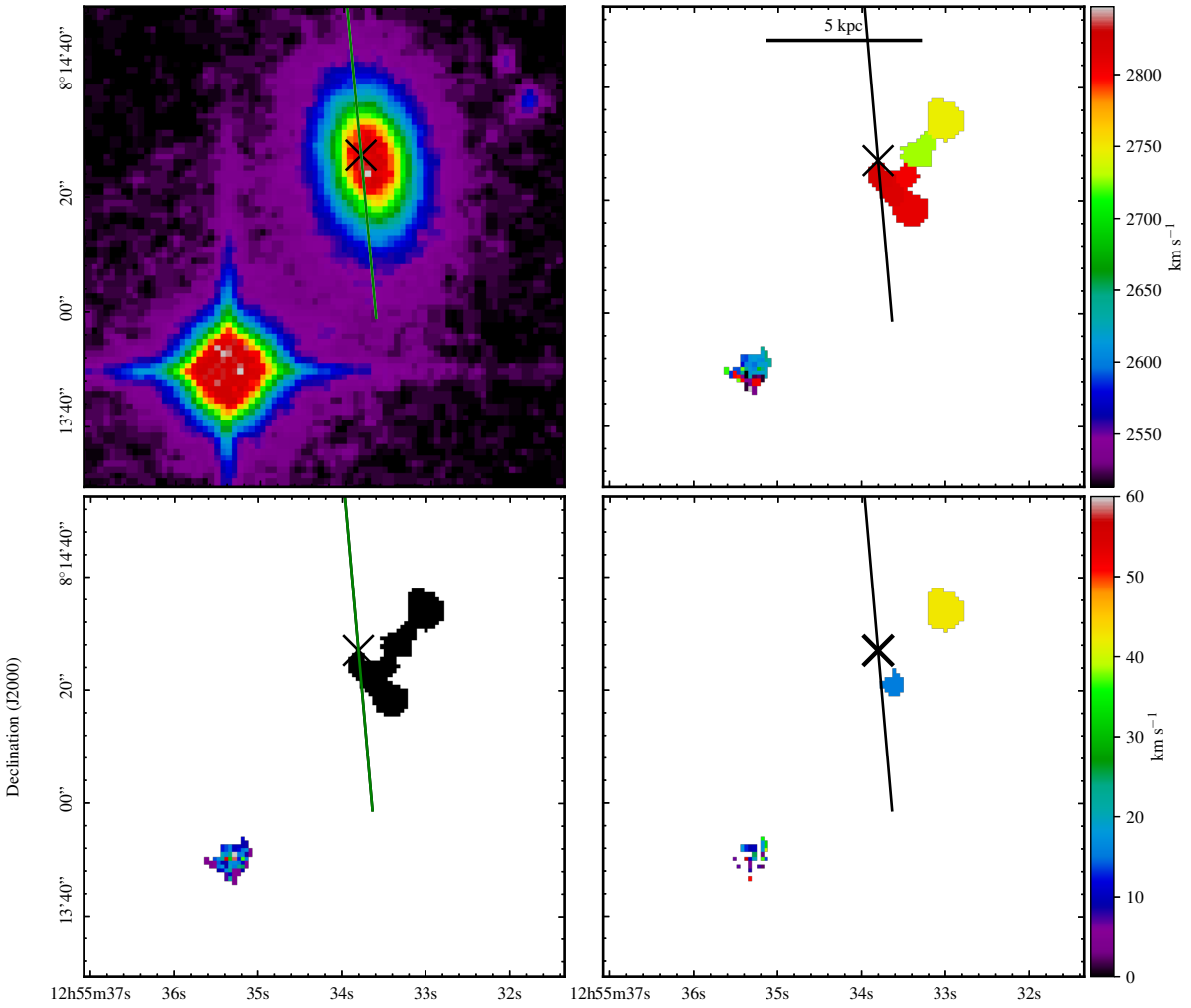
5 kpc
2800
2750
2700
2650
2600
2550
km s^{-1}
60
50
40
30
20
10
0
km s^{-1}
8° 14' 40"
20"
00"
13' 40"
Declination (J2000)
12h55m37s
36s
35s
34s
33s
32s
Right ascention (J2000)
HRS282

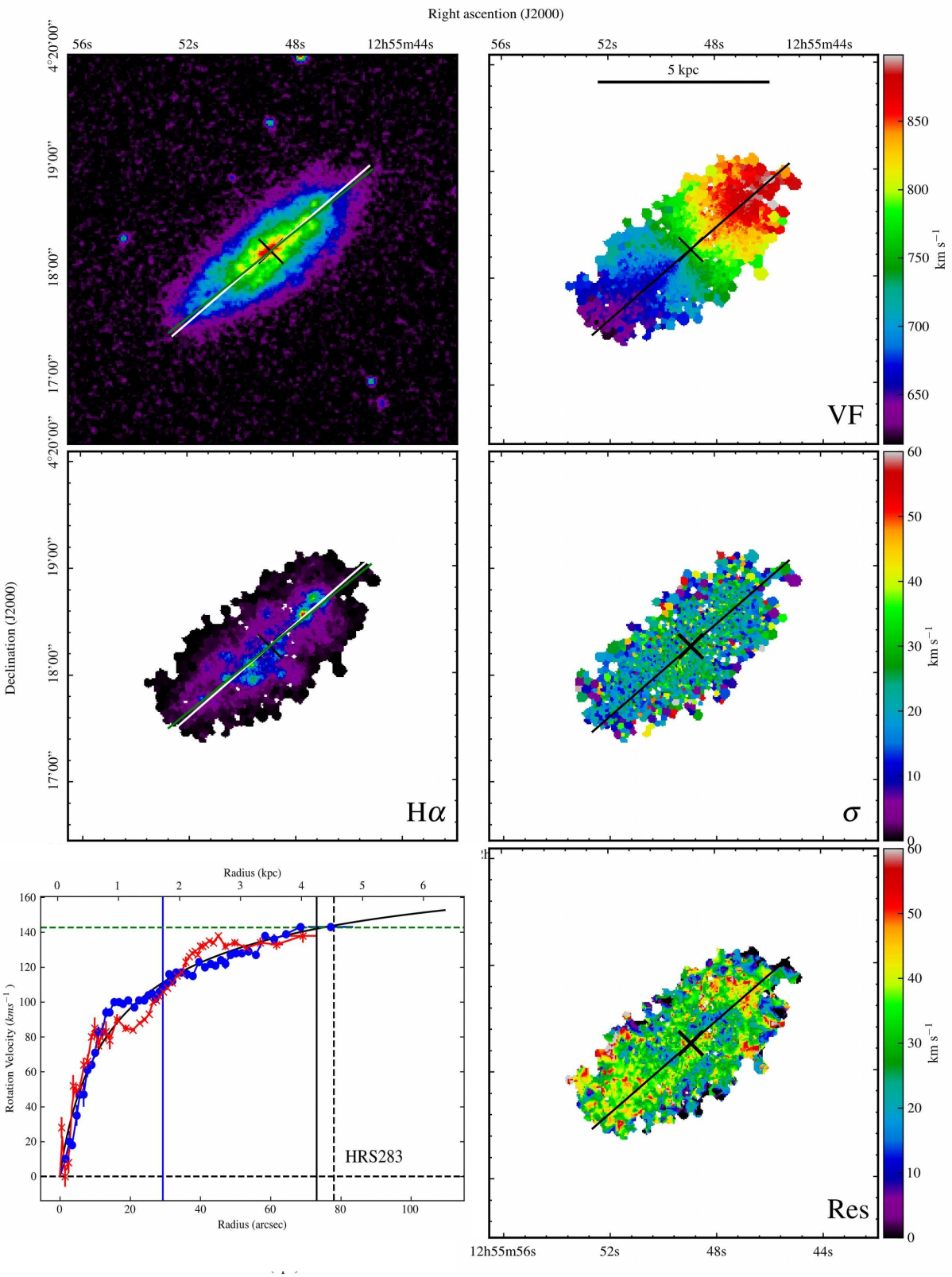
Right ascention (J2000)
Declination (J2000)
56s
52s
48s
12h55m44s
12h55m56s
44s
4°20'00"
19'00"
18'00"
17'00"
5 kpc
VF
Hα
σ
Res
km s−1
Radius (kpc)
Rotation Velocity (kms−1)
Radius (arcsec)
HRS283

HRS283

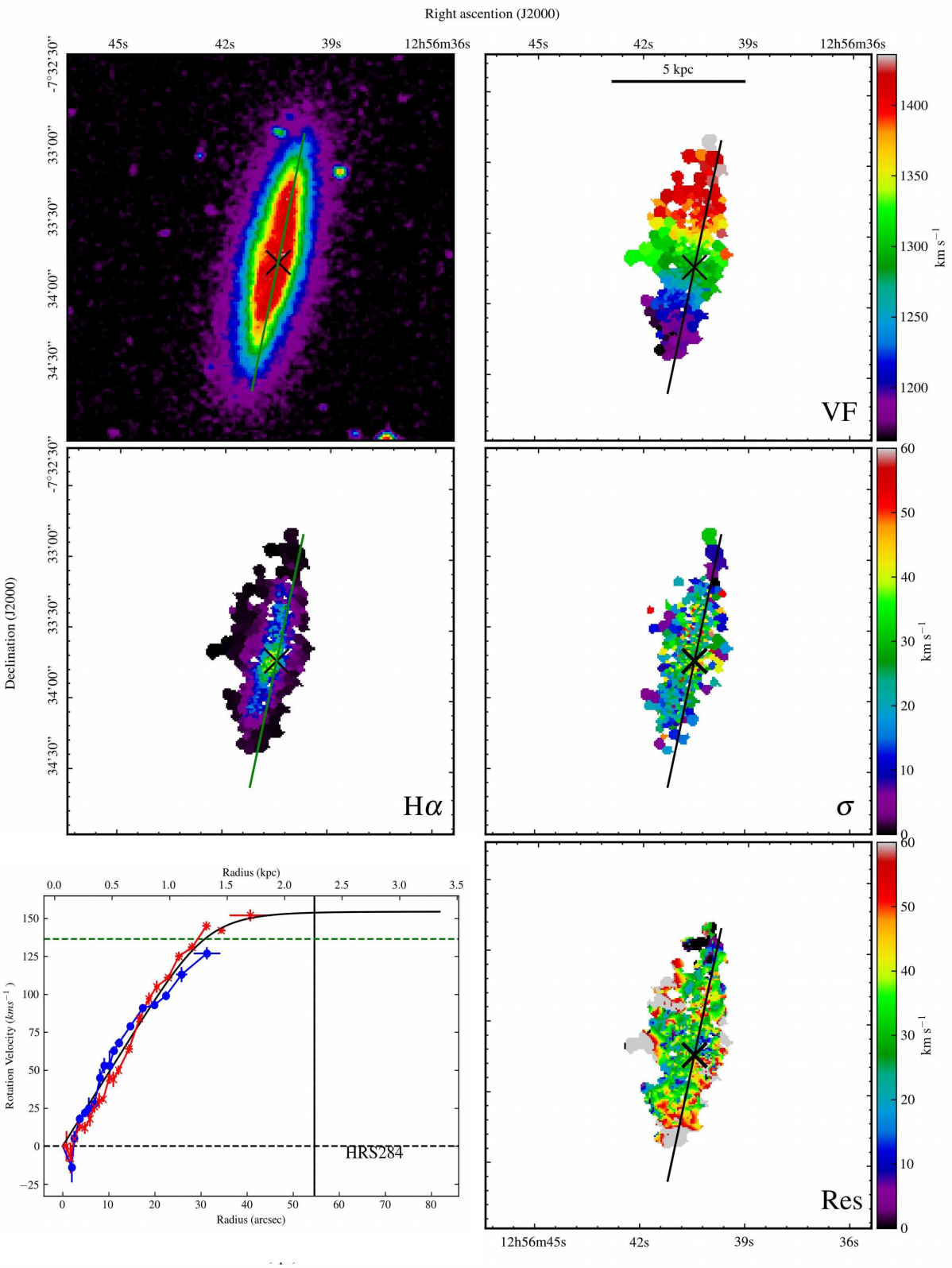
Right ascention (J2000)
45s
42s
39s
12h56m36s
-7°32'30"
33'00"
33'30"
34'00"
34'30"
Declination (J2000)
5 kpc
VF
Hα
σ
Res
km s⁻¹
1400
1350
1300
1250
1200
60
50
40
30
20
10
0
12h56m45s
42s
39s
36s
Radius (kpc)
0.0
0.5
1.0
1.5
2.0
2.5
3.0
3.5
Rotation Velocity (kms⁻¹)
150
125
100
75
50
25
0
−25
HRS284
0
10
20
30
40
50
60
70
80
Radius (arcsec)

HRS284

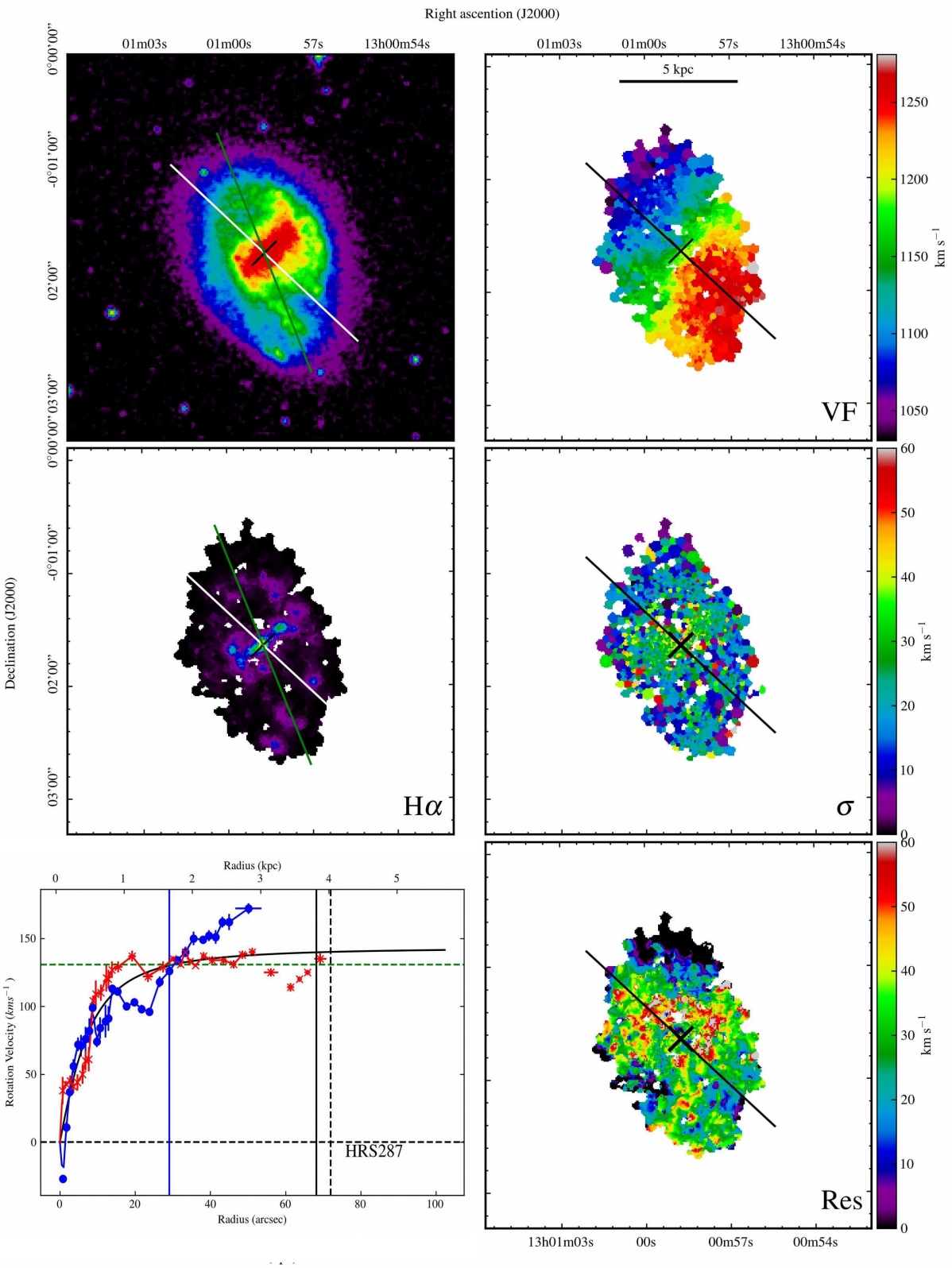
Right ascention (J2000)
Declination (J2000)
01m03s
01m00s
57s
13h00m54s
0°00'00"
-0°01'00"
02'00"
03'00"
5 kpc
VF
Hα
σ
Res
km s⁻¹
Radius (kpc)
Rotation Velocity (kms⁻¹)
Radius (arcsec)
HRS287
13h01m03s
00s
00m57s
00m54s

HRS287

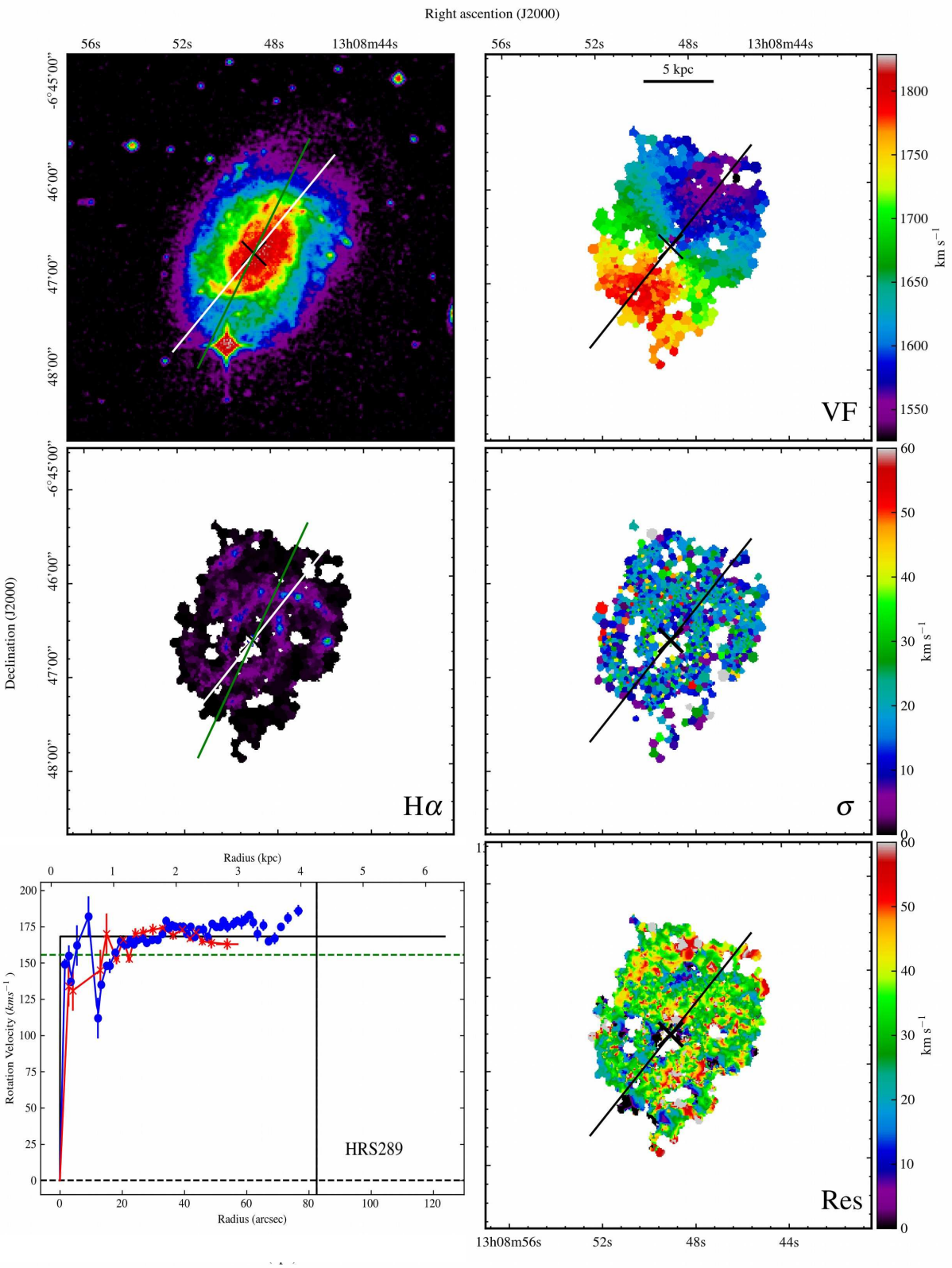
Right ascention (J2000)
56s
52s
48s
13h08m44s
-6°45'00"
46'00"
47'00"
48'00"
Declination (J2000)
5 kpc
VF
Hα
σ
Res
km s⁻¹
1800
1750
1700
1650
1600
1550
60
50
40
30
20
10
0
13h08m56s
52s
48s
44s
Radius (kpc)
0
1
2
3
4
5
6
Rotation Velocity (kms⁻¹)
200
175
150
125
100
75
50
25
0
Radius (arcsec)
0
20
40
60
80
100
120
HRS289

HRS289

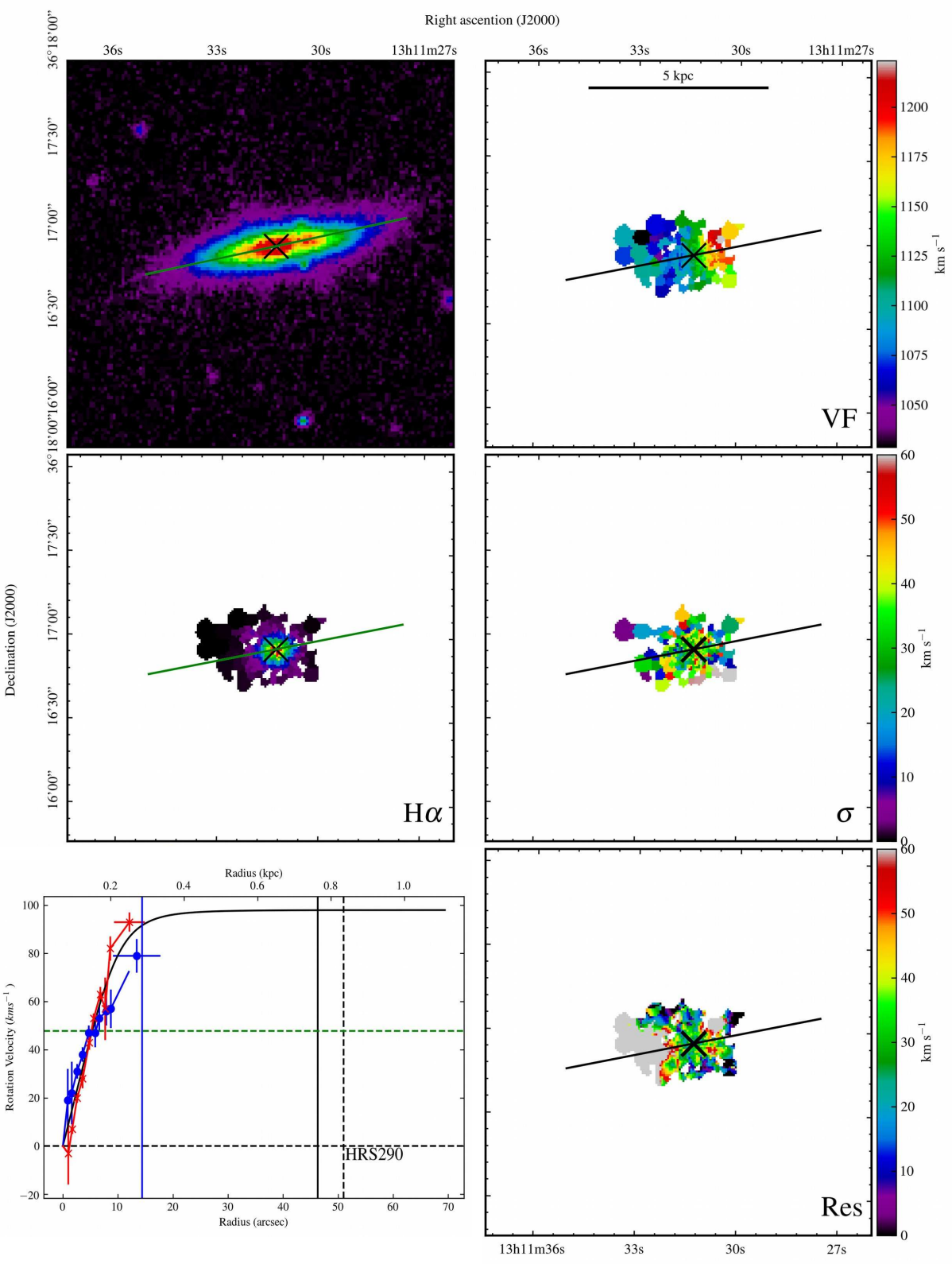
Right ascention (J2000)
Declination (J2000)
36s
33s
30s
13h11m27s
13h11m36s
27s
36°18'00"
17'30"
17'00"
16'30"
16'00"
5 kpc
VF
Hα
σ
Res
km s−1
1200
1175
1150
1125
1100
1075
1050
60
50
40
30
20
10
0
Radius (kpc)
0.2
0.4
0.6
0.8
1.0
Rotation Velocity (kms−1)
Radius (arcsec)
HRS290

HRS290

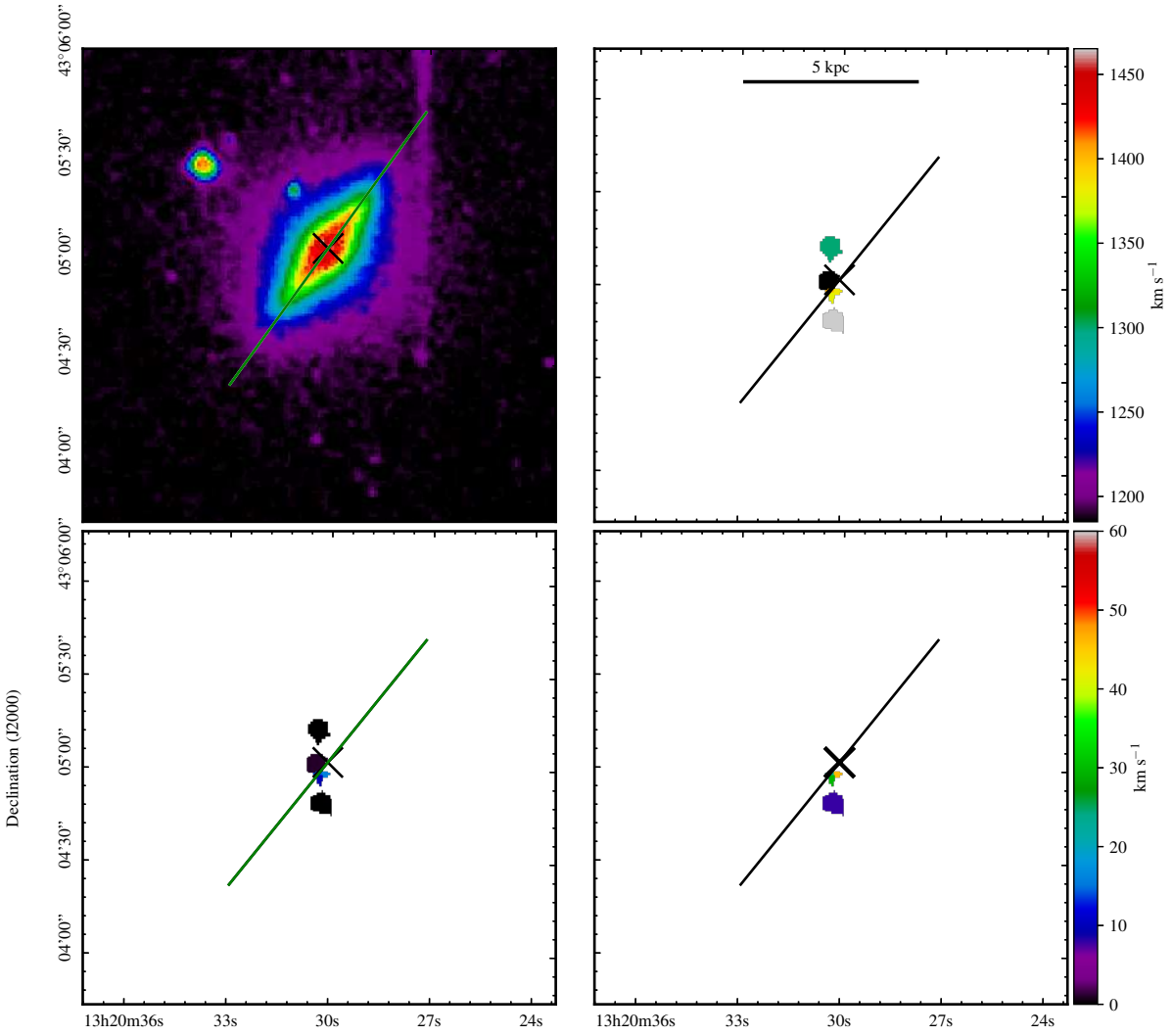
5 kpc
Declination (J2000)
43°06'00"
05'30"
05'00"
04'30"
04'00"
13h20m36s
33s
30s
27s
24s
km s^{-1}
1450
1400
1350
1300
1250
1200
60
50
40
30
20
10
0
Right ascention (J2000)
HRS291

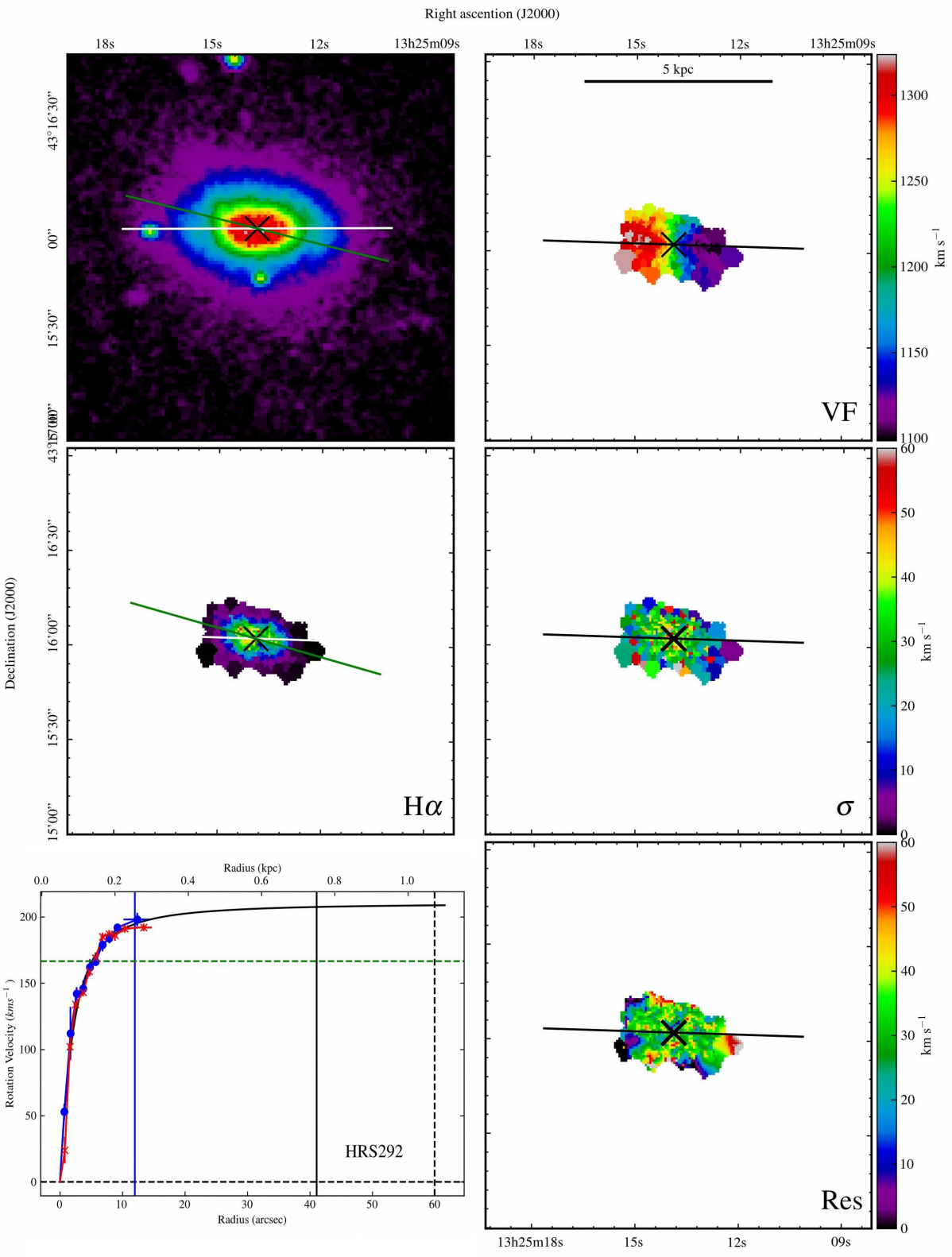
Right ascention (J2000)
18s
15s
12s
13h25m09s
Declination (J2000)
43°16'30"
00"
15'30"
16'00"
16'30"
15'00"
5 kpc
VF
Hα
σ
Res
km s⁻¹
1300
1250
1200
1150
1100
60
50
40
30
20
10
0
Radius (kpc)
0.0
0.2
0.4
0.6
0.8
1.0
Rotation Velocity (kms⁻¹)
200
150
100
50
0
Radius (arcsec)
HRS292
13h25m18s
09s

HRS292

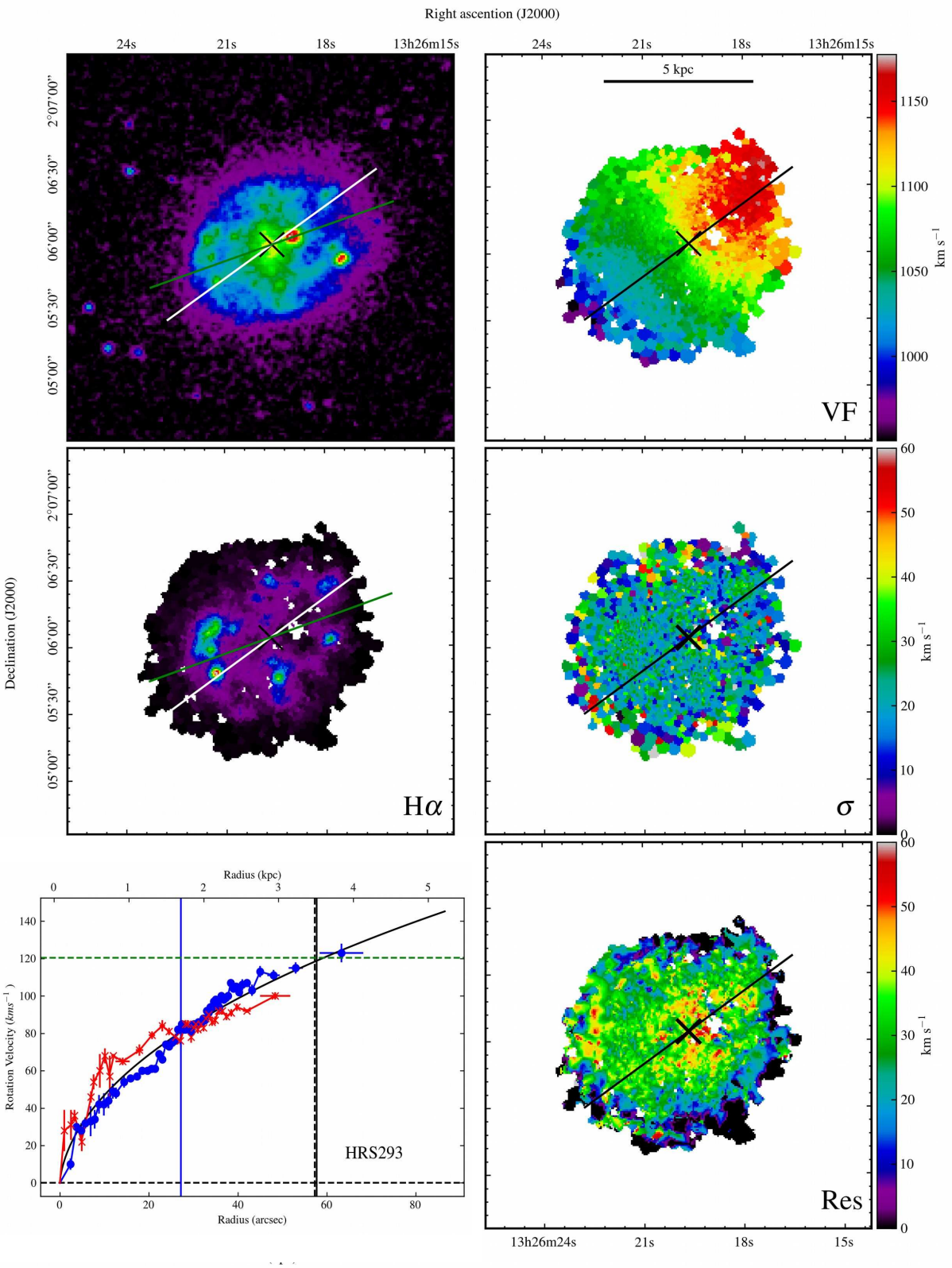
Right ascention (J2000)
24s
21s
18s
13h26m15s
Declination (J2000)
2°07'00"
06'30"
06'00"
05'30"
05'00"
5 kpc
VF
Hα
σ
Res
km s⁻¹
Radius (kpc)
Rotation Velocity (kms⁻¹)
Radius (arcsec)
HRS293
13h26m24s

HRS293

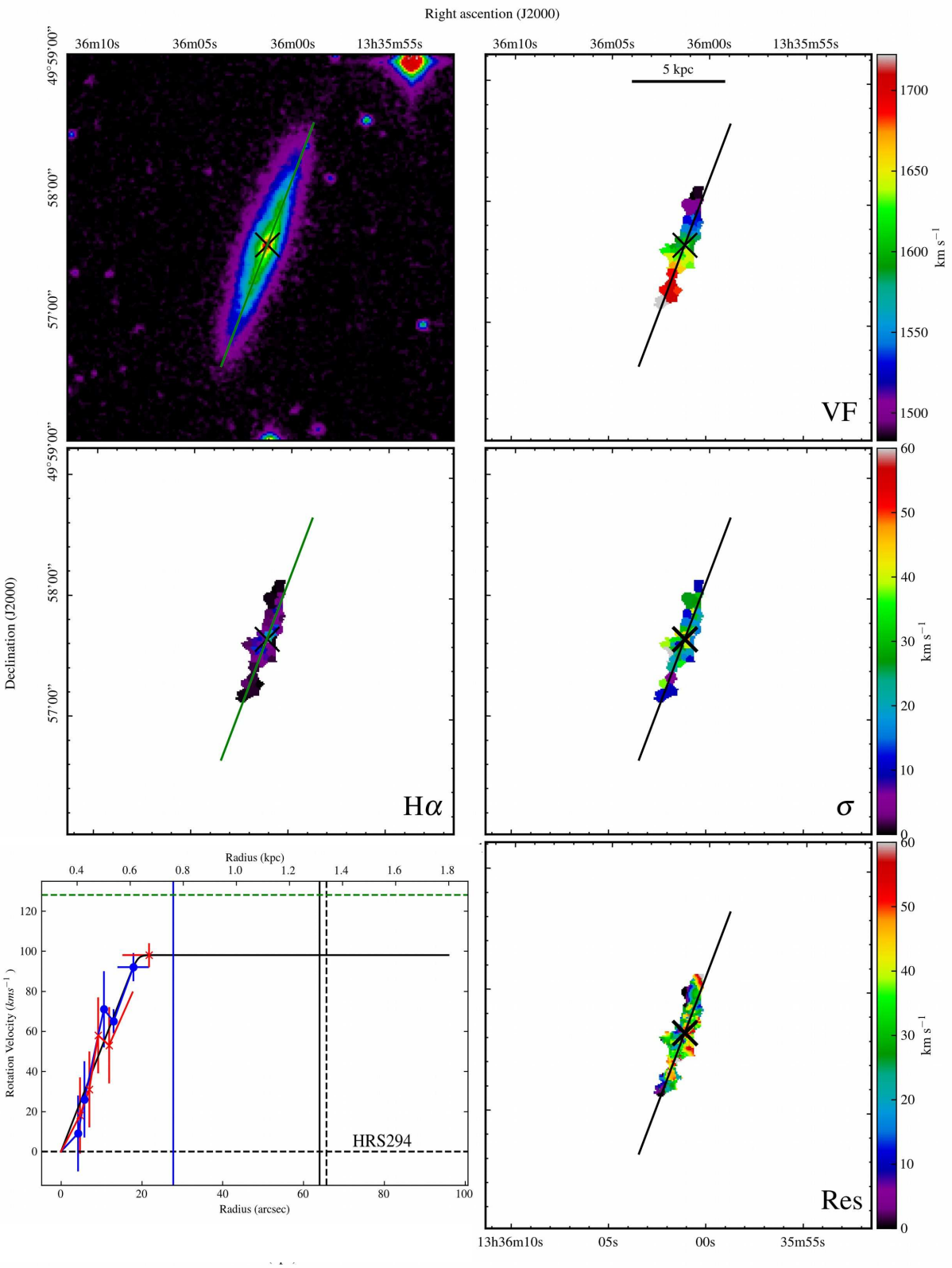
Right ascention (J2000)
Declination (J2000)
36m10s
36m05s
36m00s
13h35m55s
49°59'00"
58'00"
57'00"
5 kpc
VF
Hα
σ
Res
km s⁻¹
1700
1650
1600
1550
1500
60
50
40
30
20
10
0
Radius (kpc)
0.4
0.6
0.8
1.0
1.2
1.4
1.6
1.8
Rotation Velocity (kms⁻¹)
120
100
80
60
40
20
0
HRS294
Radius (arcsec)
0
20
40
60
80
100
13h36m10s
05s
00s
35m55s

HRS294

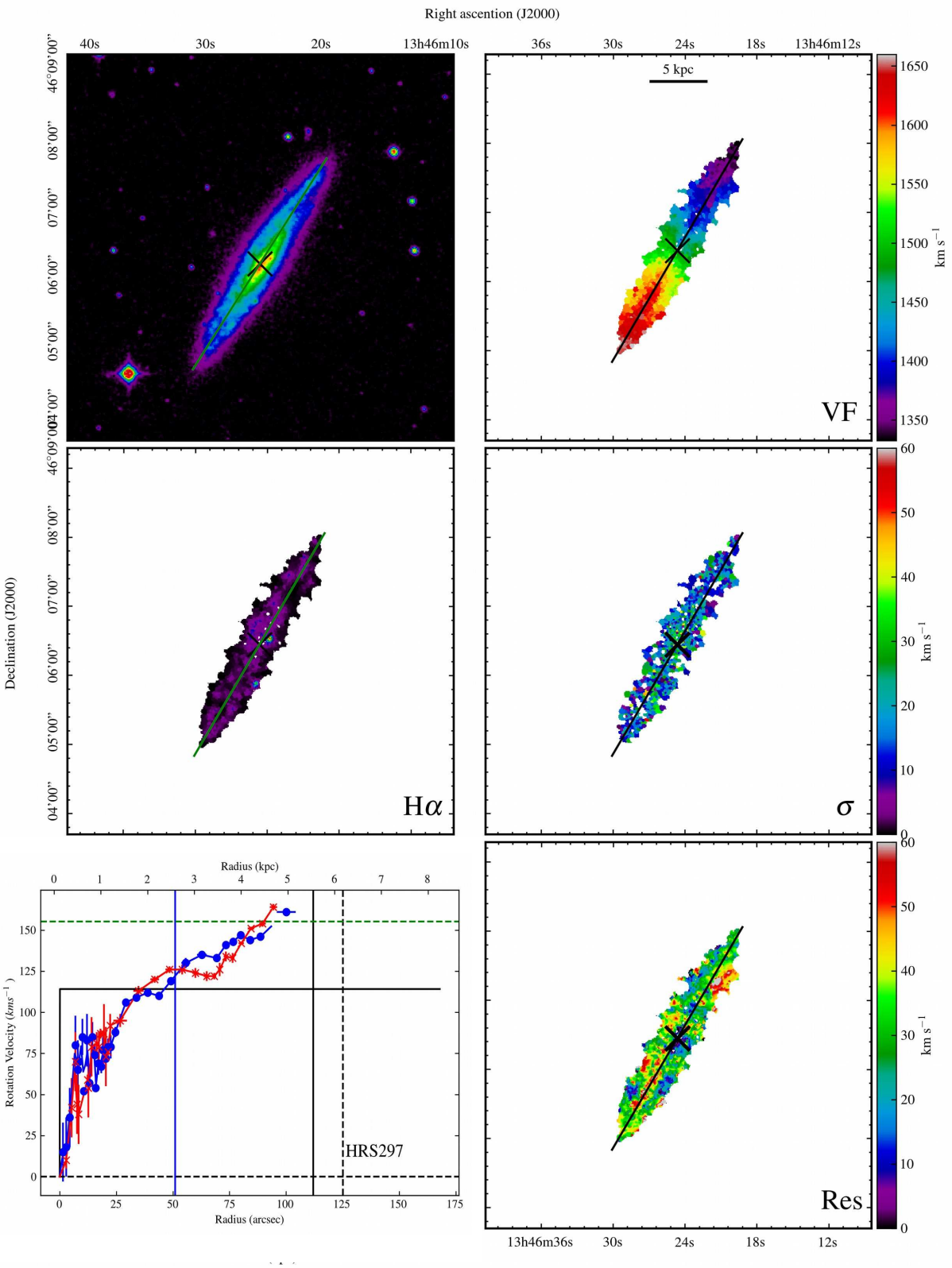
Right ascention (J2000)
Declination (J2000)
5 kpc
VF
Hα
σ
Res
km s⁻¹
Radius (kpc)
Radius (arcsec)
Rotation Velocity (kms⁻¹)
HRS297

HRS297

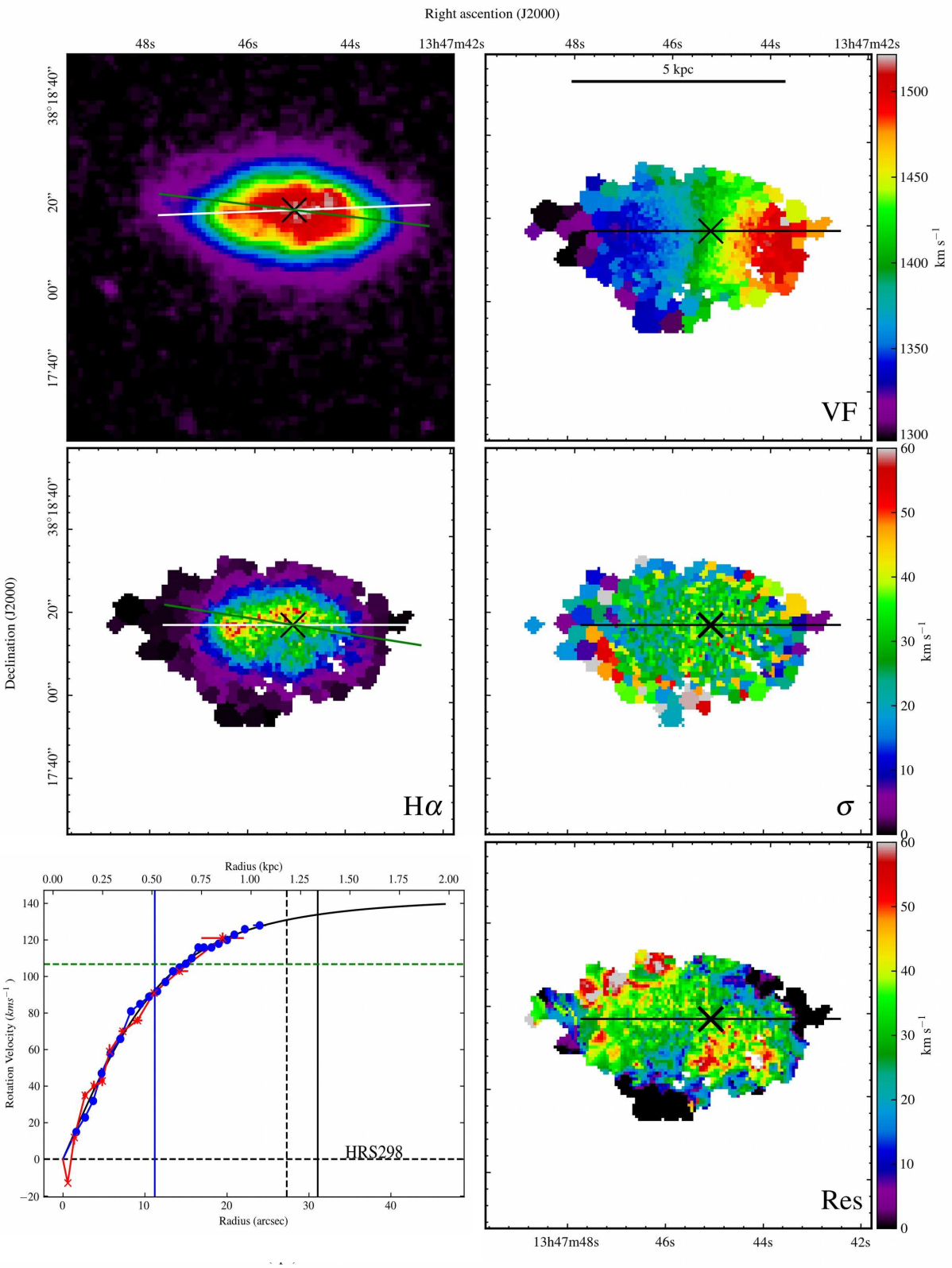
Right ascention (J2000)
48s
46s
44s
13h47m42s
38°18'40"
20"
00"
17'40"
Declination (J2000)
5 kpc
VF
Hα
σ
Res
km s⁻¹
1500
1450
1400
1350
1300
60
50
40
30
20
10
0
13h47m48s
42s
Radius (kpc)
0.00
0.25
0.50
0.75
1.00
1.25
1.50
1.75
2.00
Rotation Velocity (kms⁻¹)
Radius (arcsec)
HRS298

HRS298

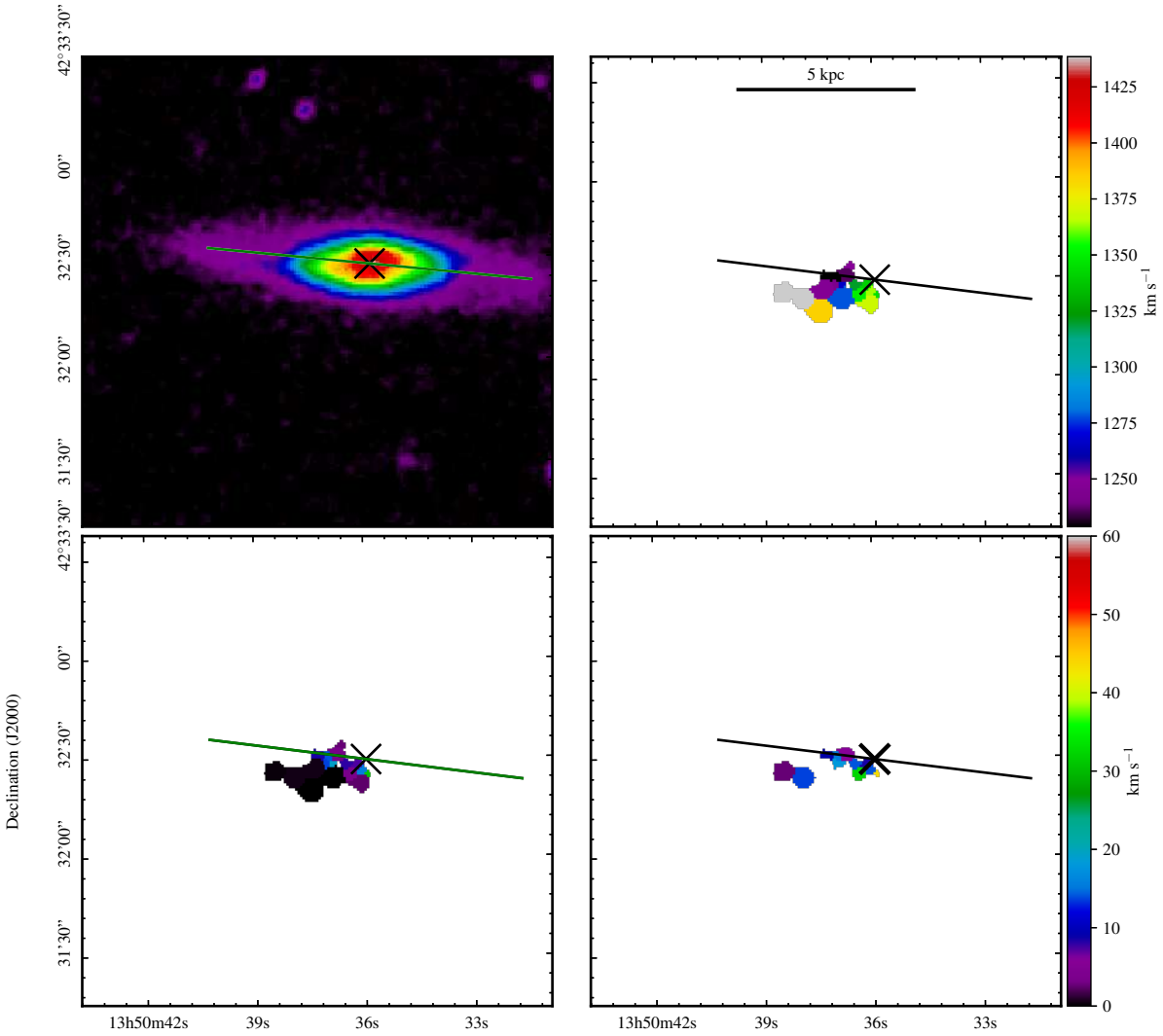

Right ascention (J2000)
HRS300

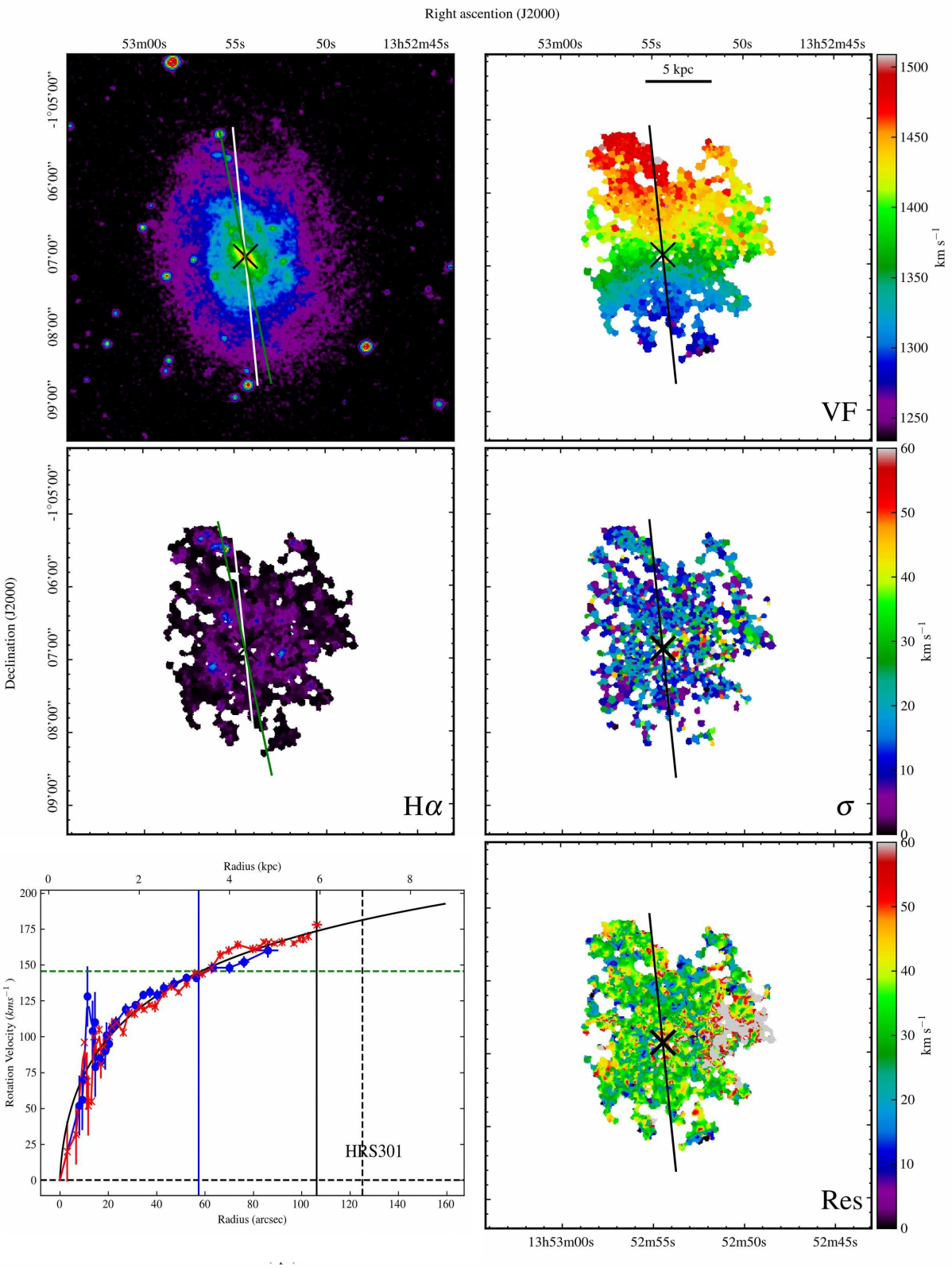
Right ascention (J2000)
53m00s
55s
50s
13h52m45s
Declination (J2000)
-1°05'00"
06'00"
07'00"
08'00"
09'00"
5 kpc
VF
Hα
σ
Res
km s⁻¹
1500
1450
1400
1350
1300
1250
60
50
40
30
20
10
0
13h53m00s
52m55s
52m50s
52m45s
Radius (kpc)
0
2
4
6
8
Rotation Velocity (kms⁻¹)
200
175
150
125
100
75
50
25
0
Radius (arcsec)
0
20
40
60
80
100
120
140
160
HRS301

HRS301

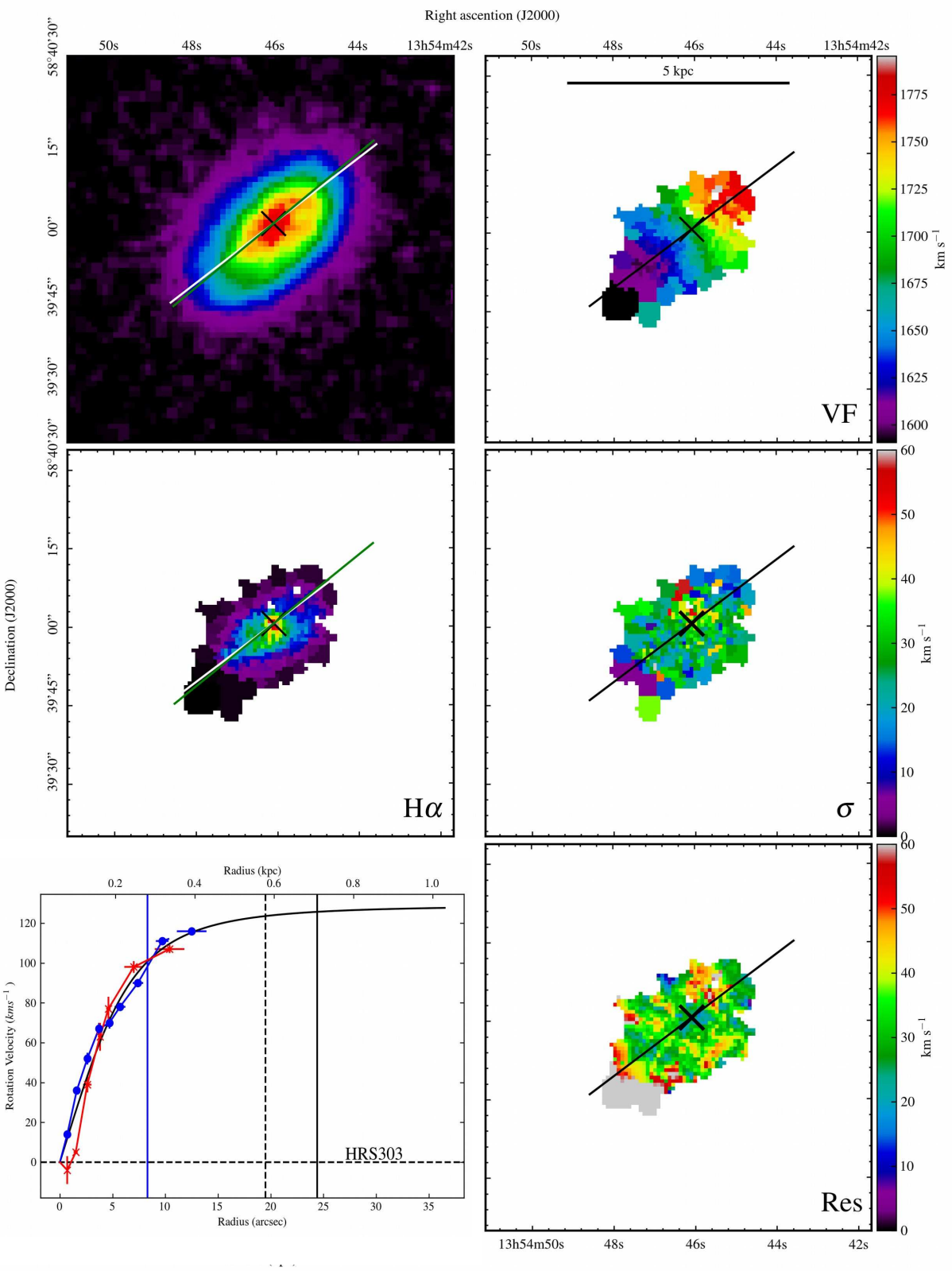
Right ascention (J2000)
50s
48s
46s
44s
13h54m42s
58°40'30"
15"
00"
39'45"
39'30"
5 kpc
VF
Hα
σ
Res
Declination (J2000)
km s^{-1}
1775
1750
1725
1700
1675
1650
1625
1600
60
50
40
30
20
10
0
Radius (kpc)
0.2
0.4
0.6
0.8
1.0
Rotation Velocity (kms^{-1})
120
100
80
60
40
20
0
HRS303
Radius (arcsec)
0
5
10
15
20
25
30
35
13h54m50s
48s
46s
44s
42s

HRS303

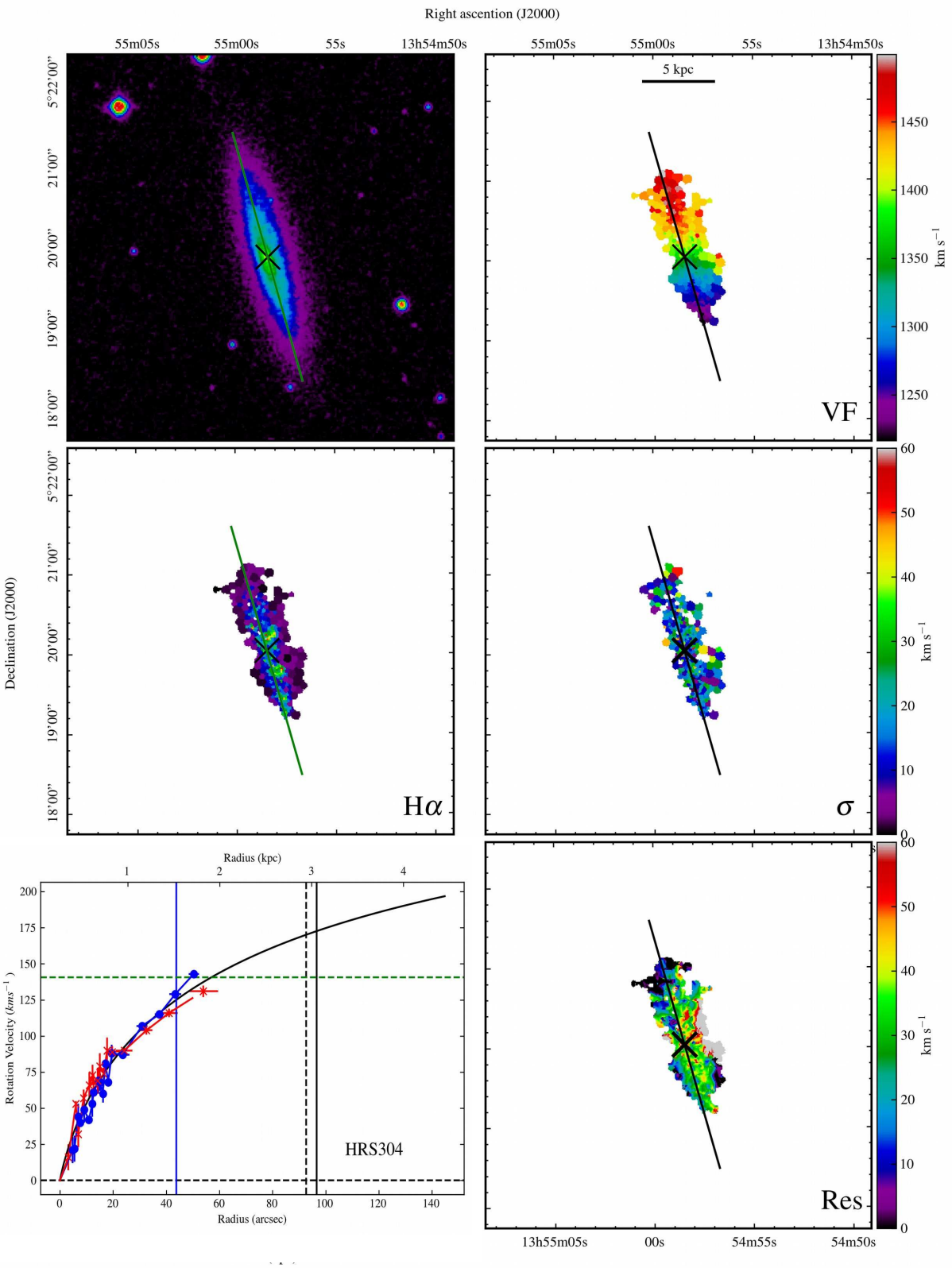
Right ascention (J2000)
55m05s
55m00s
55s
13h54m50s
Declination (J2000)
5°22'00"
21'00"
20'00"
19'00"
18'00"
5 kpc
VF
Hα
σ
Res
km s⁻¹
Radius (kpc)
Rotation Velocity (kms⁻¹)
Radius (arcsec)
HRS304
13h55m05s
00s
54m55s
54m50s

HRS304

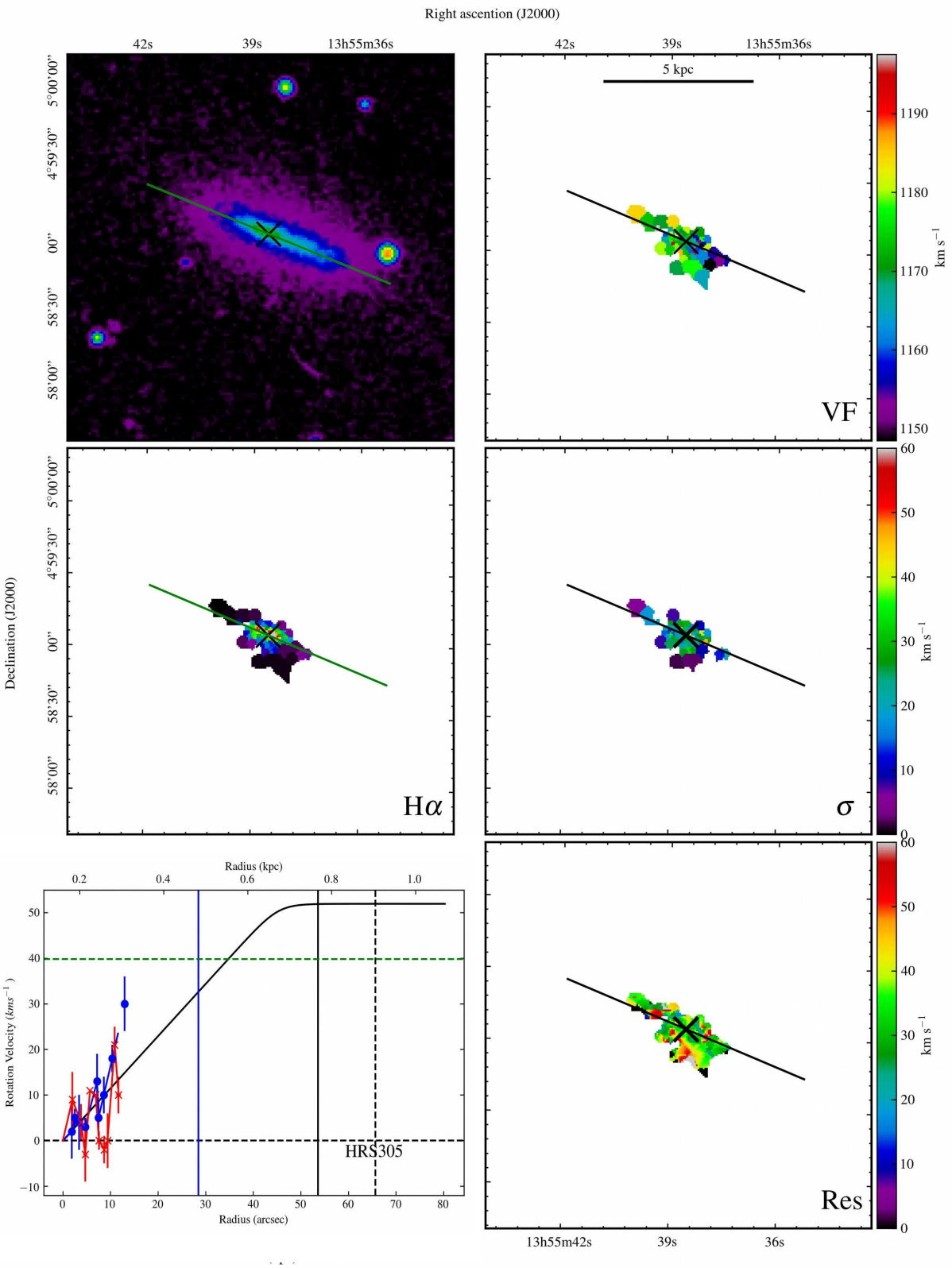
Right ascention (J2000)
42s
39s
13h55m36s
5°00'00"
4°59'30"
00"
58'30"
58'00"
Declination (J2000)
5 kpc
VF
Hα
σ
Res
km s⁻¹
1190
1180
1170
1160
1150
60
50
40
30
20
10
0
Radius (kpc)
0.2
0.4
0.6
0.8
1.0
Rotation Velocity (kms⁻¹)
Radius (arcsec)
HRS305
13h55m42s
39s
36s

HRS305

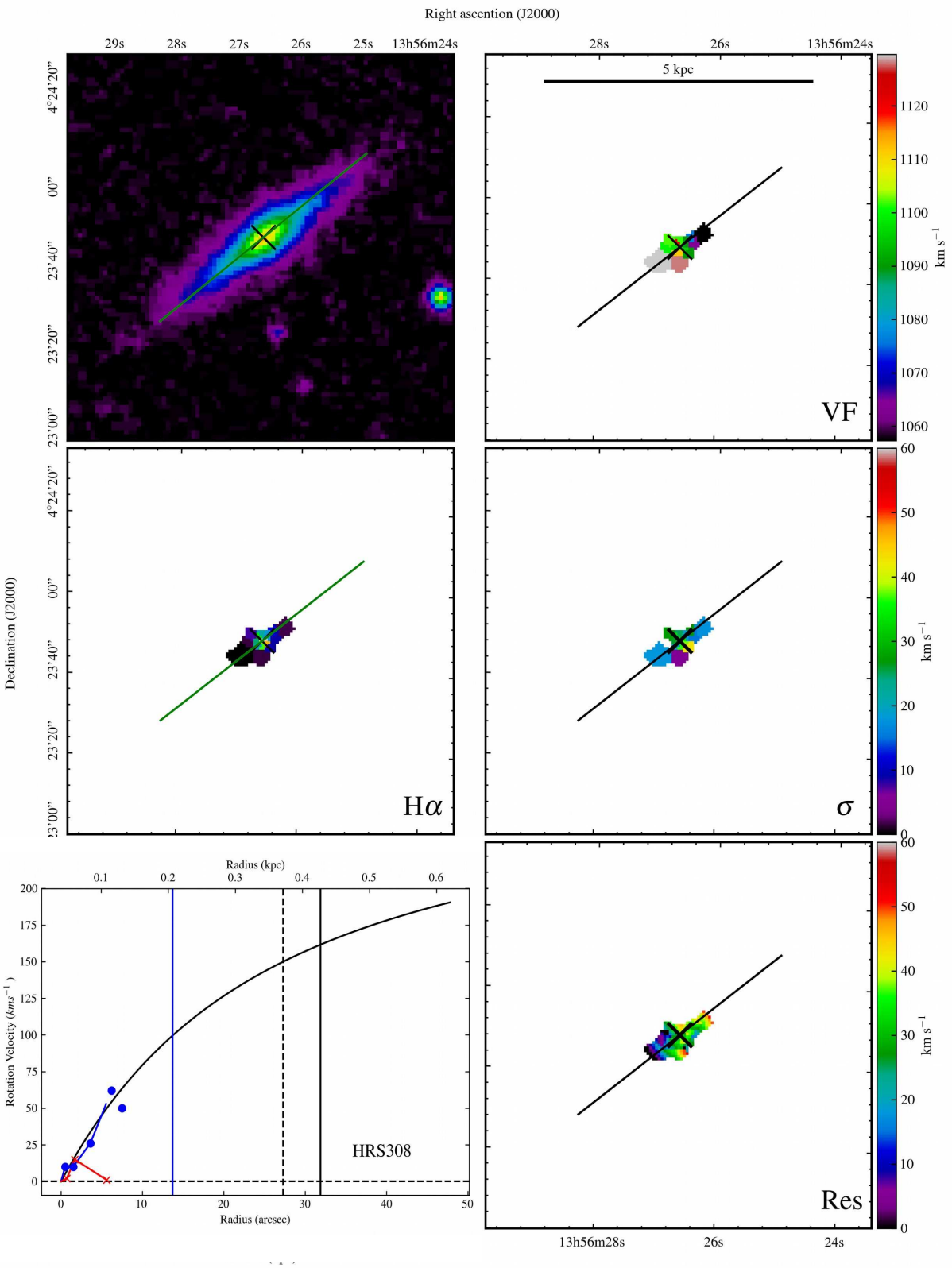
Right ascention (J2000)
29s
28s
27s
26s
25s
13h56m24s
28s
26s
13h56m24s
4°24'20"
00"
23'40"
23'20"
23'00"
5 kpc
VF
Hα
σ
Res
Declination (J2000)
km s⁻¹
1120
1110
1100
1090
1080
1070
1060
60
50
40
30
20
10
0
Radius (kpc)
0.1
0.2
0.3
0.4
0.5
0.6
Rotation Velocity (kms⁻¹)
200
175
150
125
100
75
50
25
0
HRS308
Radius (arcsec)
0
10
20
30
40
50
13h56m28s
26s
24s

HRS308

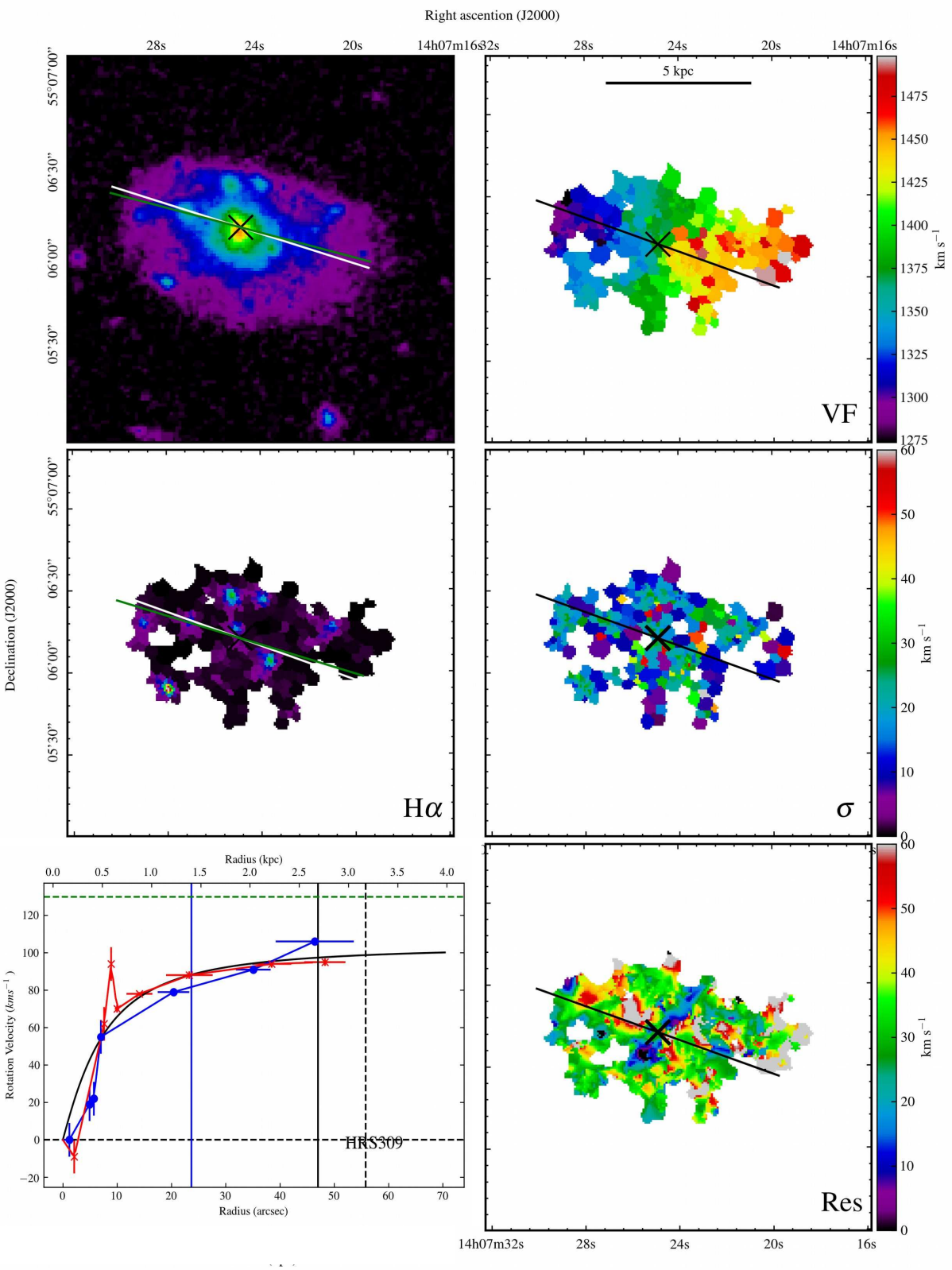
Right ascention (J2000)
Declination (J2000)
5 kpc
VF
Hα
σ
Res
km s⁻¹
Radius (kpc)
Radius (arcsec)
Rotation Velocity (kms⁻¹)
HRS309

HRS309

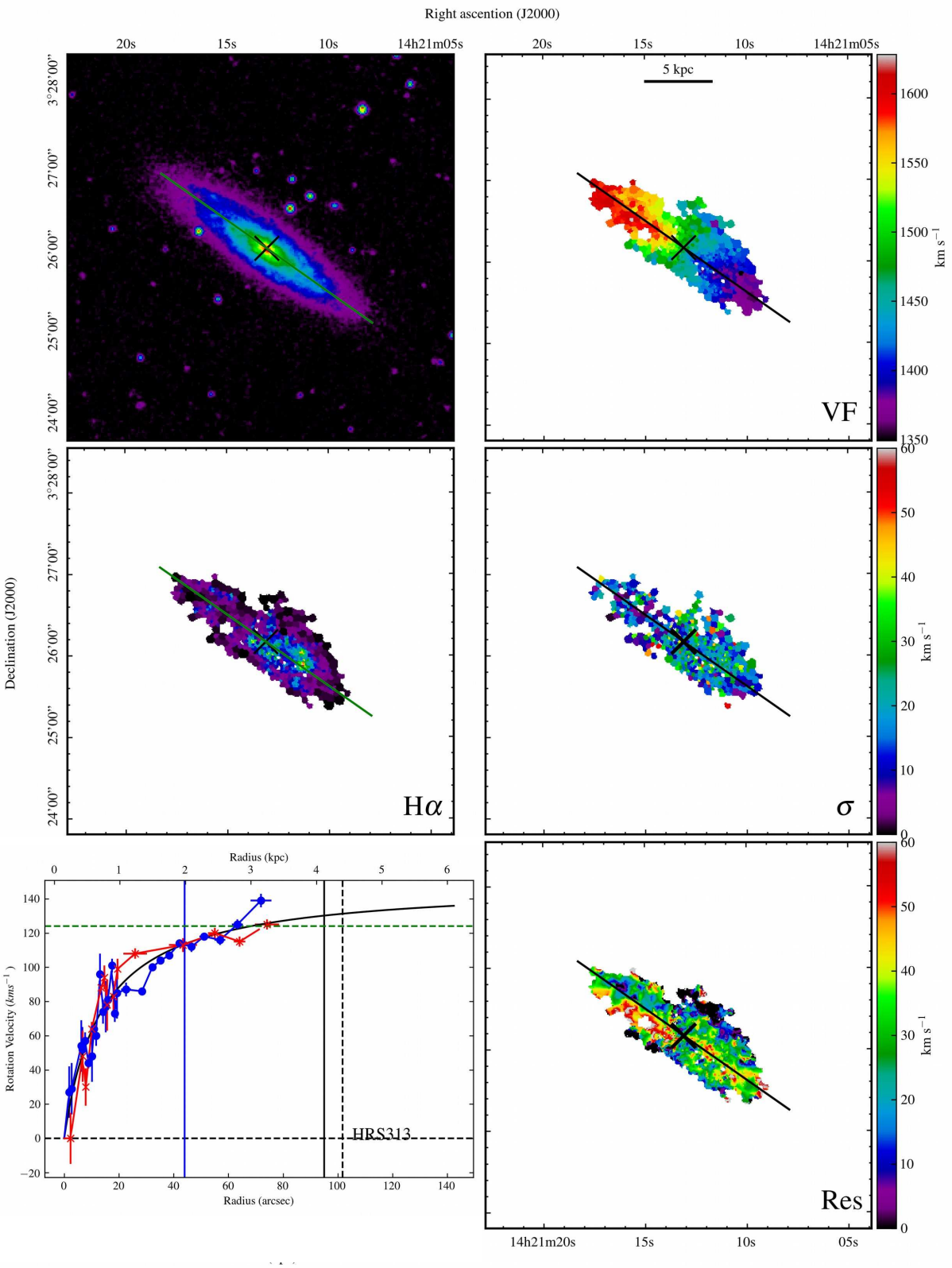
Right ascention (J2000)
20s
15s
10s
14h21m05s
Declination (J2000)
3°28'00"
27'00"
26'00"
25'00"
24'00"
5 kpc
VF
Hα
σ
Res
km s⁻¹
1600
1550
1500
1450
1400
1350
60
50
40
30
20
10
0
Radius (kpc)
Rotation Velocity (kms⁻¹)
Radius (arcsec)
HRS313
14h21m20s
05s

HRS313

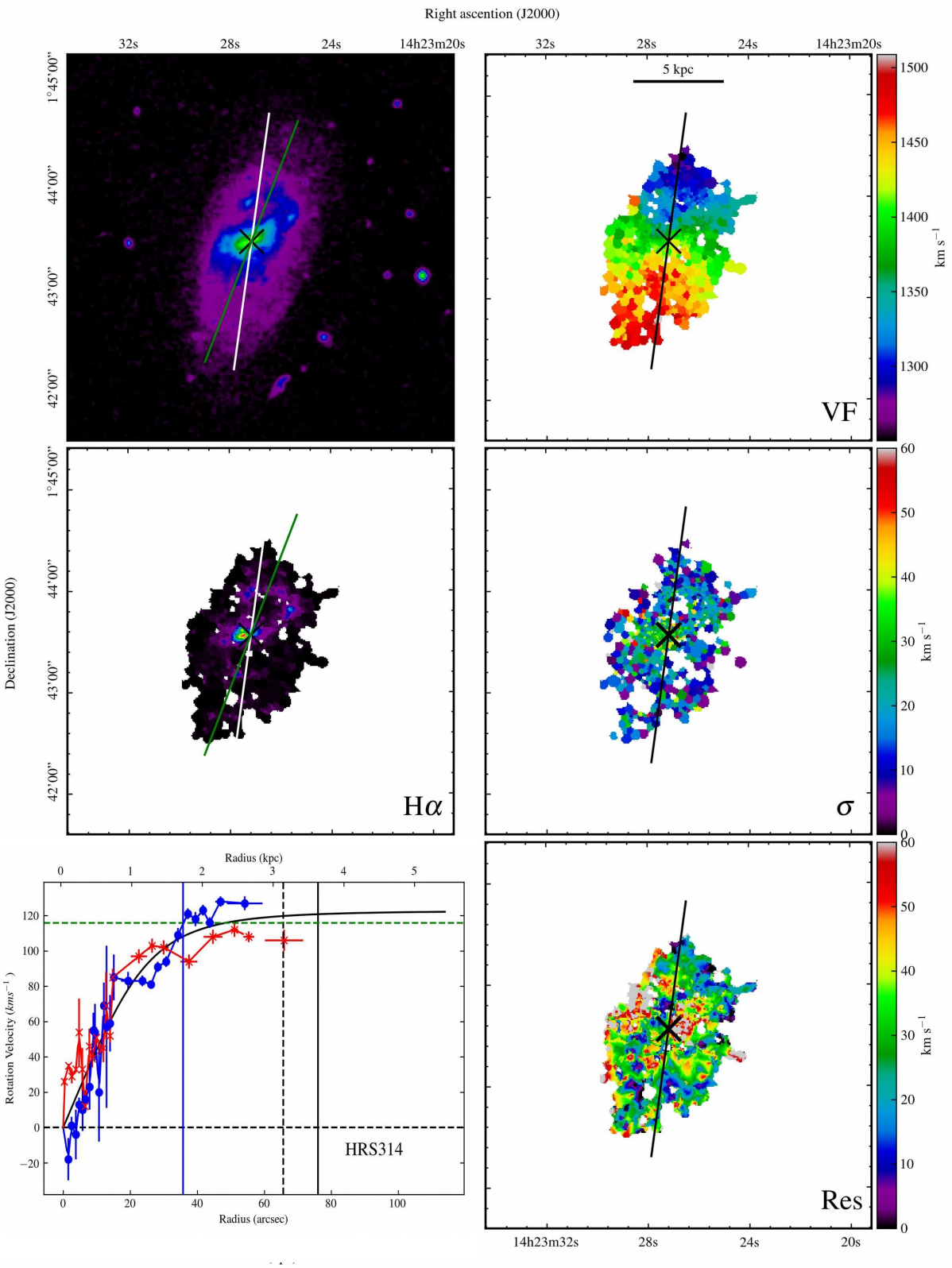
Right ascention (J2000)
32s
28s
24s
14h23m20s
1°45'00"
44'00"
43'00"
42'00"
Declination (J2000)
5 kpc
VF
Hα
σ
Res
km s⁻¹
1500
1450
1400
1350
1300
60
50
40
30
20
10
0
14h23m32s
Radius (kpc)
Rotation Velocity (kms⁻¹)
Radius (arcsec)
HRS314

HRS314

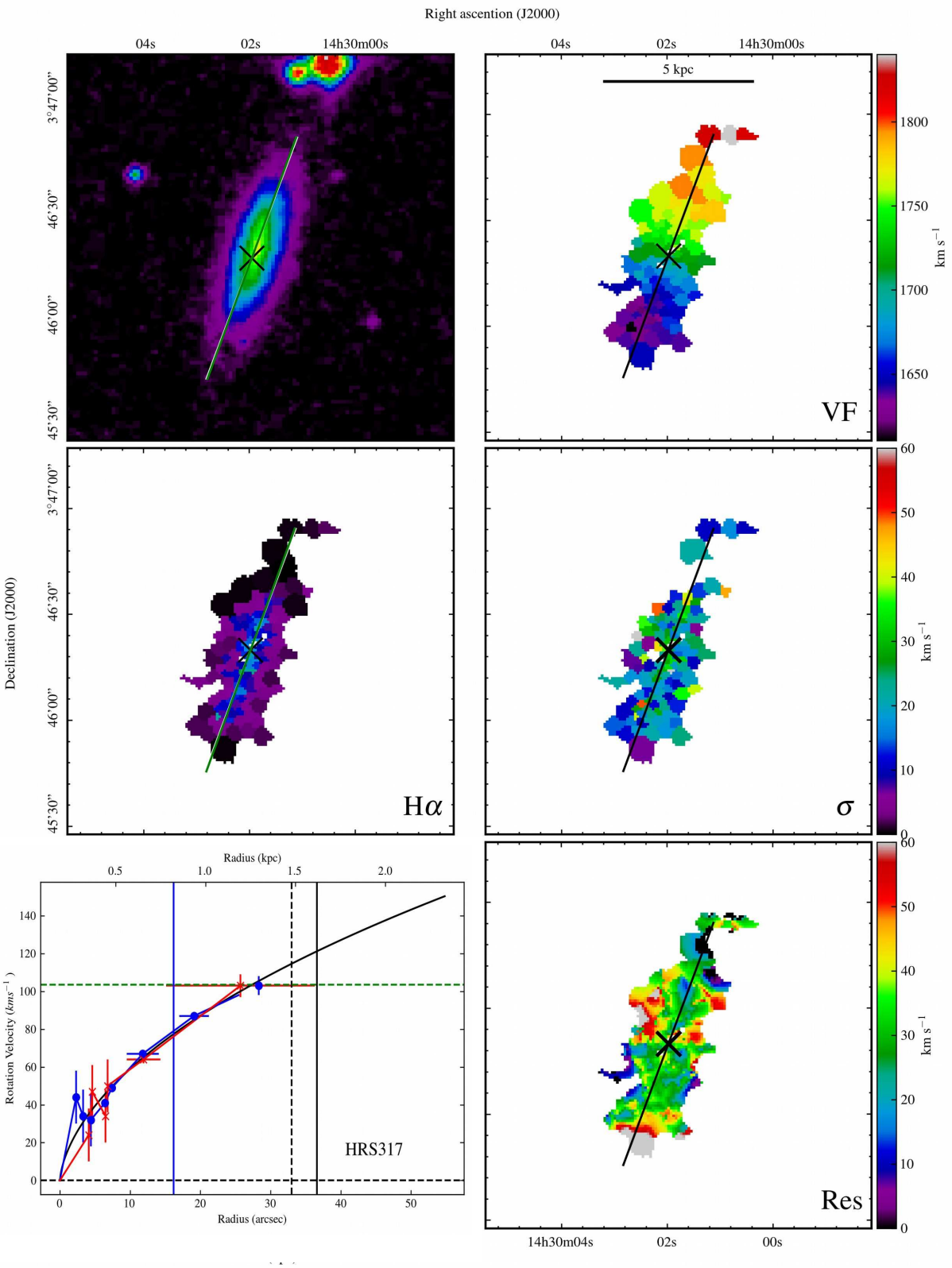
Right ascention (J2000)
04s
02s
14h30m00s
3°47'00"
46'30"
46'00"
45'30"
Declination (J2000)
5 kpc
VF
Hα
σ
Res
km s⁻¹
14h30m04s
00s
Radius (kpc)
0.5
1.0
1.5
2.0
Rotation Velocity (kms⁻¹)
Radius (arcsec)
HRS317

HRS317

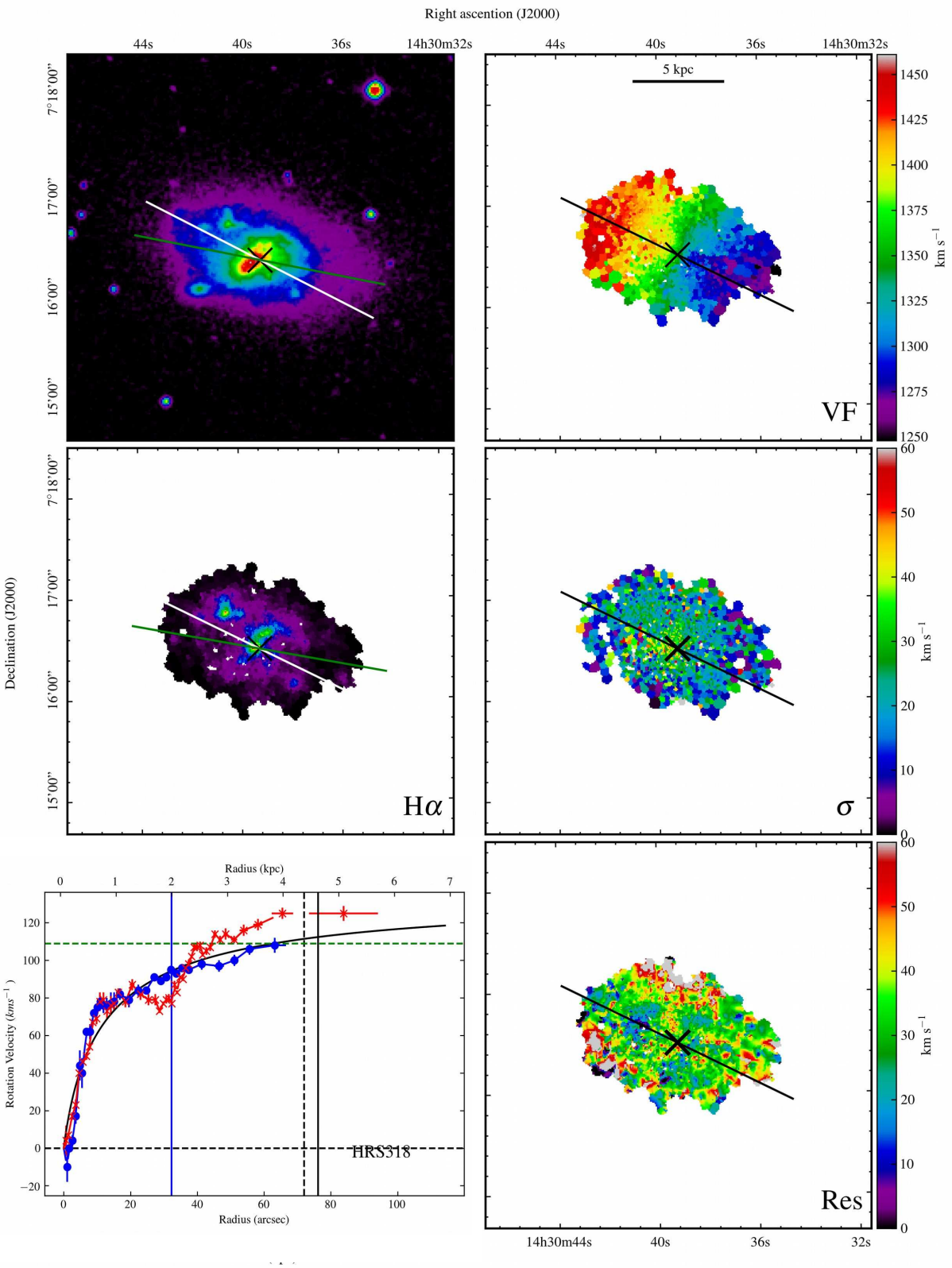
Right ascention (J2000)
44s
40s
36s
14h30m32s
7°18'00"
17'00"
16'00"
15'00"
Declination (J2000)
5 kpc
VF
Hα
σ
Res
km s⁻¹
Radius (kpc)
Rotation Velocity (kms⁻¹)
Radius (arcsec)
HRS318
14h30m44s
32s

HRS318

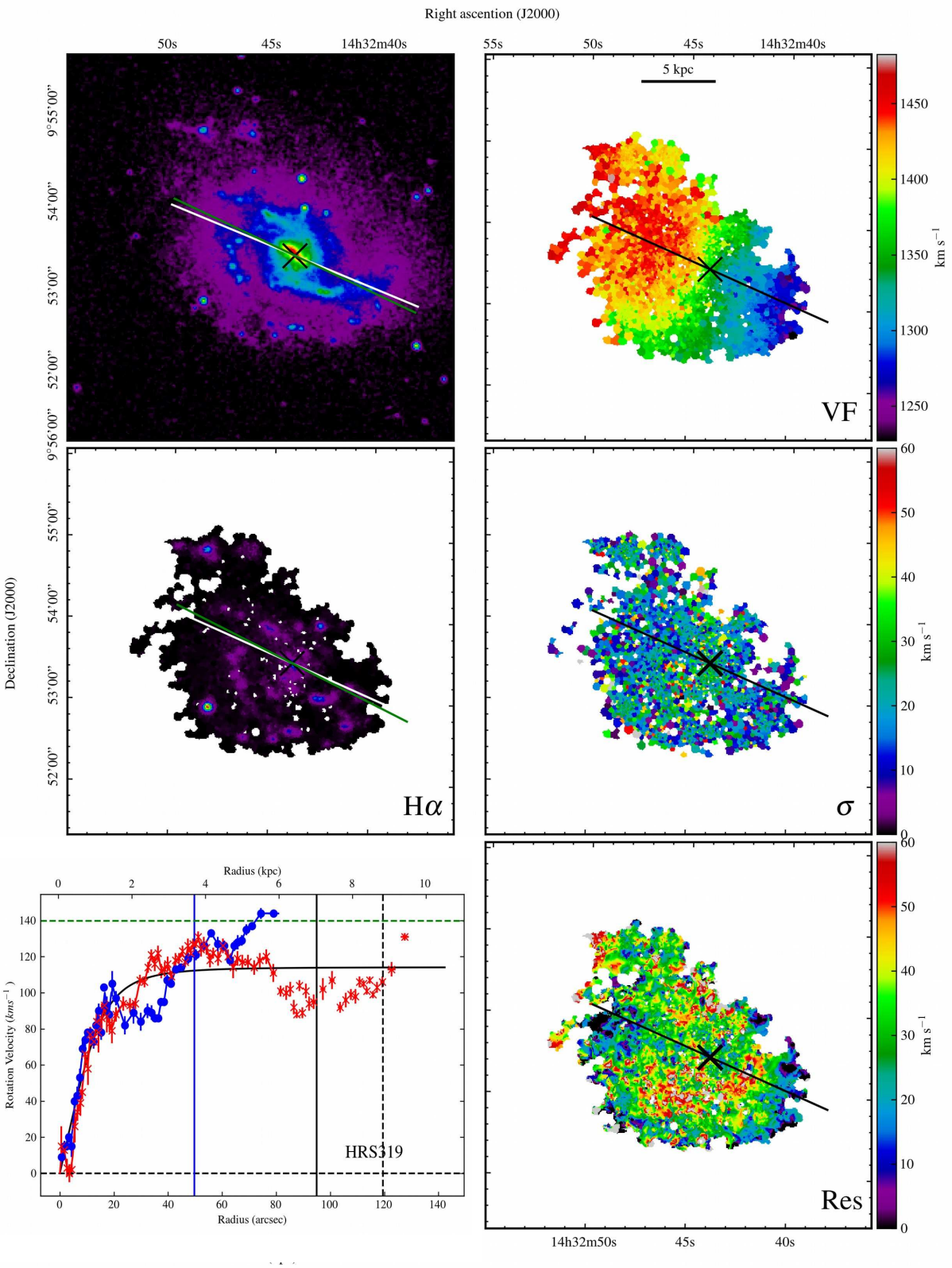
Right ascention (J2000)
50s
45s
14h32m40s
55s
50s
45s
14h32m40s
5 kpc
9°55'00"
54'00"
53'00"
52'00"
9°56'00"
55'00"
54'00"
53'00"
52'00"
Declination (J2000)
VF
Hα
σ
Res
km s⁻¹
1450
1400
1350
1300
1250
60
50
40
30
20
10
0
Radius (kpc)
0
2
4
6
8
10
Rotation Velocity (kms⁻¹)
140
120
100
80
60
40
20
0
Radius (arcsec)
0
20
40
60
80
100
120
140
HRS319
14h32m50s
45s
40s

HRS319

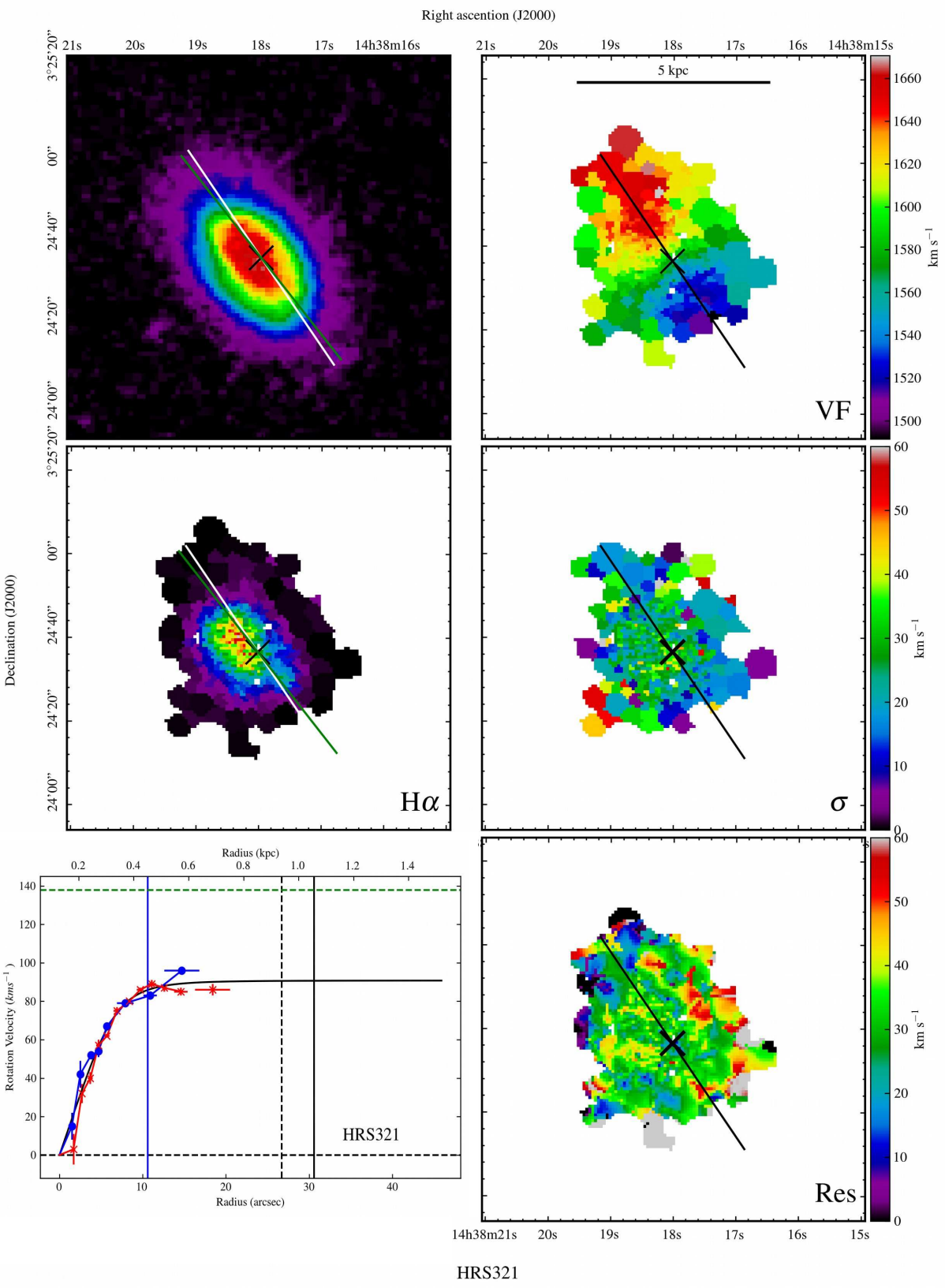
Right ascention (J2000)
Declination (J2000)
5 kpc
VF
Hα
σ
Res
km s⁻¹
Radius (kpc)
Rotation Velocity (kms⁻¹)
Radius (arcsec)
HRS321

HRS321

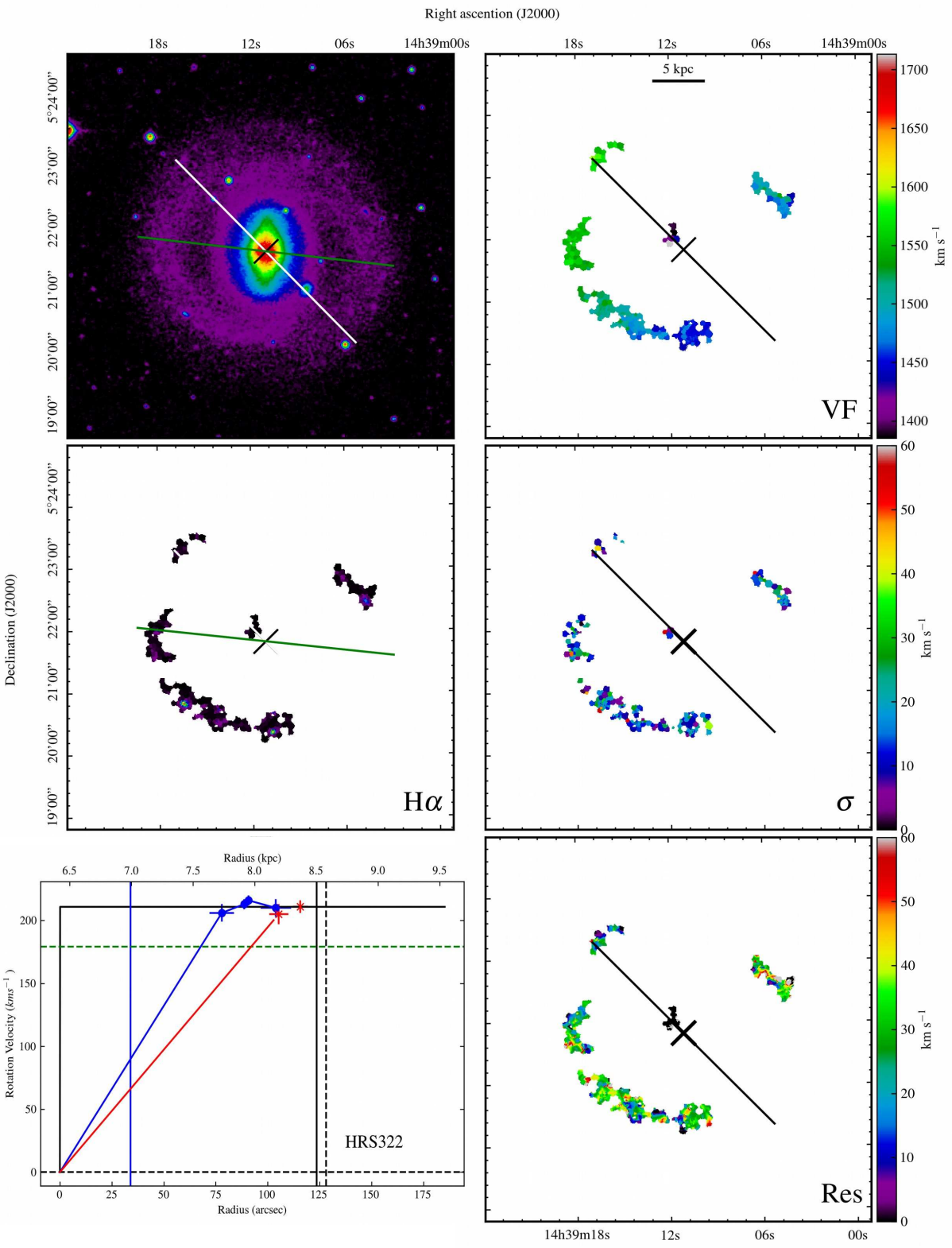
Right ascention (J2000)
18s
12s
06s
14h39m00s
Declination (J2000)
5°24'00"
23'00"
22'00"
21'00"
20'00"
19'00"
5 kpc
VF
Hα
σ
Res
km s⁻¹
1700
1650
1600
1550
1500
1450
1400
60
50
40
30
20
10
0
14h39m18s
00s
Radius (kpc)
6.5
7.0
7.5
8.0
8.5
9.0
9.5
Rotation Velocity (kms⁻¹)
200
150
100
50
0
HRS322
Radius (arcsec)
25
75
125
175

HRS322

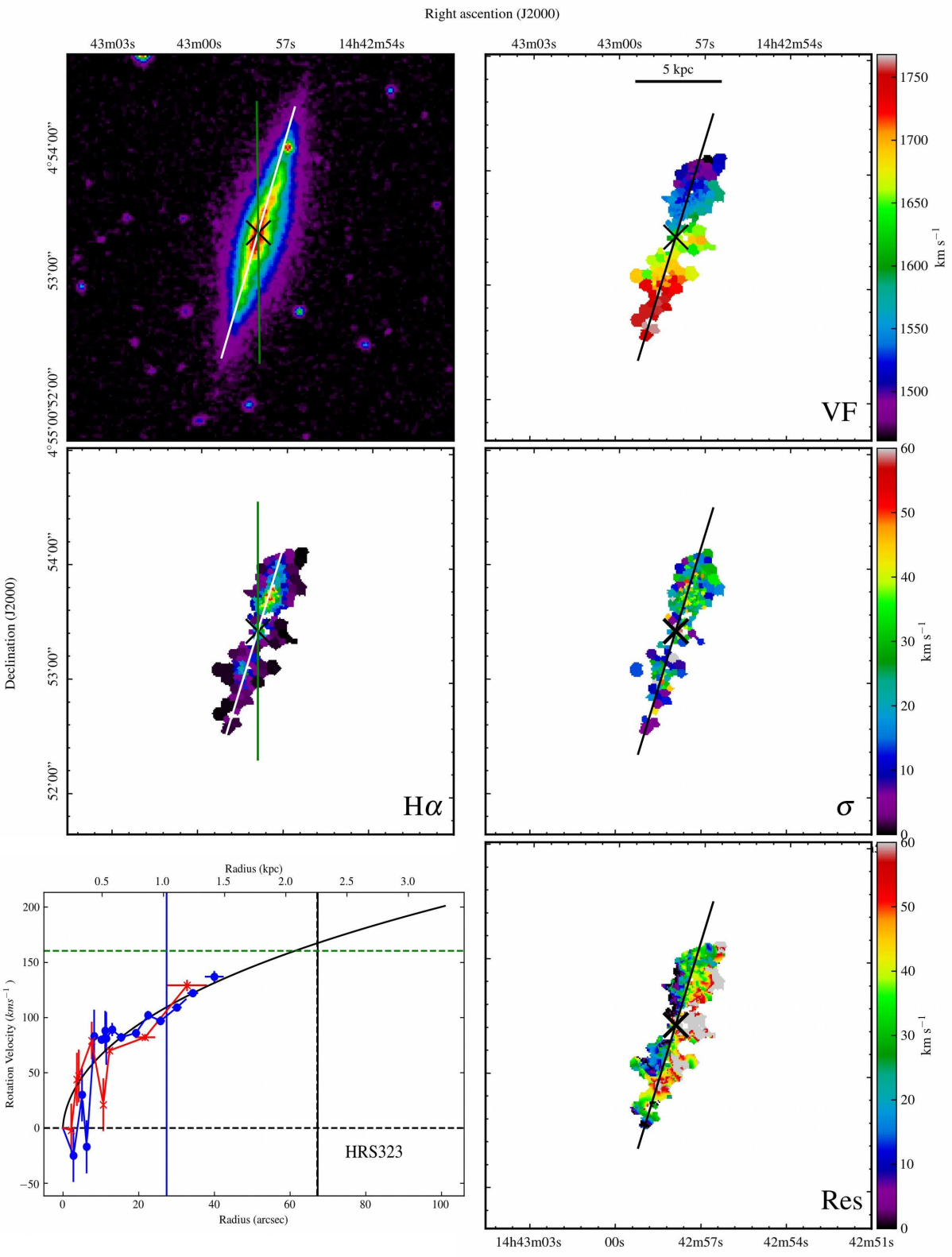
Right ascention (J2000)
43m03s
43m00s
57s
14h42m54s
Declination (J2000)
4°54'00"
53'00"
52'00"
4°55'00"
5 kpc
VF
Hα
σ
Res
km s⁻¹
Radius (kpc)
0.5
1.0
1.5
2.0
2.5
3.0
Rotation Velocity (kms⁻¹)
HRS323
Radius (arcsec)
14h43m03s
00s
42m57s
42m54s
42m51s

HRS323